

fatigue resistance of welded joints
in aluminium high-speed craft:

A TOTAL STRESS CONCEPT

J.H. den Besten

**fatigue resistance of welded joints
in aluminium high-speed craft:
A TOTAL STRESS CONCEPT**

J.H. den Besten

**fatigue resistance of welded joints
in aluminium high-speed craft:
A TOTAL STRESS CONCEPT**

PROEFSCHRIFT

ter verkrijging van de graad van doctor
aan de Technische Universiteit Delft,
op gezag van de Rector Magnificus Prof. ir. K.C.A.M. Luyben;
voorzitter van het College voor Promoties,
in het openbaar te verdedigen op
donderdag 3 september 2015 om 15.00 uur

door

Johannes Hendrik (Henk) DEN BESTEN

werktuigbouwkundig- en scheepsbouwkundig ingenieur,
geboren te Krimpen aan den IJssel

Dit proefschrift is goedgekeurd door de promotoren:

Prof. dr. ir. M.L. Kaminski
Prof. dr. ir. R.H.M. Huijsmans

Samenstelling promotiecommissie:

Rector Magnificus	voorzitter
Prof. dr. ir. M.L. Kaminski	Technische Universiteit Delft, promotor
Prof. dr. ir. R.H.M. Huijsmans	Technische Universiteit Delft, promotor

Onafhankelijke leden:

Prof. dr. P. Dong	University of Michigan
Prof. dr. -ing. W. Fricke	Technische Universität Hamburg-Harburg
Prof. dr. T. Lassen	Universitetet i Agder
Prof. dr. ir. J. Maljaars	Technische Universiteit Eindhoven
Prof. dr. A.V. Metrikine	Technische Universiteit Delft
Prof. dr. I.A. Richardson	Technische Universiteit Delft, reservelid

Research partners:

Delft University of Technology, Ship Hydromechanics & Structures Department
STW, Dutch Technology Foundation (Utrecht)
Damen Shipyards (Gorinchem)
TNO, Research Institute (Delft)
MARIN, Maritime Research Institute Netherlands (Wageningen)
Bureau Veritas (Rotterdam; Paris, France)
Lloyd's Register (Rotterdam)
United States Coast Guard (Baltimore, USA)
American Bureau of Shipping (Houston, USA)

Keywords: high-speed craft, aluminium, fatigue, welded joint, total stress concept

ISBN: 978-94-6233-040-5

Printed by Gildeprint, Enschede, The Netherlands

Copyright © 2015 by J.H. den Besten

All rights reserved. No part of the material protected by this copyright notice may be reproduced or utilised in any form or by any means, electronic or mechanical, including photocopying, recording, or by any information storage and retrieval system, without written permission of the copyright owner.

my tribute

Contents

Summary / Samenvatting	ix
Nomenclature	xvii
1 Introduction	1
1.1 Motivation	1
1.2 Research objective.	8
2 Weld Notch Stress Distributions	13
2.1 Introduction	13
2.2 Welded joint classification.	15
2.3 V-shaped notch stress	19
2.4 Weld load carrying stress	24
2.5 Structural field stress.	26
2.6 Weld toe notch stress distribution	27
2.6.1 Non-symmetry	28
2.6.2 Symmetry	36
2.7 Weld root notch stress distribution.	47
2.7.1 Non-symmetry	49
2.7.2 Symmetry	53
2.8 Size effects	54
2.8.1 Weld dimensions	55
2.8.2 Notch radius	61
2.8.3 Plate thickness.	70
2.9 Weld seam analysis	74
2.10 Residual stress distribution.	81
2.11 Total stress concept.	84
2.12 Conclusions	94
3 Weld Notch Stress Intensities	95
3.1 Introduction	95
3.2 Definition.	96
3.3 Far field factor	98
3.3.1 Single edge crack	98
3.3.2 Double edge crack	102
3.3.3 Centre crack	104
3.4 Notch factor.	106
3.5 Weld toe notch stress intensity factor	108
3.5.1 Non-symmetry	108
3.5.2 Symmetry	119
3.6 Weld root notch stress intensity factor	131
3.6.1 Non-symmetry	131
3.6.2 Symmetry	137

3.7	Size effects	142
3.7.1	Weld dimensions	142
3.7.2	Notch radius	145
3.7.3	Plate thickness.	150
3.8	Residual stress intensity factor	152
3.9	Conclusions	156
4	Crack Growth at Notches	157
4.1	Introduction	157
4.2	Two-stage crack growth model.	159
4.2.1	Far field stress	166
4.2.2	Notch geometry	168
4.2.3	Elastoplasticity	170
4.2.4	Mean stress	172
4.3	Crack growth at (weld) root notches.	178
4.3.1	Single edge notch	178
4.3.2	Double edge notch	190
4.3.3	Centre notch	193
4.4	Crack growth at weld toe notches	199
4.4.1	Specimens	199
4.4.2	Test setup	201
4.4.3	Digital image correlation principles	203
4.4.4	Texture quality	205
4.4.5	Far field region analysis.	209
4.4.6	Notch region analysis	216
4.4.7	Time series analysis	229
4.5	Conclusions	232
5	Welded Joint Fatigue Resistance	233
5.1	Introduction	233
5.2	Total stress parameter	234
5.3	Fatigue resistance statistics.	244
5.4	Small scale specimen CA fatigue resistance	249
5.4.1	Artificial T-joint data	249
5.4.2	As-welded joint data	264
5.5	Large scale specimen CA fatigue resistance	291
5.5.1	One-bay {frame, plate-stiffener, stiffened panel} data.	291
5.5.2	Three-bay stiffened panel data	294
5.6	Small scale specimen VA fatigue resistance	312
5.7	Full scale structure VA fatigue damage estimate.	318
5.8	Conclusions	330
A	Weld Notch Stress Equations	331
B	Large Scale Specimen Data	341
	Review	347
	Bibliography	349

Summary

Crew transfers, surveillance duties and {security, rescue, interception} operations at sea typically require high-speed craft. Aluminium is quite often selected as hull structure material because of its weight save potential in comparison to steel. The fatigue strength, however, may become a point of concern because of the decreased Young's modulus. Bottom slamming is identified as a dominant type of repeated loading, meaning fatigue is a governing limit state in aluminium high-speed craft design. Particular attention in that respect is paid to arc-welded joints connecting the hull structure components, {plates, shells}, since the weld geometry introduces notches; fatigue sensitive locations.

Fatigue physics cover an extensive range of scales and modelling may require a multi-scale approach. Adopting a structural response parameter S available at FSS level using global information only, however, seems attractive since S controls plasticity – required to facilitate fatigue damage: crack initiation, growth, propagation and fracture – at macro (structural)- as well as meso and micro (material) scale, but pays off in fatigue resistance data scatter and life time estimate uncertainty. Including physics at smaller scale, local information, improves the accuracy. A continuous increase of the considered scale range of physics as observed in fatigue assessment concepts developed over time – proposed to be classified according to approach, criterion, parameter and process zone – is however typically associated to increased (computational) effort and concept complexity. At the same time, similarity; proper scaling, meaning equal parameter values should yield the same fatigue resistance, seems still incomplete since all concepts available involve multiple fatigue resistance curves rather than one. From {MCF, HCF} design perspective, a local continuum mechanics approach seems sufficient and a total stress concept is proposed to balance accuracy, effort and complexity, improving similarity at the same time to obtain one aluminium arc-welded joint fatigue resistance curve.

The weld geometry introduces at least a notch at the weld toe and depending on penetration level another one at the weld root. Cracks may initiate at both fatigue sensitive locations, grow principally in {plate, shell} thickness direction and continue to propagate in general either along or perpendicular to the weld seam through {plate, shell} because of the structure orthotropic stiffness characteristics, suggesting a {plate, shell} thickness based (detectable repair) criterion to be an appropriate fatigue design parameter. The total through-thickness weld notch stress distribution along the expected crack path $\{\sigma_n^T, \sigma_{nr}^T\}$, including both the ocean/sea waves induced cyclic remote mechanical loading- and welding process related quasi-constant thermal residual part, is assumed to be a key element. The predominant remote mechanical loading mode-I contribution $\{\sigma_n, \sigma_{nr}\}$ has been examined to distinguish the involved stress components. A self-equilibrating weld geometry stress – consisting of a local V-shaped notch- and weld load carrying part – and

equilibrium equivalent global structural field stress are identified; a refinement of a well-known definition. The semi-analytical formulations are related to the welded joint far field stress, calculated using a relatively coarse meshed {plate, shell} FE model as typically available for fatigue design purposes. Exploiting (non-)symmetry conditions, a generalised formulation demonstrating stress field similarity has been obtained and extends to the welding induced thermal residual stress distributions $\{\sigma_n^r, \sigma_{nr}^r\}$. Fatigue scaling requires both the (zone 1) peak value and (zone 2 notch affected and zone 3 far field dominated) gradient to be incorporated, meaning a damage criterion should take the complete distribution into account.

The SIF K seems to meet this criterion, though, the intact geometry related notch stress distributions should be correlated to crack damaged equivalents; fatigue is assumed to be a crack growth (dominated) process. At the same time, hull structure arc-welded joints inevitably contain flaws or crack nuclei (defects) at the weld toe- and root notches, i.e. using the damage tolerant mode-I parameter K_I seems justified since fatigue associated to the {MCF, HCF} life time range at both locations will predominantly be a matter of micro- and macro-crack growth. The zone 3 related equilibrium equivalent stress contribution has been used to obtain a far field factor, distinguishing different type of cracks related to (non-) symmetry conditions for both (quasi) 2D- and 3D configurations. A notch factor incorporates the zone {1, 2} governing self-equilibrating stress. Remote mechanical weld toe- and weld root stress intensities show the zone {1, 2} notch affected- and zone 3 far field dominated parts define a micro- and macro-crack region, turning the stress field similarity into a stress intensity similarity. Each stress component dominates a certain crack length range: the notch stress the micro-crack region, the structural field stress the macro-crack region; the weld load carrying stress determines the transition (i.e. apex) location. The welding induced and displacement controlled mode-I residual stress intensity factor K_I^r is acquired for both weld toe and weld root notches to complete the total weld notch stress intensity similarity factor formulation K_I^T .

Cyclic remote mechanical- and quasi-constant thermal residual loading turn K_I^T into a crack growth driving force ΔK_I^T and defects may develop into cracks. The crack growth rate (da/dn) of micro-cracks emanating at notches show elastoplastic wake field affected anomalies, i.e. monotonically increasing or non-monotonic behaviour beyond the material threshold. Modifying Paris' equation, a two-stage micro- and macro-crack growth law similarity is proposed to include both the weld notch- and far field characteristic contributions, elastoplasticity as well as remote mechanical- and thermal residual mean stress effects. Small/short crack growth data obtained using standard specimens including {SEN, DEN, CEN} in crack configuration – representing weld root notch geometries at the same time – available in literature has been reinvestigated for the alternating material zones in (aluminium) arc-welded joints: WM and HAZ zone containing respectively the weld root- and weld toe notch fatigue damage location, as well as BM for comparison. Fatigue testing series have been developed to identify crack growth behaviour at

weld toe notches in aluminium arc-welded joints, adopting a typical fillet weld DS T-joint geometry. Using DIC, the required far field- and notch region parameters are obtained. Spatial displacement fields are estimated on a general kinematic basis using commercial DIC software (Istra4D, Dantec Dynamics). A posteriori, as a mechanical filtering process, the displacement fields are decomposed onto a selected kinematic basis, i.e. an Airy stress function. The displacement amplitudes, least squares solutions, present in a one-to-one correspondence the crack growth governing parameters: linear far field stress distribution, SIF and crack tip location. A sequence of images provides the temporal solution; weld toe crack growth data series showing both far field characteristics and notch affected (non-monotonic) anomalies.

Crack growth model integration yields a (MCF) single slope resistance relation, a joint S_T - N curve correlating arc-welded joint life time N and the total stress parameter S_T ; a line (equivalent point) criterion to estimate hull structure longevity ensuring {SSS, LSS, FSS} welded joint fatigue resistance similarity. A dual slope (i.e. random fatigue limit) formulation has been adopted to incorporate HCF taking the transition in fatigue damage mechanism (i.e. growth dominant turns into initiation controlled for decreasing load level), a slope change, into account. Regression analysis (i.e. a likelihood approach) is adopted to estimate model parameters, managing both complete- and right-censored data; failures and run-outs. Artificial fatigue test data of DS T-joints is investigated to determine the S_T parameter quality. The fatigue life uncertainty is about a factor 2 ($T_S \approx 1:1.2$). As-welded SSS (T-T) CA data available in literature has been used to establish a family of (damage tolerant engineering) joint S_T - N fatigue resistance design curves to be able to estimate the fatigue life time N of welded joints (production quality is average) knowing the joint geometry and far field structural response. The MCF life time uncertainty bandwidth increases up to a factor 6, i.e. ($T_S \approx 1:1.6$). In the hull structure (HCF) design region uncertainty is significant, predominantly because of lacking complete data. Full scale structure representative {T-T literature, T-C} CA LSS data has been examined to verify a SSS data scatter band fit. Since CA {SSS, LSS} fatigue resistance is principally used to estimate a VA FSS value adopting the Palmgren-Miner hypothesis, VA SSS data available in literature is examined and a scatter band fit is observed. The involved equivalent total stress parameter $S_{T,eq}$ is obtained adopting an extended rain flow counting algorithm to capture the damage cube. Last but not least, hourly fatigue damage estimates D_h are obtained for some frame-stiffener connections in the slamming zone of an aluminium high-speed craft, using the FSS response as measured for several trials at the North Sea. The wave (loading) statistics induced D_h uncertainty is about a factor 2.5 comparing the measurement- and simulation structural response based values; quite close to the MCF fatigue design resistance value of 3 (R99Cxx – R50Cxx).

The TS concept is implemented in a high-speed craft fatigue design tool, available to all research partners. Using the welded joints geometry- and loading induced far field structural response information, the fatigue damage estimate $D(S_T)$ of all notch locations is calculated and the governing one identified to obtain life time N .

Samenvatting

Het overzetten van bemanning, het uitvoeren van surveillance taken en {beveiligings-, reddings-, onderscheppings-} operaties op zee vereisen typisch hogesnelheidsschepen. Vaak wordt er gebruik gemaakt van aluminium als constructiemateriaal voor de romp i.v.m. gewichtsbesparing t.o.v. staal. De vermoeiingssterkte vraagt in dat geval extra belangstelling vanwege de lagere elasticiteitsmodulus. Bodem impact is geïdentificeerd als een karakteristieke repeterende belasting, zodat vermoeiing een bepalend bezwijkmechanisme is voor het ontwerp van aluminium hogesnelheidsschepen. In dat verband wordt er veel zorg besteed aan boogglasverbindingen van de rompconstructie onderdelen, {platen, schalen}, omdat de lasgeometrie vermoeiingsgevoelige locaties introduceert; zogenaamde kerven.

De vermoeiingsfysica omvat verschillende schalen en modelvorming vraagt daarom eigenlijk een multi-schaal benadering. De keuze voor een constructierespons parameter S die beschikbaar is op FSS niveau en alleen gebruik maakt van globale informatie lijkt echter aantrekkelijk omdat S plasticiteit – een vereiste voor vermoeiingsschade: scheurinitiatie, groei, propagatie en uiteindelijk breuk – controleert op macro (constructie) schaal en dientengevolge ook op meso en micro (materiaal) schaal. De rekening wordt evenwel betaald in termen van spreiding van de vermoeiingsweerstand en onzekerheid van de geschatte levensduur. Het toevoegen van fysica op kleinere schaal, lokale informatie, verhoogt de nauwkeurigheid. Het alsmaar betrekken van meer fysica op (nog) kleinere schaal zoals waargenomen bij de vermoeiingsbeoordeling concepten die de afgelopen decennia zijn ontwikkeld – er wordt voorgesteld om deze te classificeren op basis van benadering, criterium, parameter en proces zone – gaat echter typisch gepaard met een toename van de te leveren inspanning (voor het uitvoeren van berekeningen) en concept complexiteit. Tegelijkertijd lijkt similariteit; het correct schalen, zodat identieke parameter waarden dezelfde vermoeiingsweerstand opleveren, nog incompleet. Alle ontwikkelde concepten bevatten tot op heden nog steeds meerdere vermoeiingsweerstand curves in plaats van één generieke. Vanuit {MCF, HCF} ontwerp perspectief lijkt een lokale benadering op continuüm mechanica niveau toereikend en er wordt een totaalspanningsconcept voorgesteld om een balans te vinden tussen nauwkeurigheid, te leveren inspanning en modelcomplexiteit, waarbij tegelijkertijd de similariteit wordt verbeterd om uiteindelijk één vermoeiingsweerstand curve voor aluminium boogglasverbindingen te kunnen genereren.

De lasgeometrie introduceert tenminste een kerf aan de teen van de las en afhankelijk van laspenetratiediepte nog één aan de wortel van de las. Scheuren kunnen initiëren op beide vermoeiingsgevoelige locaties, groeien in principe in {plaat, schaal} dikterichting en propageren vervolgens grofweg langs of loodrecht op

de lasnaad door de {plaat, schaal} vanwege de orthotrope stijfheidskarakteristiek van de (romp)constructie. Dit suggereert dat een op {plaat, schaal} dikte gebaseerd (detecteerbaar reparatie) criterium een geschikte parameter voor vermoeiingsontwerp kan zijn. De totale door-de-dikte laskerfspanningsverdeling langs het veronderstelde scheurpad $\{\sigma_n^T, \sigma_{nr}^T\}$, inclusief de golfbelasting geïnduceerde cyclisch extern mechanische bijdrage alsook de lasproces gerelateerde quasi-constante thermische restspanning, wordt verondersteld een belangrijk element te zijn. De dominante extern mechanische mode-I bijdrage $\{\sigma_n, \sigma_{nr}\}$ is onderzocht om de betrokken spanningscomponenten te kunnen onderscheiden. Een lasgeometrie afhankelijke spanning die intrinsiek in evenwicht is – bestaande uit een lokale V-vormige kerf- en lasdragend deel – en een evenwicht equivalente globale constructie veldspanning zijn geïdentificeerd: een verfijning van een welbekende definitie. De semi-analytische formuleringen zijn gerelateerd aan de verre veldspanning van de lasverbinding, berekend m.b.v. een relatief grofmazig {plaat, schaal} FE model wat typisch beschikbaar is voor vermoeiingsontwerp doeleinden. Gebruik makend van (niet-)symmetrie condities is een gegeneraliseerde formulering verkregen dat een spanningsveld similariteit vertoont, wat zich uitstrekt naar de lasproces geïnduceerde thermische restspanningsverdelingen $\{\sigma_n^r, \sigma_{nr}^r\}$. Correct schalen van vermoeiing vereist dat zowel de (zone 1) piekwaarde als de (zone 2 kerf beïnvloede en zone 3 verre veldspanning gedomineerde) gradiënt worden meegenomen, wat betekent dat een schade criterium de gehele door-de-dikte spanningsverdeling in rekening dient te brengen.

De SIF K lijkt aan dit criterium te voldoen, hoewel de intacte geometrie gerelateerde kerfspanningsverdeling dient te worden gecorreleerd aan een door een scheur beschadigd equivalent; vermoeiing wordt verondersteld een scheurgroei gedomineerd proces te zijn. Tegelijkertijd bevatten lasverbindingen in de romp-constructie onvermijdelijk gebreken, scheurkernen (defecten) aan de kerf van de las {teen, wortel}. Ofwel, gebruik van een schade tolerante mode-I parameter K_I lijkt gerechtvaardigd omdat vermoeiing geassocieerd met het {MCF, HCF} levensduur bereik voor beide locaties voornamelijk een kwestie is van micro- en macroscheurgroei. De zone 3 gerelateerde evenwicht equivalente bijdrage is gebruikt om een verre veldfactor te formuleren, waarbij onderscheid is gemaakt tussen verschillende type scheuren die gerelateerd zijn aan de (niet-)symmetrie condities voor zowel (quasi) 2D- als 3D configuraties. Een kerffactor brengt de intrinsieke evenwichtscomponent in rekening die zone {1, 2} domineert. De extern mechanische spanningsintensiteit van de las {teen, wortel} vertoont dan ook een zone {1, 2} kerf beïnvloede- en zone 3 verre veld gedomineerd deel, waarbij een micro- en macroscheurgebied wordt gedefinieerd. De veldspanning similariteit is hierbij omgezet in een spanningsintensiteit similariteit. Elke spanningscomponent domineert een bepaald scheurlengte gebied: de kerfspanning het micro-scheurgebied, de constructie veldspanning het macro-scheur gebied; de lasdragende spanning bepaald het transitie punt. De las geïnduceerde- en verplaatsingsbepaalde mode-I restspanning intensiteitsfactor K_I^r is onderzocht voor de kerf van de las {teen, wortel} ter completering van de totale laskerfspanningsintensiteit K_I^T .

De cyclisch extern mechanische belasting en quasi-constante thermische restspanning, veranderen K_I^T in een scheurgroei stuwende kracht ΔK_I^T en defecten kunnen zich ontwikkelen tot scheuren. De scheurgroeisnelheid (da/dn) van micro-scheuren die ontstaan bij kerven vertonen afwijkingen onder invloed van elastoplasticiteit in het spoor van de kerf, d.w.z. monotoon stijgend of niet-monotoon gedrag boven de materiaal drempelwaarde. Middels het wijzigen van de Paris' vergelijking wordt een twee fasen micro- en macro-scheurgroei similariteitswet voorgesteld dat zowel de laskerf- als de verre veld karakteristieke eigenschappen, elastoplasticiteit alsook de gemiddelde waarde van de extern mechanische- en thermische restspanning in rekening brengt. Groeidata van korte scheuren verkregen m.b.v. standaard proefstukgeometrieën inclusief {SEN, DEN, CEN} in scheurconfiguratie – die tegelijkertijd de laswortel geometrie vertegenwoordigen – zoals beschikbaar in de literatuur is opnieuw geanalyseerd voor de verschillende materiaal zones in (aluminium) gelaste verbindingen: WM en HAZ zone die respectievelijk de vermoeiingsschade locatie van de kerf aan de las {wortel, teen} bevatten, evenals BM ter vergelijking. Een serie vermoeiingstesten is ontwikkeld om het scheurgroei gedrag aan de kerf van een teen van de las in aluminium gelaste verbindingen te identificeren m.b.v. een dubbelzijdige T-verbinding geometrie voorzien van een typische hoeklas. Met behulp van DIC zijn de vereiste parameters van het verre veld- en kerfgebied verkregen. Ruimtelijke verplaatsvelden zijn geschat m.b.v. een generieke kinematische basis, gebruik makend van commerciële software (Istra4D, Dantec Dynamics). Vervolgens zijn, als in een mechanisch filtering proces, de verplaatsingsvelden opgespannen in een specifieke kinematische basis; een Airy spanningsfunctie. De amplitudes van de verplaatsingen, kleinste kwadraten oplossingen, vertegenwoordigen één-op-één de scheurgroei bepalende parameters: de lineaire verre veldspanningsverdeling, de SIF en de scheurtip locatie. Een serie foto's verschaft de oplossing in de tijd; scheurgroei data series aan een teen van de las die zowel de verre veld- als de (niet-monotone) kerf beïnvloede afwijkingen zichtbaar maken.

Integratie van het scheurgroei model levert een (MCF) weerstandsrelatie met enkelvoudige helling, een S_T - N curve die de levensduur N van booglasverbindingen en de totaalspanningsparameter S_T correleert; een lijn (equivalent punt) criterium om de levensduur van de rompconstructie te kunnen schatten, waarbij men van {SSS, LSS, FSS} vermoeiingsweerstand similariteit verzekerd is. Een dubbele hellingsformulering is gebruikt om HCF op te nemen waarbij de transitie in vermoeiingsmechanisme (groei gedomineerd gaat over in initiatie bepaald voor een afnemend belastingniveau), een helling verandering, wordt meegenomen. Regressie analyse (een likelihood benadering) is gebruikt om de model parameters te schatten, waarbij zowel complete als incomplete data is verwerkt; gefaalde en niet gefaalde booglasverbindingen. Artificiële vermoeiingsdata van dubbelzijdige T-verbindingen is onderzocht om de kwaliteit van S_T te bepalen. De onzekerheid van de vermoeiingslevensduur bedraagt ongeveer een factor 2 ($T_S \approx 1:1.2$). Onbewerkte booglasverbindingen in SSS (T-T) CA data zoals beschikbaar in de literatuur is gebruikt om een familie van (schade tolerante engineering) S_T - N

vermoeiingsweerstand curves voor booglasverbindingen – productiekwaliteit is gemiddeld – te bepalen, zodat de levensduur N kan worden geschat, uitgaande van bekende verbinding geometrie en verre veld constructierespons. De bandbreedte van de MCF levensduuronzekerheid is toegenomen tot een factor 6, ($T_S \approx 1:1.6$). In het rompconstructie (HCF) ontwerpgebied is de onzekerheid enorm, voornamelijk vanwege het gebrek aan complete data. CA LSS {T-T literatuur, T-C} data van een representatieve ware grootte constructie is met succes onderzocht ter verificatie van de SSS data spreidingsband match. Omdat CA {SSS, LSS} vermoeiingsweerstand in de regel wordt gebruikt om een VA FSS waarde te schatten m.b.v. de Palmgren-Miner hypothese, is VA SSS data zoals beschikbaar in de literatuur onderzocht met een spreidingsband match als resultaat. De betrokken equivalente totaalspanningsparameter $S_{T,eq}$ is bepaald m.b.v. een uitgebreide versie van het regenstroom tel algoritme ter vaststelling van de schade. Ten slotte is de vermoeiingsschade per uur D_h geschat voor een aantal frame – verstijver verbindingen in de impact zone van een aluminium hogesnelheidsschip, op basis van de FSS respons zoals gemeten tijdens verschillende trials op de Noordzee. De golf(belasting) statistiek geïnduceerde onzekerheid van D_h bedraagt ongeveer een factor 2.5 wanneer de resultaten op basis van de gemeten en gesimuleerde constructierespons worden vergeleken. Dit is nagenoeg gelijk aan de MCF vermoeiingsweerstand ontwerpwaarde van 3 (R99Cxx – R50Cxx).

Het TS concept is geïmplementeerd in vermoeiingsontwerp software voor hogesnelheidsschepen en beschikbaar voor alle onderzoek partners. Met behulp van de geometrie en belasting geïnduceerde verre veld constructierespons van de booglasverbindingen wordt de geschatte vermoeiingsschade $D(S_T)$ van alle kerf locaties berekend en de maatgevende geïdentificeerd om levensduur N te bepalen.

Nomenclature

Latin symbols

C	{crack growth, fatigue} resistance constant / scaling factor
C_{bw}	weld load carrying stress coefficient
D	(total) fatigue damage
D_h	hourly fatigue damage
$E(\cdot)$	complete elliptical integral of the 2 nd kind
E	bulk modulus of elasticity
$F(\mu, \sigma)$	cumulative distribution function
F_i	force at node i
G	shear modulus
H	Hessian
H_s	significant wave height
I_N	notch crack growth integral
J	strain energy release rate
$K(\cdot)$	complete elliptical integral of the 1 st kind
K	stress intensity factor
K'	work hardening coefficient
K_C	fracture toughness
K_f	notch factor
K_I	mode-I stress intensity factor
K^N	notch stress intensity factor
K_I^N	mode-I notch stress intensity factor
K_{II}^N	mode-II notch stress intensity factor
K_I^r	mode-I residual stress intensity factor
K_I^T	mode-I total stress intensity factor
K_{sa}	additional stress concentration factor
K_t	theoretical stress concentration factor
K_ε	strain concentration factor
L	likelihood
L_r	normalised/relative parameter profile likelihood
\mathcal{L}	log-likelihood
M_{kn}	Battelle notch factor
N	(total) number of cycles until failure (i.e. through-thickness crack)
$N(\mu, \sigma)$	Normal distribution
N_c	cycle coalescence point
N_g	number of cycles corresponding to crack growth
N_i	number of cycles corresponding to crack initiation
$2N$	(total) number of reversals
S	stress range / stress structural response parameter
S_c	stress coalescence point

S_e	effective (notch) stress range
S_h	hot spot stress range
S_n	nominal stress range
S_s	Battelle structural stress range
S_T	total stress range
S_∞	fatigue limit
T_S	response scatter range index
T_N	lifetime range index
V_s	ship speed
W	energy range / energy structural response parameter
$W(\mu, \sigma)$	Weibull distribution
Y_f	far field factor
Y_f^r	residual field factor
Y_{fb}	far field factor bending component
Y_{fm}	far field factor membrane component
Y_{fw}	weld reinforcement affected far field factor
Y_n	notch factor
Y_{nl}	linear unit stress notch factor
Y_{nr}	root notch factor
Y_n^r	residual notch factor
a	crack size
a_0	critical crack size
a_c	coalescence (crack) size
a_e	effective crack size
a_f	final crack size / fictitious crack size
a_i	(real) defect- or initial crack size
a_n	(root) notch size
a_t	crack transition size
b	cyclic fatigue strength exponent
b_b	base plate and weld reinforcement equivalent thickness
b_c	cross plate and weld reinforcement equivalent thickness
b_p	plate and weld reinforcement equivalent thickness
c	cyclic fatigue strain exponent / half width of semi-elliptical crack
d_n	notch depth / undercut
e	strain range / strain structural response parameter
e_e	effective (notch) strain range
f	frequency
$f(\mu, \sigma)$	probability density function
f_i	line force at finite element i
f_m	line membrane force
f_s	line shear force
f_y	line membrane force in y -direction
f_z	line membrane force in z -direction
k	notch stress intensity weight function

k_1	mode-I notch stress intensity weight function
k_2	mode-II notch stress intensity weight function
l_c	cover plate length
l_i	finite element length (along weld seam)
l_w	weld leg length
h_w	weld leg height
m	fatigue resistance slope
m_1	fatigue resistance HCF slope
m_2	fatigue resistance MCF slope
m_b	line bending moment
m_{bb}	bending moment induced weld load carrying line bending moment
m_{bm}	membrane force induced weld load carrying line bending moment
m_x	line bending moment about x -axis
n	number of cycles / elasto-plasticity coefficient
n'	work hardening exponent
n_e	notch elasto-plasticity coefficient
p_f	Battelle crack face pressure
p_s	Battelle structural pressure
p_r	Battelle structural pressure ratio
$r^{(r)}$	radial coordinate
r_0	radial distance coordinate system origin to notch root
r_l	remote mechanical load ratio
r_p	plastic zone size
r_s	structural bending stress ratio
r_{sr}	structural bending root stress ratio
r_t	Battelle notch-far field transition depth
s	notch support factor
t_p	plate thickness
t_p'	artificial plate thickness
t_b	base plate thickness
t_b'	artificial base plate (related) thickness
t_c	{connecting, cross, cover} plate thickness
t_c'	artificial cross plate (related) thickness
t_w	weld throat thickness
\mathbf{u}	displacement vector
u_r	r -displacement
u_θ	θ -displacement
u_x	x -displacement
u_y	y -displacement
x'	local Cartesian coordinate (along weld seam)
y'	local Cartesian coordinate (perpendicular to weld seam)
z'	local Cartesian coordinate (through-thickness direction)

Greek symbols

$\Gamma(\cdot)$	(complete) Gamma function
ΔK_I	mode-I crack growth driving force
ΔK_I^N	mode-I notch crack growth driving force
ΔK_I^T	total mode-I crack growth driving force
ΔK_f	far field crack growth driving force component
ΔK_{th}	crack growth threshold
Δd_z	out-of-plane displacement range
Δp	pressure range
$\Delta \mu \varepsilon$	micro-strain range
$\Delta \sigma$	stress range
$\Delta \sigma_s$	structural stress range
$\Delta \sigma_E$	fatigue/endurance limit (general)
$\Delta \sigma_0$	fatigue/endurance limit (plane geometry)
P	(co-)variance or correlation matrix
Ψ	basis function vector
Ω	basis function vector
α	(half) notch angle
β	stress angle
γ	load ratio coefficient / welded joint cross plate angle
δ	data type {complete = 1, censored = 0}
ε	residual
ε_e	elastic strain component
ε_f'	cyclic fatigue strain coefficient
ε_p	plastic strain component
ε_{rr}	radial strain component (polar coordinates)
$\varepsilon_{r\theta}$	shear strain component (polar coordinates)
$\varepsilon_{\theta\theta}$	tangential strain component (polar coordinates)
ε_{xx}	normal strain component in x -direction (Cartesian coordinates)
ε_{xy}	shear strain component in xy -plane (Cartesian coordinates)
ε_{yy}	normal strain component in y -direction (Cartesian coordinates)
$\{\zeta_a, \zeta_s\}$	first blunt body eigenvalue of (anti-)symmetry part
η	stress concentration coefficient
θ	parameter vector
θ	angular coordinate
κ	Kolosov's constant
λ	eigenvalue
λ_i	eigenvalue (asymptotic solution)
$\{\lambda_a, \lambda_s\}$	first eigenvalue of (anti-)symmetry part
μ	mean
$\{\mu_a, \mu_s\}$	stress amplitude of (anti-)symmetry part
μ_i	stress component amplitude
ν	Poisson ratio

$\{\xi_1, \xi_2\}$	(auto)correlation radii
ρ	(real) notch radius
ρ_e	effective notch radius
ρ_f	fictitious notch radius
ρ_{ij}	correlation coefficient
ρ_r	reference notch radius
ρ^*	micro-structural support length
σ	stress / standard deviation
σ_b	structural bending stress component
σ_{br}	structural bending root stress component
σ_{bw}	weld load carrying stress distribution
σ_f	{structural, welded joint far} field stress distribution
σ_f'	cyclic fatigue strength coefficient
σ_{fr}	structural field root stress distribution
σ_h	hot spot stress (amplitude)
σ_m	mean stress / structural membrane stress component
σ_{mr}	structural membrane root stress component
σ_{max}	(zone 1) peak stress
σ_n	nominal stress (amplitude) / weld toe notch stress distribution
σ_n^r	weld toe notch residual stress distribution
σ_n^T	total weld toe notch stress distribution
σ_{nr}	weld root notch stress distribution
σ_{nr}^r	weld root notch residual stress distribution
σ_{nr}^T	total weld root notch stress distribution
σ_p	principal stress
σ_{rr}	radial stress component (polar coordinates)
$\sigma_{r\theta}$	shear stress component (polar coordinates)
$\sigma_{\theta\theta}$	tangential stress component (polar coordinates)
σ_s	structural stress (amplitude)
σ_s^t	Battelle structural stress
σ_{se}	self-equilibrating stress part
σ_{ser}	self-equilibrating root stress part
σ_{sr}	structural root stress (amplitude)
σ_{us}	material ultimate strength
σ_{xx}	normal stress component in x -direction (Cartesian coordinates)
σ_{xy}	shear stress component in xy -plane (Cartesian coordinates)
σ_{yy}	normal stress component in y -direction (Cartesian coordinates)
$\sigma_{y(s)}$	material yield stress / strength
φ	Airy stress function
$\{\chi_a, \chi_s\}$	first eigenvalue coefficient of (anti-)symmetry part
χ_i	eigenvalue coefficient of asymptotic solution
$\{\omega_a, \omega_s\}$	first blunt body eigenvalue coefficient of (anti-)symmetry part

Abbreviations

AIC	Akaike's information criterion
AW	as welded
BC	boundary condition
BEA	boundary element analysis
BM	base material
BS	British standard
BSS	Battelle structural stress
CA	constant amplitude
CB	confidence bound
CC	centre crack
CI	confidence interval
CT	compact tension
CDF	cumulative distribution function
CEN	Comité Européen de Normalisation
CL	clamped
CN	centre notch
DC	displacement controlled
DEC	double edge crack
DEN	double edge notch
DFT	discrete Fourier transformation
DIC	digital image correlation
DoF	degree(s) of freedom
DS	double sided
ERAAS	European recommendations for aluminium alloy structures
EV	extreme value
FAT	fatigue class
FE	finite element
FEA	finite element analysis
FP	fully penetrated
FSS	full scale structure
HAZ	heat affected zone
HCF	high cycle fatigue; life time range $N = O(5 \cdot 10^6 \dots 10^9)$
HS	hot spot
IIW	International Institute of Welding
ISSC	International Ship and offshore Structures Congress
LEFM	linear elastic fracture mechanics
LB	lower bound
LC	load carrying / load controlled
LoF	lack of fusion
LoP	lack of penetration
LS	least squares
LSS	large scale specimen
M	specimen series far field stress: membrane

MBN	specimen series far field stress: membrane and bending (non-monotonic)
MBM	specimen series far field stress: membrane and bending (monotonic)
MCF	medium cycle fatigue; life time range $N = O(10^4 \dots 5 \cdot 10^6)$
MLE	maximum likelihood estimate
NLC	non-load carrying
NSIF	notch stress intensity factor
PDF	probability density function
PL	profile likelihood
PP	partially penetrated
RCT	round compact tension
RFL	random fatigue limit
RSIF	residual stress intensity factor
SCF	stress concentration factor
SEC	single edge crack
SEN	single edge notch
SG	strain gauge
SIF	stress intensity factor
SNR	signal to noise ratio
SR	stress relieved
SS	single sided / simply supported
SSS	small scale specimen
TS	total stress
T-C	tension – compression
T-T	tension – tension
UB	upper bound
UIT	ultrasonic impact treatment
VA	variable amplitude
WM	weld material
X-FEM	extended finite element method
ZOI	zone of interest

1

Introduction

A good scientist is a person with original ideas. A good engineer is a person who makes a design (assessment concept) that works with as few original ideas as possible.

Freeman Dyson (1923, physicist)

1.1 Motivation

Crew transfers, surveillance duties and {security, rescue, interception} operations at sea typically require high-speed craft (Fig. 1.1). Aluminium is quite often selected as hull structure material, e.g. because of its weight saving potential in comparison to steel aiming for a reduction of installed power and fuel consumption. The fatigue strength, however, may become a point of concern because of the decreased Young's modulus.

Impact, bottom slamming in particular, is identified as a dominant type of repeated loading (i.e. remote mechanical load ratio $r_l \sim 0$), meaning fatigue – a cyclic loading induced local, progressive, structural damage mechanism (Schijve, 2009) – is a governing limit state in aluminium high-speed craft design. Particular attention in that respect is paid to arc-welded joints connecting the hull structure components, i.e. {plates, shells}, since the weld geometry introduces notches; fatigue sensitive locations.



Figure 1.1: Damen high speed craft, {Stan Patrol 1204, Fast Crew Supplier 1605}.

Overview

Fatigue physics cover an extensive range of scales (Fig. 1.2) and modelling may require a multi-scale approach. Notwithstanding, typically a structural response parameter $\{S, e, W\}$; a continuum mechanics based $\{\text{stress, strain, energy}\}$ macro-scale fatigue resistance engineering criterion, is adopted since $\{S, e, W\}$ controls plasticity at macro (structural)- as well as meso and micro (material) scale, required to facilitate fatigue damage: crack initiation at microscopic stress concentrations (i.e. to move dislocations, to develop (persistent) slip bands and to introduce micro-cracks), growth (up to macro scale), propagation and fracture. Macroscopic stress concentrations, hot spots (e.g. at weld notches), facilitate the microscopic ones.

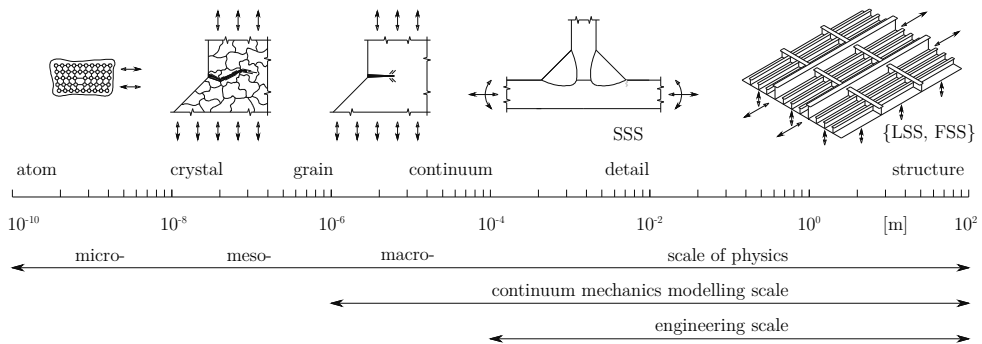


Figure 1.2: Fatigue physics range of scales.

Because of material imperfections and welding induced flaws, defects, the hull structure welded joint fatigue design strategy is principally fail safe or even damage tolerant. Life time is typically expressed in a number of cycles N and estimates are generally required in the $\{\text{medium, high}\}$ cycle fatigue (MCF, HCF) range; i.e. $N = O(10^4 \dots 10^9)$. Different $\{S, e, W\}$ - N assessment concepts and corresponding resistance curves have been developed over time and reviewed (Cui, 2002; Fricke, 2003; Maddox, 2003; Radaj, Sonsino and Fricke, 2006; Hobbacher, 2009a; Rizzo, 2011; Radaj and Vormwald, 2013), proposed to be classified according to (Fig. 1.3):

- $\{\text{global, local}\}$ approach
- $\{\text{stress (intensity), strain (intensity), energy (density)}\}$ criterion
- $\{\text{intact, crack damaged}\}$ geometry parameter
- $\{\text{point, line, area/volume}\}$ process zone.

The parameter scale relative to the hot spot defines the approach. Depending on $\{\text{work hardening, elastoplasticity, multi-axiality}\}$ examinations an appropriate criterion can be established. Model philosophy assumptions, i.e. is initiation (crack nucleation and micro-crack growth) governing or is (micro- and macro crack) growth dominant, determine if the parameter will be an intact geometry- or crack damaged one. Notch effectivity (size effects; scaling) considerations define the adopted process zone.

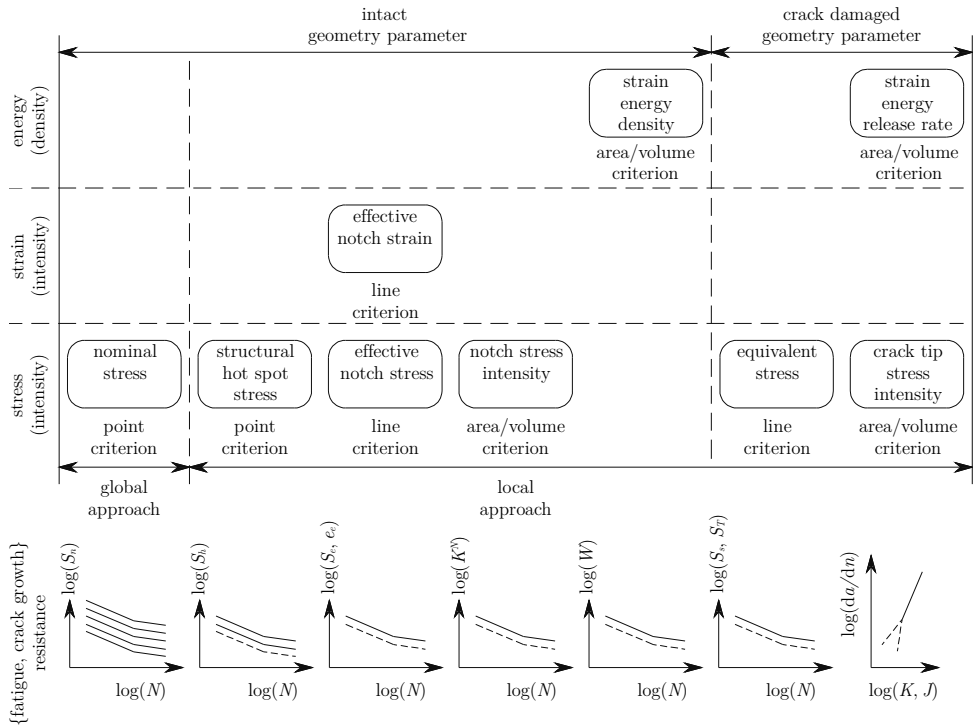


Figure 1.3: Fatigue assessment concept overview.

Nominal stress concept

Evaluating the {MCF, HCF} resistance of welded structural details using a global approach involves typically a nominal stress range criterion $S_n = \Delta\sigma_n$ (Fig. 1.4); a structural detail reference- and intact geometry parameter, assuming the major part of life time N is related to crack initiation (i.e. is spent in the weld notch affected region) rather than crack growth. Constant amplitude (CA) fatigue resistance information is commonly obtained using small- or large scale (beam) specimen (SSS, LSS) and expressed in terms of FATigue classes. Theoretically, an infinite number of different structural details exist, although in hull structures it might be rather a matter of varying dimensions than the actual diversity in welded joints. The number of defined FAT classes is limited to ~80 (CEN: Eurocode 9, 2007; IIW recommendations: Hobbacher, 2009b).

As long as geometry, loading (generally a membrane component only), failure location (weld toe- or weld root notch) and quality (metallurgical and {offset, angular} imperfections) fit the FAT class description, computational effort is limited and concept complexity is relatively low. However, (local) dimension variations are not explicitly considered paying off in terms of fatigue resistance accuracy (i.e. estimated life time uncertainty) since S_n is processed as point criterion, as ‘local’ nominal stress, meaning (stress gradient induced) size effects are not taken into account. In case the structural detail configuration identified in the

full scale structure (FSS) is running out the classified one, i.e. does not perfectly match the FAT class geometry, the ‘local’ nominal stress requires identification of stress concentration components already incorporated and missing ones. Complications increase if the ‘local’ S_n has to be extracted from a finite element (FE) model of a relatively complex (hull) structure.

Although a spatial description of a {load, structural response} cycle requires 2 parameters, e.g. a range and remote mechanical load ratio, $r_l = (F_{min}/F_{max}) = (\sigma_{min}/\sigma_{max})$ is not explicitly considered since the FSS stress level in the notch affected region is assumed to be highly tensile anyway (at yield magnitude) because of the welding induced residual stress component. Any {SSS, LSS} fatigue test result obtained at relatively low load ratio has been translated to $r_l \sim 0.5$ using a far field mean stress correction. The Basquin (type of) relation $S_n = \{\sigma_f' \cdot (2N)^b, C \cdot N^m\}$ provides the S_n - $(2N)$ fatigue resistance curves involving the FAT class characteristic fatigue strengths $\{\sigma_f', C\}$; the damage mechanism is assumed to be similar for all structural details, meaning the slopes $\{b, m\}$ are invariant.

Structural hot spot stress concept

Local approaches provide the opportunity to reflect explicitly geometry and loading contributions. A criterion like the structural hot spot stress range $S_h = \Delta\sigma_h$ (Niemi, Fricke and Maddox, 2006); an intact geometry parameter, involves the equilibrium equivalent far field stress (Fig. 1.4) solving the ‘local’ nominal stress issue. However, the local geometry parameter $\{t_b, t_c, l_w, h_w, a_n, \rho\}$ affected self-equilibrating part is not considered, meaning the number of fatigue resistance curves is theoretically still infinite. Since the self-equilibrating stress defines up to what extent the notch is load carrying, in terms of fatigue resistance the extremes have been defined: non-load carrying (NLC) and load-carrying (LC); 2 FAT classes; 2 S_h - N curves, Basquin (type of) relations. Selection is based on engineering judgement.

A hot spot stress concept based fatigue assessment is limited to weld toe induced failures; a design principle because of weld root fatigue detection issues. Originated from strain gauge (SG) measurements, S_h is typically a FE (non-) linear surface extrapolation calculated – fictitious – stress that cannot be measured itself. Alternatively, through-thickness linearisation can be used to obtain S_h , meaning no model limitation exist to determine S_h for weld root notches as well. Note S_h is a point criterion, i.e. size effect corrections are still required. Any {offset, angular} imperfections affecting the far field stress should explicitly be included. Residual stress considerations remain unchanged in comparison to the nominal stress concept. Generally speaking, life time estimate uncertainty should decrease because of reduced scatter, at the price of increased structural response modelling time and local {geometry, loading} information; increased effort and concept complexity. However, uncertainty may not be so much related to a N estimate as well to S_h FE type and mesh size sensitivity, meaning the FE recommendations associated with the S_h - N curve have to be used.

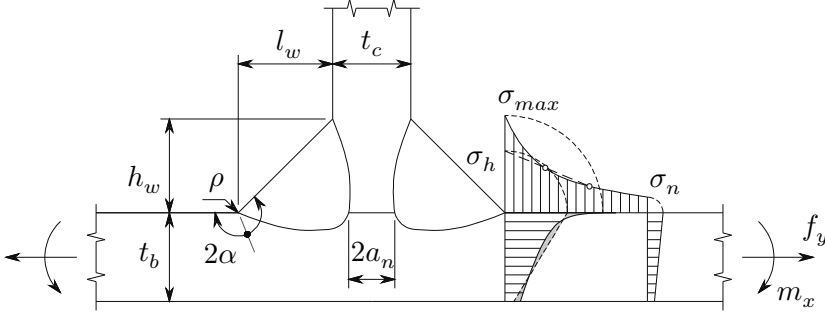


Figure 1.4: PP DS T-joint weld (toe) notch stress distribution.

Effective notch {stress, strain} concept

The (as-)weld(ed) notch radius is typically small ($\rho \rightarrow 0$) and the theoretical stress concentration is not fully effective, meaning a (local) peak stress fatigue resistance criterion $S_{max} = \Delta\sigma_{max}$ (Fig. 1.4) would be too conservative. Adopting a micro-structural notch support hypothesis, the notch stress is averaged along the (presumed) crack path over a material characteristic micro-structural length ρ^* to include the notch stress gradient contribution. The real ρ value is artificially enlarged employing a fictitious component $\rho_f = s \cdot \rho^*$ to obtain the effective one $\rho_e = \rho + \rho_f$ and the corresponding notch stress range $S_e = \Delta\sigma_e = \Delta\sigma_{av} = \Delta\sigma_{max}(\rho_e)$ of the original geometry (Neuber, 1937; Sonsino et al., 2012); an intact geometry parameter and line (equivalent point) criterion (Fig. 1.5).

Support factor s depends predominantly on loading mode (uni-axial, mixed i.e. multi-axial), response condition (plane stress, plane strain), notch angle ($2\alpha = \{5\pi/4, 2\pi\}$ for respectively idealised fillet weld toe- and weld root notches), notch shape (blunt hyperbolic, root hole or blunt circular for the weld toe; elliptic, key-hole or U-hole for the weld root) and last but not least the adopted strength criterion (e.g. an equivalent one like Von Mises). Values are in the range (1, 10).

Micro-structural length ρ^* is typically obtained in an implicit way. Using fatigue test data, S_e - N curve parameters can be estimated. Assuming the data correlation is at maximum for the actual ρ^* , its most likely value can be identified. Although ρ^* is a material characteristic parameter, {HAZ, WM} effects for respectively weld toe and weld root notches are generally ignored. A most likely ρ_e (engineering) value can be established directly as well, meaning average $\{\rho, \rho_f\}$ contributions are involved.

For engineering applications, one fatigue resistance curve (i.e. Basquin type of relation $S_e = C \cdot N^m$) corresponding to one reference radius $\rho_r = \rho_e = 1$ [mm] has been proposed (for both steel and aluminium weld {toe, root} notches) because of the simplifications (regarding notch angle, elastoplasticity, notch acuity, etc.) w.r.t. the original concept. The ρ_r value requires plate thickness $t_p \geq 5$ [mm] because of artificial cross-sectional weakening in case of weld root notches. Strengthening of weld toe notches is ignored. In both cases structural stress corrections should be applied. Concerning notch shape, root notches are obviously critical and {key, U}-hole configurations are respectively classified as {conservative, non-conservative}

based on a Round Robin (Fricke et al., 2013), although main criterion should be that the adopted shape as used to obtain the fatigue resistance curve and the one employed for fatigue assessment are in agreement. Note that only the absolute notch acuity has been taken into account, meaning size effects still have to be corrected for. Reference radius ρ_r is proposed to be replaced by a relative one (Schijve, 2012), although – at least for weld toe notches – involving the plate thickness, (ρ/t_p) , seems a better solution than a weld leg length. In case $t_p < 5$ [mm], $\rho_r = 0.05$ [mm] has been selected based on a completely different hypothesis, i.e. the relationship between the stress intensity factor (SIF) and notch stress as well as crack tip blunting. At the same time, it is a compromise w.r.t. FE modelling and calculation of a reasonable local stress component (Sonsino et al., 2012).

Embedded in an elastic far field condition, the weld notch structural response is typically elastoplastic, introducing the cyclic stress-strain (hardening) curve $(\varepsilon_e + \varepsilon_p) = (\sigma/E) + (\sigma/K')^{1/n'}$; the Ramberg-Osgood equation, turning the fatigue resistance curve into a (two-slope) Coffin-Manson-Basquin relation: $(\varepsilon_e + \varepsilon_p) = \{(\sigma_f' - \sigma_m)/E\} \cdot (2N)^b + \varepsilon_f'(2N)^c$. Morrow's mean stress correction is included. Adopting a macro- and micro-structural notch support hypothesis to relate the effective notch stress- and strain concentrations to the far field stress, an e_e -(2) N curve can be obtained.

Notch stress intensity concept

For decreasing ρ , the linear elastic notch stress becomes asymptotic and rather than a(n effective) local stress Williams' notch stress solution $\sigma(r, \theta)$ based weld notch stress intensity factor (NSIF) can be introduced (Verreman and Nie, 1996); an intact geometry parameter and notch stress gradient (area/volume) criterion: $K^N = \lim_{r \rightarrow 0^+} \{\sigma(r, \theta)/(2\alpha \cdot r)^{\lambda-1}\}$ turning into the SIF K definition for a weld root notch in crack configuration. The NSIF can be rewritten: $K^N = k\sigma t_p^{1-\lambda}$ (Lazzarin and Tovo, 1998) taking (only) the plate thickness based absolute notch acuity into account. The curve fitted weight function k is remote mechanical loading and joint geometry dependent. For a weld root notch $K^N \rightarrow K = k\sigma a_n^{1-\lambda}$. Note the eigenvalue is notch angle dependent $\lambda(2\alpha)$, meaning both the {NSIF, SIF} units and the scaling parameter for weld toe and weld root notches (respectively $t_p^{1-\lambda}$ and $a_n^{1-\lambda}$) are different. Combining fatigue resistance data involving hot spots with different notch angles (i.e. weld toe and weld root induced failures) to obtain one K^N - N or ΔK^N - N curve; a Basquin type of equation, is impossible.

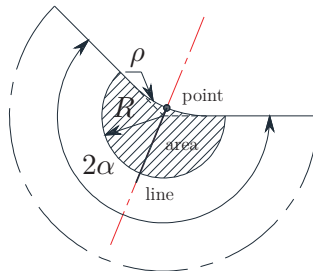


Figure 1.5: Weld notch process zones.

Strain energy density concept

To be able to incorporate work hardening, elastoplasticity, multi-axiality and mean stress effects, local {stress, strain} components should be involved and a hot spot energy criterion can be adopted: $W = f(\sigma_{ij}, \varepsilon_{ij})$. In case ($\rho \rightarrow 0$), W should be averaged to incorporate notch effectivity, introducing the energy density $\bar{W} = (W/A)$. Using Williams' asymptotic solution $\sigma(r, \theta)$ and a constitutive relation $\varepsilon_{ij} = f(\sigma_{ij})$, $\bar{W} = f(K_i^N(\sigma), A)$; an intact geometry parameter and area (or volume averaged point) criterion (Fig. 1.5). Area $A = 2\alpha \cdot R$, meaning radius R becomes the material characteristic micro-structural support parameter. A most likely value can be obtained using test data and a (Basquin type of) fatigue resistance relation, minimising the error. Alternatively, an R value can be retrieved using ($\Delta\sigma = \Delta\sigma_0$), i.e. the plane geometry fatigue limit estimate. For weld root notches, the (N)SIF should turn into the crack growth threshold $\Delta K^N \rightarrow \Delta K_{th}$ as well. Although $\bar{W} = f(K_i^N(\sigma), A)$ solves the (N)SIF units problem, the scaling issue still exists, meaning it is still not feasible to combine weld toe- and weld root induced failures and establish a \bar{W} - N or $\Delta\bar{W}$ - N fatigue resistance curve as has been proposed (Liviari and Lazzarin, 2005).

Battelle structural stress concept

The structural response for relatively complex hull structures is typically obtained using finite element analysis (FEA); welded joint fatigue life times are estimated using the structural hot spot stress concept. To reduce the S_h element type and mesh size sensitivity, nodal forces have been proposed to be used to obtain the far field stress distribution along the weld seam, including a virtual node procedure to accommodate weld ends. Assuming hull structure welded joints inevitably contain defects, a Battelle structural stress (BSS) criterion has been developed; a crack damaged- rather than intact geometry parameter (Dong and Hong, 2004).

The intact geometry through-thickness weld notch stress distribution has been bi-linearly approximated and translated to a crack damaged equivalent; the SIF K . A two-stage (notch affected micro- and far field dominated macro-) crack growth model has been proposed and turned into an equivalent (effective) stress criterion S_s incorporating the absolute and relative crack acuity, i.e. proper scaling. Fatigue resistance master curve(s), MCF S_s - N Basquin type of relations, have been derived for steel as-welded joints; toe and root induced failures separately, predominantly because of a far field stress inconsistency.

Developments

From engineering perspective, adopting a structural response parameter $\{S, e, W\}$ using only global information and available at FSS level seems attractive, but pays off in fatigue resistance data scatter and life time estimate uncertainty. Including physics at smaller scale, local information, improves the accuracy. Physics not considered typically appear as fatigue influence factors (ISSC proceedings, 2012). Approaching the continuum mechanics scale lower bound (i.e. defect size order of magnitude), intuitively a multi-scale approach might be considered as next step. Correlating $\{S, e, W\}$ to the netherworld (i.e. to meso- or even micro-scale models)

however is a challenge; to prove the hypotheses experimentally in particular. The remaining question is whether a popular multi-scale parameter like the Dang Van criterion (Dang Van, 1993) – a safe life parameter – is applicable. Providing a ‘Danger’ criterion rather than lifetime estimate, it is impossible to characterise arc-welded joint {MCF, HCF} resistance, although still applied in engineering (Dang Van et al., 2001). The only way out seems to incorporate the {MCF, HCF} normal- and shear fatigue resistance rather than the estimated(!) fatigue limits. Since the Dang Van (point) criterion applied to notched geometries does not include scaling, a notch effectivity hypothesis is required anyway. The translation from a meso- to macroscopic response distinguishing hydrostatic- and deviatoric components remains unaffected, meaning a multi-scale parameter seems a possibility indeed...

A continuous increase of the considered scale range of physics (including even granular mechanics) as observed in fatigue assessment concept development over time to increase accuracy, however, is typically associated with increased (computational) effort requirements and concept complexity (Fig. 1.6).

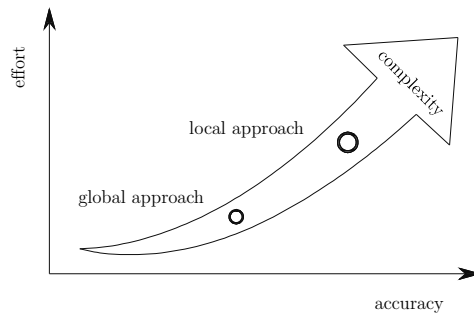


Figure 1.6: Typical fatigue assessment concept {accuracy, effort, complexity} relation.

At the same time, similarity; proper scaling, meaning equal $\{S, e, W\}$ should yield the same fatigue resistance (i.e. number of cycles N), seems still incomplete since all concepts available still involve multiple fatigue resistance curves rather than one.

1.2 Research objective

Looking at the scale of physics already considered and the accuracy achieved, the fatigue resistance data scatter and estimated life time uncertainty seem hard to improve. Different parameters defined at the same scale provide similar accuracy levels (modifications disappear in uncertainties) and – provided the micro-structural material imperfections and welding induced flaws level of scale as well as stochastics do not change – continuing the decrease of fatigue scale of physics seems inefficient. From {MCF, HCF} design perspective, a local continuum mechanics approach seems sufficient and focus will be on developing a fatigue assessment concept to balance accuracy, effort and complexity (Fig. 1.7).

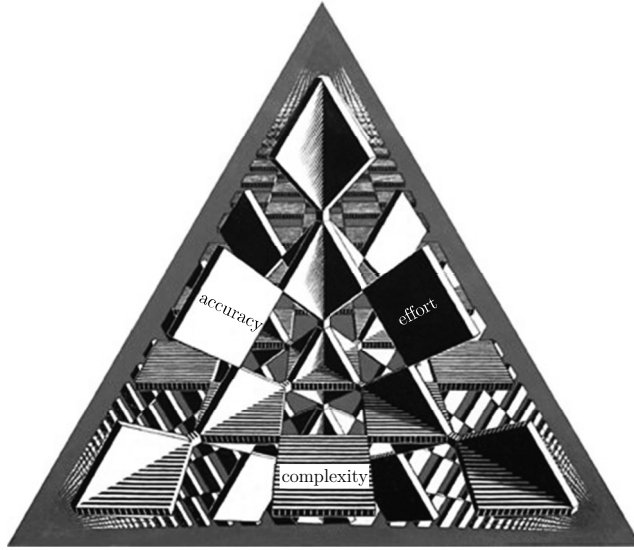


Figure 1.7: Three Intersecting Planes (M.C. Escher),
i.e. {accuracy, effort, complexity} cross roads.

Although a hull structure longevity estimate – welded joints fatigue strength and life time – require a {loading, structural response} analysis and fatigue resistance assessment, emphasis will be on fatigue resistance design in relation to the structural response. In order to improve similarity (generalising the fatigue resistance parameter at the same time) and to obtain one aluminium arc-welded joint fatigue resistance curve, a total stress concept is proposed (Fig. 1.8 and 1.9).

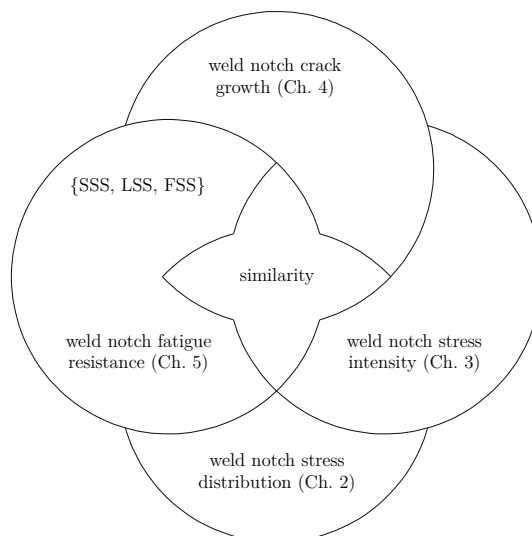


Figure 1.8: Elements of the total stress concept.

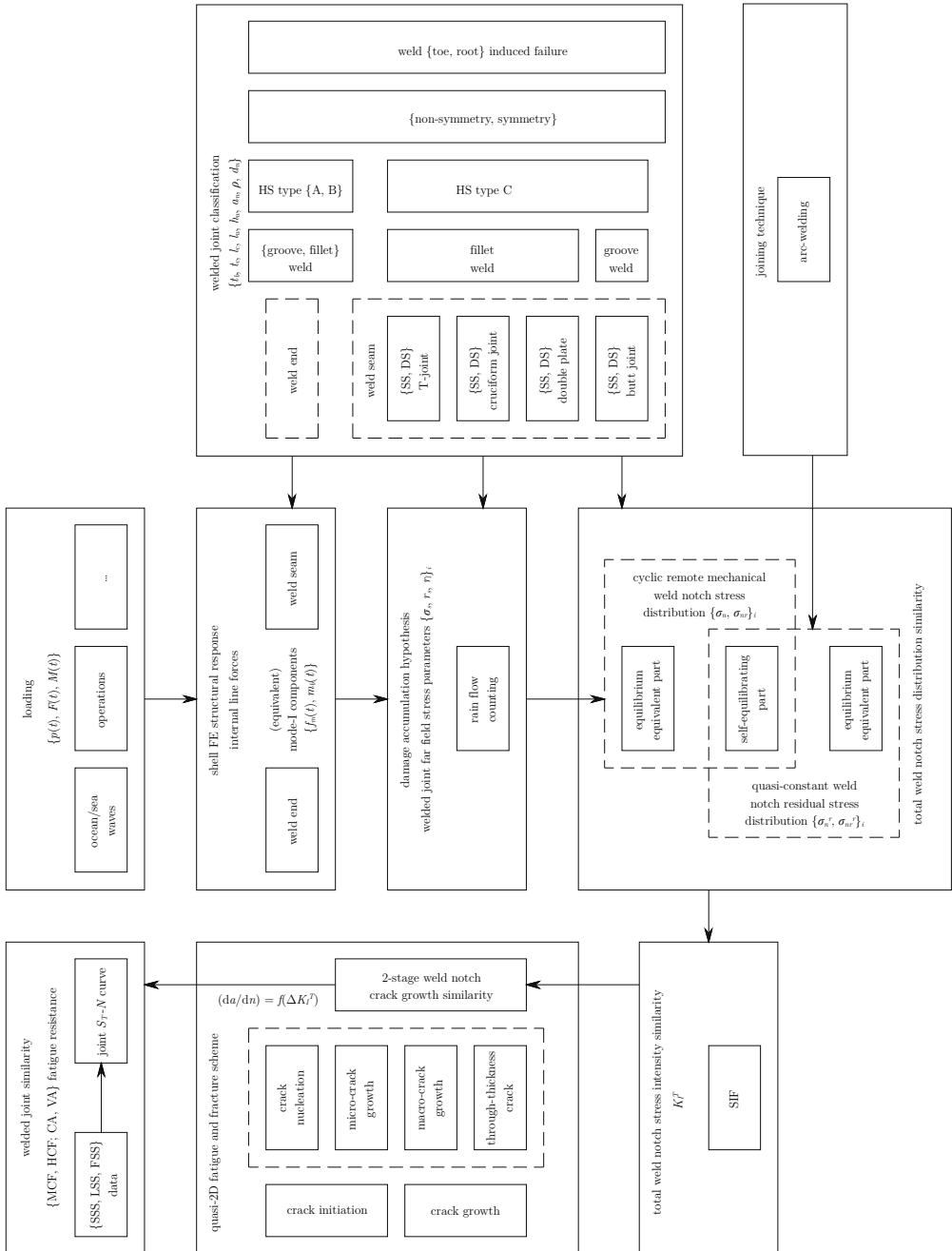


Figure 1.9: Research road map.

Thesis outline

To calculate the global hull structural response for fatigue design purposes, a relatively coarse meshed shell- and plate FE model should be sufficient. The local weld geometry is not included, meaning that corresponding notch information is missing. However, the remote mechanical loading induced (linear) predominant mode-I far field stress distribution $\sigma_f(\sigma_s, r_s)$ in each cross-section along the weld seam is available and will be related to the corresponding through-thickness weld {toe, root} notch stress distribution formulations $\{\sigma_n, \sigma_{nr}\}$ along the expected (2D) crack path: an assumed key element in defining an appropriate fatigue design (and detectable repair) criterion. Exploiting (non-)symmetry conditions, a generalised formulation is aimed for to demonstrate stress field similarity (Chapter 2) and should extend to the welding induced thermal residual stress distributions $\{\sigma_n^r, \sigma_{nr}^r\}$. A linear superposition of the two distributions provides $\{\sigma_n^T, \sigma_{nr}^T\}$; the total ones.

Fatigue scaling requires both the peak value and gradient to be incorporated, meaning a damage criterion should take the complete distribution into account. The stress intensity (similarity) factor (SIF) K seems to meet this criterion, though, the intact geometry related notch stress distributions $\{\sigma_n^T, \sigma_{nr}^T\}$ should consistently be correlated to a crack damaged equivalent (Chapter 3); the (total) mode-I weld (toe and root) notch stress intensity similarity parameter K_I^T . At the same time, assuming that arc-welded joints inevitably contain flaws, defects at the weld toe- and root notches, fatigue damage at both locations will primarily be a matter of notch affected micro- and far field dominated macro-crack growth, justifying a damage tolerant parameter like the SIF.

Cyclic remote mechanical- and quasi-constant thermal residual loading turn K_I^T into a crack growth driving force ΔK_I^T and defects may develop into cracks. The crack growth rate (da/dn) of micro-cracks emanating at notches show elastoplastic wake field affected anomalies. Modifying Paris' equation, a two-stage micro- and macro-crack growth law similarity is proposed (Chapter 4) to include both the weld notch- and far field characteristic contributions.

Crack growth model integration will provide a (MCF) single slope resistance relation, a joint S_T - N curve (Chapter 5) correlating life time N and total stress parameter S_T (Fig. 1.3); a line (equivalent point) criterion to ensure {small, large} scale specimen and full scale structure (SSS, LSS, FSS) welded joint fatigue resistance similarity. A (random) fatigue limit model, a dual slope formulation, has been adopted to incorporate HCF taking the transition in fatigue damage mechanism (i.e. growth dominant turns into initiation controlled for decreasing load level), a slope change, into account.

2

Weld Notch Stress Distributions

There has to be a mathematical explanation for how elegant weld notch stress distributions look like.

2.1 Introduction

In aluminium high-speed craft, {MCF, HCF} is a governing design limit state. Arc-welded joints connecting the hull structure stiffened (curved) panel assembly components, (thin) plates and shells, are a matter of concern in that respect (Chapter 1). The weld geometry introduces at least a notch at the weld toe and depending on penetration level another one at the weld root. Cracks may initiate at both fatigue sensitive locations, grow principally in {plate, shell} thickness direction and continue to propagate in general either along or perpendicular to the weld seam through {plate, shell} because of the structure orthotropic stiffness characteristics, suggesting a {plate, shell} thickness based (detectable repair) criterion to be an appropriate fatigue design parameter. The total through-thickness weld notch stress distribution, including both the ocean/sea waves induced cyclic remote mechanical loading- and welding process related quasi-constant thermal residual part, is assumed to be a key element.

Outline

Typical hull structure welded joints will be identified first and classified taking weld type, notch location and geometric symmetry into account (Paragraph 2.2). The predominant remote mechanical loading mode-I induced through-thickness weld notch stress distributions $\{\sigma_n, \sigma_{nr}\}$, e.g. at a base plate related weld toe and weld root for respectively a partial penetrated double sided T-joint and butt joint; plate thickness $t_p = t_b$ and $t_p' = t_b'$, will be examined to distinguish the contributing stress components. A weld geometry stress – consisting of a local V-shaped notch- and weld load carrying component (Paragraph 2.3 and 2.4) – and global structural field stress (Paragraph 2.5) are identified and a generalised formulation demonstrating stress field similarity (Fig. 2.1) will be obtained.

For increasing notch radius ρ , the notch peak stress value σ_{max} decreases meaning the corresponding zone 1 size increases, shifting its (right) boundary to the right. The other way around, if ρ decreases σ_{max} will increase; the boundary moves left and its influence reduces. The limit case: $\rho \rightarrow 0$ and zone 1 becomes infinitesimally small. The weld geometry stress defined zone 2 size increases for increasing notch angle 2α ; the V-shaped notch stress is modified. The upper limit case $2\alpha = 2\pi$ is the crack configuration as typically turns up at a weld root. Zone 2 as well as zone 1 vanish for the lower limit case $2\alpha = \pi$; a plane geometry. At the same time 2α increases the notch stress gradient increases as well; the weld dimensions $\{l_w, h_w\}$ and root notch size/length a_n dependent weld load carrying stress contribution defines the final value. The linear(ised) structural (root) field stress $\{\sigma_f, \sigma_{fr}(\sigma_f)\}$ gradient – either positive or negative – determines the zone 3 boundary location.

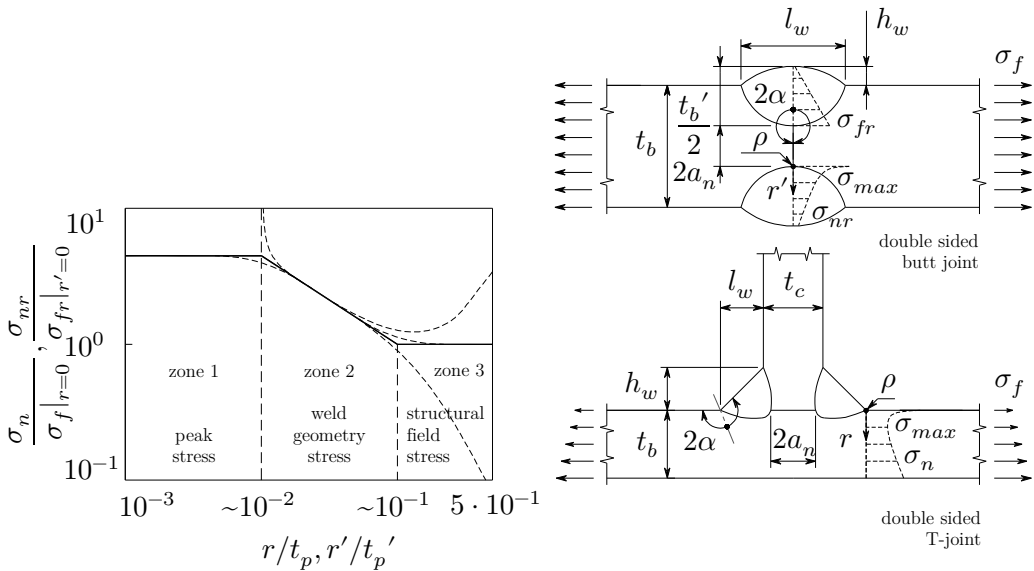


Figure 2.1: Generalised weld notch stress distribution $\{\sigma_n/\sigma_f|_{r=0}, \sigma_{nr}/\sigma_{fr}|_{r'=0}\}$.

The fatigue resistance of a welded joint depends on its dimensions, meaning an appropriate scaling parameter is required. The zone 1 peak stress and zone {2, 3} stress gradients provide important information in that respect, i.e. the highly stressed material volume around the notch is defined, explaining why linear elastic (deformations are presumed to be small), semi-analytical, parametric remote mechanical loading induced through-thickness notch stress distribution formulations $\{\sigma_n, \sigma_{nr}\}$ are developed for the weld toe as well as weld root (Paragraph 2.6 and 2.7). Size effects of {weld dimensions, notch radius, plate thickness} are investigated and include the possibility to optimise the weld geometry (Paragraph 2.8).

The $\{\sigma_n, \sigma_{nr}\}$ distributions are related to the joint far field stress, calculated using a relatively coarse meshed {plate, shell} FE hull structural design model in a weld seam analysis procedure (Paragraph 2.9). The opportunity to take proportional far field multi-axiality into account adopting an equivalent stress is provided.

Observation of numerical simulation- and {neutron, synchrotron} diffraction measurement results indicate how welding process induced (thermal residual) notch stress distributions may look like (Paragraph 2.10). Comparison of the remote mechanical- and thermal residual stress parts shows that the generalised formulation and stress field similarity can be extended. Finally, the total stress concept will be derived (Paragraph 2.11).

2.2 Welded joint classification

Theoretically, an infinite number of different welded joints exist. However, for a typical hull (i.e. bottom) structure (Fig. 2.2) it is rather a matter of varying dimensions than the actual diversity in welded joints.

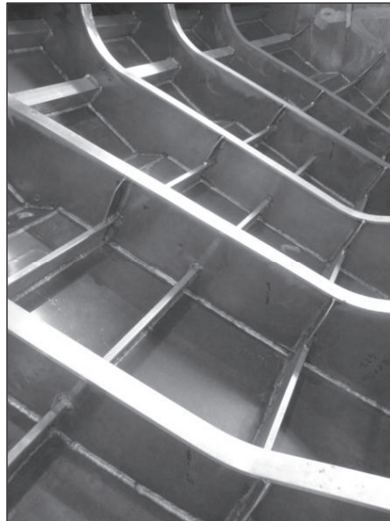


Figure 2.2: Damen high-speed craft bottom structure.

Four – quasi 2D – commonly applied welded joints in double sided (DS) and single sided (SS) configuration are identified and selected, linking a continuous base plate – thickness t_b – and {connecting, cross, cover} plate – thickness t_c (Fig. 2.3). The remote mechanical line forces $\{f_m, m_b, f_s\}$ should satisfy static equilibrium, although for each notch location and corresponding through-thickness stress distribution only the relevant mode-I membrane and bending components $\{f_m, m_b\}$ are taken into account; the shear line force f_s (mode-II component) is disregarded. For the butt joints (Fig. 2.3 a, b) t_b and t_c may be different and the off-set between the plate centre lines can be non-zero. The centre lines for the T-joint (Fig. 2.3 c, d) and cruciform joint (Fig. 2.3 e, f) need not necessarily to be perpendicular to each other; the SS configurations (Fig. 2.3 d,f) are mainly a result of chain or staggered intermittent welding. An attachment with out-of-plane thickness - t_c - will introduce 3D effects, to be taken care of using $\{f_m, m_b\}$. The cover- or double plate is a special one with in-plane thickness t_c (Fig. 2.3 g, h); the base plate may be discontinuous.

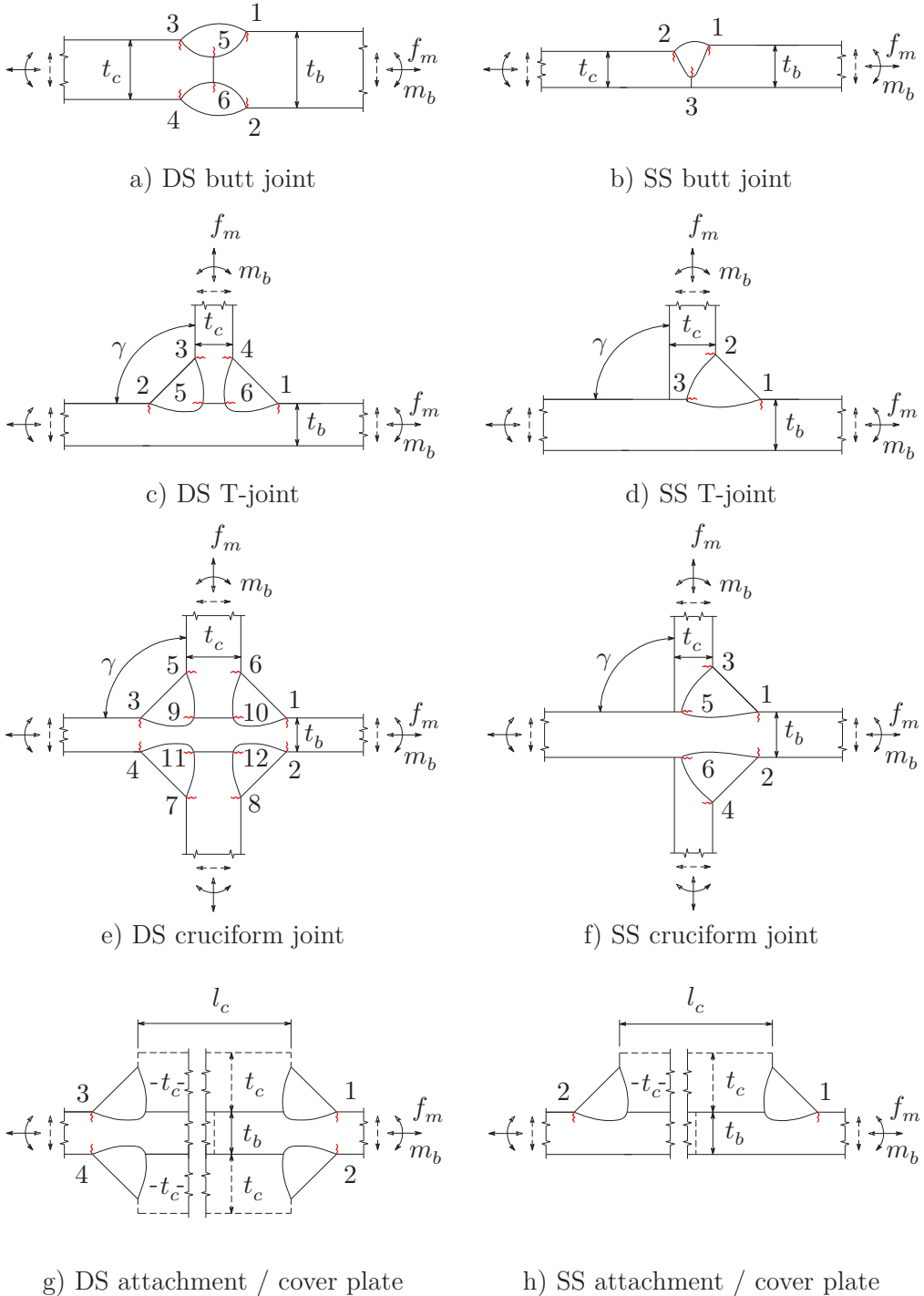


Figure 2.3: Commonly applied welded joints (incl. mode-I cracks) in hull structures.

Characteristic features defined from geometry and through-thickness weld notch stress distribution perspective include:

- weld type; groove- (Fig. 2.3 a, b) and fillet welds (Fig. 2.3 c-h) are distinguished, ideally assumed to be respectively arc- and tri-angular shaped.
- notch location; potential loading mode-I fatigue sensitive weld toe- and weld root notches are identified and numbered for convenience (Fig. 2.3).
- symmetry with respect to $(t_p/2)$, either $t_p = t_b$ or $t_p = t_c$; a pre-requisite to obtain the correct stress gradient and appropriate scaling.
- the structural hot spot (HS) classification (Fricke, 2002); restricted to weld toe notches, is proposed to be generalised (Fig. 2.4).

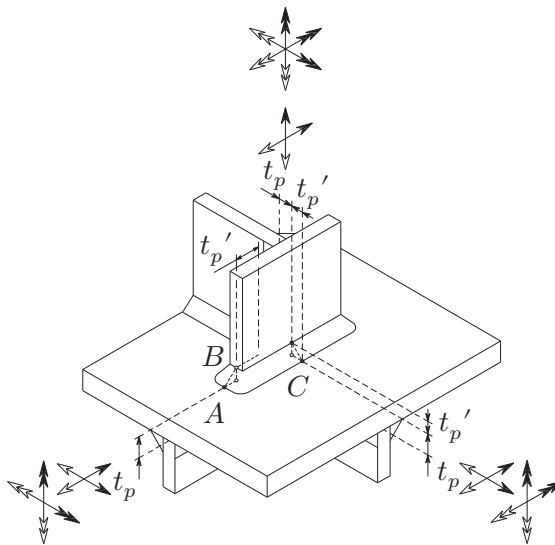


Figure 2.4: Hot spot type classification.

- HS type *C*: notch along the weld seam.
- HS type *A* or *B*: notch at the weld end.

Any particular notch in a cross-section of an arbitrary joint (Fig. 2.3 a-f) is defined as HS type *C*, including the cover plate (Fig. 2.3 g, h); using half the attachment geometries – HS type *A* specials – the generalised weld end HS types $\{A, B\}$ can be obtained (Fig. 2.5). Examples are the weld ends at respectively a (soft toe) bracket and bulkhead-bottom stiffener connection (Fig. 2.6). The weld toe HS type *B* plate thickness t_p' , defined along the weld seam, is artificial – a through-thickness criterion does not necessarily mean

through plate thickness – like for a weld root HS type *C* either along a weld leg or weld throat. To incorporate 3D weld end effects, particularly important for (weld toe) HS's type *A*, the line forces $\{f_m, m_b\}$ have to be used to obtain an equivalent structural field stress σ_f .

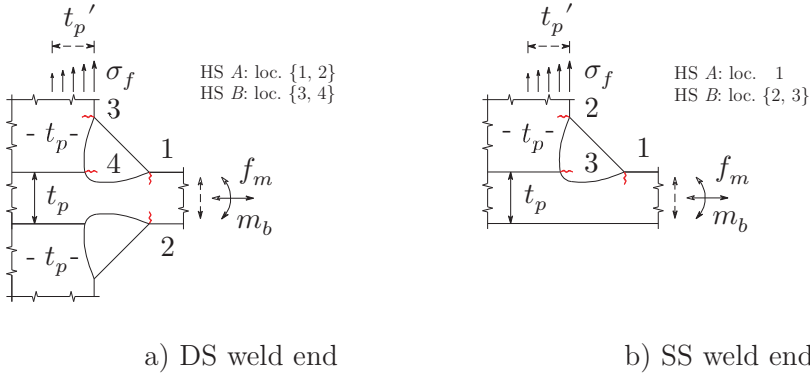


Figure 2.5: Generalised hot spot type $\{A, B\}$ incl. mode-I cracks.

The weld penetration level, full (FP) or partial (PP), is a useful denotation from production point of view, although strictly speaking the former is a PP limit case, i.e. $a_n = 0$; the general cases are shown (Fig. 2.3). Defining welds as load carrying (LC) or non-load carrying (NLC), e.g. the DS cruciform joint (Fig. 2.3e) from respectively t_b or t_c perspective, seems inappropriate. All welds are load carrying up to some extent. The $\{LC, NLC\}$ qualification just represents the extremes and is considered to be incomplete.

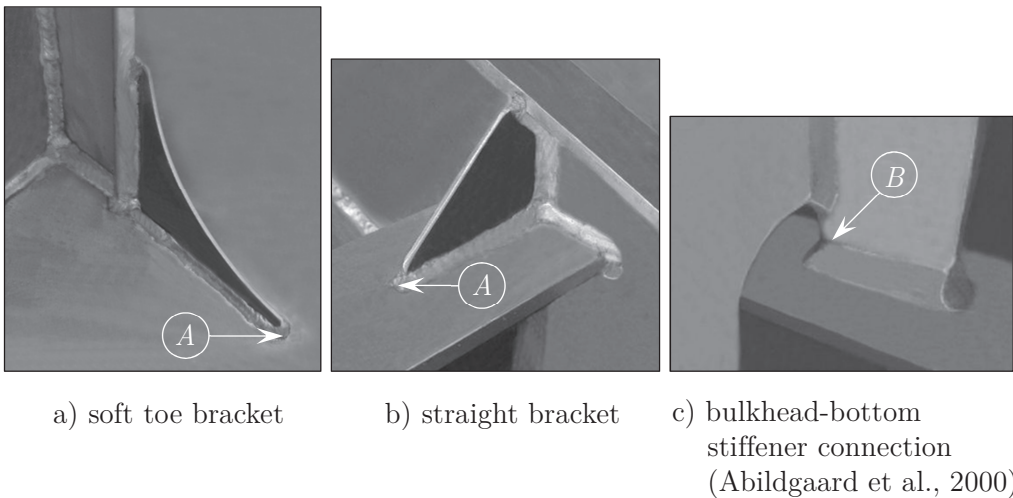


Figure 2.6: Weld end HS type $\{A, B\}$ in hull structures.

With respect to the stress concepts widely used nowadays, the welded joint selection (Fig. 2.3 and 2.5) includes a significant part of the nominal stress concept related detail categories (CEN: Eurocode 9, 2007; IIW recommendations: Hobbacher, 2009b) and significantly increases the number of considered notch locations in comparison to the weld toe analysis limited structural hot spot stress concept (Niemi, Fricke and Maddox, 2006).

2.3 V-shaped notch stress

Using linear elastic continuum mechanics, an Airy stress function φ in polar coordinates has been introduced (Williams, 1952) to obtain the (singular) stress distribution at a V-shaped notch with notch radius $\rho = 0$, i.e. the zone 1 peak stress and zone 2 stress gradient contribution (Fig. 2.1) for a fillet weld- or groove weld geometry (Fig. 2.7):

$$\varphi = r^{\lambda+1} \cdot [C_1 \cos\{(\lambda+1)\theta\} + C_2 \cos\{(\lambda-1)\theta\} + C_3 \sin\{(\lambda+1)\theta\} + C_4 \sin\{(\lambda-1)\theta\}] \quad (2.1)$$

Equilibrium (body forces are assumed to be zero) and compatibility requirements – deformations without any gaps or overlaps – are identically satisfied, i.e. the bi-harmonic equation $\nabla^4\varphi = \nabla^2(\nabla^2\varphi) = 0$ with

$$\nabla^2\varphi = \frac{\partial^2\varphi}{\partial r^2} + \frac{1}{r} \frac{\partial\varphi}{\partial r} + \frac{1}{r^2} \frac{\partial^2\varphi}{\partial\theta^2} \quad (2.2)$$

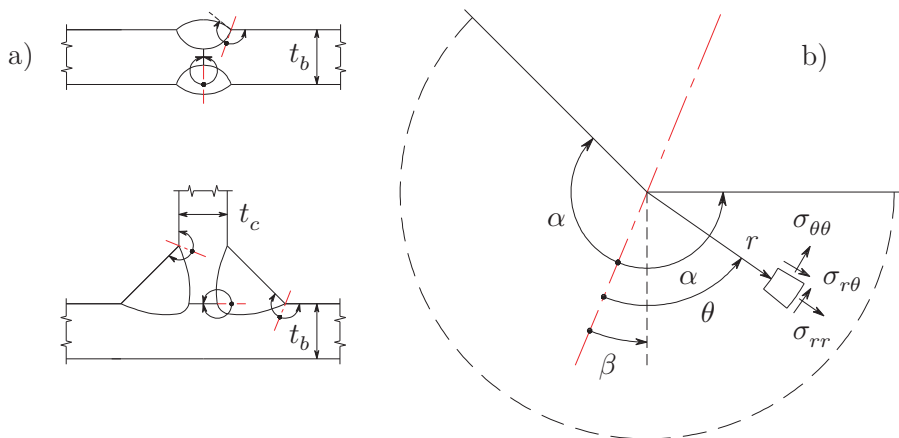


Figure 2.7: a) V-shaped notch locations and b) parameters.

Airy stress function φ (Eq. 2.1) consists of two symmetric $\cos(\cdot)$ - and two anti-symmetric $\sin(\cdot)$ terms. By definition, the {radial, tangential, shear} stress components yield:

$$\begin{aligned}\sigma_{rr} &= \frac{1}{r} \frac{\partial \varphi}{\partial r} + \frac{1}{r^2} \frac{\partial^2 \varphi}{\partial \theta^2} \\ \sigma_{\theta\theta} &= \frac{\partial^2 \varphi}{\partial r^2} \\ \sigma_{r\theta} &= -\frac{\partial}{\partial r} \left(\frac{1}{r} \frac{\partial \varphi}{\partial \theta} \right)\end{aligned}\tag{2.3}$$

The boundary conditions to be applied at the traction free surfaces:

$$\begin{aligned}\sigma_{\theta\theta}|_{\theta=\alpha} &= 0 & \sigma_{r\theta}|_{\theta=\alpha} &= 0 \\ \sigma_{\theta\theta}|_{\theta=-\alpha} &= 0 & \sigma_{r\theta}|_{\theta=-\alpha} &= 0\end{aligned}\tag{2.4}$$

Substitution of φ (Eq. 2.1) into the stress components (Eq. 2.3) subjected to the boundary conditions (Eq. 2.4) yield four equations. After adding and subtracting the two equations for each surface, two independent systems of equations – two eigenvalue problems – can be obtained for $\{C_1, C_2\}$ and $\{C_3, C_4\}$; the amplitudes of respectively the symmetric and anti-symmetric terms:

$$\begin{bmatrix} (\lambda + 1) \sin\{(\lambda + 1)\alpha\} & (\lambda - 1) \sin\{(\lambda - 1)\alpha\} \\ (\lambda + 1) \cos\{(\lambda + 1)\alpha\} & (\lambda + 1) \cos\{(\lambda - 1)\alpha\} \end{bmatrix} \begin{Bmatrix} C_1 \\ C_2 \end{Bmatrix} = \begin{Bmatrix} 0 \\ 0 \end{Bmatrix}\tag{2.5}$$

$$\begin{bmatrix} (\lambda + 1) \cos\{(\lambda + 1)\alpha\} & (\lambda - 1) \cos\{(\lambda - 1)\alpha\} \\ (\lambda + 1) \sin\{(\lambda + 1)\alpha\} & (\lambda + 1) \sin\{(\lambda - 1)\alpha\} \end{bmatrix} \begin{Bmatrix} C_3 \\ C_4 \end{Bmatrix} = \begin{Bmatrix} 0 \\ 0 \end{Bmatrix}\tag{2.6}$$

Non-trivial system (Eq. 2.5 and 2.6) solutions can be found solving respectively:

$$\left. \begin{aligned}\lambda \sin(2\alpha) + \sin(\lambda 2\alpha) &= 0 \\ \lambda \sin(2\alpha) - \sin(\lambda 2\alpha) &= 0\end{aligned} \right\} \forall (\lambda > 0, \lambda \neq 1)\tag{2.7}$$

$$\left. \begin{aligned}\lambda \sin(2\alpha) + \sin(\lambda 2\alpha) &= 0 \\ \lambda \sin(2\alpha) - \sin(\lambda 2\alpha) &= 0\end{aligned} \right\} \forall (\lambda > 0, \lambda \neq 1)\tag{2.8}$$

System (Eq. 2.7 and 2.8) solutions should satisfy $\lambda > 0$ because of the energy criterion: the strain energy must be finite (Barber, 2002). The eigenvalue $\lambda = 1$ is an unfeasible one since a null-form is obtained for the last φ term (Eq. 2.1): $C_4 \sin(0)$, meaning the Airy stress function should be modified. In a graphical presentation (Fig. 2.8), the solutions – the intersections between the $\sin(\cdot)$ term and the linear terms – are shown for a few notch angles 2α . The intersections with the continuous

lines (positive slope) correspond to the eigenvalues for the symmetric part; the intersections with the dashed lines (negative slope) to the eigenvalues for the non-symmetric part. For $2\alpha = 1.17\pi$ [rad] and $2\alpha = 1.25\pi$ [rad], the symmetric part contains only one eigenvalue. For the anti-symmetric part principally two eigenvalues can be found, however, the first one is unfeasible: $\lambda = 1$. The slope of the dashed line decreases for increasing notch angle up to $2\alpha \approx 1.43\pi$ [rad]; a limit case without feasible eigenvalue solution, in terms of a fillet weld geometry corresponding to a flank angle $\arctan(h_w/l_w) \approx 77.4$ [deg]. Continuing the 2α increase, the slope of the dashed line will increase and feasible λ values are obtained again.

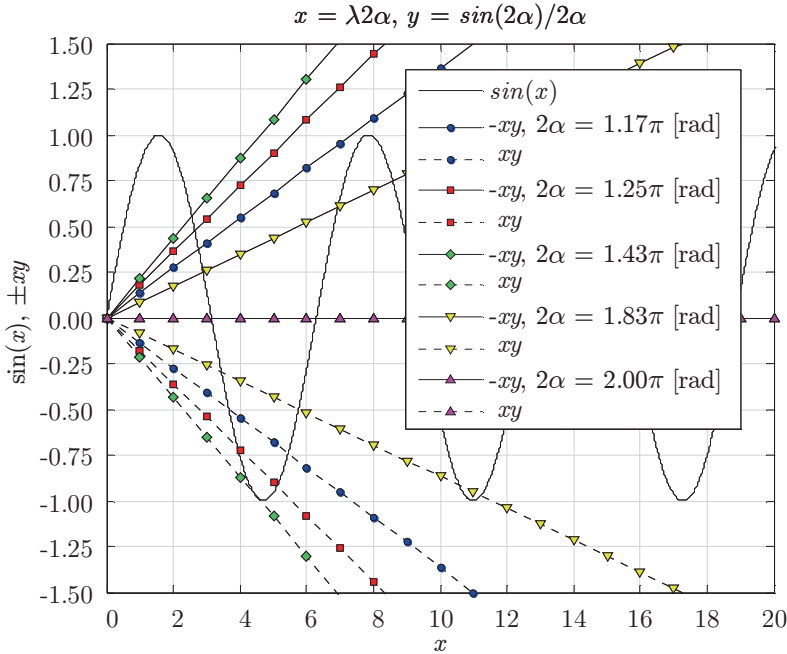


Figure 2.8: System (Eq. 2.7 and 2.8) solutions.

For all weld toe notch angles, at least one valid eigenvalue for the symmetric (mode-I) and anti-symmetric (mode-II) part, λ_s and λ_a , exists. In case of multiple values, only the first (feasible) one for each part will be considered (Fig. 2.9); ($0.5 \leq \lambda_{s,1} < 1$) and ($0.5 \leq \lambda_{a,1} < 2$) for ($\pi \leq 2\alpha \leq 2\pi$). Starting in half-plane configuration, $2\alpha = \pi$, no (feasible) eigenvalue solutions exist: no notch, no singularity. Increasing 2α , a V-shaped notch develops and $\{\lambda_{s,1}, \lambda_{a,1}\}$ decrease monotonically up to $\lambda_{s,1} = \lambda_{a,1}$ for $2\alpha = 2\pi$ [rad].

Rewriting the 2nd equation of both systems (Eq. 2.5 and 2.6) in terms of $\{C_2, C_4\}$ and substitution in φ (Eq. 2.1), the stress components (Eq. 2.3) for a particular stress angle $\theta = \beta$ become:

$$\begin{aligned} \sigma_{rr} \left(\frac{r}{t_p} \right) = -\sigma_s \left\{ \left(\frac{r}{t_p} \right)^{\lambda_s-1} \mu_s \lambda_s [(\lambda_s + 1) \cos\{(\lambda_s + 1)\beta\} - \right. \\ \left. \chi_s (\lambda_s - 3) \cos\{(\lambda_s - 1)\beta\}] + \right. \\ \left. \left(\frac{r}{t_p} \right)^{\lambda_a-1} \mu_a \lambda_a [(\lambda_a + 1) \sin\{(\lambda_a + 1)\beta\} - \right. \\ \left. \chi_a (\lambda_a - 3) \sin\{(\lambda_a - 1)\beta\}] \right\} \end{aligned} \quad (2.9)$$

$$\begin{aligned} \sigma_{\theta\theta} \left(\frac{r}{t_p} \right) = \sigma_s \left\{ \left(\frac{r}{t_p} \right)^{\lambda_s-1} \mu_s \lambda_s (\lambda_s + 1) [\cos\{(\lambda_s + 1)\beta\} - \right. \\ \left. \chi_s \cos\{(\lambda_s - 1)\beta\}] + \right. \\ \left. \left(\frac{r}{t_p} \right)^{\lambda_a-1} \mu_a \lambda_a (\lambda_a + 1) [\sin\{(\lambda_a + 1)\beta\} - \right. \\ \left. \chi_a \sin\{(\lambda_a - 1)\beta\}] \right\} \end{aligned} \quad (2.10)$$

$$\begin{aligned} \sigma_{r\theta} \left(\frac{r}{t_p} \right) = \sigma_s \left\{ \left(\frac{r}{t_p} \right)^{\lambda_s-1} \mu_s \lambda_s [(\lambda_s + 1) \sin\{(\lambda_s + 1)\beta\} - \right. \\ \left. \chi_s (\lambda_s - 1) \sin\{(\lambda_s - 1)\beta\}] - \right. \\ \left. \left(\frac{r}{t_p} \right)^{\lambda_a-1} \mu_a \lambda_a [(\lambda_a + 1) \cos\{(\lambda_a + 1)\beta\} - \right. \\ \left. \chi_a (\lambda_a - 1) \cos\{(\lambda_a - 1)\beta\}] \right\} \end{aligned} \quad (2.11)$$

with the eigenvalue coefficients

$$\chi_s = \frac{\cos\{(\lambda_s + 1)\alpha\}}{\cos\{(\lambda_s - 1)\alpha\}}, \quad \chi_a = \frac{\sin\{(\lambda_a + 1)\alpha\}}{\sin\{(\lambda_a - 1)\alpha\}}$$

The amplitudes $\mu_s = (C_1 t_p^{\lambda_s - 1} / \sigma_s)$ and $\mu_a = (C_3 t_p^{\lambda_a - 1} / \sigma_s)$ replaced respectively C_1 and C_3 to achieve a far field parameter dependent (Paragraph 2.5) – i.e. structural stress σ_s related – formulation including dimensionless coordinates ($r \rightarrow r/t_p$). The plate thickness $t_p = t_b$ for a base plate notch and $t_p = t_c$ for a {connecting, cross, cover} plate related one.

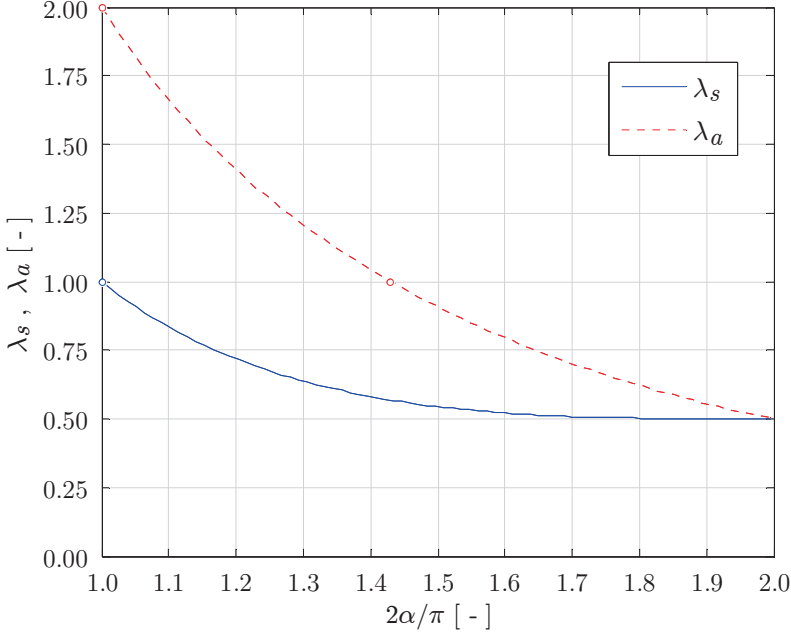


Figure 2.9: Eigenvalue solutions $\{\lambda_s = \lambda_{s,1}, \lambda_a = \lambda_{a,1}\}$.

For $2\alpha = 2\pi$ [rad], the crack configuration as typically encountered at weld root notches, the (asymptotic) solutions of both eigenvalue problems are similar:

$$\lambda_{s,i} = \lambda_{a,i} = \lambda_i = \left(\frac{n}{2}\right), \quad n = 1, 3, 5, 7, 9, \dots \quad (2.12)$$

Substituting the 1st equation of system (Eq. 2.5) and the 2nd one of system (Eq. 2.6) in terms of $\{C_2, C_4\}$ into (Eq. 2.1), the stress components (Eq. 2.3) denote:

$$\begin{aligned} \sigma_{rr} \left(\frac{r'}{t_p}\right) = -\sigma_{sr} \sum_{i=1}^n \left\{ \left(\frac{r'}{t_p}\right)^{\lambda_i - 1} \lambda_i (\mu_{1i} [(\lambda_i + 1) \cos\{(\lambda_i + 1)\beta\} - \right. & (2.13) \\ & \chi_i (\lambda_i - 3) \cos\{(\lambda_i - 1)\beta\}] + \\ & \mu_{3i} [(\lambda_i + 1) \sin\{(\lambda_i + 1)\beta\} - \\ & \left. (\lambda_i - 3) \sin\{(\lambda_i - 1)\beta\}] \right\} \end{aligned}$$

$$\sigma_{\theta\theta} \left(\frac{r'}{t_p'} \right) = \sigma_{sr} \sum_{i=1}^n \left\{ \left(\frac{r'}{t_p'} \right)^{\lambda_i-1} \lambda_i (\lambda_i + 1) (\mu_{1i} [\cos\{(\lambda_i + 1)\beta\} - \chi_i \cos\{(\lambda_i - 1)\beta\}] + \mu_{3i} [\sin\{(\lambda_i + 1)\beta\} - \sin\{(\lambda_i - 1)\beta\}]) \right\} \quad (2.14)$$

$$\sigma_{r\theta} \left(\frac{r'}{t_p'} \right) = \sigma_{sr} \sum_{i=1}^n \left\{ \left(\frac{r'}{t_p'} \right)^{\lambda_i-1} \lambda_i (\mu_{1i} [(\lambda_i + 1) \sin\{(\lambda_i + 1)\beta\} - \chi_i (\lambda_i - 1) \sin\{(\lambda_i - 1)\beta\}] - \mu_{3i} [(\lambda_i + 1) \cos\{(\lambda_i + 1)\beta\} - (\lambda_i - 1) \cos\{(\lambda_i - 1)\beta\}]) \right\} \quad (2.15)$$

with the eigenvalue coefficients

$$\chi_{1,i} = \chi_i = \frac{(\lambda_i + 1)}{(\lambda_i - 1)}, \quad \chi_{3,i} = 1$$

To distinguish the weld toe and weld root notch coordinate system, $r \rightarrow r'$; the artificial plate thickness t_p' substitutes t_p . Amplitudes $\{\mu_{1i} = (C_{1,i} t_p^{\lambda_i-1} / \sigma_{sr})\}$, $\mu_{3i} = (C_{3,i} t_p^{\lambda_i-1} / \sigma_{sr})\}$ replaced $\{C_1, C_3\}$. Note that only the first stress terms show (square root) singular behaviour.

2.4 Weld load carrying stress

The weld geometry causes a local change in stiffness; a shift in neutral axis (Fig. 2.10), meaning the weld becomes load carrying up to some extent. In case the structural discontinuity shows linear behaviour, the response is a bending moment. The corresponding bending stress formulation $\sigma_{bw}(r/t_p)$ depends on type of joint, notch location and symmetry with respect to half the plate thickness, either $(t_p/2) = (t_b/2)$ or $(t_p/2) = (t_c/2)$. Considering a weld toe notch as typically encountered in a PP DS T-joint at the base plate t_b without symmetry (Fig. 2.10a), a counter-clockwise bending moment is introduced for f_m pointing to the right and clockwise m_b and the weld load carrying (bending) stress distribution – a loading mode-I component contributing in particular to the zone 2 stress gradient (Fig. 2.1) – yields:

$$\sigma_{bw} \left(\frac{r}{t_p} \right) = \sigma_s C_{bw} \left\{ 2 \left(\frac{r}{t_p} \right) - 1 \right\} \vee \left\{ 0 \leq \left(\frac{r}{t_p} \right) \leq 1 \right\} \quad (2.16)$$

The structural stress σ_s is a far field parameter. Approximate C_{bw} values can be obtained using beam finite element (FE) models. If geometric symmetry with respect to $(t_p/2)$ is detected, like for a PP DS butt joint (Fig 2.10b), σ_{bw} is defined for half the plate thickness only:

$$\sigma_{bw} \left(\frac{r}{t_p} \right) = \sigma_s C_{bw} \left\{ 4 \left(\frac{r}{t_p} \right) - 1 \right\} \vee \left\{ 0 \leq \left(\frac{r}{t_p} \right) \leq \left(\frac{1}{2} \right) \right\} \quad (2.17)$$

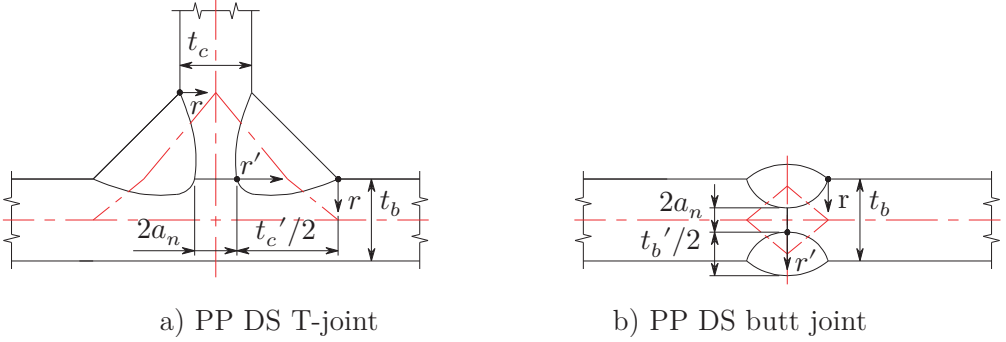


Figure 2.10: Weld geometry induced shift of neutral axis.

Weld toe notches may demonstrate non-linear structural behaviour in case the weld dimensions are relatively small and the root notch size a_n large, like for (discontinuous) cross plates related ones of PP T-joints and PP cruciform joints meaning the contribution of another (non-linear) weld load carrying component is required. Its formulation is based on engineering judgement and related to C_{bw} as well. For non-symmetry:

$$\sigma_{bw} \left(\frac{r}{t_p} \right) = \sigma_s C_{bw} \left[\left\{ 2 \left(\frac{r}{t_p} \right) - 1 \right\} + 12 \left(\left\{ \left(\frac{r}{t_p} \right) - \frac{1}{2} \right\}^2 - \frac{1}{12} \right) \right] \quad (2.18)$$

and symmetry:

$$\sigma_{bw} \left(\frac{r}{t_p} \right) = \sigma_s C_{bw} \left[\left\{ 4 \left(\frac{r}{t_p} \right) - 1 \right\} + 6 \left(\left\{ \left(\frac{r}{t_p} \right) - \frac{1}{2} \right\}^2 - \frac{1}{12} \right) \right] \quad (2.19)$$

The 1st and 2nd order polynomial terms are force self-equilibrating. Note that the considered linear and non-linear weld load carrying behaviour is in agreement with the structural hot spot stress concept related (non-)linear surface extrapolation procedures. The formulations (Eq. 2.16 to 2.19) principally hold for weld root notches, replacing the structural stress σ_s and plate thickness t_p with the root equivalents σ_{sr} and t_p' . However, σ_{bw} is naturally included using the non-singular terms of Williams' asymptotic solution for the crack configuration (Eq. 2.13 to 2.15).

2.5 Structural field stress

The linearised structural field stress distribution in the cross-section at a weld toe (Fig. 2.11), in compliance with the fracture mechanics defined far field stress (Niemi, 1995; Dong, 2001), is characterised using the structural stress σ_s and structural bending stress ratio r_s :

$$\sigma_f \left(\frac{r}{t_p} \right) = \sigma_s \left\{ 1 - 2r_s \left(\frac{r}{t_p} \right) \right\} \quad \forall \quad \left\{ 0 \leq \left(\frac{r}{t_p} \right) \leq 1 \right\} \quad (2.20)$$

Loading mode-I is assumed to be dominant, since the hull structure is a stiffened (curved) panel assembly with orthotropic stiffness properties consisting of (thin) plates and shells with t_p as governing parameter, i.e. the remote mechanical or far field loading predominantly consists of a membrane and bending stress component $\{\sigma_m, \sigma_b\}$ normal to the weld seam. The structural stress σ_s can be obtained using the line forces f_m (either f_y or f_z), m_b (m_x) and plate thickness t_p (t_b or t_c):

$$\sigma_s = \sigma_m + \sigma_b \quad (2.21)$$

with

$$\sigma_m = \frac{f_m}{t_p}, \quad \sigma_b = 6 \cdot \frac{m_b}{t_p^2}$$

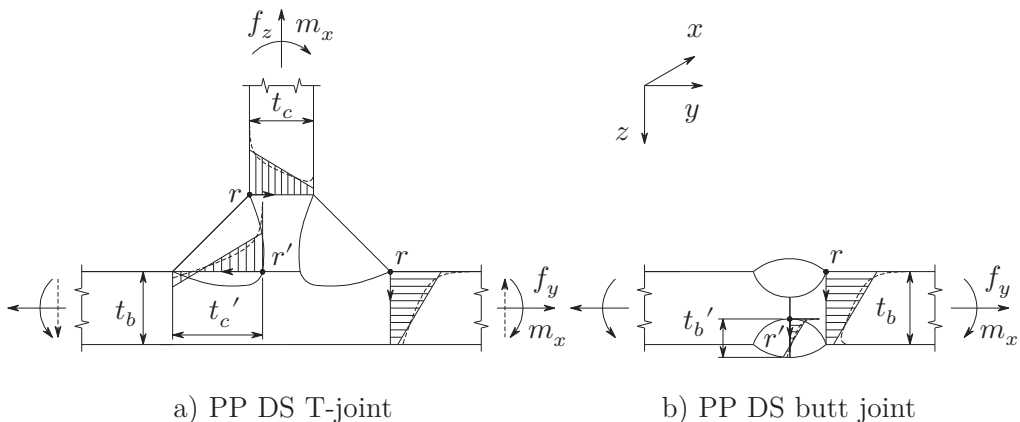


Figure 2.11: Far field load case dependent structural field (root) stress distributions.

The line forces – m_b is clockwise positive – are computed using shell FE model calculated nodal forces and corresponding element sizes. Note the x -axis is defined along the weld seam. The structural bending stress ratio ($-\infty < r_s \leq 1$) represents the relative contribution of σ_b to σ_s , i.e. the zone 3 far field stress gradient:

$$r_s = \frac{\sigma_b}{\sigma_s} \quad (2.22)$$

Rewriting $\{\sigma_m, \sigma_b\}$ in terms of σ_s (Eq. 2.21) and r_s (Eq. 2.22) yield:

$$\sigma_m = \sigma_s(1 - r_s) \quad (2.23)$$

$$\sigma_b = r_s \sigma_s$$

The structural field root stress distribution $\sigma_{fr}(r'/t_p')$, either along weld leg or weld throat, is far field stress dependent (Fig. 2.11). Its formulation is similar to σ_f (Eq. 2.20) replacing $\{\sigma_s, r_s\}$ with the root equivalents $\{\sigma_{sr}, r_{sr}\}$. The corresponding membrane and bending stress components $\{\sigma_{mr}, \sigma_{br}\}$ are obtained first applying equilibrium conditions to the cross-sectional nodal (line) forces: coarse (9 node Lagrange element) meshed parametric solid plane strain FE model solutions.

2.6 Weld toe notch stress distribution

The remote mechanical loading controlled mode-I based linear elastic through-thickness notch stress distribution at the weld toe (Fig. 2.12) – along the expected (2D) crack path – is assumed to be a linear superposition of an equilibrium equivalent stress part (the linear structural field stress, equal to the welded joint global far field stress; Paragraph 2.5) governing in zone 3 and a self-equilibrating stress part (the weld geometry stress consisting of the local non-linear notch stress- and weld load carrying stress components; Paragraph 2.3 and 2.4) dominating zone $\{1, 2\}$. It is a refinement of a well-known definition (Niemi, 1995; den Besten and Huijsmans, 2010).

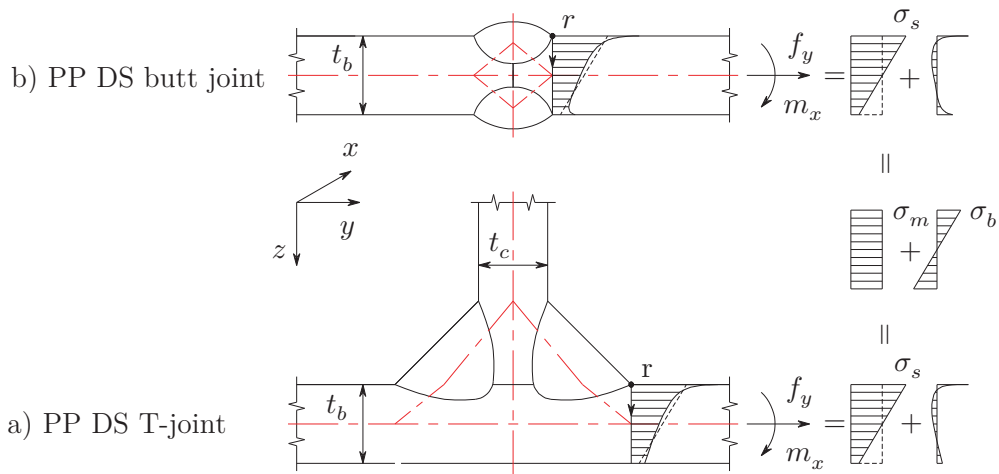


Figure 2.12: Weld toe notch stress distributions at location 1.

The expected crack path is in agreement with experimental observations, as shown for a FP DS T-joint ($\rho > 0$; Fig. 2.13b) obtained using digital image correlation based crack growth measurements (Chapter 4) and turns out to be similar to a predicted one (Fig. 2.13a) captured using FRANC2D crack growth modelling software (Cornell Fracture Group, 2010). Note that for simulations only the cyclic remote mechanical loading has been taken into account; experiments include the welding process induced quasi-constant residual stress contribution as well.

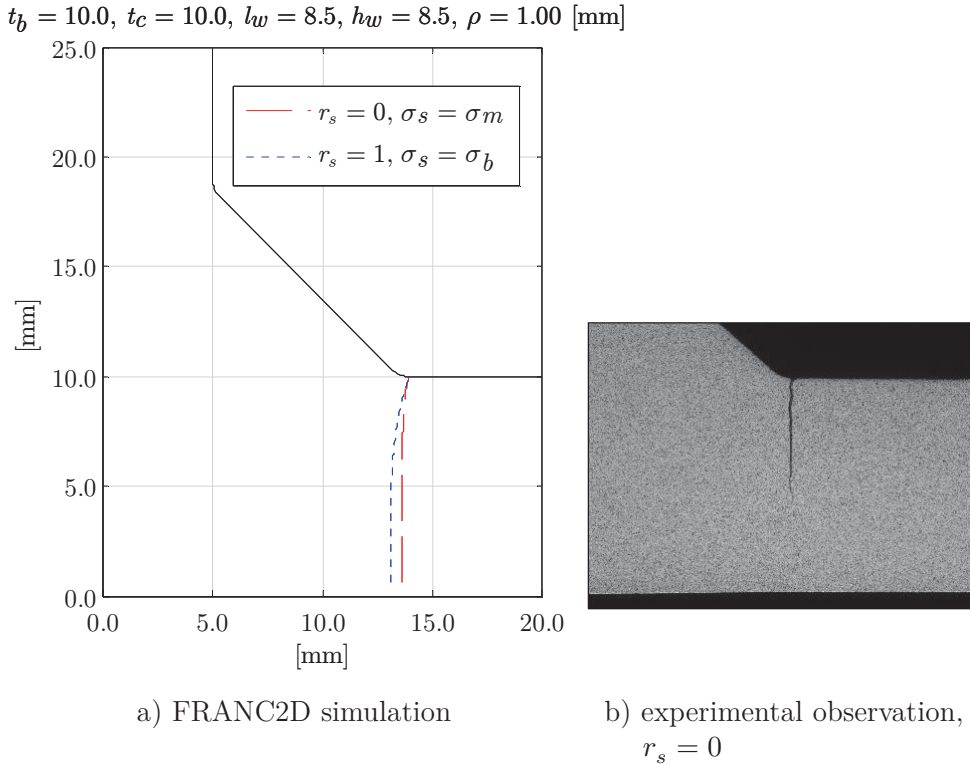


Figure 2.13: FP DS T-joint weld toe crack path similarity.

Given the notch location, (geometric) non-symmetry and symmetry with respect to $(t_p/2)$ can be distinguished. To involve the weld type classification criteria, both the fillet weld- (PP DS and SS T-joint, DS cover plate, PP DS cruciform joint) and groove weld geometry (PP DS butt joint) will be used for illustration purposes.

2.6.1 Non-symmetry

The weld notch stress distribution for the non-symmetry case has been obtained employing the weld flank angle induced tangential notch stress component $\sigma_{\theta\theta}$ (Eq. 2.10), the weld load carrying stress σ_{bw} (Eq. 2.16 – shown – or 2.18) and structural field stress formulation σ_f (Eq. 2.20):

$$\begin{aligned}
\sigma_n \left(\frac{r}{t_p} \right) = \sigma_s \left[\left(\frac{r}{t_p} \right)^{\lambda_s - 1} \mu_s \lambda_s (\lambda_s + 1) [\cos\{(\lambda_s + 1)\beta\} - \right. \\
\left. \chi_s \cos\{(\lambda_s - 1)\beta\}] + \right. \\
\left. \left(\frac{r}{t_p} \right)^{\lambda_a - 1} \mu_a \lambda_a (\lambda_a + 1) [\sin\{(\lambda_a + 1)\beta\} - \right. \\
\left. \chi_a \sin\{(\lambda_a - 1)\beta\}] + \right. \\
\left. C_{bw} \left\{ 2 \left(\frac{r}{t_p} \right) - 1 \right\} - 2r_s \left(\frac{r}{t_p} \right) \right]
\end{aligned} \tag{2.24}$$

Although principally the V-shaped normal notch stress component in Cartesian coordinates is required, a transformation does not affect the formulation: $\sigma_{yy} = \sigma_{rr} \cos^2(\beta) + \sigma_{\theta\theta} \sin^2(\beta) - \sigma_{r\theta} \sin(\beta) \cos(\beta) = \mu_s' (r/t_p)^{\lambda_s - 1} + \mu_a' (r/t_p)^{\lambda_a - 1}$ and $\sigma_{\theta\theta}$ has been used. The symmetric as well as anti-symmetric $\sigma_{\theta\theta}$ terms are incorporated, i.e. both loading mode- $\{I, II\}$ are involved since the local stress state is multi-axial by definition. The (unit) weld geometry stress, the self-equilibrating stress part + 1, is scaled and projected – using σ_s and r_s – onto the structural field stress. For $r_s > 0$ the weld notch stress distribution will be monotonic; in case $r_s \leq 0$ non-monotonic. The amplitudes $\{\mu_s, \mu_a\}$ will be determined using force and moment equilibrium (boundary) conditions in a weak form (Eq. 2.25), meaning σ_n (Eq. 2.24) is the same for both plane $\{\text{stress, strain}\}$ structural response conditions, since all boundary conditions are expressed in terms of tractions (i.e. free surface and far field stress) rather than displacements. If the compatibility equation is expressed in terms of the stress function φ , the Young's modulus E and Poisson ratio ν appear in every term, meaning the stress field for the considered simply connected elastic body is independent of material properties (Barber, 2002).

$$\begin{aligned}
\int_0^1 \left\{ \sigma_n \left(\frac{r}{t_p} \right) \right\} d \left(\frac{r}{t_p} \right) &= \int_0^1 \sigma_s \left\{ 1 - 2r_s \left(\frac{r}{t_p} \right) \right\} d \left(\frac{r}{t_p} \right) \\
\int_0^1 \left\{ \sigma_n \left(\frac{r}{t_p} \right) \right\} \left(\frac{r}{t_p} \right) d \left(\frac{r}{t_p} \right) &= \int_0^1 \sigma_s \left\{ 1 - 2r_s \left(\frac{r}{t_p} \right) \right\} \left(\frac{r}{t_p} \right) d \left(\frac{r}{t_p} \right)
\end{aligned} \tag{2.25}$$

Executing the integral operators yield:

$$\begin{bmatrix} C_{11} & C_{12} \\ C_{21} & C_{22} \end{bmatrix} \begin{Bmatrix} \mu_s \\ \mu_a \end{Bmatrix} = \begin{Bmatrix} F_1 \\ F_2 \end{Bmatrix} \tag{2.26}$$

with

$$C_{11} = (\lambda_s + 1)[\cos\{(\lambda_s + 1)\beta\} - \chi_s \cos\{(\lambda_s - 1)\beta\}]$$

$$C_{12} = (\lambda_a + 1)[\sin\{(\lambda_a + 1)\beta\} - \chi_a \sin\{(\lambda_a - 1)\beta\}]$$

$$C_{21} = \lambda_s[\cos\{(\lambda_s + 1)\beta\} - \chi_s \cos\{(\lambda_s - 1)\beta\}]$$

$$C_{22} = \lambda_a[\sin\{(\lambda_a + 1)\beta\} - \chi_a \sin\{(\lambda_a - 1)\beta\}]$$

$$F_1 = 1$$

$$F_2 = \left(\frac{1}{2} - \frac{C_{bw}}{6}\right)$$

Solving the system (Eq. 2.26) denote:

$$\mu_s = \frac{C_{bw}(\lambda_a + 1) + 3(\lambda_a - 1)}{6(\lambda_a - \lambda_s)[\cos\{(\lambda_s + 1)\beta\} - \chi_s \cos\{(\lambda_s - 1)\beta\}]} \quad (2.27)$$

$$\mu_a = -\frac{C_{bw}(\lambda_s + 1) + 3(\lambda_s - 1)}{6(\lambda_a - \lambda_s)[\sin\{(\lambda_a + 1)\beta\} - \chi_a \sin\{(\lambda_a - 1)\beta\}]}$$

Note that σ_n (Eq. 2.24) becomes β independent. The weld load carrying (bending) stress $\sigma_s C_{bw}$ is assumed to be a linear superposition of a structural field membrane and bending stress induced component:

$$\begin{aligned} \sigma_s C_{bw} &= \sigma_m C_{bm} + \sigma_b C_{bb} \\ &= \sigma_s \{C_{bm} - r_s (C_{bm} - C_{bb})\} \end{aligned} \quad (2.28)$$

with

$$C_{bm} = \frac{m_{bm} \left(\frac{6}{t_p}\right)}{\sigma_s (1 - r_s)}, \quad C_{bb} = \frac{m_{bb} \left(\frac{6}{t_p}\right)}{\sigma_s r_s}$$

The bending moments $\{m_{bm}, m_{bb}\}$ are the calculated FE beam model nodal forces at the weld toe cross-section as shown for a PP DS T-joint (Fig. 2.14). Note that only weld toe notch locations 1 and 2 show non-symmetry with respect to $(t_p/2)$. The cross plate element thickness in between the welds is reduced to $t_c - 2a_n$. For relatively small weld dimensions, rigid connections (dashed lines) are introduced. The notch angle α and stress angle β in terms of the fillet weld leg length l_w and weld leg height h_w denote respectively:

$$\alpha = \frac{1}{2} \left\{ \pi + \arctan \left(\frac{h_w}{l_w} \right) \right\} \quad (2.29)$$

$$\beta = \alpha - \frac{\pi}{2} \quad (2.30)$$

The weld element thickness t_w equals the throat size:

$$t_w = l_w \sin(\pi + 2\alpha) \quad (2.31)$$

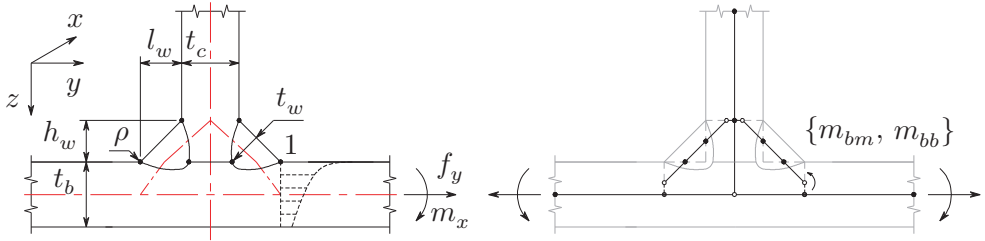


Figure 2.14: a) PP DS T-joint parameters, b) notch loc. 1 FE beam model.

Monotonic through-thickness weld toe notch stress distributions at location 1 are shown (Fig. 2.15 and 2.16) for a pure bending ($r_s = 1$) and combined load case ($r_s = 1/3$); the bending moment is applied clockwise. Non-monotonic ones are shown for a pure membrane ($r_s = 0$) and (different) combined load case ($r_s = -1$) with counter-clockwise bending moment (Fig. 2.17 and 2.18). The joint dimensions are arbitrary but realistic for aluminium high-speed craft.

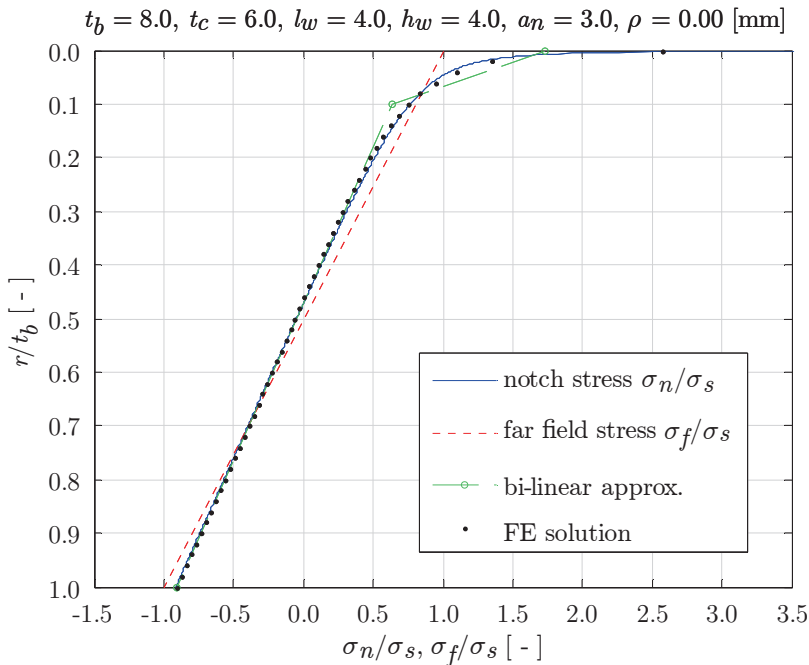


Figure 2.15: PP DS T-joint weld notch stress distr. (loc. 1), $r_s = 1$.

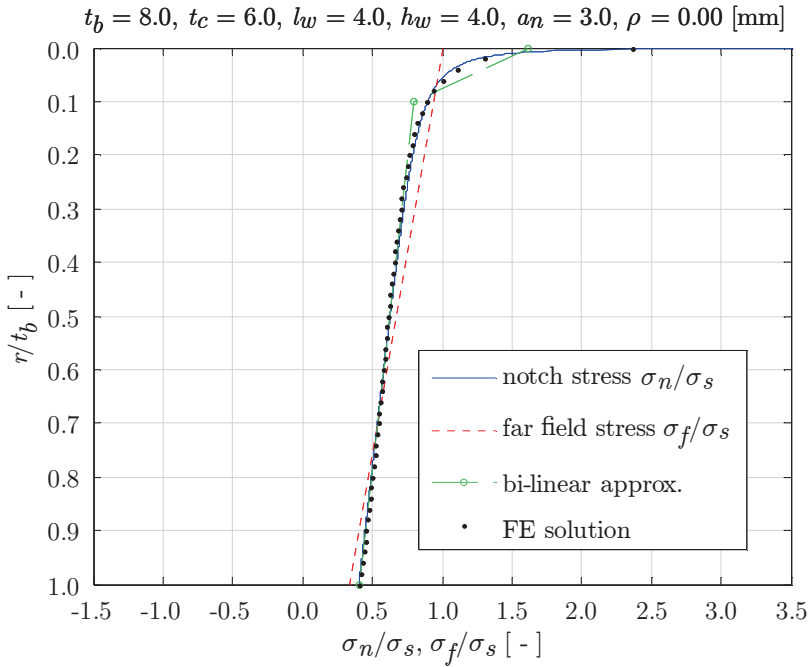


Figure 2.16: PP DS T-joint weld toe notch stress distr. (loc. 1), $r_s = (1/3)$.

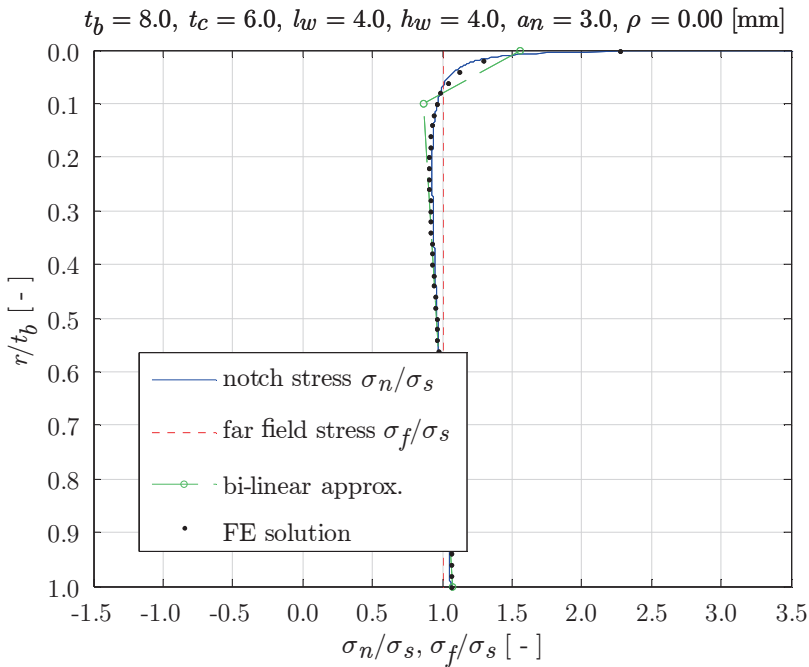


Figure 2.17: PP DS T-joint weld toe notch stress distr. (loc. 1), $r_s = 0$.

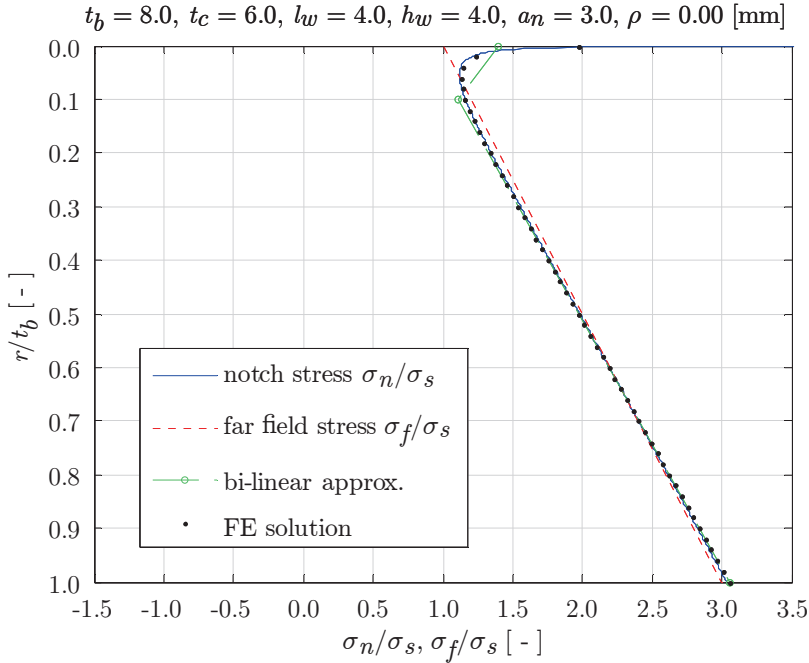


Figure 2.18: PP DS T-joint weld toe notch stress distr. (loc. 1), $r_s = -1$.

Comparing the weld toe notch stress- and far field stress distribution indicates that equilibrium is satisfied indeed. Converged solid FE solutions at node locations (Gauss point extrapolations) – rather good σ_n estimates – are displayed for convenience using dots to represent its discrete nature rather than mesh size; data points in between are disregarded in favour of a clear plot.

Generally speaking, the weld geometry contribution – the self-equilibrating stress part, assumed to be important for crack initiation at the considered notch location – decreases for $(r/t_b) \rightarrow 0.1$ in case the weld load carrying level is low, explaining why a bi-linear approximation σ_{nb} has been introduced (Dong, Hong and Cao, 2003); an important element of the Battelle structural stress (BSS) concept. The transition depth r_t for through-thickness stress distributions and non-symmetry with respect to $(t_p/2)$ is defined at 10 [%] of the plate thickness, i.e. $0.1t_p$ relative to the notch; a scaling criterion distinguishing a notch- and far field dominated stress part. Note that it seems to be a better approximation for a monotonic notch stress distribution than for a non-monotonic one. The bi-linear formulation is obtained using solid FE model solutions (either nodal forces or stresses), equilibrium conditions and a traction continuity requirement. The stress at the weld toe is finite, even for $\rho = 0$; the singular case. It should be emphasised that, rather than estimating the (structural) hot spot stress, i.e. the stress at the weld toe ($r/t_b = 0$) without weld geometry effects; quite often subject to an incorrect interpretation (Poutiainen, Tanskanen and Marquis, 2004a; Radaj, Sonsino and Fricke, 2006), the bi-linear formulation is meant to obtain the fracture mechanics

related notch stress intensity. For the same reason, the weld toe notch stress distribution σ_n (Eq. 2.24) with the characteristic singularity for ($\rho = 0$) is formulated, however, without solid FE modelling, transition depth assumption and compromised zone 2 stress gradient.

To get an idea about the weld load carrying (bending) stress contribution, $\sigma_n(r/t_p)$ is shown (Fig. 2.19 and 2.20) with and without C_{bw} term for respectively a monotonic ($r_s = 1$) and non-monotonic case ($r_s = 0$). Like for all continuous (base) plate related weld notch stress distributions at location 1, the notch angle component $\sigma_{\theta\theta}(r/t_b)$ dominates the self-equilibrating stress part:

$$\sigma_{se} = \sigma_n \left(\frac{r}{t_p} \right) - \sigma_f \left(\frac{r}{t_p} \right) \quad (2.32)$$

The σ_{bw} component is quite small and will increase slightly for increasing weld dimensions $\{l_w, h_w\}$; a_n sensitivity is negligible. Although small, neglecting this term is considered to be no option at the moment as it eliminates a welded joint and notch specific stress component.

The far field bending induced C_{bw} contribution turns out to be larger in comparison to the far field membrane case as expected, since the weld is more effective in the neutral axis shift induced stress redistribution. For decreasing notch affected zone size, C_{bw} sensitivity will increase even if the weld load carrying stress σ_{bw} is relative small.

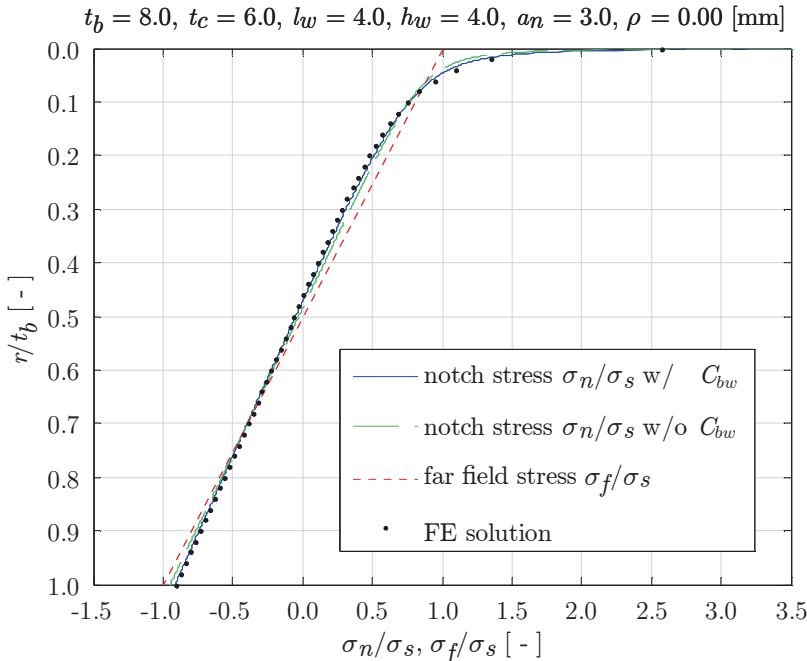


Figure 2.19: PP DS T-joint loc. 1 C_{bw} contribution to $\sigma_n(r/t_b)$, $r_s = 1$.

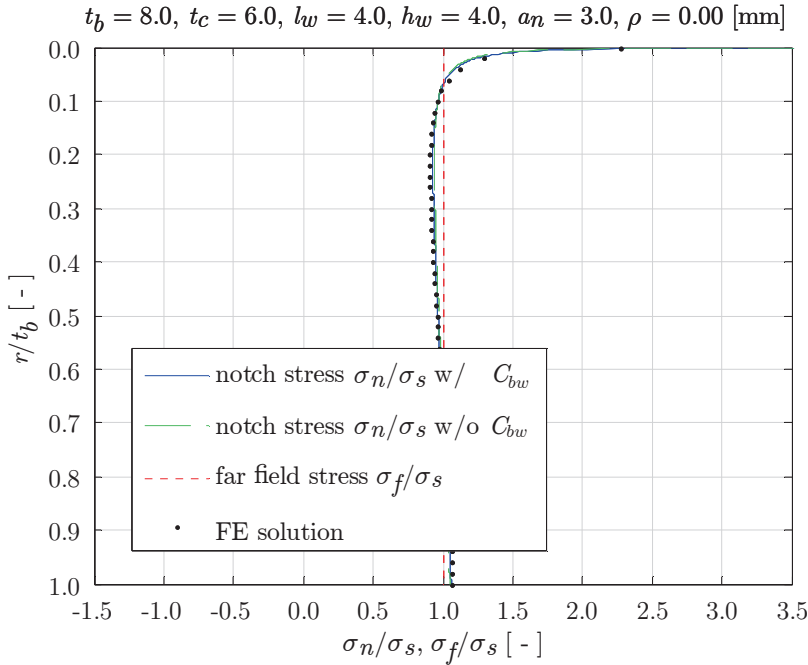


Figure 2.20: PP DS T-joint loc. 1 C_{bw} contribution to $\sigma_n(r/t_b)$, $r_s = 0$.

For a discontinuous (cross) plate related weld toe notch like location 2 of a PP SS T-joint (Fig. 2.21) in loading mode-I, the weld load carrying force increases and the stress distribution will be inaccurate if only the 1st order σ_{bw} component is included. Adding the 2nd order term (Eq. 2.18) to the weld notch stress formulation (Eq. 2.24) does not affect the system (Eq. 2.26) and $\{\mu_s, \mu_a\}$ remain unchanged.

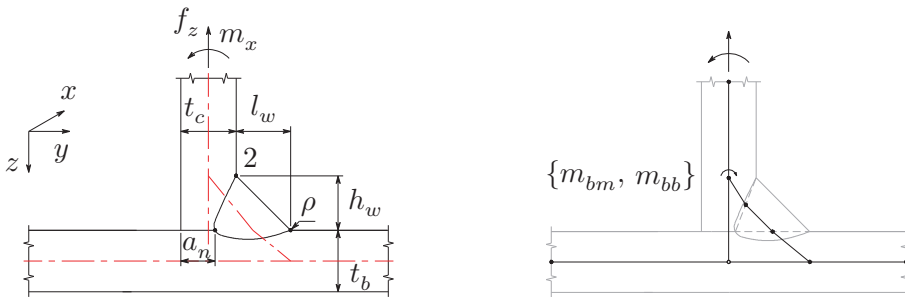


Figure 2.21: a) PP SS T-joint parameters, b) notch loc. 2 FE beam model.

The FE beam model nodal forces ($\{m_{bm}, m_{bb}\}$; Fig. 2.21) have been used to approximate both the 1st and 2nd order term. For decreasing weld dimensions, rigid connections will be introduced, like for the DS T-joint (Fig. 2.14) with decreasing $\{l_w, h_w\}$. The cross plate element thickness at the weld is equal to $(t_c - a_n)$.

However, even if a weld is significantly load carrying, it does not necessarily mean that the notch affected zone size increases. If C_{bw} becomes negative, i.e. counteracts the far field stress like for location 2 of the PP- SS T-joint (Fig. 2.22), the notch affected zone size may significantly reduce and the stress state even turn into a compressive one.

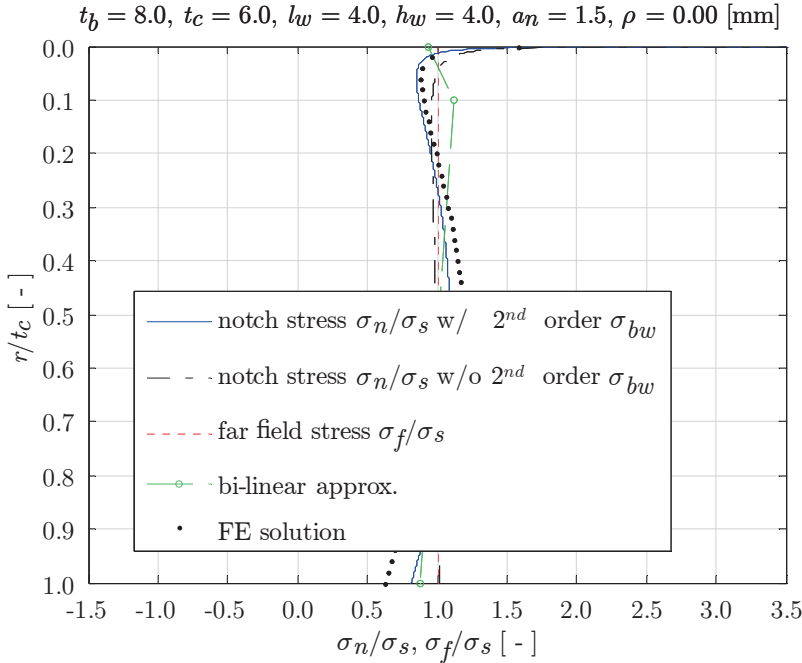


Figure 2.22: PP SS T-joint weld toe notch stress distr. (loc. 2), $r_s = 0$.

In comparison to the FE solution, the 2nd order σ_{bw} term improves the notch stress distribution (Fig. 2.22), especially the stress gradient. At the same time however, $\sigma_n(r/t_p)$ is running up against the model limits in this particular case, i.e. the number of contributing stress components is restricted and boundary conditions are satisfied using a weak formulation. The bi-linear approximation already has passed the limits. Non-monotonic distributions $\sigma_n(r/t_p)$ require particular attention in that respect.

2.6.2 Symmetry

Weld toe notches appear at both sides of a plate if stress distribution symmetry with respect to $(t_p/2)$ is detected, as shown for a PP DS butt joint (Fig. 2.23). The weld geometry related self-equilibrating stress part components $\{\sigma_{\theta\theta}, \sigma_{bw}\}$, assumed to be important for crack initiation at the considered notch location only, will be ignored for the symmetry part. For a pure far field membrane load case, ($\sigma_s = \sigma_m$) and ($C_{bw} = C_{bm}$), the notch stress formulation with 1st order weld load carrying stress (Eq. 2.17) becomes:

$$\begin{aligned}
\sigma_{nm} \left(\frac{r}{t_p} \right) &= \sigma_s \cdot f \left(\frac{r}{t_p} \right) \tag{2.33} \\
&= \sigma_s \cdot \left[\left(\frac{r}{t_p} \right)^{\lambda_s - 1} \mu_s \lambda_s (\lambda_s + 1) [\cos\{(\lambda_s + 1)\beta\} - \right. \\
&\quad \left. \chi_s \cos\{(\lambda_s - 1)\beta\}] + \right. \\
&\quad \left. \left(\frac{r}{t_p} \right)^{\lambda_a - 1} \mu_a \lambda_a (\lambda_a + 1) [\sin\{(\lambda_a + 1)\beta\} - \right. \\
&\quad \left. \chi_a \sin\{(\lambda_a - 1)\beta\}] + \right. \\
&\quad \left. C_{bw} \left\{ 4 \left(\frac{r}{t_p} \right) - 1 \right\} \right] \vee \left\{ 0 \leq \left(\frac{r}{t_p} \right) \leq 1 \right\}
\end{aligned}$$

It is assumed that no σ_{bw} correction is required for $\{1/2 < (r/t_p) \leq 1\}$ since the far field stress component dominates this region.

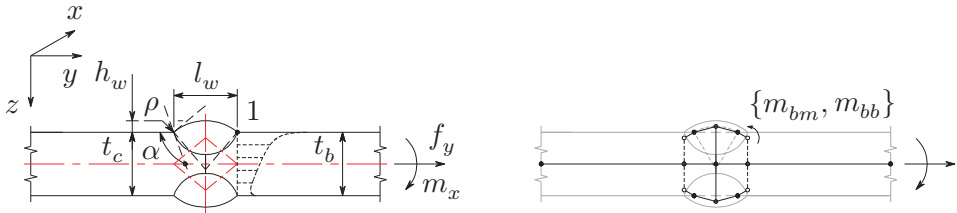


Figure 2.23: a) PP DS butt joint parameters, b) notch loc. 1 FE beam model.

To calculate $\{\mu_s, \mu_a\}$, half the plate thickness is considered. Using force and moment equilibrium only is not sufficient and a symmetry condition is added as 3rd equation:

$$\begin{aligned}
\int_0^{\frac{1}{2}} \left\{ \sigma_{nm} \left(\frac{r}{t_p} \right) \right\} d \left(\frac{r}{t_p} \right) &= \int_0^{\frac{1}{2}} \sigma_s d \left(\frac{r}{t_p} \right) \\
\int_0^{\frac{1}{2}} \left\{ \sigma_{nm} \left(\frac{r}{t_p} \right) \right\} \left(\frac{r}{t_p} \right) d \left(\frac{r}{t_p} \right) &= \int_0^{\frac{1}{2}} \sigma_s \cdot \left(\frac{r}{t_p} \right) d \left(\frac{r}{t_p} \right) \tag{2.34} \\
\frac{d\sigma_{nm} \left(\frac{r}{t_p} \right)}{d \left(\frac{r}{t_p} \right)} \bigg|_{\left(\frac{r}{t_p} \right) = \left(\frac{1}{2} \right)} &= 0
\end{aligned}$$

Executing the integral operators yield:

$$\begin{bmatrix} C_{11} & C_{12} \\ C_{21} & C_{22} \\ C_{31} & C_{32} \end{bmatrix} \begin{Bmatrix} \mu_s \\ \mu_a \end{Bmatrix} = \begin{Bmatrix} F_1 \\ F_2 \\ F_3 \end{Bmatrix} \quad (2.35)$$

with

$$C_{11} = \left(\frac{1}{2}\right)^{\lambda_s} (\lambda_s + 1) [\cos\{(\lambda_s + 1)\beta\} - \chi_s \cos\{(\lambda_s - 1)\beta\}]$$

$$C_{12} = \left(\frac{1}{2}\right)^{\lambda_a} (\lambda_a + 1) [\sin\{(\lambda_a + 1)\beta\} - \chi_a \sin\{(\lambda_a - 1)\beta\}]$$

$$C_{21} = \left(\frac{1}{2}\right)^{\lambda_s+1} \lambda_s [\cos\{(\lambda_s + 1)\beta\} - \chi_s \cos\{(\lambda_s - 1)\beta\}]$$

$$C_{22} = \left(\frac{1}{2}\right)^{\lambda_a+1} \lambda_a [\sin\{(\lambda_a + 1)\beta\} - \chi_a \sin\{(\lambda_a - 1)\beta\}]$$

$$C_{31} = \left(\frac{1}{2}\right)^{\lambda_s-2} \lambda_s (\lambda_s + 1) (\lambda_s - 1) \cdot$$

$$[\cos\{(\lambda_s + 1)\beta\} - \chi_s \cos\{(\lambda_s - 1)\beta\}]$$

$$C_{32} = \left(\frac{1}{2}\right)^{\lambda_a-2} \lambda_a (\lambda_a + 1) (\lambda_a - 1) \cdot$$

$$[\sin\{(\lambda_a + 1)\beta\} - \chi_a \sin\{(\lambda_a - 1)\beta\}]$$

$$F_1 = \frac{1}{2}$$

$$F_2 = \frac{1}{8} - \frac{C_{bw}}{24}$$

$$F_3 = -4C_{bw}$$

For the (over determined) system (Eq. 2.35) a least squares solution can be obtained. However, it has been found that allowing some relaxation, ignoring moment equilibrium, already show quite accurate results. Solving the reduced system provides:

$$\begin{aligned} \mu_s &= \frac{\left(\frac{1}{2}\right) \lambda_a (\lambda_a - 1) + C_{bw}}{C_s [\cos\{(\lambda_s + 1)\beta\} - \chi_s \cos\{(\lambda_s - 1)\beta\}]} \\ \mu_a &= -\frac{\left(\frac{1}{2}\right) \lambda_s (\lambda_s - 1) + C_{bw}}{C_a [\sin\{(\lambda_a + 1)\beta\} - \chi_a \sin\{(\lambda_a - 1)\beta\}]} \end{aligned} \quad (2.36)$$

with

$$C_s = \left(\frac{1}{2}\right)^{\lambda_s} (\lambda_s + 1) \{\lambda_a(\lambda_a - 1) - \lambda_s(\lambda_s - 1)\}$$

$$C_a = \left(\frac{1}{2}\right)^{\lambda_a} (\lambda_a + 1) \{\lambda_a(\lambda_a - 1) - \lambda_s(\lambda_s - 1)\}$$

To acquire the pure bending notch stress distribution $\sigma_{nb}(r/t_p | \sigma_s = \sigma_b, C_{bw} = C_{bb})$ in a similar formulation as for non-symmetry (Eq. 2.24), i.e. including a far field bending stress projection, $\sigma_{nm}(r/t_p)$ needs to be shifted first by $\{1 - f(r/t_p = 1/2)\}$ in order to meet the condition $\sigma_{nb}(r/t_p = 1/2) = 0$. To satisfy anti-symmetry, the σ_{nb} gradient at $(r/t_p = 1/2)$ should be equal to the far field bending value -2. Subtracting the shift in terms of a bending stress gradient $-2\{1 - f(r/t_p = 1/2)\}$ from the unit stress 1, the obtained formulation needs to be scaled according to $\{2f(r/t_p = 1/2) - 1\}$ and becomes:

$$\sigma_{nb} \left(\frac{r}{t_p} \right) = \sigma_s \left\{ 2f \left(\frac{r}{t_p} = \frac{1}{2} \right) - 1 \right\} \cdot \left[f \left(\frac{r}{t_p} \right) + \left\{ 1 - f \left(\frac{r}{t_p} = \frac{1}{2} \right) \right\} - 2 \left(\frac{r}{t_p} \right) \right] \quad (2.37)$$

with

$$f \left(\frac{r}{t_p} = \frac{1}{2} \right) = \frac{(\lambda_a - \lambda_s)(\lambda_s \lambda_a - 2C_{bw})}{\lambda_a(\lambda_a - 1) - \lambda_s(\lambda_s - 1)} + C_{bw} \quad (2.38)$$

Finally, adopting a linear superposition principle, the mode-I through-thickness weld toe notch stress distribution for symmetry in terms of $\{\sigma_s, r_s\}$ can be obtained using the membrane- and bending formulation (Eq. 2.33 and 2.37) and structural stress relations (Eq. 2.23):

$$\sigma_n \left(\frac{r}{t_p} \right) = \sigma_s \left(\left[1 - 2r_s \left\{ 1 - f \left(\frac{r}{t_p} = \frac{1}{2} \right) \right\} \right] f \left(\frac{r}{t_p} \right) + r_s \left\{ 2f \left(\frac{r}{t_p} = \frac{1}{2} \right) - 1 \right\} \left[\left\{ 1 - f \left(\frac{r}{t_p} = \frac{1}{2} \right) \right\} - 2 \left(\frac{r}{t_p} \right) \right] \right) \quad (2.39)$$

The PP DS butt joint groove weld (Fig 2.23a) is assumed to be arc-shaped and the notch angle α in terms of weld length l_w and weld height h_w denotes:

$$\alpha = \left(\frac{1}{2} \right) \left\{ \pi + \arctan \left(\frac{4l_w h_w}{l_w^2 - 4h_w^2} \right) \right\} \quad (2.40)$$

Stress angle β depends on α only (Eq. 2.30). The weld geometry and structural field stress affected weld load carrying stress coefficient C_{bw} (Eq. 2.28; $t_p = t_p/2$) is approximated using an FE beam model (Fig. 2.23b). Although the weld is of the PP type, the base- and connecting plate element in between the weld reinforcements are joined; thickness is reduced to $(t_b - 2a_n)$. The weld elements – thickness equal to h_w – are connected to the base plate at the weld toe using rigid connections (dashed lines); the elements in extension of the notch – thickness equal to l_w – ensure sufficient stiffness in z -direction.

Monotonic through-thickness weld toe notch stress distributions σ_n at location 1 for the far field load cases $\{r_s = 1, r_s = 1/3\}$ are shown (Fig. 2.24 and 2.25) as well as non-monotonic ones (Fig. 2.26 and 2.27); $\{r_s = 0, r_s = -1\}$. Observation of the weld toe notch stress- and far field stress distributions show that for $\{0 \leq (r/t_b) \leq (1/2)\}$ equilibrium conditions are (approximately) satisfied as imposed. The root notch size a_n is relative small and using the linear σ_{bw} component only is sufficient. For the symmetry part $\{(1/2) \leq (r/t_b) \leq 1\}$, the (anti-)symmetry condition ensures a stress gradient close to r_s ; the self-equilibrating stress part definition is lost here. The former, however, is more important from notch stress intensity point of view.

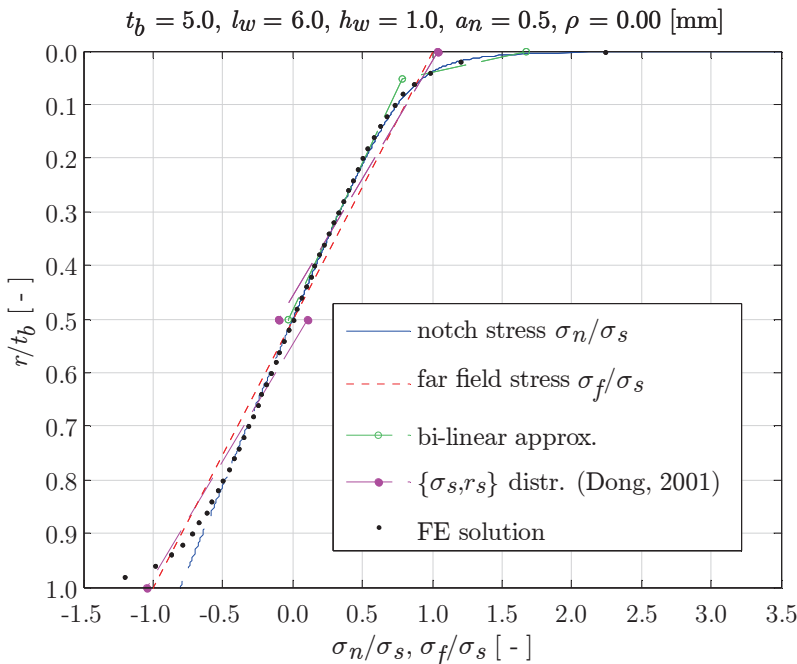


Figure 2.24: PP DS butt joint weld toe notch stress distr. (loc. 1), $r_s = 1$.

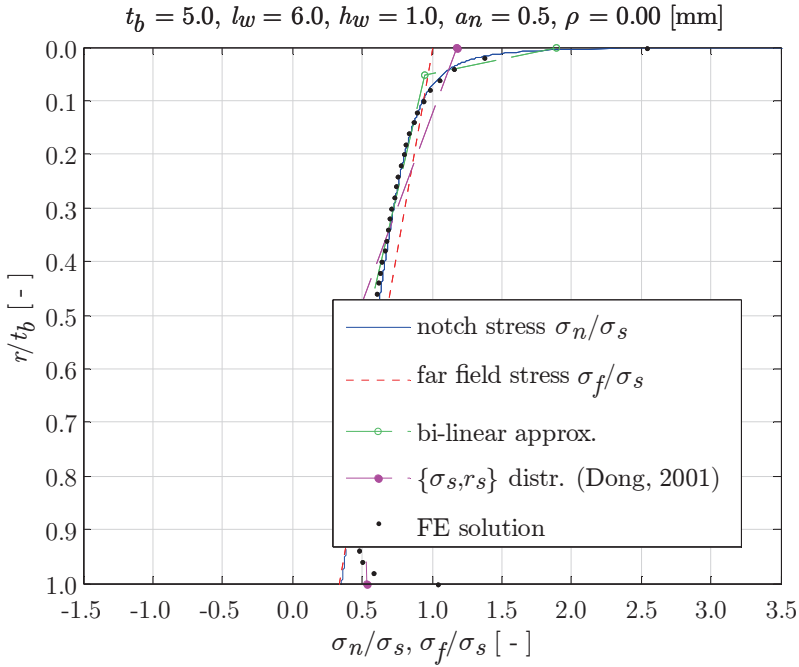


Figure 2.25: PP DS butt joint weld toe notch stress distr. (loc. 1), $r_s = (1/3)$.

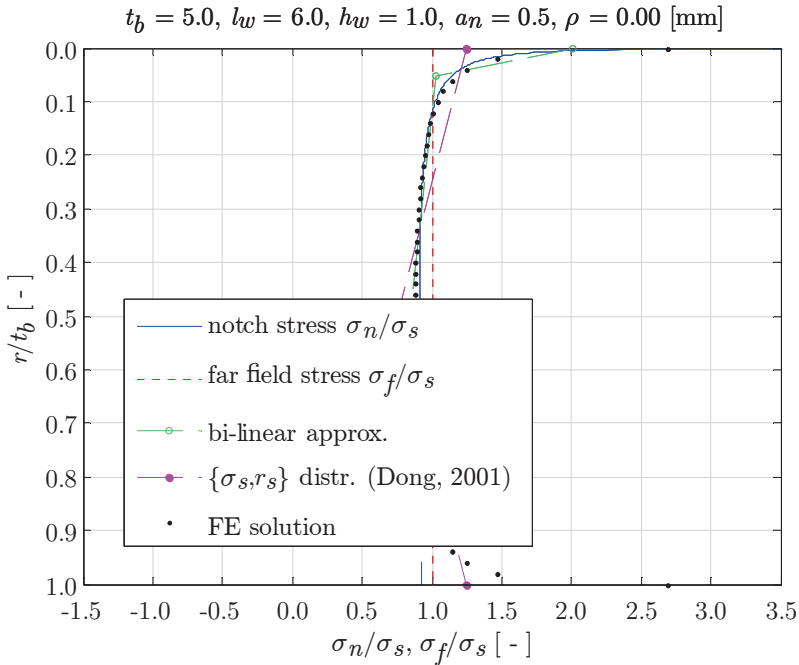


Figure 2.26: PP DS butt joint weld toe notch stress distr. (loc. 1), $r_s = 0$.

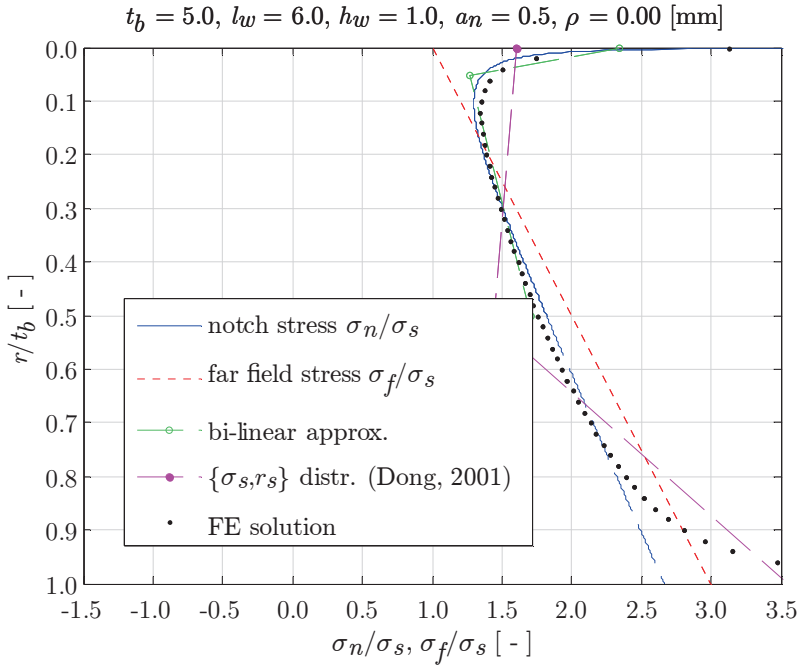


Figure 2.27: PP DS butt joint weld toe notch stress distr. (loc. 1), $r_s = -1$.

The $\{\sigma_s, r_s\}$ structural field stress distribution (Dong, 2001) as applied in the BSS concept is defined for $\{0 \leq (r/t_b) \leq (1/2)\}$ considering notch location 1 and has some serious modelling consequences. First of all, $\{\sigma_s, r_s\}$ does not comply anymore with the far field stress as defined in the fracture mechanics context. For the ($r_s = 1$) case, a reasonable $\{\sigma_s, r_s\}$ approximation can be obtained using a shell/plate FE model (Dong, 2004) as shown (Fig. 2.24), but generally speaking solid elements have to be used. Accordingly, the bi-linear approximation is defined for $\{0 \leq (r/t_b) \leq (1/2)\}$. The transition depth, distinguishing a notch and far field stress dominated region, is defined at 10 [%] of the ‘considered’ plate thickness. For symmetry cases, it is equal to $(t_p/2)$, meaning a transition depth at $0.1(t_p/2)$. The notch stress intensity that is aimed for might be rather insensitive to transition depth as long as the appropriate zone 3 far field stress gradient r_s is captured (Dong, Hong and Cao, 2003), but in comparison to the non-symmetry case at least a double standard is introduced concerning zone 2 (Fig. 2.28). Even more important: the plate thickness as scaling parameter has been used inconsistently. Comparing the self-equilibrating stress part for a DS T-joint and its symmetry equivalent (the DS cruciform joint), the stress gradient turns out to be more pronounced in the notch dominated region (zone 2) for the non-symmetry case. The bi-linear approximation shows in fact the opposite behaviour.

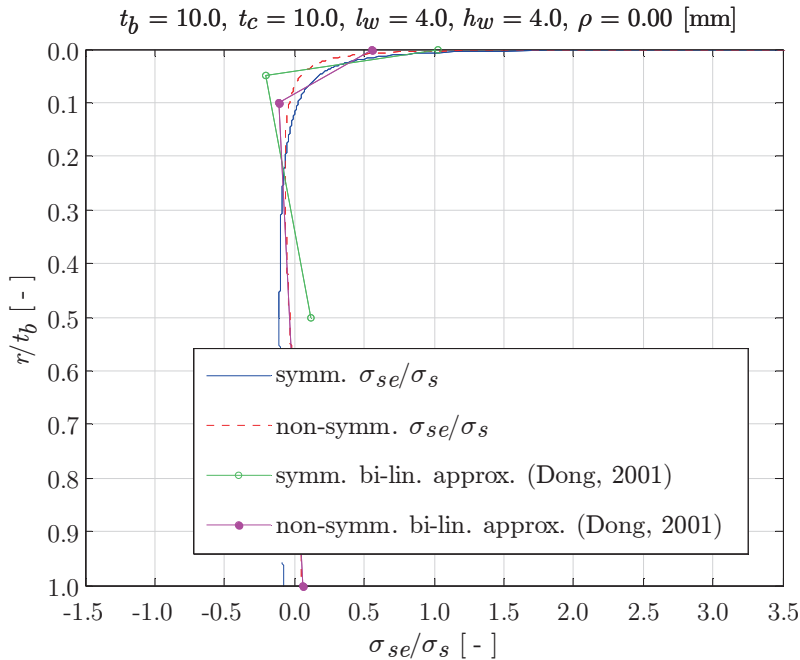


Figure 2.28: Self-equilibrating stress part comparison regarding symmetry using a PP DS T-joint and PP DS cruciform joint (loc. 1), $r_s = 0$.

Using the structural hot spot stress concept, weld geometry effects are – by definition – not considered explicitly. However, to take the load carrying effects (implicitly) into account for fillet welds, FAT classes are defined for the non-load carrying and full load carrying case, i.e. the extremes. An additional stress concentration factor (SCF) K_{sa} has been introduced (Poutiainen and Marquis, 2004b; 2006) to deal with partial load carrying fillet welds as well.

In case of symmetry with respect to $(t_p/2)$, a modified weld size dependent multi-linear through-thickness structural (field) stress distribution has been proposed, meant to obtain the additional weld load carrying induced structural stress at the hot spot; the weld toe. The average normal stress component in the weld throat cross-section as shown for a DS cover plate (Fig. 2.29a), obtained using relatively coarse meshed solid FE models, is considered to be a criterion for the level of weld load carrying effectiveness and translated to a bending stress contribution in terms of K_{sa} in the cross-section at the weld toe (Fig. 2.30). The weld load carrying affected zone is related to the weld length l_w rather than the adopted symmetry condition (Eq. 2.17), i.e. the structural field stress transitions are defined at (l_w/t_p) and $\{1 - (l_w/t_p)\}$ if $\{l_w < (t_p/2)\}$; a tri-linear formulation that turns into a bi-linear one for $\{l_w \geq (t_p/2)\}$ with the transition at $(t_p/2)$. Far field force equilibrium is maintained, meaning the plate thickness is involved as well and it is claimed that K_{sa} includes size effects since the stress gradient is involved.

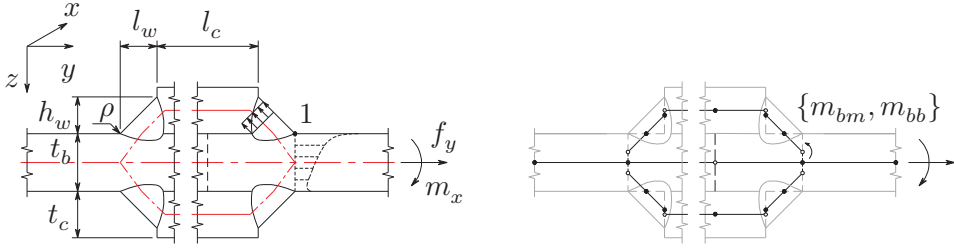


Figure 2.29: a) DS cover plate parameters, b) notch loc. 1 FE beam model

Depending on the far field load case, either one or both FE beam model cover plate centre nodes (Fig. 2.29b) are constrained in z -direction to prevent for bending induced deformation across the base plate.

For the considered example (Fig. 2.30), $K_{sa} \approx 1.34$ [-]; not really close to $(1 + C_{bw}) \approx 1.11$ [-]. In terms of weld load carrying stress the former predicts a value more than twice as large. Even if the base plate is discontinuous (Fig. 2.31), the difference persists: $K_{sa} \approx 1.74$ [-] and $(1 + C_{bw}) \approx 1.30$ [-]. Though, the normal weld stress is weld load carrying stress σ_{bw} as well as notch stress $\sigma_{\theta\theta}$ induced; after all, both are σ_{se} components representing the weld geometry effect. The notch stress, however, is not supposed to be part of the structural hot spot stress in the first place.

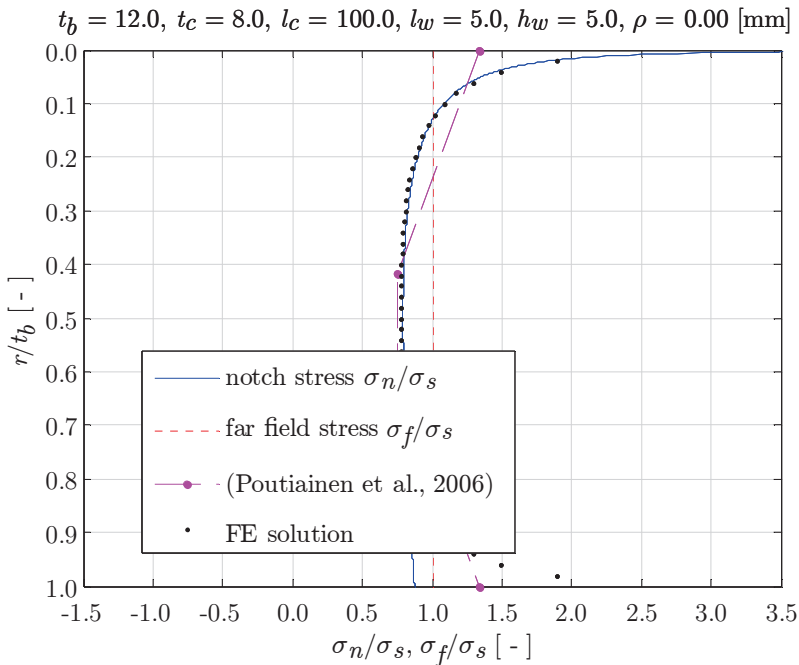


Figure 2.30: DS cover plate – continuous base plate – (loc. 1) weld toe notch stress distribution; $(1 + C_{bw}) \approx 1.11, r_s = 0$.

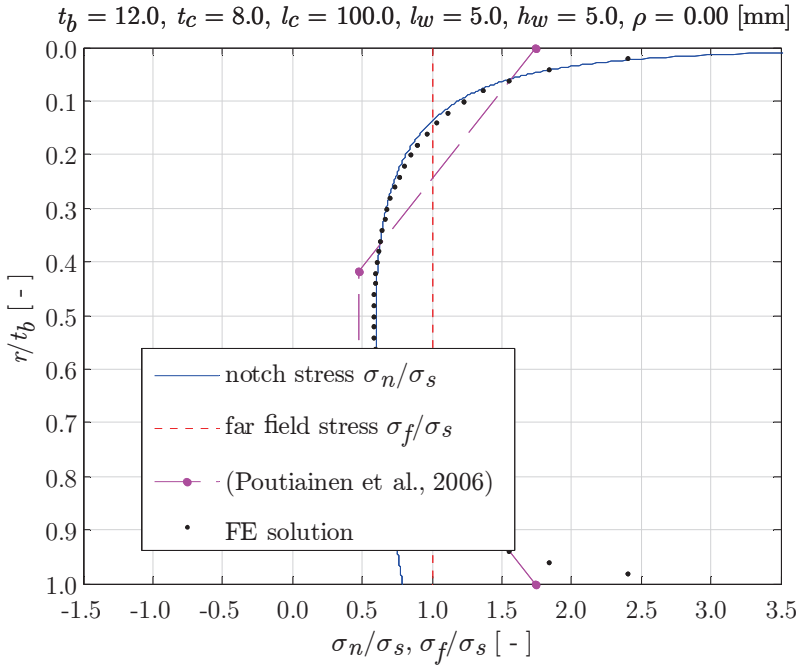


Figure 2.31: DS cover plate – discontinuous base plate – (loc. 1) weld toe notch stress distribution; $(1 + C_{bw}) \approx 1.30, r_s = 0$.

The transition depth dividing the notch affected zone and the far field dominated region is principally σ_{se} defined, i.e. includes a $\sigma_{\theta\theta}$ and σ_{bw} contribution. If artificially imposed in case of bi- or tri-linearisation assuming only weld size dependency (Poutiainen et al., 2006), turns out to be a limited measure. Adopting a plate thickness dependent criterion (Dong, Hong and Cao, 2003), i.e. $\{0.1t_p, 0.1(t_p/2)\}$ for respectively non-symmetry and symmetry w.r.t. $(t_p/2)$, seems restricted to $(\sigma_{bw} \rightarrow 0)$ cases.

The weld load carrying stress for the DS cover plate in discontinuous base plate configuration (Fig. 2.31) is quite substantial: its magnitude is approximately 30 [%] of the far field stress. Using the linear σ_{bw} term only is considered to be sufficient, although the model limit is coming closer. Generally speaking, the extremes are obtained for a cross plate related weld toe notch of a PP DS cruciform joint (Fig. 2.32). The cross plate finite element thickness in between the welds is reduced to $(t_c - 2a_n)$. Adding a nonlinear term (Fig. 2.33), $K_{sa} \approx 1.83$ [-] and $(1 + C_{bw}) \approx 1.40$ [-] using the DS cover plate dimensions.

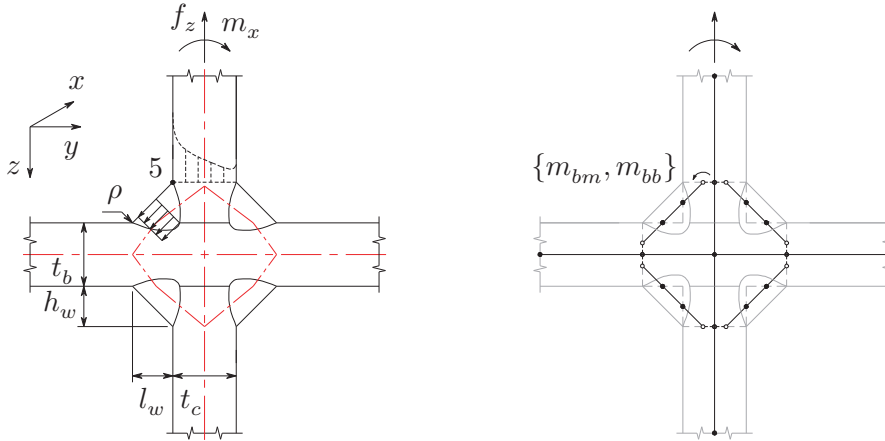


Figure 2.32: a) PP DS cruciform joint parameters, b) notch loc. 5 FE beam model

For the same joint in FP configuration ($a_n = 0$), another extreme can be found: $K_{sa} \approx 1.16$ [-] and $(1 + C_{bw}) \approx 1.01$ [-]. In terms of weld load carrying stress – using the linear term only is sufficient – the difference is about one order of magnitude and the normal weld stress is predominantly $\sigma_{\theta\theta}$ rather than σ_{bw} determined.

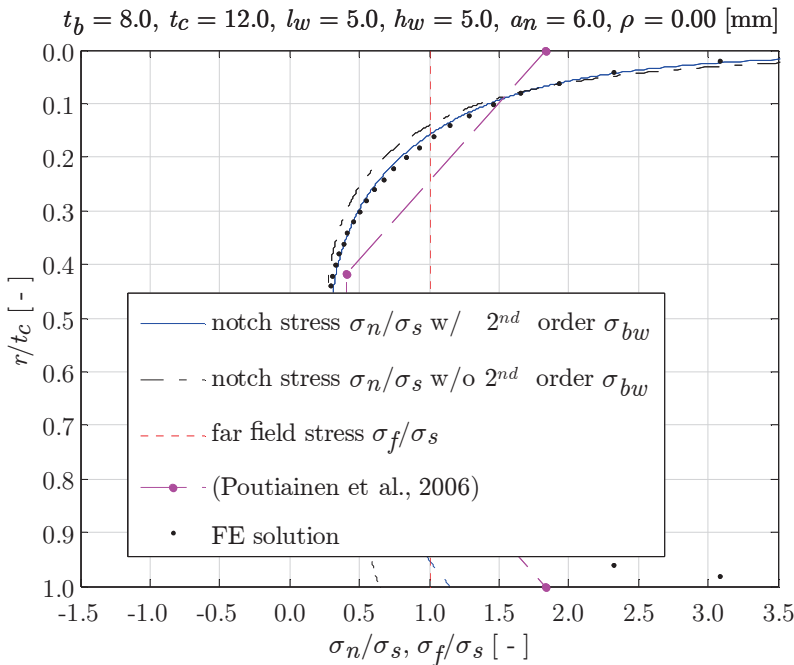


Figure 2.33: PP DS cruciform joint (loc. 5) weld toe notch stress distribution; $(1 + C_{bw}) \approx 1.40, r_s = 0$.

Adding the 2nd order term (Eq. 2.19) to the weld notch stress formulation (Eq. 2.33), the force element (Eq. 2.35) yields $F_2 = (1/8 - C_{bw}/24 + C_{bw}/32)$. Solving the corresponding system of equations, the equilibrium coefficients $\{\mu_s, \mu_a\}$ can be obtained. Note that the solutions allowing bending moment relaxation (Eq. 2.36) do not change.

2.7 Weld root notch stress distribution

For fabrication reasons, welds are only partial penetrated to a great extent and in some cases not penetrated at all, i.e. show a lack of penetration (LoP) introducing a root notch (size a_n); both notch locations, weld toe and weld root, become fatigue sensitive. In fact, fully penetrated welds may initiate fatigue cracks at both locations as well because of the welding process induced risk of a non-fused root face (LoF).

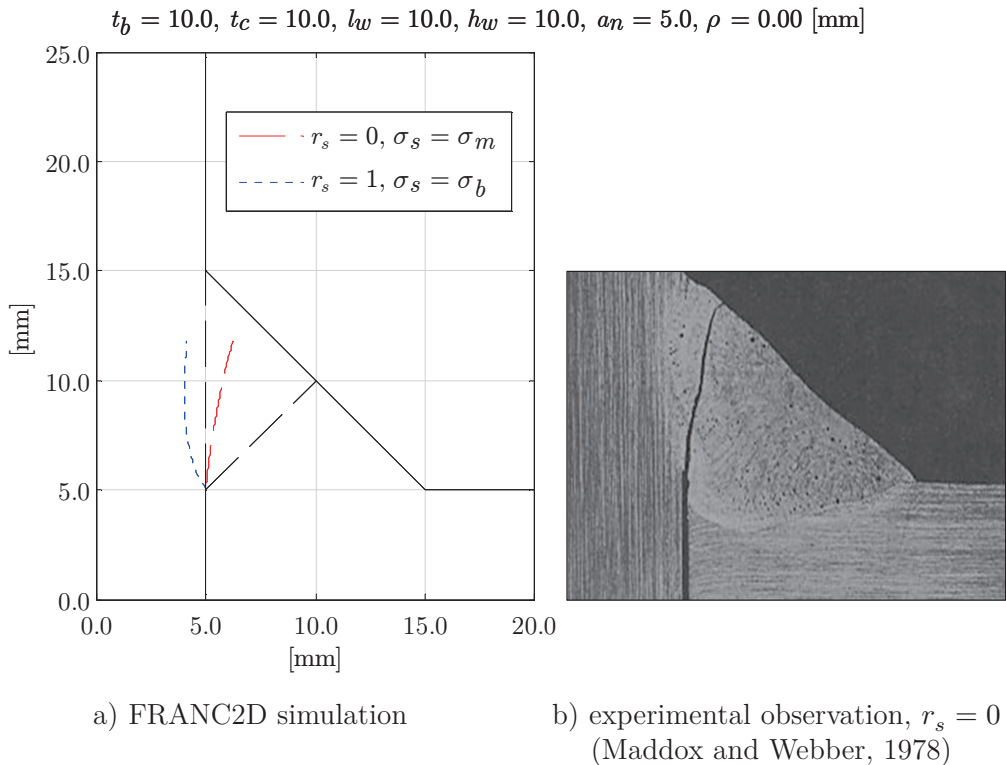


Figure 2.34: PP DS cruciform joint weld root crack path similarity.

Generally speaking, fillet weld root cracks start to grow at the notch root along the weld leg (mode-I) and continue by tearing (mode-II) through the weld throat (Frank and Fisher, 1979). Assuming that crack initiation (i.e. micro-crack growth) dominates the total fatigue life time, the weld leg section is the favourable crack path for weld root damage evaluation. Crack growth simulations show that if the (remote mechanical) far field loading predominantly consists of a membrane and

bending component, the entire crack path is closer to the weld leg section than to the weld throat (Fig. 2.34a), simply because the stress state in the weld leg section is membrane and bending dominated as well; the (average) shear stress contribution is insignificant (Fricke, Kahl and Paetzold, 2005; Fricke and Kahl, 2008; Hong, 2010). Note that an experimentally obtained crack (Fig. 2.34b), including both remote mechanical membrane loading and welding induced residual stress, has been developed similarly. In conclusion, the weld leg section is adopted as root crack path for fillet welds, associated with the $\{t_p, l_w, h_w, a_n\}$ dependent artificial plate thickness t_p' . The weld throat section is the most likely one for groove welds (Fig. 2.35a); $t_p'(t_p, h_w, a_n)$. It is loading mode-I dominated as well.

The linear superposition principle and (non-)symmetry considerations as presented for weld toe notch stress distributions hold for the weld root. However, joint symmetry with respect to $(t_p/2)$, either $(t_p = t_b)$ or $(t_p = t_c)$, does not necessarily mean that the (weld) root notch stress distributions require symmetry conditions as well (Fig. 2.35b). The only relevant geometry is the double edge notch (DEN) standard crack growth specimen (Fig. 2.35c); for the selected welded joints it is no issue.

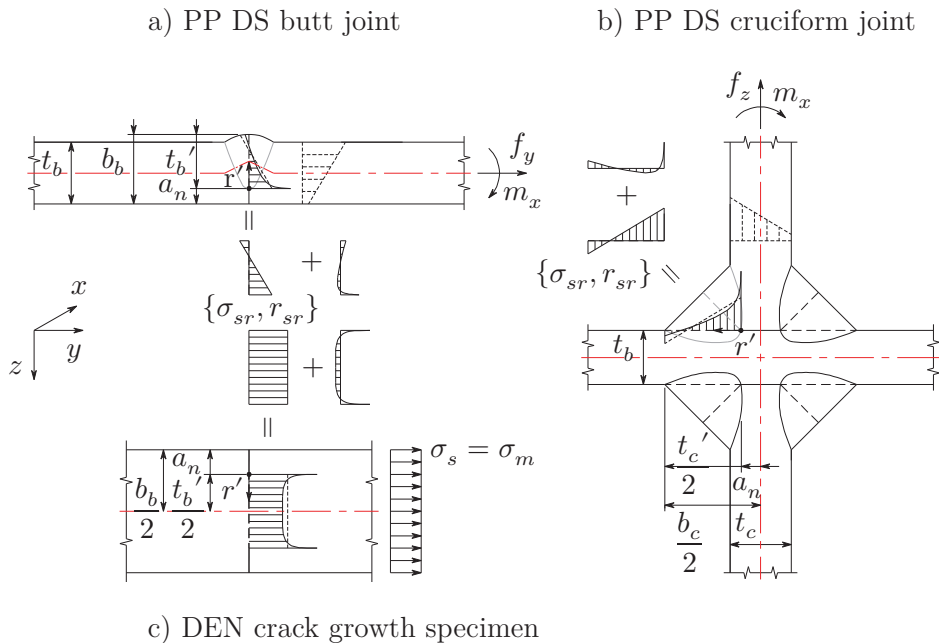


Figure 2.35: Far field stress dependent weld root notch stress distributions.

To illustrate the (weld) root notch stress formulations in case of (non-)symmetry, the PP SS butt joint, PP DS cruciform joint and DEN specimen will be used.

2.7.1 Non-symmetry

To acquire the weld root notch stress distribution $\sigma_{nr}(r'/t_p')$ in case of non-symmetry, the $\sigma_{\theta\theta}$ component of Williams' truncated solution for the crack configuration (Eq. 2.14) can be used. The number of terms included is based on engineering judgement; 5 terms have been found effective in comparison to FE solutions. The first term is the notch angle induced square root singular one; the following (non-singular) terms include the weld geometry- and root notch size induced weld load-carrying and structural root field stress contributions. For both fillet- and groove welds, the assumed root crack path is an extension of the notch a_n , meaning $\beta = 0$ for all cases and $\sigma_{\theta\theta}$ (Eq. 2.14) reduces to:

$$\begin{aligned} \sigma_{nr} \left(\frac{r'}{t_p'} \right) &= \sigma_{\theta\theta} \left(\frac{r'}{t_p'} \right) \\ &\approx \sigma_{sr} \sum_{i=1}^5 \left\{ \left(\frac{r'}{t_p'} \right)^{\lambda_i-1} \mu_i \lambda_i (\lambda_i + 1) (1 - \chi_i) \right\} \end{aligned} \quad (2.41)$$

The coefficients ($\mu_i = \mu_{1i}$) will be determined using equilibrium conditions as well as (strong) constraints. The former requires the structural root field stress distribution $\sigma_{fr}(r'/t_p')$; the equilibrium equivalent stress part, characterised by $\{\sigma_{sr}, r_{sr}\}$ and obtained using the nodal forces along the assumed root crack path of a coarse (9 node Lagrange element) meshed parametric solid plane strain FE model. Applied loading is the far field stress distribution. The latter uses three stress points $\sigma_{nr(i)}(r'_{(i)}/t_p')$ determined with the same FE model. The system of equations to be solved yield:

$$\begin{bmatrix} C_{11} & \cdots & C_{15} \\ \vdots & \ddots & \vdots \\ C_{51} & \cdots & C_{55} \end{bmatrix} \begin{Bmatrix} \mu_1 \\ \vdots \\ \mu_5 \end{Bmatrix} = \begin{Bmatrix} F_1 \\ \vdots \\ F_5 \end{Bmatrix} \quad (2.42)$$

with:

$$\begin{aligned} C_{1i} &= (\lambda_i + 1)(1 - \chi_i) & F_1 &= 1 - r_{sr} \\ C_{2i} &= \lambda_i(1 - \chi_i) & F_2 &= \frac{1 - r_{sr}}{2} - \frac{r_{sr}}{6} \\ C_{3i} &= \lambda_i(\lambda_i + 1)(1 - \chi_i) \left(\frac{r_1}{t_p'} \right)^{\lambda_i-1} & F_3 &= \frac{\sigma_{nr1}}{\sigma_{sr}} \\ C_{4i} &= \lambda_i(\lambda_i + 1)(1 - \chi_i) \left(\frac{r_2}{t_p'} \right)^{\lambda_i-1} & F_4 &= \frac{\sigma_{nr2}}{\sigma_{sr}} \\ C_{5i} &= \lambda_i(\lambda_i + 1)(1 - \chi_i) \left(\frac{r_3}{t_p'} \right)^{\lambda_i-1} & F_5 &= \frac{\sigma_{nr3}}{\sigma_{sr}} \end{aligned}$$

The (weld) root notch stress distribution (Eq. 2.41) is far field stress dependent (Fig. 2.35). Separate zone 2 and zone 3 stress gradient related terms cannot be identified like for σ_n (Eq. 2.24) and requires calculation of the self-equilibrating stress part first:

$$\sigma_{ser} = \sigma_{nr} \left(\frac{r'}{t_p'} \right) - \sigma_{fr} \left(\frac{r'}{t_p'} \right) \quad (2.43)$$

For a PP SS butt joint (Fig. 2.36), the weld root notch stress distribution at location 3 is shown for a far field bending load case $r_s = 1$ (Fig. 2.37); the bending moment is applied counter-clockwise. The cross-section is of the same size as the base plate thickness, i.e. $a_n = h_w$, and $\sigma_{fr}(r'/t_p')$ remains a pure bending formulation.

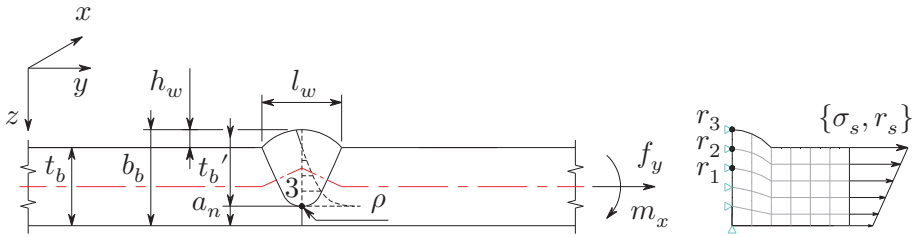


Figure 2.36: a) PP SS butt joint parameters, b) notch loc. 3 FE solid model.

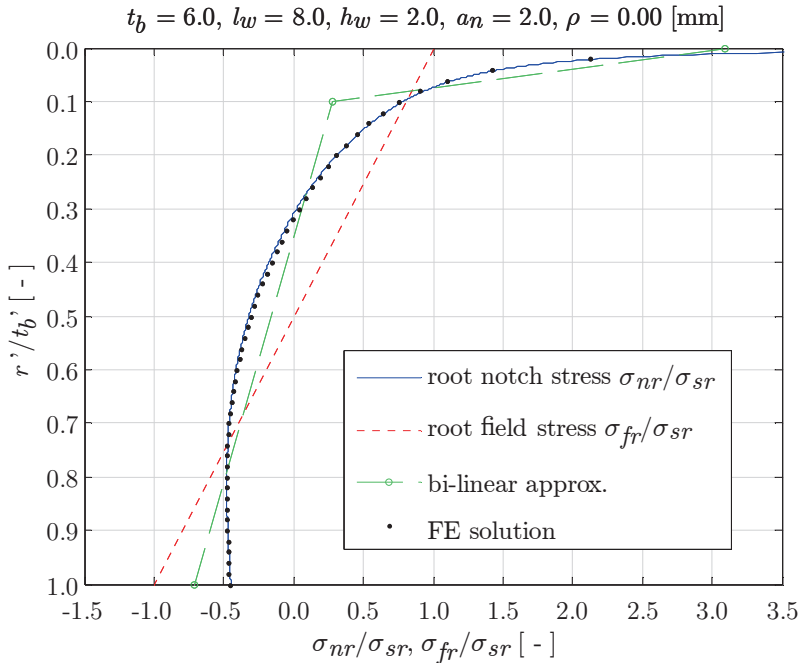


Figure 2.37: PP SS butt joint weld root notch stress distr. (loc. 3), $r_s = 1$.

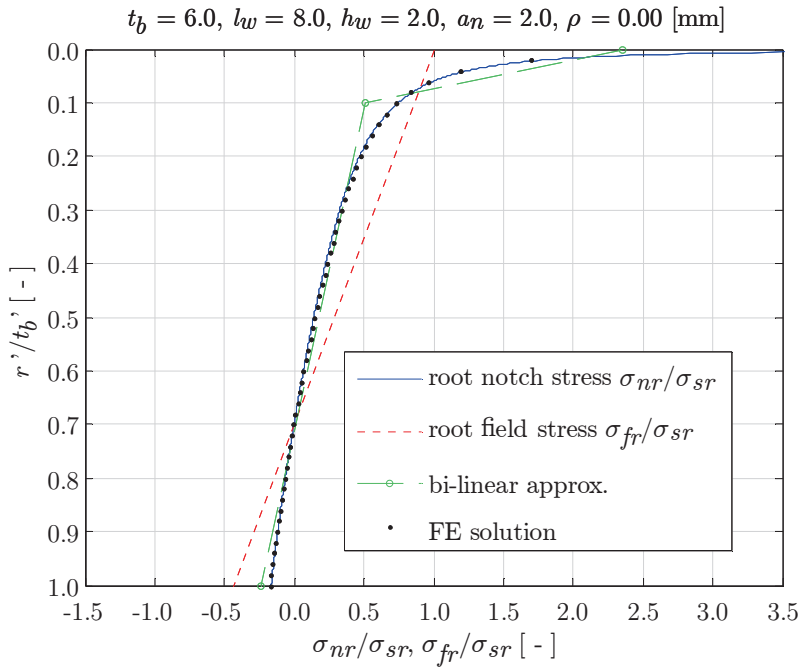


Figure 2.38: PP SS butt joint weld root notch stress distr. (loc. 3), $r_s = (1/3)$.

The notch dominated region demonstrates (non-singular term induced) relaxation, i.e. an increased notch affected region and smaller zone 2 stress gradient, in comparison to a combined load case $r_s = (1/3)$ showing, on the other hand, concentration (Fig. 2.38). However, this behaviour is not reflected in the bi-linear approximation.

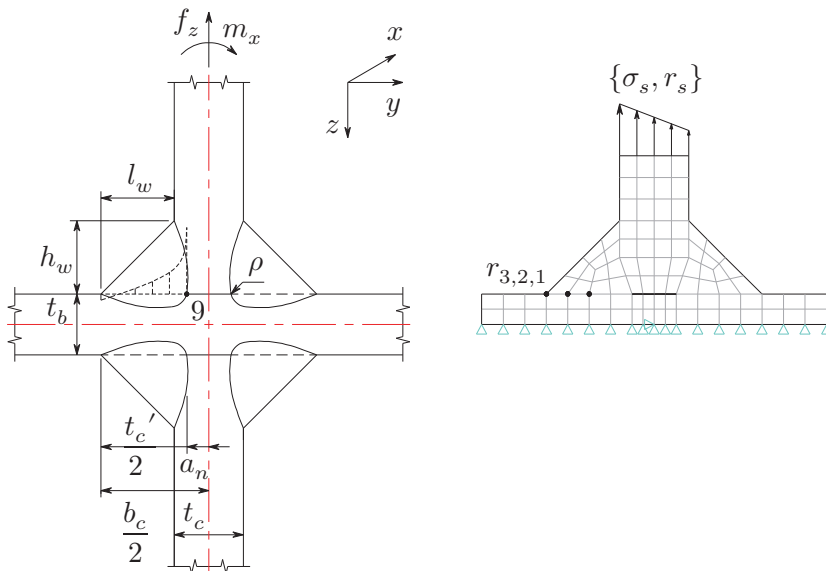


Figure 2.39: a) PP DS cruciform joint parameters, b) notch loc. 9 FE solid model.

Even more important: for the bi-linear approximation it is relatively easy to make the notch effect completely disappear and from weld notch fatigue perspective a fixed transition depth at 10 [%] of the ‘considered’ thickness asks for improvement. An example will be shown for a PP DS cruciform joint (Fig. 2.39). The location 9 weld root notch stress distribution (Fig. 2.40) is far field bending induced; $r_s = 1$. The self-equilibrating stress part (Eq. 2.43) shows in comparison to its bi-linear approximated equivalent even opposite behaviour in the notch affected region: tensile versus compressive.

Note that the weld root field stress distribution $\sigma_{fr}(r'/t_p')$ equals the $\{\sigma_s, r_s\}$ Battelle structural field stress distribution (Dong, 2001), meaning that the fracture mechanics context (welded joint) far field stress definition is violated like for the weld toe notch stress distributions including symmetry with respect to half the plate thickness ($t_p/2$).

In case the BSS concept is adopted and a fillet weld geometry is involved, it is recommended to use the weld throat section as root crack path if no detailed root notch size information is available (Hong, 2010). For $a_n = (t_p'/2)$, a very common assumption, the root structural stress σ_{sr} for the weld throat section exceeds its weld leg equivalent; a conservative approach. However, σ_{sr} cannot be related to the welded joint far field stress, for it does not meet the loading mode-I criterion, explaining why the linearised weld throat stress distribution is selected as far field stress instead.

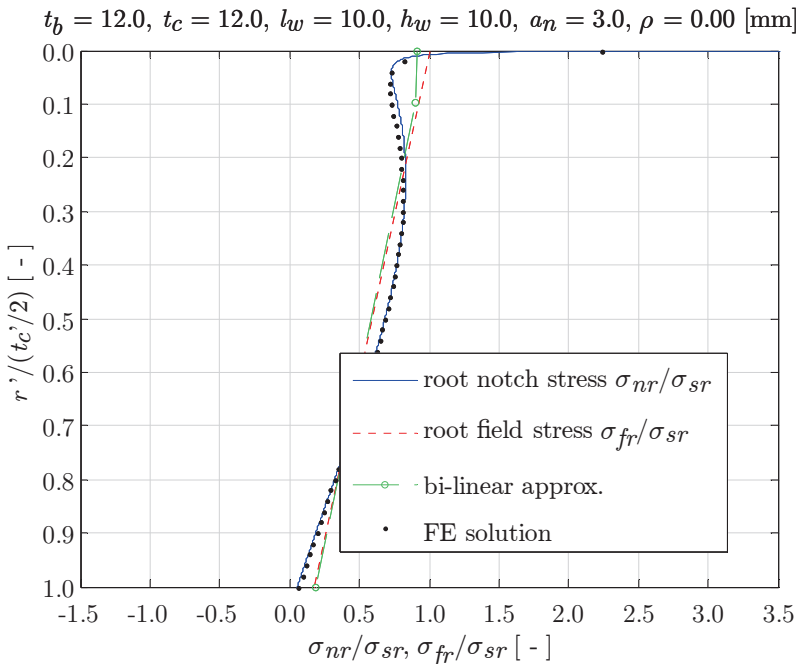


Figure 2.40: PP DS cruciform joint weld root notch stress distr. (loc. 9), $r_s = 1$.

The far field stress definition seems to be a matter of modelling principles. Being consistent, the welded joint far field stress and structural field stress distribution should be in agreement, rather than adopting the equilibrium equivalent stress part along the considered crack path as remote loading induced far field stress like for the BSS concept, meaning that (notch) symmetry effects with respect to $(t_p/2)$ are ignored by definition. All stress distributions are related to a single edge notch (SEN) configuration, ignoring the DEN and centre notch (CN) configurations, naturally corresponding to respectively several weld toe notch stress distributions for symmetry (e.g. DS cruciform joint, loc. 1 and 2) and weld root notch stress distribution for non-symmetry (e.g. DS butt joint, loc. 5 and 6).

2.7.2 Symmetry

The DEN geometry (Fig. 2.41), used in standard crack growth specimen, is symmetric with respect to $(b_b/2)$ and requires a symmetry condition to obtain the root notch stress distribution.

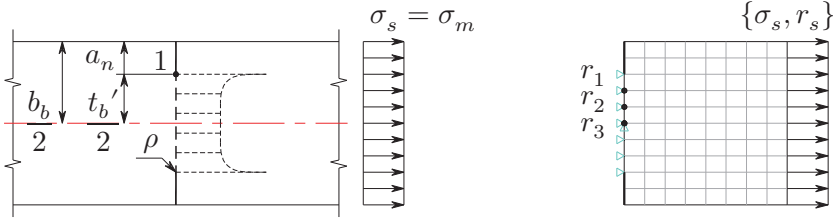


Figure 2.41: a) DEN(T) specimen parameters, b) notch loc. 1 solid model.

For $(r'/t_p') \rightarrow \{r'/(t_p'/2)\}$ the weld root notch stress formulation (Eq. 2.41) still applies, meaning that only the 2nd equation in the system (Eq. 2.42) has to be replaced like for the weld toe notch stress distribution including symmetry; moment equilibrium is ignored. The matrix and vector coefficients C_{ij} and F_i become:

$$\begin{aligned}
 C_{1i} &= (\lambda_i + 1)(1 - \chi_i) & F_1 &= 1 - r_{sr} \\
 C_{2i} &= \lambda_i(\lambda_i + 1)(1 - \chi_i)(\lambda_i - 1) & F_2 &= 0 \\
 C_{3i} &= \lambda_i(\lambda_i + 1)(1 - \chi_i) \left(\frac{r_1}{t_p'/2} \right)^{\lambda_i - 1} & F_3 &= \frac{\sigma_{nr1}}{\sigma_{sr}} \\
 C_{4i} &= \lambda_i(\lambda_i + 1)(1 - \chi_i) \left(\frac{r_2}{t_p'/2} \right)^{\lambda_i - 1} & F_4 &= \frac{\sigma_{nr2}}{\sigma_{sr}} \\
 C_{5i} &= \lambda_i(\lambda_i + 1)(1 - \chi_i) \left(\frac{r_3}{t_p'/2} \right)^{\lambda_i - 1} & F_5 &= \frac{\sigma_{nr3}}{\sigma_{sr}}
 \end{aligned} \tag{2.44}$$

The most common load case for DEN(T) crack growth testing ($r_s = 0$; tensile loading) provides a non-monotonic stress distribution (Fig. 2.42).

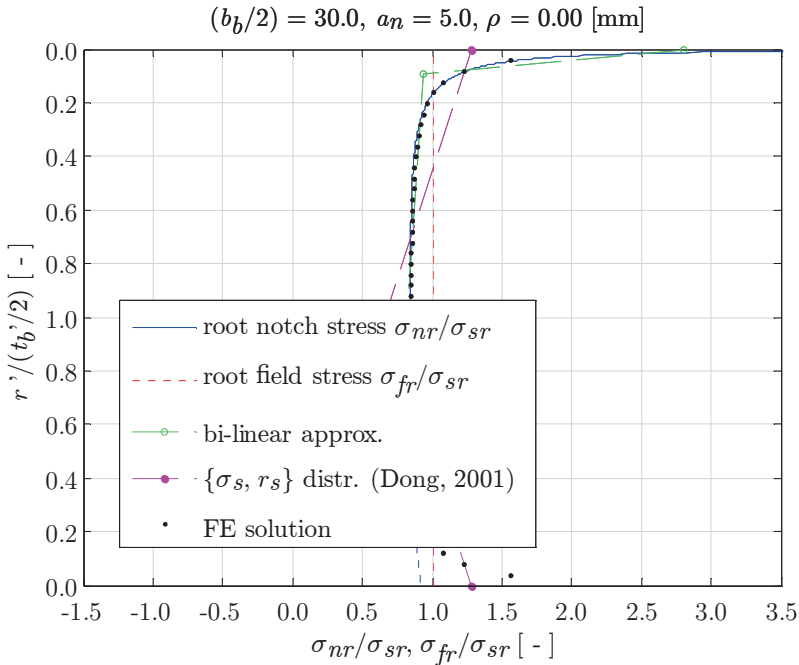


Figure 2.42: DEN(T) specimen root notch stress distr. (loc. 1), $r_s = 0$.

Comparing the (root) field stress distribution $\sigma_{fr}(r'/t_p')$ and the $\{\sigma_s, r_s\}$ Battelle structural field stress distribution (Dong, 2001) illustrates the difference for a DEN and SEN based formulation. The former takes crack growth at both notches into account while the latter ignores (non-conservatively) the effect of a crack growing at the same time in the symmetry part. Although crack initiation may hardly be influenced, the macro-crack growth behaviour will definitely be affected.

2.8 Size effects

Changing welded joint geometry dimensions modifies the notch stress distribution zone 1 peak value and zone $\{2, 3\}$ gradients. Fatigue scaling requires these size effects to be taken into account. The nominal stress- or structural hot spot stress range $\{S_n, S_h\}$ fatigue resistance measures, respectively a global and local (zone 1) point criterion, are incomplete in that respect and the IIW (Niemi, Fricke and Maddox, 2006) and CEN (Eurocode 9, 2007) introduced a plate thickness correction factor to incorporate a zone 2 stress gradient correction. The effective notch stress range S_e , an equivalent local zone $\{1, 2\}$ line criterion, includes a fictitious notch radius component to deal with size effects. Common denominator is the selection of a single geometry parameter, supposed to be dominant given certain modelling assumptions, meaning incomplete scaling anyway.

However, rather than looking for a governing parameter to include scaling, the contribution of the different stress components to the analytical weld notch stress distribution formulations involving all geometry parameters will be used to investigate and illustrate the peak value- and gradient consequences for varying weld dimensions $\{\alpha, l_w, h_w, a_n\}$, notch radius ρ and plate thickness t_p .

2.8.1 Weld dimensions

The local weld geometry related V-shaped notch stress $\sigma_{\theta\theta}$ (Eq. 2.10), a component of the self-equilibrating stress part σ_{se} (Eq. 2.32), incorporates the weld notch angle 2α . For (ideal) groove- and fillet welds, the 2α dependent weld toe flank angles are different affecting the σ_{se} distributions as shown for some extreme values, (l_w/h_w) variations (Fig. 2.43). Results are joint independent, since the weld load carrying bending stress component ($C_{bw} = 0$) is omitted to focus exclusively on flank angle effects first. It turns out that predominantly the $\{0 \leq (r/t_p) \leq 0.1\}$ region is affected. Differences between zone 2 stress gradients are relative small. For $(r/t_p) \rightarrow 0$ the notch stress increases for increasing flank angle as expected, although at the same time the notch affected region decreases since self-equilibrium requires compensation; for the symmetry case even in a stronger degree if compared to its non-symmetry equivalent.

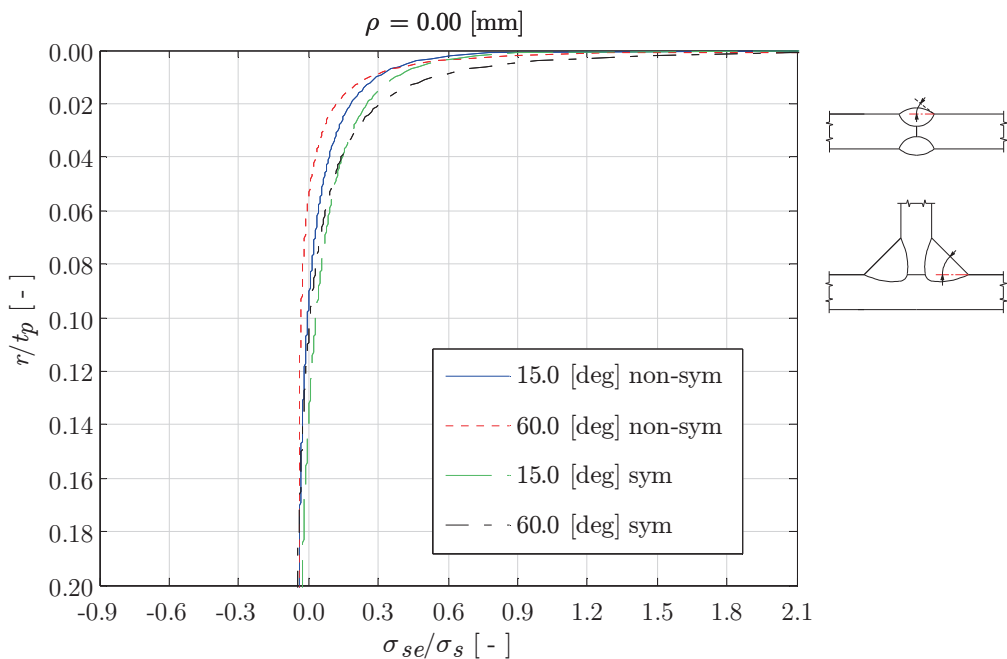


Figure 2.43: Self-equilibrating stress at different weld flank angles, ($C_{bw} = 0$).

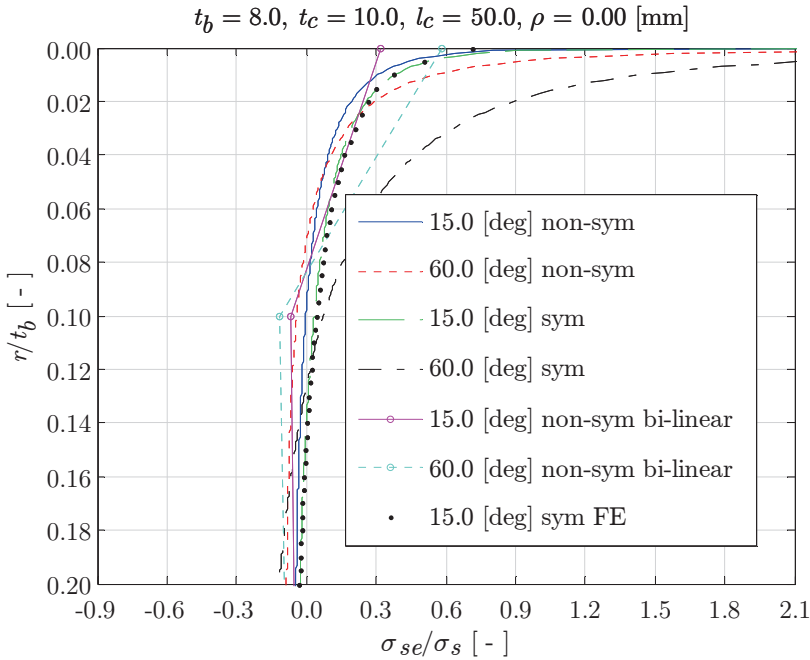


Figure 2.44: SS cover plate (non-sym.) and DS cover plate (sym.) – continuous base plate – loc. 1 self-equilibrating stress at different fillet weld flank angles and constant weld throat size $a_t = 4$ [mm], $r_s = 0$.

Including the other self-equilibrating stress part component, the $\{l_w, h_w\}$ dependent weld load carrying stress σ_{bw} (Eq. 2.16 or 2.18), amplifies this behaviour as shown for notch location 1 of a SS and DS cover plate (Fig. 2.44). At the same time, it explains reasonably well why the geometric 1 [mm] stress concept (Xiao and Yamada, 2004) has been introduced: the notch stress contribution vanishes at this distance and the corresponding stress value that keeps the stress gradient induced size effects to a minimum is preferred rather than a parameter that will take scaling explicitly into account. However, it is an absolute criterion, meaning that for increasing t_p the notch affected region will be entered. The range of application in terms of plate thickness seems limited to prevent for scaling issues. The BSS concept related bi-linear notch stress approximation (Dong, Hong and Cao, 2003) incorporates the notch angle and weld dimension effects in a rather crude and implicit way.

The structural hot spot stress does not include local weld geometry effects explicitly. The same FAT class is assigned to both groove- and fillet weld toes (Niemi, Fricke and Maddox, 2006) and the weld flank angle – put under restrictions – is implicitly taken into account, i.e. it is left in the fatigue resistance data scatter just like the symmetry effect. Obviously, the influence of notch angle 2α is supposed to be small. The (l_w/h_w) dependent weld load carrying effectiveness has been proposed to be included using an additional SCF K_{sa} (Poutiainen and Marquis, 2004b; 2006); in fact a local weld geometry stress related parameter. Although not directly comparable to $(1 + C_{bw})$; K_{sa} contains both $\sigma_{\theta\theta}$ and σ_{bw} contributions, behaviour

should be similar and Table 2.1 shows the results for notch location 1 of a PP DS cruciform joint with varying weld dimensions; far field load cases $\{r_s = 0, r_s = 1\}$. For increasing weld size, on the one hand K_{sa} decreases exponentially for the membrane as well as bending load case. On the other hand, $(1 + C_{bw})$ increases for increasing weld size, since the zone 2 notch stress gradient increases for $(r/t_b) \rightarrow 0$ (Fig. 2.45); the weld becomes more load carrying. Its values are quite small because of the continuous base plate. The $\sigma_{\theta\theta}$ component turns out to dominate σ_{bw} for decreasing weld size. The far field membrane induced weld load carrying effectiveness exceeds the bending contribution; a zone 3 stress gradient effect.

far field load case	weld dimensions [mm]	K_{sa} [-]	$1 + C_{bw}$ [-]
$r_s = 0$	$l_w = h_w = 7.1$	1.11	1.02
$r_s = 1$	$l_w = h_w = 7.1$	1.06	1.00
$r_s = 0$	$l_w = h_w = 11.3$	1.06	1.03
$r_s = 1$	$l_w = h_w = 11.3$	1.02	1.00
$r_s = 0$	$l_w = h_w = 17.0$	1.03	1.07
$r_s = 1$	$l_w = h_w = 17.0$	1.01	1.01

Table 2.1: PP DS cruciform joint ($t_b = t_c = 12, a_n = 6$) weld load carrying factors K_{sa} and $(1 + C_{bw})$ at loc. 1; far field stress and weld dimension effects.

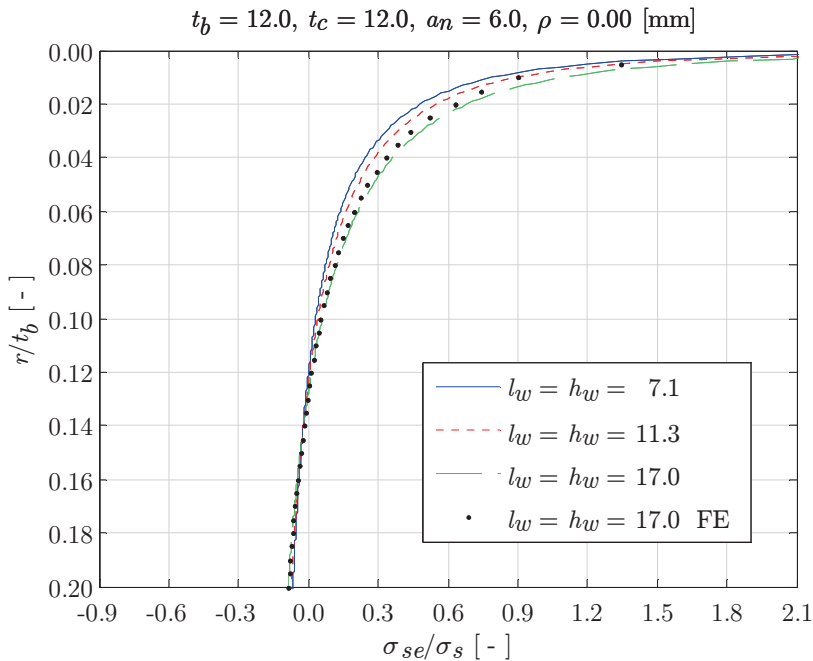


Figure 2.45: PP DS cruciform joint loc. 1 self-equilibrating stress for varying fillet weld dimensions and constant flank angle, $r_s = 0$.

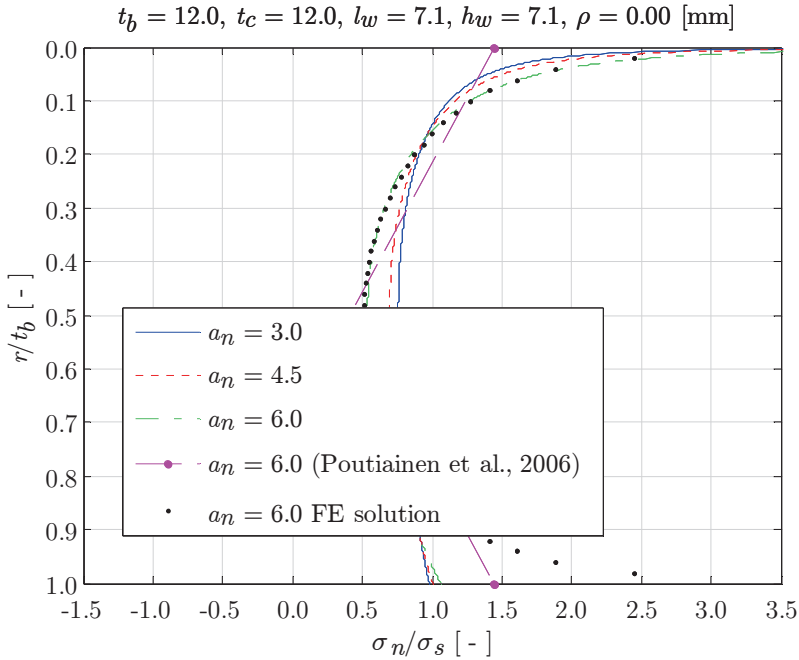


Figure 2.46: PP DS cruciform joint loc. 5 weld notch stress distribution for different root notch sizes, $r_s = 0$.

Generally speaking, continuous plate related weld toe notch stress distributions are hardly root notch size a_n affected. At a discontinuous plate, e.g. location 5 of a PP DS cruciform joint (Fig. 2.3), the weld load carrying induced bending stress component σ_{bw} however significantly increases for increasing a_n (Fig. 2.46), approximately up to half σ_s for a relative small full load carrying weld ($a_n = 6$) as shown in Table 2.2, meaning both stress values are of the same order of magnitude. Important fact: a_n cannot be detected using visual inspection.

Note that the linear as well as non-linear weld load carrying stress component (Eq. 2.19) is included, explaining $(1 + 2C_{bw})$. Both weld load carrying factors K_{sa} and $(1 + 2C_{bw})$ show the same trend; σ_{bw} tends to dominate $\sigma_{\theta\theta}$ for increasing a_n .

notch size a_n [mm]	K_{sa} [-]	$1 + 2C_{bw}$ [-]
3.0	1.29	1.19
4.5	1.35	1.27
6.0	1.44	1.48

Table 2.2: PP DS cruciform joint weld load carrying factors K_{sa} and $(1 + C_{bw})$ at loc. 5; influence of root notch size, $r_s = 0$.

Self-equilibrating stress part distributions are notch location-, welded joint geometry- and far field stress dependent. For the weld root, the notch angle is reasonably assumed to be the same in any case: ($2\alpha = 2\pi$). A joint independent representation of 2α effects like for weld toe notches is impossible since the non-singular stress terms (Eq. 2.41) contain both the weld load carrying stress- as well as the structural field stress component, i.e. C_{bw} is implicitly included. To prevent for any bending contribution, a far field membrane loaded PP reinforcement removed SS or DS butt joint should be adopted and root notch size $a_n \rightarrow 0$. At the same time, however, the notch disappears. Note: a microscopic notch is considered to be a flaw; defect (size a_i). The high degree of variety in zone 2 notch stress gradient is a result of different weld leg lengths $\{l_w, h_w\}$, but predominantly of root notch size a_n as shown for some DS and SS butt joint extremes (Fig. 2.47). The notch affected region does not exceed ($r'/t_p' = 0.1$), although σ_{ser} is more pronounced in comparison to the weld toe cases (Fig. 2.44). The order of magnitude is the same.

For weld toe notches, varying weld dimensions predominantly affects the zone 2 stress gradient; the zone 3 stress gradient is structural field stress dependent and the weld geometry is not involved. However, $\{l_w, h_w, a_n\}$ variations for weld root notches influence both zone $\{2, 3\}$ stress gradients since at the same time the structural field stress is modified (Fig. 2.48). Note it is principally a plate thickness effect as well: $t_p' = f(t_p, l_w, h_w, a_n)$. Increasing the root notch size a_n increases predominantly the structural root stress σ_{sr} , meaning for a far field bending loaded SS butt joint the root notch stress distribution σ_{nr} remains more or less unaffected.

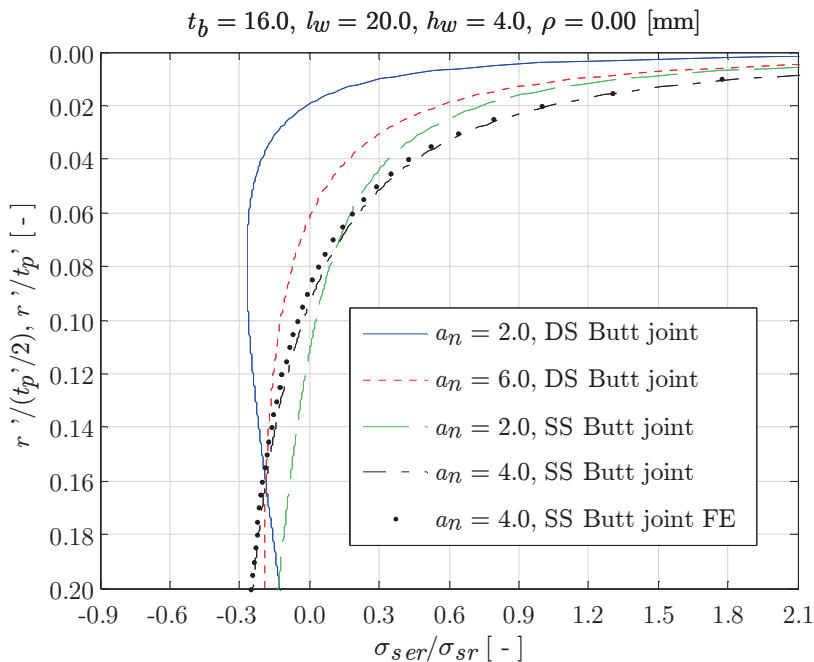


Figure 2.47: PP DS butt joint (loc. 5) and PP SS butt joint (loc. 3) self-equilibrating stress for different root notch sizes, $r_s = 1$.

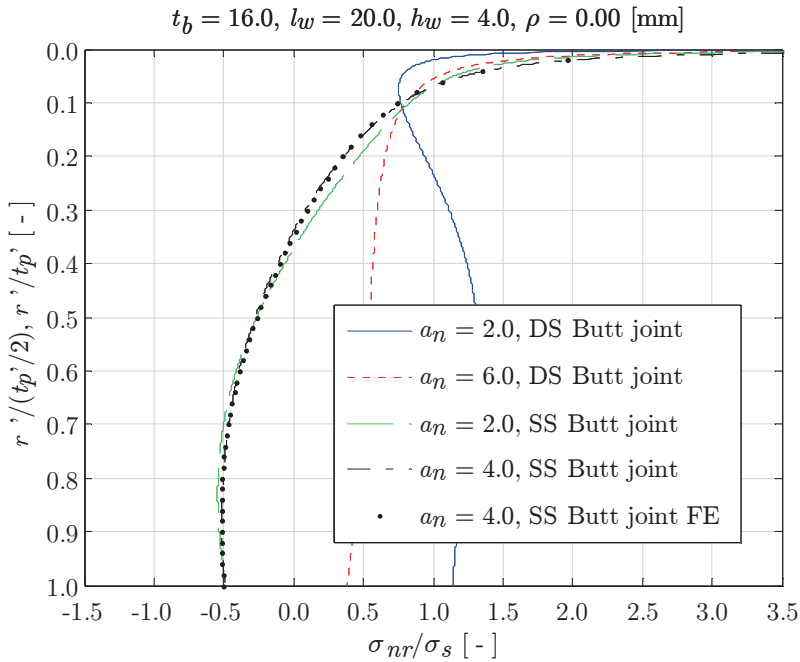


Figure 2.48: PP DS butt joint (loc. 5) and SS butt joint (loc. 3) weld notch stress distribution for different root notch sizes, $r_s = 1$.

The FAT28 class assigned to weld root fatigue for the structural (hot spot) stress concept – linearisation of the stress distribution along weld leg should replace the weld toe related surface extrapolation to obtain a structural interpolated(!) stress omitting the notch component – drops considerably in comparison to the LC weld toe FAT36 class (Fricke, 2013). Quite remarkable from geometry point of view, since it is the self-equilibrating stress part that should explain the difference. However, similar distributions for weld toe and weld root have been observed (Fig. 2.44 and 2.47). It has been argued (Brandt, Lawrence and Sonsino, 2001; Ribeiro and De Jesus, 2011) that weld root fatigue predominantly consists of crack growth rather than crack initiation. Passing the question why, if so, still a crack initiation related intact geometry parameter is selected, it seems confusing that a weld root notch and crack share the same square root singular behaviour. The adopted crack growth models ignore the notch specific behaviour (Paragraph 2.11). Besides, the $S-N$ curve slopes are the same, meaning a different fatigue mechanism – governing initiation or growth – is out of question. The weld quality could be different because of an increased weld root fatigue test data scatter, although the effective notch stress concept guideline (Fricke, 2012), another IIW report, applies the same – average – fictitious notch radius (Zhang, Sundermeier and Sonsino, 2012) and FAT class to weld toe and weld root notches for the same welded joints.

2.8.2 Notch radius

Remote mechanical loaded weld geometries introduce stress concentrations, meaning the linear elastic notch stress distributions $\{\sigma_n, \sigma_{nr}\}$ contain a peak stress at $\{(r/t_p) = 0, (r'/t_p') = 0\}$. It is related to the far field (reference) stress using the theoretical SCF K_t ; an intact geometry related crack initiation zone 1 parameter, independent of material properties. However, for a notch radius $\rho = 0$ an artificial (worst) limit case is identified: $K_t \rightarrow \infty$. To eliminate this singularity and obtain a meaningful zone 1 value, $\rho > 0$ is required. Except the real ρ component, the notch radius is the parameter to be used to include micro-structural support – a notch stress gradient hypothesis (Sonsino et al., 2012) – and is the only one to incorporate the statistical weld volume effect adequately, since investigation of actual weld seams shows that ρ is widely scattered along the weld length (Lassen et al., 2005; 2006).

Using Kolossoff-Muskhelishvili's method based on complex Airy stress functions and conformal mapping, the stress components $\{\sigma_{rr}, \sigma_{\theta\theta}, \sigma_{r\theta}\}$ for ($\rho > 0$) can be obtained (Lazzarin and Tovo, 1996; Atzori, Lazzarin and Tovo, 1997), a solution that has been improved significantly for increased opening angles $2(\pi - \alpha)$ and a relative small notch radius ρ (Filippi, Lazzarin and Tovo, 2002) in particular, as typically encountered in welded joints. In this blunt body case (Fig. 2.49), the stress components (Eq. 2.9 to 2.11) include additional terms (Appendix A, Eq. A1 to A3).

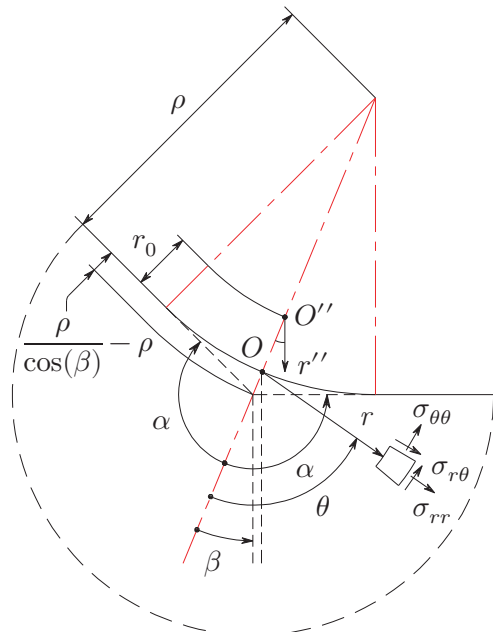


Figure 2.49: Blunt V-shaped notch parameters.

The coordinate system origin will be transformed ($O'' \rightarrow O$) and $\{\sigma_n, \sigma_{nr}\}$ will be formulated in the corresponding cross-section. At ($r/t_p = 0$), the maximum (principal) notch stress location, the crack is most likely to be initiated. The non-linear transformation – keeping the polar axis parallel to the original one – yields:

$$\left(\frac{r''}{t_p}\right)^2 = \left(\frac{r}{t_p}\right)^2 + 2\cos(\beta - \theta_t) \left(\frac{r_t}{t_p}\right) \left(\frac{r}{t_p}\right) + \left(\frac{r_t}{t_p}\right)^2 \quad (2.45)$$

$$\tan(\beta'') = \frac{\left(\frac{r}{t_p}\right) \sin(\beta) + \left(\frac{r_t}{t_p}\right) \sin(\theta_t)}{\left(\frac{r}{t_p}\right) \cos(\beta) + \left(\frac{r_t}{t_p}\right) \cos(\theta_t)} \quad (2.46)$$

with

$$r_t = r_0 = \rho \left(1 - \frac{\pi}{2\alpha}\right), \quad \theta_t = 0$$

The stress angle has been approximated ($\beta'' \approx \beta$) and the weld toe notch stress distribution for the non-symmetry case and 1st order σ_{bw} becomes:

$$\begin{aligned} \sigma_n \left(\frac{r}{t_p}\right) = \sigma_s \left[\mu_s \left\{ \left(\frac{r''}{t_p}\right)^{\lambda_s-1} \lambda_s (\lambda_s + 1) [\cos\{(\lambda_s + 1)\beta\} - \right. \right. & (2.47) \\ & \chi_s \cos\{(\lambda_s - 1)\beta\}] + \\ & \left. \left(\frac{r''}{t_p}\right)^{\zeta_s-1} \left(\frac{r_0}{t_p}\right)^{\lambda_s-\zeta_s} \lambda_s \frac{\left(\frac{2\alpha}{\pi}\right)}{4 \left\{\left(\frac{2\alpha}{\pi}\right) - 1\right\}} \right. \\ & \left. [\omega_{s1} \cos\{(\zeta_s + 1)\beta\} + \right. \\ & \left. \omega_{s2}(\zeta_s + 1) \cos\{(\zeta_s - 1)\beta\}] \right\} + \\ \mu_a \left\{ \left(\frac{r''}{t_p}\right)^{\lambda_a-1} \lambda_a (\lambda_a + 1) [\sin\{(\lambda_a + 1)\beta\} - \right. & \\ & \chi_a \sin\{(\lambda_a - 1)\beta\}] + \\ & \left(\frac{r''}{t_p}\right)^{\zeta_a-1} \left(\frac{r_0}{t_p}\right)^{\lambda_a-\zeta_a} \lambda_a \frac{1}{4(\zeta_a - 1)} \right. \\ & \left. [\omega_{a1} \sin\{(\zeta_a + 1)\beta\} + \right. \\ & \left. \omega_{a2}(\zeta_a + 1) \sin\{(\zeta_a - 1)\beta\}] \right\} + \\ C_{bw} \left[2 \left(\frac{r}{t_p}\right) - 1 \right] - 2r_s \left(\frac{r}{t_p}\right) \end{aligned}$$

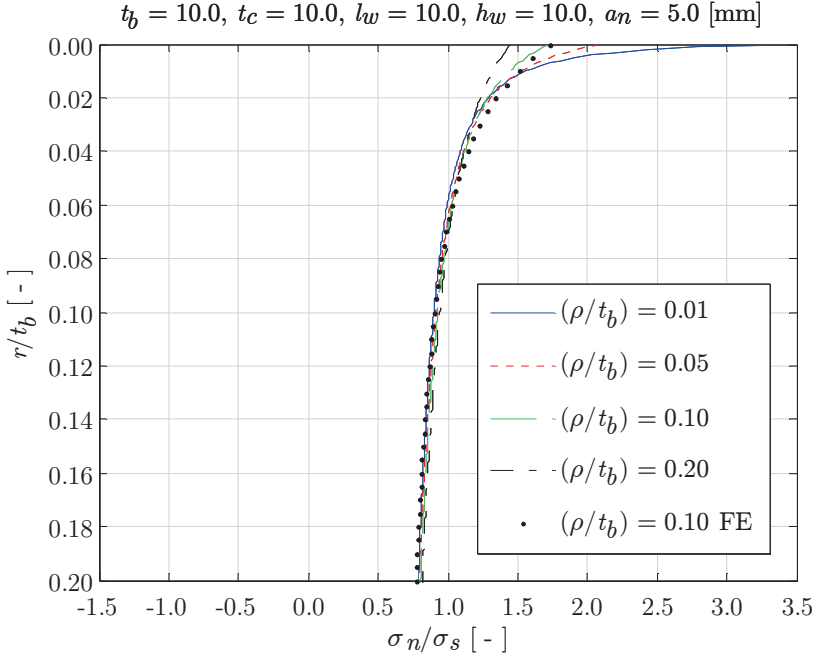


Figure 2.50: PP DS T-joint weld toe notch stress distribution (loc. 1) for different notch radii, $r_s = (1/3)$.

The notch radius is assumed to be relatively small and scaling of t_p and σ_s according to the increased cross-section is ignored. The blunt body eigenvalues $\{\zeta_s, \zeta_a\}$, corresponding eigenvalue coefficients $\{\omega_{s1}, \omega_{s2}, \omega_{a1}, \omega_{a2}\}$ and the system of equations to be solved for $\{\mu_s, \mu_a\}$ can be found in appendix A (Eq. A.4 and A.5).

Changing the notch radius modifies the peak stress value as well as the zone 2 stress gradient, like shown for the weld toe notch stress distributions of a PP DS T-joint (Fig. 2.50). Using $\{\sigma_{rr}, \sigma_{\theta\theta}, \sigma_{r\theta}\}$, i.e. (Eq. A1 to A5), the 1st principal stress σ_{p1} based SCF K_t can be calculated. Note that $\sigma_{p1,2}$ are invariant, i.e. independent of coordinate system:

$$\sigma_{p1,2} = \left\{ \frac{\sigma_{\theta\theta} \left(\frac{r}{t_p} = 0 \right) + \sigma_{rr} \left(\frac{r}{t_p} = 0 \right)}{2} \right\} \pm \sqrt{\left\{ \frac{\sigma_{\theta\theta} \left(\frac{r}{t_p} = 0 \right) - \sigma_{rr} \left(\frac{r}{t_p} = 0 \right)}{2} \right\}^2 + \left\{ \sigma_{r\theta} \left(\frac{r}{t_p} = 0 \right) \right\}^2} \quad (2.48)$$

Results are compared to FE solutions (Table 2.3). Although the notch stress components $\{\sigma_{rr}, \sigma_{\theta\theta}, \sigma_{r\theta}\}$ have been developed to be applied for a relative small notch radius ρ , the error increases for decreasing notch radius – no doubt it is a

result of the way it has been used – and K_t is predominantly (somewhat) underestimated. Tsuji's boundary element analysis (BEA) based curve fitted formulae (Iida and Uemura, 1996) are added for convenience and show errors having the same order of magnitude and bandwidth, although K_t is mainly (conservatively) overestimated. The SCF increases for decreasing ρ like it should be, implying a decreased fatigue resistance from crack initiation point of view.

(ρ/t_b) [-]	K_t [-] FEA	K_t [-] (Eq. 2.48)	error [%]	K_t [-] (Iida et al, 1996)	error [%]
0.01	4.19	3.89	-7.2	4.12	-1.7
0.05	2.51	2.40	-4.4	2.54	1.2
0.10	2.03	1.99	-2.0	2.13	4.9
0.20	1.67	1.69	1.2	1.83	9.6

Table 2.3: PP DS T-joint weld toe (loc. 1) SCF's for different notch radii; $r_s = (1/3)$.

For the weld toe symmetry case – 1st order weld load carrying stress – including ρ , σ_{nb} (Eq. 2.37) can be used with:

$$\begin{aligned}
 f\left(\frac{r}{t_p}\right) = & \mu_s \left\{ \left(\frac{r''}{t_p}\right)^{\lambda_s-1} \lambda_s (\lambda_s + 1) [\cos\{(\lambda_s + 1)\beta\} - \right. & (2.49) \\
 & \left. \chi_s \cos\{(\lambda_s - 1)\beta\}] + \right. \\
 & \left. \left(\frac{r''}{t_p}\right)^{\zeta_s-1} \left(\frac{r_0}{t_p}\right)^{\lambda_s-\zeta_s} \lambda_s \frac{\left(\frac{2\alpha}{\pi}\right)}{4 \left\{ \left(\frac{2\alpha}{\pi}\right) - 1 \right\}} \cdot \right. \\
 & \left. [\omega_{s1} \cos\{(\zeta_s + 1)\beta\} + \right. \\
 & \left. \omega_{s2}(\zeta_s + 1) \cos\{(\zeta_s - 1)\beta\}] \right\} + \\
 & \mu_a \left\{ \left(\frac{r''}{t_p}\right)^{\lambda_a-1} \lambda_a (\lambda_a + 1) [\sin\{(\lambda_a + 1)\beta\} - \right. \\
 & \left. \chi_a \sin\{(\lambda_a - 1)\beta\}] + \right. \\
 & \left. \left(\frac{r''}{t_p}\right)^{\zeta_a-1} \left(\frac{r_0}{t_p}\right)^{\lambda_a-\zeta_a} \lambda_a \frac{1}{4(\zeta_a - 1)} \cdot \right. \\
 & \left. [\omega_{a1} \sin\{(\zeta_a + 1)\beta\} + \right. \\
 & \left. \omega_{a2}(\zeta_a + 1) \sin\{(\zeta_a - 1)\beta\}] \right\} + \\
 & C_{bw} \left\{ 4 \left(\frac{r}{t_p}\right) - 1 \right\}
 \end{aligned}$$

To obtain $f(r/t_p = 1/2)$, the coordinate system transformation (Eq. 2.45, 2.46) have to be used; simplifications like for the ($\rho = 0$) case (Eq. 2.38) seem impossible. Appendix A provides the system (Eq. A.6) required to solve for the constants $\{\mu_s, \mu_a\}$.

Comparing the loc. 1 weld toe notch stress distributions for a PP DS T-joint (Fig. 2.50) and PP DS cruciform joint (Fig. 2.51) with the same dimensions, the symmetry condition at ($t_p/2$) for the latter forces a more pronounced notch affected region, i.e. increased SCF's. Table 2.4 shows the corresponding K_t values as well as results obtained using curve fitted formulae: availability and application is limited because of typical restrictions like $\{t_b = t_c, l_w = h_w\}$ and a lack of far field bending formulations.

(ρ/t_b) [-]	K_t [-] FEA	K_t [-] (Eq. 2.48)	error [%]	K_t [-] (Iida et al, 1996)	error [%]
0.01	4.69	4.65	-0.9	5.64	20.2
0.05	2.76	2.78	0.7	2.78	0.0
0.10	2.21	2.25	1.8	2.18	-1.4
0.20	1.81	1.84	1.7	1.78	-1.7

Table 2.4: PP DS cruciform joint weld toe (loc. 1) SCF's at different notch radii; $r_s = (1/3)$.

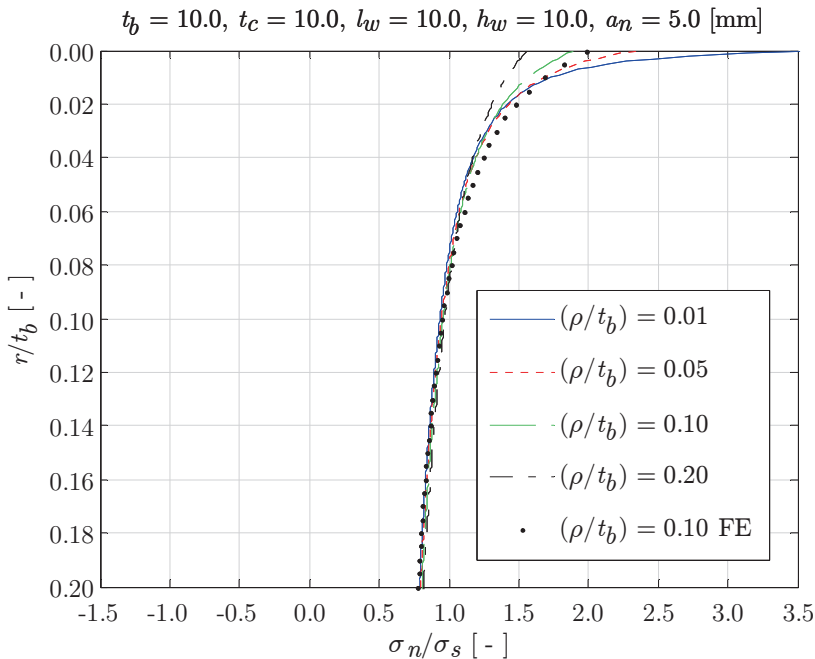


Figure 2.51: PP DS cruciform joint weld toe notch stress distribution (loc. 1) for different notch radii, $r_s = (1/3)$.

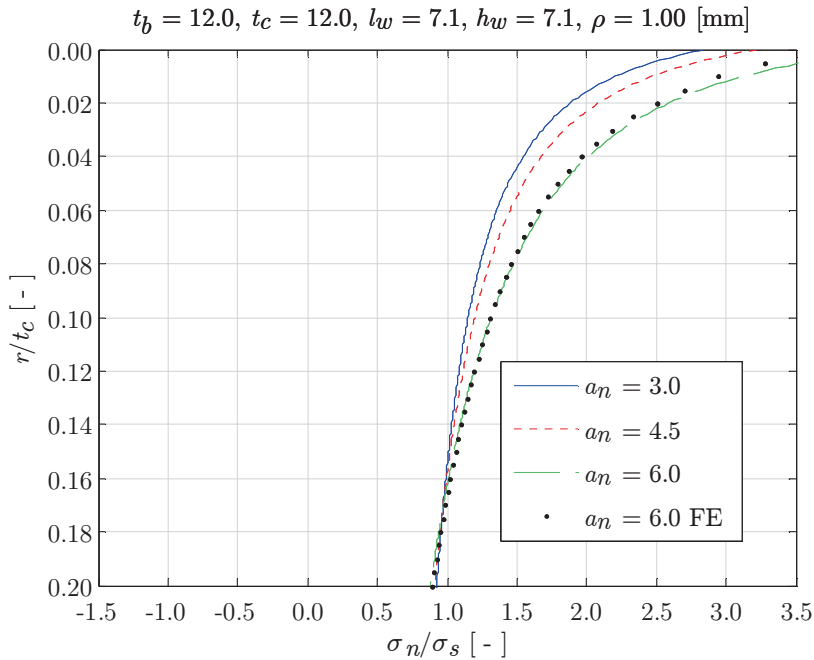


Figure 2.52: PP DS cruciform joint weld toe notch stress distribution (loc. 5) for ($\rho = 1.00$) and varying root notch size, $r_s = 0$.

The cross plate related weld toe notches, e.g. loc. 5 of a PP DS cruciform joint (Fig. 2.52), are significantly a_n affected for ($h_w < t_c$). Both the 1st and 2nd order weld load carrying stress components are included. The considered geometry may look familiar; it has been used as example in the fatigue assessment guide line for the effective notch stress concept (Fricke, 2012) and is included for comparison.

ρ [mm]	a_n [mm]	K_t [-] FEA	K_t [-] (Eq. 2.48)	K_t [-], (error [%]) (Radaj et al, 1990)	K_t [-], (error [%]) (Anthes et al, 1993)
0.5	3.0	3.77	3.91 (-0.9)	4.97 (31.8)	3.76 (-0.3)
0.5	4.5	4.54	4.43 (-2.4)	5.24 (15.4)	4.53 (-0.2)
0.5	6.0	5.49	5.74 (4.6)	5.44 (-0.9)	5.79 (5.5)
1.0	3.0	3.08	3.12 (2.7)	3.79 (23.1)	3.15 (2.3)
1.0	4.5	3.70	3.52 (-4.9)	3.99 (7.8)	3.82 (3.2)
1.0	6.0	4.51	4.52 (0.2)	4.15 (-8.0)	4.91 (8.9)

Table 2.5: PP DS cruciform joint weld toe (loc. 5) SCF's for different root notch size and notch radii; $r_s = 0$.

Welding practice shows that like the notch radius, the root notch size is not easy to control and varies a lot along the weld seam; ($a_n = t_c/2$) is a conservative assumption. Decreasing ρ at the same time (Table 2.5), the fatigue resistance reduces quite efficiently; a worst case scenario easily doubles K_t , not to mention the reduction in fatigue life. Obviously, the range of application for the curve fitted formula (Radaj and Zhang, 1990) is limited; for (Anthes, Köttgen and Seeger, 1993) results are close to the FEA estimates, but a geometry restriction requires ($t_b = t_c$).

The weld root notch stress distributions including ρ contribution – both non-symmetric and symmetric – can be obtained as well. Appendix A provides the corresponding V-shaped notch stress components (Eq. A.7 to A.9) as well as the system (Eq. A.11) to be solved for μ_i and σ_{nr} (Eq. 2.41) becomes:

$$\sigma_{nr} \left(\frac{r'}{t_p'} \right) = \sigma_{sr} \sum_{i=1}^5 \mu_i \left[\left(\frac{r''}{t_p'} \right)^{\lambda_i-1} \lambda_i (\lambda_i + 1) (1 - \chi_i) + \left(\frac{r''}{t_p'} \right)^{\zeta_i-1} \left(\frac{r_0}{t_p'} \right)^{\lambda_i-\zeta_i} \left(\frac{\lambda_i}{2} \right) \{ \omega_{1i} + \omega_{2i} (\zeta_i + 1) \} \right] \quad (2.50)$$

with

$$\left(\frac{r''}{t_p'} \right)^2 = \left(\frac{r'}{t_p'} \right)^2 + 2 \left(\frac{r_t}{t_p'} \right) \left(\frac{r'}{t_p'} \right) + \left(\frac{r_t}{t_p'} \right)^2$$

and

$$r_t = r_0 = \left(\frac{\rho}{2} \right)$$

ρ [mm]	a_n [mm]	K_t [-] FEA	K_t [-] (Eq. 2.48)	K_t [-], (error [%]) (Radaj et al, 1990)	K_t [-], (error [%]) (Anthes et al, 1993)
0.5	3.0	4.65	4.34 (-6.7)	5.23 (12.5)	4.50 (-3.2)
0.5	4.5	5.85	5.77 (-1.4)	6.23 (6.5)	5.98 (2.2)
0.5	6.0	7.31	7.57 (3.5)	7.05 (-3.6)	7.57 (3.6)
1.0	3.0	3.57	3.45 (-3.4)	4.04 (13.2)	3.46 (-3.1)
1.0	4.5	4.48	4.62 (3.1)	4.82 (7.6)	4.60 (2.7)
1.0	6.0	5.64	6.13 (8.7)	5.45 (-3.4)	5.83 (3.7)

Table 2.6: PP DS cruciform joint weld root loc. 9 Stress Concentration Factors for different root notch size and notch radii; $r_s = 0$.

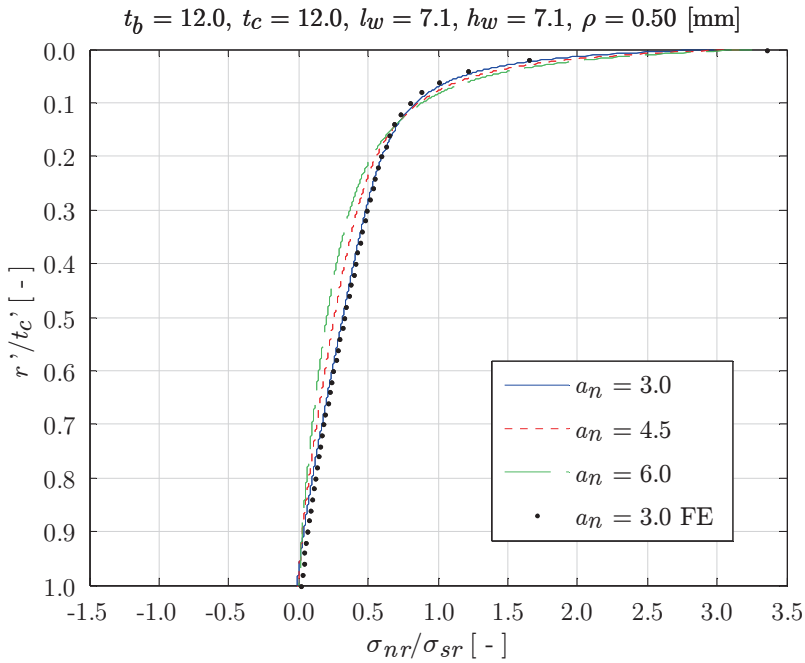


Figure 2.53: PP DS cruciform joint weld root notch stress distribution at loc. 9 for ($\rho = 0.50$) and varying root notch size, $r_s = 0$.

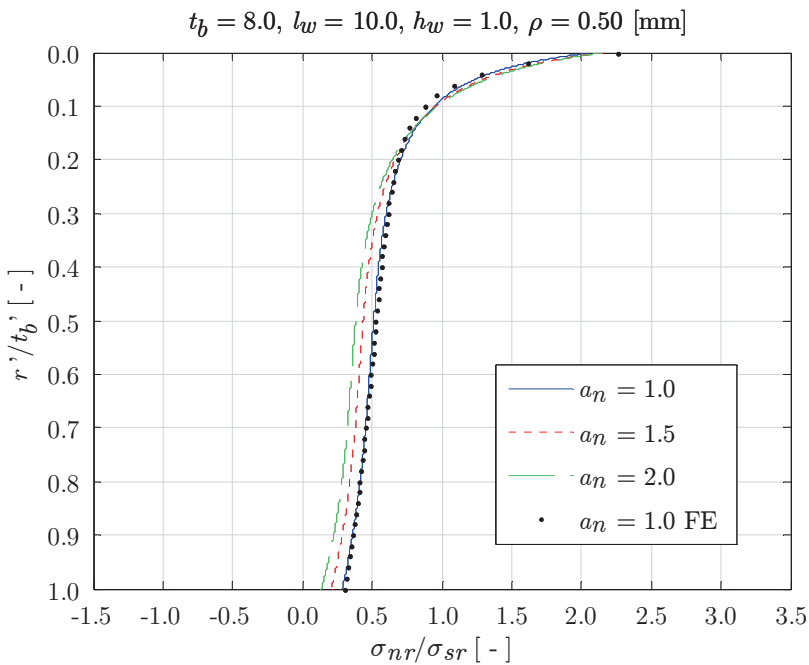


Figure 2.54: PP DS but joint weld root notch stress distribution (loc. 5) for ($\rho = 0.50$) and varying root notch size, $r_s = 0$.

Still considering the same PP DS cruciform joint, K_t results can be obtained for the weld root, location 9, as well (Table 2.6). Comparing the weld toe and weld root SCF's (Table 2.5 and 2.6), the weld root is governing, meaning a bad welded joint design anyway since weld root fatigue damage is hard to detect.

It is typical for moderate a_n sizes that the weld root notch stress distributions (Fig. 2.53) remain approximately the same since the structural root field stress parameters $\{\sigma_{sr}, r_{sr}\}$ change linear accordingly. The notch radii applied denote the fictitious $\rho_f(\alpha)$ values for aluminium welded joints, respectively $\rho_f = 1.0$ [mm] and $\rho_{fr} = 0.5$ [mm] for weld toe and weld root (Zhang, 2012; Zhang, Sonsino and Sundermeier, 2012), as proposed for the effective notch stress concept. For decreasing root notch size, weld root fatigue shows a typical lower bound hole-in-plate solution (Table 2.7): $K_t = 3.0$ [-], as shown for a PP DS butt joint (Fig. 2.54). Note that a fictitious notch radius – after all, fatigue is a real life problem – in FE models artificially modifies the structure and may introduces some peculiarities, e.g. for relative small weld dimensions the structural stiffness is reduced quite a lot. Although the analytical weld notch stress formulations are not explicitly meant to be used to obtain SCF's as crack initiation parameter – a competition with FE results in terms of accuracy will be lost a priori, it may still be useful if the effective notch stress concept is adopted for fatigue design. From efficiency point of view, K_t estimates are similar or even better in comparison to results obtained using available curve fitted formulae.

ρ [mm]	a_n [mm]	K_t [-] FEA	K_t [-] (Eq. 2.48)	error [%]
0.50	1.0	3.69	3.46	-6.2
0.50	1.5	4.50	4.53	0.7
0.50	2.0	5.36	5.68	6.0
1.00	1.0	3.00	2.92	-2.7
1.00	1.5	3.56	3.85	8.2
1.00	2.0	4.25	4.89	15.1

Table 2.7: PP DS butt joint weld root (loc. 5) SCF's at different notch radii; $r_s = 0$.

Note that weld (toe) notch stress distributions for $\rho > 0$ can be used to explain (partially) the effects of a post-welding improvement procedure like weld toe grinding. At the same time, an undercut or notch depth d_n appears reducing the effective plate thickness and increasing the structural stress parameters $\{\sigma_s, r_s\}$. However, one important weld geometry parameter, the initial crack size a_i , is not taken into account in a crack initiation based concept and – whatever the as-welded (AW) value might be – it will definitely be different after the grinding procedure and affects the fatigue life up to a large extent.

2.8.3 Plate thickness

Although experimental research shows that the fatigue resistance of a welded joint depends on all its dimensions, it is often reduced to a plate thickness t_p effect (Gurney, 1991; Maddox, 1995; van Straalen and Soetens, 1995; Atzori and Meneghetti, 1998). For some reason it is considered to be a weld toe related issue only. Point of concern is the decrease in fatigue resistance for increasing t_p because of:

- The increased welded material volume involved. Although the defect size remains more or less unaffected, the probability of present defects increases as well as the fatigue damage likelihood; a statistical effect.
- The increased restrained material volume. The welding induced residual stress level increases and surface quality reduces, decreasing the welded joint fatigue resistance; a welding technology effect.
- The increased highly stressed material volume or notch affected region; a remote mechanical loading induced (zone 2) stress gradient effect.

The latter is commonly assumed to be the dominating factor (Niemi, 1995) and will be examined since geometry and far field stress dependent scaling is involved. The well-known thickness correction or scaling factor – as required for the global and local zone 1 nominal stress and structural hot spot stress fatigue resistance measures – turning up in the IIW recommendations (Niemi, Fricke and Maddox, 2006) and CEN design handbook (Eurocode 9, 2007) is $(t_{p,ref}/t_p)^k$, with $\{0 < k < 1\}$ and $\{t_p > t_{p,ref}\}$, showing a detrimental effect on fatigue life for increasing t_p . Common applied curve fitting based exponential values for mixed groove- and fillet weld configurations include $k = \{0.25, 0.30\}$. Assuming the crack will grow along the bisector ($\beta = 0$), the zone 2 symmetric V-shaped notch stress exponent, eigenvalue λ_s , has been adopted (Atzori and Meneghetti, 1998): $k = (1 - \lambda_s)$ and values quite close to the curve fitted ones have been obtained, i.e. for a 30 and 45 [deg] flank angle, the exponent becomes respectively $k \approx \{0.23, 0.33\}$. The adopted reference plate thickness denotes $t_{p,ref} = 25$ [mm]. The specimen plate thickness of the experimental data used to obtain a fatigue design curve yield ($t_p \leq t_{p,ref}$). The involved standard deviation already includes the related scaling induced scatter.

For a continuous base plate related weld toe notch, e.g. location 1 of a PP DS T-joint, non-symmetric stress distributions for increasing t_b are shown (Fig. 2.55). The weld- and cross plate dimensions are reasonably assumed to scale accordingly. The relative size of the highly stressed material volume turns out to be constant, justifying a scaling parameter like $(r/t_p) = 0.1$ (Dong, Hong and Cao, 2003) to define a transition depth and distinguish a notch affected- and far field dominated region. The $\{l_w, h_w\}$ induced σ_{bw} contribution is limited, even if $\{l_w, h_w, t_c\}$ are fixed, meaning the stress distribution in the notch affected region is the same for varying plate thickness. Since the zone 2 stress gradient is hardly affected, the nominal stress- and structural hot spot stress concept related correction factor is very useful. Different far field loading conditions will not change this behaviour.

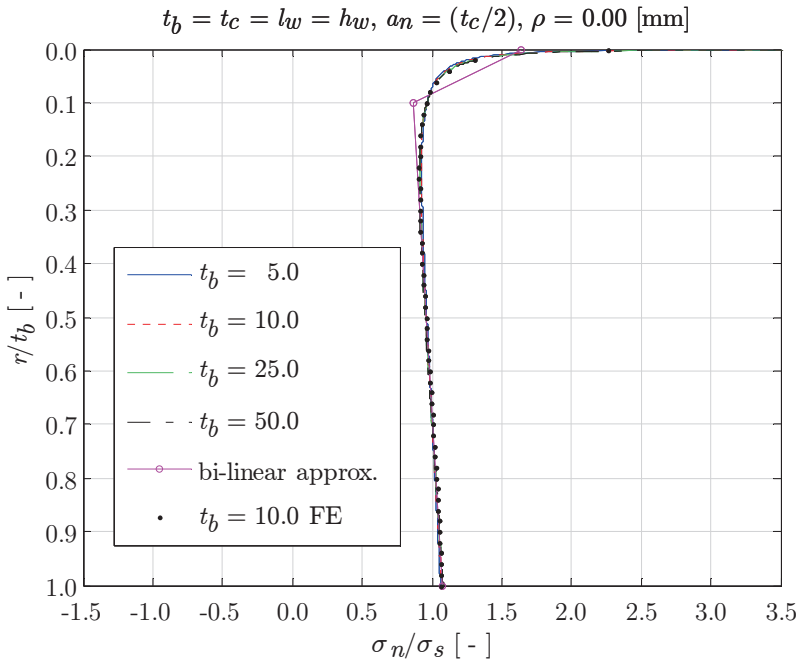


Figure 2.55: Plate thickness effect on $\sigma_n(r/t_b)$ of a PP DS T-joint (loc. 1), $r_s = 0$.

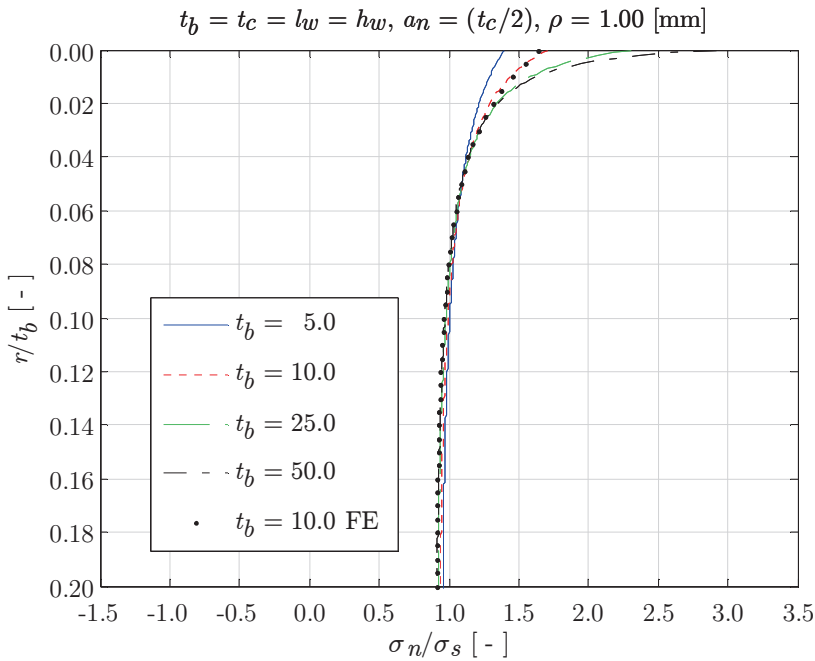


Figure 2.56: Plate thickness effect on $\sigma_n(r/t_b)$ of a PP DS T-joint (loc. 1), $r_s = 0$.

Using the effective notch stress concept, a constant ρ_e value has to be applied taking only the absolute notch acuity is taken into account. However, for increasing t_b the relative notch acuity changes (ρ_f/t_b), meaning that except the zone 1 peak stress the zone 2 stress gradient – in average already included – is affected as well (Fig. 2.56). Although mentioned that scaling is incorporated (Fricke, 2012), it seems to be incomplete.

Symmetry cases show similar behaviour, even if the weld toe notch is related to a discontinuous plate as shown for a PP DS cruciform joint (Fig. 2.57). The root notch size a_n is scaled accordingly to keep the weld load-carrying behaviour similar. The structural hot spot stress concept related additional SCF (Poutiainen and Marquis, 2004b; 2006) remains constant as well, $K_{sa} = 1.15 [-]$, meaning t_p effects are not involved at all. In fact, it is already excluded by definition since $K_{sa} = 1.0 [-]$ for a non-load carrying weld no matter the plate thickness. The original correction factor $(t_{p,ref}/t_p)^k$ still has to be applied.

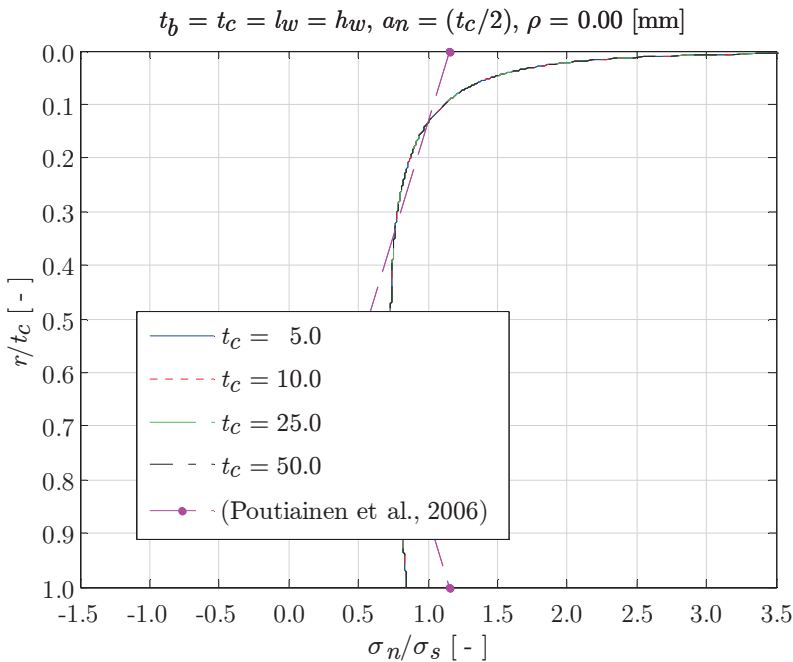


Figure 2.57: Effect of t_p on $\sigma_n(r/t_b)$ of a PP DS cruciform joint (loc. 5), $r_s = 0$.

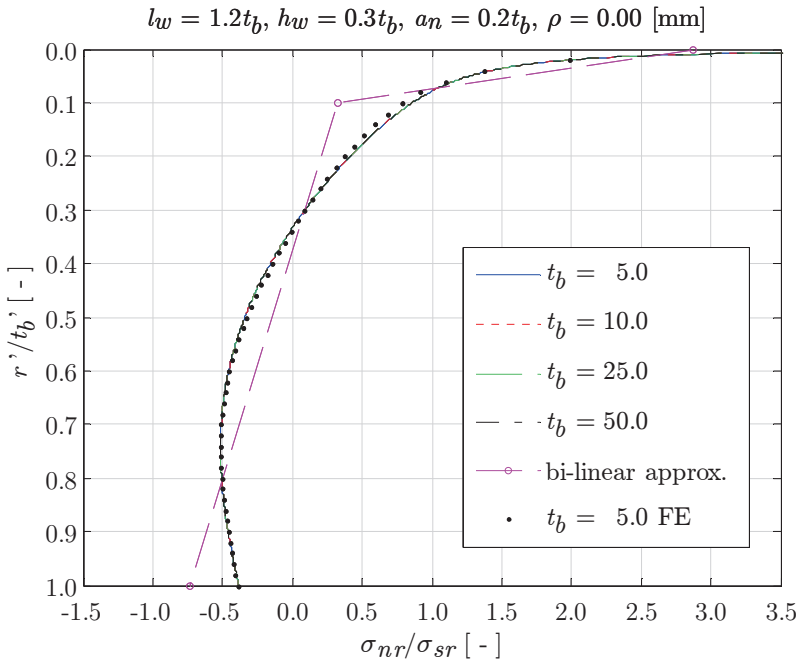


Figure 2.58: Effect of t_p on $\sigma_{nr}(r'/t_b')$ of a PP SS butt joint (loc. 3), $r_s = 1$.

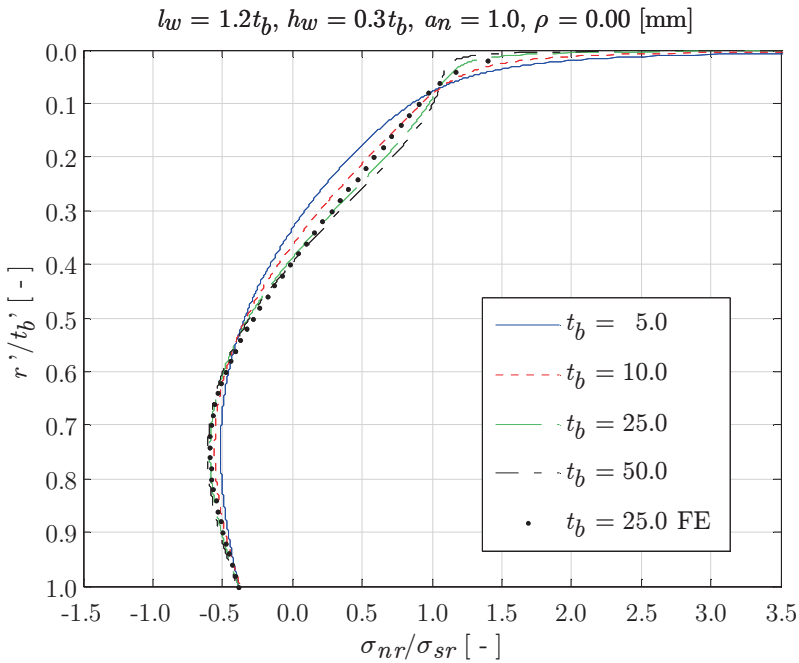


Figure 2.59: Effect of t_p on $\sigma_{nr}(r'/t_b')$ of a PP SS butt joint (loc. 3), $r_s = 1$.

For a weld root notch, e.g. location 3 at a PP SS butt joint, principally no changes appear as long as all other geometry parameters scale accordingly (Fig. 2.58). If not, both zone {2,3} stress gradients may be adjusted (Fig. 2.59).

Generally speaking, if an incomplete fatigue scaling parameter like the nominal- or structural hot spot stress is adopted, the well-known plate thickness correction factor is very useful for both weld toe and weld root fatigue as long as the other geometry parameters scale accordingly – a reasonable assumption – since the zone 2 stress gradient remains unaffected. Modifying the notch related plate thickness only, the correction factor becomes incomplete. Effects might be limited for continuous plate related notches; for discontinuous plate related ones – both weld toe and weld root – effects may become significant. For the latter, the zone 3 stress gradient might even be affected.

2.9 Weld seam analysis

Hull structures may contain $O(10^3)$ metres weld seam. A fatigue assessment of all (identified critical) weld notch locations, hot spots, is a challenging task. The nominal stress as fatigue resistance measure often applied for welded joint fatigue design uses global loading and geometry information only, meaning the required effort is relatively low and calculated fatigue strength- and life time estimate uncertainty is limited. Adding local (structural hot spot- or notch stress) information improves the result. Effort increases, however, in particular for the typically FEA calculated structural response. Challenge is to reduce (computational) effort maintaining accuracy, i.e. use the remote mechanical loading induced welded joint far field stress obtained employing relatively coarse meshed plate/shell FE models – excluding weld geometry, the (idealised) welded joint geometry parameters and the semi-analytical formulations (Eq. 2.24, 2.39, 2.41) to construct the mode-I through-thickness weld notch stress distributions along the weld seam. The procedure will be illustrated for the different type of hot spots {A, B, C} using small scale specimen (SSS) as generally involved to obtain fatigue resistance information.

In a quasi-2D cross-sectional approach along the weld seam – HS's type C – of the first specimen (Matic et al., 2005; Fig. 2.60), the SS cover plate can be identified; one of the classified welded joints (Fig. 2.3). An offset has been used to model the cover plate in the shell FE model. To obtain the welded joint far field stress (Eq. 2.21), line forces f_i rather than stresses are proposed to be used (Dong, 2004) to reduce mesh-size sensitivity. The required nodal forces F_i however are typically calculated in a global Cartesian coordinate system and need to be translated using a rotation matrix to the local weld coordinate system, i.e. $\{x', y'\}$ -axis respectively along and perpendicular to the weld seam and z' -axis in thickness direction (Fig. 2.61). Depending on the element formulation order, f_i can be determined; i.e. in a 1st order (linear) case using:

$$\begin{Bmatrix} F_1 \\ F_2 \\ \vdots \\ F_{n-1} \\ F_n \end{Bmatrix} = \begin{bmatrix} \frac{l_1}{3} & \frac{l_1}{6} & 0 & \dots & 0 \\ \frac{l_1}{6} & \frac{l_1+l_2}{3} & \frac{l_2}{6} & 0 & \dots & \vdots \\ 0 & \frac{l_2}{6} & \frac{l_2+l_3}{3} & \frac{l_3}{3} & \ddots & 0 \\ \vdots & \vdots & \vdots & \vdots & \frac{l_{n-2}+l_{n-1}}{3} & \frac{l_{n-1}}{6} \\ 0 & \dots & 0 & \frac{l_{n-1}}{6} & \frac{l_{n-1}}{3} \end{bmatrix} \begin{Bmatrix} f_1 \\ f_2 \\ \vdots \\ f_{n-1} \\ f_n \end{Bmatrix} \quad (2.51)$$

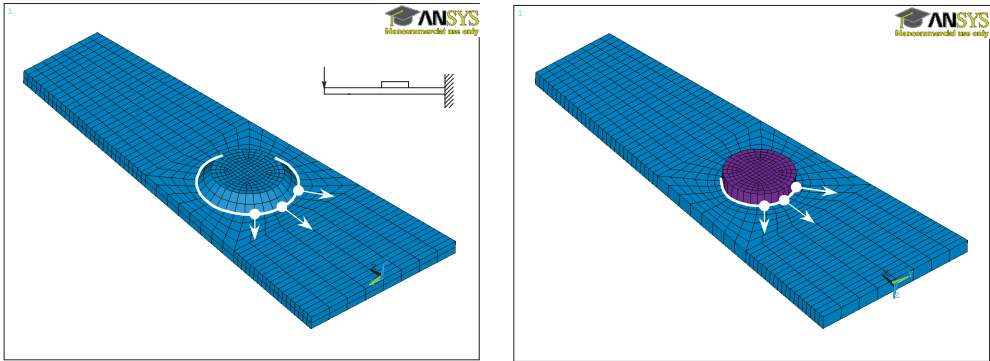


Figure 2.60: Solid (coarse mesh shown for convenience) and shell FE model of SS cover plate SSS (Matic et al., 2005).

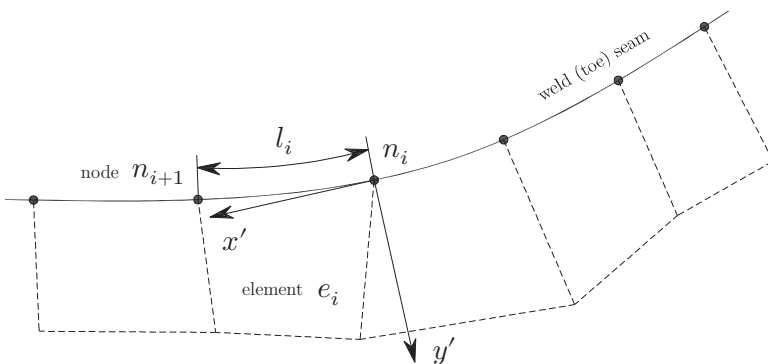


Figure 2.61: Local coordinate system at node along the weld seam in FE model.

The (element) length l_i denotes the distance in between 2 consecutive nodes n_i and n_{i+1} ; the (line) force vectors contain either the membrane forces or the bending moments, $\{F = F_m \vee F = M_b\}$ and $\{f = f_m \vee f = m_b\}$.

The specimen (Fig. 2.60) is constrained as cantilever; loading is applied at the free end in terms of displacement, meaning the response is bending dominated. The obtained semi-analytical formulation (Fig. 2.62) in the critical location along the weld seam is compared to a solid FE model result; stresses in the notch affected region are missing since the mesh size is a trade-off between accuracy and calculation time. Note the shell/plate FE model does not contain the weld geometry as it is local information to be included using the semi-analytical formulation.

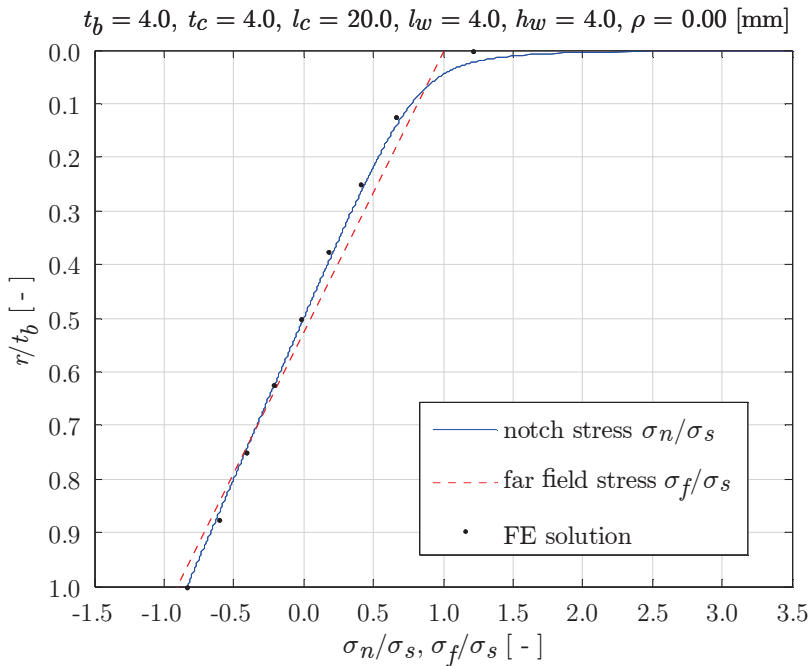


Figure 2.62: PP SS cover plate weld notch stress distr. (loc. 1) at critical location; loading according to test setup (Matic et al., 2005).

Another HS type *C* example is a SSS tubular SS T-joint (Mann, 2006; Fig. 2.63). The brace has been loaded in bending, i.e. the weld toe in the corner at the chord is the governing fatigue sensitive location. The corresponding far field stress distribution consists predominantly of bending as well (Fig. 2.64). The semi-analytical solution overestimates the far field stress gradient a little.

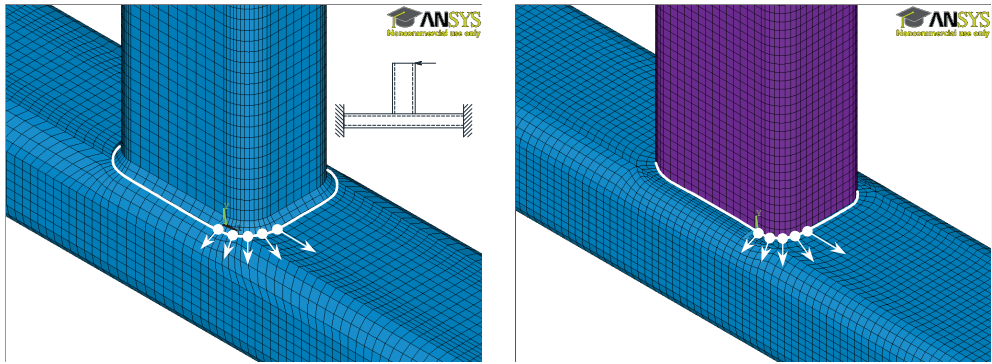


Figure 2.63: Solid (coarse mesh shown for convenience) and shell FE model of tubular SS T-joint SSS (Mann, 2006).

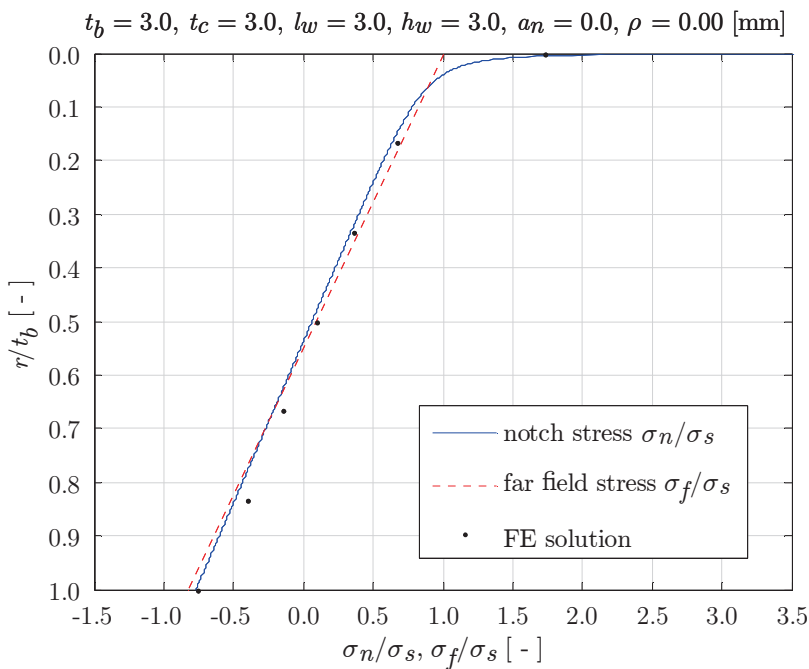


Figure 2.64: PP SS T-joint weld notch stress distr. (loc. 1) at critical location; loading according to test setup (Mann, 2006).

The weld ends require particular attention. Using solid FE models, for HS's type *A* principally the same procedure as for HS type *C* can be applied. However, in case of shell/plate FE models the procedure changes because of the 1 node weld end presentation. If the element size is relatively small, i.e. $\leq (l_w, h_w)$, the average line force along the weld end length $\{t_b + 2l_w, t_c + 2h_w\}$ can be adopted and should be

calculated using the nodal forces along the weld end perpendicular to the weld seam as shown for a DS attachment (Haagensen et al., 1998; Fig. 2.65). However, if the element size is relatively large, i.e. $\gg (l_w, h_w)$, the virtual node method can be adopted (Dong, Hong, Osage and Prager, 2002; Fig. 2.66). Using static equilibrium, the nodal forces $\{F_1, F_2\}$ of the element next to the weld end are redistributed over its length l , assuming the line force f_1 is constant over the weld end length l_1 and decreases linearly over $(l_1 - l)$:

$$f_1 = \frac{F_1(l_1 + l) + F_2(l_1 - l)}{l_1 \cdot l} \quad (2.52)$$

$$f_2 = \frac{F_1(l_1^2 + l^2) + F_2(l_1^2 - 2l_1 \cdot l - l^2)}{l_1 \cdot l(l_1 - l)}$$

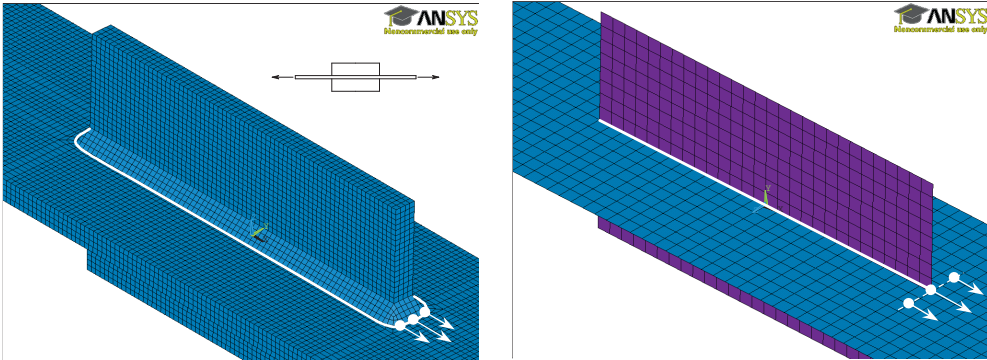


Figure 2.65: Solid (coarse mesh shown for convenience) and shell FE model of DS attachment SSS (Haagensen et al., 1998).

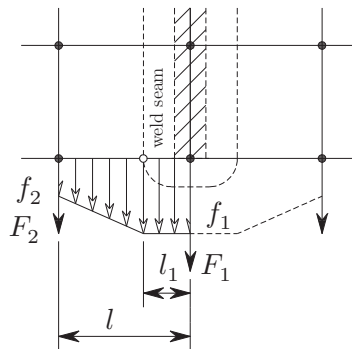


Figure 2.66: Weld end HS type A equivalent line force using virtual node.

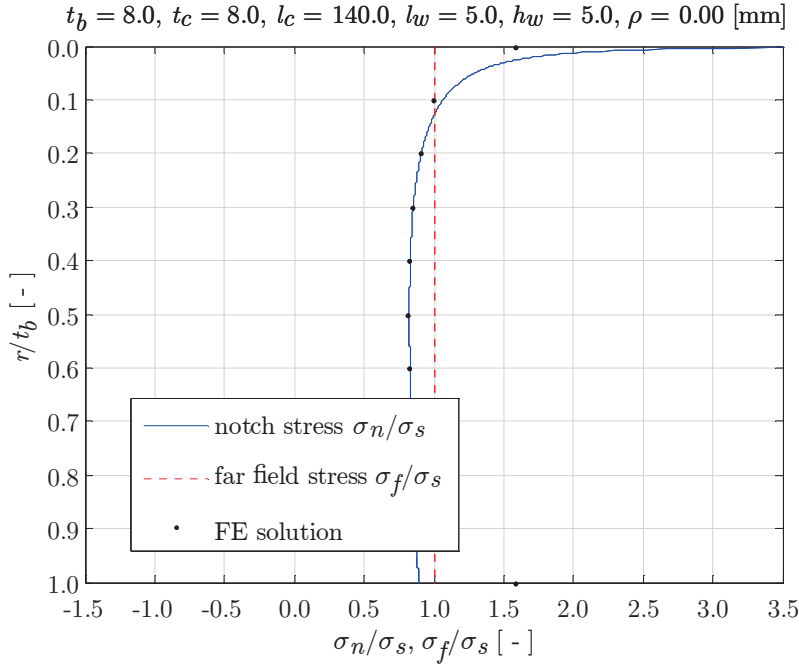


Figure 2.67: PP DS attachment weld notch stress distr. (loc. 1); loading according to test setup (Haagensen, 1998).

Comparing the results obtained using a semi-analytical formulation and a solid FE model, the weld load carrying stress turns out to be in agreement since the match is perfect at $(r/t_b) = 0.5$; FE stresses in the notch affected region are not available because of a relative coarse mesh size (Fig. 2.67).

For weld end HS's type *B*, an artificial crack length t_p' has to be defined. Typically, $t_p' = t_p$ is adopted. The mode-I nodal forces F_i along the presumed crack path as shown for a DS gusset plate (Daniels, 2001; Fig. 2.68) have been used to calculate the far field stress components:

$$\sigma_m = \frac{\sum(F_i)}{t_p \cdot t_p'}$$

$$\sigma_b = \frac{6 \left\{ \sum(F_i \cdot x_i) - \sigma_m \cdot \frac{(t_p')^2}{2} \right\}}{t_p \cdot (t_p')^2} \quad (2.53)$$

Obviously the origin of the σ_n coordinate system is adopted. Although the DS gusset plate shows symmetry w.r.t. half the specimen width, ($t_p' < w_p$) meaning σ_n is non-symmetric (Fig. 2.69). The bending contribution, i.e. C_{bw} , is somewhat underestimated.

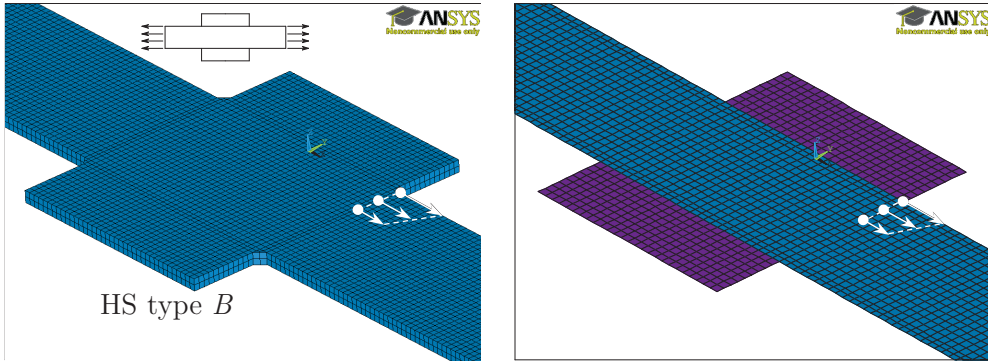


Figure 2.68: Solid and shell (coarse meshed) FE model of DS gusset plate SSS (Daniels, 2001).

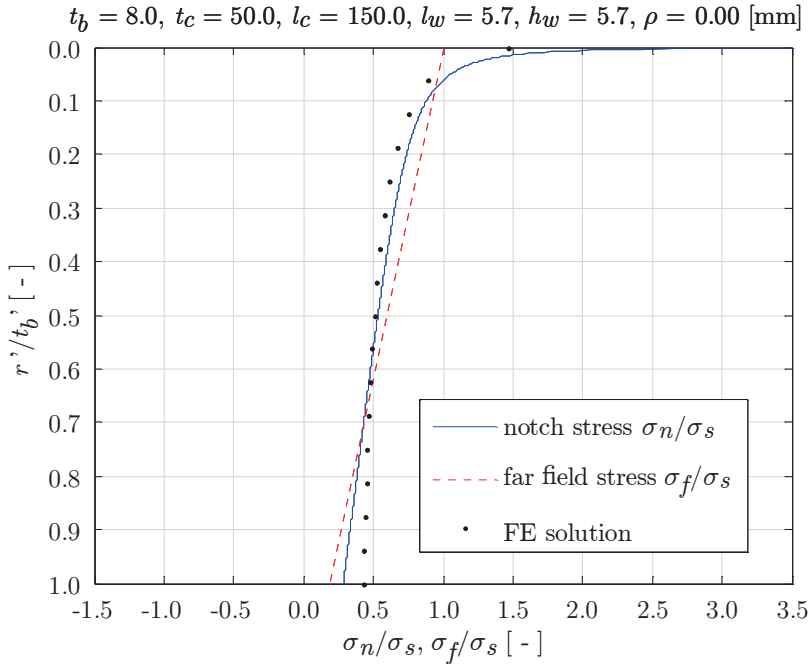


Figure 2.69: PP SS attachment weld notch stress distr. (loc. 1); loading according to test setup (Daniels, 2001).

2.10 Residual stress distribution

Welding, a material fusion process, introduces thermal loading to the plates and shells being joined. After cooling down however, residual stresses around the weld seam are still present because of (local) material yielding and (global) structural deformation restraints. Rapid advances in computational modelling introduced the possibility to simulate the welding process and investigate the residual stress characteristics. Except for modelling of the temperature dependent material properties (phase transformations), the way the arc-welding torch is modelled, e.g. using Goldak's heat source (Ferro, Berto and Lazzarin, 2005), as well as the degree of far field displacement constraints have been found to be governing parameters. Concerning the latter, the through-thickness mode-I distributions along the expected crack path have been classified as “bending” and “self-equilibrating” type as shown for a PP SS T-joint (Dong and Hong, 2001; Fig. 2.70). The qualification may be suitable for pipe girth welds (Song, Dong and Zhang, 2011), for welded joints in hull structures however the “bending” type should be replaced by “equilibrium” type.

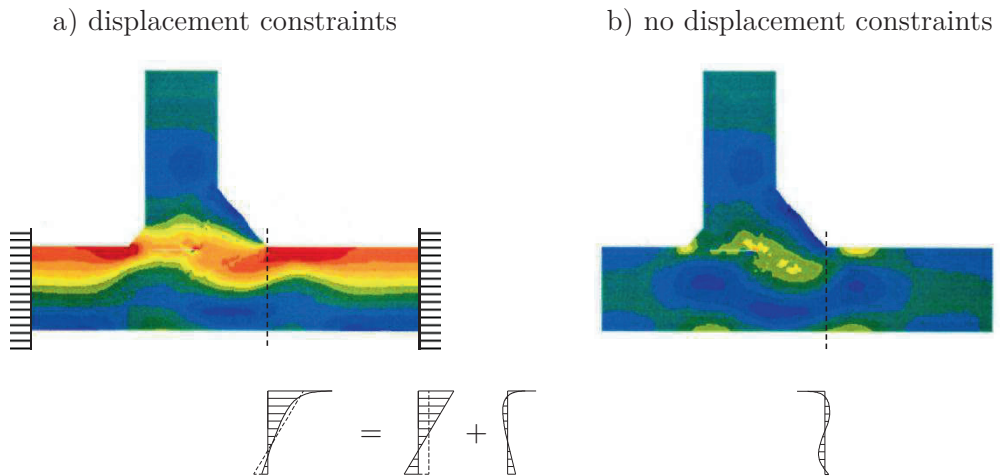


Figure 2.70: Quasi-2D mode-I residual stress distributions for a PP SS T-joint, obtained using numerical simulation (Dong and Hong, 2001).

Like the remote mechanical loading induced notch stress, the “equilibrium” type residual stress distribution (Fig. 2.70a) is assumed to be a linear superposition of an equilibrium equivalent- and self-equilibrating part. The former may contain both a membrane and bending component, i.e. the “bending” type definition has become incomplete. The involved (full) displacement constraints physically represent the as-welded (AW) joint embedded in the ship structure far field material. Without displacement constraints the equilibrium equivalent stress part tends to become zero and the residual stress distribution will be of the “self-equilibrating” type (Fig. 2.70b). The same type appears for a constrained joint subjected to a post-welding stress relieving (SR) procedure; an heat treatment for example.

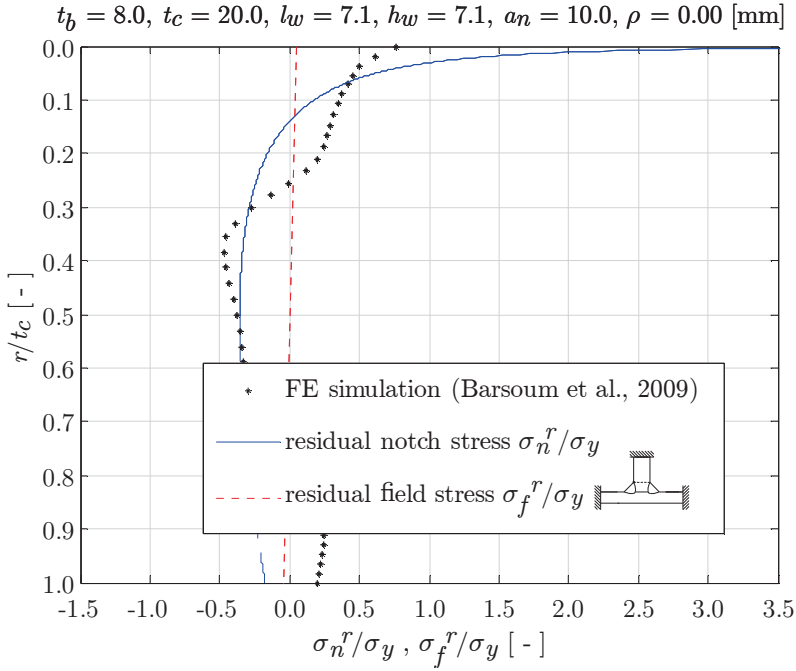


Figure 2.71: PP DS T-joint weld notch residual stress distr. (loc. 3).

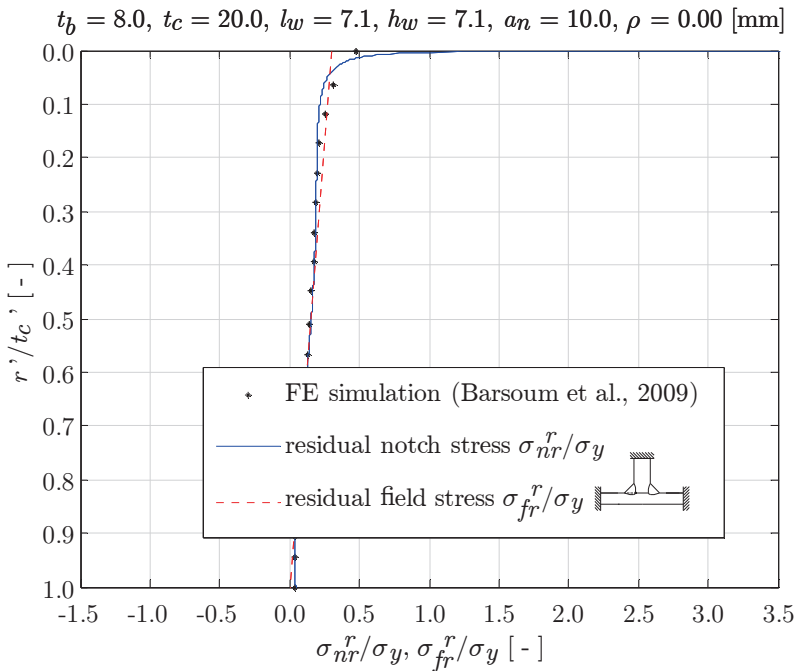


Figure 2.72: PP DS T-joint weld root notch residual stress distr. (loc. 6).

Measurements performed using neutron or synchrotron diffraction – sufficient density in plate thickness direction is required – confirm the “equilibrium” type residual stress distribution at the weld toe for a DS attachment (Nitschke-Pagel and Dilger, 2011). Actually, the loading and geometry considerations introduced for the remote mechanical loading controlled stress at weld toe and weld root seems to hold for the thermal loading induced residual stress, meaning both distributions show the same stress field similarity (Fig. 2.1).

The equilibrium equivalent residual stress part magnitude depends on level of heat input including the number of weld passes and axial displacement constraint; the zone 3 stress gradient is predominantly a matter of rotational displacement constraint and joint symmetry with respect to $(t_p/2)$. The self-equilibrating stress part however is principally weld geometry dependent. The V-shaped notch stress component $\sigma_{\theta\theta}$ (Eq. 2.10) for remote mechanical loading will not change for steady state thermal loading (Ferro, Berto and Lazzarin, 2005). In comparison to the welding process transient thermal loading induced notch stress, differences are quite small. Assuming the weld load carrying stress behaves similarly means the self-equilibrating stress part for both remote mechanical and welding induced thermal loading is approximately the same.

Simulations for a full displacement constrained PP DS T-joint (Barsoum and Lundbäck, 2009) show residual stress distributions of the (approximately) “self-equilibrating”- and “equilibrium” type for a weld toe and weld root, respectively a symmetry and non-symmetry case (Fig. 2.71 and 2.72). Because of an involved simplified heat source formulation, i.e. a constant flux rather than Goldak’s heat source or equivalent, the residual stress in the notch affected region is underestimated using a semi-analytical formulation.

The residual stress is often assumed to be highly tensile, about yield magnitude. However, following both the simulation and measurement results, it is limited to the notch affected region $(r/t_p) \rightarrow 0$, i.e. zone $\{1,2\}$, in particular for the “equilibrium” type. A linear elastic residual stress formulation seems to be justified, although notch plasticity can be taken into account modifying the V-shaped notch stress formulation (Lazzarin, Zambardi and Livieri, 2001). At the same time, cyclic (over)loading induced stress redistribution effects will be limited to the notch affected region as well. Its influence can still be considerable if a significant part of the fatigue life is related to crack initiation. The “self-equilibrating” type on the other hand can be compressive in the notch affected region as shown for a PP SS T-joint (Fig. 2.70) as confirmed in a similar investigation (Ferro, Berto and Lazzarin, 2005) for a FP SS butt joint. If both the remote mechanical- and welding induced thermal loading related stress distributions contribute to fatigue damage at weld notches and crack initiation will be governing, the fatigue life time for a constrained AW joint – the equilibrium equivalent residual stress is irrelevant – is smaller in comparison to a non-constrained or SR joint for the same far field loading applied, as experimentally observed (Bertini, Fontanari and Straffellini, 1998).

2.11 Total stress concept

Fatigue is concerned with crack initiation and crack growth (Fig. 2.73). Governing parameter in the initiation period, a (near) surface phenomenon, is the SCF. Micro-crack growth is typically included because of the low crack growth rate, although the initiation-growth transition definition is a qualitative one. If a crack penetrates into the material, the macro-crack growth resistance – a material bulk property – is taking over control. The stress intensity factor (SIF) is the crack growth period dominant parameter. Both SCF and SIF are defined as loading and (respectively intact and cracked damaged) geometry dependent.

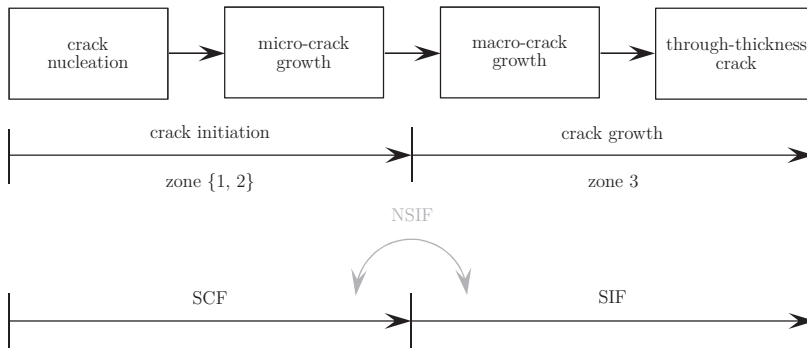


Figure 2.73: Quasi-2D fatigue and fracture scheme.

The SCF K_t is meant to be a loading and geometry controlled zone 1 similarity parameter, i.e. the (cyclic) remote mechanical loading induced linear elastic (peak) stress range S required to initiate a fatigue crack in an intact plane geometry like a FP reinforcement removed butt joint ($K_t = 1$): $S = \Delta\sigma$, should be the same as for a notched geometry ($K_t > 1$): $S = K_t \Delta\sigma$. However, the effective stress concentration often turns out to be smaller, similarity is violated and the fatigue- or endurance limit $\Delta\sigma_E$ related notch factor $K_f = \{\Delta\sigma_E(K_t = 1) / \Delta\sigma_E(K_t > 1)\}$ has been introduced. Assuming at least a significant part of the welded joint fatigue life in number of cycles N is related to crack initiation rather than crack growth, the K_f definition can be translated to any stress range $\Delta\sigma$ in the medium and high-cycle fatigue region; $K_f = \eta K_t \in (0 < \eta \leq 1)$. Similarity requires K_f to consider loading (amplitude, gradient, load ratio r_l), geometry (absolute and relative notch acuity, i.e. notch radius ρ , notch angle α , root notch size a_n and size effect) as well as material (i.e. quality, hardness, surface condition and elastoplastic notch behaviour); the latter in particular for ductile alloys like the aluminium 5xxx and 6xxx series.

To estimate the K_f zone 2 stress gradient contribution, a micro-structural notch support hypothesis (Neuber, 1937; Sonsino et al., 2012) can be adopted, averaging the notch stress over a material-characteristic micro-structural support length ρ^* and taking loading and geometry effects into account using a notch support factor s . Zone 3 stress gradient effects are included implicitly as far as the notch affected zone is concerned. The real notch radius ρ is artificially enlarged employing a fictitious one $\rho_f = s(r_l, \alpha, \dots) \cdot \rho^*$ to obtain the effective notch stress of the original

geometry. At the same time, investigation of the actual weld seam shows however that ρ is widely scattered, meaning the statistical weld volume effect has to be incorporated as well. The effective notch radius $\rho_e = \rho(\mu, \sigma) + \rho_f(s, \rho^*)$ and notch factor $K_f = K_t(\rho_e)$ define the effective notch stress concept principle. Optimum ρ_e values (i.e. average ones; s is loading and geometry dependent) for weld toe and weld root have been obtained fitting $S-N$ welded joint fatigue data in order to achieve a Basquin type of relation: $\log(N) = C - m \cdot \log\{S(K_f, \Delta\sigma)\}$, an optimum standard deviation σ and least squares solutions for the welded joint fatigue resistance constant C and curve slope m , incorporating the (quasi-constant) welding process induced thermal effects implicitly. The real notch radius component is assumed to be a worst case value ($\rho = 0$); σ contains the statistical part. Based on ρ_e estimates one reference value ρ_r has been proposed to be used in engineering applications for both weld toe and weld root notches (Zhang, 2012; Zhang, Sonsino and Sundermeier, 2012). However, things should be made as simple as possible, but not any simpler. Notch plasticity – whether a result of high remote mechanical loading, welding induced residual stress or both – introducing the (cyclic) work hardening exponent n , a material parameter, is ignored and K_f is limited to be used for a predominant linear elastic structural response. Although mentioned that size effects are included (Fricke, 2012), only the absolute notch acuity has been taken into account and K_f as scaling parameter is still incomplete. The relative part has been proposed to be incorporated – without experimental validation – using one of the weld dimensions $\{l_w, h_w\}$ rather than plate thickness t_p (Schijve, 2012). For weld toe induced fatigue, however, the plate gets damaged and it seems obvious to adopt t_p rather than $\{l_w, h_w\}$. The $\{t_p, l_w, h_w, a_n\}$ dependent artificial plate thickness t_p' should be involved for the weld root; scaling is not exclusively a matter of weld size.

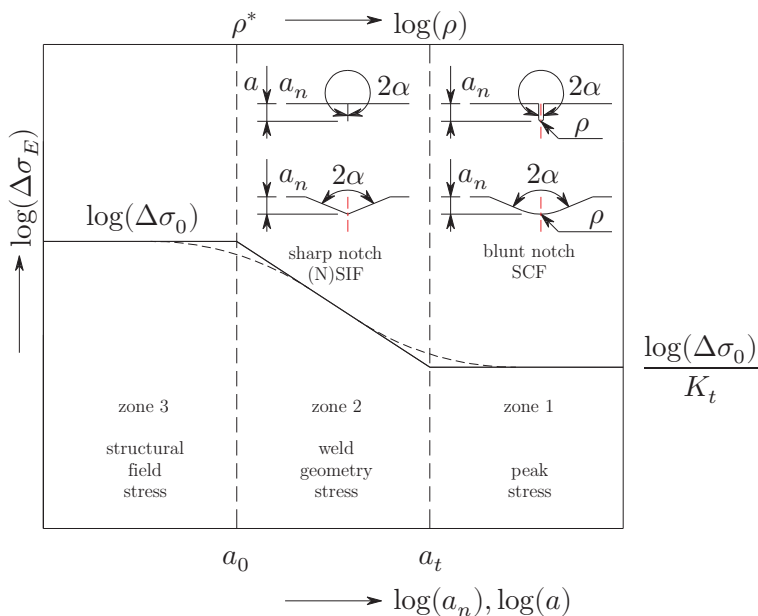


Figure 2.74: Notch and defect sensitivity correlation; endurance limit similarity.

The plane geometry fatigue- or endurance limit ($\Delta\sigma_E = \Delta\sigma_0$) is a material parameter, a threshold value defining on the one hand an upper limit that cannot be exceeded (Fig. 2.74). On the other hand, a fully effective notch ($K_f = K_t$) defines the lower limit: $\Delta\sigma_E = (\Delta\sigma_0/K_t)$, a structure parameter. Decreasing a_n of a blunt notch, the notch sensitivity increases and the peak stress becomes conservative ($K_f < K_t$). At the same time, for decreasing ρ the notch factor $K_f(K_t)$ decreases as well until some point a_t ; K_t may still increase although K_f remains constant and the K_f - K_t relation becomes insufficient. For $\rho \rightarrow 0$, the peak stress and zone 1 parameter K_t approach infinity and become inapplicable; the lower limit $\Delta\sigma_E = (\Delta\sigma_0/K_t) \rightarrow 0$ and the zone 2 weld geometry stress becomes governing. If the sharp notch denotes a crack, i.e. ($2\alpha = 2\pi$) and ($a_n = a$), the KT diagram (Kitagawa and Takahashi, 1976; Fig. 2.74) is obtained. Continuing the a_n decrease, a critical notch or crack size a_0 (El Haddad et al., 1979) – a material defect sensitivity parameter having the same physical meaning as intact geometry parameter ρ^* (Radaj et al., 2013) – appears. For ($a_n < a_0$) the root notch size hardly influences the endurance value and approaches the plane geometry upper limit: $\Delta\sigma_E \rightarrow \Delta\sigma_0$, a zone 3 field stress parameter. For ($a_0 < a_n < a_t$), the zone 2 notch stress loading mode-I component $\sigma_{\theta\theta}$ along the bi-sector ($\beta = 0$) is assumed to be dominant (Atzori and Lazzarin, 2000; Atzori, Meneghetti and Susmel, 2002) and the endurance limit scales according to $\Delta\sigma_E a_n^{1-\lambda_s} = C$, introducing similarity. A critical sized crack, ($a_n = a_0$) and $\{\lambda_s = \lambda_1 = (1/2)\}$, yields the material crack growth threshold: $\Delta K_{th} \pi^{\lambda_1-1} = \Delta\sigma_0 a_0^{1-\lambda_1}$.

For a crack initiation dominated fatigue life, the notch stress gradient based endurance limit similarity can be translated to the medium- and high-cycle fatigue range, introducing the mode-I notch stress intensity factor (NSIF): $K_I^N = (2\alpha)^{1-\lambda_s} \cdot \lim_{r \rightarrow 0^+} \{r^{1-\lambda_s} \sigma_{\theta\theta}(r, \theta = 0)\}$. In case of a crack K_I^N turns into the SIF K_I definition, i.e. K_I^N bridges the crack initiation- and crack growth parameter (Fig. 2.73), respectively $K_f(K_t)$ and K_I . Like the SCF, the NSIF is a remote loading dependent and intact geometry linear elastic response parameter, although notch elastoplasticity can be taken into account (Lazzarin, Zambardi and Livieri, 2001). Using the weld toe notch stress formulation (Eq. 2.10), the NSIF can be rewritten: $K_I^N = k_1 \sigma_s t_p^{1-\lambda_s}$ (Lazzarin and Tovo, 1998); $\Delta K_I^N = k_1 \Delta\sigma_s t_p^{1-\lambda_s}$, taking (only) the absolute notch acuity into account. The curve fitted remote loading and joint geometry dependent correction function k_1 implicitly includes the zone 2 weld load carrying stress contribution as well as zone 3 stress gradient effects in the notch affected zone. For a weld root notch $K_I^N = K_I = k_1 \sigma_s a_n^{1-\lambda_1}$. However, like the NSIF and SIF units ($\lambda_s \neq \lambda_1$), the scaling parameter for weld toe and weld root notches, respectively $t_p^{1-\lambda_s}$ and $a_n^{1-\lambda_1}$, turn out to be different, meaning it is principally wrong to combine weld toe and weld root fatigue data; not even if $\{\Delta K_I^N, \Delta K_I\}$ are translated to energy density as proposed (Livieri and Lazzarin, 2005; Fricke, 2012) solving only the units part. Besides, the NSIF implies a sharp notch assumption (Fig. 2.74). Although a reasonable worst case scenario for welded joints – from physical point of view ($\rho = 0$) seems rather fictitious than ($\rho = \rho_f$) – it is impossible to include weld volume effects and the corresponding uncertainty should be part of the Basquin relation $\{\log(N) = C - m \cdot \log(\Delta K_I^N)\}$ residual, i.e. standard deviation σ .

The total welded joint fatigue life N consists of a crack initiation and crack growth contribution: $N = N_i + N_g$ (Fig. 2.73). Although not easy to distinguish because of the gradual transition, some two-stage parameter models have been proposed (Brandt, Lawrence and Sonsino, 2001; Lassen and Recho et al., 2005, 2006 and 2009). Key element is an assumed(!) micro-crack coalescence size a_c , respectively 0.25 and 0.10 [mm] based on different arguments: theoretical (e.g. fracture mechanics modelling restrictions), practical (e.g. detectability) as well as typical ($a_c = \rho_f$) but still artificial, affecting the (N_i/N_g) ratio up to a large extent.

With respect to crack initiation, the linear elastic part of the Coffin-Manson equation including Morrow's mean stress correction has been adopted: $\log(2N_i) = m_1 \cdot \log\{2(\sigma_f' - \sigma_m)\} - m_1 \cdot \log\{K_f \Delta\sigma_s\}$. The involved zone 1 parameter $K_f(K_t)$ requires a notch radius ρ . Proposed values include either a micro-structural notch support hypothesis based worst case effective value $\rho_e = \rho_f$ similar for weld toe and weld root notches (Brandt, Lawrence and Sonsino, 2001) or an extreme value $EV(a_r)$ including the real statistical component (Lassen and Recho et al., 2006), respectively obtained using notched weld (root) material specimen fatigue test $S-N$ data assuming ($N \approx N_i$) and weld geometry measurement results. The material parameters, fatigue strength coefficient σ_f' and curve slope m_1 , are determined using smooth hour-glass shaped weld (root) material specimen in strain controlled tests (Brandt, Lawrence and Sonsino, 2001) or material dependent empirical relations calibrated using welded joint $S-N_i$ fatigue test data covering the number of cycles up to the micro-crack transition size (Lassen and Recho, 2009). The mean stress σ_m is obtained using either cyclic stress-strain measurement data of the hour-glass shaped specimens (Brandt, Lawrence and Sonsino, 2001) or is simply assumed to be at yield magnitude because of the welding induced residual stress (Lassen and Recho et al., 2006).

For arc-welded joints it seems inevitable that crack nuclei (defects), already exist – at least in a worst but realistic case scenario – naturally introducing the linear elastic fracture mechanics (LEFM) crack damaged geometry parameter K_I (Fig. 2.73). LEFM can straightforward be applied for cracks ($a > a_0$), provided the far field stress induced degree of notch plasticity is limited. To get some idea about order of magnitude: for Al5083 base material, $a_0 \approx 30..40$ [μm] independent of remote loading ratio r_l (Kranenburg, 2000); the AW joint average heat affected zone and weld material value (Livieri and Lazzarin, 2005) $a_0 \sim 140$ [μm]. The SIF K_I naturally allows to incorporate the total mode-I weld notch stress distribution. For a weld toe geometry $K_I = Y_n(\sigma_{se}, a)Y_f(r_s, a)\sigma_s(\pi a)^{1-\lambda_1}$. The weight function $Y_f(r_s, a)$ and structural stress σ_s represent the zone 3 macro-crack related equilibrium equivalent far field stress contribution; $Y_n(\sigma_{se}, a)$ the zone {1, 2} micro-crack associated self-equilibrating stress part. A weld root notch a_n introduces a geometric notch and crack similarity, turning the SIF into $K_I = Y_f(Y_{fw}, r_s, a_n + a)\sigma_s\{\pi(a_n + a)\}^{1-\lambda_1}$; Y_{fw} takes the weld geometry into account. Note that a (virtual) crack path assumption is required what might be considered as disadvantage, although for weld {toe, root} notches in predominant orthotropic and mode-I governing hull structures it will likely be in plate thickness $\{t_p, t_p'\}$ direction.

The cyclic remote mechanical loading turns K_I into a driving force ΔK_I and may initiate crack growth. The sigmoidal shaped large/long (macro-)crack growth characteristic $(da/dn)-\Delta K_I$ (Fig. 2.75) is divided into:

- region-I (crack growth near threshold)
- region-II (linear, steady state crack growth)
- region-III (unstable crack growth up to final fracture).

Below the threshold ΔK_{th} cracks principally do not grow. The region-III fatigue life time contribution is quite small because of the high crack growth rate (da/dn) and considered not that important from fatigue (design) point of view. Although micro-cracks emanating at notches show anomalous growth rates (Fig. 2.75) – explaining why $K_f(K_t)$ should include elastoplastic notch behaviour – for the two-stage two-parameter models, N_i is supposed to include region-I micro-crack growth and the region-II Paris equation $\log(da/dn) = C' + m_2 \cdot \log\{\Delta K_I(\Delta\sigma_s, Y_f, a)\}$ is sufficient to obtain the Basquin type of relation for the macro-crack growth part: $\log(N_g) = C - m_2 \cdot \log\{\int f(\Delta K_I) da\}$. Typically standard crack growth specimens are used to acquire the macro-crack growth resistance coefficient C' and slope m_2 (Brandt, Lawrence and Sonsino, 2001; Lassen and Recho et al., 2005, 2006 and 2009). Relative notch- or crack-acuity is not taken into account.

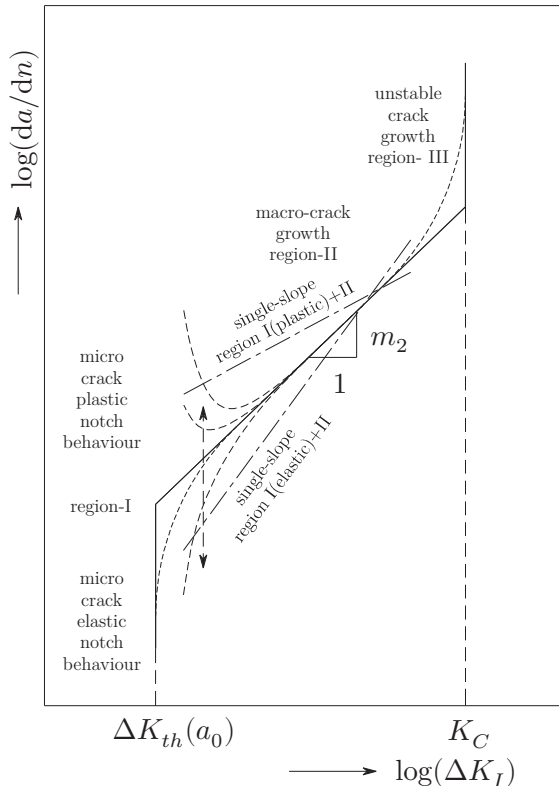


Figure 2.75: Anomalous growth rates for micro-cracks emanating at notches.

Intuitively, crack initiation and crack growth are different fatigue mechanisms, meaning the slopes $\{m_1, m_2\}$ will likely be different. It seems obvious that up to a certain transition (coalescence) point $N_c(\Delta\sigma_c)$ crack initiation (i.e. micro-crack growth) dominates; macro-crack growth is governing beyond, justifying a two-stage model that – by the way – should apply to constant amplitude (CA) as well as variable amplitude (VA) loading. Question is whether a two-parameter concept is the best solution to include two-stage behaviour. Except for the micro-crack transition size a_c , the actual AW joint fatigue test data is only used for calibration purposes of some crack initiation model parameters or not involved at all, assuming a series of initiation and growth similarity conditions for (standard) specimen and AW joints rather than a one-to-one correspondence between model life time estimates and $S-N$ test data; a welded joint fatigue resistance similarity. Scaling issues are still unsolved.

The one-stage one-parameter notch stress- and notch stress intensity factor concepts involve respectively the zone $\{1, 2\}$ intact geometry parameters $K_f = K_t(\rho_e)$ and K_I^N , assuming that crack initiation is governing. A two-stage two-parameter concept incorporates both initiation and growth, i.e. K_f or K_I^N as well as K_I . However, rather than a one-stage one-parameter or two-stage two-parameter concept, a two-stage one-parameter concept using the total stress S_T is proposed. The complete remote mechanical loading controlled through-thickness weld toe- or weld root notch stress distribution $\{\sigma_n(r/t_p), \sigma_{nr}(r'/t_p')\}$ is taken into account, meaning all zone $\{1, 2, 3\}$ governing stress components are involved. Limiting the structural response to linear elastic behaviour, stress field similarity (Fig. 2.1) – a modification of an existing representation (Atzori and Lazzarin, 2000; Atzori, Meneghetti and Susmel, 2002) – has already been demonstrated (Paragraph 2.6 and 2.7) using linear superposition of an equilibrium equivalent and self-equilibrating part. The latter, the weld geometry stress, controls zone $\{1, 2\}$; the former, the structural field stress, dominates zone 3. All welded joint geometry parameters $\{t_b, t_c, l_c, l_w, h_w, a_n, \rho\}$ are involved, i.e. the absolute notch acuity has been taken into account. Conceptually, the same stress field similarity has been observed for the thermal loading induced residual stress distribution (Paragraph 2.10). Typical hull structure AW joints show displacement constraint control up to some extent, i.e. are considered to be of the “equilibrium” type.

The total through-thickness weld $\{\text{toe, root}\}$ notch stress distribution $\{\sigma_n^T, \sigma_{nr}^T\}$ is a linear superposition of the cyclic remote mechanical- and quasi-constant welding induced thermal part, often referred to as respectively the primary- and secondary stress component. Although the actual loading sequence is the other way around, the former involves a stress range with corresponding load ratio; the latter a residual mean stress. Looking at crack paths originated at both weld toe and weld root notches as shown for FRANC2D (Cornell Fracture Group, 2010) simulations in comparison to experimental observations (Fig. 2.13 and 2.34), a crack path similarity has been identified. The former includes only the cyclic remote mechanical loading induced stress; the latter the quasi-constant welding induced thermal residual stress, a mean stress contribution, as well. Since the crack growth direction for the simulations is based on maximum (1st) principal

stress, the zone $\{2, 3\}$ stress gradient seems hardly residual stress affected no matter the different conditions, respectively loading and displacement controlled. Using $\{\sigma_n(r/t_p), \sigma_{nr}(r'/t_p')\}$ only, it will be assumed that stress gradient induced scaling effects can be reasonably well estimated.

The number of weld passes and restrained material volume increase for increasing plate thickness t_p and weld dimensions $\{l_w, h_w\}$. The “equilibrium” type residual stress distribution has already been found highly tensile (Fig. 2.70) – in particular for the zone $\{1, 2\}$ notch affected region – and its magnitude will increase even further, introducing a size- or welding technology effect. Remote mechanical (over) loading may shake down the thermal residual mean stress; its equilibrium equivalent part in particular, however, because of the stress distribution similarity the zone $\{1, 2\}$ mean stress including both residual stress and remote load ratio effects is assumed to remain highly tensile anyway and the influence of residual stress scaling will be limited. For zone 3, the remote mechanical load ratio r_l is taking over control.

Assuming the total fatigue life predominantly consists of crack growth, the macro-crack growth parameter K_I will be adopted. Cracks emanating at weld toe- or weld root notches show however anomalous growth rates (da/dn). Depending on the degree of notch and/or crack tip elastoplasticity, small/short cracks (initially) may tend to grow slower or faster in comparison to cracks in plane geometries for the same ΔK_I and accelerate or decelerate respectively to the large/long crack growth characteristic; similarity – the same crack growth rate for similar crack driving force – is violated (Fig. 2.75). A significant part of the welded joint fatigue life time is expected to be related to anomalous micro-crack growth because of the low (da/dn). The linear superposition of the predominantly elastic remote mechanical- and welding induced thermal notch stress distribution may significantly increase the total stress level and the possibility of notch and crack tip plasticity, introducing the (cyclic) work hardening exponent n as material parameter. Rather than introducing an effective (initial) crack size (El Haddad et al., 1979), the zone $\{2, 3\}$ stress gradient of the cyclic remote mechanical part that has been found to be crack path direction governing, will be employed to estimate the anomalous micro-crack growth elastoplastic behaviour as well, in particular the weld geometry stress, i.e. the self-equilibrating stress part $\{\sigma_{se}, \sigma_{ser}\}$ that contains the notch characteristic properties. A two-stage micro- and macro-crack growth region- $\{I, II\}$ model is proposed to achieve similarity, modifying the Paris equation:

$$\log\left(\frac{da}{dn}\right) = C' + n \cdot \log\{Y_n(\sigma_{se}, a)\} + m_2 \cdot \log[f\{\Delta\sigma_s, Y_f(r_s, a), a\}] \quad (2.54)$$

The 2nd term yields the micro-crack growth behaviour in the notch affected region; n denotes a notch stress elastoplasticity correction (Filippi, Ciavarella and Lazzarin, 2002). Straightforward integration still yields a Basquin type fatigue resistance relation, since the total stress parameter S_T (i.e. an equivalent line criterion) includes the anomalous micro-crack growth behaviour:

$$\log(N) = C - m_2 \cdot \log(S_T) \quad (2.55)$$

with

$$S_T = \frac{\Delta\sigma_s}{t_p^{(r) \frac{2-m_2}{2m_2}} I_N^{\frac{1}{m_2}}}$$

and

$$I_N = \int_{\left(\frac{a_i}{t_p^{(r)}}\right)}^{\left(\frac{a_f}{t_p^{(r)}}\right)} f \left\{ Y_n \left(\frac{a}{t_p^{(r)}} \right), Y_f \left(\frac{a}{t_p^{(r)}}, r_s \right), \left(\frac{a}{t_p^{(r)}} \right), n, m_2 \right\} d \left(\frac{a}{t_p^{(r)}} \right)$$

The geometry-, zone 1 peak stress- and zone {2, 3} stress gradient dependent notch crack growth integral I_N is proportional to N , meaning it is quite easy to determine how much of the total fatigue life is involved reaching a certain (relative) crack length.

Starting in the medium-cycle fatigue range, for decreasing $S_T(\Delta\sigma_s)$ the notch affected micro-crack growth behaviour may turn (gradually) from elastoplastic into elastic. The elastoplastic n value as well as its implicitly required transition point to elastic behaviour is unknown in advance and might be solved for. Another way to deal with elastoplasticity is to estimate the (average) MCF n value and apply an elastoplasticity induced HCF slope correction, introducing a two-slope formulation:

$$\log(N) = C - m_2 \cdot \log(S_T) - \left\{ \left(\frac{m_2}{m_1} \right) - 1 \right\} \cdot \log[1 + \exp\{\log(S_T) - \log(S_c)\}^{-m_1}] \quad (2.56)$$

It is non-linear on log-log scale (Fig. 2.76). Beyond the total stress transition point S_c notch elastoplasticity is governing; below it becomes elastic. The model may be simplified applying the Paris equation separately to the medium- and high-cycle fatigue range. The slopes $\{m_1, m_2\}$ will both be corrected for the missing elastoplastic micro-crack growth behaviour. The total stress parameter definition S_T remains unaffected; the notch crack growth integral I_N will be modified. For ($m_1 \rightarrow \infty$) the two-slope formulation (Eq. 2.56) will turn into a (random) fatigue limit formulation:

$$\log(N) = C - m_2 \log(S_T - S_\infty) \quad (2.57)$$

The total stress parameter S_T requires an initial crack or defect size a_i (assumption). It is often argued to be a critical parameter (Schijve, 2012) and for a two-stage model two-parameter concept it is indeed. However, if the total fatigue life is

involved and welded joint fatigue resistance similarity will be satisfied, within certain limits it can be any value since predominantly the fatigue resistance constant C will be affected, shifting the S_T-N curve up or down. The real value includes a statistical component $a_i(\mu, \sigma)$, required to include the weld volume effect because of a significant scatter along the weld seam. In comparison to the effective notch radius ρ_e , artificial enlarging may be required for ($a < a_0$) (Smith and Miller, 1978; El Haddad et al., 1981) and the effective (initial) crack size yields: $a_e = a_i(\mu, \sigma) + a_f$. Note the a_e and ρ_e similarity. At the same time, a difficulty may be introduced that needs to be resolved. The total stress parameter S_T includes ρ as well as a . Both parameters contain a real-, fictitious- and statistical component, respectively assumed to be governing for the micro- and macro-crack growth governing parameters K_f and K_I . Besides, ρ affects the elastoplastic behaviour in the notch affected region as well.

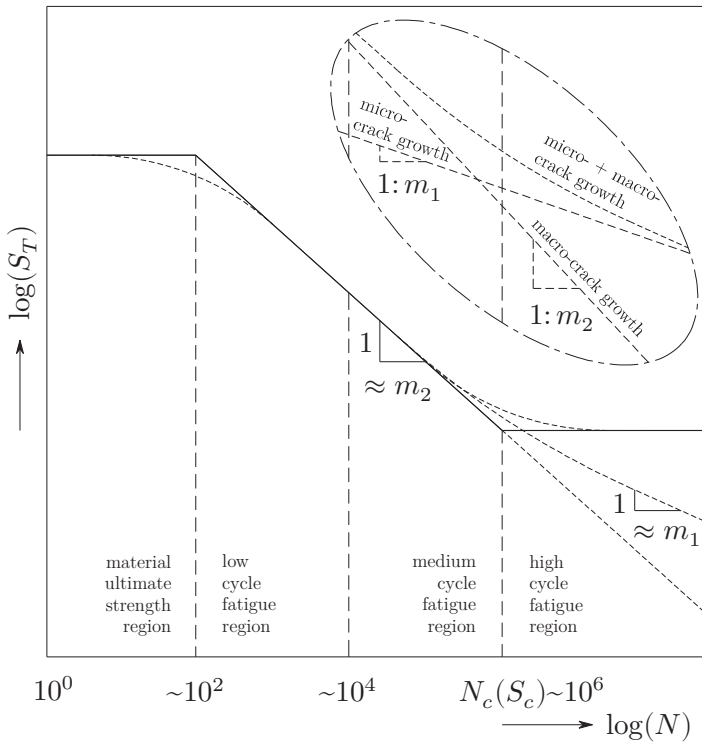


Figure 2.76: Medium and high-cycle fatigue joint S_T-N curve.

To include the relative (notch) crack acuity, it seems obvious to select the plate thickness $\{t_p, t_p'\}$. This parameter is naturally introduced for the weld notch stress distribution and SIF because of the crack path. Last but not least, in terms of welded joint fatigue resistance similarity it is a parameter that small- and large scale laboratory specimen as well as full scale hull structures have in common. Note that the relative defect size ($a_i/t_p^{(i)}$) in that respect is considered to be the

explanation for the plate thickness correction factor (Maddox, 1987). For decreasing $(a_i/t_p^{(i)})$, the notch crack growth integral I_N tend to show asymptotic behaviour (Maddox and Webber, 1978; Dong and Hong, 2004) for $(a_i/t_p^{(i)}) \rightarrow O(10^{-3})$, i.e. for $(a \rightarrow 0)$ the total stress S_T becomes an endurance limit parameter. Although difficulties may be introduced with respect to physical interpretation and LEFM modelling limitations, an asymptotic $I_N(a_i/t_p^{(i)})$ value would be an engineering solution and ρ_e would be the remaining parameter to deal with notch effectivity (although the stress gradient is incorporated already) and statistical effects. In terms of geometric notch and crack similarity, the absolute and relative (notch) crack acuities may be taken into account using $t_p^{(i)}$, $(a_{(e)}/t_p^{(i)})$ and $(\rho_{(e)}/t_p^{(i)})$.

The resistance formulations (Eq. 2.55, 2.56 and 2.57) are principally joint S_T - N curves (Fig. 2.76): medium- and high-cycle fatigue damage at notches in the classified (aluminium) arc-welded joints can be calculated. A S_T based welded joint fatigue resistance similarity will be assumed between model estimates and actual test data concerning small scale- and large scale laboratory specimens (SSS and LSS considering respectively the welded joint only and including some neighbour structural members as identified in stiffened panels, frames or trusses) as well as full scale hull structures (FSS) to estimate the fatigue life N , meaning the fatigue damage should be the same. The classification {SSS, LSS, FSS} is not related to welded joint dimensions as well up to what extent neighbour structural members are involved. The remote-mechanical stress is principally not affected; the residual stress part is and may require correction.

The total stress parameter S_T definition and two-slope S_T - N relation is principally argued from welded joint geometry and (cyclic) remote mechanical loading similarity point of view. The parameters $\{C, m_1, m_2, S_c\}$ or $\{C, m_2, (S_\infty)\}$, material properties, will be obtained fitting SSS fatigue test data and include the (quasi-constant) welding process related thermal effects, i.e. the (mean) residual stress effects as well as (WM and HAZ) material structure, i.e. hardness, cyclic hardening coefficient, etc. The average {defect size, notch radius} might be obtained optimising the residual uncertainty. Since the stress gradient and notch / crack tip elastoplasticity are explicitly taken into account, the optima might be real- rather than effective values, since the fictitious components have become obsolete. The statistical component (distribution) should be determined using direct measurements anyway and can be used to deal with different weld qualities as well. Using LSS should achieve the same results. For FSS's similarity is supposed to be maintained; validation in a measurement campaign is usually limited to the stress field (distribution).

To deal with FSS production tolerances, i.e. offset- and angular misalignments, (zone 3) far field knock down factors $\{K_{mm}, K_{mb}\}$ have to be introduced for adequate fatigue life time estimates, since SSS and LSS misalignment induced far field stress corrections are aimed for to be taken into account in order to identify uncertainties rather than arriving at an uncertain residual uncertainty.

2.12 Conclusions

Remote mechanical loading induced through-thickness weld toe- and weld root notch stress distributions $\{\sigma_n, \sigma_{nr}\}$ have been examined to distinguish the involved stress components. A self-equilibrating weld geometry stress – consisting of a local V-shaped notch- and weld load carrying part – and equilibrium equivalent global structural field stress are identified; a refinement of a well-known definition. The obtained semi-analytical formulations are related to the welded joint far field stress, calculated using a relatively coarse meshed {plate, shell} FE model as typically available for fatigue design purposes. Exploiting (non-) symmetry conditions, a generalised formulation demonstrating stress field similarity has been observed and extends to the welding induced thermal residual stress distributions $\{\sigma_n^r, \sigma_{nr}^r\}$.

Fatigue scaling requires both the (zone 1) peak value and (zone 2 notch affected and zone 3 far field dominated) gradient to be incorporated, meaning a damage criterion should take the complete distribution into account; a prelude to {crack growth, welded joint fatigue resistance} similarity and finally a total stress concept.

3

Weld Notch Stress Intensities

Symmetry, as wide or narrow its meaning may be defined, is one idea that through the ages has been used to comprehend and create order, beauty and perfection.

Hermann Klaus Hugo Weyl (1885-1955, mathematician)

3.1 Introduction

The remote mechanical loading induced mode-I through-thickness weld notch stress distributions $\{\sigma_n, \sigma_{nr}\}$, including a (local) zone 1 peak value and zone 2 stress gradient in the notch affected region as well as a (global) zone 3 structural field stress gradient, proved to be generalised formulations and stress field similarity has been demonstrated exploiting symmetry (Chapter 2). Conceptually, the same applies to the welding process related residual stress distributions.

Scaling of welded joint fatigue damage requires a total stress parameter definition taking all zone $\{1, 2, 3\}$ remote- and residual stress contributions into account. The stress intensity (similarity) factor (SIF) K seems to meet this criterion, though, the intact geometry related notch stress distributions should be correlated to crack damaged equivalents; fatigue is assumed to be crack growth (dominated) process. At the same time, hull structure arc-welded joints inevitably contain flaws or crack nuclei (defects) – assumed to be mechanically or physically small – at the weld toe- and root notches, i.e. using the damage tolerant parameter K seems justified, since fatigue associated with the medium and high-cycle life time range at both locations will predominantly be a matter of $\{\text{micro, macro}\}$ -crack growth.

Outline

Identifying the different contributions for remote loading controlled mode-I SIF's at weld toe- and weld root notches, the corresponding K_I definitions will be considered first (Paragraph 3.2). The zone 3 associated equilibrium equivalent stress contribution will be used to obtain a far field factor, distinguishing different type of cracks related to (non-) symmetry conditions (Paragraph 3.3) for both (quasi) 2D- and 3D configurations. A notch factor incorporates the zone $\{1, 2\}$ governing self-equilibrium equivalent stress (Paragraph 3.4). Weld toe- and weld root notch stress intensities

are derived and illustrated (Paragraph 3.5 and 3.6) in order to investigate a notch affected micro- and far field dominated macro-crack region. Using a parameter sensitivity study of weld dimensions, including notch radius and plate thickness, size effects have been investigated (Paragraph 3.7). Finally, the welding induced and displacement controlled mode-I residual stress intensity factor (RSIF) K_I^r is acquired for both weld toe and weld root notches (Paragraph 3.8) to complete the total weld notch stress intensity similarity factor formulation $K_I^T = K_I + K_I^r$.

3.2 Definition

The linear elastic stress field at an infinitely sharp crack tip (Eq. 2.13 to 2.15) shows square root singular behaviour for $(r'/t_p') \rightarrow 0$. To quantify its magnitude, the SIF K – a loading and geometry dependent LFM similarity parameter – has been defined. The stress field components $\{\sigma_{\theta\theta}, \sigma_{rr}, \sigma_{r\theta}\}$ correspond respectively to the linear independent crack surface displacement opening mode-I, sliding mode-II and tearing mode-III (Fig. 3.1).

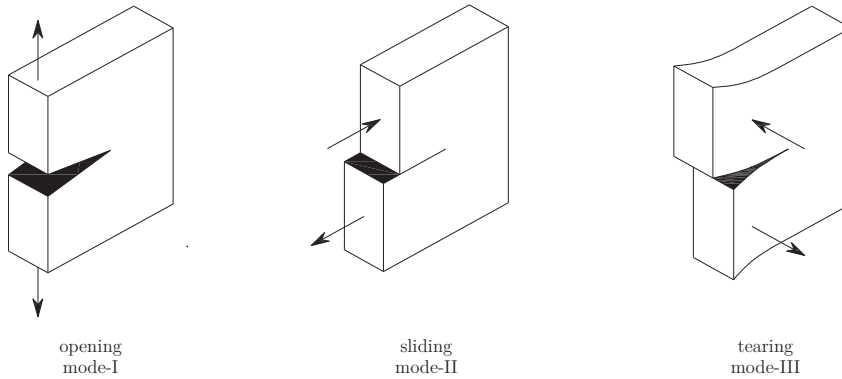


Figure 3.1: Crack surface displacement modes (Janssen et al., 2002).

Sliding mode-II becomes irrelevant in case of a thin {plate, shell} assumption since through-thickness shear forces are neglected, meaning any hull structure multi-axial far field stress distribution is at most a bi-axial one. Opening mode-I however is considered to be dominant because of the stiffened (curved) panel induced orthotropic stiffness characteristics. The corresponding SIF K_I is a 1st order damage tolerant parameter, i.e. only the 1st (singular) $\sigma_{\theta\theta}$ term (Eq. 2.14) is incorporated. The linear elastic principle and quasi-2D infinite plane solution for a remote mechanically loaded crack (Fig. 3.2), size $2a$, yields:

$$\begin{aligned}
 K_I &= (2\pi)^{1-\lambda_1} \lim_{r' \rightarrow 0^+} \{(r')^{1-\lambda_1} \sigma_{\theta\theta,1}(r', \theta = 0)\} \\
 &= \sigma_s \sqrt{\pi a}
 \end{aligned} \tag{3.1}$$

The singular $\sigma_{\theta\theta}$ behaviour has been eliminated (Gross and Mendelson, 1972); $(2\pi)^{1-\lambda_1}$ refers to the mode-I intensity for $2\alpha = 2\pi$. To obtain the SIF for groove- and fillet weld geometries, weight functions (Albrecht and Yamada, 1977) will be introduced. Consistently using the intact geometry related weld notch stress distribution σ_n superposition (Paragraph 2.6), K_I includes for weld toe cracks $\{Y_n, Y_f\}$; a size/length dependent notch- and far field factor:

$$K_I = \sigma_s Y_n Y_f \sqrt{\pi a} \quad (3.2)$$

The equilibrium equivalent stress part related far field factor Y_f incorporates the remote mechanical loading- and crack related geometry effects, i.e. both the membrane and bending component for finite plane dimensions (plate thickness) and free surface behaviour. The non-square root singular notch behaviour is taken into account using the self-equilibrating stress part induced notch factor Y_n .

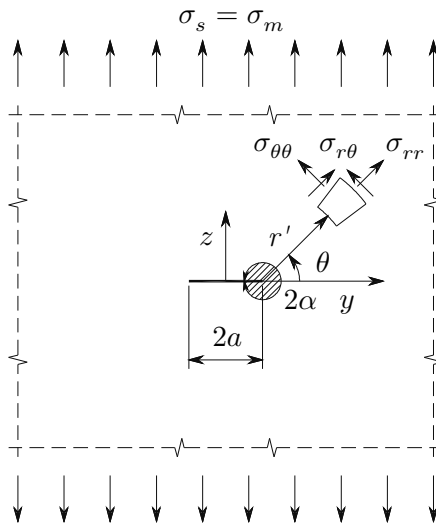


Figure 3.2: Mode-I remote mechanically loaded crack in an infinite plane.

Weld root cracks initiate at a notch in crack configuration (size a_n), meaning the crack tip and root notch share the same square root stress field singularity and the SIF K_I will be computed for a fictitious crack length ($a_n + a$). The far field factor should take the weld reinforcement geometry into account $Y_f(Y_{fw})$:

$$K_I = \sigma_s Y_f(Y_{fw}) \sqrt{\pi(a_n + a)} \quad (3.3)$$

Obviously $Y_n \neq 1$, although a separate notch contribution is not involved since the SIF already includes the square root singular behaviour. Adding the notch induced component would require a SIF redefinition since K_I would become singular again. The weld geometry induced SIF contribution for a weld toe and weld root turns out to be respectively notch- and far field dominated.

3.3 Far field factor

The linear far field stress distribution in the fracture mechanics context is consistent with the one defined for the welded joint (Eq. 2.20). A superposition of the involved membrane and bending zone 3 component translated to the (unit) structural stress formulation (Eq. 2.21 to 2.23) applies to the far field factor as well. For a weld toe:

$$Y_f = Y_{fm} - r_s(Y_{fm} - Y_{fb}) \quad (3.4)$$

The intact welded joint geometries (Fig. 2.3 and 2.5) should be related to crack damaged equivalents to obtain Y_f , taking the characteristic features: notch location, symmetry and HS type into account (Paragraph 2.2). Single- and double edge crack geometries match respectively the weld toe non-symmetry and symmetry cases with respect to $(t_p/2)$; the single edge- and centre notch geometries correspond to the weld root notch induced (non-)symmetry cases. Including the weld reinforcement contribution to comply with the welded joint far field stress definition yield:

$$Y_f = Y_{fw} \{Y_{fm} - r_s(Y_{fm} - Y_{fb})\} \quad (3.5)$$

To continue the quasi-2D approach adopted for HS's type *C*, weld notches along the seam (Paragraph 2.2 and 2.9), Y_f should be dealt with similarly. At the weld ends, HS's type *B* require a 2D formulation by definition (Fig. 2.4); 3D effects have to be incorporated for HS's type *A* only. Both HS type $\{A, B\}$ appear to be predominantly weld toe notches.

3.3.1 Single edge crack

Weld toe notches along the weld seam – quasi-2D HS's type *C* – showing non-symmetry with respect to $(t_p/2)$, require far field stress induced plate thickness and free surface effects to be taken into account with respect to the principle solution (Eq. 3.1): a single edge crack (SEC) geometry correction, like identified at location 1 of a DS T-joint or SS butt joint (Fig. 3.3a).

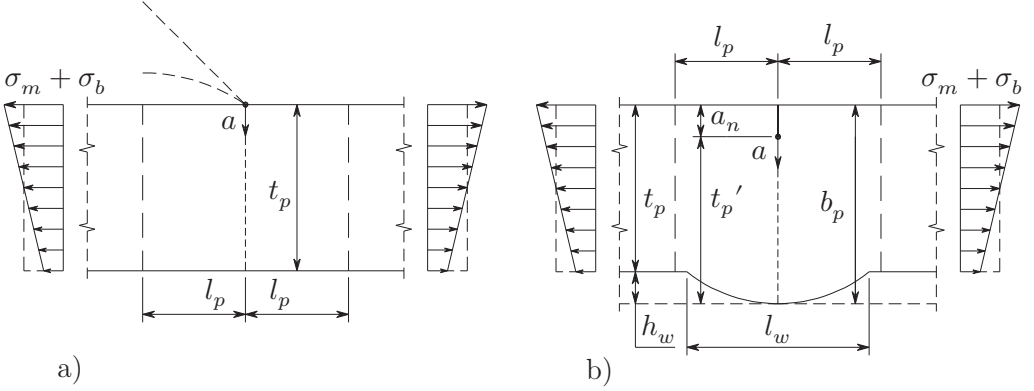


Figure 3.3: Single edge crack at a) weld toe- and b) at (weld) root notch.

Fortunately, a SEC geometry is often encountered in standard crack growth specimen, meaning handbook solutions are available (Tada, Paris and Irwin, 2000). The far field membrane and bending component $\{Y_{fm}, Y_{fb}\}$ are mentioned to be better than 0.5 [%] for any (a/t_p) in comparison to FE results, provided the far field stress distance criterion $(l_p/t_p) \geq 1$ is satisfied.

$$Y_{fm} \left(\frac{a}{t_p} \right) = \sqrt{\left(\frac{2}{\pi} \right) \tan \left(\frac{\pi}{2} \cdot \frac{a}{t_p} \right)} \cdot \frac{0.752 + 2.20 \left(\frac{a}{t_p} \right) + 0.370 \left\{ 1 - \sin \left(\frac{\pi}{2} \cdot \frac{a}{t_p} \right) \right\}^3}{\sqrt{\left(\frac{a}{t_p} \right) \cos \left(\frac{\pi}{2} \cdot \frac{a}{t_p} \right)}} \quad (3.6)$$

$$Y_{fb} \left(\frac{a}{t_p} \right) = \sqrt{\left(\frac{2}{\pi} \right) \tan \left(\frac{\pi}{2} \cdot \frac{a}{t_p} \right)} \cdot \frac{0.923 + 0.199 \left\{ 1 - \sin \left(\frac{\pi}{2} \cdot \frac{a}{t_p} \right) \right\}^4}{\sqrt{\left(\frac{a}{t_p} \right) \cos \left(\frac{\pi}{2} \cdot \frac{a}{t_p} \right)}} \quad (3.7)$$

The only geometry parameter involved turns out to be the plate thickness t_p , meaning $\{Y_{fm}, Y_{fb}\}$ are basically welded joint independent. Crack growth specimen however typically contain – like a PP SS butt joint (Fig. 3.3b) – a single edge notch (SEN) with, i.e. a (weld root) notch in crack configuration (size a_n) where the crack is supposed to initiate and the fictitious crack length becomes $(a_n + a)$:

$$\left(\frac{a}{t_p} \right) = \left(\frac{a_n}{b_p} \right) + \left(\frac{t_p'}{b_p} \right) \left(\frac{a}{t_p'} \right) \quad (3.8)$$

For a SEN crack growth specimen ($b_p = t_p$) and ($t_p' = t_p - a_n$), meaning Y_f does principally not change. A weld geometry introduces a reinforcement to be included; ($b_p = t_p + h_w$) and ($t_p' = t_p + h_w - a_n$) for root notch location 3 of a SS butt joint. To maintain compliance with the far field stress definition, Y_f needs to be modified using a weld geometry component Y_{fw} . Parametric curve fitted Y_{fw} solutions available are quite often limited concerning welded joint dimensions. Using the coarse meshed FE models as applied for the weld root notch stress distributions (e.g. Fig. 2.36), K_I is obtained for different (a/t_p') adopting a stiffness derivative technique rather than the J -integral (Banks-Sills, 1991). Both methods require a virtual crack extension and are equivalent in terms of accuracy. The former however just needs the displacement field; the latter requires a strain field, derivative(!) information. The crack tip adjacent nodes are moved to the isometric (1/4) and (3/8) positions – the latter for the centre node only – to introduce the square root singular crack tip behaviour. The calculated weld geometry far field function Y_{fw} is a curve fitted 4th order polynomial approximation:

$$Y_{fw} \left(\frac{a}{t_p} \right) = \frac{K_I}{\sigma_s \sqrt{\pi a} Y_f} \quad (3.9)$$

$$= c_0 + c_1 \left(\frac{a}{t_p} \right) + c_2 \left(\frac{a}{t_p} \right)^2 + c_3 \left(\frac{a}{t_p} \right)^3 + c_4 \left(\frac{a}{t_p} \right)^4$$

With respect to the non-symmetric (weld root) notch stress distribution in the cross-section of the crack, the structural field root- or equilibrium equivalent stress part is included implicitly.

For weld end HS's type *B*, predominantly weld toe notches, Y_f as obtained for the HS's type *C* (Eq. 3.4 and 3.5) can still be used, since a 2D edge crack formulation is required by nature. Only the plate thickness notation needs to be modified: ($t_p \rightarrow t_p'$).

Like the 3D far field stress effects (Paragraph 2.9), the weld toe related semi-elliptical crack formulations are required to incorporate 3D crack shape effects at weld end HS's type *A*, introducing the crack aspect ratio (a/c) as illustrated (Fig. 3.4). Handbook solutions are available (Newman and Raju, 1981; Murakami, 1987); the latter has been adopted because of the (a/t_p) range of application.

$$Y_{fm} \left(\frac{a}{t_p} \right) = \frac{M_1 + M_2 \left(\frac{a}{t_p} \right)^2 + M_3 \left(\frac{a}{t_p} \right)^4}{\Phi} \quad (3.10)$$

$$Y_{fb} \left(\frac{a}{t_p} \right) = \left\{ 1 + G_1 \left(\frac{a}{t_p} \right) + G_2 \left(\frac{a}{t_p} \right)^2 \right\} Y_{fm} \left(\frac{a}{t_p} \right) \quad (3.11)$$

with

$$M_1 = 1.13 - 0.09 \left(\frac{a}{c} \right)$$

$$M_2 = -0.54 + \frac{0.89}{0.2 + \left(\frac{a}{c} \right)}$$

$$M_3 = 0.50 - \frac{1}{0.65 + \left(\frac{a}{c} \right)} + 14 \left\{ 1 - \left(\frac{a}{c} \right) \right\}^{24}$$

$$G_1 = -1.22 - 0.12 \left(\frac{a}{c} \right)$$

$$G_2 = 0.55 - 1.05 \left(\frac{a}{c} \right)^{0.75} + 0.47 \left(\frac{a}{c} \right)^{1.50}$$

and

$$\begin{aligned} \Phi &= \int_0^{\frac{\pi}{2}} \sqrt{1 - \left\{ 1 - \left(\frac{a}{c} \right)^2 \right\}^2 \sin^2(\varphi)} \, d\varphi \\ &\approx \left(\frac{\pi}{2} \right) \left[1 - \left(\frac{1}{4} \right) \left\{ 1 - \left(\frac{a}{c} \right)^2 \right\} - \left(\frac{3}{64} \right) \left\{ 1 - \left(\frac{a}{c} \right)^2 \right\}^2 - \right. \\ &\quad \left. \left(\frac{5}{1024} \right) \left\{ 1 - \left(\frac{a}{c} \right)^2 \right\}^3 - \left(\frac{175}{65536} \right) \left\{ 1 - \left(\frac{a}{c} \right)^2 \right\}^4 \right] \end{aligned}$$

The elliptical integral of the 2nd kind Φ has been approximated using a Maclaurin series expansion considering the first 5 terms only. The far field component formulations (Eq. 3.10 and 3.11) are mentioned to be accurate within 5.0 [%] for $\{(a/t_p) \leq 0.8\}$ and $\{0.0 \leq (a/c) \leq 1.0\}$ in comparison to FE results.

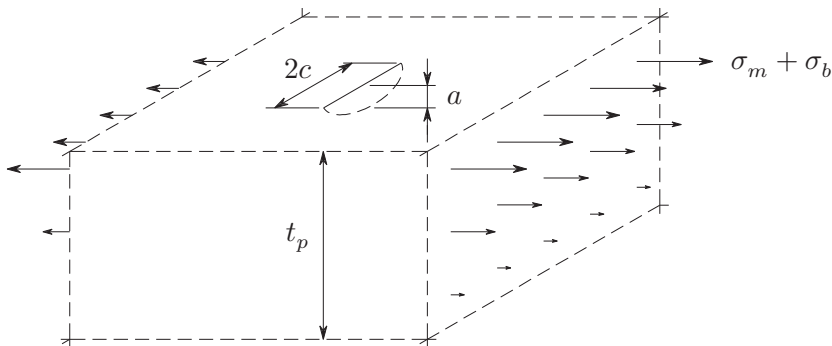


Figure 3.4: Semi-elliptical edge crack.

3.3.2 Double edge crack

Considering the weld toe notch locations of a DS cruciform joint, DS cover plate or DS butt joint (Fig. 3.5a), quasi-2D HS type C examples, Y_f requires except the plate thickness and free surface corrections a symmetry condition with respect to $(t_p/2)$ to be satisfied as well, introducing the double edge crack (DEC) geometry.

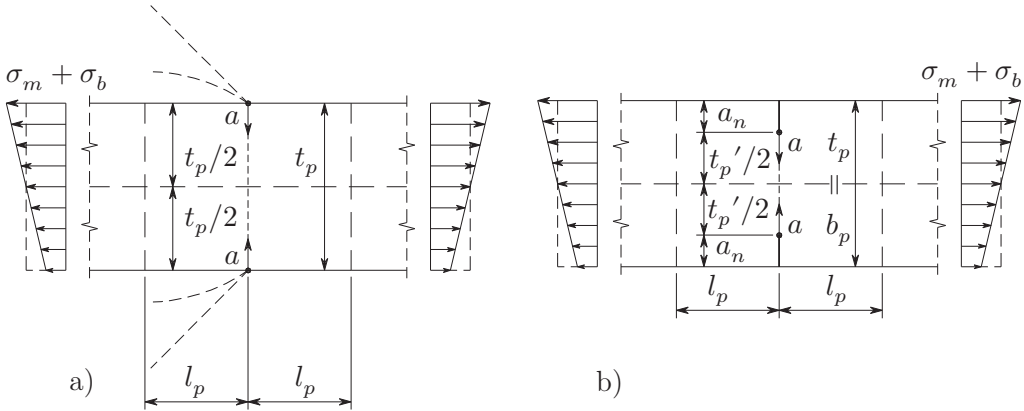


Figure 3.5: Double edge crack at a) weld toe notches and at b) root notches in crack growth specimen.

The handbook solution is limited to Y_{fm} (Tada, Paris and Irwin, 2000). In terms of accuracy it is better than 0.5 [%] for any (a/t_p) in comparison to FE results, provided the far field stress distance criterion $(l_p/t_p) \geq 1$ is satisfied. The far field bending component Y_{fb} is a FE curve fitting result as well. Note that for $(r_s = 1)$ induced cyclic remote mechanical loading the cracks are alternately loaded in tension and compression mode.

$$Y_{fm} \left\{ \frac{a}{\left(\frac{t_p}{2}\right)} \right\} = \frac{1}{\sqrt{1 - \left\{ \frac{a}{\left(\frac{t_p}{2}\right)} \right\}^2}} \cdot \left[1.122 - 0.561 \left\{ \frac{a}{\left(\frac{t_p}{2}\right)} \right\} - 0.205 \left\{ \frac{a}{\left(\frac{t_p}{2}\right)} \right\}^2 + 0.471 \left\{ \frac{a}{\left(\frac{t_p}{2}\right)} \right\}^3 + 0.190 \left\{ \frac{a}{\left(\frac{t_p}{2}\right)} \right\}^4 \right] \quad (3.12)$$

$$\begin{aligned}
 Y_{fb} \left\{ \frac{a}{\left(\frac{t_p}{2}\right)} \right\} &= \frac{1}{\sqrt{1 - \left\{ \frac{a}{\left(\frac{t_p}{2}\right)} \right\}}} \cdot \\
 &\left[1.123 - 1.358 \left\{ \frac{a}{\left(\frac{t_p}{2}\right)} \right\} + 5.553 \left\{ \frac{a}{\left(\frac{t_p}{2}\right)} \right\}^2 - \right. \\
 &\quad \left. 9.687 \left\{ \frac{a}{\left(\frac{t_p}{2}\right)} \right\}^3 + 8.776 \left\{ \frac{a}{\left(\frac{t_p}{2}\right)} \right\}^4 \right]
 \end{aligned} \tag{3.13}$$

Cracks initiating at weld root notches in symmetry configuration with respect to $(t_p/2)$, introduce a double edge notch (DEN) geometry as often applied in standard crack growth specimen, i.e. $t_p = b_p$ (Fig. 3.5b) with:

$$\left\{ \frac{a}{\left(\frac{t_p}{2}\right)} \right\} = \left\{ \frac{a_n}{\left(\frac{b_p}{2}\right)} \right\} + \left\{ \frac{\left(\frac{t_p'}{2}\right)}{\left(\frac{b_p}{2}\right)} \right\} \left\{ \frac{a}{\left(\frac{t_p'}{2}\right)} \right\} \tag{3.14}$$

The welded joint selection (Fig. 2.3 and 2.5) does not contain similar quasi-2D HS type *C* weld root notches along the weld seam, just like weld notches of HS type *B*. Because rarely needed, double edge semi-elliptical surface crack formulations required for HS's type *A* are not available; the SEN Y_f will be used instead.

3.3.3 Centre crack

Only (weld) root notches facing symmetry with respect to $(t_p/2)$, either in a quasi-2D standard crack growth specimen, PP DS T-joint, PP DS cruciform joint or PP DS butt joint (Fig. 3.6), may develop a centre crack (CC) at the root notch (size $2a_n$) already present; a centre notch (CN) geometry.

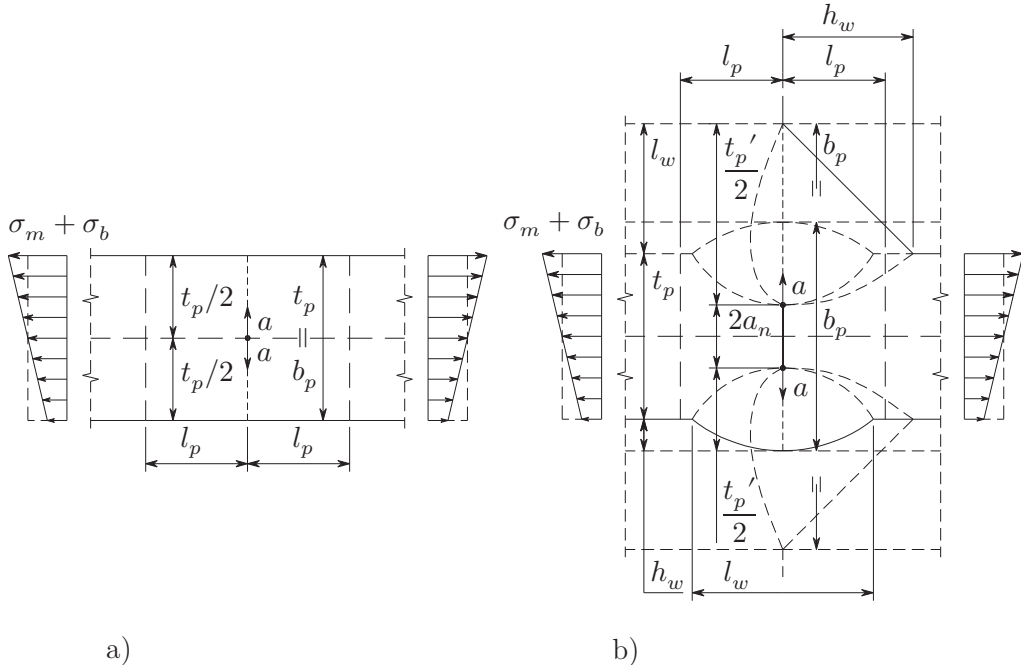


Figure 3.6: Centre crack a) in plate and b) at (weld) root notches.

In case of far field bending, alternately half the crack is loaded in tension mode; the other half in compression, like for the DEC geometry. The $\{Y_{fm}, Y_{fb}\}$ handbook solutions, better than 1.0 [%] for any (a/t_p) in comparison to FE results if the far field stress distance criterion $(l_p/t_p) \geq 1$ is satisfied, yield (Murakami, 1987; Tada, Paris and Irwin, 2000):

$$Y_{fm} \left\{ \frac{a}{\left(\frac{t_p}{2}\right)} \right\} = \sqrt{\sec \left\{ \frac{\pi}{2} \cdot \frac{a}{\left(\frac{t_p}{2}\right)} \right\}} \cdot \left[1 - 0.025 \left\{ \frac{a}{\left(\frac{t_p}{2}\right)} \right\}^2 + 0.06 \left\{ \frac{a}{\left(\frac{t_p}{2}\right)} \right\}^4 \right] \quad (3.15)$$

$$\begin{aligned}
 Y_{fb} \left\{ \frac{a}{\left(\frac{t_p}{2}\right)} \right\} = & 2 \left\{ \frac{a}{\left(\frac{t_p}{2}\right)} \right\} \cdot \frac{\sqrt{1 - 2 \left\{ \frac{a}{\left(\frac{t_p}{2}\right)} \right\}}}{\left[1 - 8 \left\{ \frac{a}{\left(\frac{t_p}{2}\right)} \right\}^3 \right]} \\
 & \left[1 + \left\{ \frac{a}{\left(\frac{t_p}{2}\right)} \right\} + 1.5 \left\{ \frac{a}{\left(\frac{t_p}{2}\right)} \right\}^2 - \right. \\
 & \left. 5.5 \left\{ \frac{a}{\left(\frac{t_p}{2}\right)} \right\}^3 + 7.424 \left\{ \frac{a}{\left(\frac{t_p}{2}\right)} \right\}^4 \right]
 \end{aligned} \tag{3.16}$$

with

$$\left\{ \frac{a}{\left(\frac{t_p}{2}\right)} \right\} = \left\{ \frac{a_n}{\left(\frac{b_p}{2}\right)} \right\} + \left\{ \frac{\left(\frac{t_p'}{2}\right)}{\left(\frac{b_p}{2}\right)} \right\} \left\{ \frac{a}{\left(\frac{t_p'}{2}\right)} \right\}$$

Because of the weld geometry, the b_p size denote either $b_c = (t_c + 2l_w - 2a_n)$ or $b_b = (t_b + 2h_w - 2a_n)$. The reinforcement correction Y_{fw} needs to be involved (Eq. 3.5) to satisfy the far field stress definition. The solutions available in literature, e.g. (Frank and Fisher, 1979; Noblett and Andrews, 2000) and (Sonsino, Radaj, Brandt and Lehrke, 1999) for respectively a PP DS cruciform joint and PP DS butt joint, are obtained using parametric geometry variations and curve fitting of the calculated SIF results. However, the former requires $(l_w/h_w) = 1$ and $(t_c/t_b) = 1$; for the latter Y_{fw} is available for membrane far field loading only. Since the weld root SIF is quite sensitive to geometry parameter variations, in particular the (l_w/h_w) ratio (Al-Mukhtar, Biermann, Henkel and Hübner, 2009), the coarse meshed FE models (e.g. Fig. 2.39) have been used in a similar procedure as applied for the SEC at SEN geometries to prevent for limitations.

Centre crack HS type $\{A, B\}$ formulations are not required, although an embedded elliptical crack handbook solution is available (BS7910, 2005) if 3D effects should be included.

3.4 Notch factor

The self-equilibrating stress part $\sigma_{se}(r/t_p)$, an intact weld toe geometry dependent distribution along the assumed or virtual crack path (Fig. 3.7), will be applied as unit crack face traction – the formulation $Y_n Y_f$ rather than $(Y_n + Y_f)$ has been adopted – to obtain Y_n , the linear σ_s dependent notch SIF zone $\{1, 2\}$ contribution, using the weight function approach (Bueckner, 1987).

$$\begin{aligned}
 Y_n &= \left(\frac{2}{\pi}\right) \int_0^a \frac{\left\{ \sigma_{se} \left(\frac{r}{t_p} \right) + 1 \right\}}{\sqrt{a^2 - r^2}} dr \\
 &= \left(\frac{2}{\pi}\right) \int_0^1 \frac{\left\{ \sigma_{se} \left(\frac{r}{a} \cdot \frac{a}{t_p} \right) + 1 \right\}}{\sqrt{1 - \left(\frac{r}{a} \right)^2}} d \left(\frac{r}{a} \right)
 \end{aligned} \tag{3.17}$$

The through-thickness crack coordinate (a/t_p) naturally replaced the through-thickness stress coordinate (r/t_p) . Note that Y_n is assumed to be a (quasi) 2D effect, even if combined with the 3D affected semi-elliptical far field factor formulations, since in front- and aft of the considered cross-section (i.e. along the weld seam) the same notch stress concentration exists. Only in thickness direction the stress level decreases, defining the (crack) path of least resistance accordingly. In case of symmetry, Y_n incorporates the corresponding notch stress contribution assumptions (Paragraph 2.6.2).

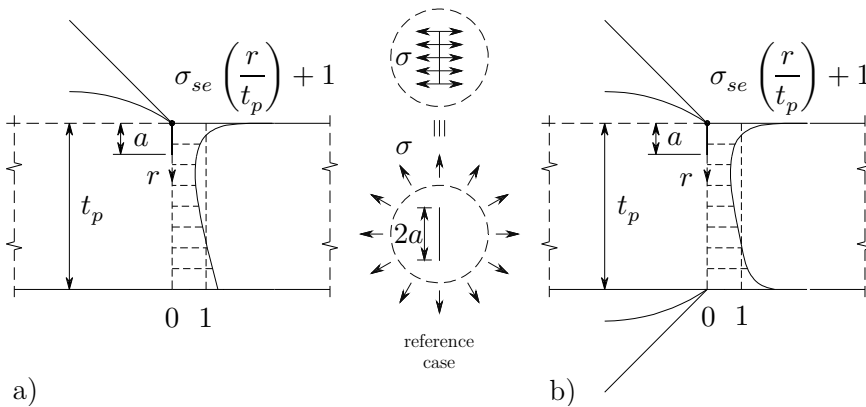


Figure 3.7: Self-equilibrating stress part applied as unit crack face traction at weld toe notches for a) non-symmetry and b) symmetry w.r.t. $(t_p/2)$.

The SIF includes the crack tip characteristic square root singular behaviour by definition. However, a weld root notch in crack configuration (Fig. 3.8), shows similar behaviour and to extract the notch effect, the root notch size a_n should be involved:

$$Y_n = \frac{Y_{nr}}{Y_{nl}} \quad (3.18)$$

with

$$Y_{nr} = \left(\frac{2}{\pi}\right) \int_{a_n}^{a_n+a} \frac{\left\{ \sigma_{ser} \left(\frac{r' - a_n}{t_p'} \right) + 1 \right\}}{\sqrt{(a_n + a)^2 - r'^2}} dr'$$

and

$$Y_{nl} = \left(\frac{2}{\pi}\right) \int_{a_n}^{a_n+a} \frac{1}{\sqrt{(a_n + a)^2 - r'^2}} dr'$$

$$= 1 - \left(\frac{2}{\pi}\right) \arcsin \left\{ \frac{\left(\frac{a_n}{b_p}\right)}{\left(\frac{a_n}{b_p}\right) + \left(\frac{t_p'}{b_p}\right) \left(\frac{a}{t_p'}\right)} \right\}$$

Note that the (linear) unit stress notch factor Y_{nl} is shown for a non-symmetry case like a SEN geometry (Fig. 3.7); in case of symmetry, e.g. a CN geometry, ($b_p \rightarrow b_p/2$) and ($t_p' \rightarrow t_p'/2$). In agreement with the weld toe notch related intact geometry formulation, $Y_{nl}(a_n = 0) = 1$ and ($Y_n = Y_{nr}$).

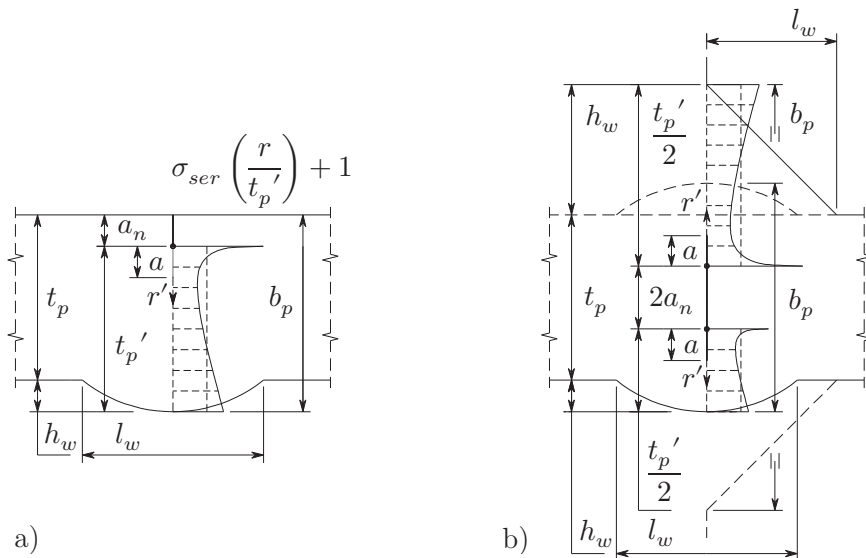


Figure 3.8: Self-equilibrating stress part applied as unit crack face traction at weld root notches for a) non-symmetry and b) symmetry w.r.t. ($t_p/2$).

3.5 Weld toe notch stress intensity factor

The non-square root singular behaviour to be taken into account using the weld geometry stress induced Y_n is a key feature of weld toe notch SIF's. A notch angle different from the crack configuration value ($0 < 2\alpha < 2\pi$) and a stress angle ($\beta > 0$) means that for a remote mechanical loading controlled mode-I based far field stress distribution σ_f and increasing crack size a , the governing axis will change (Fig. 3.9) from notch dominant ($a \sim 0^+$) to crack controlled ($a \gg 0$).

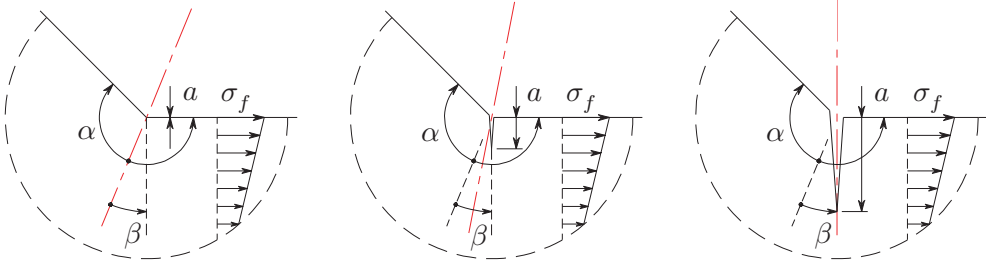


Figure 3.9: Increasing the crack size at a weld toe notch changes the governing axis.

Adding the {SEC, DEC} far field contribution Y_f allows to deal consistently with geometric non-symmetry and symmetry with respect to $(t_p/2)$ and to obtain the weld toe notch characteristic stress intensity $Y_n Y_f$. The same examples used in Paragraph 2.6 for illustration purposes will be considered to involve the weld type classification criteria, i.e. the fillet weld- (PP DS and SS T-joint, DS cover plate, PP DS cruciform joint) and groove weld geometry (PP DS butt joint).

3.5.1 Non-symmetry

The unit crack face traction needs $\sigma_{se}(r/t_p) + 1$, i.e. the weld toe notch stress distribution (Eq. 2.24) excluding the structural stress σ_s and far field bending stress projection $2r_s(r/t_p)$. Using the Y_n definition (Eq. 3.17) yield:

$$\begin{aligned}
 Y_n \left(\frac{a}{t_p} \right) &= \left(\frac{2}{\pi} \right) \left[\left(\frac{a}{t_p} \right)^{\lambda_s - 1} \mu_s \left(\frac{\sqrt{\pi}}{2} \right) \frac{\Gamma \left(\frac{\lambda_s}{2} \right)}{\Gamma \left(\frac{\lambda_s + 1}{2} \right)} \lambda_s (\lambda_s + 1) \cdot \right. & (3.19) \\
 &\quad \left[\cos\{(\lambda_s + 1)\beta\} - \chi_s \cos\{(\lambda_s - 1)\beta\} \right] + \\
 &\quad \left(\frac{a}{t_p} \right)^{\lambda_a - 1} \mu_a \left(\frac{\sqrt{\pi}}{2} \right) \frac{\Gamma \left(\frac{\lambda_a}{2} \right)}{\Gamma \left(\frac{\lambda_a + 1}{2} \right)} \lambda_a (\lambda_a + 1) \cdot \\
 &\quad \left[\sin\{(\lambda_a + 1)\beta\} - \chi_a \sin\{(\lambda_a - 1)\beta\} \right] + \\
 &\quad \left. C_{bw} \left\{ 2 \left(\frac{a}{t_p} \right) - \frac{\pi}{2} \right\} \right]
 \end{aligned}$$

Note that the notch factor (Eq. 3.19) and the weld toe notch stress distribution (Eq. 2.24) show similar singular behaviour (den Besten and Huijsmans, 2011). The integral solutions introduce $\Gamma(\cdot)$; the (complete) gamma function.

The non-monotonic weld toe notch stress intensities $Y_n Y_f$ for location 1 of the PP DS T-joint, a HS type C, as a result of the 4 far field load cases applied (Fig. 2.14 to 2.18), are shown (Fig. 3.10 to 3.13). Quasi-2D SEC geometry formulations (Eq. 3.6 and 3.7) have been adopted to describe the far field effect Y_f . For welds showing limited load carrying behaviour, i.e. C_{bw} is rather small, Y_n turns out to be governing for $\{0 < (a/t_p) \leq 0.2\}$; the zone $\{1, 2\}$ weld geometry stress (concentration) affected micro-crack region in which crack size a is considered to be technically small. It is divided into respectively a notch dominated and a weld load carrying controlled part. The apex shifts to the left for decreasing r_s , meaning the micro- and macro-crack region respectively increases and decreases at the same time. Far field factor Y_f rules the zone 3 far field stress related macro-crack region $\{0.2 < (a/t_p) \leq 1.0\}$, meaning that all 3 defined stress components (Paragraph 2.3 to 2.5) are decisive in a certain crack length region. The FE solutions, obtained for plane strain conditions, prove to be rather good $Y_n Y_f$ estimates.

Comparing the pure bending ($r_s = 1$) and pure membrane ($r_s = 0$) far field load case results (Fig. 3.10 and 3.12), the notch induced behaviour for $\{(a/t_p) \rightarrow 0\}$ is similar because of the same weld angle; the C_{bw} affected weld load carrying region shows smaller values in case of bending. The difference in macro-crack behaviour is quite large in favour of bending as a result of the zone 3 far field stress gradient.

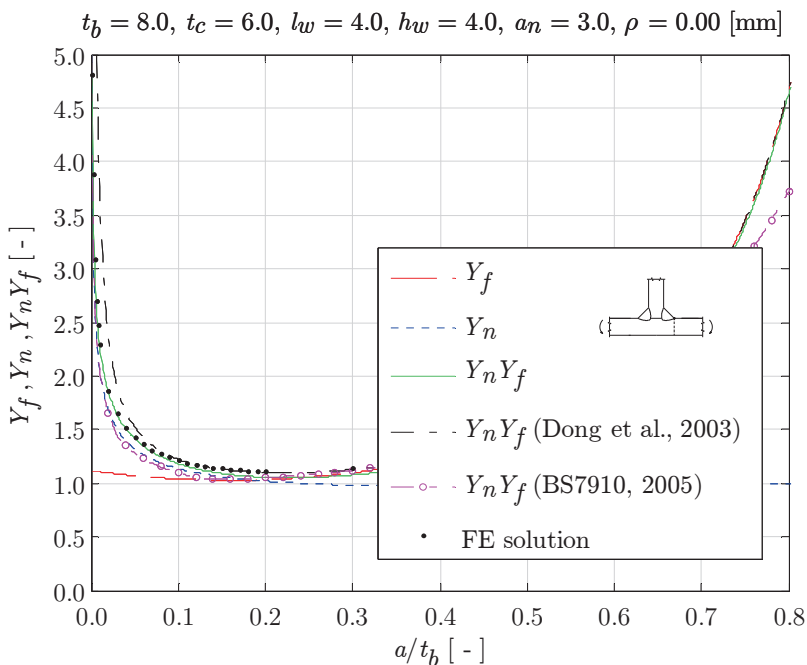


Figure 3.10: PP DS T-joint SIF far field- and notch contribution (loc. 1), $r_s = 1$.

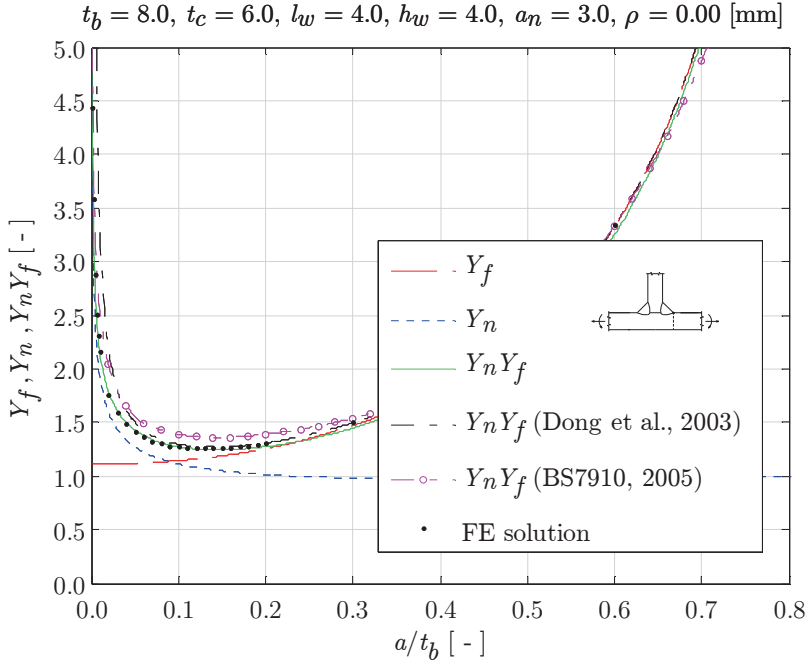


Figure 3.11: PP DS T-joint SIF far field- and notch contribution (loc. 1), $r_s = (1/3)$.

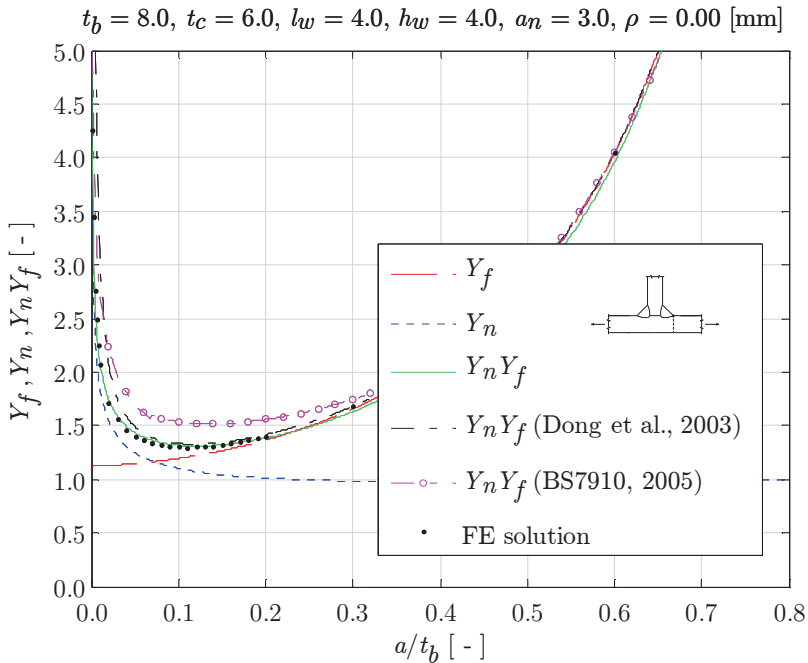


Figure 3.12: PP DS T-joint SIF far field- and notch contribution (loc. 1), $r_s = 0$.

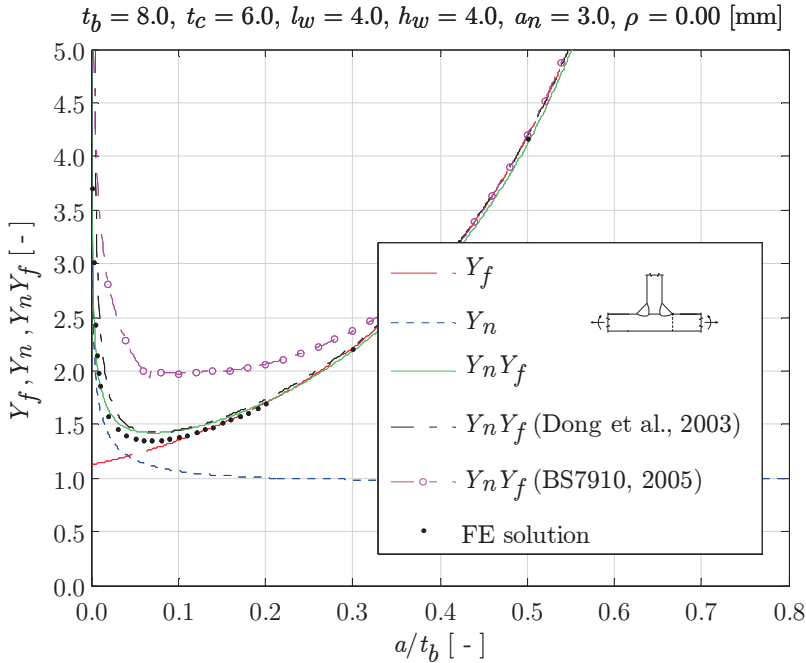


Figure 3.13: PP DS T-joint SIF far field- and notch contribution (loc. 1), $r_s = -1$.

Applying a bending moment clockwise or counter clockwise makes a big difference, i.e. the combined far field load cases ($r_s = 1/3$) and ($r_s = -1$) show for a monotonic weld notch stress distribution the notch affected micro-crack region is twice as large. Note that $Y_n Y_f$ for the ($r_s = -1$) case is C_{bw} sensitive at $\{0.1 < (a/t_p) \leq 0.2\}$, like the corresponding notch stress distribution (Fig. 2.18).

Although general handbook solutions for weld toe notch SIF's do not exist, some FE solution based curve fitted formulations are available (Maddox, Lechocki and Andrews, 1986; Hobbacher, 1993). The former is outlined in the British Standard (BS7910, 2005). The considered joint geometry does not encounter inconvenience from the fixed 45 [deg] weld flank angle limitation. Except for the pure bending case (Fig. 3.10), the notch affected micro-crack region estimates seem however rather conservative (Fig. 3.11 to 3.13); none of the far field load cases show a good match. A plate and weld size dependent transition in curve fitting function constants introduces a small step, identified at $\{(a/t_b) \approx 0.07\}$. In comparison to other calculation results, the macro-crack region BS7910 far field effects diverge for $\{(a/t_b) > 0.65\}$ because of different Y_f formulation (Fig. 3.10 and 3.11).

One of the BSS concept features is that the bi-linear notch stress approximation σ_{nb} (Paragraph 2.6) has been used to obtain K_I (Dong, Hong and Cao, 2003; 2004). Relating the involved transition depth to the crack size ($r_t = a$) is supposed to yield a crack face traction $p_f = p_s \{1 - 2r_p(r/a)\} \in r = [0, a]$. For varying a , equilibrium is maintained using the structural traction and associated bending traction ratio; $p_s(a, t_p, \sigma_{nb}) = (p_m + p_b)$ and $p_r(a, t_p, \sigma_{nb}) = (p_b/p_s)$,

meaning that for $(a \rightarrow t_p)$ the notch stress affected SIF solution converges (approximately) to the BSS $\sigma_s^t = (\sigma_m^t + \sigma_b^t)$ induced one and $p_s \{1 - 2r_p(r/a)\} \rightarrow \sigma_s^t \{1 - 2r_s^t(r/t_p)\}$. Rewriting $\{\sigma_s^t, r_s^t\}$ of the σ_f^t based SIF in terms of the structural traction parameters $\{p_s, p_r\}$, i.e. $\{\sigma_s = p_s, r_s = (t_p/a)p_r\}$, a blend notch and structural field factor $Y_n Y_f^t$ has been obtained since $K_I = \sigma_s^t Y_f(r_s^t) \sqrt{\pi a}$ turns into $K_I = p_s \{Y_{fm} - (t_p/a)p_r(Y_{fm} - Y_{fb})\} \sqrt{\pi a}$. Note that σ_s^t is not equal to the welded joint far field stress σ_s by definition (Chapter 2); the notch affected region upper bound previously identified turns out to be in between the BSS concept- and BS7910 value: $\{0.1 < (a/t_p)_{UB} < 0.3\}$. Although notch stress intensities are in agreement with the FE solutions (Fig. 3.10 to 3.13), $Y_n Y_f$ is consistently overestimated for $\{(a/t_p) < 0.1\}$. However, it is not a matter of a notch radius ($\rho > 0$) applied to the FE model as explained for several examples (Dong, Hong and Cao, 2003; 2004; Dong, 2008), neither a consequence of the bi-linear notch stress approximation nor the result of assumed transition depth; the SIF estimation procedure has proven to be robust (Dong, Hong, Osage and Prager, 2002). It is a peculiarity that seems to be a result of incorporating the notch characteristic behaviour as far field contribution; Y_f corresponds to a crack length a invariant through-thickness linear- rather than an a dependent bi-linear (notch) stress distribution. The crack face traction definition (Eq. 3.17) has been ignored and the (normalised) SIF consequences are serious as shown for the considered welded joint notch location and far field load cases (Fig. 3.14 to 3.17).

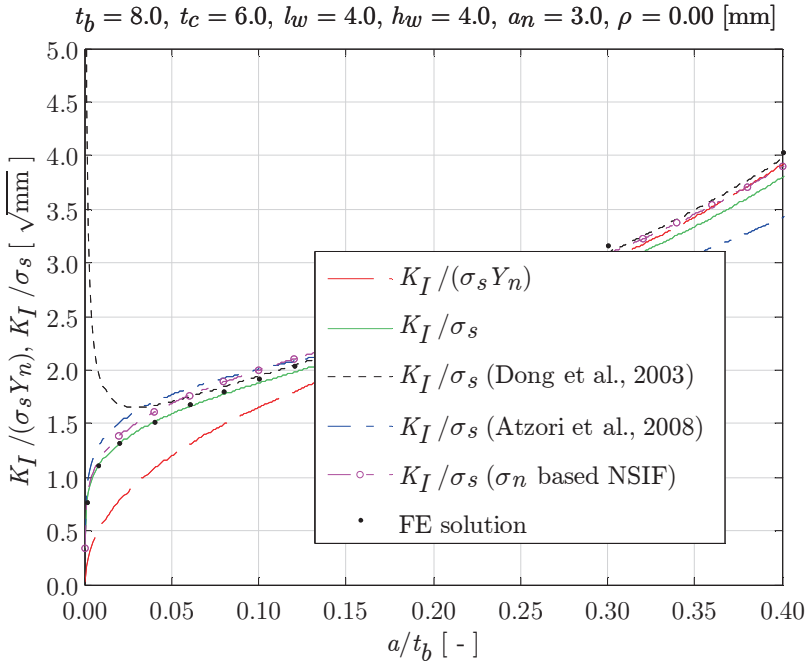


Figure 3.14: PP DS T-joint SIF (loc. 1), $r_s = 1$.

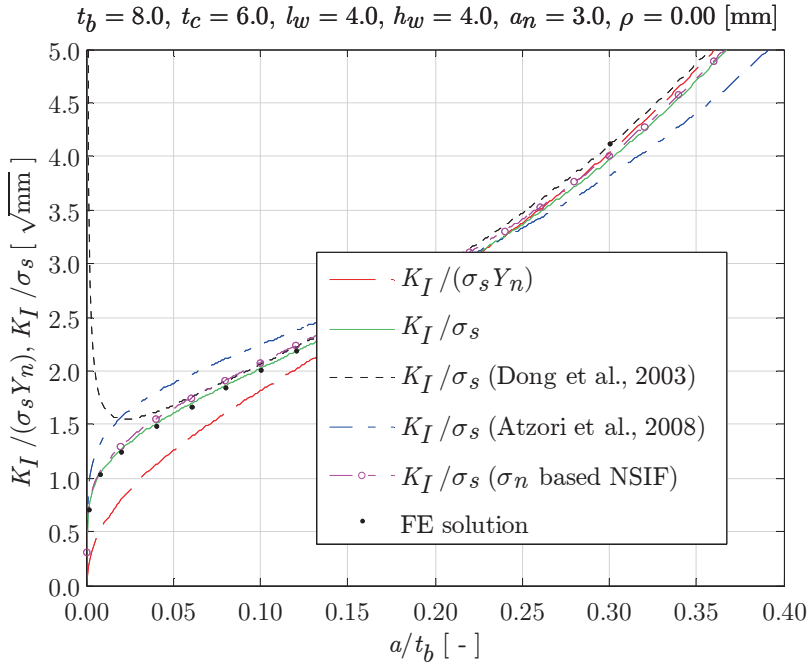


Figure 3.15: PP DS T-joint SIF (loc. 1), $r_s = (1/3)$.

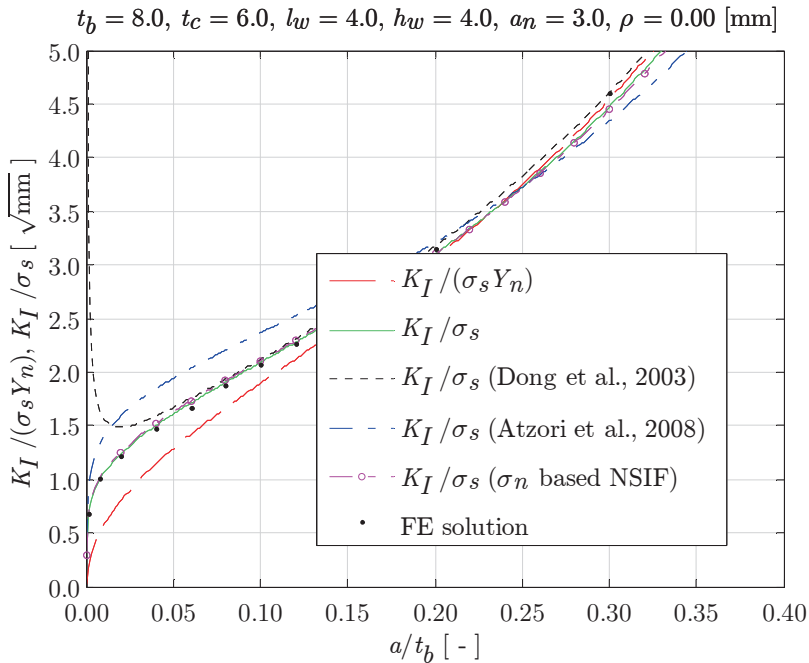


Figure 3.16: PP DS T-joint SIF (loc. 1), $r_s = 0$.

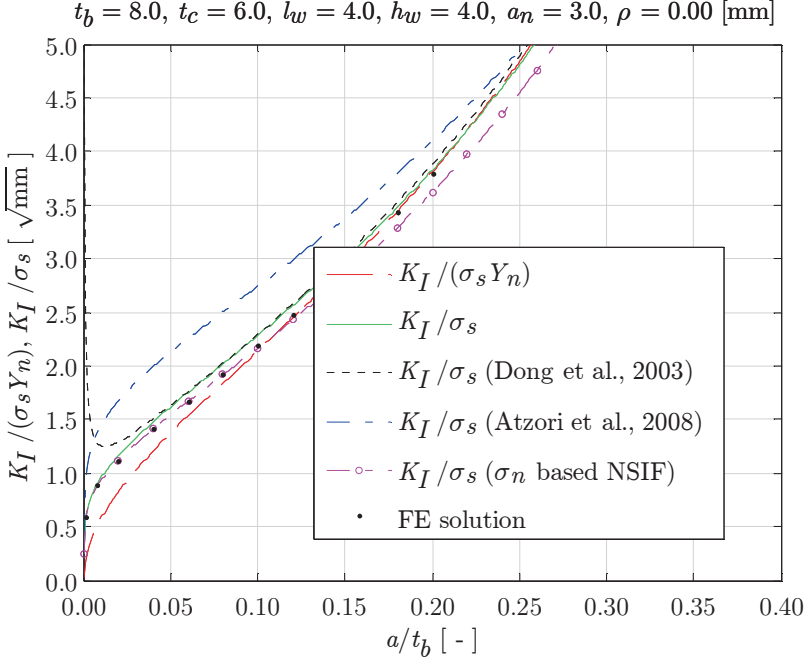


Figure 3.17: PP DS T-joint SIF (loc. 1), $r_s = -1$.

The non-monotonic K_I distribution is explained to be a higher order SIF effect, important for small cracks (Dong, Hong and Cao, 2003). However, since the notch stress intensities $Y_n Y_f$ are qualified as good estimates in comparison to (1st order) FE results (Dong, Hong. and Cao, 2004), it is surprising that the actual SIF would include higher order effects. The singular behaviour for $\{(a/t_p) \rightarrow 0\}$ seems fictitious anyway. By definition, K_I is a 1st order damage tolerant parameter (Eq. 3.1), taking the dominant crack(!) tip stress field singularity into account. Non-singular higher order terms (Eq. 2.14) may add a finite contribution at most as been illustrated (Ritchie, Yu, Holm and Blom, 1988), even if the notch(!) induced singularity becomes governing (Fig. 3.10 – 3.13). Regardless the non-monotonic $Y_n Y_f$ behaviour, i.e. $\{\lambda_s, \lambda_a\} \geq 0.5$ (Fig. 2.9), the SIF should remain a monotonically increasing function because of the 1st order $\sqrt{\pi a}$ factor.

The SIF's (Eq. 3.2) in normalised formulation (K_I/σ_s) perfectly match the FE solutions as shown (Fig. 3.14 to 3.17). If a significant part of the fatigue life time is related to the weld geometry affected micro-crack region $\{0 < (a/t_b) \leq 0.2\}$, ignoring the notch contribution $K_I/(\sigma_s Y_n)$ would have substantial consequences of the non-conservative type.

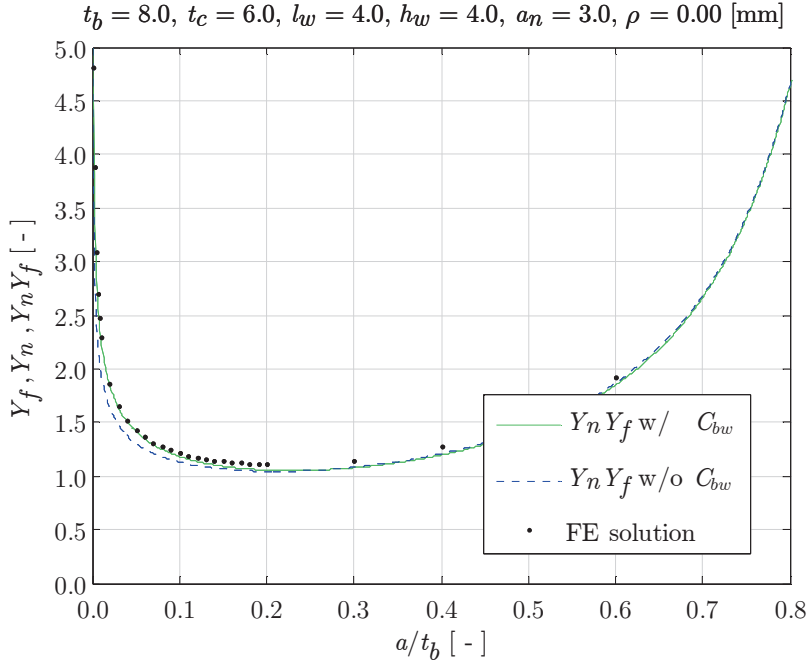
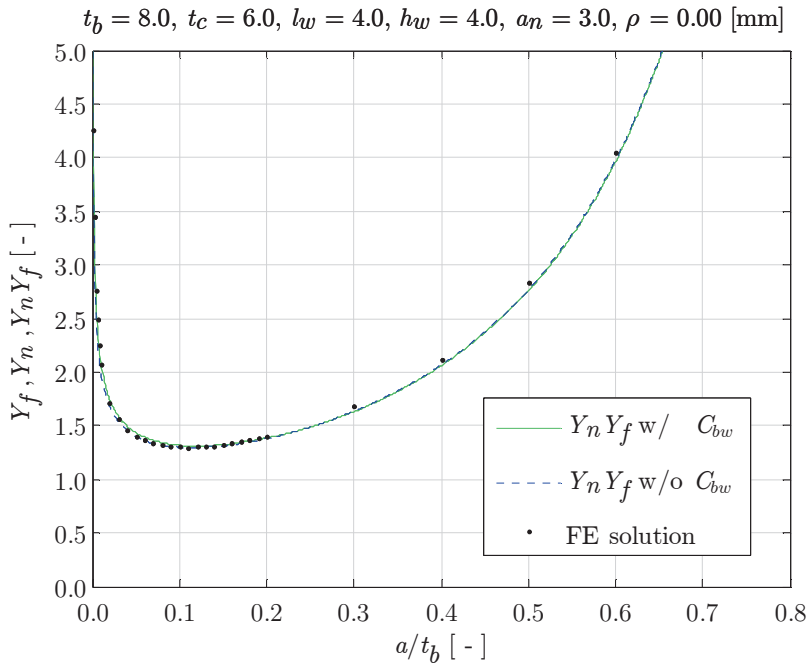
Using the crack initiation and growth bridging intact geometry parameters $\{K_I^N, K_{II}^N\}$, NSIF's, the notch SIF K_I can be obtained as well (Atzori, Lazzarin and Tovo, 1999; Atzori, Lazzarin and Meneghetti, 2008). The mode-II component should be involved since K_I has to be calculated for $(\theta = \beta)$. Using the notch stress components (Eq. 2.10, 2.11), the symmetry and anti-symmetry related NSIF's denote:

$$\begin{aligned}
K_I^N &= (2\alpha)^{1-\lambda_s} \lim_{r \rightarrow 0^+} \{r^{1-\lambda_s} \sigma_{\theta\theta}(r, \theta = 0)\} & (3.20) \\
&= (2\alpha)^{1-\lambda_s} \sigma_s t_p^{1-\lambda_s} \mu_s \lambda_s (\lambda_s + 1) (1 - \chi_s) \\
&= k_1 \sigma_s t_p^{1-\lambda_s}
\end{aligned}$$

$$\begin{aligned}
K_{II}^N &= (2\alpha)^{1-\lambda_a} \lim_{r \rightarrow 0^+} \{r^{1-\lambda_a} \sigma_{r\theta}(r, \theta = 0)\} & (3.21) \\
&= (2\alpha)^{1-\lambda_a} \sigma_s t_p^{1-\lambda_a} \mu_a \lambda_a \{(\lambda_a + 1) - \chi_a (\lambda_a - 1)\} \\
&= k_2 \sigma_s t_p^{1-\lambda_a}
\end{aligned}$$

Rewriting $\{K_I^N, K_{II}^N\}$ in terms of the equilibrium coefficients $\{\mu_s, \mu_a\}$ and substitution into $\{\sigma_{\theta\theta}, \sigma_{r\theta}\}$, i.e. (Eq. 2.10 and 2.11) yield the notch stress components in terms of the NSIF's $\{\sigma_{\theta\theta}(K_I^N), \sigma_{r\theta}(K_{II}^N)\}$. If applied as crack face traction, a linear superposition returns the notch factor $Y_n(K_I^N, K_{II}^N)$ and the notch SIF $K_I(K_I^N, K_{II}^N)$ can be calculated. The required NSIF's can easily be obtained using the parametric joint geometry and remote loading dependent $\{k_1, k_2\}$ formulations (Eq. 3.20, 3.21); curve fitted FE results limited to a 45 [deg] weld flank angle (Lazzarin and Tovo, 1998; Lazzarin and Livieri, 2001). For the considered examples (Fig. 3.14 to 3.17), the SIF's are overestimated in the micro-crack region. Application of the $K_I(K_I^N, K_{II}^N)$ formulations is mentioned to be limited to $\{0 < (a/t_p) \leq 0.3\}$. Although the small SEC far field factor ($Y_f = 1.12$) has been replaced by an extended formulation (Eq. 3.4) to improve the results in the macro-crack region, still some non-conservative behaviour is observed because $\{Y_n(K_I^N, K_{II}^N) < 1\}$; defining an engineering constraint ($Y_n \geq 1$) like for the BS7910 solution increases the performance. Although $\{\mu_s, \mu_a\}$ have been calculated taking only $\sigma_{\theta\theta}(\theta = \beta)$ into account, the notch stress distribution can be used alternatively to approximate the required NSIF's (Eq. 3.20 and 3.21) as well. The $\{K_I^N, K_{II}^N\}$ values for the two approaches are very different; however, the σ_n based solutions show better agreement. The $\{K_I^N, K_{II}^N\}$ definition (Eq. 3.20 and 3.21) has been modified to meet the one adopted for the NSIF concept (Lazzarin and Tovo; 1998) to stick to the $K_I(K_I^N, K_{II}^N)$ formulations (Atzori, Lazzarin and Meneghetti, 2008). For one reason or another, the crack configuration related $(2\pi)^{1-\lambda_1}$ factor has been used rather than the generalised $\{(2\alpha)^{1-\lambda_s}, (2\alpha)^{1-\lambda_a}\}$ formulation; depending on the notch angle, $\{K_I^N, K_{II}^N\}$ values may become significantly different.

The Y_n weld geometry C_{bw} contribution turns out to be larger for far field bending (Fig. 3.18) in comparison to the membrane case (Fig. 3.19) as already identified for the weld notch stress distributions (Fig. 2.19 and 2.20); a matter of weld effectiveness.

Figure 3.18: PP DS T-joint SIF notch C_{bw} effect (loc. 1), $r_s = 1$.Figure 3.19: PP DS T-joint SIF notch C_{bw} effect (loc. 1), $r_s = 0$.

The PP SS T-joint (Fig. 2.21) needs an additional (2nd order) weld load carrying term $Y_{n,bw}$ to improve the notch stress intensity (Eq. 3.19) in the micro-crack region (Fig. 3.20). Although σ_n (Fig. 2.22) shows some error in comparison to the FE solution, its gradient is still good explaining the Y_n accuracy.

$$Y_{n,bw} = \left(\frac{2}{\pi}\right) C_{bw} \left[\pi \left\{ 3 \left(\frac{a}{t_p}\right)^2 + 1 \right\} - 12 \left(\frac{a}{t_p}\right) \right] \quad (3.22)$$

As expected from the bi-linear notch stress approximation, the corresponding $Y_n Y_f$ solution (Dong, Hong and Cao, 2003) becomes negative for $(a/t_p) \rightarrow 0$. BS7910 formulations are not available, nor NSIF based notch SIF estimates (Atzori, Lazzarin and Meneghetti, 2008).

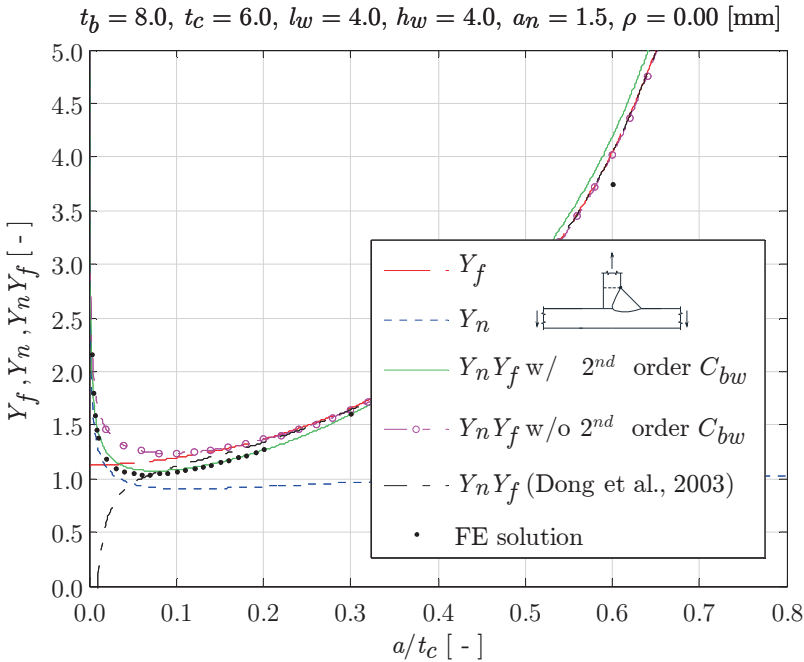


Figure 3.20: PP SS T-joint SIF notch 2nd order C_{bw} effect (loc. 2), $r_s = 0$.

Considering the DS T-joint again, although this time a FP one developing a semi-elliptical surface crack rather than SEC, 3D effects will be investigated. The 2D weld notch stress distributions still have been used to obtain Y_n , a reasonable approximation since for respectively a pure bending and membrane far field load case $\{r_s = 1, r_s = 0\}$ it seems to be predominantly a Y_f (Eq. 3.4, 3.10 and 3.11) or macro-crack effect (Fig. 3.21 and 3.22). Results are related to the deepest crack point (Fig. 3.4). Differences in the macro-crack region for the different $Y_n Y_f$ formulations is because of the different Y_f formulations involved.

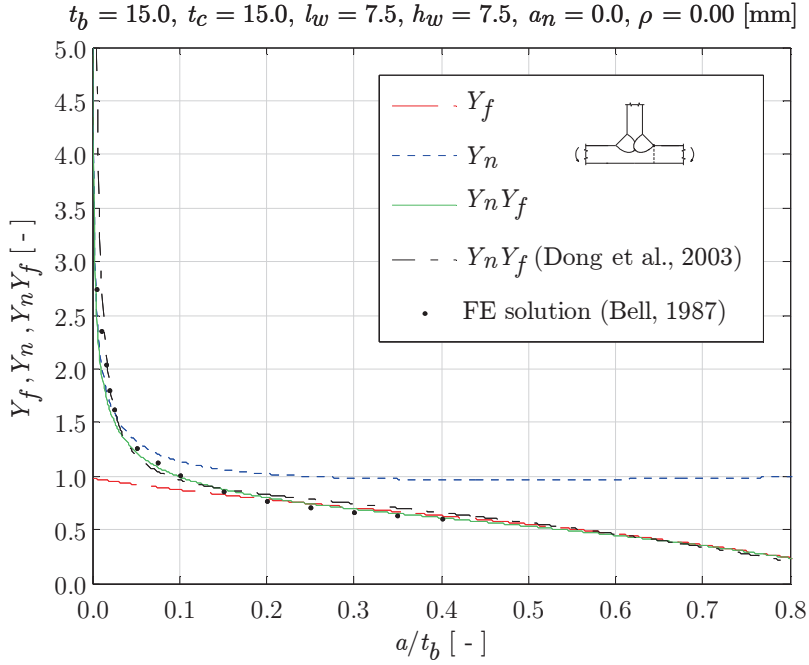


Figure 3.21: FP DS T-joint SIF (loc. 1) semi-elliptical crack $\{(a/c) = 0.25\}, r_s = 1$.

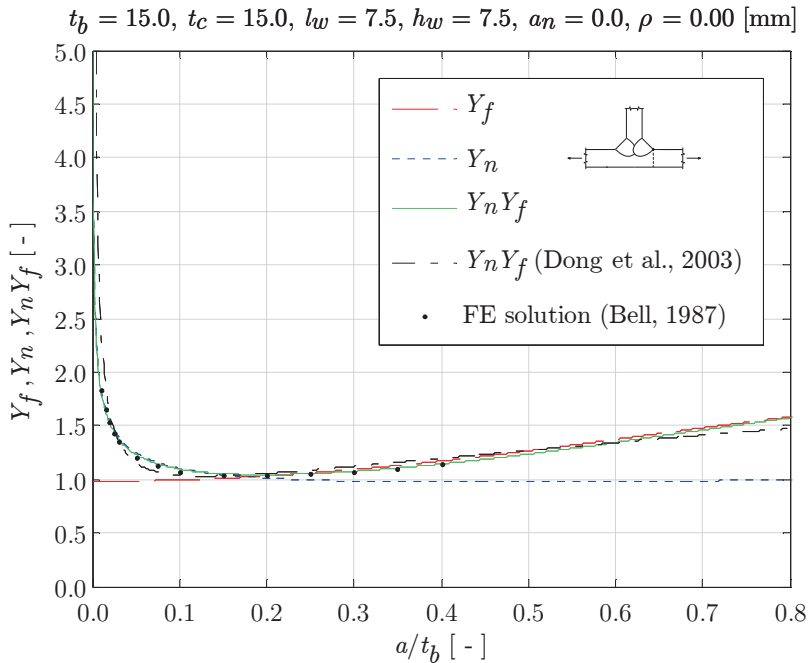


Figure 3.22: FP DS T-joint SIF (loc. 1) semi-elliptical crack $\{(a/c) = 0.25\}, r_s = 0$.

Far field bending induced compressive stress decreases the stress intensity for increasing crack size (Fig. 3.21). Insufficient curve fitting may cause ($Y_f < 0$) for $(a/t_b) \rightarrow 1$ meaning crack arrest and is important to keep in mind for crack growth calculations.

The $Y_n Y_f$ (Dong et al., 2003) micro-crack region overestimation as already identified before seems no coincidence, although the FE solutions (Bell, 1976) include a non-zero notch radius; $\rho = 0.6$ [mm] for the considered examples, not taken into account for the moment.

3.5.2 Symmetry

Any influence of another crack at a weld toe notch in the plane of symmetry at $(t_p/2)$ is assumed to be a macro-crack effect, i.e. considering one notch at the time is sufficient. Subtracting the far field bending stress projection $2r_s(r/t_p)$ from the corresponding notch stress distribution σ_n (Eq. 2.39) yields approximately $\sigma_{se}(r/t_p) + 1$. If applied as (unit) crack face traction, the notch factor involving the linear weld load carrying component becomes:

$$Y_n \left(\frac{a}{t_p} \right) = \left(\frac{2}{\pi} \right) \left(\left[1 - 2r_s \left\{ 1 - f \left(\frac{a}{t_p} = \frac{1}{2} \right) \right\} \right] f \left(\frac{a}{t_p} \right) + \right. \quad (3.23)$$

$$r_s \left\{ 2f \left(\frac{a}{t_p} = \frac{1}{2} \right) - 1 \right\} \left[\left\{ 1 - f \left(\frac{a}{t_p} = \frac{1}{2} \right) \right\} \left(\frac{\pi}{2} \right) - \right.$$

$$\left. \left. 2 \left(\frac{a}{t_p} \right) \right] + 2r_s \left(\frac{a}{t_p} \right) \right)$$

with

$$f \left(\frac{a}{t_p} \right) = \left(\frac{a}{t_p} \right)^{\lambda_s - 1} \mu_s \left(\frac{\sqrt{\pi}}{2} \right) \frac{\Gamma \left(\frac{\lambda_s}{2} \right)}{\Gamma \left(\frac{\lambda_s + 1}{2} \right)} \lambda_s (\lambda_s + 1) \cdot$$

$$[\cos\{(\lambda_s + 1)\beta\} - \chi_s \cos\{(\lambda_s - 1)\beta\}] +$$

$$\left(\frac{a}{t_p} \right)^{\lambda_a - 1} \mu_a \left(\frac{\sqrt{\pi}}{2} \right) \frac{\Gamma \left(\frac{\lambda_a}{2} \right)}{\Gamma \left(\frac{\lambda_a + 1}{2} \right)} \lambda_a (\lambda_a + 1) \cdot$$

$$[\sin\{(\lambda_a + 1)\beta\} - \chi_a \sin\{(\lambda_a - 1)\beta\}] +$$

$$C_{bw} \left\{ 4 \left(\frac{a}{t_p} \right) - \frac{\pi}{2} \right\}$$

and

$$f\left(\frac{a}{t_p} = \frac{1}{2}\right) = f\left(\frac{r}{t_p} = \frac{1}{2}\right) = \frac{(\lambda_a - \lambda_s)(\lambda_s \lambda_a - 2C_{bw})}{\lambda_a(\lambda_a - 1) - \lambda_s(\lambda_s - 1)} + C_{bw}$$

To obtain the non-monotonic weld toe notch stress intensities $Y_n Y_f$ for location 1 of a PP DS butt joint, a HS type C, as a result of 4 different far field load cases (Fig. 3.23 to 3.26), the quasi-2D DEC geometry formulations (Eq. 3.12 and 3.13) have been adopted to include the far field effects. The non-symmetry defined micro- and macro-crack region definitions appear still to be the same, although related to half the plate thickness because of the symmetry induced DEC configuration. Although weld load carrying stress dependent, generally speaking Y_n dominates the micro-crack region $\{0 < a/(t_p/2) \leq 0.2\}$; Y_f the macro-crack region $\{0.2 < a/(t_p/2) \leq 1.0\}$. The $Y_n Y_f$ estimates and FE plane strain solutions match fairly good. The stress state becomes compressive (Fig. 3.26) for $\{(a/t_p) > 0.7\}$ in case ($r_s = -1$).

The BSS concept formulation $Y_n Y_f$ (Dong et al., 2003) has been defined for half the plate thickness only (Fig. 2.23 to 2.27). Consequences regarding symmetry in terms of notch stress distribution (a Y_n governing issue) – r_t is defined at $0.1(t_p/2)$ – and presence of another crack right across (predominantly a Y_f matter) are ignored. Deviations in the macro-crack region are the result of adopting a SEC-rather than DEC far field description (Fig. 3.24 to 3.26); in any case, a combination of membrane and bending. For comparison reasons, $Y_n Y_f$ (Dong et al., 2003) includes the scale factor (σ_s^t/σ_s) to deal with the BSS definition for symmetry (Dong, 2004). Generally speaking, the notch stress intensity is still consistently overestimated in the micro-crack region, in particular for $(a/t_p) \rightarrow 0$.

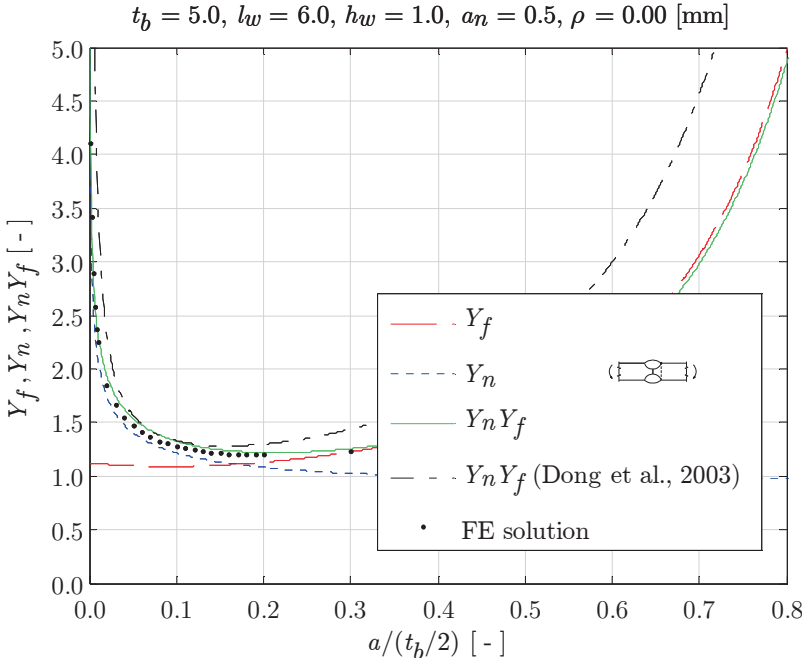


Figure 3.23: PP DS butt joint SIF far field- and notch effect (loc. 1), $r_s = 1$.

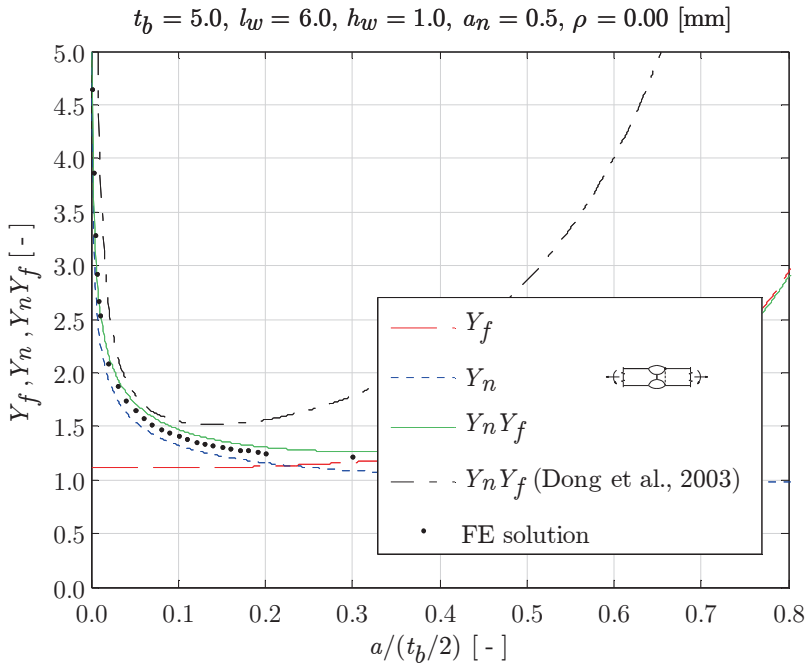


Figure 3.24: PP DS butt joint SIF far field- and notch effect (loc. 1), $r_s = (1/3)$.

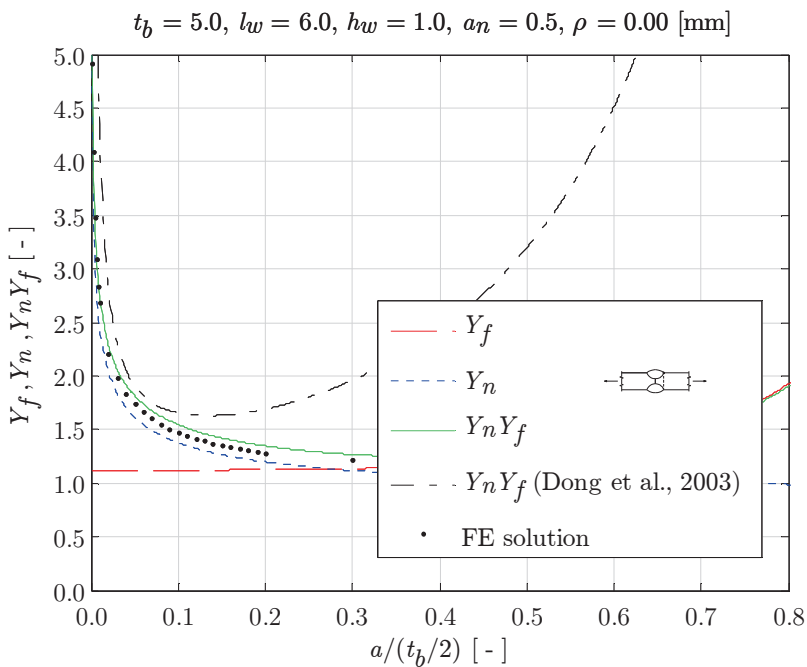


Figure 3.25: PP DS butt joint SIF far field- and notch effect (loc. 1), $r_s = 0$.

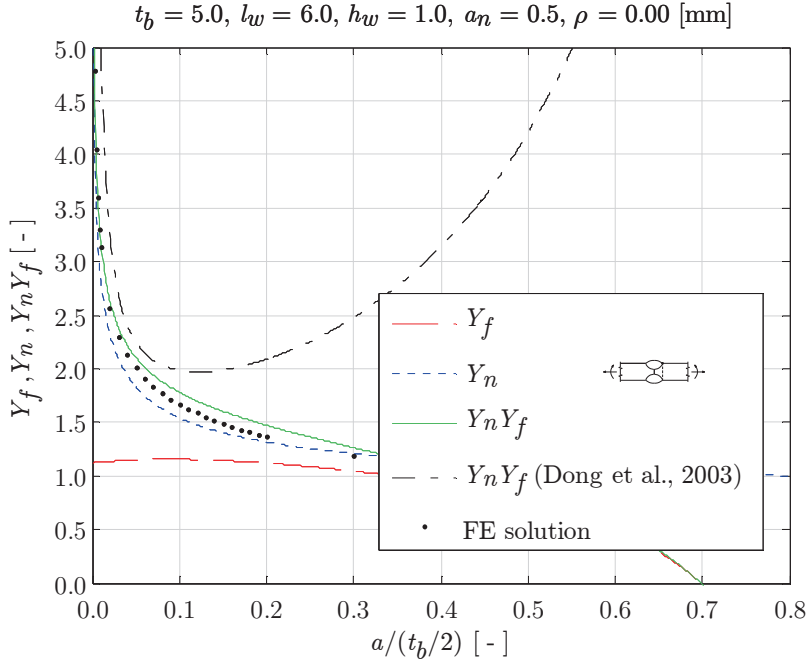


Figure 3.26: PP DS butt joint SIF far field- and notch effect (loc. 1), $r_s = -1$.

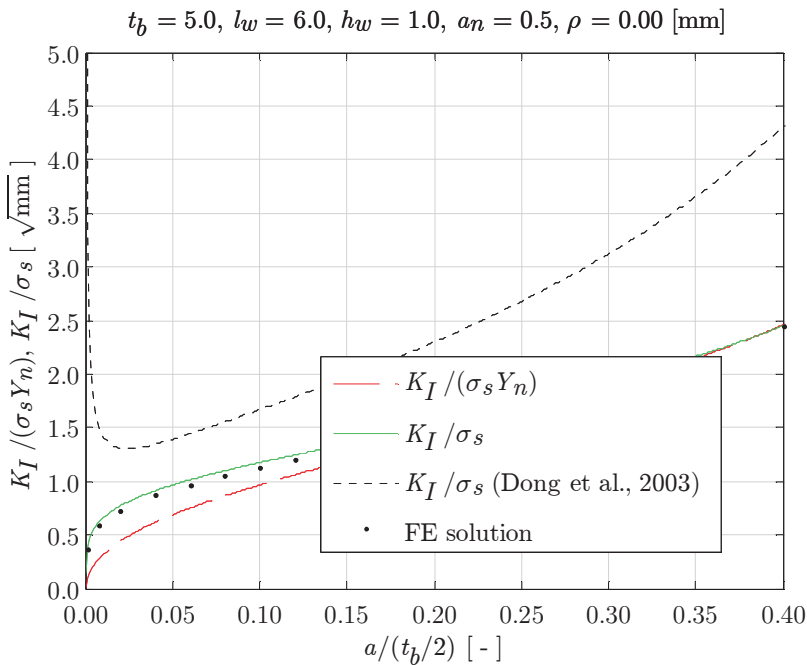


Figure 3.27: PP DS butt joint SIF (loc. 1), $r_s = 1$.

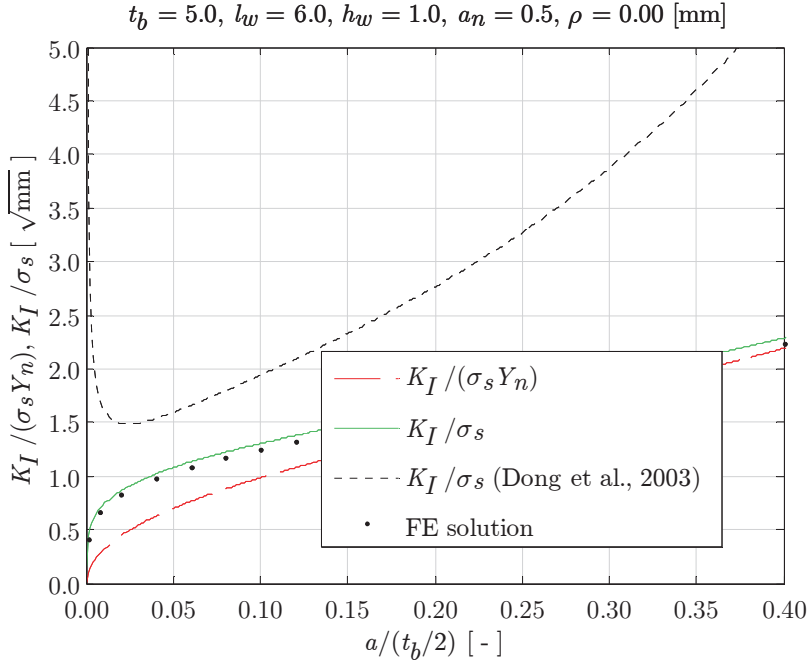


Figure 3.28: PP DS butt joint SIF (loc. 1), $r_s = (1/3)$.

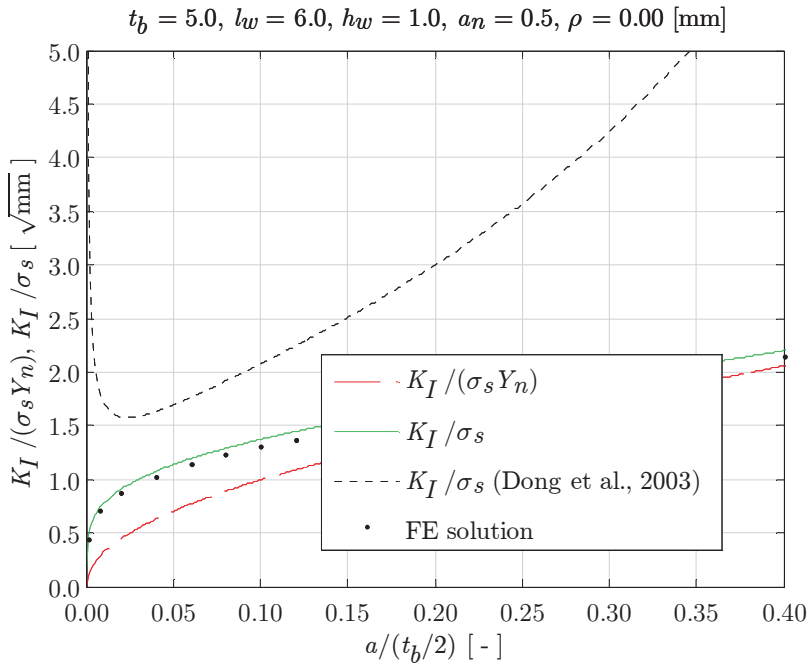


Figure 3.29: PP DS butt joint SIF (loc. 1), $r_s = 0$.

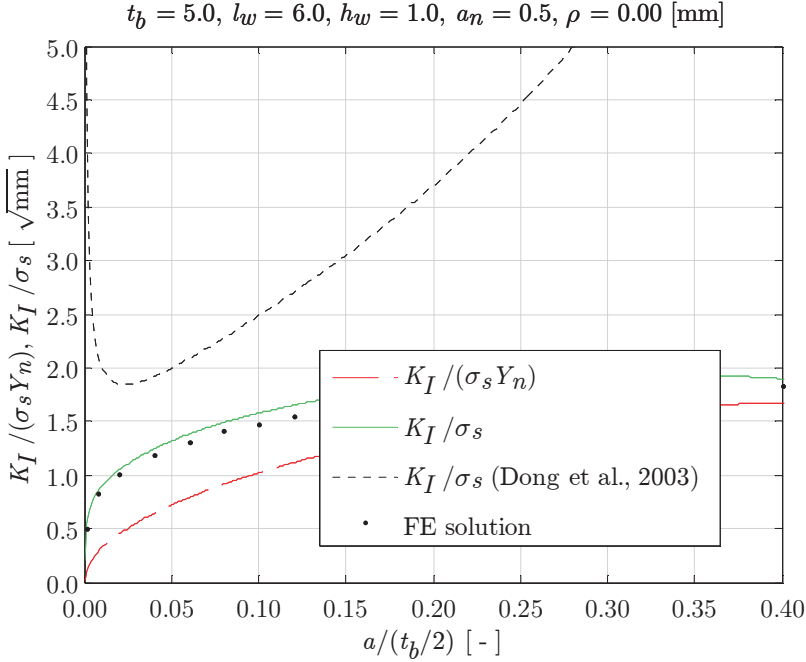


Figure 3.30: PP DS butt joint SIF (loc. 1), $r_s = -1$.

The normalised SIF's (K_I/σ_s) and FE solutions have a close match (Fig. 3.27 to 3.30). While the ($r_s = -1$) case (Fig. 3.26 and 3.30) may suggest crack arrest, the notch in the symmetry plane experiences ($r_s = 1/3$), meaning fatigue in the considered cross-section is still an issue. Ignoring the notch contribution $K_I/(\sigma_s Y_n)$ underestimates the SIF substantially in the micro-crack region. The BSS concept SEC based (K_I/σ_s) estimates (Dong et al., 2003) show rather conservative behaviour and include the characteristic singularity and non-monotonic behaviour. To ensure a level playing field, it is normalised using σ_s as well rather than the BSS defined σ_s^t value, related to half the plate thickness (Dong, 2004).

Although inconsistent from symmetry perspective, a probably more realistic SEC approach – as adopted for the British Standard (BS) – can be applied as well. Likely, one of the weld toe notches contain a governing defect or initial crack size that justifies the one in the symmetry plane to be ignored. Since at $\{0.5 < (a/t_p) \leq 1\}$ far field stress equilibrium conditions are not satisfied and a weld load carrying stress correction is disregarded, the DEN based notch factor Y_n introduces some error in this region, i.e. (small) deviations from the equilibrium value 1. Notwithstanding, the $Y_n Y_f$ estimates and FE solutions are nearly the same in both micro- and macro-crack region since C_{bw} is rather small (Fig. 3.31 to 3.34). Given the BS limitation, i.e. a general a_n induced PP modification to the ideal fillet weld based notch factor, the $Y_n Y_f$ (BS7910, 2005) estimates are conservative as shown for the non-symmetry examples (Fig. 3.10 to 3.13), mainly because of the membrane far field component.

Comparing the DEC and SEC $Y_n Y_f$ estimates (Fig. 3.23 to 3.26 and 3.31 to 3.34), the far field membrane component results are rather different; for bending approximately the same. However, in absolute terms it seems to be the other way around. The DEC micro- and macro-crack region sizes are half the SEC related ones and the membrane results appear to be comparable; for bending different. For both a DEC and SEC assumption the Y_n formulation is the same, meaning a crack growing at the same time in the symmetry part is indeed a macro-crack effect. The SEC case turns out to be the conservative one. Which one to adopt is a matter of choice, provided consistency is preserved. Select either plate thickness t_p and its corresponding weld notch stress distribution no matter symmetry and a SEC based SIF formulation, or relate t_p and SEC; ($t_p/2$) and DEC, for respectively non-symmetry and symmetry. In any case, the far field stress relation should be maintained. Fatigue relevance is questioned (Radaj, Sonsino and Fricke, 2006) concerning the bi-linear notch stress approximation, as defined for symmetry cases (Dong, 2004) considering half the plate thickness ($t_p/2$) only (Paragraph 2.6). In case of a DEC assumption however, it is very useful to obtain Y_n . Though, because of the coupled $Y_n Y_f$ (Dong et al., 2003) formulation, the far field stress relation is lost and a SEC formulation must be adopted. Mixing things up seems to be the actual problem.

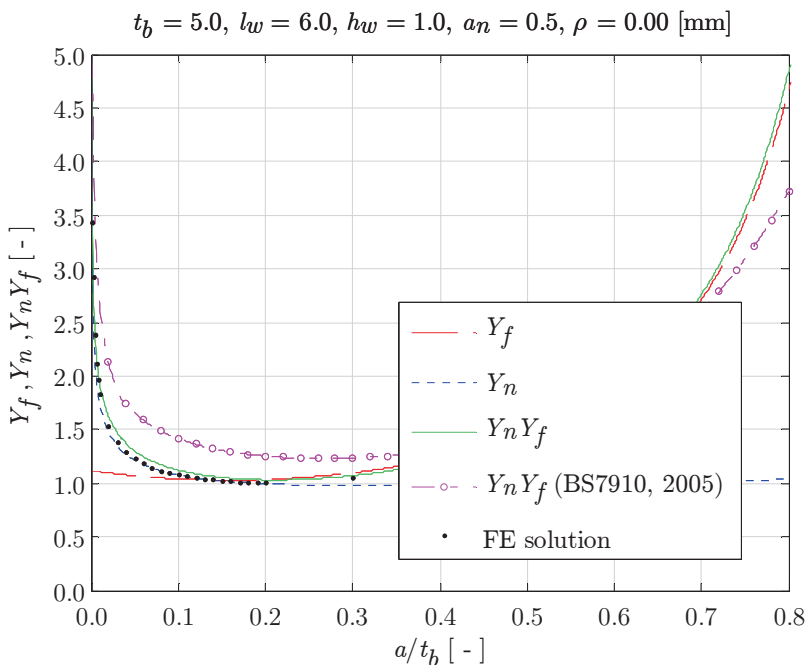


Figure 3.31: PP DS butt joint Y_f SEC formulation (loc. 1), $r_s = 1$.

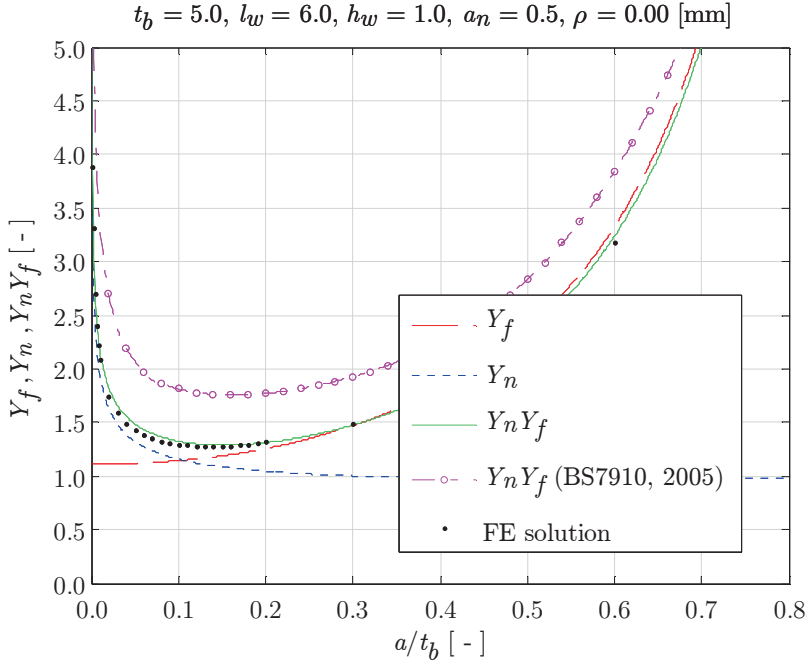


Figure 3.32: PP DS butt joint Y_f SEC formulation (loc. 1), $r_s = (1/3)$.

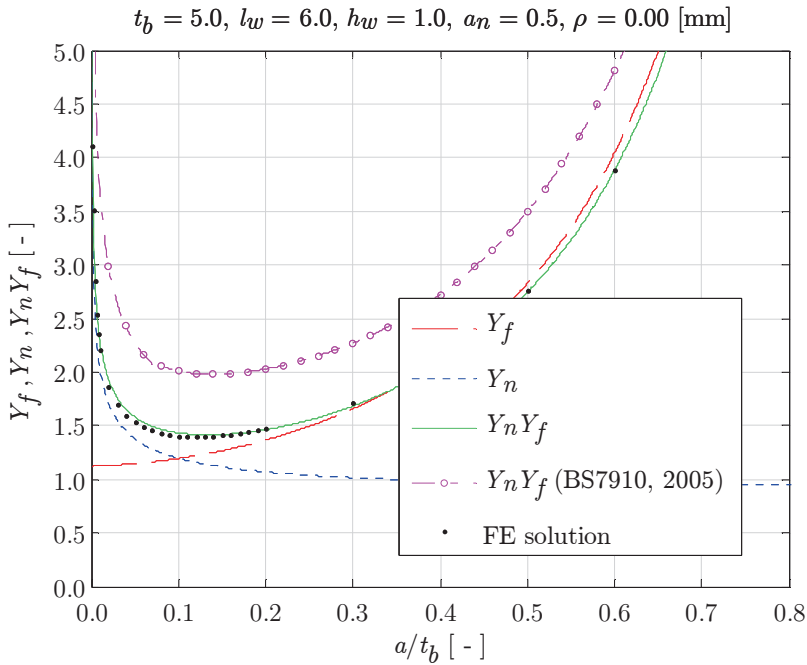


Figure 3.33: PP DS butt joint Y_f SEC formulation (loc. 1), $r_s = 0$.

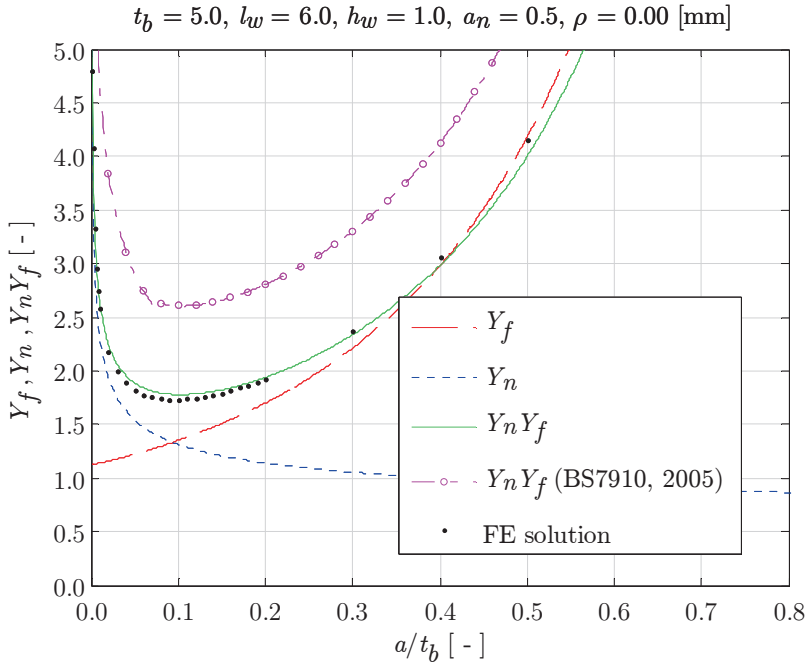


Figure 3.34: PP DS butt joint Y_f SEC formulation (loc. 1), $r_s = -1$.

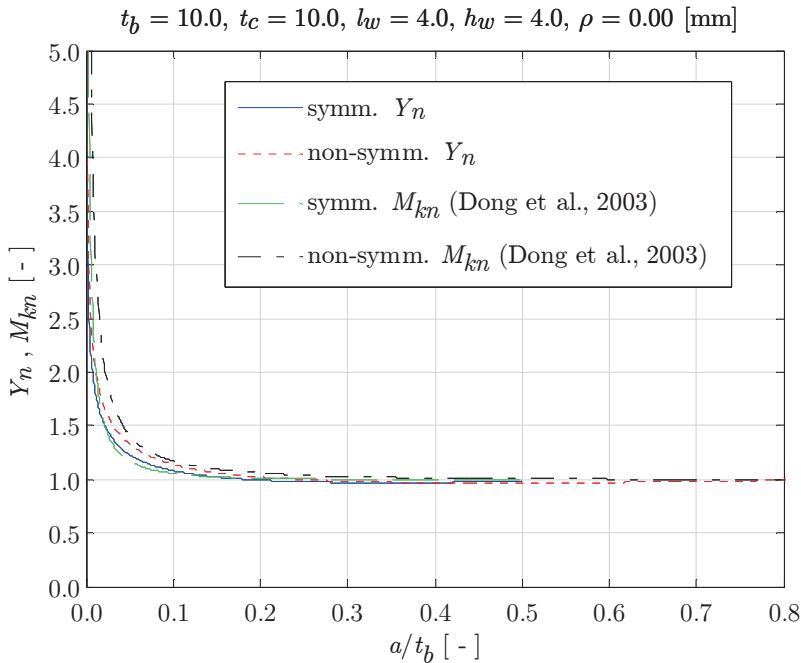


Figure 3.35: Y_n symmetry effect (PP DS T-joint and cruciform joint; loc. 1), $r_s = 1$.

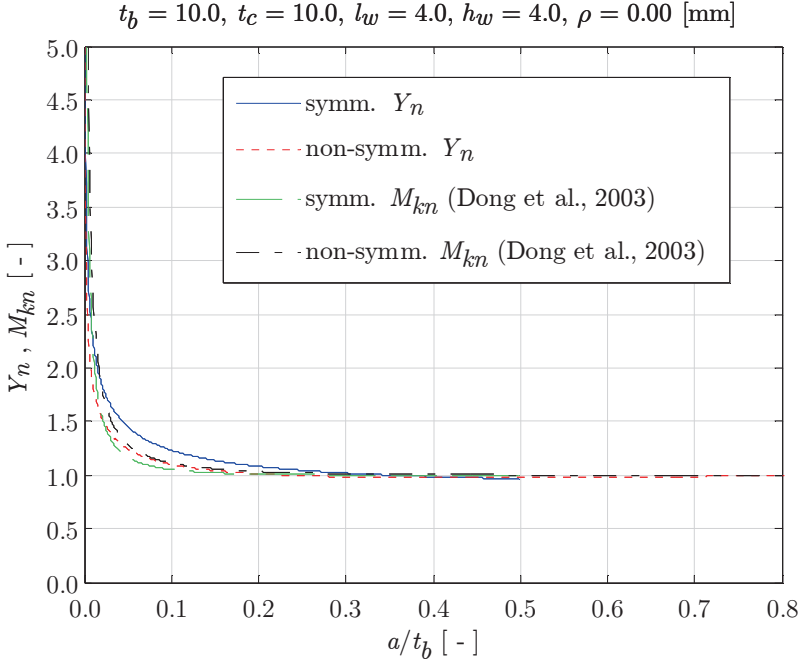


Figure 3.36: Y_n symmetry effect (PP DS T-joint and cruciform joint; loc. 1), $r_s = 0$.

Notch symmetry effects for a PP DS T-joint and its symmetry equivalent, the PP DS cruciform joint, at notch location 1 can be identified (Fig. 3.35 and 3.36). The pure bending far field case shows that the Y_n gradient is more pronounced for non-symmetry; it is the other way around if pure membrane far field loading is applied: a matter of (anti-)symmetry induced load carrying effectiveness. For the BSS concept coupled $Y_n Y_f$ formulation, the notch factor M_{kn} is defined as the ratio of K_I with notch- and K_I without notch effect (Dong, Hong and Cao, 2003). The self-equilibrating stress part related Y_n (Eq. 3.17) satisfies this definition as well. Comparing M_{kn} and Y_n with respect to (non-)symmetry, the same behaviour is identified for ($r_s = 1$). If ($r_s = 0$), it is in fact the opposite as already observed for the weld toe notch stress distributions (Fig. 2.28); a consequence of the bi-linear notch stress approximation.

If the weld becomes more effective, significantly load carrying, as regularly encountered in case of symmetry like for a DS cover plate in discontinuous base plate configuration (Fig. 2.29), C_{bw} increases and Y_n (Eq. 3.23) needs the 2nd order component (Eq. 2.19) to be included:

$$Y_{n,bw} = \left(\frac{2}{\pi}\right) C_{bw} \left(\frac{1}{2}\right) \left[\pi \left\{ 3 \left(\frac{a}{t_p}\right)^2 + 1 \right\} - 12 \left(\frac{a}{t_p}\right) \right] \quad (3.24)$$

A consistent use of the symmetry based Y_n DEN and Y_f DEC formulation pays off in accurate $Y_n Y_f$ estimates (Fig. 3.37). Although Y_n does not include the notch in the symmetry plane, the involved (anti-)symmetry condition at $\{(r/t_p) = (1/2)\}$ and correct C_{bw} value are important. The notch affected- or micro-crack region is considerably increased up to $\{a/(t_p/2) = 0.5\}$, e.g. in comparison to a $Y_n Y_f$ case with substantial smaller C_{bw} (Fig. 3.25), meaning that the micro- and macro-crack region transition, the apex location, is principally C_{bw} determined and shifts towards the right for increasing weld load carrying behaviour. Note that $Y_n Y_f$ (Dong et al., 2003) still limits the notch affected region to $\{0 < a/(t_p/2) \leq 0.1\}$ because of the transition depth assumption. If the weld is hardly weld load-carrying, it seems a reasonable assumption; for increasing C_{bw} , the estimated notch contribution is rather non-conservative.

Inconsistency, i.e. adopting a Y_n DEN and Y_f (SEC) assumption, comes at a price, in particular for significantly weld load carrying welds (Fig. 3.38). Obviously, Y_n is responsible since SEN based unit equilibrium is hard to identify because of the (anti-)symmetry condition at $\{(r/t_p) = (1/2)\}$ and the far field equilibrium lost in the symmetry part. The error already introduced in the micro-crack region continues to increase in the macro-crack region. Although the DEC and SEC assumption was supposed to be predominantly Y_f induced, for increasing C_{bw} the DEN based Y_n considering symmetry is the bottleneck and a SEN formulation should be used to recover consistency.

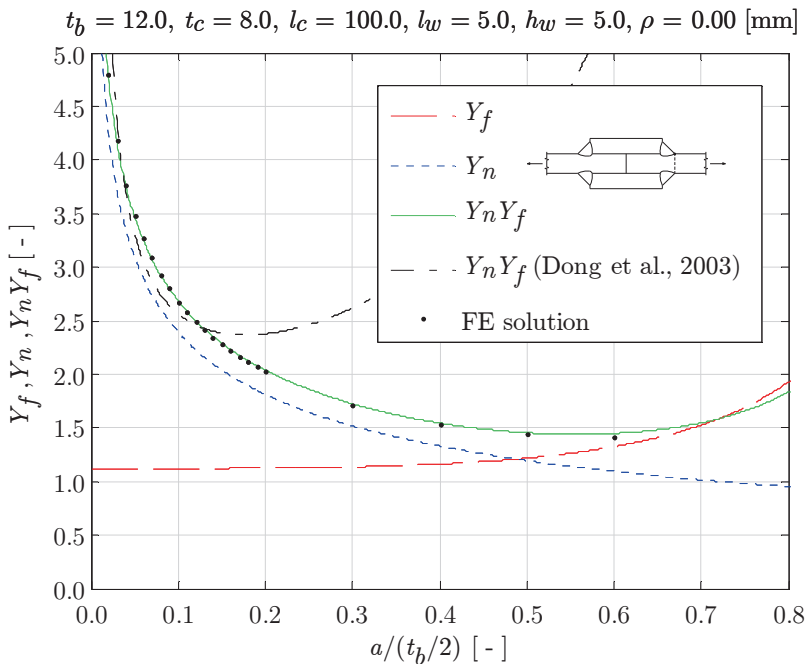


Figure 3.37: DS cover plate (loc. 1) – discontinuous base plate – SIF notch effect including 2nd order C_{bw} contribution, $r_s = 0$.

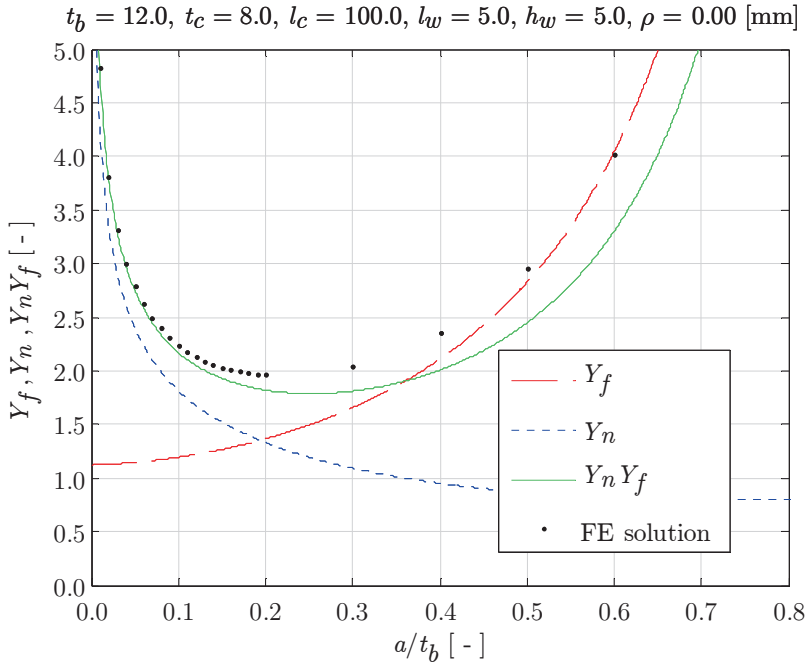


Figure 3.38: DS cover plate (loc. 1) – discontinuous base plate – Y_f SEC far field effect and 2nd order C_{bw} notch contribution, $r_s = 0$.

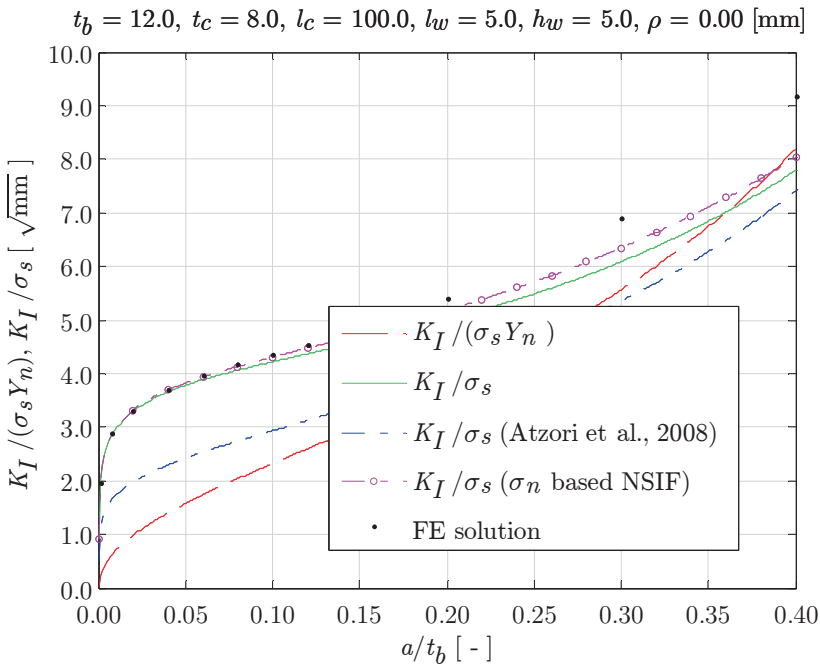


Figure 3.39: DS cover plate (loc. 1) – discontinuous base plate – Y_f SEC formulation and 2nd order C_{bw} notch contribution, $r_s = 0$.

The corresponding normalised SIF's (Fig. 3.39) show the same behaviour. The NSIF and SEC based K_I/σ_s (Atzori et al., 2008) estimate is added for convenience. The involved $\{k_1, k_2\}$ formulations (Eq. 3.20, 3.21); curve fitted FE results (Lazzarin and Tovo, 1998), are derived for a continuous base plate explaining the large deviation. Results are improved using the σ_n based NSIF.

3.6 Weld root notch stress intensity factor

Partial weld penetration introduces a root notch (Fig. 2.34), principally in crack configuration, meaning that an infinitely sharp root notch and crack initiating at that location share the same square root singular behaviour. Besides, the assumed crack path is an extension of the weld root notch, i.e. the governing axis ($\beta = 0$) is the same for both root notch and crack (Fig. 3.40) and the SIF (Eq. 3.3) does – by definition – not include an explicit notch related contribution. An isolated Y_n formulation however can be obtained (Eq. 3.18) if separate notch and crack induced components are required, like for a 2-stage crack growth model. Anyway, $Y_n \neq 1$.

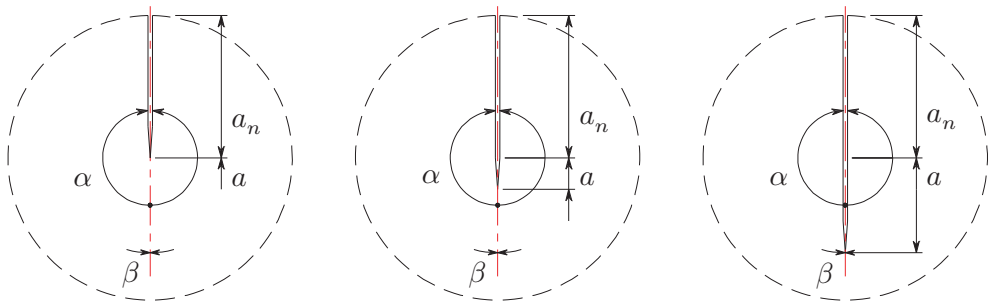


Figure 3.40: The weld root notch- and crack governing axis is one and the same.

The SEN and $\{CN, DEN\}$ related far field components $Y_f(Y_{fw})$ include the weld reinforcement correction to satisfy the welded joint far field stress definition for respectively non-symmetry and symmetry with respect to $(t_p/2)$ and represent the weld root notch crack characteristic SIF behaviour. For illustration purposes, the PP SS butt joint (non-symmetry) and PP DS cruciform joint (symmetry) will be considered using the same dimensions as selected for the weld root notch stress distributions (Paragraph 2.7).

3.6.1 Non-symmetry

Although no explicit part of the weld root notch SIF, the root notch factor Y_{nr} will be determined first in order to calculate Y_n (Eq. 3.18). The notch stress distribution σ_{nr} (Eq. 2.41) needs the root field bending stress projection to be subtracted to obtain the unit crack face traction. Using:

$$\sigma_{ser} \left(\frac{r' - a_n}{t_p'} \right) + 1 = \sum_{i=1}^5 \left\{ \left(\frac{r' - a_n}{t_p'} \right)^{\lambda_i - 1} \mu_i \lambda_i (\lambda_i + 1) (1 - \chi_i) \right\} + \quad (3.25)$$

$$2r_{sr} \left(\frac{r' - a_n}{t_p'} \right)$$

the root notch factor denotes:

$$Y_{nr} = \left(\frac{2}{\pi} \right) \left[\sum_{i=1}^5 \{ F_i \cdot \mu_i \lambda_i (\lambda_i + 1) (1 - \chi_i) \} + \quad (3.26)$$

$$\frac{2r_{sr}}{\left(\frac{t_p'}{b_p} \right)} \left(\sqrt{\left(\frac{t_p'}{b_p} \cdot \frac{a}{t_p'} \right) \left(2 \cdot \frac{a_n}{b_p} + \frac{t_p'}{b_p} \cdot \frac{a}{t_p'} \right)} - \right.$$

$$\left. \left(\frac{a_n}{b_p} \right) \left[\left(\frac{\pi}{2} \right) - \arcsin \left\{ \frac{\left(\frac{a_n}{b_p} \right)}{\left(\frac{a_n}{b_p} + \frac{t_p'}{b_p} \cdot \frac{a}{t_p'} \right)} \right\} \right] \right) \right]$$

with

$$F_1 = \frac{f_1}{\left(\frac{t_p'}{b_p} \right)^{-\frac{1}{2}}} K(m)$$

$$F_2 = - \frac{f_1 f_2}{\left(\frac{t_p'}{b_p} \right)^{\frac{1}{2}}} \left\{ K(m) - \frac{E(m)}{f_3} \right\}$$

$$F_3 = \frac{f_1 f_2}{3 \left(\frac{t_p'}{b_p} \right)^{\frac{3}{2}}} \left\{ f_4 K(m) - f_5 \frac{E(m)}{f_3} \right\}$$

$$F_4 = - \frac{f_1 f_2}{15 \left(\frac{t_p'}{b_p} \right)^{\frac{5}{2}}} \left\{ f_6 K(m) - f_7 \frac{E(m)}{f_3} \right\}$$

$$F_5 = \frac{f_1 f_2}{105 \left(\frac{t_p'}{b_p} \right)^{\frac{7}{2}}} \left\{ f_8 K(m) - f_9 \frac{E(m)}{f_3} \right\}$$

and

$$f_1 = \frac{\sqrt{2}}{\left(\frac{a_n}{b_p} + \frac{t_p'}{b_p} \cdot \frac{a}{t_p'}\right)}$$

$$f_2 = \left(2 \cdot \frac{a_n}{b_p} + \frac{t_p'}{b_p} \cdot \frac{a}{t_p'}\right)$$

$$f_3 = 1 - \frac{\left(\frac{t_p'}{b_p} \cdot \frac{a}{t_p'}\right)}{2 \left(\frac{a_n}{b_p} + \frac{t_p'}{b_p} \cdot \frac{a}{t_p'}\right)}$$

$$f_4 = \left(4 \cdot \frac{a_n}{b_p} + \frac{t_p'}{b_p} \cdot \frac{a}{t_p'}\right)$$

$$f_5 = 4 \left(\frac{a_n}{b_p}\right)$$

$$f_6 = \left\{ 32 \left(\frac{a_n}{b_p}\right)^2 + 18 \left(\frac{a_n}{b_p} \cdot \frac{t_p'}{b_p} \cdot \frac{a}{t_p'}\right) + 9 \left(\frac{t_p'}{b_p} \cdot \frac{a}{t_p'}\right)^2 \right\}$$

$$f_7 = \left\{ 32 \left(\frac{a_n}{b_p}\right)^2 + 26 \left(\frac{a_n}{b_p} \cdot \frac{t_p'}{b_p} \cdot \frac{a}{t_p'}\right) + 9 \left(\frac{t_p'}{b_p} \cdot \frac{a}{t_p'}\right)^2 \right\}$$

$$f_8 = \left\{ 48 \left(\frac{a_n}{b_p}\right)^2 + 58 \left(\frac{a_n}{b_p} \cdot \frac{t_p'}{b_p} \cdot \frac{a}{t_p'}\right) + 25 \left(\frac{t_p'}{b_p} \cdot \frac{a}{t_p'}\right)^2 \right\} \left(8 \cdot \frac{a_n}{b_p} + \frac{t_p'}{b_p} \cdot \frac{a}{t_p'}\right)$$

$$f_9 = \left\{ 24 \left(\frac{a_n}{b_p}\right)^2 + 26 \left(\frac{a_n}{b_p} \cdot \frac{t_p'}{b_p} \cdot \frac{a}{t_p'}\right) + 13 \left(\frac{t_p'}{b_p} \cdot \frac{a}{t_p'}\right)^2 \right\} \left(16 \cdot \frac{a_n}{b_p}\right)$$

The complete elliptical integrals of respectively the 1st and 2nd kind $\{K(m), E(m)\}$ are expressed as function of parameter m rather than the elliptical modulus k ; ($k^2 = m$), with:

$$m = \frac{\left(\frac{t_p'}{b_p} \cdot \frac{a}{t_p'}\right)}{2 \left(\frac{a_n}{b_p} + \frac{t_p'}{b_p} \cdot \frac{a}{t_p'}\right)}$$

The Y_n distributions for a PP SS butt joint (loc. 3) in $\{r_s = 1, r_s = (1/3)\}$ far field loading conditions (Fig. 3.41 and 3.42) reflect the self-equilibrating root stress part induced crack face traction, i.e. an increased notch affected region for the pure bending case as could be expected based on the weld root notch stress distributions (Fig. 2.37 and 2.38).

The SEN based $Y_f(Y_{fw})$ root stress intensities show good agreement with the FE solutions. Since the far field stress definition should be maintained and ($t_b < b_b$) as shown (Fig. 3.3), $\{Y_f(Y_{fw}) < 1\}$ may be identified for smaller crack sizes, like typically encountered for the ($r_s = 1$) far field case (Fig. 3.41); the stress state in the weld throat cross-section is pure bending as well. Adding a membrane component increases the bending contribution and overrules this kind of behaviour (Fig. 3.42).

The BSS concept consistently uses a SEC assumption for weld root notches as well (Hong, 2010), meaning that the σ_{nr} induced stress intensities $Y_n Y_f$ (Dong et al., 2003) as shown for comparison (Fig. 3.41 and 3.42) include an explicit notch- and far field contribution like the weld toe formulations; $Y_n Y_f(Y_{fw})$ would show comparable non-monotonic SIF behaviour. At first glance, the far field contribution seems similar for far field bending (Fig. 3.41). However, it is because the equilibrium equivalent part of the weld root notch stress equals the welded joint far field stress; $\{\sigma_{sr}, r_{sr}\} = \{\sigma_s, r_s\}$. The former, i.e. the structural root stress distribution, has been adopted as far field stress, satisfying its definition for a SEC if and only if the crack is considered not to be a weld root notch extension. From SIF perspective, the root notch geometry introduces the notch behaviour at an intact geometry, similar to the weld toe notches. It is considered beneficial that Y_{fw} has become obsolete. For the sake of a proper comparison, the BSS solutions include the scale factor (σ_s^t/σ_s), i.e. (σ_{sr}/σ_s). Obviously, ($\sigma_{sr} \gg \sigma_s$) for the $r_s = (1/3)$ far field load case (Fig. 3.42). Modelling consequences can be explained as well using the σ_s normalised SIF's (Fig. 3.43 and 3.44). Results excluding the notch contribution $K_I/(\sigma_s M_{kn})$ visualise that the a_n crack like behaviour is ignored in contrast to the SEN based solution, i.e. $\{K_I(a/t_b' = 0)/\sigma_s \neq 0\}$. Taking the notch effect into account, K_I/σ_s (Dong et al., 2003) still shows the artificial and singular stress intensity behaviour for $(a/t_b') \rightarrow 0$. Even if a shared stress field singularity for crack tip and root notch from stress intensity point of view would not last and explicit notch and crack induced far field contributions should be considered; a matter of definition. The SIF $K_I = \sigma_s Y_n Y_f(Y_{fw}) \sqrt{\pi a}$ as 1st order parameter must still be finite and monotonically increasing. The BSS SIF estimates are rather non-conservative in comparison to the FE solutions. Obviously, the SEN and SEC based far field crack stress intensity gradients are similar.

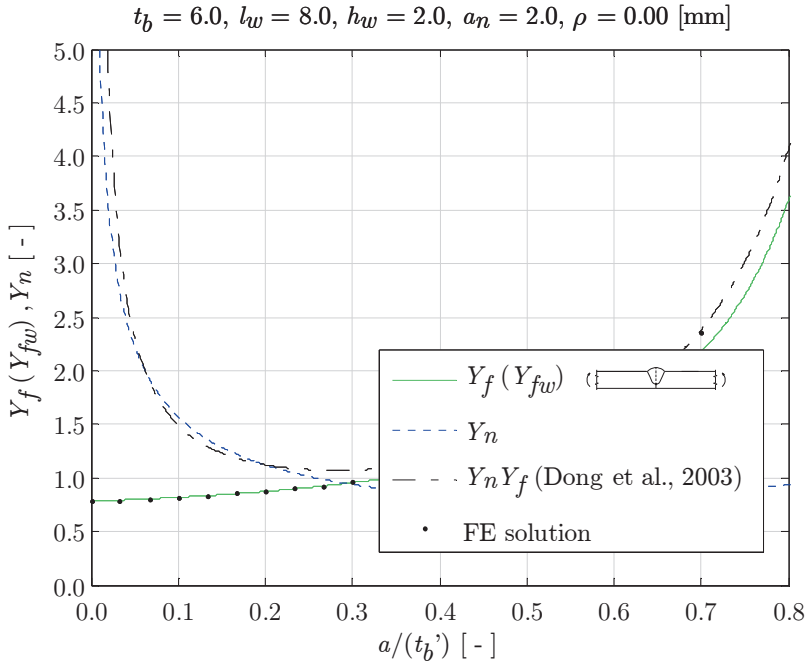


Figure 3.41: PP SS butt joint SIF far field- and notch effect (loc. 3), $r_s = 1$.

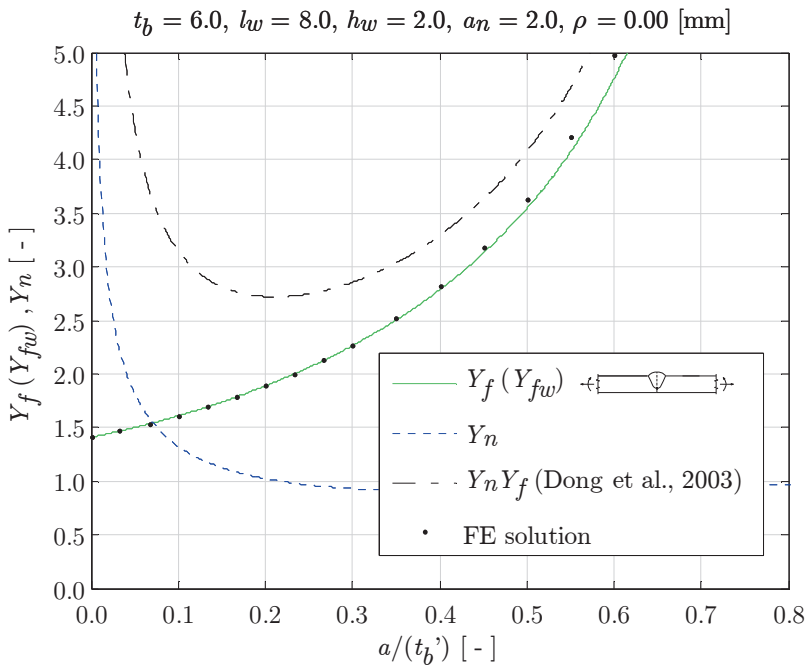
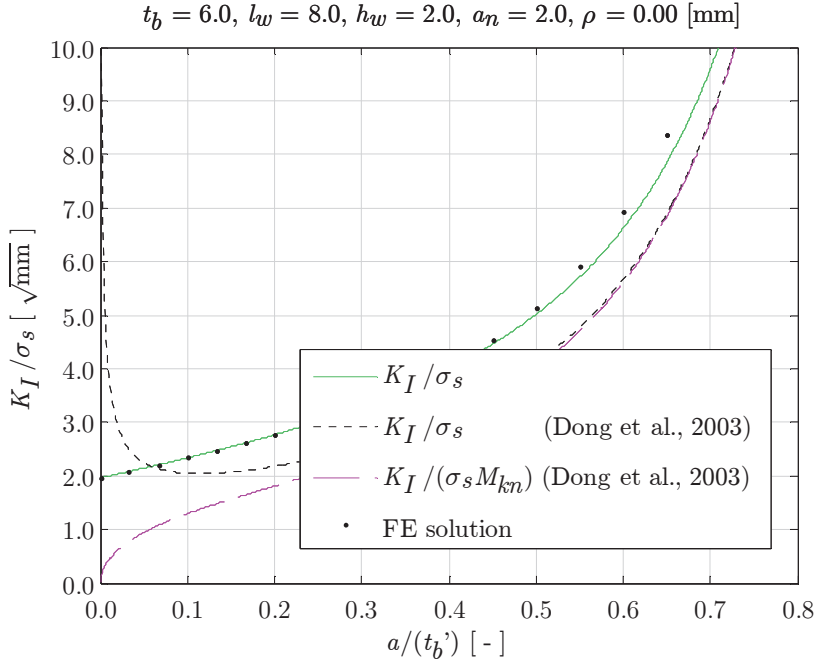
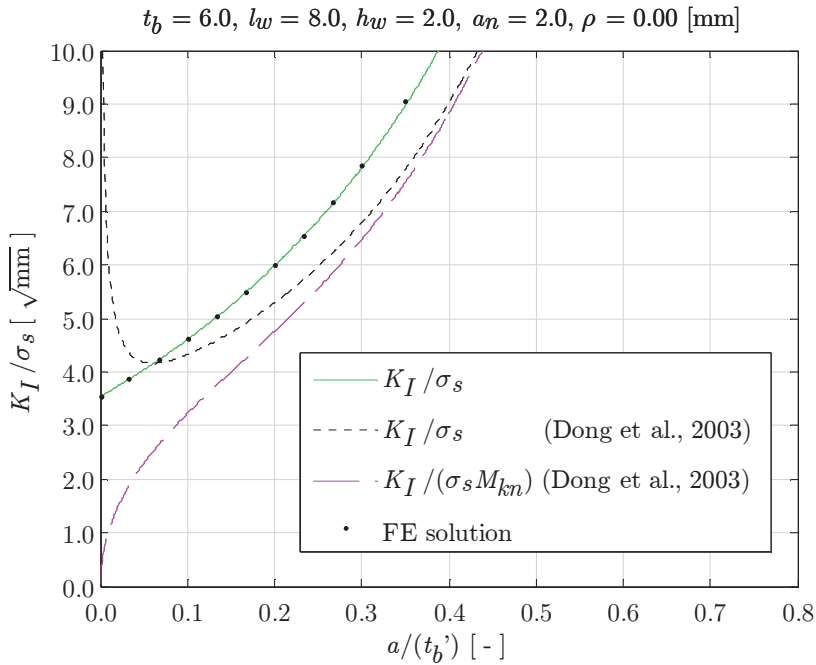


Figure 3.42: PP SS butt joint SIF far field- and notch effect (loc. 3), $r_s = (1/3)$.

Figure 3.43: PP SS butt joint SIF (loc. 3), $r_s = 1$.Figure 3.44: PP SS butt joint SIF (loc. 3), $r_s = (1/3)$.

3.6.2 Symmetry

Since the weld root notch stress formulation σ_{nr} (Eq. 2.41) applies to non-symmetry as well as symmetry with respect to $(t_p/2)$, the root notch factor Y_{nr} (Eq. 3.26) is principally the same for both cases as well, except that symmetry requires the plate thickness related parameters to be modified: ($b_p = b_p/2$) and ($t_p' = t_p'/2$).

Notches in crack configuration facing symmetry include the DEN- (Fig. 3.5) and CN geometry (Fig. 3.6). The latter is a special one. Although the notch geometry demonstrates symmetry, a Y_f effect, non-symmetry is involved concerning σ_{nr} (e.g. Fig. 2.42) – Y_{nr} accordingly – as shown for a $\{r_s = 1, r_s = (1/3)\}$ remote mechanical loaded PP DS cruciform joint at location 9 (Fig. 3.45 and 3.46); a kind of hybrid case.

The $Y_f(Y_{fw})$ estimates and matching FE solutions show that from weld root fatigue perspective far field bending reduces relatively speaking fatigue life time just slightly if the root notch size a_n is not too large; obviously, the membrane component is governing. The geometry property ($t_c/2 < t_c'/2$) and crack stress intensities $Y_f(Y_{fw}) < 1$ are in agreement. Involving the notch component Y_n would cover both a notch and crack contribution, meaning $Y_n Y_f(Y_{fw})$ would include the characteristic non-monotonic behaviour. The Y_n governing micro-crack region turns out to be rather small for pure far field bending in comparison to the $r_s = (1/3)$ case.

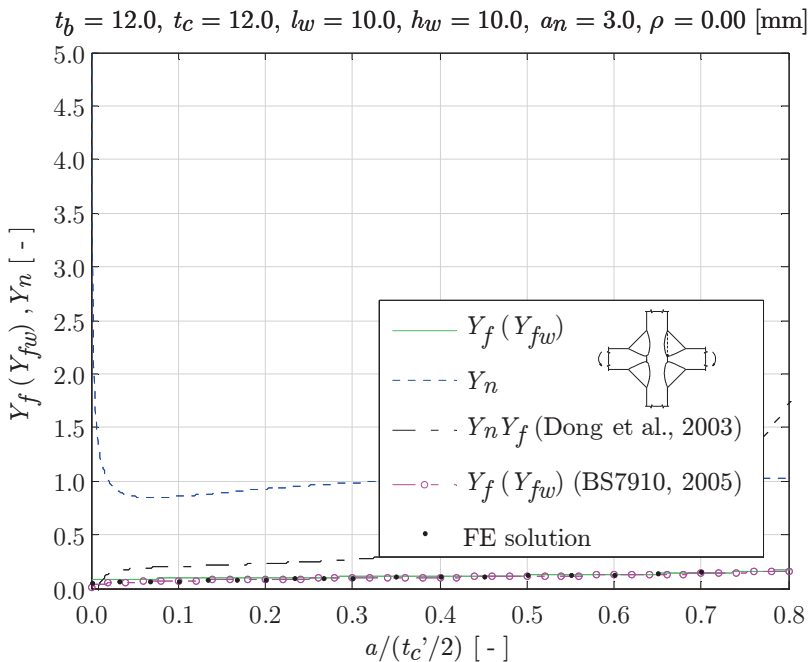


Figure 3.45: PP DS cruciform joint SIF contributions (loc. 9), $r_s = 1$.

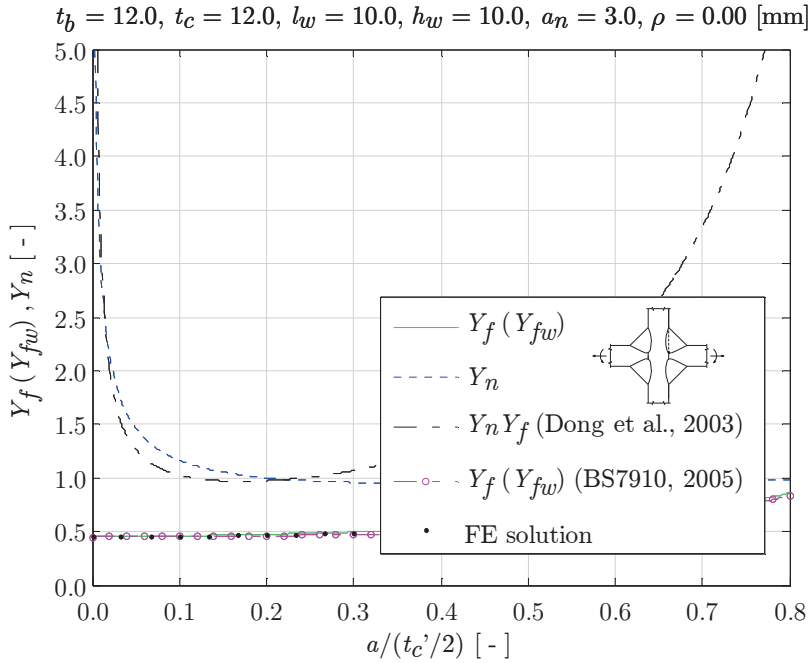


Figure 3.46: PP DS cruciform joint SIF contributions (loc. 9), $r_s = (1/3)$.

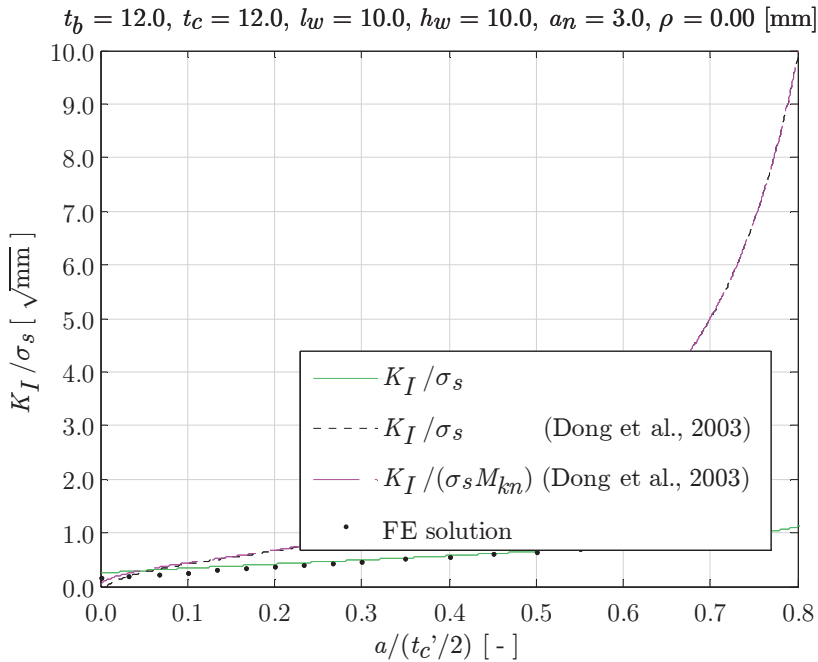


Figure 3.47: PP DS cruciform joint SIF (loc. 9), $r_s = 1$.

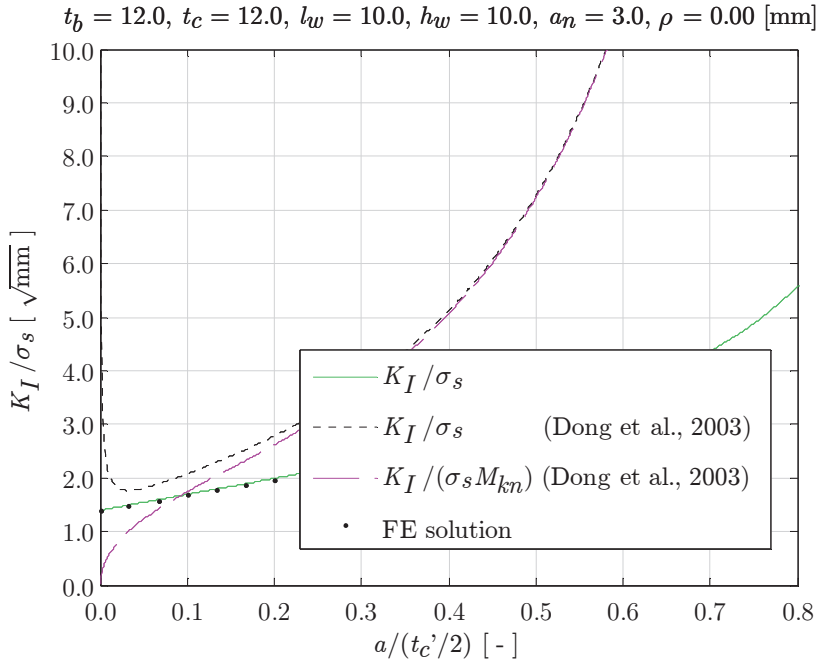


Figure 3.48: PP DS cruciform joint SIF (loc. 9), $r_s = (1/3)$.

An available British Standard (BS7910, 2005) CN solution for PP DS cruciform joint weld root notch SIF's includes only the crack contribution $Y_f (Y_{fw})$; a FE results based curve fitted function.

If the BSS bi-linear root notch stress approximation is adopted, the notch effect disappears for far field bending because of the small notch affected region (Fig. 2.40) and $Y_n Y_f$ (Dong et al., 2003), scaled because structural stress definition, becomes negative for $a / (t_p' / 2) \rightarrow 0$ (Fig. 3.45). The far field behaviour is different since the SEC rather than CN geometry has been selected. In case the fillet weld throat section is assumed to be the crack path – a conservative recommendation if weld root notch size information is not available (Hong, 2010) – rather than a weld leg section, the a_n induced crack-like behaviour must be ignored if a SIF mode-I approach should be adequate. The crack will be no extension of the weld root notch and would introduce a mode-II component. The structural weld throat stress distribution, a solid FE model calculation result, becomes the far field stress. The weld root SIF's (Fig. 3.47 and 3.48) show that as long as notch behaviour with moderate accuracy is included, the SEC based K_I / σ_s (Dong et al., 2003) estimates are rather conservative.

Although no commonly applied welded joints (Fig. 2.3) contain symmetry with respect to $(t_p'/2)$ from both notch and root stress perspective, a DEN standard crack growth specimen does. The Y_{nr} formulation (Eq. 3.26) and modified plate thickness related parameters still apply since σ_{nr} takes care of the symmetry conditions (Eq. 2.44). For the common crack growth testing (tension) load case, $r_s = r_{sr} = 0$, Y_f (Eq. 3.12 and 3.14, Fig. 3.49) – Y_{fw} is not involved – and corresponding K_I/σ_s (Fig. 3.50) prove to be good estimates in comparison to FE solutions. Using Y_n as reference, $Y_n Y_f$ (Dong et al, 2003) contains a smaller notch contribution because of the bi-linear notch stress related transition depth assumption: $0.1(t_p'/2)$.

Since the SEC induced BSS K_I estimates in case of symmetry with respect to $\{(t_p/2), (t_p'/2)\}$ for weld toe- and weld root notches are not very accurate (Fig. 3.50), a different approach has been adopted for crack growth specimen involving notch symmetry (Dong, Hong and Cao, 2003), i.e. the CN and DEN geometry, to obtain improved experimental data analysis results (Chapter 4). The presumed crack face traction $p_{fr} = p_{sr}[1 - 2r_{pr}\{(r' - a_n)/a\}]$ is imposed using the weight function approach (Eq. 3.18), meaning that a crack damaged geometry- rather than intact geometry stress distribution $\{\sigma_{ser}((r' - a_n)/(t_p'/2)) + 1\}$ is involved to acquire Y_{nr} . Results are clearly improved in the macro-crack region, although the way the BSS SIF is calculated has lost its consistency. The BSS notch factor M_{kn} , ratio of K_I with- and without notch effect, i.e. $(p_s Y_{nr} Y_f \sqrt{a_n + a})/(\sigma_s^t Y_{lr} Y_f \sqrt{a_n + a})$, needs Y_{lr} to be calculated first. It has been obtained applying the structural field stress $\sigma_s^t\{1 - 2r_s^t((r' - a_n)/(t_p'/2))\}$ as crack face traction (Dong, Hong and Cao, 2003).

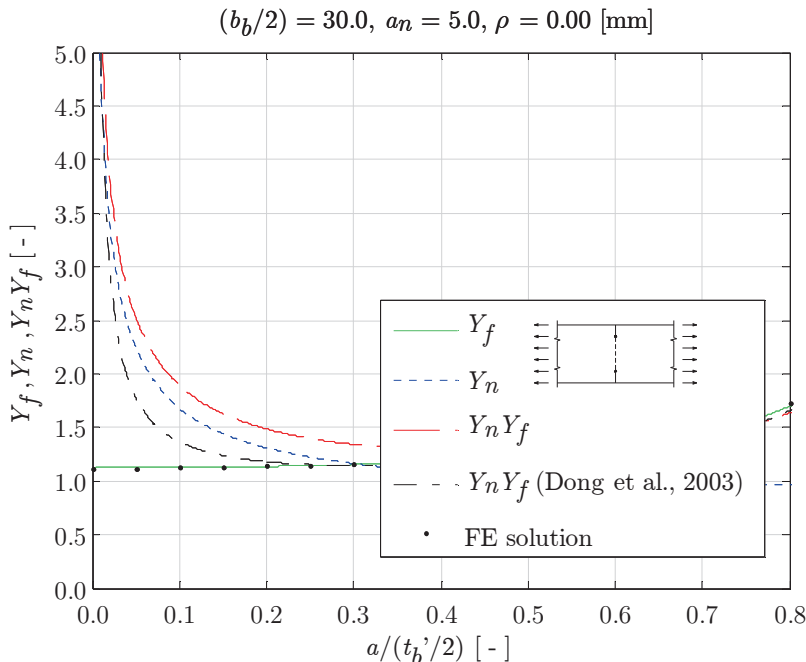


Figure 3.49: SIF contributions DEN(T) crack growth specimen; $r_s = 0$.

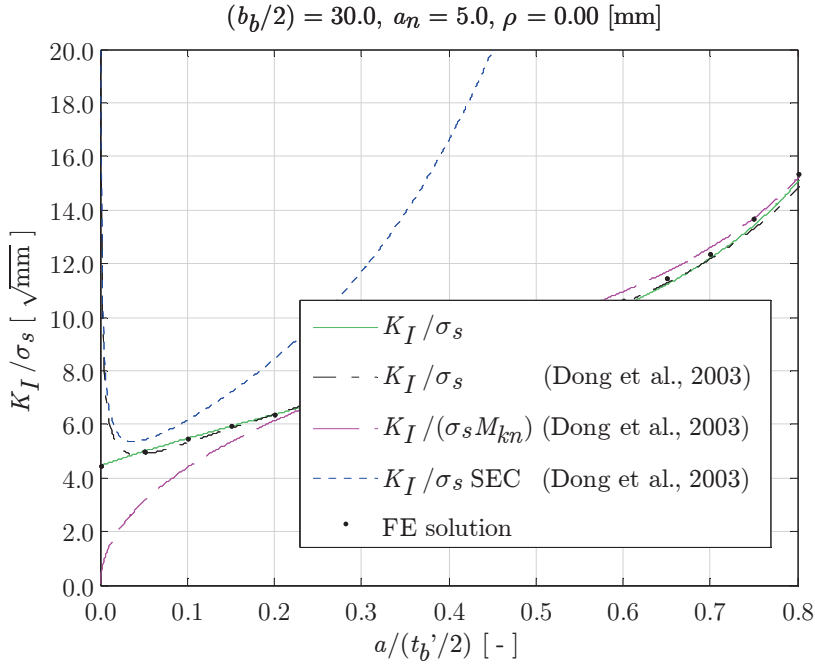


Figure 3.50: SIF contributions DEN(T) crack growth specimen; $r_s = 0$.

Although strictly speaking the weight function definition is violated, $p_f = p_s\{1 - 2p_r(r/a)\}$ could (consistently) be imposed as crack face traction for weld notches as well. The SEC induced SIF including notch effects would simply become $K_I = p_s\{1 - (2/\pi)2r_p\}Y_f\sqrt{\pi a}$. The (artificial) notch affected region results change up to some extent. However, it is considered quite well within the range in comparison to the implications of all the model assumptions.

3.7 Size effects

Modification of the intact geometry notch stress distributions $\sigma_{n(r)}$ for changing weld dimensions – to be taken into account for appropriate fatigue scaling – has already been investigated and illustrated (Paragraph 2.8). Consequences for the crack damaged equivalent, i.e. notch SIF K_I , will be shown varying the same weld dimensions $\{\alpha, l_w, h_w, a_n\}$, notch radius ρ and plate thickness t_p .

3.7.1 Weld dimensions

For (ideal) groove- and fillet welds, the flank angle influences Y_n in a similar way σ_{se} has been affected (Fig. 2.43), as shown for some extreme $\{l_w, h_w\}$ variations (Fig. 3.51). Decreasing $(a/t_p) \rightarrow 0$, the notch factor increases for increasing flank angle, for symmetry even in a stronger degree in comparison to its non-symmetry equivalent. Since the weld load carrying stress increases for increasing flank angle, the weld becomes more effective, as shown for a SS and DS cover plate with continuous base plate (Fig. 3.52). The BSS notch stress intensity M_{kn} (Dong, Hong, and Cao, 2003) becomes conservative for $(a/t_b) \rightarrow 0$ in any case.

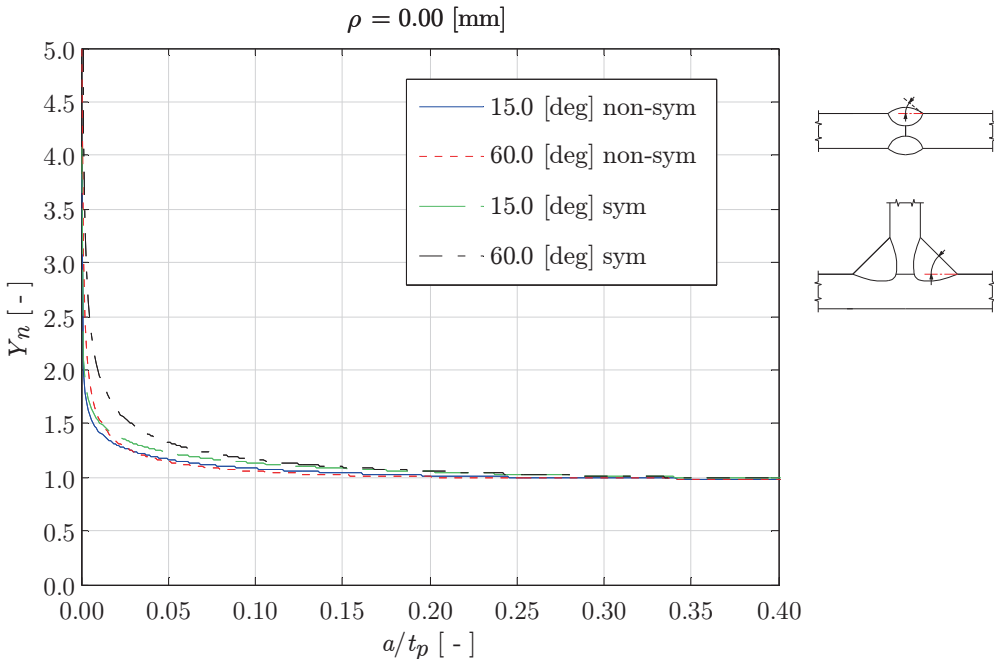


Figure 3.51: Notch factor Y_n at different weld flank angles, ($C_{bw} = 0$).

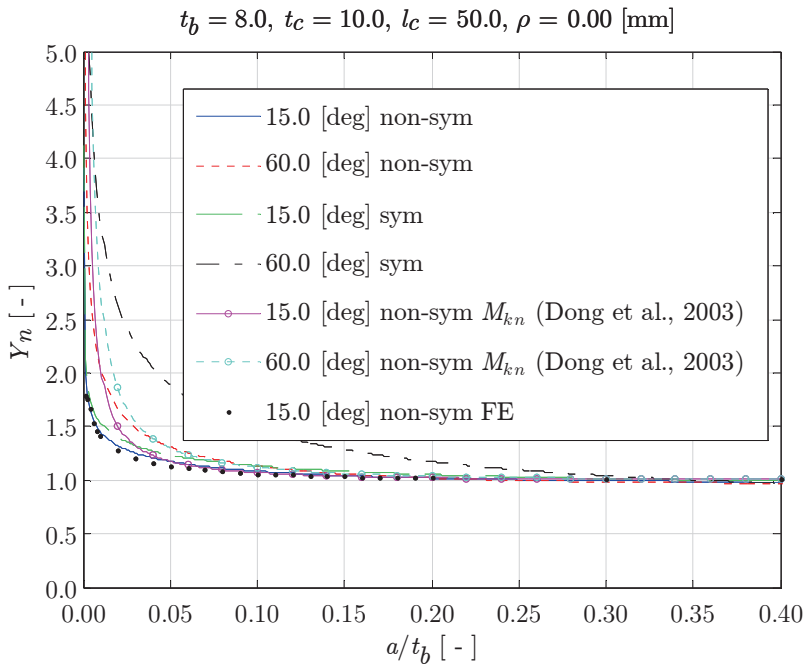


Figure 3.52: SS cover plate (non-sym.) and DS cover plate (sym.) – continuous base plate – loc. 1 notch factor Y_n at different fillet weld flank angles and constant weld throat size $a_t = 4$ [mm], $r_s = 0$.

For partial penetrated welds, except $\{l_w, h_w\}$ the root notch a_n forces the weld to carry more load, meaning the notch stress intensity $Y_n Y_f$ increases in the micro-crack region as shown for a PP DS cruciform joint developing a SEC (Fig. 3.53). The consequences of a DEN based Y_n in combination with a SEC induced Y_f is obvious: a respectively conservative and non-conservative stress intensity estimate in the micro- and macro-crack region because of the high weld load carrying level. The BS7910 estimate includes a $\sqrt{t_c/t_w}$ correction reasonable at $\{0 < (a/t_b) < 0.1\}$. However, because the notch contribution converges very slowly to 1, at least not in agreement with the actual one, the macro-crack growth region estimate is quite conservative.

Increasing the root notch size a_n increases predominantly the structural root stress σ_{sr} , meaning for a far field bending loaded SS butt joint the (fictitious) notch stress intensity $Y_n Y_f (Y_{fw})$ remains more or less unaffected like the root notch stress distribution. Even if σ_{nr} changes, in particular in the far field dominated region (Fig. 2.48), the zone 3 stress gradient can be approximately the same as shown for a DS butt joint, meaning the macro-crack stress intensity is similar (Fig. 3.54). Because $\{(t'_p/2) > (t_p/2)\}$, the weld geometry correction $\{Y_f(Y_{fw}) < 1\}$. The FE solution does not include the notch contribution because of the shared crack tip and notch singularity.

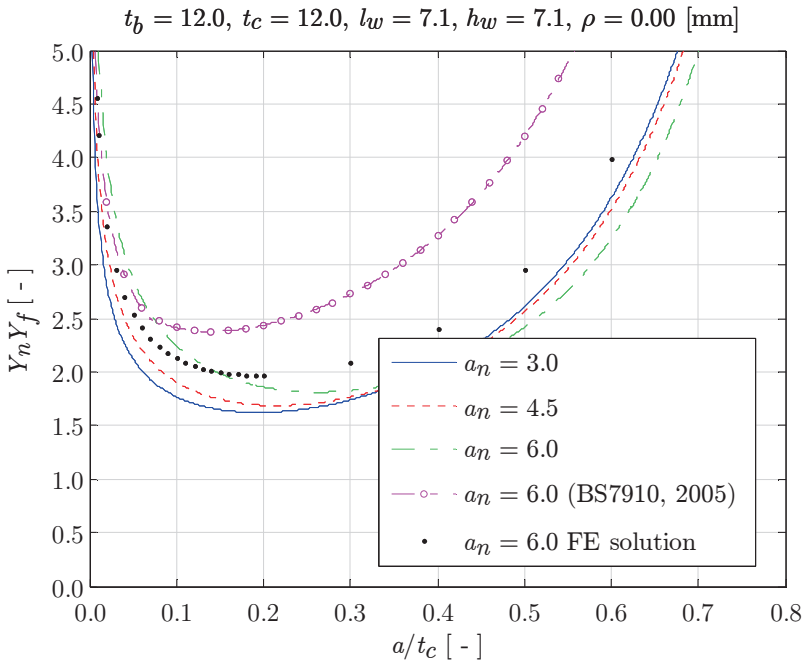


Figure 3.53: PP DS cruciform joint SEC notch stress intensity (loc. 5), $r_s = 0$.

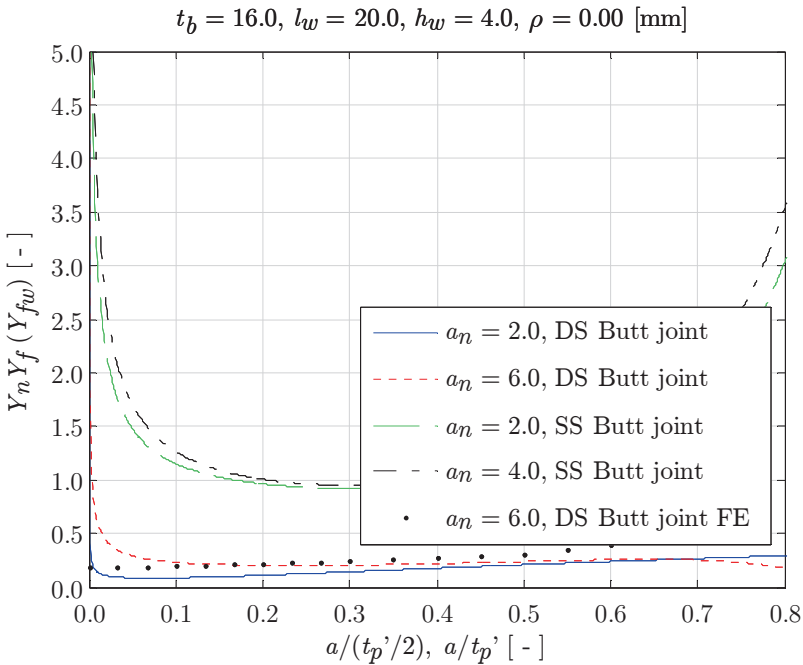


Figure 3.54: PP {DS, SS} butt joint {loc. 5, loc. 3} stress intensity, $r_s = 1$.

3.7.2 Notch radius

For cracks emanating at notches (Fig. 3.55) satisfying ($\rho > 0$), the SIF can be approximated over the crack size range ($a > 0$) using an asymptotic interpolation solution (Wormsen, Fjeldstad and Härkegård, 2006; Liu and Mahadevan, 2009) and involves an equivalent crack length:

$$K_I = \sigma_s Y_f \sqrt{\pi \left(d_n \left[1 - \exp \left\{ - \left(\frac{a}{d_n} \right) \left(\frac{K_t^2}{Y_f^2} - 1 \right) \right\} \right] + a \right)} \quad (3.27)$$

with the two extremes

$$K_I = \sigma_s K_t Y_f \sqrt{\pi a} \quad \text{for } (d/a_n) \rightarrow 0$$

$$K_I = \sigma_s Y_f \sqrt{\pi(d_n + a)} \quad \text{for } (d/a_n) \rightarrow \infty$$

The first one involves a micro-crack in the notch affected region; a simplified expression obtained using the 1st order (Maclaurin) series expansion, $\exp\{\cdot\} = 1 - (a/a_n)(K_t^2 - 1)$. In comparison to the K_I formulation as previously defined for groove- and fillet weld geometries (Eq. 3.2), the SCF K_t representing the zone 1 peak stress has replaced the notch factor $Y_n(a/t_p)$. Note that K_I (Eq. 3.27) approximates the zone 2 notch stress gradient using the $\exp\{\cdot\}$ function. The second extreme concerns a macro crack in the far field dominated region. At the same time, for sharp notches ($\rho \rightarrow 0$), the SCF ($K_t \rightarrow \infty$) and the asymptotic solution (Eq. 3.27) reduces to $K_I = \sigma_s Y_f \sqrt{\pi(d_n + a)}$ as well. The notch depth equals the notch length ($d_n = a_n$) in case of a weld root, although the crack tip stress intensity does not include a notch contribution because of shared singularity. On the other hand, for a weld toe it is not obvious how d_n should be defined – introducing the same kind of peculiarities as identified for the NSIF K_I^N (Paragraph 1.1 & 2.11) – but the SIF includes a notch component; i.e. application to weld notches is controversial anyway.

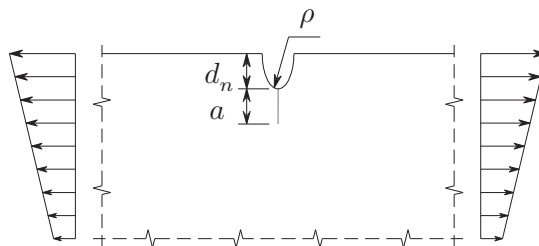


Figure 3.55: Crack emanating at notch; ($\rho > 0$).

Using the notch stress formulation (Eq. 2.47) and crack face traction definition (Eq. 3.17), Y_n in case of non-symmetry becomes for 1st order σ_{bw} :

$$Y_n = \left(\frac{2}{\pi}\right) \int_0^a \frac{\left\{ \sigma_{se} \left(\frac{r''}{t_p} \right) + 1 \right\}}{\sqrt{a^2 - r^2}} dr \quad (3.28)$$

$$\begin{aligned} Y_n = \left(\frac{2}{\pi}\right) & \left[\mu_s \left\{ I_{\lambda_s} \left(\frac{a}{t_p} \right) \cdot \lambda_s (\lambda_s + 1) [\cos\{(\lambda_s + 1)\beta\} - \right. \right. \\ & \left. \left. \chi_s \cos\{(\lambda_s - 1)\beta\}] + \right. \right. \\ & \left. I_{\zeta_s} \left(\frac{a}{t_p} \right) \cdot \left(\frac{r_0}{t_p} \right)^{\lambda_s - \zeta_s} \lambda_s \frac{\left(\frac{2\alpha}{\pi} \right)}{4 \left\{ \left(\frac{2\alpha}{\pi} \right) - 1 \right\}} \cdot \right. \\ & \left. [\omega_{s1} \cos\{(\zeta_s + 1)\beta\} + \right. \\ & \left. \left. \omega_{s2} (\zeta_s + 1) \cos\{(\zeta_s - 1)\beta\}] \right\} + \right. \\ & \left. \mu_a \left\{ I_{\lambda_a} \left(\frac{a}{t_p} \right) \cdot \lambda_a (\lambda_a + 1) [\sin\{(\lambda_a + 1)\beta\} - \right. \right. \\ & \left. \left. \chi_a \sin\{(\lambda_a - 1)\beta\}] + \right. \right. \\ & \left. I_{\zeta_a} \left(\frac{a}{t_p} \right) \cdot \left(\frac{r_0}{t_p} \right)^{\lambda_a - \zeta_a} \lambda_a \frac{1}{4(\zeta_a - 1)} \cdot \right. \\ & \left. [\omega_{a1} \sin\{(\zeta_a + 1)\beta\} + \right. \\ & \left. \left. \omega_{a2} (\zeta_a + 1) \sin\{(\zeta_a - 1)\beta\}] \right\} + \right. \\ & \left. C_{bw} \left\{ 2 \left(\frac{a}{t_p} \right) - \left(\frac{\pi}{2} \right) \right\} \right] \end{aligned}$$

with

$$I_x \left(\frac{a}{t_p} \right) = \int_0^1 \frac{\left\{ \left(\frac{r}{a} \cdot \frac{a}{t_p} \right)^2 + 2 \cos(\beta) \left(\frac{r}{t_p} \right) \left(\frac{r}{a} \cdot \frac{a}{t_p} \right) + \left(\frac{r}{t_p} \right)^2 \right\}^{\frac{x-1}{2}}}{\sqrt{1 - \left(\frac{r}{a} \right)^2}} d \left(\frac{r}{a} \right)$$

and

$$x = \{ \lambda_s, \lambda_a, \zeta_s, \zeta_a \}$$

The 4 integrals I_x have to be calculated numerically for each crack step. Because of the involved boundary singularity, a Gauss-Kronrod integration scheme is adopted. In case of symmetry, the original formulation (Eq. 3.23) has be used with $f(a/t_p) = Y_n$ (Eq. 3.28) and modified σ_{bw} contribution: $C_{bw}\{4(a/t_p) - (\pi/2)\}$. For root notches involving non-symmetry:

$$\begin{aligned}
 Y_{nr} = \left(\frac{2}{\pi}\right) & \left[\sum_{i=1}^5 \mu_i \left[I_{\lambda_i} \left(\frac{a}{t_p}\right) \cdot \lambda_i(\lambda_i + 1)(1 - \chi_i) + \right. \right. \\
 & I_{\zeta_i} \left(\frac{a}{t_p}\right) \cdot \left(\frac{r_0}{t_p'}\right)^{\lambda_i - \zeta_i} \cdot \\
 & \left. \left. \left(\frac{\lambda_i}{2}\right) \{\omega_{1i} + \omega_{2i}(\zeta_i + 1)\} \right] + \right. \\
 & \left. \frac{2r_{sr}}{\left(\frac{t_p'}{b_p}\right)} \left(\sqrt{\left(\frac{t_p'}{b_p} \cdot \frac{a}{t_p'}\right) \left(2 \cdot \frac{a_n}{b_p} + \frac{t_p'}{b_p} \cdot \frac{a}{t_p'}\right)} - \right. \right. \\
 & \left. \left. \left(\frac{a_n}{b_p}\right) \left[\left(\frac{\pi}{2}\right) - \arcsin \left\{ \frac{\left(\frac{a_n}{b_p}\right)}{\left(\frac{a_n}{b_p} + \frac{t_p'}{b_p} \cdot \frac{a'}{t_p'}\right)} \right\} \right] \right) \right]
 \end{aligned} \tag{3.29}$$

with

$$I_x \left(\frac{a}{t_p}\right) = \int_{a_n}^{a_n+a} \frac{\left\{ \sqrt{\left(\frac{r}{t_p}\right)^2 + 2 \left(\frac{r_t}{t_p}\right) \left(\frac{r}{t_p}\right) + \left(\frac{r_t}{t_p}\right)^2} - \left(\frac{a_n}{t_p}\right) \right\}^{x-1}}{\sqrt{(a_n + a) - r^2}} d(r)$$

and

$$x = \{\lambda_i, \zeta_i\}$$

The symmetry case requires only the plate thickness related parameters to be modified: ($b_p = b_p/2$) and ($t_p' = t_p'/2$). The linear unit stress notch factor Y_{nl} does principally not change since a_n already includes the ρ correction (Fig. 3.55).

For increasing ρ , the zone 1 peak stress reduces as well as the zone 2 stress gradient, meaning predominantly the micro-crack region is affected. The Y_n contribution for respectively a non-symmetry- (PP DS T-joint; Fig. 3.56) and symmetry case (PP DS cruciform joint; Fig. 3.57) is similar, although the symmetry condition forces Y_n to be more pronounced.

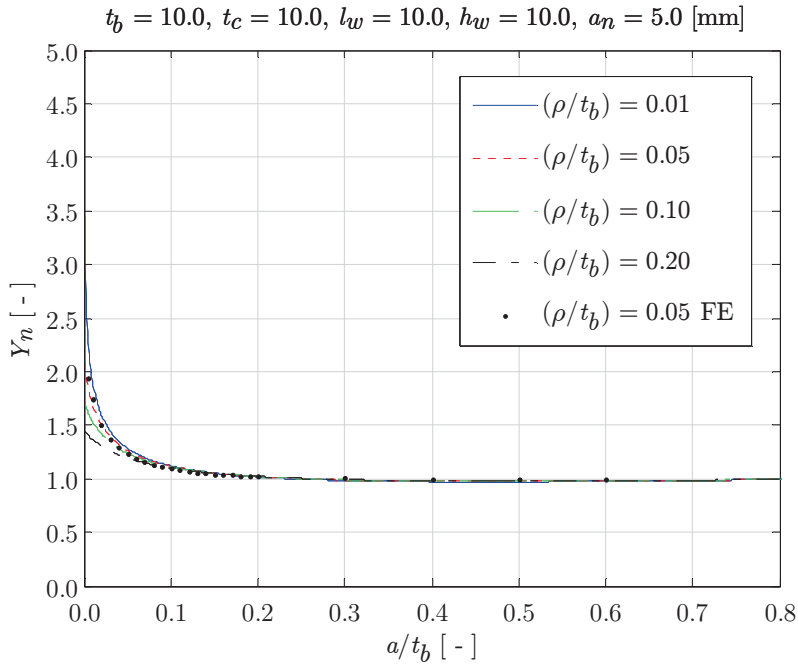


Figure 3.56: PP DS T-joint notch stress intensity (loc. 1), $r_s = (1/3)$.

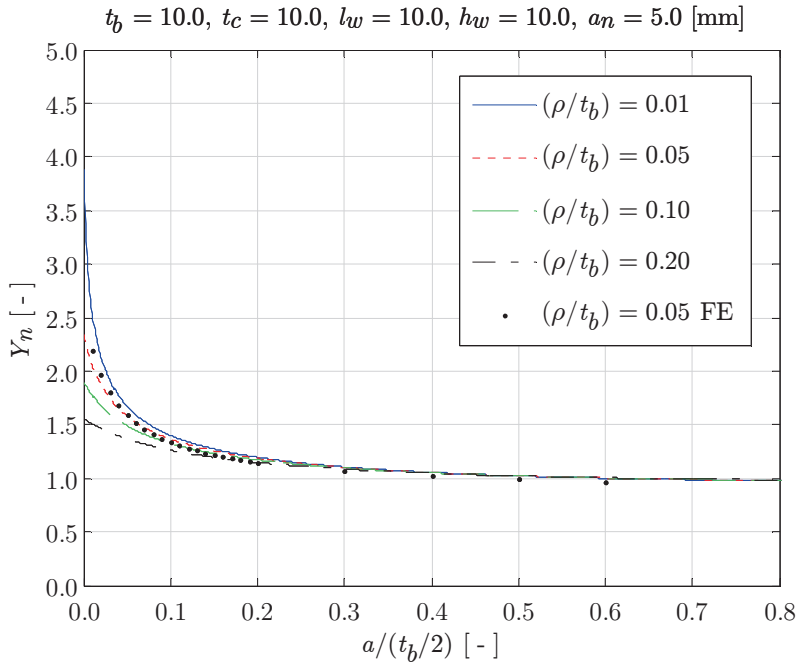


Figure 3.57: PP DS cruciform joint notch stress intensity (loc. 1), $r_s = (1/3)$.

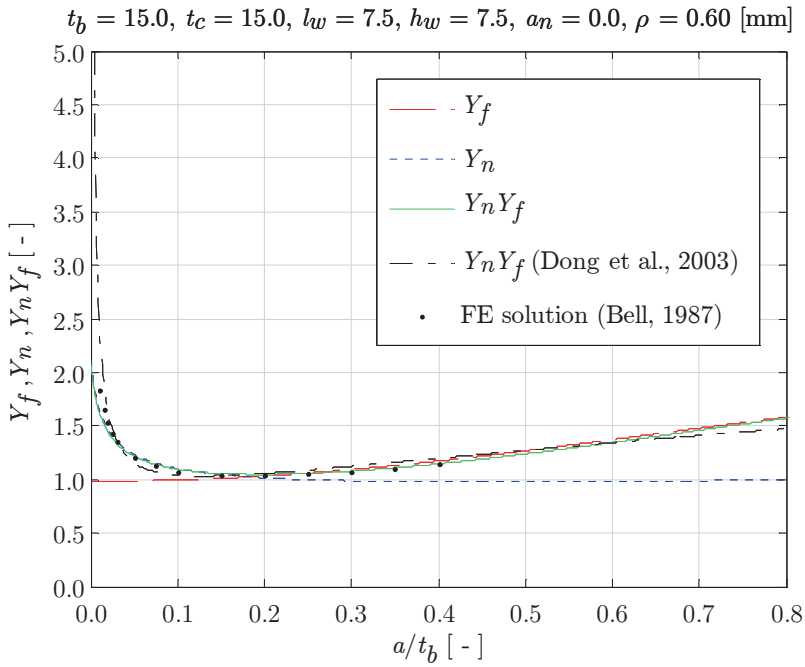


Figure 3.58: PP DS T-joint SIF (loc. 1) semi-elliptical crack $\{(a/c) = 0.25\}, r_s = 1$.

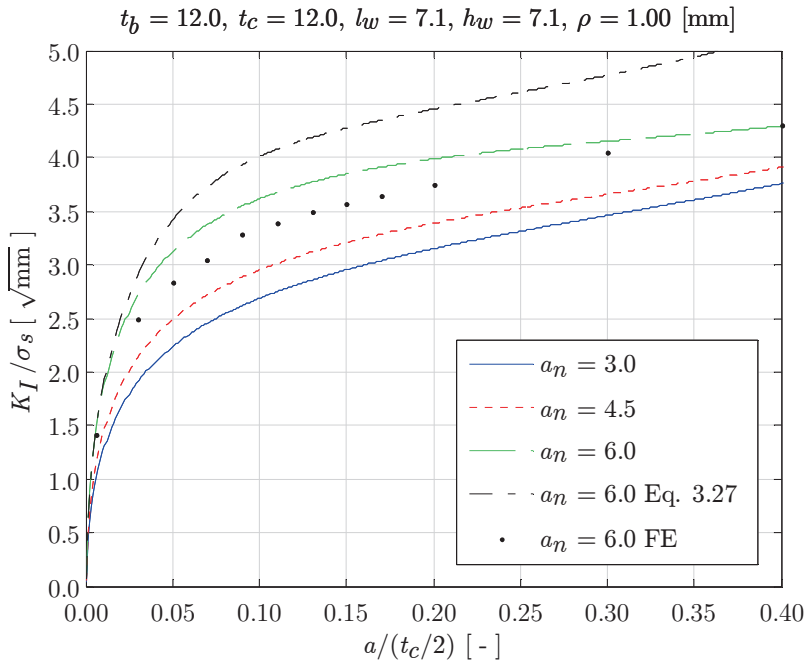


Figure 3.59: PP DS cruciform joint SIF (loc. 5), $r_s = 0$.

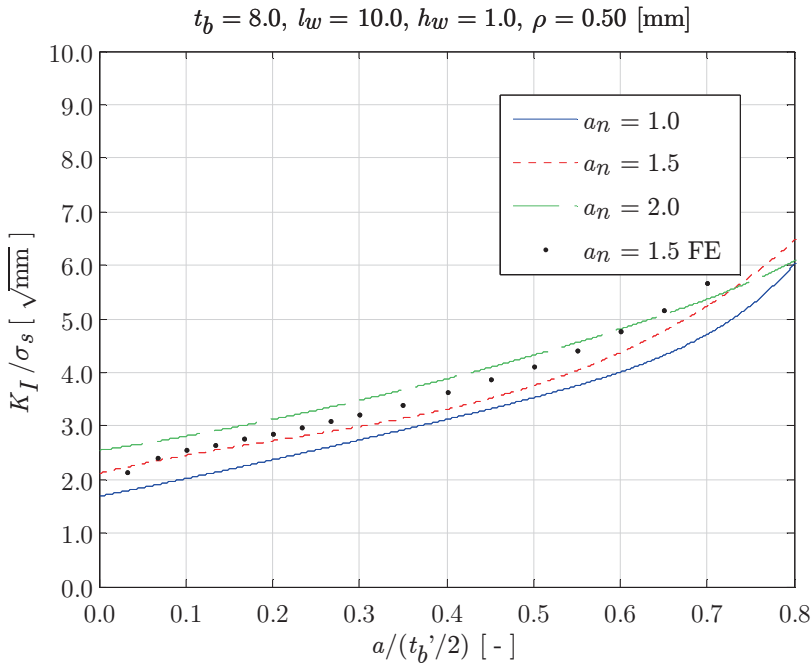


Figure 3.60: PP DS butt joint SIF (loc. 5), $r_s = 0$.

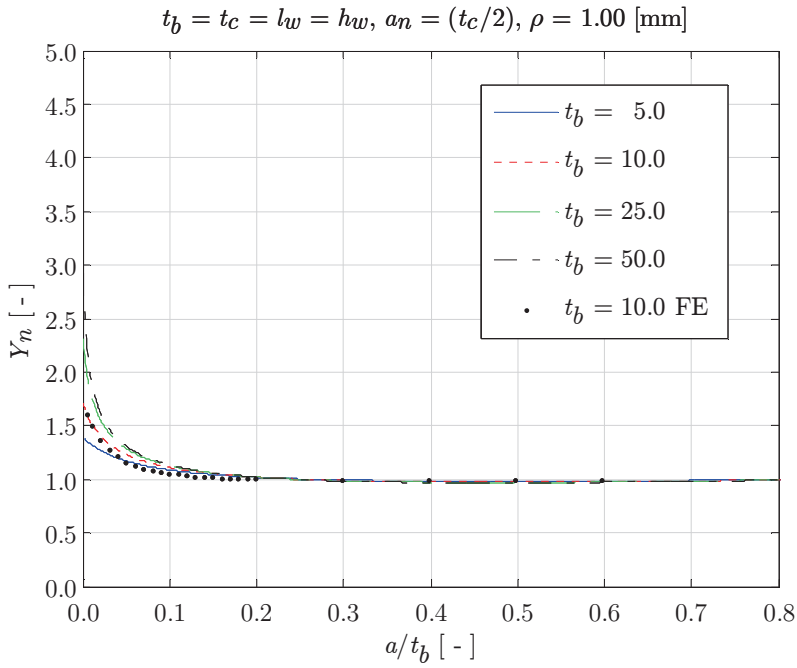
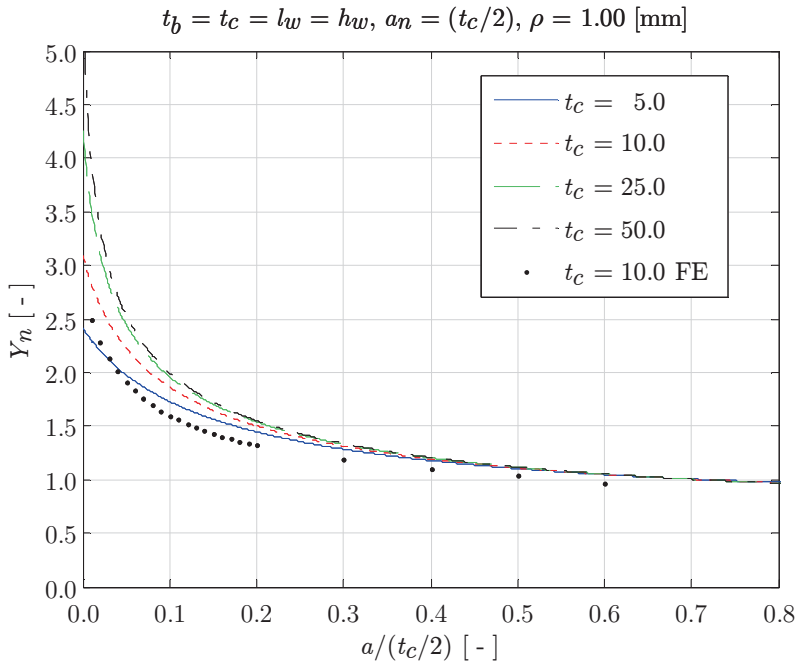
Reanalysis of the semi-elliptical crack stress intensity (Fig. 3.22) including ρ effect emphasizes the difference in comparison to the the BSS estimate (Fig. 3.58).

The SIF for an extreme (non-linear) load carrying weld of a PP DS cruciform joint (Fig. 3.59) is principally overestimated, although not to the extent of the asymptotic interpolation solution (Eq. 3.27); the fictitious notch depth is defined as $d_n = \cos[\{\pi - \text{atan}(l_w/h_w)\}/2] \cdot (l_w^2 + h_w^2)^{0.5}$.

Since the PP DS butt joint weld root notch stress distribution remains approximately the same for varying a_n , K_I shifts with increasing structural root stress σ_{sr} (Fig. 3.60).

3.7.3 Plate thickness

The weld notch stress distributions already revealed that as long as all welded joint dimensions scale according to t_p , $\{\sigma_n, \sigma_{nr}\}$ hardly change (Paragraph 2.8.3). Focus on the deviating cases shows for weld toe and root notches the same effect: scaling is incomplete. One example is a fixed (effective) notch radius as shown for (non-) symmetry (Fig. 3.61 and 3.62). The relative notch acuity (ρ/t_p) decreases for increasing t_p and $Y_n(\rho > 0) \rightarrow Y_n(\rho = 0)$, meaning the weld notch stress intensity in the σ_n zone $\{1, 2\}$ related micro-crack region changes. The conservative estimate compared to the FE solution in case of symmetry is a matter of inaccurate C_{bw} ; a weakness of the way it has been obtained (using an FE beam model).

Figure 3.61: PP DS T-joint SIF plate thickness effect (loc. 1), $r_s = 0$.Figure 3.62: PP DS cruciform joint SIF plate thickness effect (loc. 5), $r_s = 0$.

3.8 Residual stress intensity factor

For the welding induced and displacement (constraints) controlled residual stress distribution showing conceptually the same stress field similarity as the remote mechanically loading induced one (Paragraph 2.10), the mode-I quasi-2D residual stress intensity factor (RSIF) K_I^r can be obtained using the weight (Green's) function approach (Tada and Paris, 1981; Bueckner, 1987). Applying both the equilibrium equivalent- and self-equilibrating residual stress part as crack face traction, the weld toe notch formulation denotes:

$$K_I^r = \sigma_s^r Y_f^r \sqrt{\pi a} + Y_n^r \sqrt{\pi a} \quad (3.30)$$

with

$$\begin{aligned} Y_f^r &= \left(\frac{2}{\pi}\right) \int_0^a \frac{\left\{1 - 2r_s^r \left(\frac{r}{t_p}\right)\right\}}{\sqrt{a^2 - r^2}} dr \\ &= \left\{1 - \left(\frac{4}{\pi}\right) r_s^r \left(\frac{a}{t_p}\right)\right\} \end{aligned}$$

and

$$Y_n^r = Y_n - 1$$

In comparison to the SIF K_I (Eq. 3.2), K_I^r is expressed as superposition since the residual stress distribution σ_n^r can be of the self-equilibrating type if no constraints are involved, meaning ($\sigma_s^r = 0$). Assemblies like hull structures typically include constraints. The residual notch factor formulation Y_n^r , principally equal to the unit-stress related Y_n , has been modified accordingly. Residual stress simulations should be available to obtain C_{bw}^r , simply using the equilibrium equivalent bending stress for $(r/t_p) \in (0, 1/2)$. One σ_n^r example of the (approximately) self-equilibrating type is identified at loc. 3 of a DS T-joint (Barsoum et al., 2009; Fig. 2.71); a symmetry case.

Like for σ_n^r (Fig. 2.71), Y_n^r turns out to be conservative in the zone $\{1, 2\}$ notch affected region $\{0 < a/(t_c/2) < 0.2\}$ for this particular case (Fig. 3.63) because of an involved simplified heat source formulation, i.e. a constant flux rather than Goldak's heat source or equivalent, and alternatively a cosine function or 2nd order polynomial – self-equilibrating by definition – can be adopted:

$$\begin{aligned}
 Y_n^r &= \left(\frac{2}{\pi}\right) \int_0^a \frac{\cos\left(2\pi \cdot \frac{r}{t_p}\right)}{\sqrt{a^2 - r^2}} dr \\
 &= J_0\left(2\pi \frac{a}{t_p}\right)
 \end{aligned}
 \tag{3.31}$$

or

$$\begin{aligned}
 Y_n^r &= \left(\frac{2}{\pi}\right) \int_0^a \frac{6 \left\{ \left(\frac{r}{t_p} - \frac{1}{2}\right)^2 - \frac{1}{12} \right\}}{\sqrt{a^2 - r^2}} dr \\
 &= 3 \left(\frac{a}{t_p}\right)^2 - \left(\frac{12}{\pi}\right) \left(\frac{a}{t_p}\right) + 1
 \end{aligned}
 \tag{3.32}$$

The cosine formulation (Eq. 3.31) introducing the Bessel function of the 1st kind $J_0(\cdot)$ already improves the approximation; the 2nd order polynomial however shows even a better fit. Note that the amplitude has been scaled using the structural residual stress corresponding to half the plate thickness. The RSIF plot (Fig. 3.64) includes the crack induced square root behaviour as well.

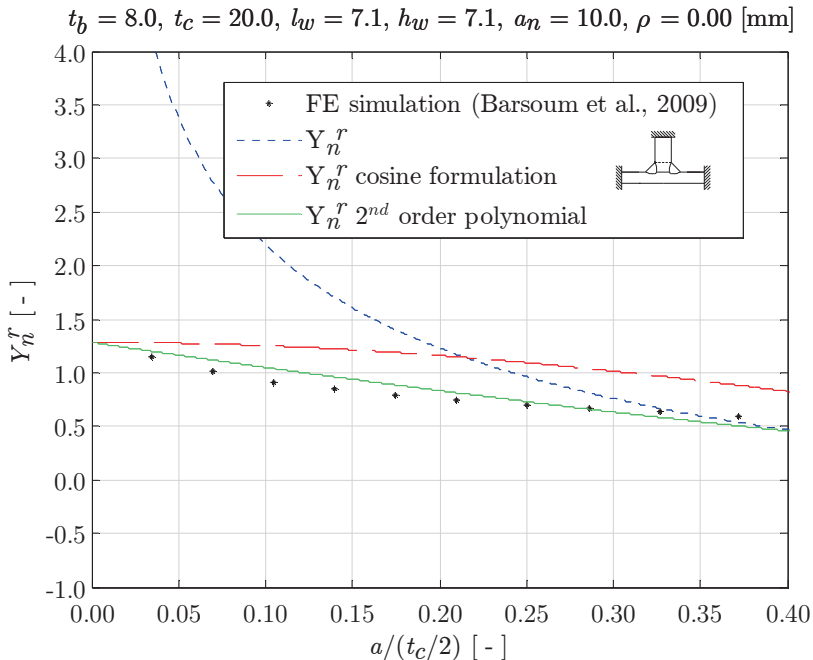


Figure 3.63: Y_n^r formulations for a PP DS T-joint (loc. 3).

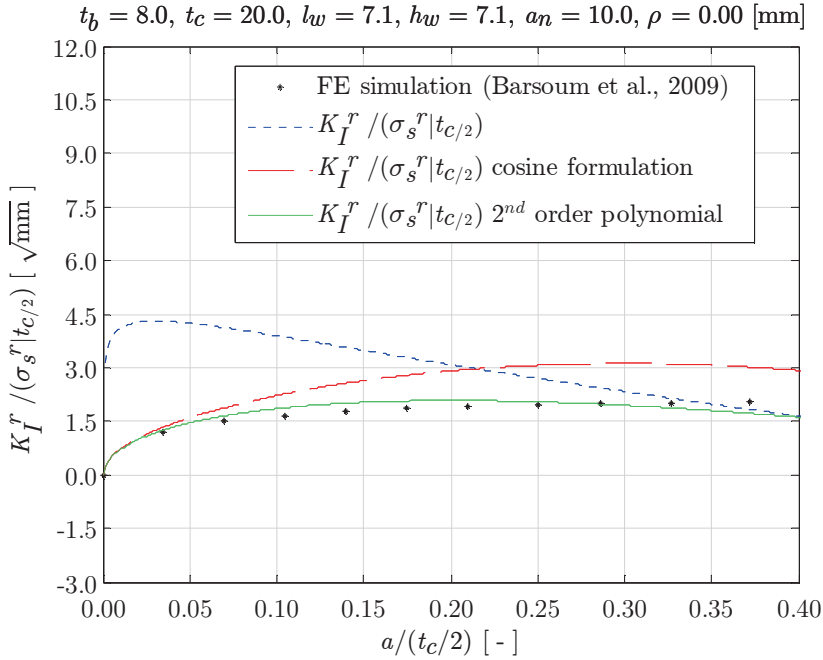


Figure 3.64: K_I^r formulations for a PP DS T-joint (loc. 3).

Interesting to mention is that the BSS concept applies the residual self-equilibrating stress as crack face traction (Dong, 2008) in contrast to the remote loading induced part (Paragraph 3.5), meaning the ‘higher order SIF effect’ is considered to be typically far field stress related. However, in case of (theoretically) similar stress distributions – either mechanical- or thermal loading induced – an inevitable question arises and is still open...

For loc. 6 of the same joint, K_I^r is related to a weld root notch. If the self-equilibrating stress part shows singular square root behaviour, its contribution is already included in the residual field part formulation. Adding the root notch contribution, the RSIF becomes:

$$K_I^r = \sigma_s^r Y_f^r \sqrt{\pi(a_n + a)} \quad (3.33)$$

The weld root notch residual stress distribution (Barsoum et al., 2009; Fig. 2.72) is of the “equilibrium” type and shows a negligible self-equilibrating residual stress σ_{se}^r , i.e. the residual field component Y_f^r defines K_I^r (Fig. 3.65 and 3.66). Note that in fact no simulation data is available for the Y_n^r governing region!

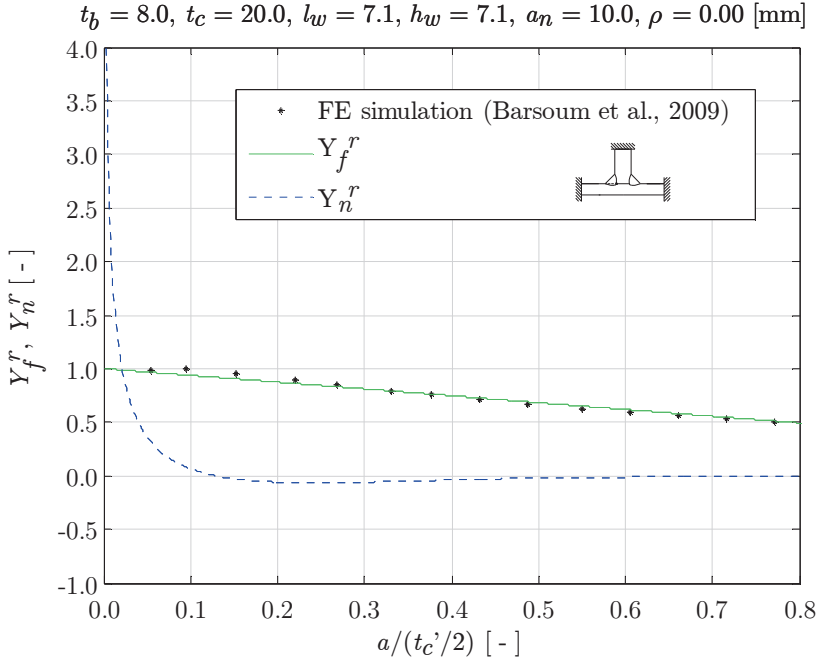


Figure 3.65: $\{Y_n^r, Y_f^r\}$ formulations for a PP DS T-joint (loc. 5).

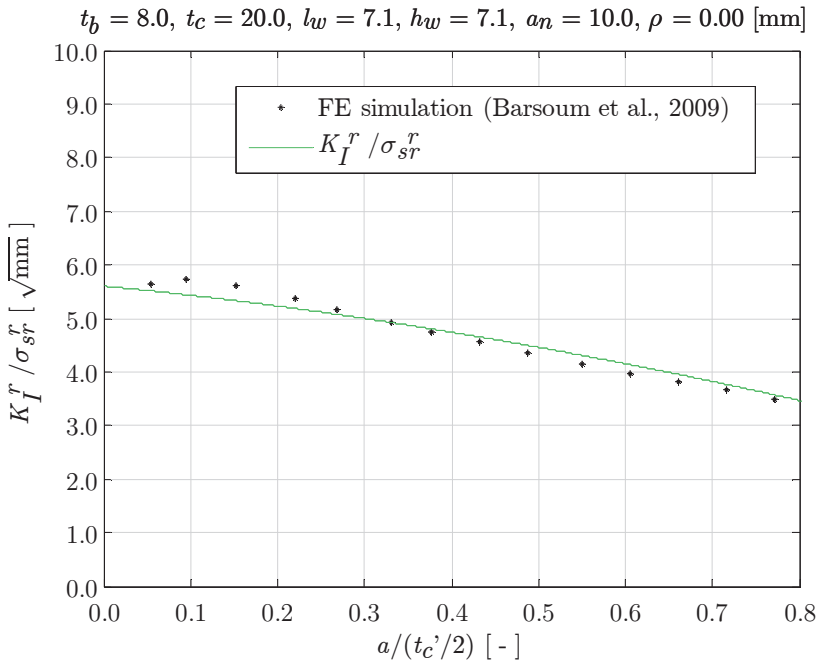


Figure 3.66: K_I^r formulation for a PP DS T-joint (loc. 5).

To obtain the FE simulation result for the equilibrium equivalent residual field stress only, σ_{nr}^r has been applied as crack face traction in total first; then Y_n^r containing the theoretical square root behaviour has been subtracted.

The total weld notch stress intensity factor is a superposition of the far field loading- and welding induced contribution, i.e. $K_I^T = K_I + K_I^r$. However, it is popular to turn the residual stress part into a crack size dependent mean stress effect $r_{s(r)}^r(a/t_p)$ to correct the crack growth formulation (Dong, 2008; Liljedahl et al., 2009; Paragraph 5.4.2).

3.9 Conclusions

The remote mechanical loading induced intact geometry weld notch stress distribution has been translated into a crack damaged equivalent exploiting (non-) symmetry conditions. The zone {1, 2} notch affected- and zone 3 far field dominated parts defined a micro- and macro-crack region, turning the stress field similarity into a stress intensity similarity. Each stress component dominates a certain crack length range: notch stress $\sigma_{\theta\theta}$ the micro-crack region, structural field stress σ_f the macro-crack region; weld load carrying stress σ_{bw} determines the transition position, i.e. apex location.

4

Crack Growth at Notches

Growth means change and change involves risk, stepping from the known to the unknown.
George Shinn (1941, former baseball team owner)

4.1 Introduction

Fatigue damage of arc-welded joints in hull structures is hypothesised to be a crack growth dominated process. Crack nucleation – a significant part of the crack initiation process – is not required to develop (near) surface microscopic stress concentrations since welding induced ones (a result of defects) are assumed to exist already (Fig. 4.1).

Cyclic loading as involved in the fatigue damage process requires the spatial remote mechanical mode-I weld notch stress distribution (Chapter 2), in particular the far field stress definition, to be extended using one more parameter, e.g. the load ratio r_l specifying the cycle degree of symmetry relative to zero: $\sigma_f(\sigma_s, r_s) \rightarrow \sigma_f(\Delta\sigma_s, r_s, r_l)$. The stress range ($\Delta\sigma_s = 2\sigma_s$) substitutes the amplitude σ_s . Temporally, a sinusoidal shape is assumed for both linear and non-linear (impact) types of ocean/sea wave induced loading as governing for high-speed craft.

For ($\sigma_s \rightarrow \Delta\sigma_s$), the mode-I (weld notch) stress intensity K_I (Chapter 3) becomes a crack growth driving force ΔK_I and defects may grow into small/short cracks. If the size a is comparable to the scale of the microstructure, one grain, a is defined as micro-structurally small/short. Crack growth however involves the mode-II mechanism, meaning it is still slip band related and considered to be part of the initiation process. A crack size up to a few grains is denoted as mechanically small/short; mode-I already becomes governing and the (notch affected) crack tip plastic zone size r_p is significant. For negligible r_p , the crack turns into a physically small/short one (Suresh and Ritchie, 1984; Krupp, 2007). Although crack size criteria are predominantly assigned using absolute numbers; $O(10^x)$, relative ones (e.g. with respect to grain size, notch size or plate thickness) would make more sense. For a small/short crack exceeding one grain in size, the far field stress amplitude will be responsible for the qualification “mechanical” or “physical”. Welding induced defects are assumed to belong to one of both categories.

Concerning crack growth at notches, another definition will be added: a is considered to be technically small/short in the notch affected micro-crack region; beyond, in the macro-crack region, a is identified as large/long.

Growth, a process of stepwise increments in crack size, both physically – considering fatigue striations – as well as numerically to obtain a fatigue life time estimate N , starts at a relatively low crack growth rate (da/dn) and may suggest fatigue is predominantly related to technically small/ short crack growth. Assuming the involved crack growth driving force components can be formulated at macro-structural (continuum mechanics)- rather than at meso- or even micro-structural scale, an adequate crack growth law similarity will be defined using the weld notch stress distribution- and intensity similarities.

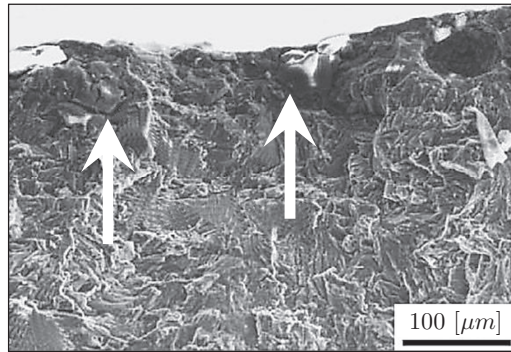


Figure 4.1: Fatigue fracture surface showing defects near a weld toe notch of a DS T-joint (Sidhom et al., 2005).

Outline

A common feature of small/short crack growth is however the anomalous behaviour in comparison to the sigmoidal shaped large/long crack (da/dn) - ΔK_I curve. The (notch dependent) elastoplastic crack tip stress wake field size and shape is assumed to be an important parameter (Schijve, 1988), suggesting the (total weld) notch stress distribution should be involved. The equilibrium equivalent- and self-equilibrating remote mechanical- and thermal residual stress parts used to define the mode-I weld notch SIF, reveal a notch affected micro-crack- and far field dominated macro-crack region. Using the corresponding crack growth driving force components, it seems obvious to adopt a two-stage crack growth model (Paragraph 4.2). Far field stress-, notch geometry-, elastoplasticity- as well as remote mechanical and thermal residual mean stress effects will be taken in to account.

Weld toe- and weld root notches are both principally V-shaped; difference is only a matter of notch angle. The latter is a special one in crack configuration, meaning weld root notch and crack (tip) share the same stress field singularity. The crack size/length a generally includes the notch size/length a_n , e.g. (Brandt, Lawrence and Sonsino, 2001; Lassen, Darcis and Recho, 2006; Fischer and Fricke, 2013), suggesting that no notch specific contribution is involved at all. The

conclusion that crack growth would dominate the – large/long crack region-II characteristic estimated – fatigue life in contrast to initiation that would be governing for weld toe notches (e.g. Ribeiro and De Jesus, 2011), is simply not true and even wrong. In fact, small/short crack growth data obtained using standard specimens including {SEN, DEN, CEN} in crack configuration – representing weld root notch geometries at the same time – shows anomalous behaviour. Some data available in literature will be reinvestigated for the alternating material zones in (aluminium) arc-welded joints (Fig. 4.2): weld material (WM) and heat affected zone (HAZ) containing respectively the weld root- and weld toe notch fatigue damage location, as well as base material (BM) for comparison (Paragraph 4.3).

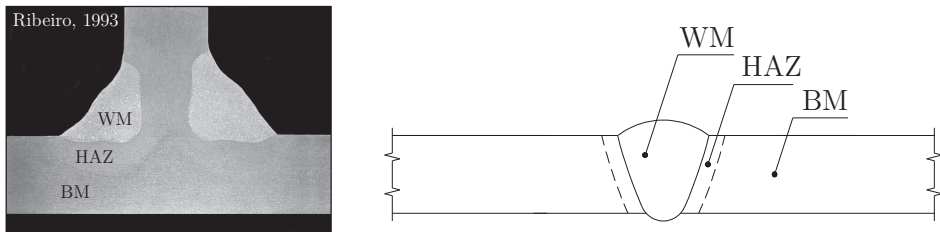


Figure 4.2: Alternating material zones for FP DS T-joint and FP SS butt joint.

Fatigue testing series have been developed to identify crack growth behaviour at weld toe notches in aluminium arc-welded joints (Paragraph 4.4), adopting a typical fillet weld DS T-joint geometry. Using digital image correlation (DIC), the required far field- and notch region parameters are obtained. Spatial displacement fields are estimated on a general kinematic basis using commercial DIC software (Istra4D, Dantec Dynamics). A posteriori, as a – mechanical – filtering process, the displacement fields are decomposed onto a selected kinematic basis, i.e. an Airy stress function. The displacement amplitudes, least squares (LS) solutions, present in a one-to-one correspondence the crack growth governing parameters: linear far field stress distribution, SIF and crack tip location. A sequence of images provides the temporal solution; crack growth data series.

4.2 Two-stage crack growth model

The well-known Paris equation (Eq. 4.1; Paris and Erdogan, 1963) is a large/long crack region-II characteristic of the sigmoidal shaped crack growth rate curve (Fig. 4.3). Assuming the crack tip wake field is predominantly elastic, the crack growth driving force $\Delta K_I(\Delta\sigma_s, Y_f, a)$ incorporates (only) the 1st order square root singular term including geometry and cyclic loading mode-I far field effects.

$$\log\left(\frac{da}{dn}\right) = \log(C) + m \cdot \log(\Delta K_I) \quad \forall \quad (\Delta K_{th} < \Delta K_I < K_C) \quad (4.1)$$

with

$$\begin{aligned}\Delta K_I &= \Delta K_f \\ &= \Delta \sigma_s Y_f \sqrt{\pi a}\end{aligned}$$

However, crack nuclei (flaws) or defects – either a result of crack initiation or welding process induced and assumed to be physically small/short – in materials or structures (at a notch location), show different subcritical growth behaviour; ($\Delta K_I < K_C$). Depending on crack(tip) and/or notch stress distribution and magnitude including its degree of elastoplasticity, small/short cracks (initially) may tend to grow slower or faster and accelerate or decelerate respectively to the large/long crack growth characteristic, meaning similarity – the same crack growth rate (da/dn) for similar crack growth driving force ΔK_f – is violated and anomalous behaviour can be identified (Fig. 4.3).

To incorporate small/short crack growth behaviour at blunt notches ($\rho > 0$), K_I (Eq. 3.27) and ΔK_I have been modified (El Haddad, Smith and Topper, 1979; Liu and Mahadevan, 2009), introducing the SCF_t K_t and an effective crack size/length $a_e = (a_n + a_0 + a)$ to include respectively a notch-, material defect sensitivity- and real crack contribution:

$$\begin{aligned}\Delta K_I &= \Delta \sigma_s Y_f \cdot \\ &\sqrt{\pi \left(a_n \left[1 - \exp \left\{ - \left(\frac{a_0 + a}{a_n} \right) \left(\frac{K_t^2}{Y_f^2} - 1 \right) \right\} \right] + a_0 + a \right)}\end{aligned}\tag{4.2}$$

with the two extremes

$$\Delta K_I = \Delta \sigma_s K_t Y_f \sqrt{\pi(a_0 + a)} \quad \text{for } (a/a_n) \rightarrow 0$$

$$\Delta K_I = \Delta \sigma_s Y_f \sqrt{\pi(a_n + a_0 + a)} \quad \text{for } (a/a_n) \rightarrow \infty$$

Both crack(tip) and notch are supposed to behave predominantly linear elastic. For $(a/a_n) \rightarrow 0$ and decreasing a , the effective crack size/length becomes even fictitious: ($a_e \rightarrow a_0$). If at the same time the remote mechanical loading is reduced up to plane geometry fatigue endurance limit level, ($\Delta \sigma_s \rightarrow \Delta \sigma_0$), the crack growth driving force turns into the structural threshold, a lower bound and region-I parameter (Paragraph 2.11): $\Delta K_I \rightarrow K_t \Delta K_{I,th} = \Delta \sigma_0 K_t Y_f \sqrt{\pi a_0}$. Obviously, small/short crack growth behaviour observed at notches may be monotonically increasing similar to a large/long crack in region-I, although beyond the material threshold ΔK_{th} (Fig. 4.3); a region-II anomaly. To take crack(tip) and notch plasticity into account, the J -integral and strain concentration factor (SCF_ε) K_ϵ have respectively been used (El Haddad, Dowling, Topper and Smith, 1980).

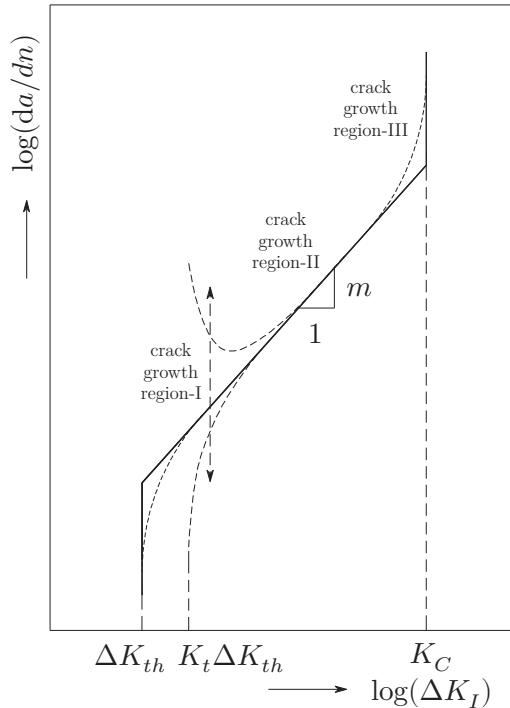


Figure 4.3: Anomalous small/short crack growth at notches.

Load ratio r_l , the 2nd parameter involved in defining cyclic far field stress, provides the tension-compression ratio affecting crack opening and closure. In case ($r_l > 0$), a crack may still be partially closed around the minimum of a far field stress cycle and a crack closure phenomenon has been introduced (Elber, 1971). The crack growth driving force is hypothesised to be not fully effective: $\Delta K_I \rightarrow \Delta K_{f,eff} = f\{\Delta\sigma_{eff}(\Delta\sigma_s, \sigma_y, a), Y_f, a\}$. The yield strength σ_y is incorporated, since reduced effectivity has been assumed to be a result of plastic wake field deformations at the crack tip. Over time, the load ratio r_l became explicitly involved, as well as work hardening- and structural response condition {plane stress, plane strain} parameters (Sehitoglu, Gall and García, 1996); an attempt to obtain a conclusive model. Rather than an effective crack size/length, crack closure; an effective SIF range $\Delta K_{f,eff}$, has been used to explain non-monotonic small/short crack growth behaviour (Fig. 4.3) at (blunt) notches as well, i.e. $\Delta\sigma_{eff}(K_t, \Delta\sigma_s, \sigma_y, a)$: the plastic wake field would not yet be fully developed (Schijve, 1988), meaning initially a lower level of crack closure and increased crack growth rate (da/dn). Anomalous growth is however identified well beyond the plastic zone; obviously at least another contributor is involved (Sehitoglu, Gall and García, 1996).

Physically small/short cracks, either in plane geometries or at notches (respectively materials or structures), show similar growth behaviour if along the (presumed) crack path the same stress distribution is involved, suggesting (non-monotonic region-II) anomalies to be a result of missing crack driving force

components rather than a matter of crack closure or even micro-structural effects (Krupp, 2007) and a total crack driving force $\Delta K_I = \Delta K_{I,tot}$ (Sadananda and Vasudevan, 1998) has been formulated. In addition to elastoplastic wake field size; the SCF_t or $SCF_\varepsilon \{K_t, K_\varepsilon\}$ in case of blunt notches, its shape is taken into account as well. For the remote mechanical cyclic loading part of weld notches, both the far field (equilibrium equivalent stress) and weld notch geometry (self-equilibrating stress) contributions have to be included: $\Delta K_{I,tot} = \Delta K_f(Y_f, a) + \Delta K_n(Y_n, a)$, even for a sharp weld root notch in crack configuration $\{\rho = 0, \alpha = \pi\}$, meaning notch and crack share the same local stress field. Note that $\Delta K_f(Y_f, a)$ includes the 1st order (crack) singular term only; $\Delta K_n(Y_n, a)$ incorporates the non-singular higher order (notch) terms as well. The crack growth similarity definition has been refined (Sadananda and Vasudevan, 1998): equal crack driving forces yield the same crack growth rates, provided the growth mechanism is the same.

Although the response condition in the structural field stress dominated zone 3 should be exclusively elastic, in the (weld) notch stress governing zone $\{1, 2\}$ however it may vary from predominantly elastic up to fully plastic. Inevitably, the crack growth mechanism will be affected and a dual slope formulation (Dong, Hong and Cao, 2003; Dong and Hong, 2004), the BSS two-stage crack growth model; a modified elastic far field stress governing Paris equation, has been introduced:

$$\log\left(\frac{da}{dn}\right) = \log(C) + 2\log(M_{kn}) + m\log(\Delta K_f) \quad (4.3)$$

In terms of crack size, growth rate behaviour from physically- to technically small/short is distinguished from technically small/short to large/long using respectively M_{kn} and ΔK_f . The notch magnification factor M_{kn} is defined as ratio of the SIF with- and without notch contribution because of the blend notch and structural field factor $Y_n Y_f^t$ (Paragraph 3.5) and includes the wake field shape along the assumed crack path; using the total stress (TS) concept, ($M_{kn} = Y_n$). Its exponent, an elastoplastic wake field size parameter, that proved to be an average value applicable to several data sets for different – base – materials, environments (temperature, water) and all types of crack geometry (single edge-, double edge- and centre cracks) is suggested to be notch plasticity related (Dong, Hong and Cao, 2003; Dong and Hong, 2004) since ($r_y \propto K_I^2$); actually a first order crack tip plasticity parameter, at least related to square root singular crack/notch behaviour. Focus is on non-monotonic small/short crack growth at sharp (weld) notches only, i.e. monotonic structural threshold affected behaviour is ignored.

Comparing Paris' large/long crack region-II characteristic (Eq. 4.1) to other formulations developed over time, a crack growth law similarity has been identified (Paris and Erdogan, 1963), i.e. $(da/dn) = C(\Delta\sigma)^m a^n$. For $n = (m/2)$, the quasi 2D infinite plane SIF solution for a remote mechanically loaded crack (Eq. 3.1) is obtained. Using dimensional analysis, it has been shown that the crack growth rate should be proportional to the crack size/length: $(da/dn) = C(\Delta\sigma)^m a$, as confirmed for several crack growth observations; $n = 1$ does the F&D model (Frost and Dugdale, 1958) appear. Since all formulations imply (partially) straight lines on

log-scale, however, an apparent agreement of different- or even contradictory laws can be identified for the same test data; the ‘correct’ one should correlate a wide range of test data rather than a single one (Paris and Erdogan, 1963).

The F&D model has particularly proved to be able to characterise growth of physically small cracks – at sharp notches in crack configuration – at low (linear elastic) stress intensity (Molent et al., 2006), i.e. is capable to collapse monotonically increasing crack growth (rates) in region-I and the lower part of region-II of the sigmoidal shaped curve into a single (near) straight line (Fig. 4.4).

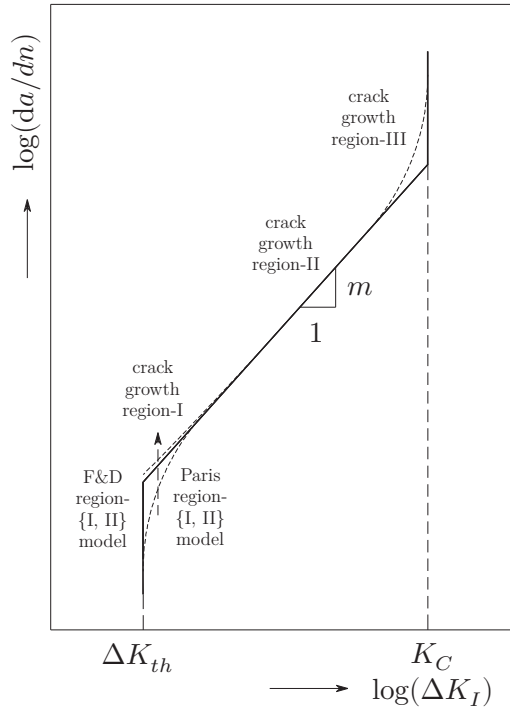


Figure 4.4: Near threshold monotonically increasing crack growth rate behaviour (Eq. 4.6) collapsed into a (near) straight line (Eq. 4.5).

Using dimensional analysis and a fractal geometry concept, the Paris law coefficient C should be crack size dependent according to a power function (Spagnoli, 2005), turning the Paris characteristic (Eq. 4.1) into:

$$\begin{aligned} \log\left(\frac{da}{dn}\right) &= \log\{C(a)\} + m\log(\Delta K_f) \\ &= \log(C) + n\log\{f(a)\} + m\log(\Delta K_f) \end{aligned} \quad (4.4)$$

The crack growth law similarity has been generalised at the same time; far field SIF contributions are included as well. One of the solutions is the generalised F&D model (Jones, Molent and Pitt, 2007a):

$$\begin{aligned} \log\left(\frac{da}{dn}\right) &= \log(C) + n\log\left(\frac{a}{a_0}\right) + m\log(\Delta K_f) \quad \forall (a_0 < a < a_C) \quad (4.5) \\ &= \log(C_0) + n\log(a) + m\log(\Delta K_f) \end{aligned}$$

with

$$n = \left(1 - \frac{m}{2}\right)$$

To eliminate the ΔK_f 1st order crack tip singularity, n includes $(-m/2)$. An explicit notch contribution is not taken into account; only the crack configuration has been investigated. The critical crack/defect size a_0 (only) became explicitly involved rather than the crack growth driving force material threshold $\Delta K_{th}(\sigma_0, Y_f, a_0)$. Note that crack growth similarity – the same crack growth rate for similar crack driving force – is violated in contrast to a modified Paris (Eq. 4.1) region- $\{I, II\}$ formulation:

$$\log\left(\frac{da}{dn}\right) = \log(C) + m\log(\Delta K_f - \Delta K_{th}) \quad \forall (\Delta K_{th} < \Delta K_f < K_C) \quad (4.6)$$

For $(m = 2)$, McEvily's model is obtained. The 1st order crack tip plasticity relation ($r_y \propto K_I^2$) and crack growth rate – crack size/length proportionality ($da/dn \propto a$) are identically satisfied at the same time; $m\log(\Delta K_f - \Delta K_{th})$ has replaced $\log(\Delta K_f^m - \Delta K_{th}^m)$ to achieve in average a better fit in the near threshold region for multiple data sets (McEvily, 1983); an engineering solution. Plasticity induced crack closure, i.e. $\{\Delta K_f = \Delta K_{f,eff}, \Delta K_{th} = \Delta K_{th,eff}\}$, has been introduced to deal with crack growth anomalies (McEvily and Minakawa, 1984).

Note that anomalous crack growth at notches (Fig. 4.3), often illustrated below the (large/long crack) threshold; e.g. (Ritchie et al., 1988; Janssen et al., 2002), is suggested to be a result of missing crack growth driving force (correction) components like K_t or Y_n . Threshold ΔK_{th} might be considered as a compressive driving force (Eq. 4.6) preventing for crack growth; a material parameter for both small/short and large/long cracks.

In order to be able to model generalised region- $\{I, II\}$ crack growth behaviour (both monotonically increasing and non-monotonic) at notches concerning structural field response (membrane and bending contribution for thin plates and shells), notch acuity (both sharp and blunt) as well as crack tip and/or notch stress condition (exclusively elastic up to fully plastic), all involved crack growth driving force components – stress distributions – along the (assumed) crack path should be taken into account, since crack tip wake field shape and size are assumed to be decisive.

The remote mechanical loading induced weld notch stress distributions (Chapter 2) have already been found important to define the weld notch SIF's (Chapter 3). Using the far field stress controlled equilibrium equivalent- and notch stress dominated self-equilibrating part $\{\sigma_f, \sigma_{se}\}$, the stress intensity far field- and notch factor $\{Y_f, Y_n\}$ are determined; linear elastic SIF weight functions incorporating

the stress wake field shape of cracks at weld toe- and weld root notches. Reflected in micro- and macro crack growth, Y_n should be governing for cracks increasing in size/length from physically- to technical small/short in the notch affected region; from technically small/short to large/long, the far field induced Y_f is assumed to be in charge. Correlating micro- and macro crack growth, a total stress (TS) concept based two-stage model satisfying similarity, $f(a) = Y_n$, a modified Paris equation, is proposed:

$$\begin{aligned} \log\left(\frac{da}{dn}\right) &= \log(C) + n\log\{f(a)\} + m\log(\Delta K_f) \\ &= \log(C) + n\log\{Y_n\} + m\log(\Delta K_f) \end{aligned} \quad (4.7)$$

with

$$n = \left(n_e - \frac{m}{2}\right)$$

Incorporating notch affected micro-crack growth using a two-stage model is not so much a peculiarity (Radaj, Sonsino and Fricke, 2006), as it is based on the reasonable hypothesis that all crack growth driving forces should be taken into account (Sadananda and Vasudevan, 1998), rather than the introduction of non-similarities (Jones, Chen and Pitt, 2007b) or dismissed as micro-structural aspects.

The scaling factor $\log(C)$ represents the material crack growth strength as usual. Assuming ρ^* and a_0 have the same physical meaning (Paragraph 2.11), the Ramberg-Osgood equation $\varepsilon = (\sigma/E) + (\sigma/K')^{1/n'}$ and Coffin-Manson-Basquin relation $(\Delta\varepsilon/2) = (\sigma'_f/E) \cdot (2N)^b + \varepsilon'_f(2N)^c$, respectively the intact geometry stabilised cyclic stress-strain- and fatigue resistance curve, can be used to prove $\log(C) = f(K', n', \sigma'_f, \varepsilon'_f, b, c)$; a true material parameter (Jones, Molent and Pitt, 2007a; Noroozi et al., 2005). The cyclic strength coefficient and work hardening exponent $\{K', n'\}$, fatigue strength- and ductility coefficients $\{\sigma'_f, \varepsilon'_f\}$ as well as fatigue strength and ductility exponents $\{b, c\}$ can be solved for using cyclic stress-strain- and life time data satisfying compatibility for the elastic and plastic parts (Nieslony et al., 2008). Cyclic stress intensity ΔK_f still controls the wake field size or magnitude $\Delta\sigma_s$ because of the involved equilibrium equivalent stress part. With respect to shape, ΔK_f incorporates the linear elastic (sharp) crack tip 1st order square root singular term as well as geometry and zone 3 cyclic loading mode-I far field stress effects governing in the macro-crack growth region. Slope m , a material parameter, characterises the corresponding crack growth mechanism.

The zone $\{1, 2\}$ governing self-equilibrating notch stress part dominates the wake field shape in the micro-crack growth region, meaning for Y_n the ΔK_f included square root singular crack tip behaviour should be subtracted: $n = (n_e - m/2)$ for $(\lambda_1 - 1) = (-1/2)$. The introduced notch elastoplasticity coefficient n_e should satisfy the criterion ($n_e \geq 1.0$). In case the notch stress distribution is elastic, ($n_e = 1.0$); if plasticity becomes involved, ($n_e > 1.0$). Like argued for cracks (Irwin, 1957; Janssen et al., 2002), it is assumed that because of plasticity the notch

behaves as if it were larger/longer than its actual physical size (Guo, Wang and Rose, 1998), meaning the effective notch size/length includes a plasticity induced fictitious component: $a_{ne} = a_n + a_{nf}$ and $Y_n = \sum C_i (a/t_p)^{\lambda_i - 1}$ turns into $Y_{ne} = \sum C_i^{n_i} (a/t_p)^{\lambda_i - 1}$. For unknown a_{ne} , the effective notch factor will be approximated using: $Y_{ne} \approx \{\sum C_i (a/t_p)^{\lambda_i - 1}\}^{n_e} = Y_n^{n_e}$. Although the order of singularity, the zone 2 stress gradient, should decrease for increasing level of plasticity (Lazzarin, Zambardi and Livieri, 2001; Filippi, Ciavarella and Lazzarin, 2002), using the elastic contribution only it will increase since a_{ne} increases.

For a positive elastoplasticity coefficient ($n > 0$) a non-monotonic crack growth rate can be identified; a monotonically increasing one if ($n \leq 0$), i.e. near (structural) threshold behaviour is observed for ($n_e < m/2$) involving two material parameters. Small cracks, either at notches or in plane geometries, show even similar growth behaviour for respectively the same notch and crack tip elastoplasticity (Li and Zhang, 2001); $Y_n = Y_c$ using the asymptotic stress distribution for a notch in crack configuration and includes the higher-order terms as well.

To achieve a crack growth rate proportional to crack size/length ($da/dn \propto a$), notch elastoplasticity coefficient $n_e = (-2 + 3m/2)$. In case ($m = 3$), a curve fitted value for different materials (Jones et al., 2007a; 2007b), still the exclusively elastic notch or crack tip distribution – a (generalised) F&D model assumption – is involved since $n = 1$.

In comparison to the BSS two-stage crack growth model, Y_n and M_{kn} serve the same purpose although obtained in different ways (Paragraph 3.4). Rather than a constant plasticity related coefficient ($n = 2$) and focus on non-monotonic crack growth at notches at the same time, crack growth behaviour may change from predominantly non-monotonic in the MCF- to monotonically increasing in the (near threshold) HCF region in terms of fatigue life time; n should be variable.

The large/long crack growth region- $\{I, II, III\}$ definitions do not apply one-to-one to notch emanated cracks in welded joints. Notch affected micro-crack growth can be identified as near structural threshold region-I (monotonically increasing) as well as region-II (non-monotonic) behaviour. Anyhow, far field dominated macro-crack growth is a region-II phenomenon. If a through-thickness crack – a design and detectable repair criterion – has been developed, it is still assumed to be stable and will continue to propagate either along or perpendicular to the weld seam. In parallel systems like hull structure stiffened panels, a load shedding mechanism – stress redistribution – may become involved (Xu and Bea, 1997) because of local stiffness loss. At some (region-III) point, the crack will become unstable and may cause fatigue induced failure. In terms of fatigue life time, the number of cycles in region-III is limited.

4.2.1 Far field stress

Hull structures are predominantly orthotropic stiffened (curved) panel assemblies consisting of (thin) plates and shells. The remote mechanical loading of arc-welded joints, the linear elastic far field stress, mainly consists of a membrane and bending stress component defining the zone 3 far field stress gradient; the structural

bending stress ratio r_s varies in between the limits ($-\infty < r_s \leq 1$). Similar to the weld notch stress distributions (Paragraph 2.6 & 2.7) and -stress intensity factors (Paragraph 3.5 & 3.6), differences in terms of crack growth rate $(da/dn) = f[\Delta K_f \{Y_f(r_s)\}]$ as well as fatigue life time N are expected to be at maximum between a pure bending ($r_s = 1$)- and combined membrane-bending case ($r_s \rightarrow -\infty$); a principle matter of notch stress distribution (non-)symmetry with respect to half the plate thickness ($t_p/2$), a {SEN, CN} or DEN geometry (Fig. 3.3, 3.5 and 3.6).

Concerning macro-crack growth in non-symmetric {SEN, CN} geometries, far field bending remains bending in the cross-section along the (assumed) crack path for increasing macro-crack size/length. Far field membrane loading on the other hand introduces an additional (dominant) bending term, meaning $Y_f(r_s)$ increases for ($r_s|_{=1} \rightarrow -\infty$) as well as $(da/dn) = f[\Delta K_f \{Y_f(r_s)\}]$ along the crack growth rate curve in region-II (Fig. 3.10 to 3.13 and Fig. 4.5); the material macro-crack growth strength and mechanism parameters, i.e. scaling factor $\log(C)$ and slope m , do not change. Since in case of symmetry, a DEN geometry, no membrane loading induced bending term is involved, $Y_f(r_s)$ and $(da/dn) = f[\Delta K_f \{Y_f(r_s)\}]$ shows in fact the opposite behaviour (Fig. 3.23 to 3.26 and Fig. 4.5), i.e. decreasing for ($r_s|_{=1} \rightarrow -\infty$).

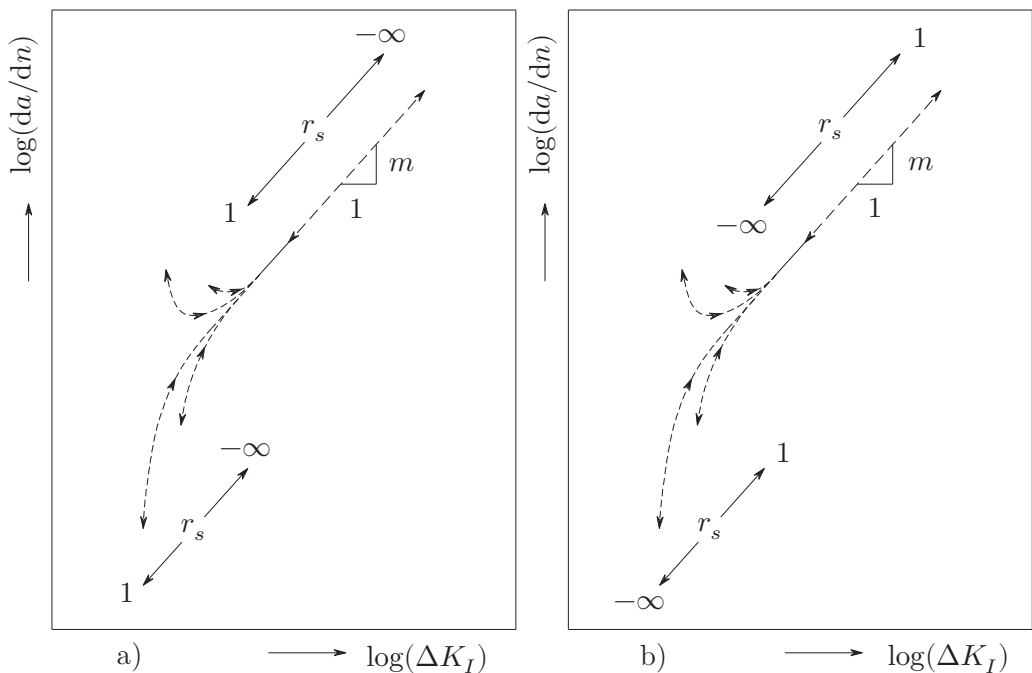


Figure 4.5: Far field stress effects in micro- and macro-crack growth region in case of a) non-symmetry and b) symmetry.

Micro-crack growth however is affected at the same time (Fig. 4.5). The $Y_n Y_f$ apex, dividing the notch affected micro- and far field dominated macro crack region, shifts for $(r_s|_{=1} \rightarrow -\infty)$ to the left in case of non-symmetry (Fig. 3.10 to 3.13), decreasing the notch affected zone size and reducing the micro-crack growth contribution – material parameter n remains unaffected. The apex shift is to the right for $(r_s|_{=1} \rightarrow -\infty)$ if symmetry is involved (Fig. 3.23 to 3.26). Increasing the notch affected zone size ensures more pronounced micro-crack growth rates.

Comparing one load case to another for either non-symmetry or symmetry (Fig. 4.5a or 4.5b), obviously, straightforward conclusions in terms of fatigue life time are inappropriate. Both micro- and macro crack growth are affected and (da/dn) consequences are different. Generally speaking, for any (non-)symmetric geometry N decreases for $\{\sigma_s, r_s|_{=1} \rightarrow -\infty\}$, despite the crack growth behaviour and naturally expected considering the far field stress gradient. On the other hand, because of the opposite crack growth behaviour, $(N|r_s = 1)$ for a {SEN, CN} geometry (slightly) exceeds its DEN equivalent; the DEN value is (somewhat) larger in comparison to the {SEN, CN} one for $(N|r_s \rightarrow -\infty)$, provided the non-symmetric and symmetric geometries are similar.

4.2.2 Notch geometry

The way key parameters like notch angle and -radius $\{2\alpha, \rho\}$ influence the (micro-) crack growth rate (da/dn) , is principally like the self-equilibrating stress part $\sigma_{se(r)}$ (Paragraph 2.8) and notch factor Y_n (Paragraph 3.7) are affected (Fig. 4.6).

Starting in half-plane configuration ($2\alpha = \pi$), any crack growth in plane material is basically identified as a long-crack region-II characteristic. For increasing notch angle 2α , micro-crack growth behaviour becomes more pronounced up to $(2\alpha \approx 1.22\pi)$; close to an ideally assumed 45 [deg] fillet weld toe angle configuration. Continuing the 2α increase up to $(2\alpha \approx 1.43\pi)$; the eigenvalues $\{\lambda_s, \lambda_a\}$ become tangent $\sin(\lambda 2\alpha)$ solutions (Fig. 2.8), the notch induced (da/dn) contribution decreases. For a persistent 2α increase up to the crack configuration $(2\alpha = 2\pi)$, micro-crack growth becomes pronounced again.

The notch angle effect on monotonically increasing and non-monotonic (da/dn) is the opposite. The former shows e.g. for increasing notch angle $(\pi < 2\alpha < 1.22\pi)$ initially smaller micro-crack growth rates to be accelerated in time to macro-crack growth level; the latter larger (da/dn) to be decelerated. The same type of behaviour can be identified for $(1.43\pi < 2\alpha < 2\pi)$; the other way around if $(1.22\pi < 2\alpha < 1.43\pi)$, a principal zone 2 stress gradient effect.

In terms of fatigue life time N , assuming crack growth is governing and monotonically increasing, weld toe notches in approximately ideal fillet angle- and weld root notches in crack configuration show the best results. The undulating N estimate for increasing notch angle is however in contradiction – a phenomenon that applies only to 2α – to crack initiation based values; i.e. for increasing notch angle $(\pi < 2\alpha < 0.75\pi)$, the SCF or notch factor $K_f(K_t)$, a(n effective) zone 1 peak stress parameter, monotonically increases for increasing 2α . Quite interesting to

note is that for non-monotonic (residual stress amplified) tensile notch stress induced crack growth both configurations are actually the worst.

To be able to deal with sharp cracks at both sharp and blunt notches, the TS concept based two-stage crack growth model (Eq. 4.7) includes the notch radius ρ as it affects the zone 2 stress gradient and controls the zone 1 peak stress. For increasing ρ , the peak value as well as stress gradient reduce in the notch affected region, meaning the level of acceleration or deceleration for respectively monotonically increasing- and non-monotonic crack growth rates reduces (Fig. 4.6); i.e. micro-crack growth behaviour becomes less pronounced.

Like for crack initiation dominated fatigue, the life time estimate N for non-monotonic crack growth governing fatigue increases for increasing ρ . In the monotonic case N reduces, since the self-equilibrating stress part – compressive in the notch affected region either thermal residual or structural threshold induced since the far field induced component must be tensile by definition – preventing for crack growth, i.e. zone 1 peak stress and zone 2 stress gradient, should be as large as possible, meaning for increased ρ a reduced fatigue life time estimate.

Note that using a bi-linearised (weld) notch stress distribution includes ρ effects implicitly, since its peak value will be finite by definition (Paragraph 2.6 and 2.7). However, the way M_{kn} has been derived (Paragraph 3.5) ensures $\{M_{kn} | (a/t_p \rightarrow 0) \rightarrow \infty\}$, meaning the BSS two-stage crack growth model (Eq. 4.3) cannot take the actual ρ contribution into account.

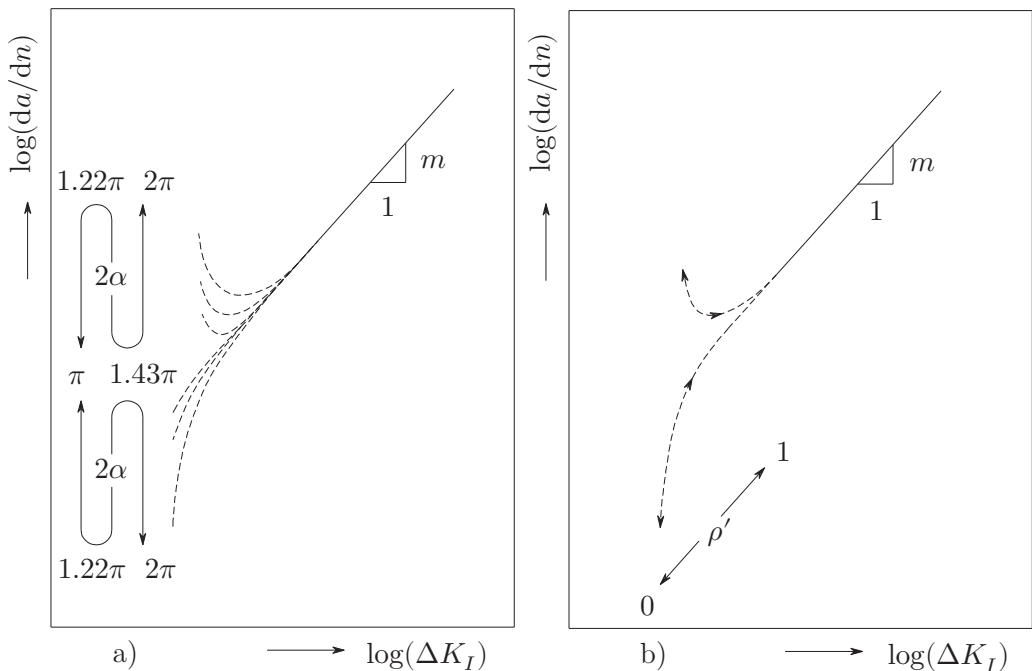


Figure 4.6: Notch geometry effects in the micro-crack growth region for varying a) notch angle- and b) radius; $\rho' = (\rho/l)$ with l a characteristic length.

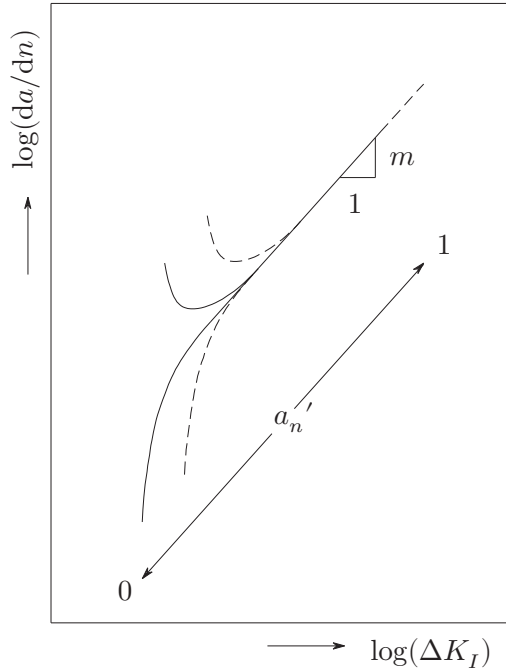


Figure 4.7: Crack growth effects for varying notch length;
 $a_n' = (a_n/l)$ with l a characteristic length.

The notch size/length a_n , a (weld) root notch parameter, affects both micro- and macro crack growth because of σ_{sr} amplitude- and zone $\{2, 3\}$ $\sigma_{n(r)}$ gradient changes; $(da/dn) = f\{Y_f(Y_{fw}, a_n + a), Y_n(Y_{nr}, Y_{nl}, a_n + a)\}$. The curve principally shifts along the region-II long crack growth characteristic (Fig. 4.7) since the amplitude contribution dominates.

4.2.3 Elastoplasticity

For $\{MCF, HCF\}$, the far field stress condition is assumed to be predominantly elastic. In the notch affected region however the zone 1 peak stress and zone 2 stress gradient may vary from exclusively elastic up to fully plastic, influencing micro-crack growth (Fig. 4.8). Whether (da/dn) is either monotonically increasing or non-monotonic depends on the macro-crack growth slope as well; $n(n_e, m)$. Starting at the notch elastoplasticity coefficient lower bound ($n_e = 1$) – the elastic case – and a common (average) slope value ($m = 3$), it is monotonically increasing. For increasing n_e , plasticity becomes involved and at some point the crack growth rate (da/dn) becomes non-monotonic. Note this explanation is in contrast to the one based on crack closure: the plastic wake field would not yet be fully developed, referring to a lack. Continuing the n_e increase means (da/dn) becomes more pronounced and acceleration increases. The SIF related crack correction ($-m/2$) remains linear elastic by definition.

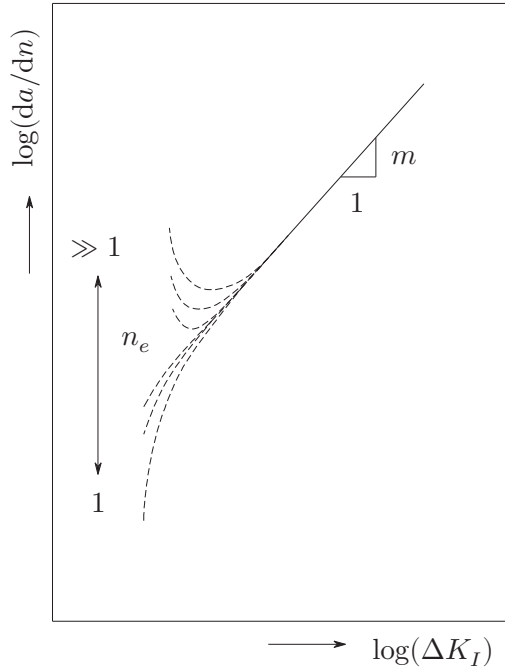


Figure 4.8: Elastoplasticity effects in the micro-crack growth region.

Elastoplastic notch crack behaviour is highly structural response condition dependent. It is plane stress at the (notch) surface, the crack initiation- or physically small/short crack location, meaning a reduced yield stress σ_y and increased (cyclic) plastic zone size r_p in comparison to the σ_y bulk value for a plane strain condition that becomes governing for increasing crack size/length a . The involved transition explains why micro-crack growth behaviour is more pronounced in thin plate specimen (Newman et al., 2000; Li and Zhang, 2001) and complicates the r_p calculation. In case ($\rho = 0$), using the mode-I NSIF (Eq. 3.20) a 1st order r_p estimate for V-shaped notches as identified at weld toe and weld root denote:

$$r_p = \left\{ \frac{1}{(2\pi)^{1-\lambda_s}} \frac{\Delta K_I^N}{C_p 2\sigma_y} \right\}^{\frac{1}{1-\lambda_s}} \quad (4.8)$$

with

$$\begin{aligned} \Delta K_I^N &= (2\pi)^{1-\lambda_s} \lim_{r \rightarrow 0^+} \{r^{1-\lambda_s} \sigma_{\theta\theta}(r, \theta = 0)\} \\ &= (2\pi)^{1-\lambda_s} \Delta \sigma_s t_p^{1-\lambda_s} \mu_s \lambda_s (\lambda_s + 1) (1 - \chi_s) \end{aligned}$$

and

$$r_p = \left\{ \frac{1}{(2\pi)^{1-\lambda_1} C_p 2\sigma_y} \Delta K_I^{Nr} \right\}^{\frac{1}{1-\lambda_1}} \quad (4.9)$$

with

$$\begin{aligned} \Delta K_I^{Nr} &= (2\pi)^{1-\lambda_1} \lim_{r \rightarrow 0^+} \{r^{1-\lambda_1} \sigma_{\theta\theta}(r, \theta = 0)\} \\ &= (2\pi)^{1-\lambda_1} \Delta\sigma_{sr} (t_p')^{1-\lambda_s} \mu_1 \lambda_1 (\lambda_1 + 1) (1 - \chi_1) \end{aligned}$$

In case of crack tip plasticity: $K_I^{Nr} = K_I$. Similar formulations can be obtained for ($\rho > 0$) using the corresponding notch stress distribution formulations (Eq. 2.47, 2.49 and 2.50). The plastic constraint factor for plane stress denotes: $C_p = 1$. Using Von Mises' yield criterion and assuming the Poisson ratio $\nu = (1/3)$, in plane strain $C_p = 3$ for a notch in crack configuration ($\lambda_1 = 1/2$), meaning r_p is 9 times smaller in comparison to the plane stress value. In thin plates and shells it is considered to be a lower bound and an intermediate plane strain value ($C_p = \sqrt{3}$) has been proposed (Irwin, 1957).

Note that notch radius ρ and elastoplasticity coefficient n_e are pushing the same button: for increasing ρ plasticity reduces and micro-crack growth becomes less pronounced.

4.2.4 Mean stress

Of all factors that may influence fatigue, mean stress has proved to be an important one (Maddox, 1975; Obrtlík, Man and Polák, 2004), although it is (still) rarely reported up to what extent micro- as well as macro crack growth at notches – in particular in the context of arc-welded joints – is affected. All contributions including the cyclic remote mechanical- and quasi-constant thermal residual stress part have to be taken into account.

Far field contribution

A remote mechanical loading induced far field structural stress cycle (Fig. 4.9) is unambiguously defined using two independent parameters, e.g. $\{\Delta\sigma_s, \sigma_{s,max}\}$, suggesting crack growth involves 2 driving force components as well (Walker, 1970; Sadananda and Vasudevan, 1998): $\Delta K_I(\Delta\sigma_s)$ and $K_{I,max}(\sigma_{s,max})$. An effective one – different from the original- and modified plasticity induced crack closure formulation, e.g. (Donald and Paris, 1999; Gavras, Lados and Donald, 2013) – can be determined taking the log-relative contributions into account:

$$\Delta K_{I,eff} = (\Delta K_I)^p (K_{I,max})^{1-p} \quad \forall \quad (0 \leq p \leq 1) \quad (4.10)$$

Assuming m to be $\{\Delta\sigma_s, \sigma_{s,max}\}$ invariant, mean stress independent, Paris' far field geometry and loading dependent region-II characteristic (Eq. 4.1) becomes:

$$\log\left(\frac{da}{dn}\right) = \log(C) + m\log\{(\Delta K_f^-)^p (K_{f,max})^{1-p}\} \quad (4.11)$$

Crack growth similarity requires macro-cracks to grow at the same rate for similar $\{\Delta K_f, K_{f,max}\}$ and material; ($K_{f,max} > 0$) is mandatory for crack growth anyway. Hypothesising at the same time that the negative part of a far field stress cycle (Fig 4.9); in fact ΔK_f^- (Kujawski, 2001), does not contribute:

$$\log\left(\frac{da}{dn}\right) = \log(C) + m\log\{(\Delta K_f^+)^p (K_{f,max})^{1-p}\} \quad (4.12)$$

The involved effective structural stress range $\Delta\sigma_{s,eff}$ can be rewritten in terms of $\Delta\sigma_s = (\sigma_{s,max} - \sigma_{s,min})$ and the remote load ratio $r_l = (\sigma_{s,min}/\sigma_{s,max})$; a far field mean stress factor defining the cycle degree of symmetry:

$$\begin{aligned} \Delta\sigma_{s,eff} &= (\Delta\sigma_s^+)^p (\sigma_{s,max})^{1-p} = \frac{\Delta\sigma_s}{(1-r_l)^{1-p}} \quad \forall \quad (r_l \geq 0) \\ \Delta\sigma_{s,eff} &= (\Delta\sigma_s^+)^p (\sigma_{s,max})^{1-p} = \frac{\Delta\sigma_s}{(1-r_l)} \quad \forall \quad (r_l < 0) \end{aligned} \quad (4.13)$$

As a matter of fact, on log-scale $K_{I,eff}(\Delta\sigma_s, r_l)$ simply shifts the crack growth relationship. Introducing a load ratio coefficient γ :

$$\begin{aligned} \log\left(\frac{da}{dn}\right) &= \log(C) + m\log\left\{\frac{\Delta K_f}{(1-r_l)^{1-\gamma}}\right\} \\ &= \log(C) + m\log(\Delta K_f) - m(1-\gamma)\log(1-r_l) \end{aligned} \quad (4.14)$$

with

$$\begin{aligned} \gamma &= p \quad \forall \quad (r_l \geq 0) \\ \gamma &= 0 \quad \forall \quad (r_l < 0) \end{aligned}$$

Although two crack driving forces are involved, $K_{f,max}$ is in control for a negative load ratio r_l since ($p = 0$); for increasing positive r_l values ΔK_f becomes governing. A geometric mean for ($r_l \geq 0$) can be adopted (Smith, Watson and Topper, 1970), i.e. the load ratio coefficient $\gamma = p = 0.5$ [-]; effects of (cyclic) material properties including fracture toughness (ductile; ($\gamma > 0.5$) meaning ΔK_f dominates like for aluminium 5xxx and 6xxx alloys, or brittle; ($\gamma < 0.5$) for governing $K_{f,max}$) and environment are disregarded – whether negligible or not.

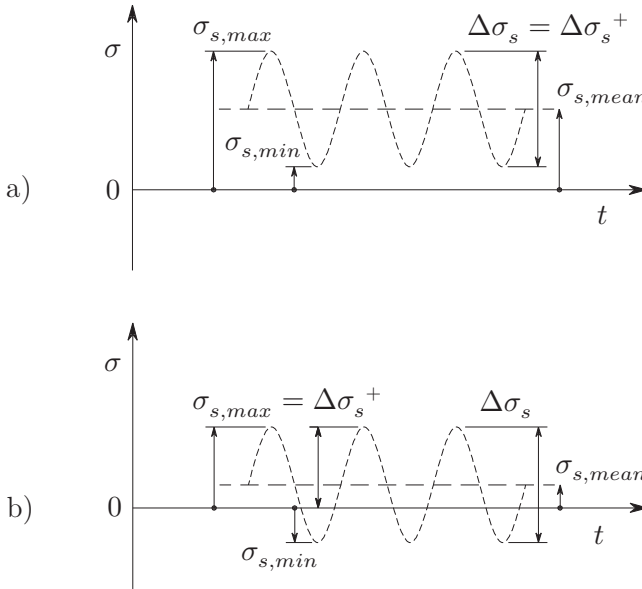


Figure 4.9: Structural stress cyclic parameters in case of respectively a) a positive- and b) negative load ratio r_l .

The generalised non-similitude F&D model (Eq. 4.5) has been modified as well to include the effective crack growth driving force $\Delta K_{I,eff}$, (Jones, Molent and Pitt, 2007a; Jones and Molent, 2010):

$$\log\left(\frac{da}{dn}\right) = \log(C) + \left(1 - \frac{m}{2}\right) \log(a) + m \log\{(\Delta K_f)^p (K_{f,max})^{1-p}\} \quad (4.15)$$

Although dedicated to model growth of physically small/short cracks, $\Delta K_{I,eff} = \Delta K_{f,eff}$ since the crack size/length induced non-similitude imposes the effective crack growth driving force principally to be considered as a far field restricted large/long growth contribution.

Weld notch contribution

In the notch affected region however, σ_{se} causes an increased local mean stress. Though, it is still remote loading induced meaning the corresponding local load ratio, $(K_t \sigma_{s,min}) / (K_t \sigma_{s,max})$ for a blunt notch, equals the equilibrium equivalent stress related r_l . Given a small/short crack, the notch affected mean stress converges for increasing crack size/length to the far field value (Fig. 4.10) as naturally included using M_{kn} in the BSS- or Y_n in the TS two-stage crack growth model (Eq. 4.3 and 4.7). Taking both crack growth driving forces $\{\Delta K_I, K_{I,max}\}$ into account, the BSS formulation (Kim and Dong et al., 2006) has become:

$$\log\left(\frac{da}{dn}\right) = \log(C) + 2\log\left\{\frac{M_{kn}}{(1-r_l)^{1-\gamma}}\right\} + m\log(\Delta K_f) \quad (4.16)$$

Coefficient $\gamma = 0.5$ for $r_l \geq 0$; $\gamma = 0$ for $r_l < 0$. At first glance the remote loading induced mean stress, i.e. $K_{I,max}(\Delta\sigma_s, r_l)$, might seem to contribute only to micro-crack growth in the notch affected region; macro-crack growth is however influenced as well. Most important is the modelling assumption that mean stress is (notch) plasticity related. The far field stress should be elastic by definition, suggesting to use $K_{f,eff}$ (Eq. 4.12). For the two-stage crack growth model (Eq. 4.7), $n_e(\sigma_{s,max}, \sigma_y)$ is principally r_l independent although some correlation will be involved because of the σ_f elasticity requirement. Both the $(\Delta\sigma_s, r_l)$ micro-crack (implicitly)- as well as macro-crack growth contribution (explicitly) are proposed to be incorporated:

$$\begin{aligned} \log\left(\frac{da}{dn}\right) &= \log(C) + n \log(Y_n) + m\log\left\{\frac{\Delta K_f}{(1-r_l)^{1-\gamma}}\right\} \\ &= \log(C) + n_e \log(Y_n) + m\log\left\{\frac{\Delta K_f}{(Y_n)^{\frac{1}{2}}(1-r_l)^{1-\gamma}}\right\} \end{aligned} \quad (4.17)$$

For ($n_e = 1$), notch and/or crack tip behaviour is elastic and (structural) threshold induced anomalous crack growth, monotonically increasing, is principally r_l invariant.

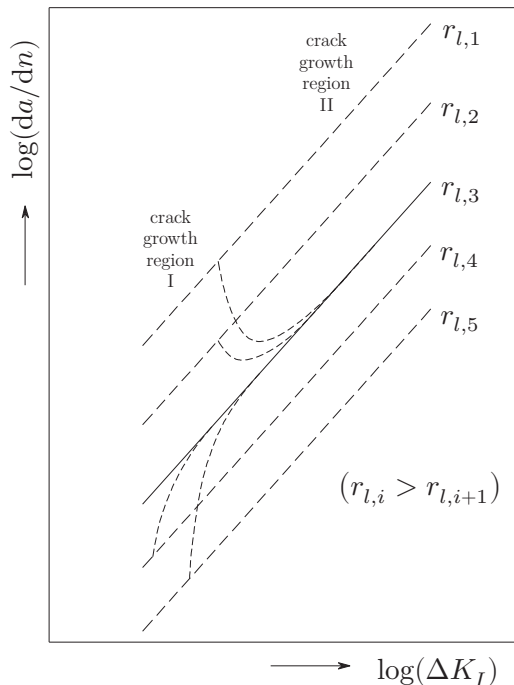


Figure 4.10: Mean stress effects in the micro-crack growth region.

To achieve notch and/or crack tip elastoplasticity ($n_e > 1$) for decreasing r_l , the stress range $\Delta\sigma_s$ should increase, implying the local mean stress increases as well. For increasing crack size/length, the mean stress reduces to the far field value, meaning plasticity induced anomalous crack growth, i.e. non-monotonic behaviour, becomes more pronounced for decreasing r_l and is predominantly identified for small (impact related) positive and negative values (Fig. 4.10) since ($\sigma_s < \sigma_y$).

Residual stress

A total weld notch stress distribution σ_n^t consists of a (cyclic) remote mechanical- and thermal loading induced (quasi-constant) residual part $\{\sigma_n, \sigma_n^r\}$ showing stress field similarity (Paragraph 2.11).

Using load-displacement records (Lados, Apelian and Donald, 2007; Gavras, Lados and Donald, 2013), the RSIF affected $K_{I,max}(K_I^r)$ can be obtained in a similar way as the plasticity induced crack closure related effective crack growth driving force component $\Delta K_{I,eff}$ and the total effective one becomes $\Delta K_{I,tot,eff} = (\Delta K_{I,eff})^p (K_{I,max})^{1-p}$.

To include the displacement (constraints) controlled residual stress contribution exploring a residual load ratio, it should be crack size/length dependent because of the involved σ_n^r redistribution: $r_l^r(a/t_p)$. Using one parameter incorporating both the remote mechanical- and thermal residual mean stress component, the load ratio may be defined as $r_l(a/t_p) = (K_{I,min} + K_I^r)/(K_{I,max} + K_I^r)$ like included in the BSS two-stage crack growth model (Dong, 2008):

$$\log\left(\frac{da}{dn}\right) = \log(C) + 2\log(M_{kn}) + m\log\left[\frac{\Delta K_f}{\{1 - r_l(a/t_p)\}^{1-\gamma}}\right] \quad (4.18)$$

For ($K_I^r = 0$), only the remote mechanical mean stress is considered. In comparison to the preceding formulation (Eq. 4.16), mean stress has changed over time to a pure macro-crack growth effect.

In case the residual stress distribution is tensile in the notch affected region, $r_l(a/t_p)$ turns out to be approximately constant and may be included in the crack growth strength coefficient $\log(C)$; if compressive, $r_l(a/t_p)$ rapidly decreases to a significant negative value in the micro-crack region, will gradually increase for increasing crack size/length and converges up to a constant in the macro-crack region (Dong, 2008). Taking a closer look to the compressive case, in terms of load ratio the obviously lower local residual stress (at yield magnitude) dominated value naturally converges for increasing crack size/length to the higher far field governing one; the higher the residual compressive stress in the notch affected region or the higher the remote mechanical r_l value, the more pronounced the monotonically increasing anomalous behaviour will be (Fig. 4.10). In fact, monotonic crack growth rate behaviour as ignored in the cyclic remote mechanical loading based BSS two-stage model (Eq. 4.16), is included using $r_l(a/t_p)$ as far as residual stress is concerned.

The TS concept crack growth formulation (Eq. 4.7 and 4.17) already contains n to include cyclic remote mechanical loading induced non-monotonic and monotonically increasing (da/dn). Since σ_n^r is estimated at or even beyond yield magnitude – either in tension or compression – in the notch affected region, the (elastic) remote mechanical r_l contribution to the total stress intensity is relatively small; i.e. assumed to negligible. Crack size dependent tensile residual stress in the notch affected micro-crack growth region would simply increase the elastoplasticity coefficient: $n_e \rightarrow n_e'$. To allow for a governing compressive crack size dependent one, a cyclic elastoplasticity coefficient ($n_e' \leq 1$) will be accepted as well. Anomalous behaviour will be pronounced anyway; Y_n remains the same because of the weld notch remote mechanical- and thermal residual stress distribution similarity.

Quasi-constant residual mean stress effects in the macro-crack growth region either tensile or compression – if any, depends on displacement constraint, i.e. “equilibrium” or “self-equilibrating” type (Paragraph 2.10 & 3.9) – will be included in the crack growth strength coefficient, $\log(C) \rightarrow \log(C')$, since quantitative values are unknown (from design perspective) and the TS concept two-stage crack growth model denotes:

$$\begin{aligned} \log\left(\frac{da}{dn}\right) &= \log(C') + n' \log(Y_n) + m \log\left\{\frac{\Delta K_f}{(1-r_l)^{1-\gamma}}\right\} \\ &= \log(C') + n_e' \log(Y_n) + m \log\left\{\frac{\Delta K_f}{(Y_n)^{\frac{1}{2}}(1-r_l)^{1-\gamma}}\right\} \end{aligned} \quad (4.19)$$

Formulations (Eq. 4.17 and 4.19) are similar and represent respectively cases with- and without welding induced residual stress effects, i.e. in terms of arc-welded joint material zones respectively a BM and {WM, HAZ} dedicated model to be used for weld toe- and weld root notches.

To achieve crack growth involving 2 driving force components $\{\Delta K_I(\Delta\sigma_s), K_{I,max}(\sigma_{s,max})\}$ or $\Delta K_I(\Delta\sigma_s, r_l)$ may suggest at the same time existence of 2 thresholds $\{\Delta K_{I,th}, K_{I,max,th}\}$; violating only 1 value would already be sufficient (Sadananda, 1998 and 2004). Generally speaking, the cyclic one $\Delta K_{I,th}$ is considered to be small, in particular for aluminium as applied in high-speed craft, meaning $K_{I,max,th}$ is assumed to decisive. However, since $K_{I,max}$ includes a remote mechanical- and (predominantly tensile) thermal residual contribution, aluminium arc-welded joint threshold values would be violated in almost any sea state. Though, question is still whether threshold values truly exist as a constant(!), at least for metallic materials (Bathias et al., 2001; Pyttel et al., 2011). Well-established crack growth threshold $\{\Delta K_{I,th}, K_{I,max,th}\}$ - as well as (random) fatigue limit $\Delta\sigma(N \rightarrow \infty)$ values in the HCF region seem to be in contrast to experimental data and is considered to be an important reason to prevent for formulations like (Eq. 4.6), including the (extended) McEvily model (Wang, Cui, Wu, Wang and Huang, 2008), explicitly involving a threshold parameter as material constant.

4.3 Crack growth at (weld) root notches

Standard specimens containing notches in crack configuration to emanate cracks and acquire growth data, principally represent arc-welded root notch geometries at the same time; specimen width b_p turns into plate thickness t_p (Fig. 3.3, 3.5 and 3.6). Data available in literature will be reinvestigated for small/short crack related anomalies, limited to far field stress constant amplitude (CA) series; i.e. the crack growth driving force ΔK_I will increase for increasing crack length a and the remote load ratio r_l remains fixed. The material focus is on {WM, HAZ, BM} aluminium 5xxx (plates) and 6xxx (extrusions) as typically applied in high-speed craft, although some crack growth data in aluminium 7xxx and steel will be used as well to demonstrate TS two-stage crack growth model features. For the different type of notches, {SEN, DEN, CN} related to (non-)symmetry conditions (Paragraph 3.3), mean stress-, elastoplasticity- and notch geometry $\{\rho|2\alpha = 2\pi\}$ effects will be examined; far field stress is limited to the membrane case.

4.3.1 Single edge notch

Employing aluminium Al5083-H321 FP DS butt joints, SEN crack growth data (Fig. 4.11) has been obtained using multiple specimens – explaining the scatter band – for BM and HAZ in L-T configuration (crack path normal to grain rolling direction). The MIG welding procedure has been applied using filler wire 5356 without pre-heating; one pass on each side. The weld reinforcement is not removed and may introduce (limited, ignored) 3D effects. Constant amplitude tests at load ratio $r_l = 0.1$ [-] and frequency $f = 10$ [Hz] have been conducted in air (Shankar and Wu, 2002).

The crack growth rates (da/dn) are monotonically increasing beyond the material threshold, i.e. $\Delta K_{th} \approx 60$ [MPa $\sqrt{\text{mm}}$] for BM, suggesting notch (structural threshold) related anomalies are involved. Rewriting the two-stage crack growth model (Eq. 4.7) to a multi-log-linear formulation (Eq. 4.20), regression analysis has been used to obtain the parameter LS estimates $\{\log(C), m, n_{e,i}\}$.

$$\log\left(\frac{da}{dn}\right) = \log(C) + m \log\left\{\frac{\Delta K_f}{(Y_n)^{\frac{1}{2}}}\right\} + \sum\{n_e \log(Y_n)\}_i \quad (4.20)$$

In agreement with modelling considerations (Paragraph 4.2), all BM notch elastoplasticity coefficients turn out to be the lower bound value ($n_{e,i} \approx 1.0$), i.e. the cyclic remote mechanical loading induced notch behaviour is predominantly linear elastic as confirmed by the average notch plastic zone size amplitude; ($r_p \approx 0.03$) for $\sigma_y = 240$ [MPa] in plane strain. The HAZ data includes welding induced residual stress σ_n^r as well. The SEN crack growth specimens, free bodies, do not contain displacement constraints, meaning σ_n^r is of the self-equilibrating type. If compressive in the notch affected region (Fig. 2.70), the local residual load ratio is smaller than the remote loading induced one ($r_l^r < r_l$), i.e. ($n_{e,i} < 1.0$) and may explain the

HAZ crack growth behaviour to be monotonically increasing as well (Fig. 4.11). The HAZ (cyclic) notch elastoplasticity coefficients however approximately equals the BM value: ($n_{e,i} \approx 1.0$), suggesting the σ_n^r contribution is limited. To visualise the results, a two-stage single slope presentation might be useful (Fig. 4.12); the better the log-log linearity, the better the data fit and model capabilities seems to be. At normal scale, the multi-log-linear formulation (Eq. 4.20) becomes:

$$\left\{ \left(\frac{da}{dn} \right) / (Y_n^{n_e})_i \right\} = C \cdot \left\{ \frac{\Delta K_f}{Y_n^{\frac{1}{2}}} \right\}^m \quad (4.21)$$

Note that to justify the development of a new fatigue model in comparison to available (competitive, alternative) ones, preventing for curve fitting to obtain model coefficients is sometimes used as argument since it would lack a physical base. The misunderstanding seems that although curve fitting itself has no physical meaning, the parameters do, meaning the argument is simply invalid. Agree to disagree concerning modelling philosophies.

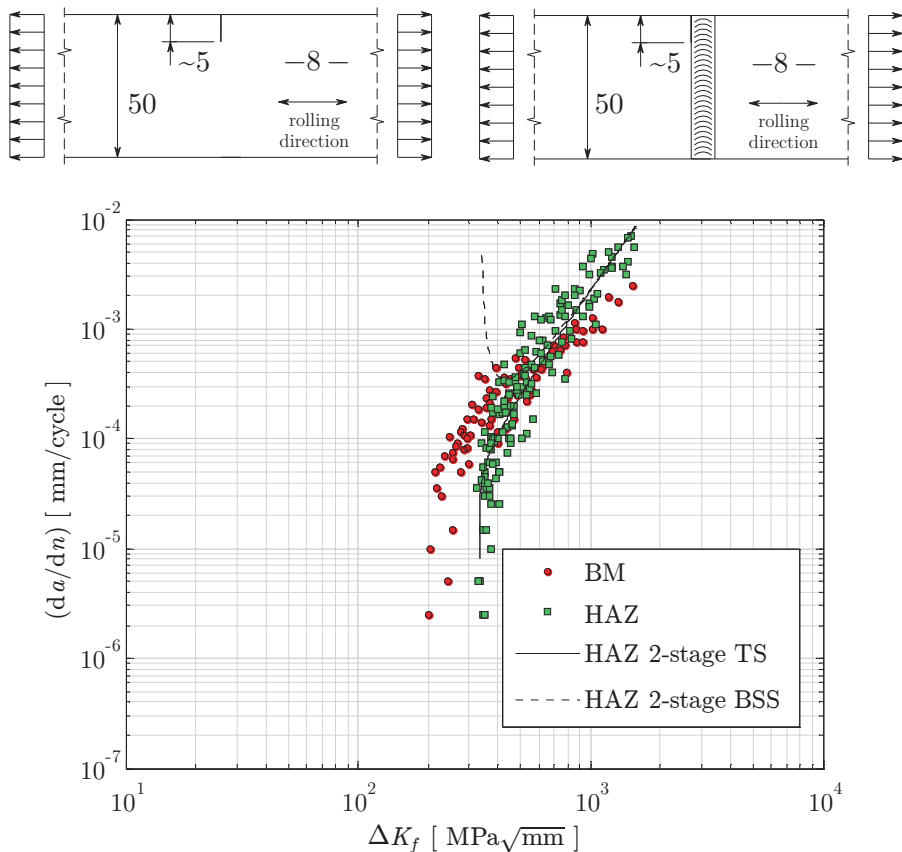


Figure 4.11: SEN Al5083-H321 large/long crack growth data presentation (Shankar and Wu, 2002) and two-stage models (Eq. 4.3 and 4.7); $r_l = 0.1$ [-].

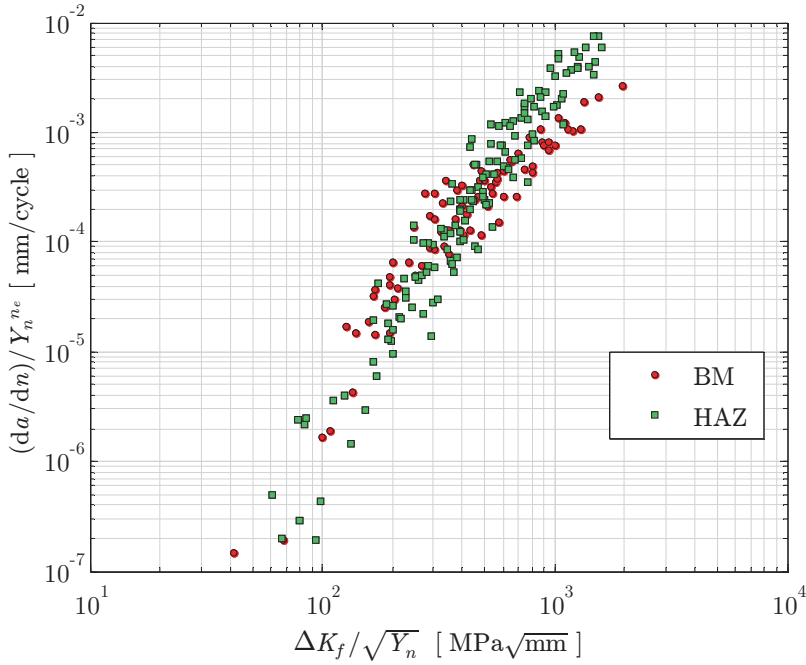


Figure 4.12: SEN A15083-H321 crack growth data (Shankar and Wu, 2002) in TS two-stage single slope presentation; $r_l = 0.1$ [-].

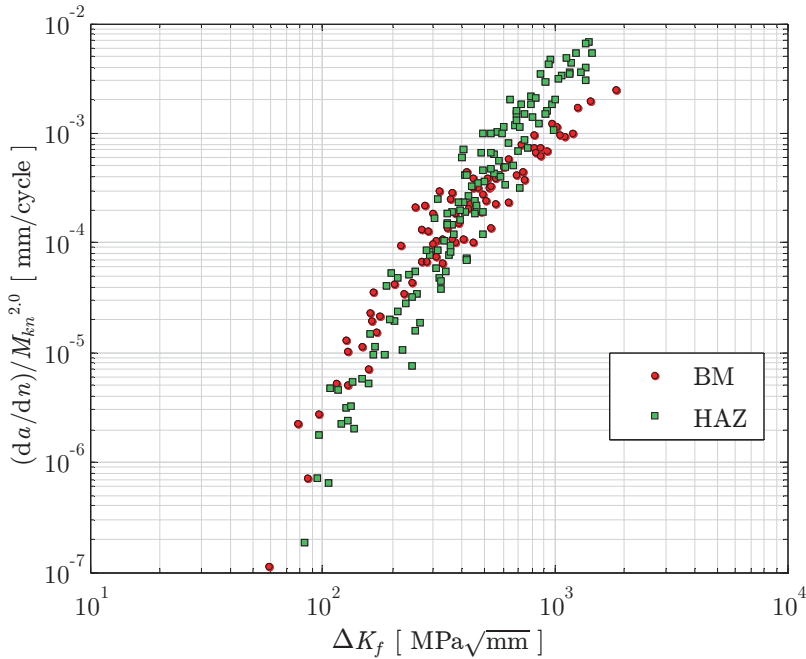


Figure 4.13: SEN A15083-H321 crack growth data (Shankar and Wu, 2002) in BSS two-stage single slope presentation; $r_l = 0.1$ [-].

Comparing {BM, HAZ} data, the average slope values $m = \{2.48, 3.15\}$ prove that cracks grow faster in the HAZ; principally a matter of different bulk material properties affecting (da/dn) . The crack growth strength in terms of scaling factors, $\log(C^{(i)}) = \{-10.31, -12.01\}$, is in favour of BM.

Application of the BSS model (Eq. 4.3) including non-monotonic crack growth behaviour only – a SEC approach is adopted for any SEN geometry like for weld toe and weld root notches (Paragraph 3.5 and 3.6) and σ_s is no far field stress anymore – seems inappropriate here as shown for the HAZ data mean (Fig. 4.11); a binary approach ($n = 1 \vee n = 2$) might be a solution to incorporate elastic notch and/or crack tip behaviour as well. In two-stage single slope presentation, however, an apparent agreement of the contradictory TS and BSS formulation has been identified (Fig. 4.12 and 4.13). Differences are hardly visible and relying on a two-stage single slope presentation only (Dong, Hong and Cao 2003; Dong and Hong 2004) may suggest a better correlation than it actually is.

Micro-crack growth BM data (L-T config.) for varying notch radius ρ has been obtained for BS4360 steel grade 50B (Shin and Smith, 1988). The SEN specimens are stress relieved to ensure no σ_n^r component is involved. Constant amplitude tests are performed at $r_l = 0.005$ [-], $f = 5$ or 10 [Hz] and ambient temperature.

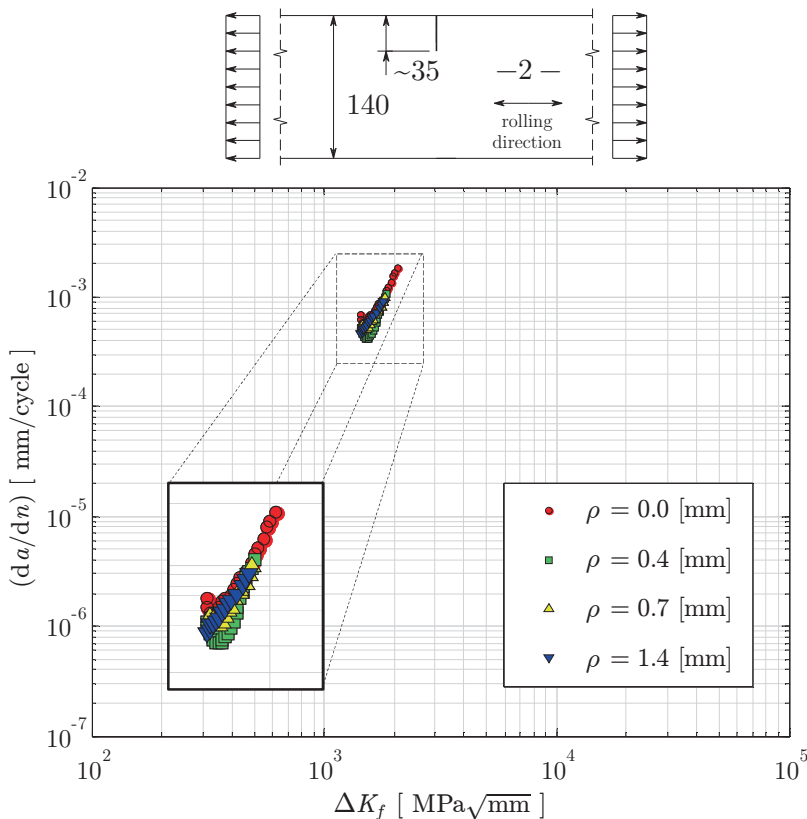


Figure 4.14: SEN BS4360 steel grade 50B large/long crack growth data presentation (Shin and Smith, 1988); $r_l = 0.05$ [-].

Non-monotonic behaviour is identified beyond the material threshold $\Delta K_{th} \approx 180$ [MPa $\sqrt{\text{mm}}$]; note the E -modulus and ΔK_{th} bulk material property ratios of steel and aluminium is approximately equal. The notch induced micro-crack growth anomaly reduces for increasing ρ (Fig. 4.14), increasing notch acuity (ρ/a_n), as included in the TS two-stage crack growth model (Eq. 4.7). Since macro-crack growth data is limited, the slope value ($m = 3.50$) is based on other test results (Shin and Smith, 1988). To obtain $\{\log(C), n_{e,i}\}$, the $m \log\{\Delta K_f/(Y_n)^{1/2}\}$ term is moved to the left hand side in the multi-log-linear relation (Eq. 4.20). Plasticity is involved; ($n_{e,i} \approx 1.88$) in average, meaning $\{(n_{e,i} - m/2) > 0\}$ as expected. A crack growth data TS two-stage single slope presentation shows a good correlation (Fig. 4.15). The 1st order notch plastic zone size exceeds the aluminium 5083-H321 BM data value by one order of magnitude, i.e. ($r_p \approx 0.74$) for $\sigma_y = 350$ [MPa] in plane stress condition; a specimen thickness related assumption, confirming that for a far field stress below σ_y plasticity induced non-monotonic micro-crack growth is predominantly limited to thin specimen. For notches at arc-welded joints however a plane strain condition seems obvious...

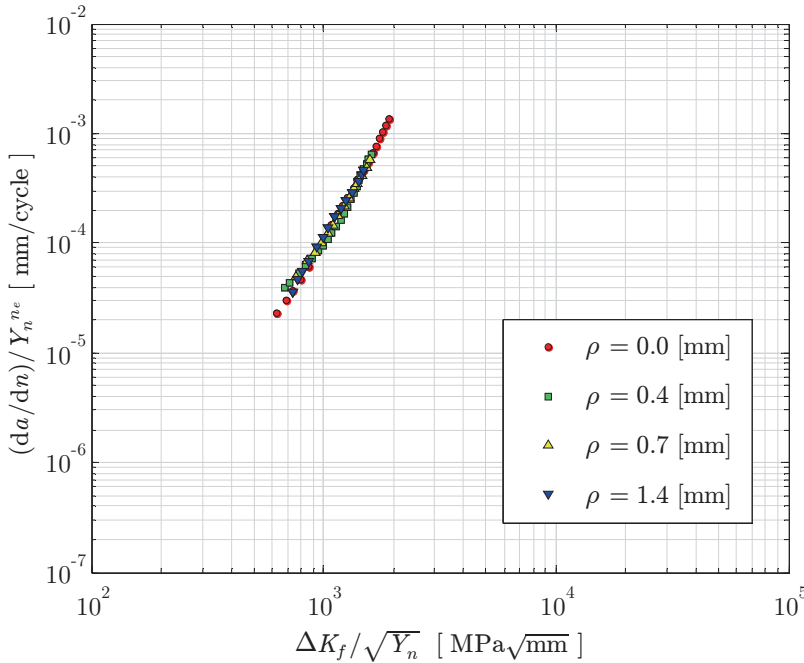


Figure 4.15: SEN BS4360 steel grade 50B crack growth data (Shin and Smith, 1988) in TS two-stage single slope presentation; $r_l = 0.05$ [-].

For the same type of specimen (non-symmetric with respect to $(b_p/2)$; Fig. 3.3b) and dimensions – only the thickness is adapted to 3 [mm] – in BS1470 aluminium 1200 (S1C), similar results have been obtained (Shin and Smith, 1988; Fig. 4.16 and 4.17). The slope value ($m = 2.7$) is a long crack growth data set value; curve fitting provides $n_{e,i} = \{1.55, 1.49, 1.39\}$.

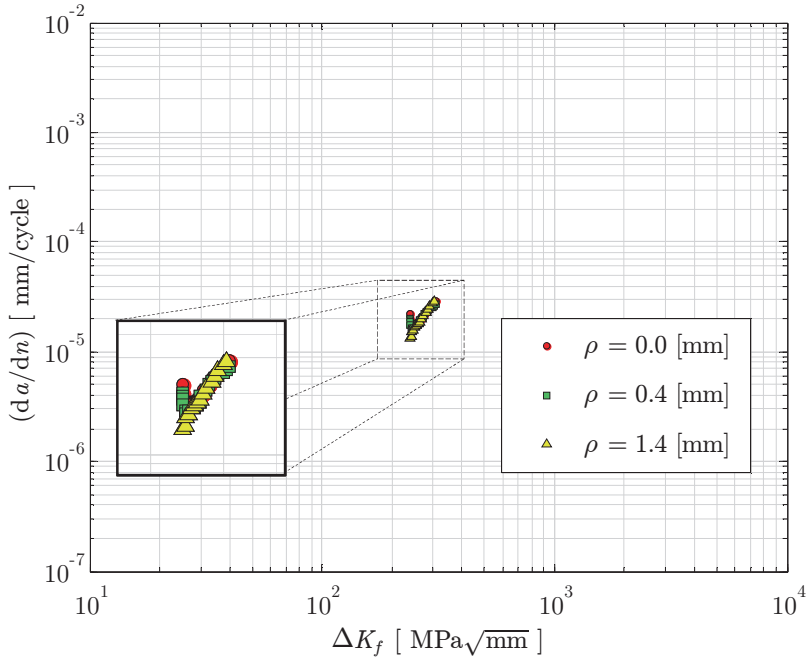


Figure 4.16: SEN BS1470 aluminium 1200 (S1C) large/long crack growth data presentation (Shin and Smith, 1988); $r_l = 0.05$ [-].

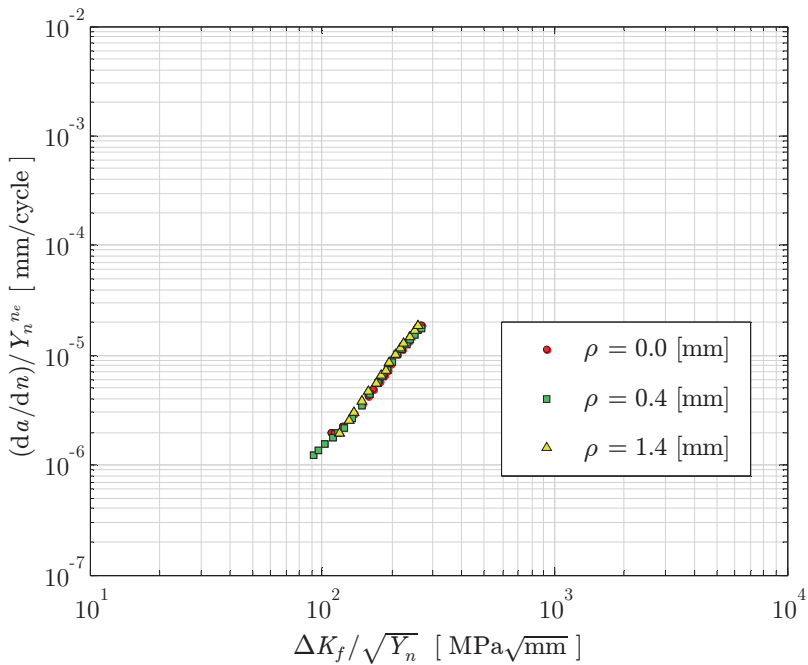


Figure 4.17: SEN BS1470 aluminium 1200 (S1C) crack growth data (Shin and Smith, 1988) in TS two-stage single slope presentation; $r_l = 0.05$ [-].

To limit SEN specimen dimensions, a Compact Tension (CT) configuration has been developed. Crack growth behaviour is established for {BM, WM, HAZ} in aluminium 6062-T651 (Ribeiro and De Jesus, 2011; Fig. 4.18) using MIG filler wire 5356 welded FP DS butt joints. The weld reinforcements have been removed. Constant amplitude data at $f = 15$ [Hz] in lab conditions is obtained for 2 remote load ratios: $r_l = \{0.10, 0.50\}$ [-]. Although the notch affected micro-crack growth contribution is limited – monotonically increasing beyond ΔK_{th} as expected based on remote loading, self-equilibrating residual stress and specimen thickness – the data allows to investigate mean stress effects, i.e. cases with- and without welding induced residual component.

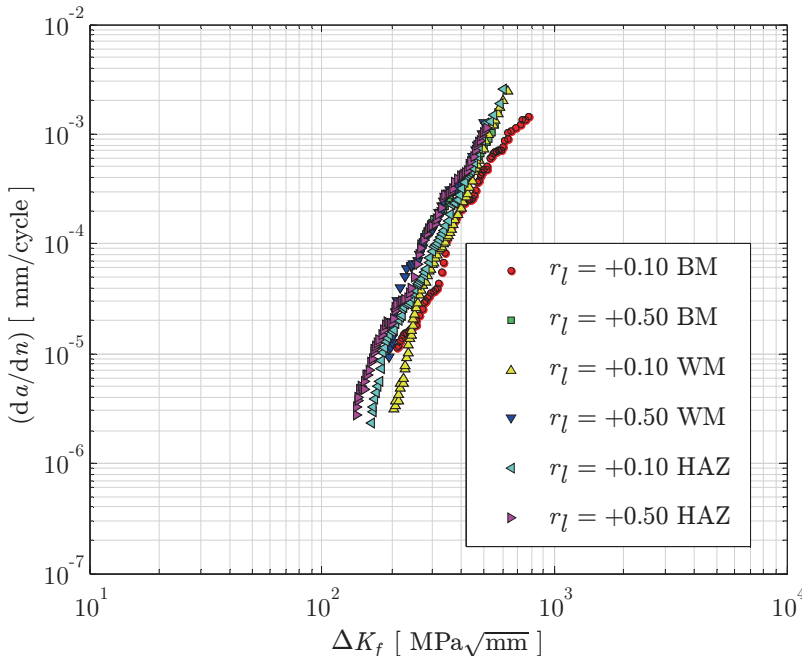
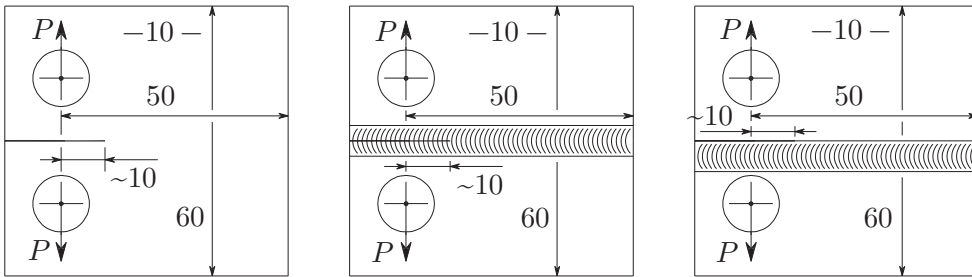


Figure 4.18: SEN CT Al6062-T651 large/long crack growth data presentation (Ribeiro and De Jesus, 2011).

Least squares estimates $\{\log(C^{(i)}), m, \gamma', n_{e,i}^{(i)}\}$ have been obtained for each material zone using regression analysis, rewriting the TS two-stage crack growth models (Eq. 4.17 and 4.19) for respectively BM and $\{\text{WM}, \text{HAZ}\}$:

$$\log\left(\frac{da}{dn}\right) = \log(C^{(i)}) + m \log\left\{\frac{\Delta K_f}{(Y_n)^{\frac{1}{2}}}\right\} + \gamma' \log(1 - r_l) + \sum \{n_e^{(i)} \log(Y_n)\}_i \quad (4.22)$$

with

$$\gamma = \frac{\gamma'}{m} + 1$$

The obtained r_l coefficients $\gamma = \{0.70, 0.73, 0.87\}$ are beyond the geometric mean, i.e. the crack growth contribution of the cyclic component ΔK_I dominates $K_{I,max}$. Although large values are no exception (Mann, 2007), the $\{\text{BM}, \text{WM}\}$ ones are typical (Dowling, Calhoun and Arcari, 2009).

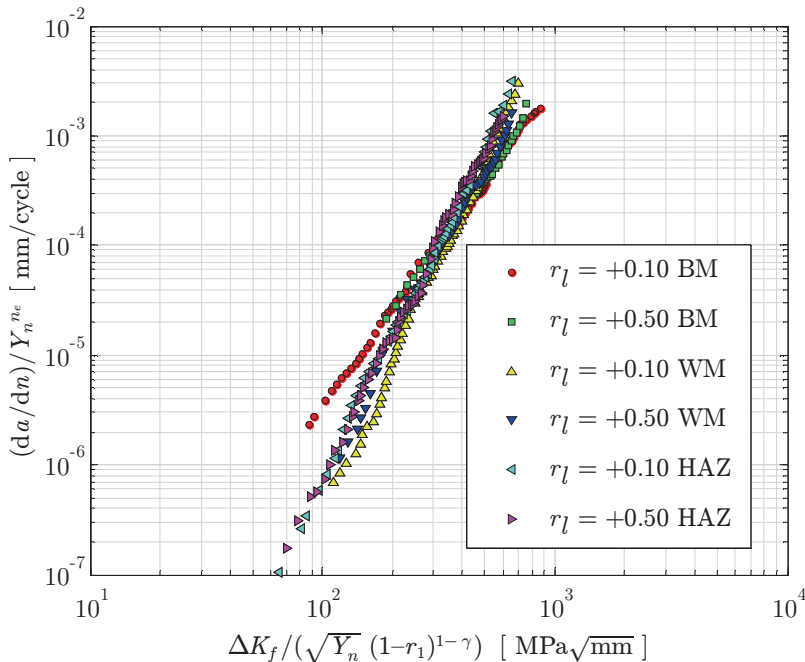


Figure 4.19: SEN CT Al6062-T651 crack growth data (Ribeiro and De Jesus, 2011) in TS two-stage single slope presentation.

The Al6061-T651 {WM, HAZ} crack growth strengths $\log(C^{(l)}) = \{-14.30, -14.65\}$ and slopes $m = \{4.07, 4.27\}$ are approximately equal (Fig. 4.19); a prerequisite to combine weld root and weld toe induced fatigue resistance data. The BM slope is obviously smaller ($m = 2.97$). Generally speaking, m values closer to the Al5083-H321 one have been found as well (Mann, 2007). If micro-crack growth behaviour is ignored and all data is incorporated to obtain m , the Paris region slope is overestimated (e.g. Ribeiro and De Jesus, 2011) and (artificially) large.

Surprisingly, the {WM, HAZ} γ coefficients are different. The only possible explanation seems to be unequal specimen residual stress, supported by the γ - $n_e^{(l)}$ correlation; $n_e^{(l)} \approx \{1.38, 1.79\}$ in average, showing plasticity (plane strain to a large extent) is involved in all cases, but dominant for HAZ.

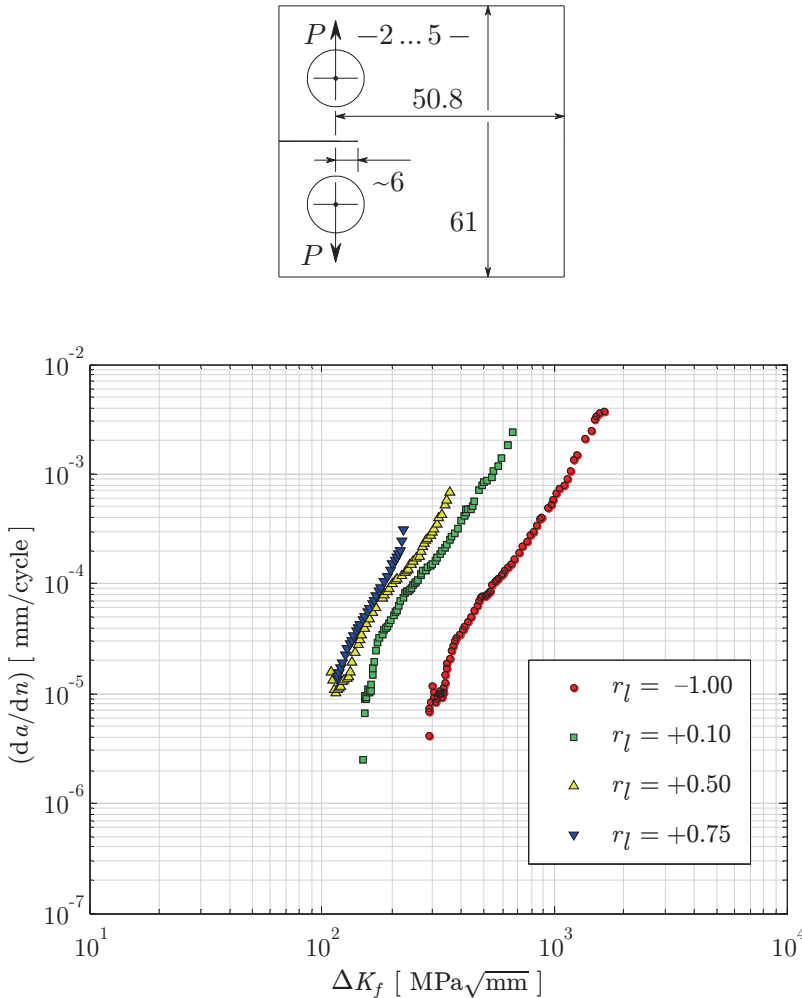


Figure 4.20: SEN CT Al7075-T651 large/long crack growth data presentation (Zhao, Zhang and Jiang, 2008).

For ($r_l \geq 0$) and exponential load ratio coefficients ($0.5 < \gamma \leq 1.0$), a decision to neglect mean stress seems reasonable if the r_l contribution disappears in the data scatter. However, as soon as ($r_l < 0$) data becomes involved – representative for deck- (sagging condition) or bottom structures (hogging condition) – mean stress effects become significant as shown for high-strength aluminium BM 7075-T651 data (T-L configuration), obtained in air at $f = 1..10$ [Hz] depending on applied loading (Zhao, Zhang and Jiang, 2008; Fig. 4.20). The plate thickness is not the same for all specimen, but ensures a predominant plane stress condition in any case. The log-linear relation (Eq. 4.22) needs to be modified.

$$\log\left(\frac{da}{dn}\right) = \log(C^{(\nu)}) + m \left[\begin{array}{l} \log\left\{\frac{\Delta K_f}{(Y_n)^{\frac{1}{2}}}\right\} \text{ for } r_l \geq 0 \\ \log\left\{\frac{\Delta K_f}{(Y_n)^{\frac{1}{2}}(1-r_l)}\right\} \text{ for } r_l < 0 \end{array} \right] + \quad (4.23)$$

$$\gamma \left[\begin{array}{l} \log(1-r_l) \text{ for } r_l \geq 0 \\ 0 \text{ for } r_l < 0 \end{array} \right] +$$

$$\sum \{n_e^{(\nu)} \log(Y_n)\}_i$$

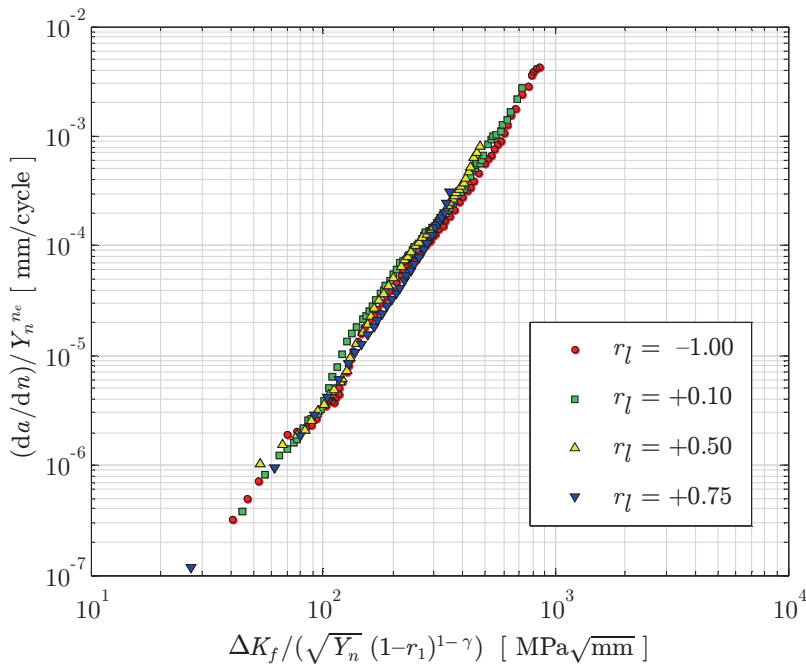


Figure 4.21: SEN CT Al7075-T651 crack growth data (Zhao, Zang and Jiang, 2011) in TS two-stage single slope presentation.

Assuming only the tensile part of the stress cycle contributes to crack growth, is a reasonable one (Fig. 4.21); the remote load ratio coefficient is beyond the geometric mean ($\gamma = 0.69$). Notch affected micro-crack growth data is limited. Both monotonically increasing- and non-monotonic behaviour is identified, showing $n_e^{(i)}$ should be determined for each individual crack growth data series indeed.

Plasticity induced micro-crack growth at notches is predominantly related to a plane stress condition and becomes more pronounced for decreasing (negative) remote load ratio r_l (Newman at al., 2000; Fig. 4.10), as shown for 1070 Steel data at a SEN in round compact tension (RCT) specimen configuration (Ding, Feng and Jiang; Fig. 4.22).

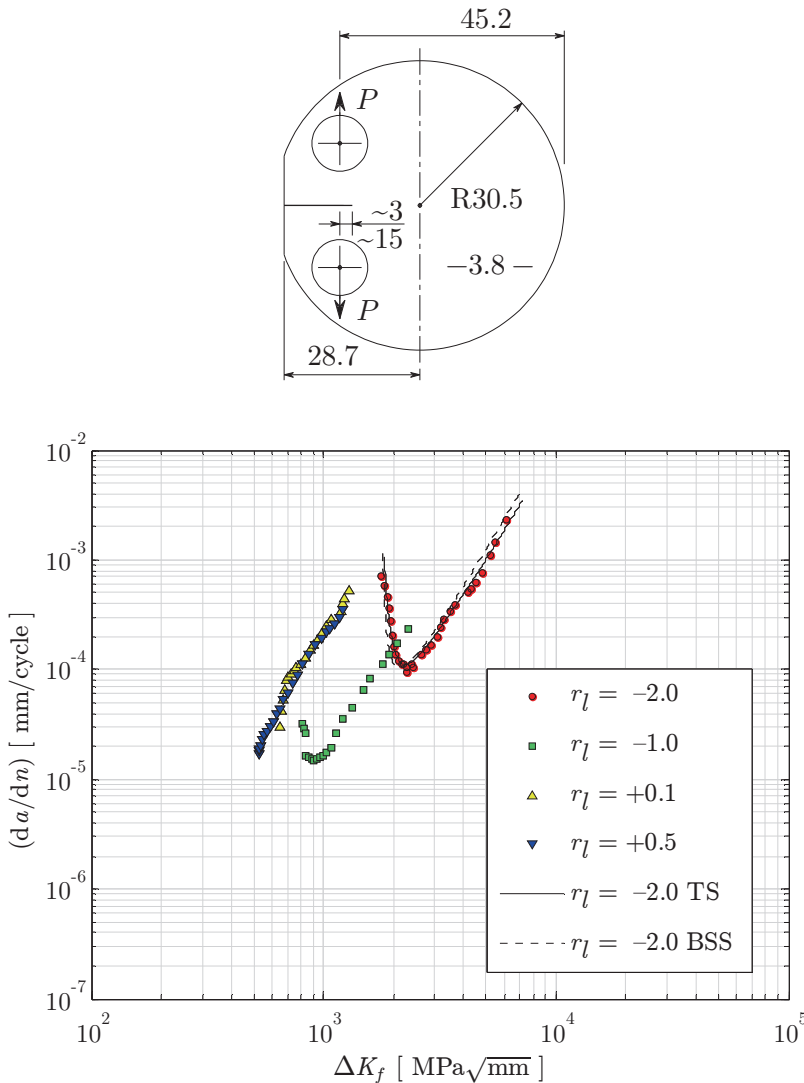


Figure 4.22: SEN RCT 1070 Steel large/long crack growth data presentation (Ding, Feng and Jiang, 2007).

Although (R)CT data is typically considered to be large/long crack related (Lados, Apelian and Donald, 2007) confusing notch- and crack size/length, non-monotonic- as well as monotonically increasing anomalies can be identified. For ($r_l \geq 0$) the applied load range seems governing, since no load ratio effect is identified; the $r_l = \{+0.1, +0.5\}$ contribution has been ignored and $\gamma \approx 1$.

The specimen thickness induced plane stress condition provides an increased plastic zone size r_p compared to a plane strain case. To achieve notch and/or crack(tip) plasticity for decreasing load ratio, the stress range $\Delta\sigma_s$ should increase like has been done for ($r_l = -1.0$) \rightarrow ($r_l = -2.0$). The non-monotonic micro-crack growth behaviour becomes more pronounced, since the increased local mean stress will gradually decrease to the far field value for increasing crack size; i.e. the significance of crack growth rate deceleration (Fig. 4.10 and 4.22) is up to some extent a self-fulfilling prophecy. Assuming that only the stress cycle tensile part contributes to crack growth seems still reasonable (Fig. 4.23).

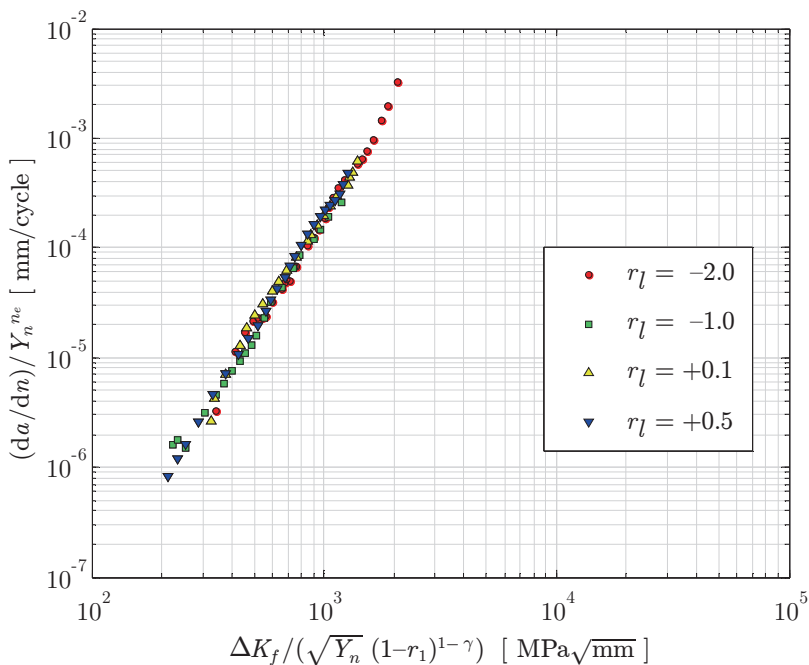


Figure 4.23: SEN RCT 1070 Steel crack growth data (Ding, Feng and Jiang, 2007) in TS two-stage single slope presentation.

Obtained elastoplasticity coefficients $n_{e,i} = \{4.55, 2.36, 1.64, 1.67\}$ and slope ($m = 3.47$) show for ($r_l = -2.0$) that the TS value $\{n = (n_e - m/2) \approx 2.82\}$ exceeds the BSS one ($n = 2.0$); model results are approximately the same (Fig. 4.22). For ($r_l = -1.0$), $n_{e,i}$ is halved with respect to the ($r_l = -2.0$) case like the applied loading ΔP , meaning the elastoplasticity coefficient includes only a cyclic contribution for ($r_l < 0$) since γ is not involved by definition. At ($r_l = +0.1$) the

load range has drastically been reduced again; $n_{e,i}$ may contain load ratio effects. The specimens notch length however, $a_n \approx 15$ [mm], increases the stress level and some plasticity is still involved. The crack growth rate has become monotonically increasing since $\{(n_e - m/2) < 0\}$. Increasing ΔP as well as the load ratio up to ($r_l = +0.5$), the level of plasticity increases slightly. Anomalous crack growth – either structural threshold or residual stress induced – is limited since the increased local mean stress is counteracted by the increased far field mean stress (i.e. increased r_l).

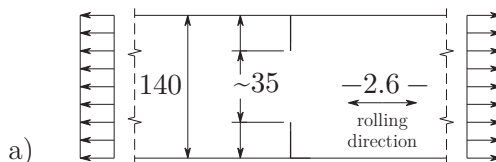
In the hull structure {WM, HAZ}, a plane strain condition at weld notches is expected, limiting the plastic zone size r_p at one hand; residual stress distributions of the (tensile) equilibrium equivalent type (displacement constraints are involved) increasing the local mean stress and r_p on the other hand. The far field stress range $\Delta\sigma_s$ seems to be decisive for the actual r_p size and determine the crack growth behaviour to be either monotonically increasing or non-monotonic; r_l determines how pronounced the anomalies will be.

4.3.2 Double edge notch

For the SEN symmetry equivalent with respect to ($t_p^{(v)}/2$) or ($b_p/2$), a DEN geometry (Fig. 3.5); cracks should emanate at both sides with equal (da/dn), micro-crack growth AISI 316 stainless steel BM data (L-T config.) has been obtained at different remote load ratios r_l and notch radii ρ (Fig. 4.24 and 4.25; Shin and Smith, 1988). The specimens are stress relieved to ensure no σ_n^r component is involved. Constant amplitude tests are performed at $f = 5$ or 10 [Hz] and ambient temperature. Macro-crack growth data is limited and the slope value ($m = 5.50$) is based on long crack growth test results (Shin and Smith, 1988). To obtain $\{\log(C), \gamma', n_{e,i}\}$, the $m\log\{\Delta K_f/(Y_n)^{1/2}\}$ term is moved to the left hand side in the multi-log-linear relation (Eq. 4.22).

Elastoplasticity reduces for the constant ρ and increasing r_l series (Fig. 4.24) and crack growth behaviour has changed from non-monotonic – the specimen thickness ensures a plane stress condition – into monotonically increasing. A nearly perfect correlation between $n_e = \{3.00, 2.53, 1.98\}$ and r_l can be identified.

Varying ρ at the same time (Fig. 4.25), the elastoplasticity coefficients become: $n_e = \{2.90, 2.41, 1.45\}$. If ρ decreases like for $r_l = \{+0.05, +0.30\}$, the peak stress increases meaning the plasticity concentration increases as well, i.e. the plastic zone size and n_e decrease will decrease. The common case ($r_l = +0.65$) n_e value however is different and suggests a considerable degree of data sensitivity. The remote load ratio coefficients are approximately the same: $\gamma \approx 0.40$ [-].



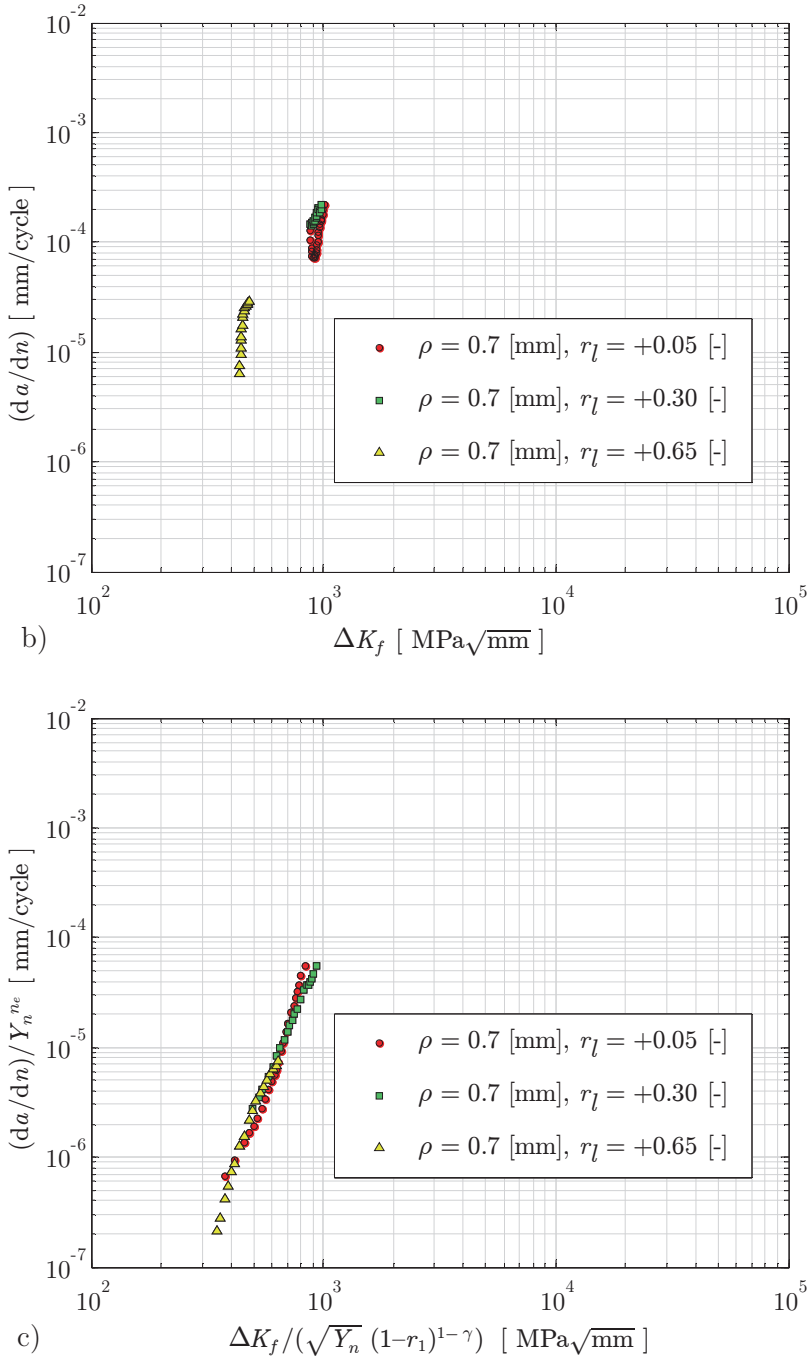


Figure 4.24: DEN AISI 316 stainless steel large/long crack growth data (Shin and Smith, 1988)- and TS two-stage single slope presentation; constant ρ .

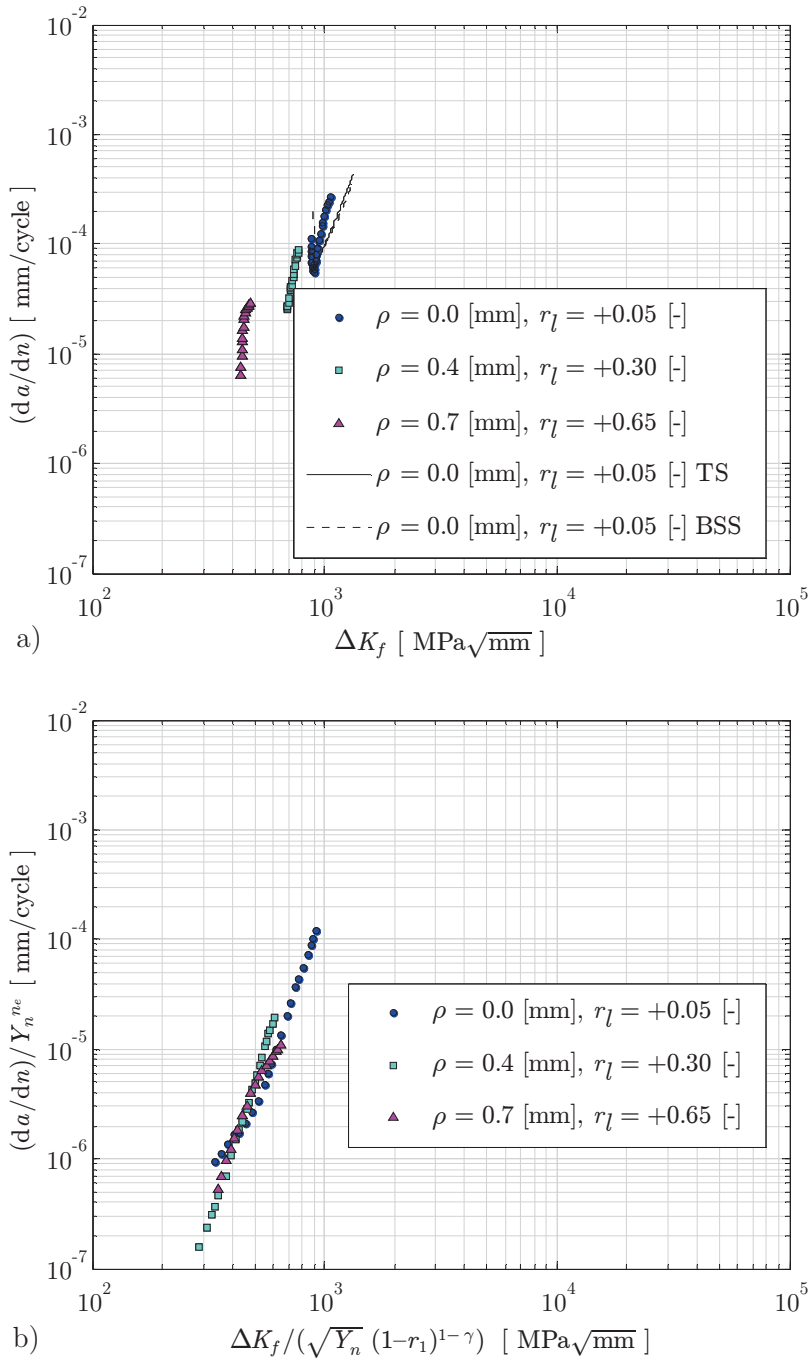


Figure 4.25: DEN AISI 316 stainless steel large/long crack growth data (Shin and Smith, 1988)- and TS two-stage single slope presentation; varying ρ .

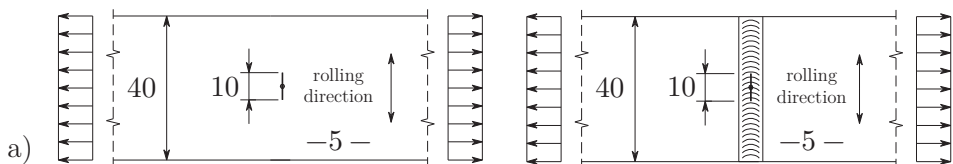
Surprisingly, the BSS crack face traction p_f (Dong, Hong and Cao, 2003; Dong and Hong, 2004; Paragraph 3.5 and 3.6) for DEN geometries is included using the weight function approach (Eq. 3.17), in contrast to the SEC formulation adopted for SEN geometries; σ_s is still no far field stress. Consistency seems lost. Note that the region-II slope ($m = 5.5$) is already taken into account (Fig. 4.25).

4.3.3 Centre notch

Weld root notches in PP DS butt- and cruciform joints, i.e. CN geometries (Fig. 3.6), show – like DEN ones – symmetry w.r.t. ($t_p/2$); the σ_{nr} distribution is however non-symmetric. Corresponding crack growth behaviour in aluminium 5083 is established for {BM, WM} in T-L configuration (crack path parallel to grain rolling direction) using multiple MIG filler wire 5183 welded FP DS butt joints (Sonsino et al., 1999 and Brandt et al., 2001; Fig. 4.26) and provides a data scatter band. The weld reinforcements have been removed. Constant amplitude data is obtained in lab conditions for 2 remote load ratios: $r_l = \{-1.0, +0.0\}$ [-]. The WM specimens are stress relieved, i.e. annealed at 200 [°C] for 1 hr. without compromising the material hardness and to prevent for σ_{nr}^r effects, explaining the very similar {BM, WM} crack growth behaviour; $\{\log(C^{(l)}), m\}$ are comparable. Notch affected micro-crack growth is monotonically increasing beyond ΔK_{th} for both data sets, in agreement with the applied remote mechanical loading, (cyclic) yield strength and specimen thickness.

Typical analysis results (Brandt et al., 2001) include the Paris equation, obtained using all data no matter crack growth anomalies, affecting the region-II parameters (Fig. 2.75). However, adopting the two-stage crack growth model, an elastic notch affected crack tip structural response has been identified ($n_e \approx 1$) as expected since r_p is negligibly small. Taking the remote mechanical mean stress into account is rather a formality since ($\gamma = 0$) in both cases (Fig. 4.27). The assumption that only the tensile part of the stress cycle contributes to crack growth seems reasonable.

Using the BSS crack face traction p_f (Dong, Hong and Cao, 2003; Dong and Hong, 2004; Paragraph 3.5 and 3.6) and a weight function approach (Eq. 3.17), the stress intensity has been calculated inconsistently since p_f rather than σ_{nr} has been used. Together with the plasticity induced non-monotonic crack growth assumption, the single-slope presentation (Fig. 4.28) is obviously misleading. Mean stress effects have not been considered.



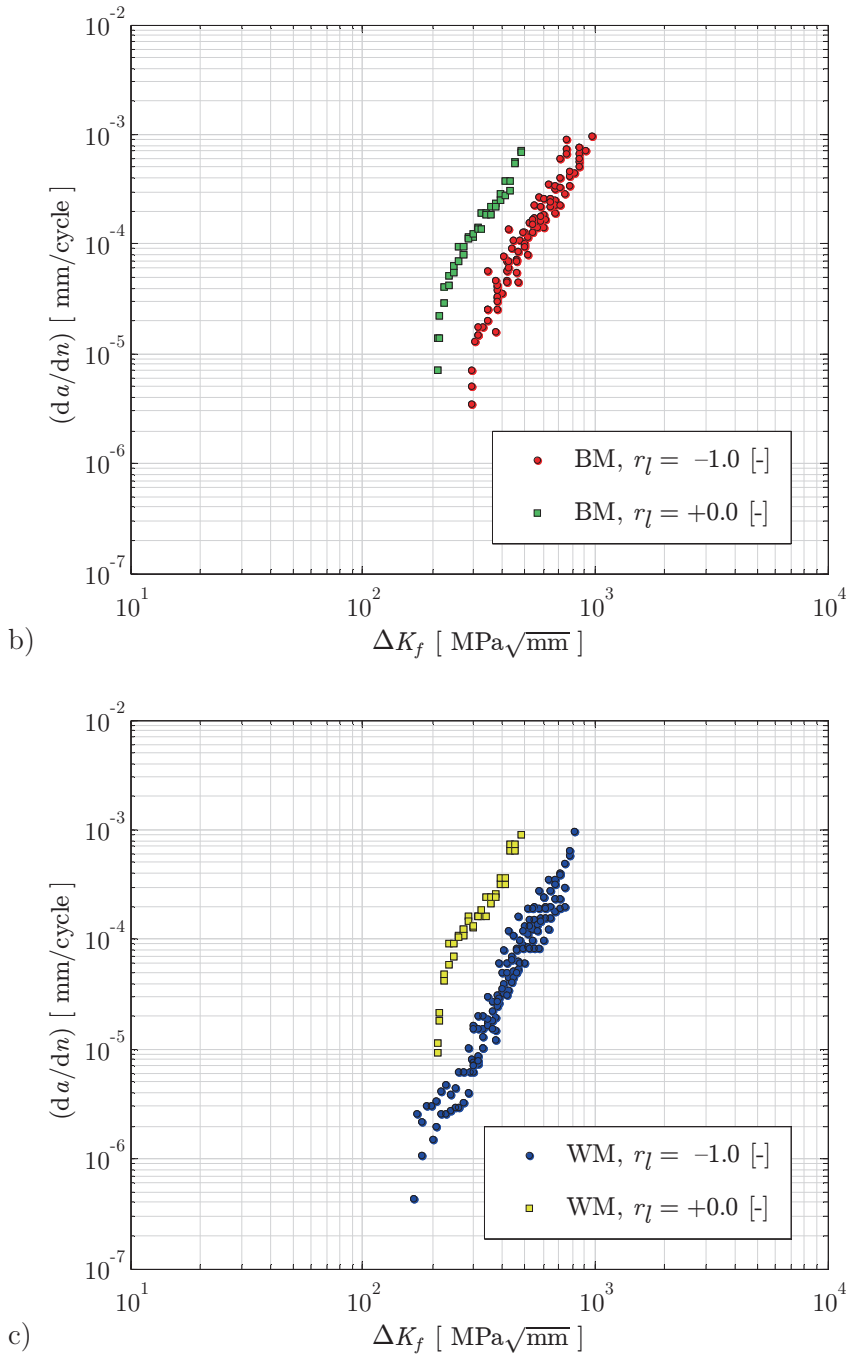


Figure 4.26: CN aluminium 5083 long crack growth data (Brandt et al., 2001).

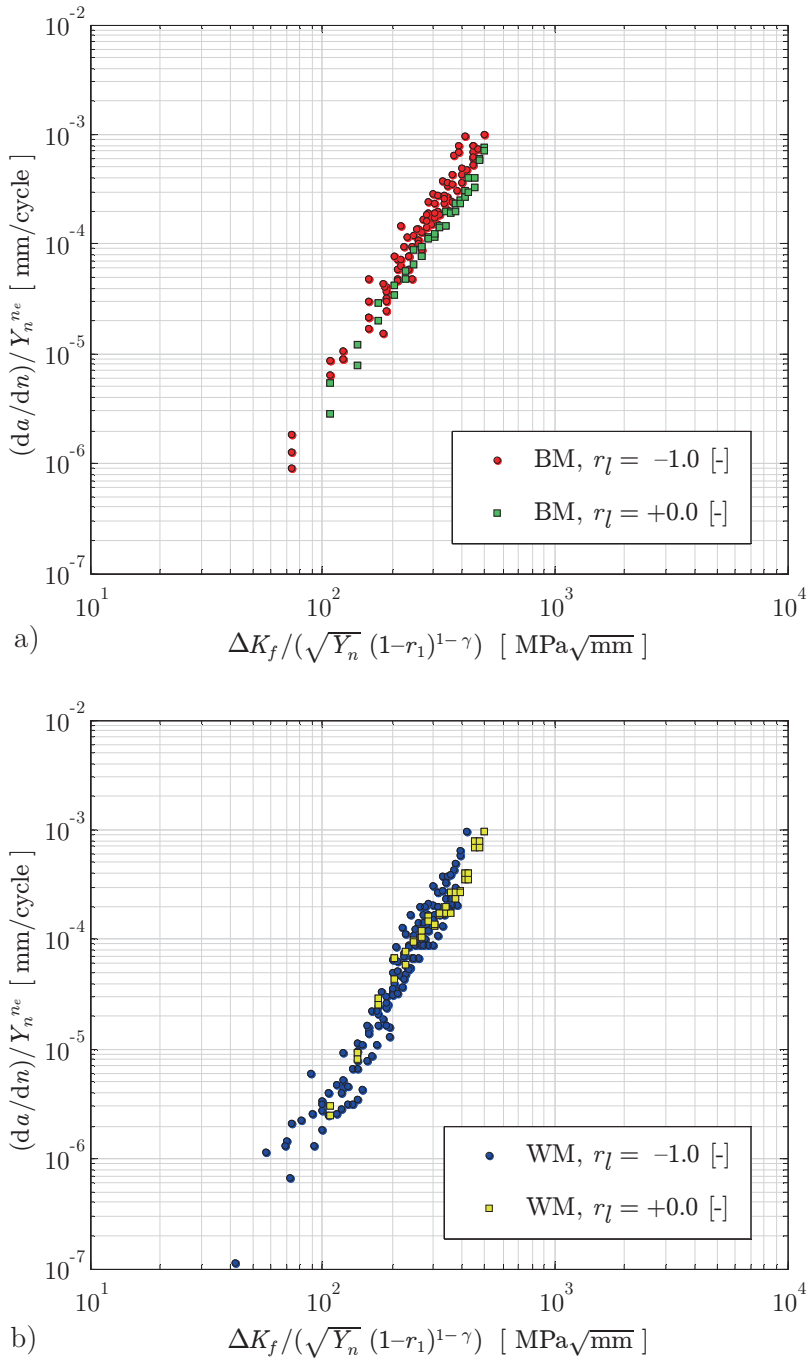


Figure 4.27: CN aluminium 5083 crack growth data in TS two-stage single slope presentation.

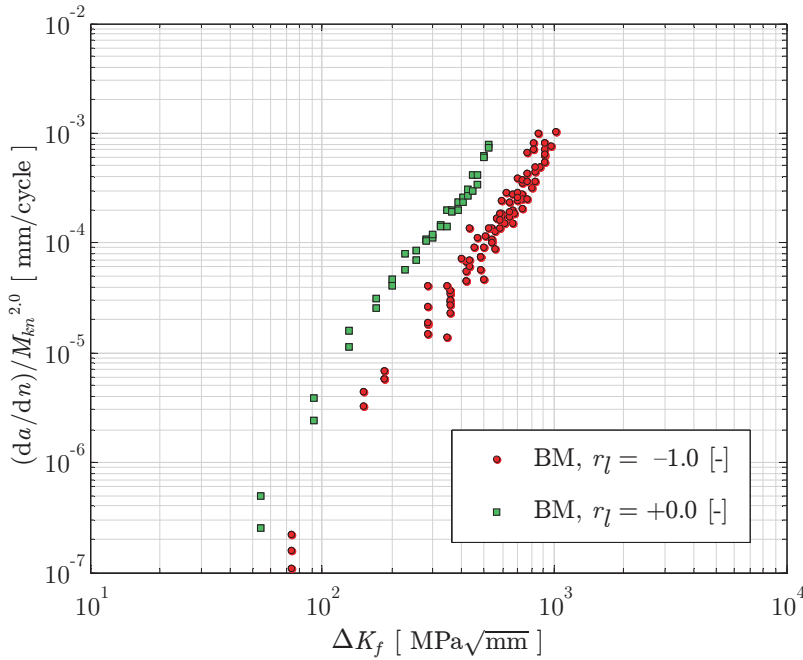


Figure 4.28: CN aluminium 5083 crack growth data in BSS two-stage single slope presentation.

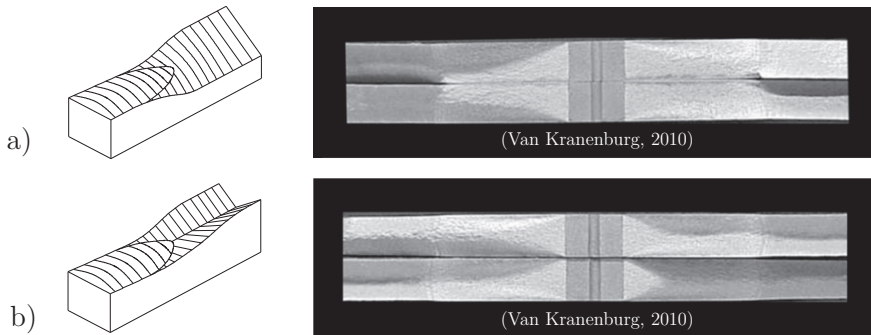


Figure 4.29: Shear lips in aluminium 5083 CN crack growth specimen for a) non-symmetry and b) symmetry w.r.t. half the plate thickness.

Shear lip development, both non-symmetric and symmetric w.r.t. $(t_p/2)$, is a well-known region-II crack growth phenomenon in standard aluminium specimens (Fig. 4.29). The initially flat fracture surface turns gradually into a slant one and introduces a mixed mode- $\{I, III\}$ loaded crack opening, meaning the slope $(da/dn) = f(\Delta K_I)$ changes at the same time up to the transition is completed as shown for aluminium 5083 BM CN test data for a range of r_l values (Fig. 4.30).

Shear lips are usually associated with plane stress conditions at the material surface (i.e. become more important for increasing specimen thickness) and includes an environmental component as well (Schijve, 1988). Although in hull structures not so much related to through-thickness crack growth as well to continuing crack propagation, adequate mode-I region-II parameters require a SIF correction, in particular for the non-symmetry case; for symmetry the mode-III contributions neutralise each other. In the shear lip affected region, K_I may reduce (log)linearly up to $K_I/\sqrt{2}$ for a 45 [deg] slant angle; a geometry (increased, effective specimen thickness)- or loading (reduced, effective stress) correction. For the considered data, the actual (final) slant angle is unknown and an average reduction factor $\{(1 + \sqrt{2})/2\}$ has been adopted. Applying the TS concept as well (Fig. 4.31), the average slope $m \approx 3.5$ is similar to the value obtained before (Fig. 4.27)

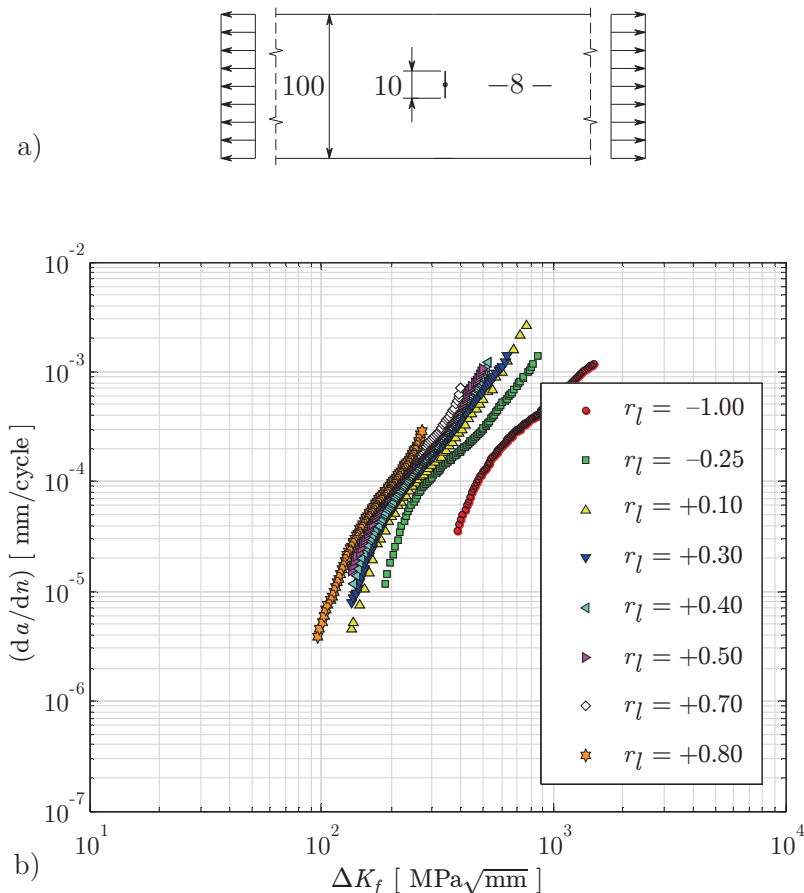


Figure 4.30: CN aluminium 5083 long crack growth data (Van Kranenburg, 2010).

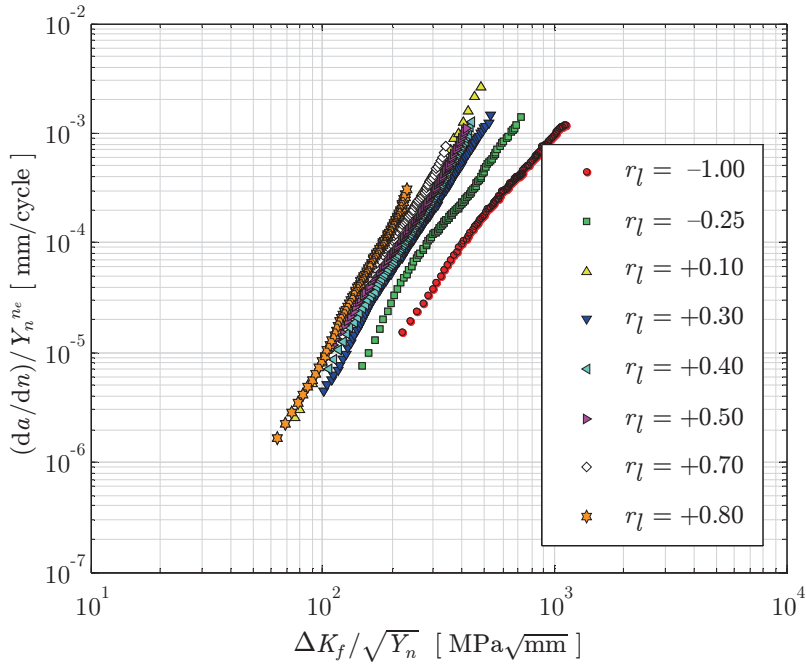


Figure 4.31: CN aluminium 5083 crack growth data in TS two-stage single slope presentation including shear lip correction.

4.4 Crack growth at weld toe notches

Fatigue testing series have been developed in a quasi-2D setup in order to identify CA crack growth behaviour at single edge weld toe notches ($0 < 2\alpha < 2\pi$) as well. Aim is to investigate influence of mode-I far field loading combinations (membrane and bending), initial crack size effects and notch elastoplasticity consequences (den Besten, Kaminski and Huijsmans, 2013).

4.4.1 Specimens

Recognising that crack growth behaviour in arc-welded joints is a complex combination of properties in the alternating material zones {WM, HAZ, BM}, in a two-series approach 45 non-welded and welded small scale specimens (SSS) have been used. The specimen geometry (including initial crack size) as well as the far field loading is controlled to prevent for related uncertainties; i.e. the SIF is both geometry and loading determined.

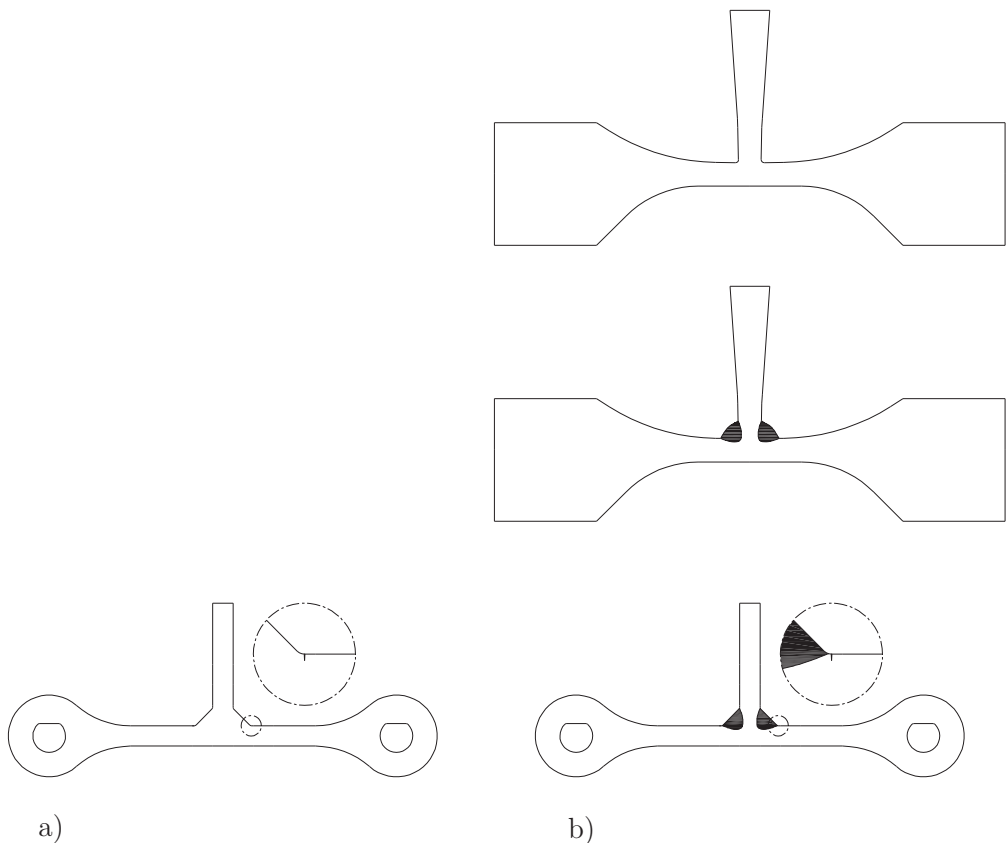


Figure 4.32: Non-welded and welded FP DS T-joint SSS geometry; $t_b = t_c = 10$, $l_w = h_w = 6\sqrt{2}$, $\rho = 1$ [mm].

The 1st series, (non-welded) FP DS T-joint geometries (Fig. 4.32a); no standard crack growth specimens, is milling machined from aluminium 5083H321, 10 [mm] sheet material. Hole eccentricity e_h [mm] has been used to achieve 3 different far field bending contributions affecting both $\{Y_n, Y_f(r_s)\}$, i.e. $e_h = \{-0.625, 0.0, 1.111\}$ corresponding to $r_s = \{-0.6, 0.0, 0.4\}$; the $\{\text{MBN}, \text{M}, \text{MBM}\}$ series, referring to the far field membrane and (non-)monotonic bending components. Chamfering has been applied to prevent for friction induced load contributions.

A SEN specimen (2α corresponding to an ideal fillet weld geometry) would provide crack growth information, but the fatigue resistance does not represent welded joint data. Applying far field bending is more difficult as well.

To obtain the same geometry for the 2nd series, welded SSS's, coarse contours are obtained first using a laser cutter machine. Fillet-welds are applied using MIG welding equipment and, subsequently, the T-joints are milling machined (Fig. 4.32b). To prevent for weld root failure in any case, the coarse contour approach is preferred rather than FP welding of base and cross-plates. The latter may introduce large deformations and aim is to keep the weld material removal to a minimum. Any residual stress left is assumed to be of the self-equilibrating type; specimens are not σ_n^r relieved.

Finally, for both series predefined artificial cracks are applied at the weld toe (one side only) using a (YAG) laser engraving technique. The initial weld toe flaw or crack size/length a_i is typically assumed (Lassen et al., 2006; Radaj, et al., 2006) to be in the range 0.10 ... 0.25 [mm] and random numbers $a_i \sim W(\mu, \sigma)$ have been generated (Fig. 4.33). The sharp flaws are wedge-shaped with a 6 [deg] top angle.

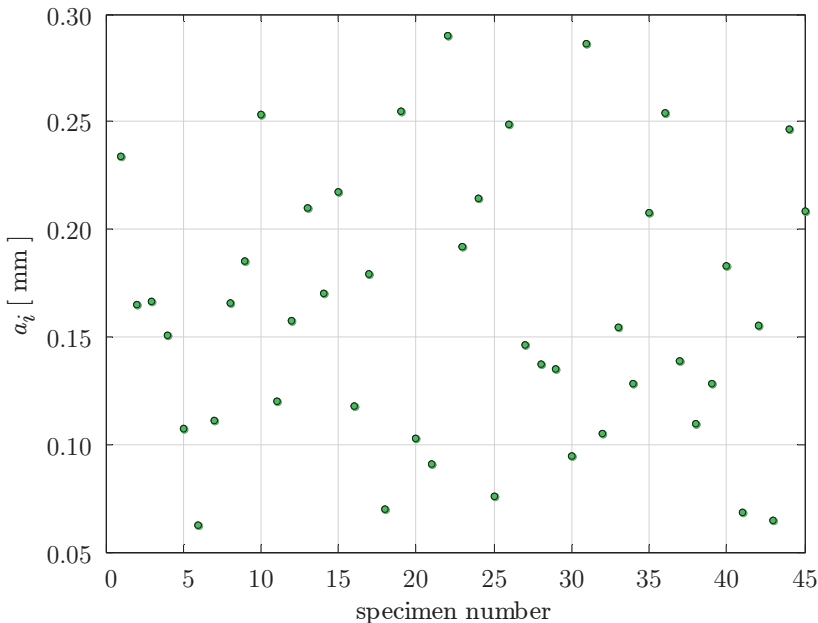


Figure 4.33: Randomly generated specimen weld toe initial crack sizes.

An artificial laser engraved crack is preferred rather than a (time consuming) pre-cracked one. Size and shape control is defined as decisive. For a pre-cracked one it is uncertain at which notch the crack will appear first – in contrast to a laser engraved crack – and it is likely to have a non-constant size and shape over specimen width. Besides, for a laser engraved flaw the size can be verified after testing using a stereo microscope (Fig. 4.34). A possible influence of laser heat input, which eventually may simulate the welding process induced heat input up to some extent, is considered of secondary importance.

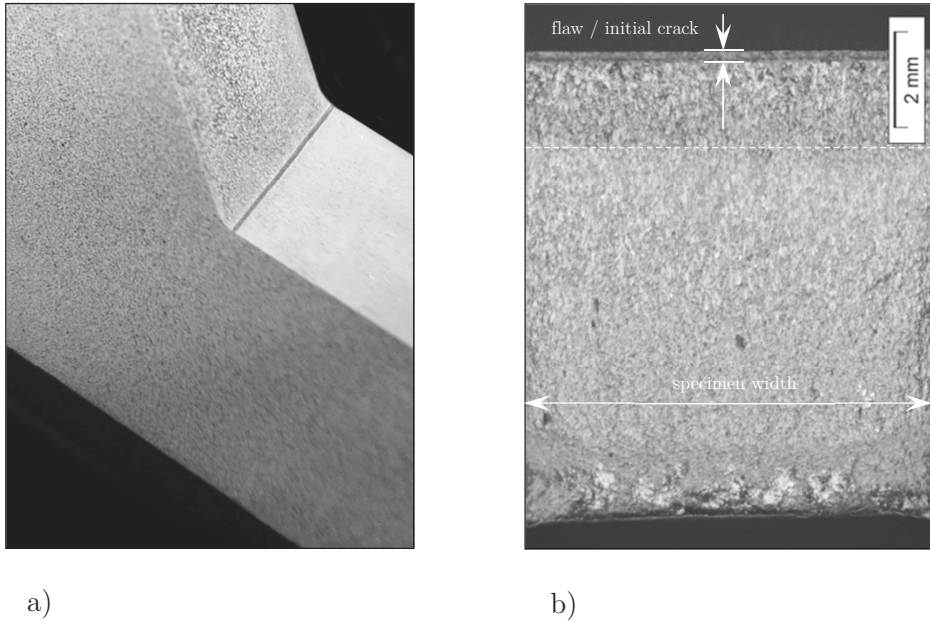


Figure 4.34: a) flaw geometry after YAG laser process, b) typical flaw; stereo microscope image after specimen failure.

The dark grey area below the flaw is the stable crack growth region (Fig. 4.34b). The (dashed) transition line to unstable crack growth (region-III) is approximately horizontal, meaning a quasi-2D edge crack has been developed indeed.

4.4.2 Test setup

To achieve full remote mechanical load control, the SSS fixtures contain Oiles sleeve bearings. Chamfered 12.9 fitting bolts have been used to mount the specimen in the machine grips (Fig. 4.35). Assuming the hinges work perfectly (i.e. frictionless), fixture misalignments; an offset puts the SSS under angle, will not affect the applied loading. Cyclic (sinusoidal) CA loading is applied at $r_l = 0.1$ [-] and $f = 10$ [Hz]. Three load range levels [N] have been defined for respectively the non-welded and welded configuration: $\Delta F_x = \{10500, 7500, 5000\}$ and $\Delta F_x = \{8500, 6500, 4500\}$, i.e. 5 specimens at each load range level for all {MBN, M, MBM} series. To capture

the SIF as governing crack growth parameter, its notch and far field information – respectively crack size/length (crack tip position) and (linear) stress distribution – is required and have been obtained using digital image correlation (DIC): a non-destructive, non-contact, direct optical observation method and surface displacement field measurement technique. Images are taken once in every 500 cycles (Fig. 4.35b) at maximum and minimum load condition $\{F_{max}, F_{min}\}$ using a stereo camera setup. To capture a notch affected crack growth anomaly like non-monotonicity – predominantly observed in plane stress condition – surface measurements seems an excellent choice indeed. SIF notch- and far field information (Fig. 4.35c) is recognised to be (already) available at different scales. However, aim is to capture all information from the same image, meaning the notch region requirements are governing. For a good spatial resolution, 5 MP cameras are used; the physical pixel size corresponds to ~ 6 $[\mu\text{m}]$.

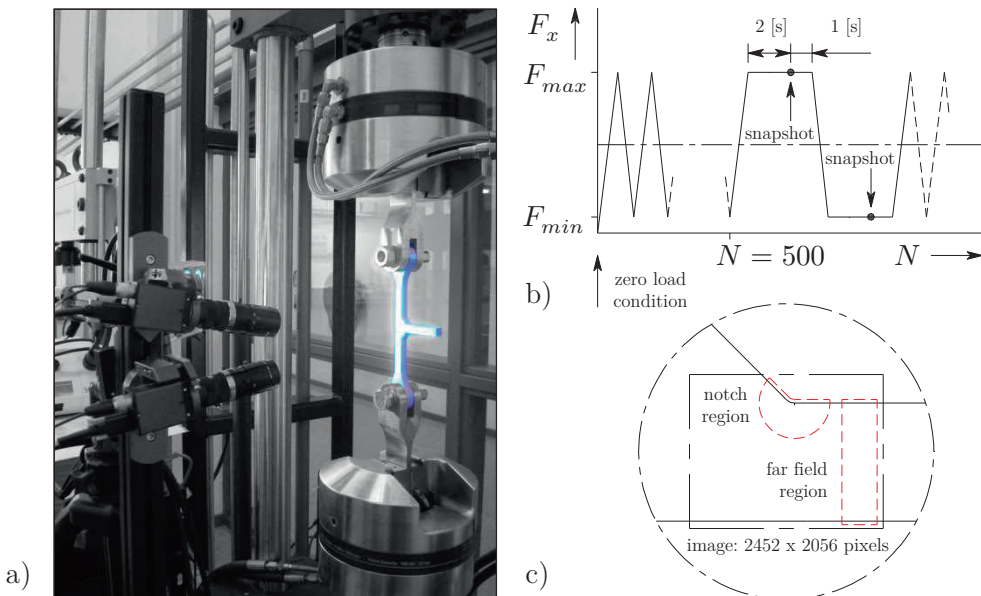


Figure 4.35: a) Test setup, b) loading scheme, c) SSS notch- and far field region.

The displacement field kinematic basis is a key issue to obtain accurate notch- and far field region information. As a first step in the analysis procedure, displacement fields are estimated on a general kinematic basis using commercial DIC software Istra4D (Dantec Dynamics). A posteriori, the displacement fields are decomposed onto a dedicated one, providing the far field stress, crack tip location and SIF. A note in advance: estimating the displacement field directly using the dedicated kinematic basis in an integrated approach may increase the accuracy (Roux and Hild, 2006) – in particular close to the specimen edges and around the crack(tip) – and is considered to be the next step, since out-of-plane displacements might be involved.

4.4.3 Digital image correlation principles

Processing 2 digital images, 1 captured before and 1 after object deformation using a single or stereo camera setup, 2D or 3D displacements $\mathbf{u}(\mathbf{x})$ and displacement derivatives can be estimated by matching (correlating) the image textures $f(\mathbf{x})$ and $g(\mathbf{x})$; light intensity (grey level) distributions, if optical flow conservation is satisfied:

$$g(\mathbf{x}) = f(\mathbf{x} + \mathbf{u}(\mathbf{x})) \quad (4.24)$$

Areas with pixels (equivalent: subset, facet, zone of interest (ZOI), correlation window) rather than single pixels are used to perform the correlation process because a single pixel has no unique signature. The system (Eq. 4.24) is ill-conditioned and require displacement field constraints, since $\mathbf{u}(\mathbf{x})$ has to be regular and smooth. Applying a low-pass filter is one option, but alternatively a subspace of suitable or even dedicated displacement functions $\mathbf{v}(\mathbf{x})$ can be adopted, e.g. FE based formulations (Hild and Roux, 2006). In particular cases, Airy stress functions like Williams' (generalised) asymptotic solution can be selected as well and operate as a mechanical filter. In order to ensure a unique grey level distribution for each subset, the texture should be random. If the observed (material) texture does not meet this criterion, an artificial random pattern must be applied.

Selecting a single subset from a 2D image before deformation (the reference image), the image after deformation is searched for the same grey level distribution (Fig. 4.36a). Assumption: the grey level distribution does not change during deformation, meaning a one-to-one correspondence exists. The displacement fields $u_x(x, y)$ and $u_y(x, y)$ force the subset centre point $P(x_p, y_p)$ to shift to $P^*(x_p^*, y_p^*)$:

$$\left\{ \begin{array}{l} x_p^* = x_p + u_x(x, y) \\ y_p^* = y_p + u_y(x, y) \end{array} \right\} \quad (4.25)$$

For a linear deformation approximation (the subset size should be small enough), the subset displacement gradients are constant and location $Q(x_q, y_q)$ in the same subset becomes $Q^*(x_q^*, y_q^*)$:

$$\left\{ \begin{array}{l} x_q^* = x_q + u_x(x, y) + \frac{\partial u_x}{\partial x} dx + \frac{\partial u_x}{\partial y} dy \\ y_q^* = y_q + u_y(x, y) + \frac{\partial u_y}{\partial x} dx + \frac{\partial u_y}{\partial y} dy \end{array} \right\} \quad (4.26)$$

The 2 displacement components and 4 displacement gradients (providing strain information) have to be solved for. Note the subset deforms as a parallelogram. The adopted subset deformation approximation is basically a smoothness assumption, meaning each subset behaves as a low-pass filter. Higher order displacement gradients can be included to allow for more complicated subset deformations.

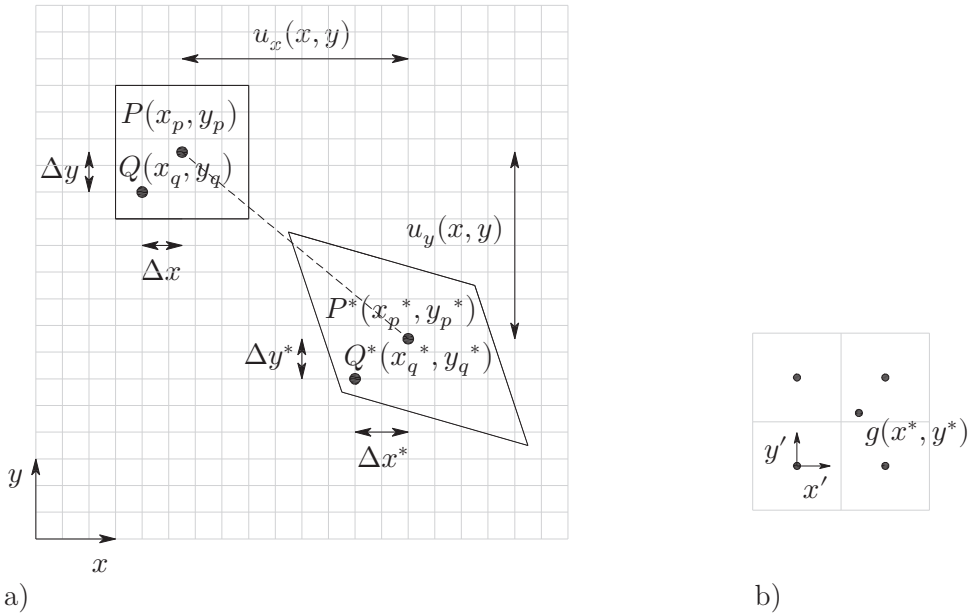


Figure 4.36: a) Subset before and after deformation, b) sub-pixel interpolation.

Generally speaking, $\{P^*, Q^*\}$ are located in between pixel positions. Grey levels are not available at these points and interpolation is required. Adopting a bi-linear interpolation scheme; an affine transformation (alternatives: bi-cubic or spline interpolation schemes), the grey level $g(x^*, y^*)$ between 4 surrounding pixels (Fig. 4.36b) is obtained as:

$$g(x^*, y^*) = a_0 + a_1 x' + a_2 y' + a_3 x' y' \quad (4.27)$$

Note that $g(x^*, y^*)$ is a continuous grey scale distribution. The constants a_n are estimated using the locations and grey level values of the surrounding pixels. To represent the correlation for each subset, a least squares based correlation coefficient Φ is defined:

$$\Phi = \sum_{\text{pixel}} \{g(x^*, y^*) - f(x, y)\}^2 \quad (4.28)$$

and at image level:

$$\Phi = \sum_{\text{subset}} \{g(\mathbf{x} + \mathbf{u}) - f(\mathbf{x})\}^2 \quad (4.29)$$

Minimising Φ , an optimisation problem, the design variables (displacements and displacement gradients) can be obtained.

The subset size strongly influences measurement accuracy (Huang, 2012). For areas with small (uniform) displacement or strain distributions, like the far field region, the random- or statistical error (noise and illumination fluctuations) associated with subset quality dominates – generally speaking – the systematic error (e.g. DIC algorithm induced). It means that an increased subset size is preferred to reduce the random error as it contains more information in terms of grey level distribution. However, the accuracy close to the specimen edge decreases because of the increased chance of a mismatch between subset boundary and specimen edge. On the other hand, for the notch region containing relative large strains because of the (weld) geometry related strain concentration and a crack induced displacement field discontinuity, a smaller subset size is recommended because of the increased systematic error. Consequently, DIC is a trade-off between displacement (and strain) accuracy and spatial resolution. Increasing the subset size increases accuracy, correlation, but decreases spatial resolution. The same applies vice versa.

4.4.4 Texture quality

To estimate a priori the predominantly texture quality determined DIC displacement measurement performance, global and local quality indicators are introduced to analyse the notch and far field area using the reference image. Painting the specimens respectively satin white (using a spray can) and black (using an airbrush system), an artificial texture (Fig. 4.37 and 4.38) is obtained.

The (8-bit depth) grey level distribution histogram, e.g. the one (Fig. 4.39) corresponding to the far field region (Fig. 4.37), is a global texture quality indicator: as wide as possible to employ the full dynamic grey level range maximising the grey level characteristic and without any (white colour) saturation to prevent for reflection.

Considering the texture random character, each subset grey level distribution is unique. To evaluate whether a subset contains enough information for a proper analysis, the subset grey level standard deviation, a local quality and sensitivity indicator, has been introduced (Hild and Roux, 2008). Note: the higher its value, the better. Adopting the normal distribution $N(\mu, \sigma)$, a practical criterion has been found to be 1 [%] of the subset grey level range: for an 8-bit depth grey level distribution the subset grey level range should approximately be in between 11, i.e. $N(\mu \pm 2\sigma)$, and 15, i.e. $N(\mu \pm 3\sigma)$. Below, the grey level gradient is not enough to capture displacements. For the considered texture, all 5-pixel subsets already satisfy this criterion (Fig. 4.40); $\sigma_{mean} \approx 16$ [pixel]. Although developed for the Q4-DIC procedure, a Q4 (bi-linear) FE based subset displacement formulation (Hild and Roux, 2008) and affine transformation (Dantec Dynamics) use the same number of constants to be estimated, i.e. the criterion is considered to be a general one since a linear kinematic basis approximation holds for many DIC procedures, regardless the different correlation procedures.

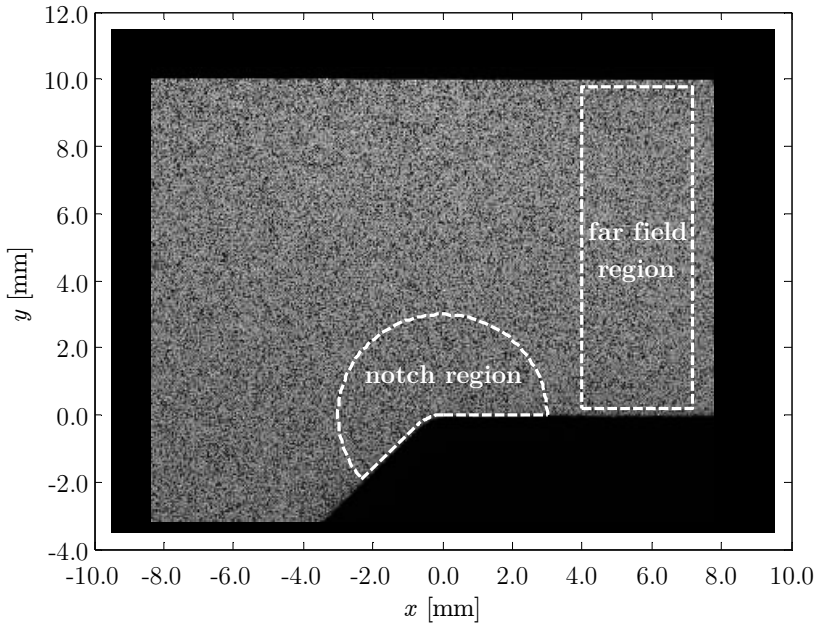


Figure 4.37: Specified far field- and notch region in typical DIC (reference) image.

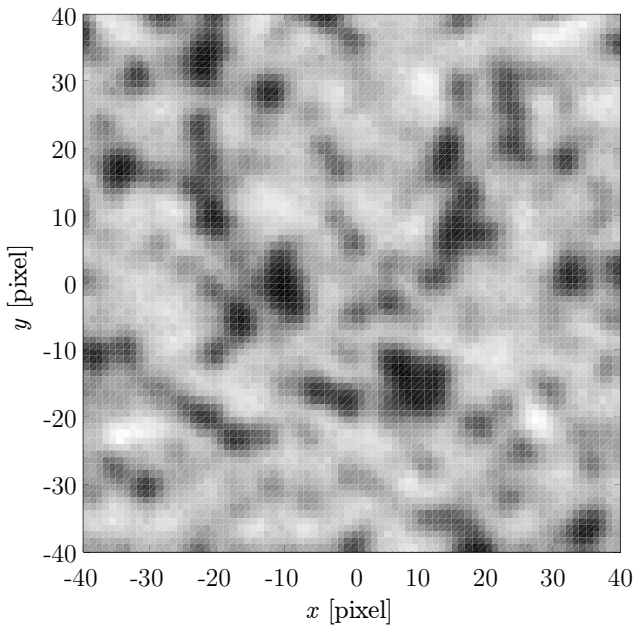


Figure 4.38: Typical texture close up (far field centre Fig. 4.37).

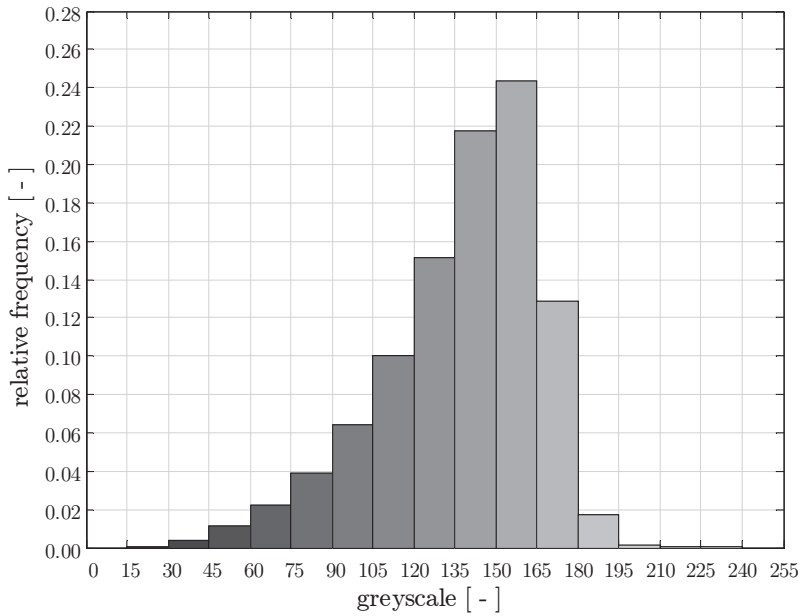


Figure 4.39: Typical (8-bit) grey level distribution histogram (far field Fig. 4.37).

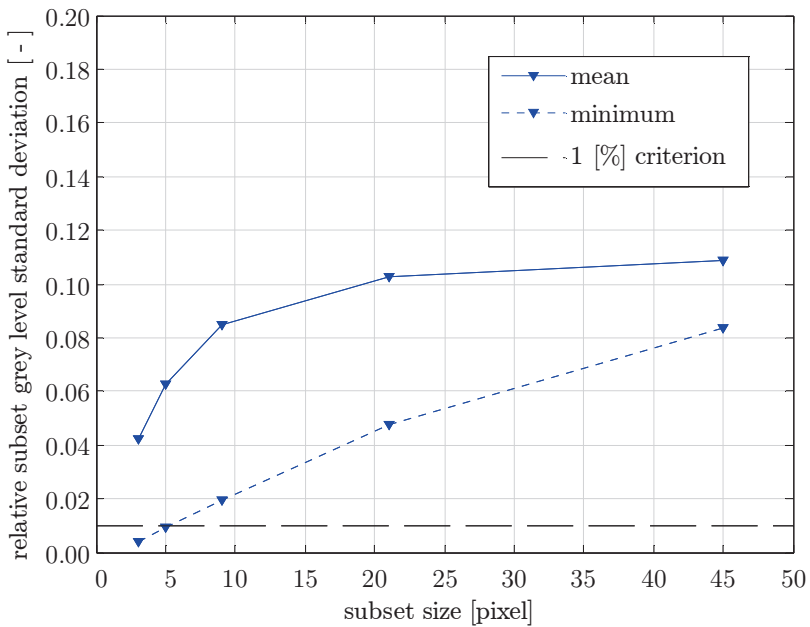


Figure 4.40: Typical subset grey level standard deviation (far field Fig. 4.37).

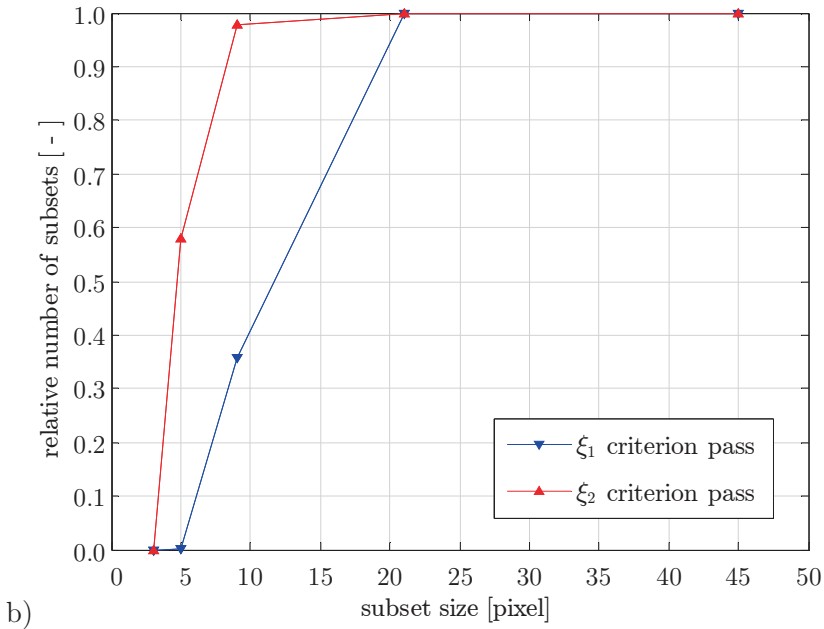
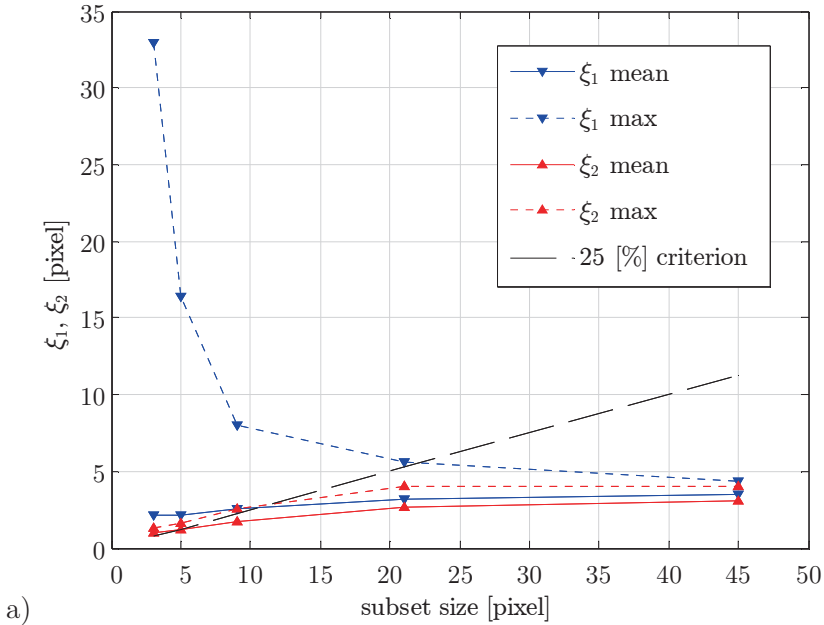


Figure 4.41: Typical subset correlation radii passing criterion (far field Fig. 4.35).

Another significant criterion involves the subset (auto)correlation radii $\{\xi_1, \xi_2\}$; physically defining an ‘equivalent’ speckle size, a self-similarity measure. For each subset $\{\xi_1, \xi_2\}$ should be as small as possible to ensure its texture grey level distribution is unique. A practical criterion has been found to be 25 [%] of the subset size (Hild and Roux, 2008). Approximate $\{\xi_1, \xi_2\}$ values are obtained using a parabolic interpolation of the autocorrelation function at the subset centre and involves only the 8 neighbour pixels, i.e. the autocorrelation radii are the ellipse principal axis lengths in $\{x, y\}$ direction. The ratio of the $\{\xi_1, \xi_2\}$ values is a texture anisotropy measure and proved typically to be quite isotropic as preferred with some outliers (Fig. 4.41). For a subset size ≥ 21 [pixels] the adopted criterion is satisfied.

4.4.5 Far field region analysis

Following the a-priori texture quality analyses results, a subset size of 21 [pixel] has been selected and the displacement fields $\{u_x, u_y\}$ are obtained using Istra4D (Fig. 4.42). Subsets close to the specimen edge are ignored because of the subset boundary and specimen edge mismatch induced inaccuracy. The observed displacement range is in the order of a few microns and some noise can be identified.

The SIF related far field information, the linear far field stress distribution, requires strain. The amplitudes are expected to be very small. Sufficiently accurate and smooth strain fields can only be obtained using (mechanically) filtered displacement fields – disregarding an increased subset size for the moment. A polynomial filter, e.g. a Savitzky-Golay smoothing and differentiation filter or Airy stress function, has the important advantage that strain, spatial displacement derivatives, quite easily can be obtained. Selecting an appropriate Airy stress function:

$$\varphi = C_{22}y^2 + C_{33}y^3 \quad (4.30)$$

the stress components σ_{ij} in Cartesian coordinates become by definition:

$$\begin{aligned} \sigma_{xx} &= \frac{\partial^2 \varphi}{\partial y^2} = 2C_{22} + 6C_{33}y \\ \sigma_{yy} &= \frac{\partial^2 \varphi}{\partial x^2} = 0 \\ \sigma_{xy} &= -\frac{\partial^2 \varphi}{\partial x \partial y} = 0 \end{aligned} \quad (4.31)$$

The bi-harmonic equation is identically satisfied. Introducing the stress-strain relations, Hooke’s law, assuming a plane stress condition – DIC is a surface measurement technique:

$$\begin{aligned}\varepsilon_{xx} &= \frac{(\kappa + 1)\sigma_{xx} - (3 - \kappa)\sigma_{yy}}{8G} = \frac{(\kappa + 1)(6C_{33}y + 2C_{22})}{8G} \\ \varepsilon_{yy} &= \frac{(\kappa + 1)\sigma_{yy} - (3 - \kappa)\sigma_{xx}}{8G} = -\frac{(3 - \kappa)(6C_{33}y + 2C_{22})}{8G}\end{aligned}\quad (4.32)$$

$$\varepsilon_{xy} = \frac{\sigma_{xy}}{2G} = 0$$

with Kolosov's constant

$$\kappa = \frac{(3 - \nu)}{(1 + \nu)}$$

and the small strain-displacement relations

$$\begin{aligned}\varepsilon_{xx} &= \frac{\partial u_x}{\partial x} \\ \varepsilon_{yy} &= \frac{\partial u_y}{\partial y}\end{aligned}\quad (4.33)$$

$$\varepsilon_{xy} = \frac{1}{2} \left(\frac{\partial u_y}{\partial x} + \frac{\partial u_x}{\partial y} \right)$$

the displacement field in complex coordinates is obtained

$$\begin{aligned}\mathbf{u}(z) &= u_x + iu_y \\ &= \sum_k C_k \Psi_k \\ &= C_x + C_y \cdot i + C_r \cdot (ix - y) + \\ &\quad \left(\frac{C_{22}}{G} \right) \cdot \frac{2(\kappa + 1)x - 2(3 - \kappa)iy}{8} + \\ &\quad \left(\frac{C_{33}}{G} \right) \cdot \frac{-3(\kappa + 1)ix^2 + 6(\kappa + 1)xy - 3(3 - \kappa)iy^2}{8}\end{aligned}\quad (4.34)$$

including the rigid body terms. Assuming the Poisson ratio $\nu = 0.33$ [-], the Istra4D displacement field is decomposed onto the dedicated kinematic basis (Eq. 4.34; Fig. 4.43). The amplitudes C_k have been obtained solving the system $[\Psi]\{C\} = \{\mathbf{u}(z)_{\text{Istra4D}}\}$. Since $[\Psi]$ is non-square (i.e. contains more rows than columns) and rank-deficient (rigid body motions are included), its inverse $[\Psi]^{-1}$ does not exist. The pseudo inverse $[\Psi]^+$ is calculated containing some, but not all, $[\Psi]^{-1}$ properties. The system is overdetermined and provides least squares approximate solutions, i.e. $\min_{\{C\}} \|[\Psi]\{C\} - \{\mathbf{u}(z)_{\text{Istra4D}}\}\|^2$, meaning $\{C\} = [\Psi]^+\{\mathbf{u}(z)_{\text{Istra4D}}\}$ is the most likely one out of the infinitely many available.

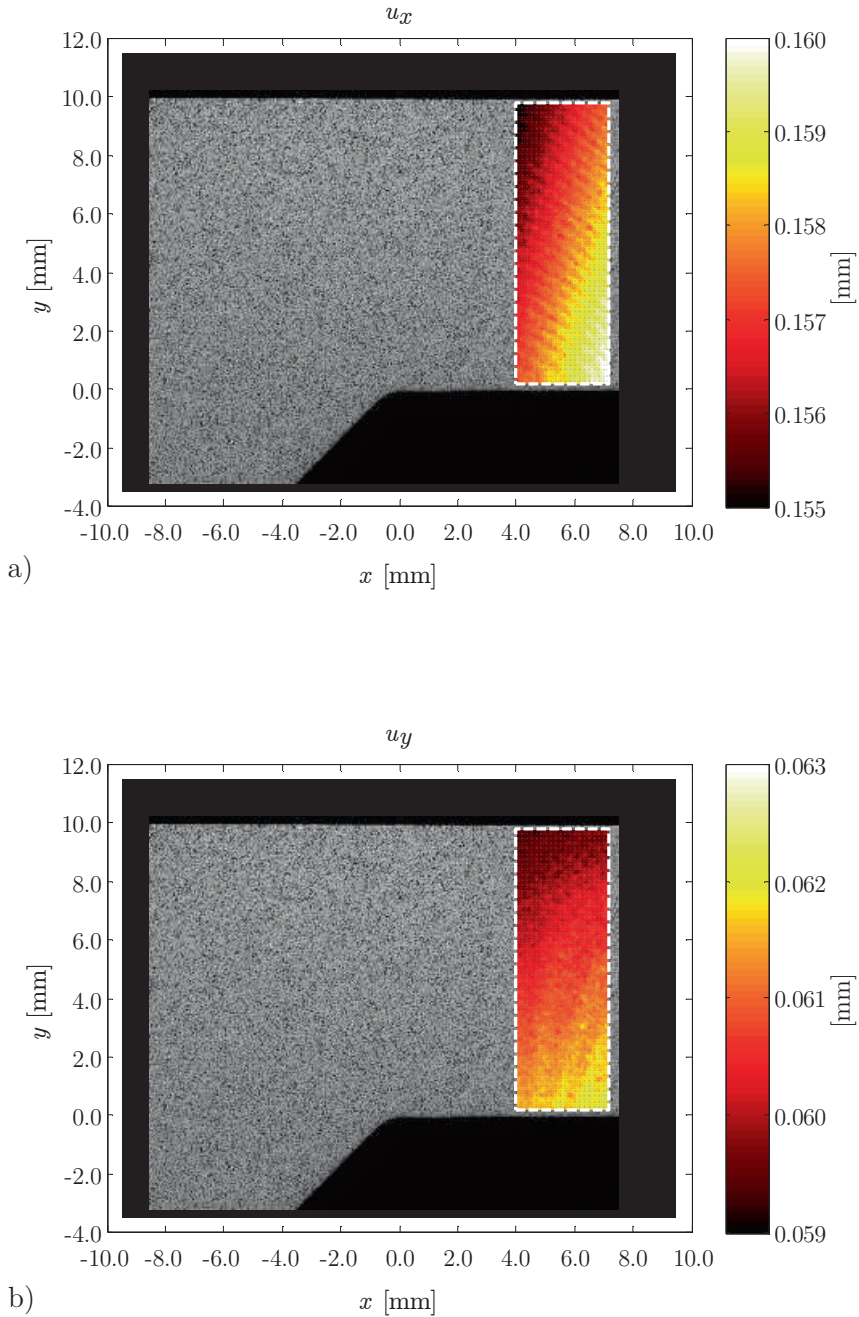


Figure 4.42: Typical Istra4D displacement fields $\{u_x, u_y\}$ including rigid body motions; M-series in maximum load condition (far field Fig. 4.35).

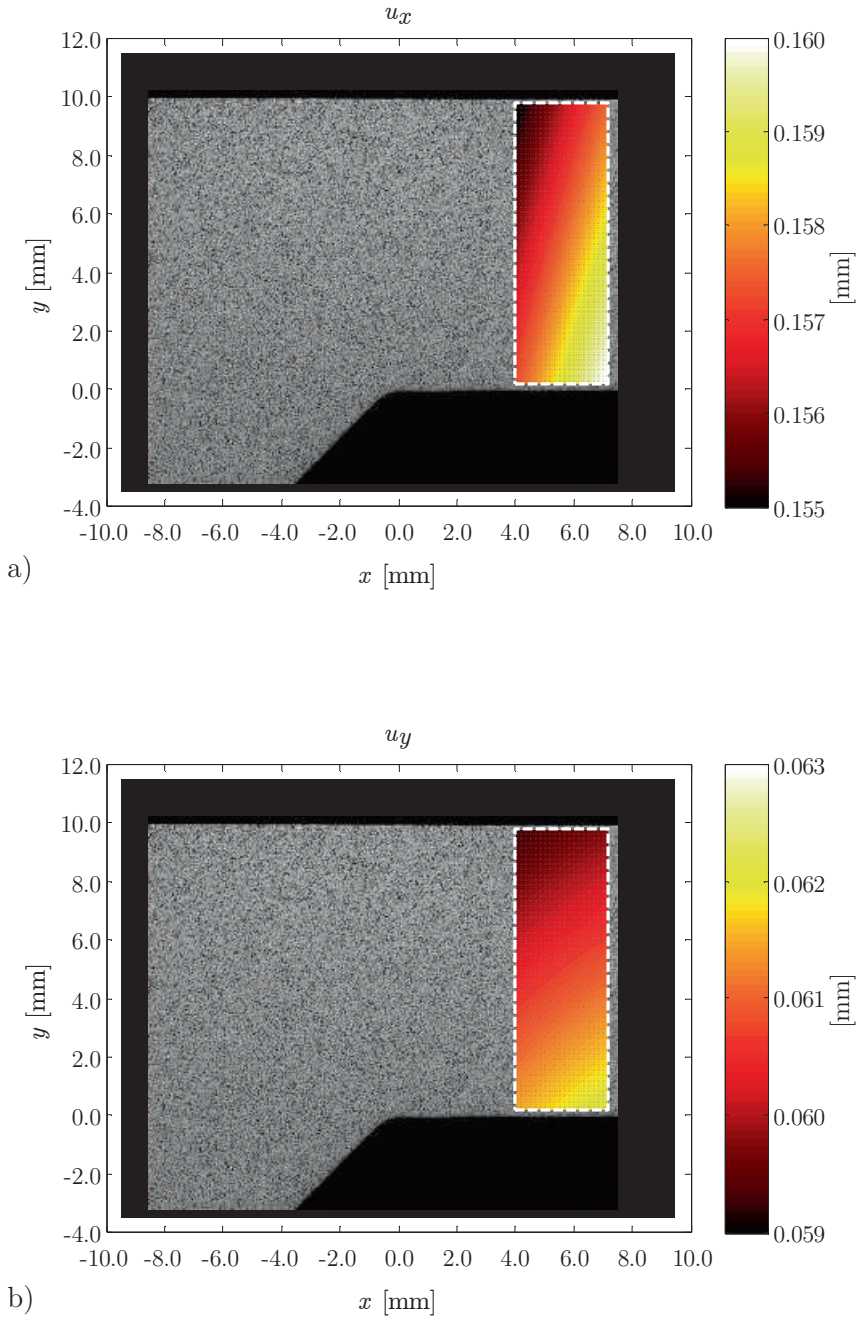


Figure 4.43: Typical subspace displacement fields (Eq. 4.34) including rigid body motions; M-series in maximum load condition (far field Fig. 4.35).

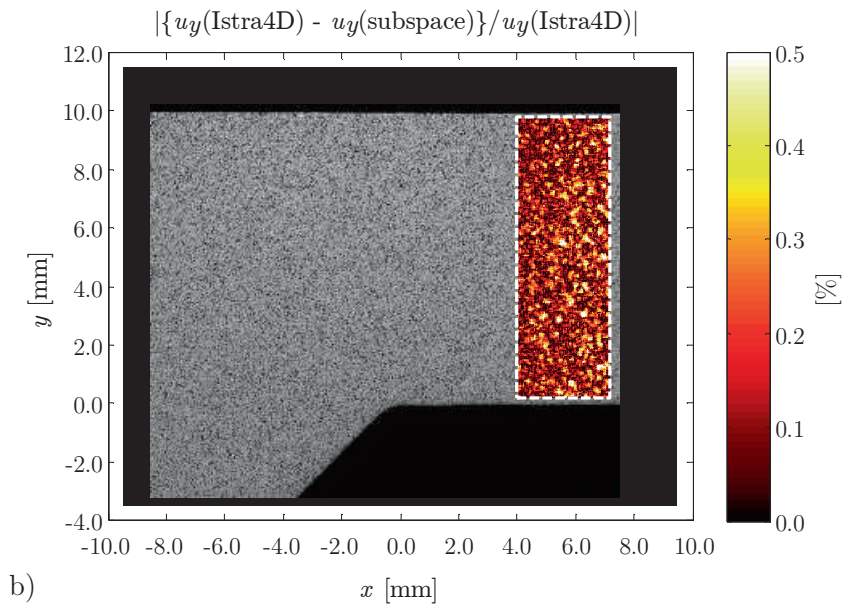
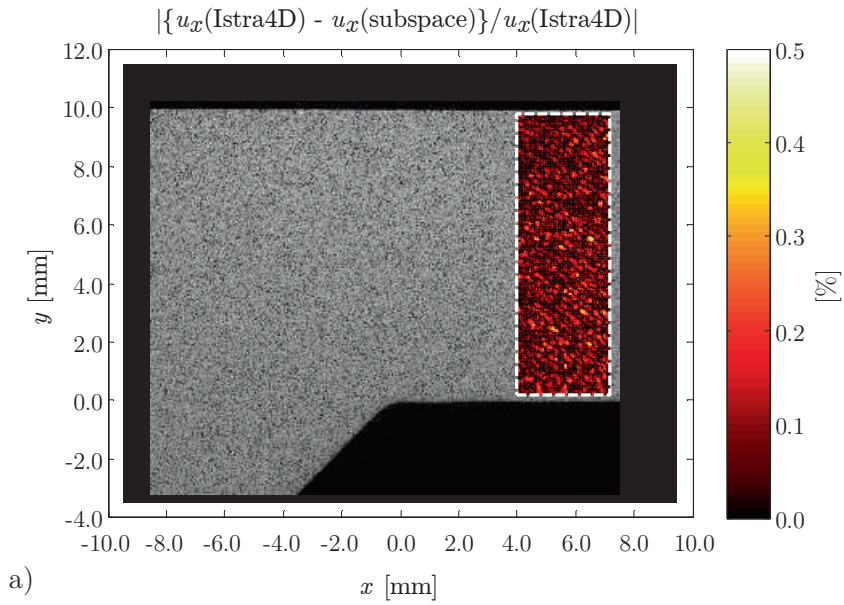


Figure 4.44: Typical displacement field error; M-series in maximum load condition (far field Fig. 4.35).

The relative displacement error (Fig. 4.44) $\sim N(0, \sigma)$ appears to be ≤ 0.5 [%]. The displacement field amplitude- and relative error ratios seem inversely proportional, i.e. the u_y error standard deviation is somewhat larger compared to the u_x value.

Using direct numerical Istra4D displacement field $\{u_x, u_y\}$ differentiation to obtain the strain fields $\{\varepsilon_{xx}, \varepsilon_{yy}, \varepsilon_{xy}\}$ without filtering is unreliable because of the noise amplification. In the adopted subspace, ε_{xx} (Eq. 4.32; Fig. 4.45) shows a linear variation in y -direction, i.e. a small bending component can be identified.

At the same time each image is taken, the applied force F_x is measured. For the considered image, $F_x = 5462$ [N]. Taking the actual specimen width $w = 9.65$ [mm] and base plate thickness $t_b = 10$ [mm] into account, the membrane stress component can be calculated: $\sigma_m = 57$ [MPa] and the shear modulus G estimated using the stress formulations (Eq. 4.31):

$$G = \frac{\sigma_m}{2 \cdot C_{02}} \quad (4.35)$$

However, $G = 25.2$ [GPa], a plane stress value and small in comparison to an engineering plane strain value $G = 26.3$ [GPa]; approximately 4 [%] difference. Other images at maximum load condition for the considered specimen ($\Delta F_x = 5000$) provide the same result. The stress components (Table 4.1, including a few more results) would become $\sigma_m = 58$ [MPa] and $\sigma_b = 1$ [MPa], meaning the structural stress and structural bending stress ratio turn out to be $\{\sigma_s, r_s\} = \{59, 0\}$.

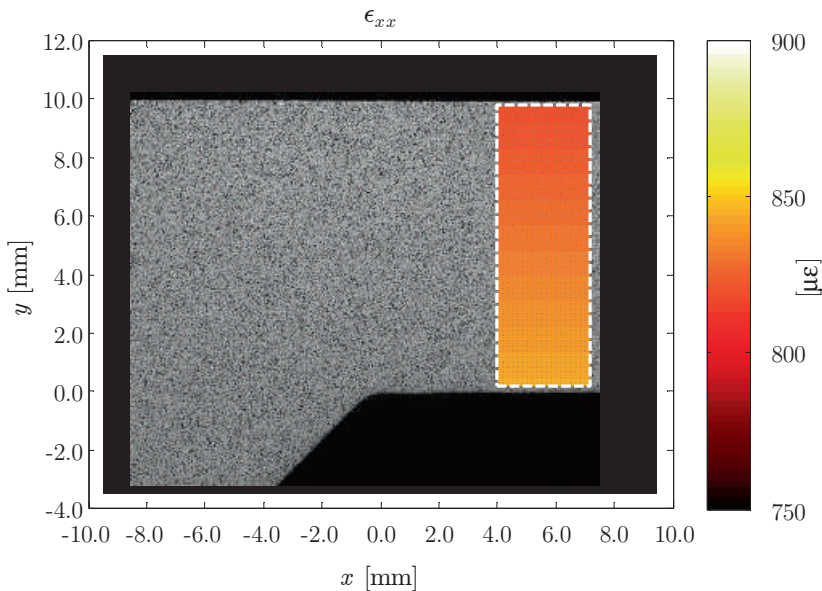


Figure 4.45: Typical subspace strain field ε_{xx} ; M-series in maximum load condition (far field Fig. 4.37).

Because of the small far field bending components, geometric non-linear behaviour might be involved. Finite element analysis results and measurement values agree quite well.

The solutions C_k are converged for a far field region width ≥ 1.5 [mm]. Normal approximated displacement amplitude confidence bounds (CB's) are calculated using the covariance matrix $[\Psi^T \Psi]^+$ to investigate the uncertainty. However, because of the limited number degrees of freedom (DoF), small grid spacing and significant far field region size, the two-sided 95 [%] CB's basically equal the LS parameter estimate.

case	F_x [N]	σ_m [MPa]	σ_m (th) [MPa]	σ_b [MPa]	σ_b (th) [MPa]	σ_b (th non-lin) [MPa]
5000 M max	5462	58	57	1	0	1
6500 M max	7138	75	74	2	0	2
10500 M max	11536	118	119	3	0	5

Table 4.1: Some SSS M-series far field stress distribution parameters; a comparison of DIC estimated- and theoretical calculated values.

Together with the analysis results in minimum load condition, the far field stress information $\{\Delta\sigma_s, r_s, r_l\}$ can be obtained at all predefined load range levels for the non-welded and welded {MBN, M, MBM} series. Any sequence of 2 images can be used, although preferably in a stage the crack size is still small. Except meant to verify the imposed loading, $\{\Delta\sigma_s, r_s, r_l\}$ is very helpful to investigate the fatigue resistance as well (Paragraph 5.4.1).

4.4.6 Notch region analysis

To obtain a reliable crack tip location and SIF estimate at the same time, the notch region is investigated as well. At a weld toe, K_I (Eq. 3.2) includes an explicit notch- and far field component $\{Y_n, Y_f\}$, respectively related to the self-equilibrating and equilibrium equivalent stress part. In an attempt to be able to distinguish the separate Y_n contribution, the intact geometry based displacement field is defined first. Adopting Williams' solution (Eq. 2.1) to include the V-shaped notch stress and selected terms of the general Michell solution in Polar coordinates (Barber, 2002) to add the (linear) weld load carrying stress, the Airy stress function becomes:

$$\begin{aligned} \varphi = r^{\lambda+1} \cdot [C_1 \cos\{(\lambda+1)\theta\} + C_2 \cos\{(\lambda-1)\theta\} + \\ C_3 \sin\{(\lambda+1)\theta\} + C_4 \sin\{(\lambda-1)\theta\}] + \\ A_{11}r^3 \cos(\theta) + B_{22}r^3 \sin(\theta) \end{aligned} \quad (4.36)$$

The notch term amplitudes $\{C_1, C_2, C_3, C_4\}$ can be related to $\{K_I^N, K_{II}^N\}$ by definition (Eq. 3.20 and 3.21). Using the (constitutive) linear stress-strain relations

$$\begin{aligned} \varepsilon_{rr} &= \frac{(\kappa+1)\sigma_{rr} - (3-\kappa)\sigma_{\theta\theta}}{8G} \\ \varepsilon_{\theta\theta} &= \frac{(\kappa+1)\sigma_{\theta\theta} - (3-\kappa)\sigma_{rr}}{8G} \end{aligned} \quad (4.37)$$

$$\varepsilon_{r\theta} = \frac{\sigma_{r\theta}}{2G}$$

and (kinematic) small strain-displacement formulations

$$\begin{aligned} \varepsilon_{rr} &= \frac{\partial u_r}{\partial r} \\ \varepsilon_{\theta\theta} &= \frac{1}{r} \frac{\partial u_\theta}{\partial \theta} + \frac{u_r}{r} \\ \varepsilon_{r\theta} &= \frac{1}{2} \left(\frac{1}{r} \frac{\partial u_r}{\partial \theta} + \frac{\partial u_\theta}{\partial r} - \frac{u_\theta}{r} \right) \end{aligned} \quad (4.38)$$

the ($\rho = 0$) notch displacement field in complex coordinates denotes:

$$\mathbf{u}(z) = C_x + C_y \cdot i + C_r \cdot i(r \cdot e^{i\theta}) + \quad (4.39)$$

$$\left(\frac{K_I^N}{G}\right) \cdot \frac{r^{\lambda_s}}{2(2\pi)^{1-\lambda_s} \lambda_s (\lambda_s + 1) (\chi_s - 1)} \cdot \{\chi_s \kappa \cdot e^{i\lambda_s \theta} - \chi_s \lambda_s \cdot e^{-i(\lambda_s - 2)\theta} + (\lambda_s + 1) \cdot e^{-i\lambda_s \theta}\} +$$

$$\left(\frac{K_{II}^N}{G}\right) \cdot i \cdot \frac{r^{\lambda_a}}{2(2\pi)^{1-\lambda_a} \lambda_a \{\chi_a (\lambda_a - 1) - (\lambda_s + 1)\}} \cdot \{\chi_a \kappa \cdot e^{i\lambda_a \theta} + \chi_a \lambda_a \cdot e^{-i(\lambda_a - 2)\theta} - (\lambda_a + 1) \cdot e^{-i\lambda_a \theta}\} +$$

$$\left(\frac{A_{11}}{G}\right) \cdot \frac{(\kappa \cdot e^{i2\theta} - 2)}{2} \cdot r^2 + \left(\frac{B_{11}}{G}\right) \cdot i \cdot \frac{(\kappa \cdot e^{-i2\theta} - 2)}{2} \cdot r^2$$

In order to verify \mathbf{u} (Eq. 4.39), a SSS geometry ($\rho = 0$) FE solution (Fig. 4.46 including white Gaussian noise; SNR = 80) – grid spacing 0.02 [mm] and notch region radius 3.0 [mm] – has been decomposed (Fig. 4.47). The relative displacement error (Fig. 4.48) shows that when passing the weld toe cross-section (from right to left) the error slightly increases, i.e. to satisfy the boundary conditions (BC's) in Quadrant-III higher order terms are required.

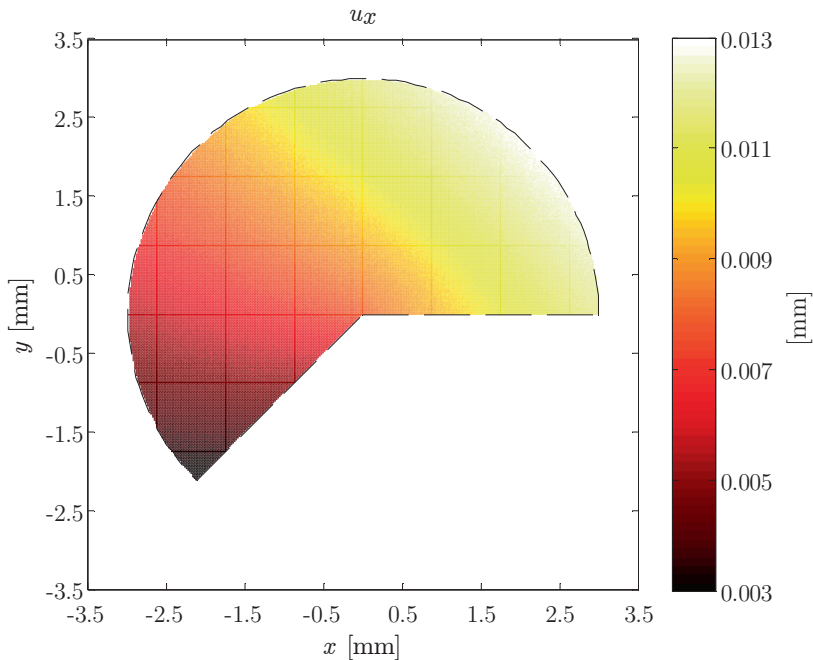


Figure 4.46: Typical SSS geometry ($\rho = 0$) Ansys notch displacement field u_x incl. white Gaussian noise; M-series in maximum load condition.

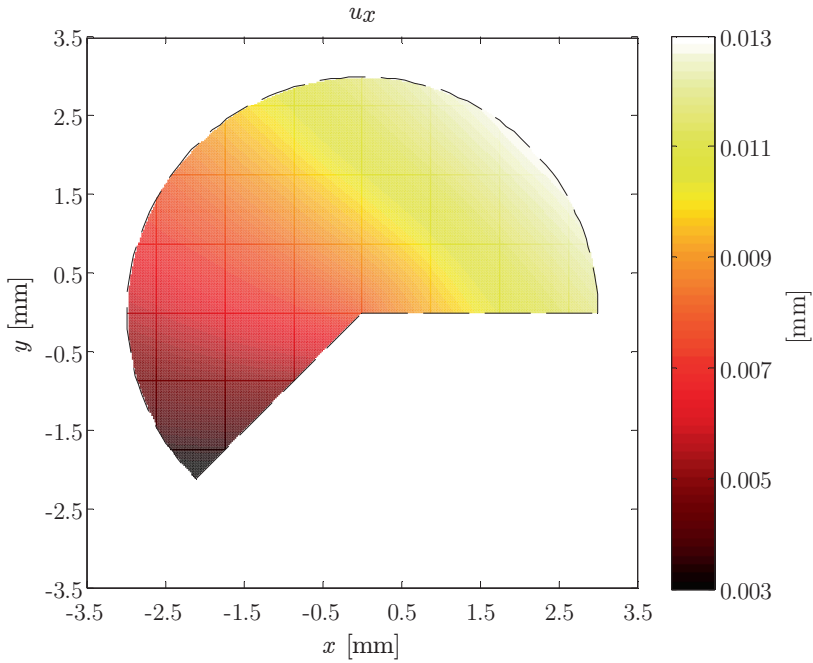


Figure 4.47: Subspace displacement field u_x ; M-series in maximum load condition.

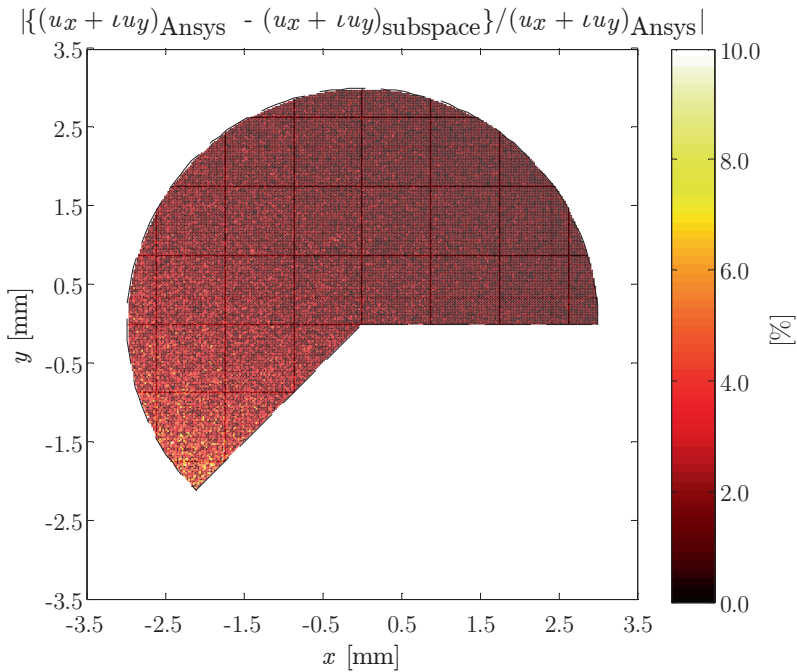


Figure 4.48: Relative displacement field error; M-series in maximum load condition.

Similarly, using the blunt body notch stress formulations (Eq. A.1 to A.3), constitutive equations (Eq. 4.37) and kinematic relations (Eq. 4.38), the ($\rho > 0$) displacement field can be derived:

$$\begin{aligned}
 \mathbf{u}(z) = & C_x + C_y \cdot i + C_r \cdot i(r'' \cdot e^{i\theta}) + \tag{4.40} \\
 & \left(\frac{K_I^N}{G}\right) \cdot \frac{1}{2(2\pi)^{1-\lambda_s} \lambda_s (\lambda_s + 1) (\chi_s - 1)} \cdot \\
 & [(r'')^{\lambda_s} \{\chi_s \kappa \cdot e^{i\lambda_s \theta} - \chi_s \lambda_s \cdot e^{-i(\lambda_s - 2)\theta} + (\lambda_s + 1) \cdot e^{-i\lambda_s \theta}\} + \\
 & r_0^{\lambda_s - \zeta_s} \cdot \frac{\left(\frac{2\alpha}{\pi}\right)}{4 \left\{\left(\frac{2\alpha}{\pi}\right) - 1\right\}} \cdot \left(\frac{\lambda_s}{\zeta_s}\right) \cdot \\
 & (r'')^{\zeta_s} \{-\omega_{s2} \kappa \cdot e^{i\zeta_s \theta} + \omega_{s2} \zeta_s \cdot e^{-i(\zeta_s - 2)\theta} + \omega_{s1} \cdot e^{-i\zeta_s \theta}\}] + \\
 & \left(\frac{K_{II}^N}{G}\right) \cdot \frac{1}{2(2\pi)^{1-\lambda_a} \lambda_a \{\chi_a (\lambda_a - 1) - (\lambda_s + 1)\}} \cdot \\
 & i \cdot [(r'')^{\lambda_a} \{\chi_a \kappa \cdot e^{i\lambda_a \theta} + \chi_a \lambda_a \cdot e^{-i(\lambda_a - 2)\theta} - (\lambda_a + 1) \cdot e^{-i\lambda_a \theta}\} + \\
 & r_0^{\lambda_a - \zeta_a} \cdot \frac{1}{4(\zeta_a - 1)} \cdot \left(\frac{\lambda_a}{\zeta_a}\right) \cdot \\
 & (r'')^{\zeta_a} \{-\omega_{a2} \kappa \cdot e^{i\zeta_a \theta} - \omega_{a2} \zeta_a \cdot e^{-i(\zeta_a - 2)\theta} - \omega_{a1} \cdot e^{-i\zeta_a \theta}\}] + \\
 & \left(\frac{A_{11}}{G}\right) \cdot \frac{(\kappa \cdot e^{i2\theta} - 2)}{2} \cdot r^2 + \left(\frac{B_{11}}{G}\right) \cdot i \cdot \frac{(\kappa \cdot e^{-i2\theta} - 2)}{2} \cdot r^2
 \end{aligned}$$

The V-shaped notch- and weld load carrying component coordinate system origin (Fig. 2.49) is respectively $\{O'', O\}$. Although somewhat arbitrary (Lazzarin and Filippi, 2006), the crack initiation related (intact geometry) NSIF parameter definitions are unchanged, meaning the $\{K_I^N, K_{II}^N\}$ values remain the same for ($\rho > 0$). SSS geometry ($\rho = 1$) FE displacement field solutions (e.g. Fig. 4.49 to 4.51) show comparable results with respect to the ($\rho = 0$) case (Fig. 4.46 to 4.48).

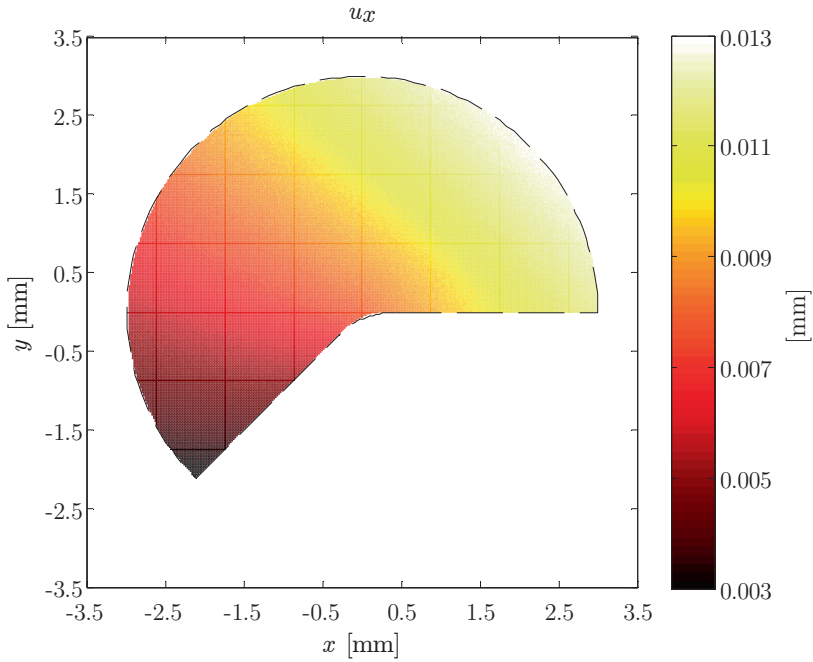


Figure 4.49: Typical SSS geometry ($\rho = 1$) Ansys notch displacement field u_x incl. white Gaussian noise; M-series in maximum load condition.

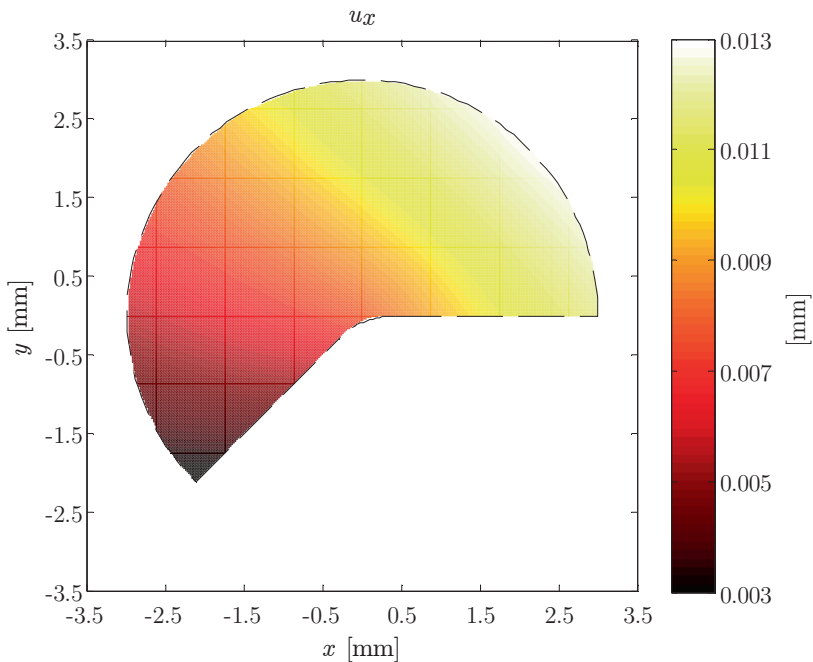


Figure 4.50: Subspace displacement field u_x ; M-series in maximum load condition.

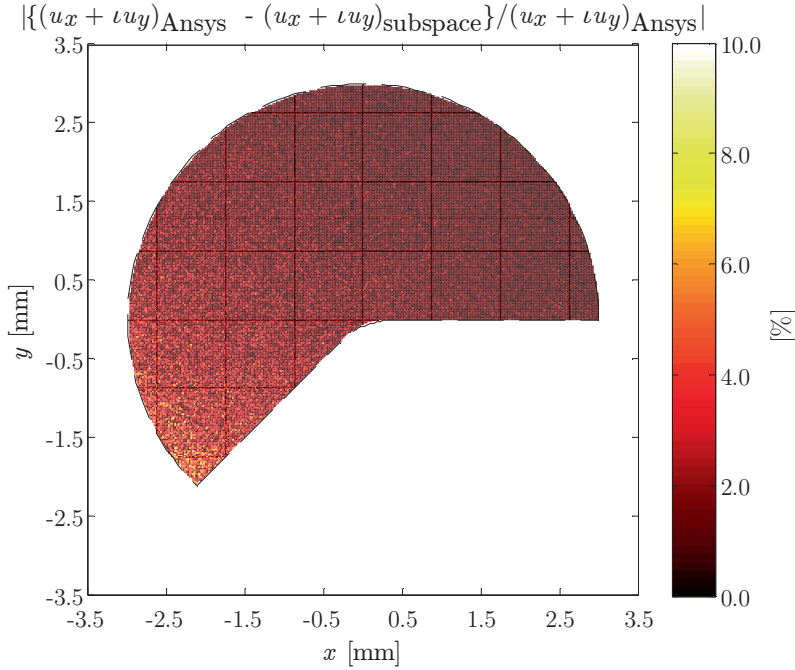


Figure 4.51: Relative displacement field error; M-series in maximum load condition.

Introducing nuclei or defects, cracks with initial size a_i , a (sharp) crack tip displacement field – Williams’ asymptotic solution in complex polar coordinates – can be obtained as well (Mathieu, Hild and Roux, 2011):

$$\mathbf{u}(z) = \sum_n \left\{ \left(\frac{\omega_n}{G} \right) \cdot \mathbf{\Omega}_n(z) + \left(\frac{v_n}{G} \right) \cdot \mathbf{\Psi}_n(z) \right\} \quad (4.41)$$

with

$$\mathbf{\Omega}_n(z) = \frac{(-1)^{\frac{1-n}{2}}}{2\sqrt{2\pi}} \cdot r^{\frac{n}{2}} \cdot \left[\kappa \cdot e^{\frac{in\theta}{2}} - \left(\frac{n}{2} \right) \cdot e^{\frac{i(4-n)\theta}{2}} + \left\{ (-1)^n + \frac{n}{2} \right\} \cdot e^{-\frac{in\theta}{2}} \right]$$

and

$$\mathbf{\Psi}_n(z) = i \cdot \frac{(-1)^{\frac{1-n}{2}}}{2\sqrt{2\pi}} \cdot r^{\frac{n}{2}} \cdot \left[\kappa \cdot e^{\frac{in\theta}{2}} + \left(\frac{n}{2} \right) \cdot e^{\frac{i(4-n)\theta}{2}} + \left\{ (-1)^n - \frac{n}{2} \right\} \cdot e^{-\frac{in\theta}{2}} \right]$$

The amplitudes ω_0 and v_0 associated with basis functions $\mathbf{\Omega}_0$ and $\mathbf{\Psi}_0$ correspond to the rigid body translations; ω_2 and v_2 coincide with the rigid body rotation and T-stress component. Amplitudes ω_1 and v_1 , correlated to the stress field singular terms (Eq. 2.13 to 2.15), yield respectively the mode-I and mode-II SIF.

The displacement field of crack damaged geometries like a weld toe notch region (Fig. 4.32) may require both a notch- and crack tip contribution. Higher order sub-singular crack tip terms ($n > 2$) accounting for effects like free surface BC's should be omitted to prevent the notch contribution (identically satisfying the BC's) to become frustrated. The SIF's (Eq. 4.41) are meant to reduce to the far field component $\{\omega_1 \rightarrow K_I^f, v_1 \rightarrow K_{II}^f\}$ and $\{K_I^N, K_{II}^N\}$ (Eq. 4.39 or 4.40) should provide the notch parts. However, both displacement formulations (Eq. 4.39 or 4.40 and Eq. 4.41) are principally local ones and the coordinate system origins are quite close to each other, in particular for small cracks. Stable $\{K_I^N, K_{II}^N, K_I^f, K_{II}^f\}$ solutions have been found difficult to obtain, even if a notch/crack tip mask is applied.

The adopted procedure to investigate the notch region is to estimate the remote mechanical loading induced SIF $\{K_I, K_{II}\}$ first using the crack tip displacement field (Eq. 4.41) including a sufficient number of sub-singular terms. The far field contribution can be reconstructed using $\{\sigma_s, r_s\}$ and available handbook solutions (Eq. 3.4); the difference provides the notch component.

For a subset size of 21 [pixel] – texture quality in notch- and far field region is similar – $\{u_x, u_y\}$ is obtained using Istra4D (Fig. 4.52). To take the displacement discontinuity around the crack into account, the notch region requires a subset match with the crack tip and free edges. However, no crack(tip) information is involved meaning a mismatch and consequently less accurate displacement field estimates.

A notch displacement field decomposition requires the crack tip position to be known. Assuming some location and introducing the first super-singular term, the amplitude ω_{-1} can be used to estimate the (1st order) crack tip offset d with respect to the exact location (Roux, Réthoré and Hild, 2009), i.e. respectively along- and normal to the crack employing the real and imaginary part.

$$d = 2 \cdot \frac{\omega_{-1}}{\omega_1} \quad (4.42)$$

Stable solutions (Fig. 4.53) have been obtained considering 1 sub-singular term only, (i.e. $n = -1..3$) and a notch region radius $r_n = 3.0$ [mm]. The relative displacement amplitude error (Fig. 4.54) is quite small; ≤ 0.5 [%]. Crack tip position convergence has been verified (Fig. 4.55). Applying a small crack tip mask; radius $r_c = 0.05$ [mm], stabilises the procedure. Because of the bias between estimated offset and actual location, the procedure is iterative. The notch related eigenvalues $\{\lambda_s, \lambda_a\}$ differ from the governing in crack configuration ($\lambda_1 = 1/2$).

Alternatively, a (sub pixel) grid of crack tip positions is considered and the minimum global residual r_g location naturally provides the actual one (Fig. 4.56; Roux and Hild, 2006).

$$r_g = \sum_i \|u_i(z)|\text{Istra4D} - u_i(z)|\text{subspace}\|^2 \quad (4.43)$$

The optimum tip position (white cross) is principally similar to the ω_{-1} estimate; 0.52 [mm] for the considered image. For small cracks, the super-singular term provides better (consistent) results.

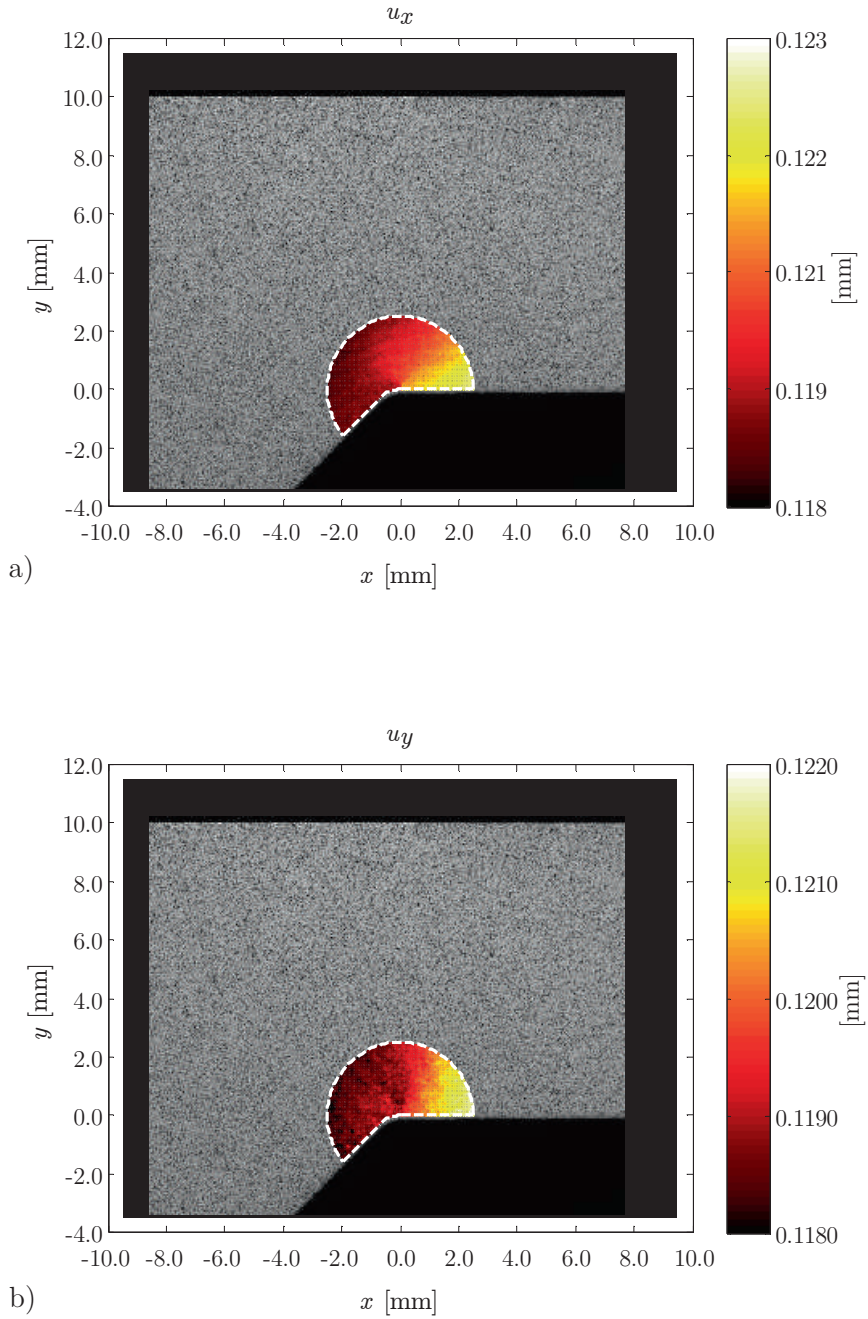


Figure 4.52: Typical Istra4D displacement fields $\{u_x, u_y\}$ including rigid body motions; M-series in max. load condition (notch Fig. 4.37; image 1001).

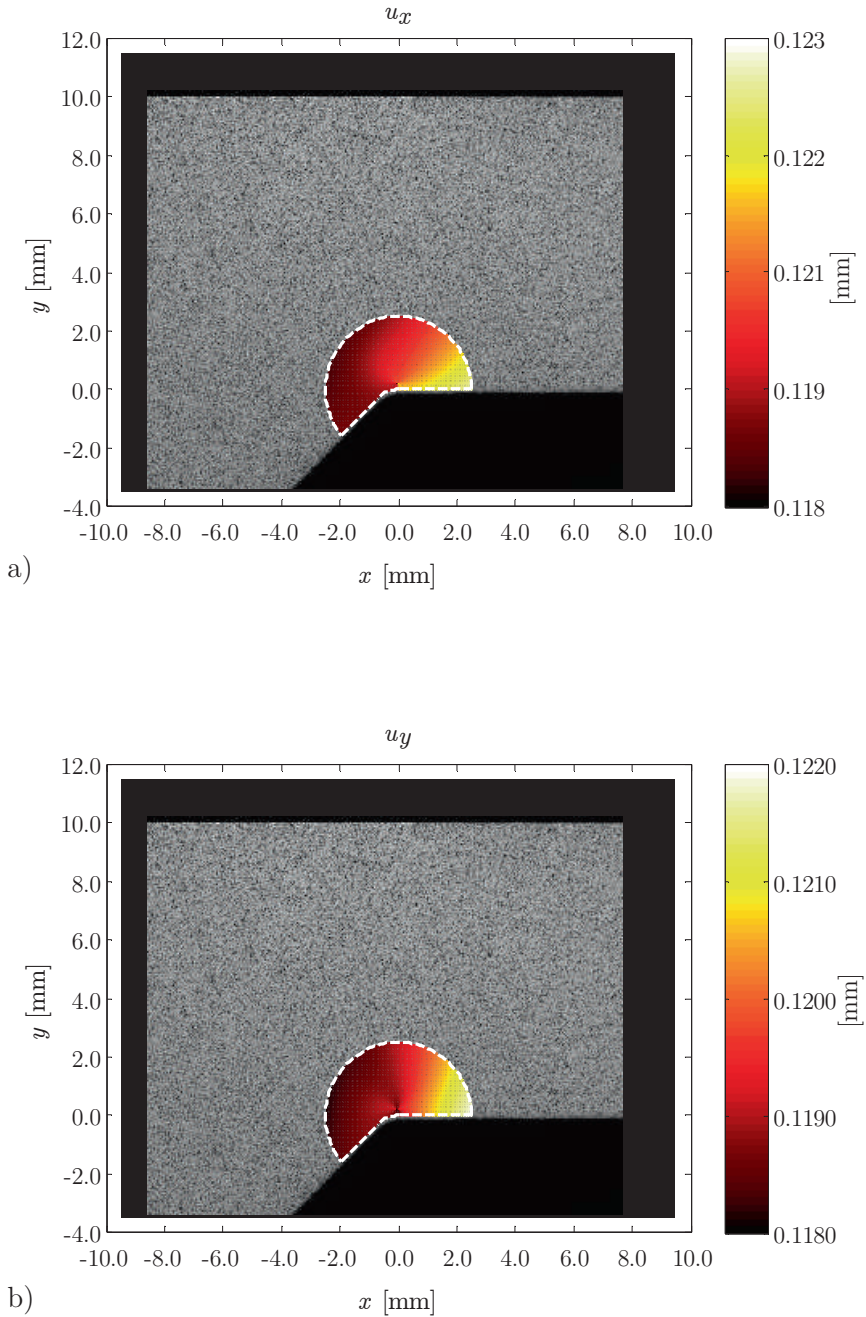


Figure 4.53: Typical subspace displacement fields $\{u_x, u_y\}$ including rigid body motions; M-series in max. load condition (notch Fig. 4.37; image 1001).

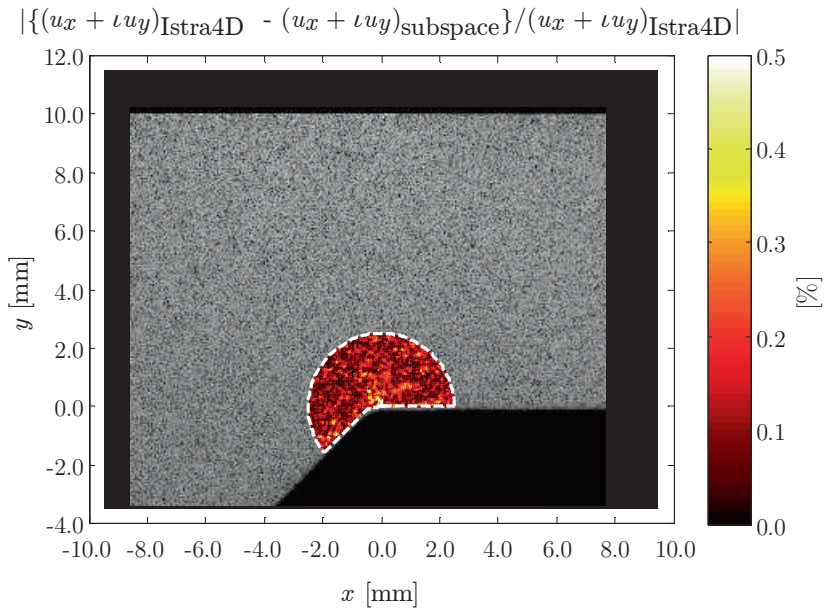


Figure 4.54: Typical displacement field error; M-series in maximum load condition (notch field Fig. 4.37; image 1001).

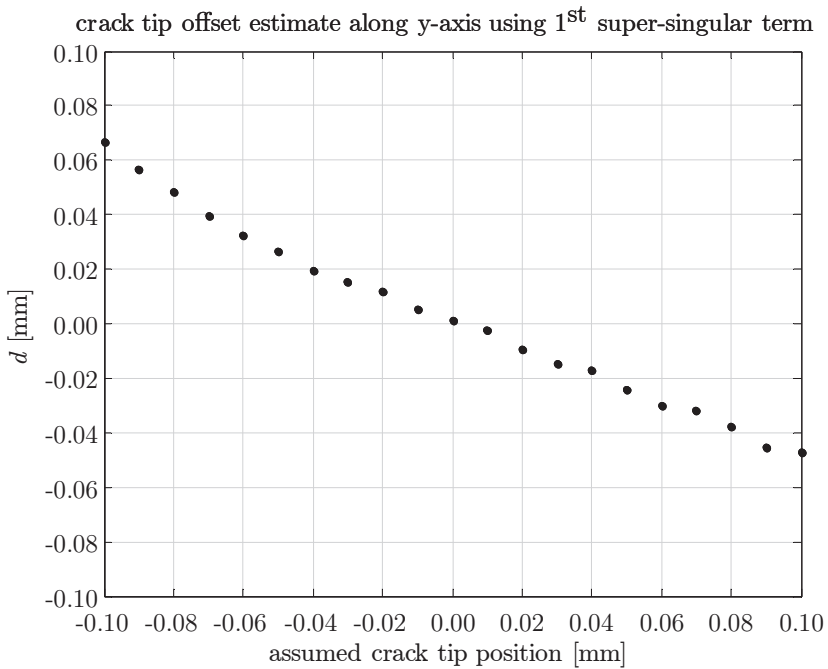


Figure 4.55: Typical crack tip offset estimate (notch field Fig. 4.35; image 1001).

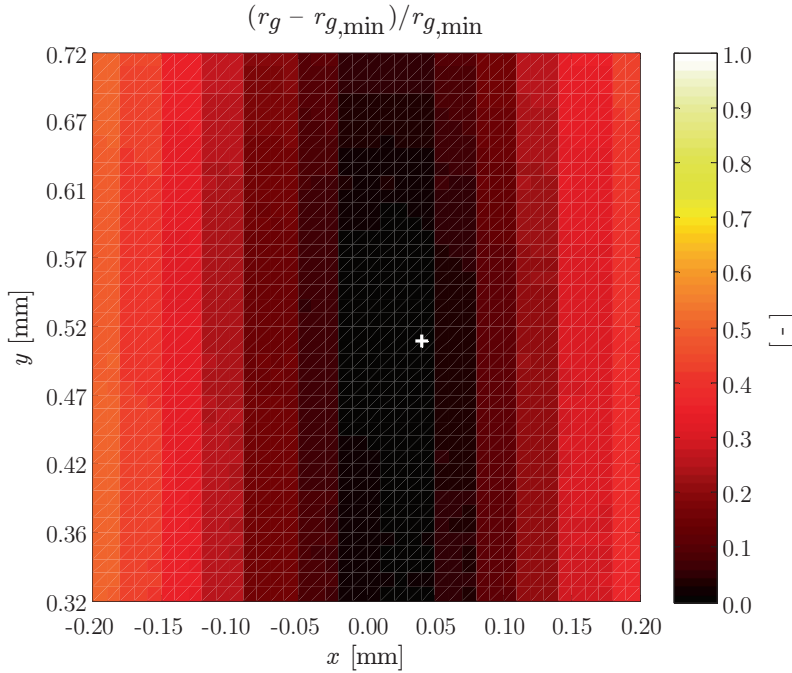


Figure 4.56: Typical crack tip position relative global residual grid; M-series in maximum load condition (notch field Fig. 4.37; image 1001).

In case of increased crack size, the colour bands are quite pronounced and indicate the crack orientation as confirmed in \mathbf{u} (Fig. 4.57). Note a crack size dependent notch region radius is adopted; $\rho_{nr} \propto (a + 2.5)$, to create a level playing field and converged SIF solutions. Obtained K_I values including Normal approximated 95 [%] CB's show in comparison to (geometric non-linear) FEA results obtained for the same crack tip location some error (Table 4.2). In general, the DIC based SIF's are overestimated because of the limited displacement DoF. The error distribution for a range of images is typically parabolic. Turning (gradually) the notch region into a crack tip region for macro-cracks ($a/t_p > 0.1$) might reduce errors.

case	image	F_x [N]	a [mm]	K_I [MPa $\sqrt{\text{mm}}$]	K_I (th. non-lin.) [MPa $\sqrt{\text{mm}}$]	error [%]
5000 M max	501	5459	0.277	86 ± 3	81	6
5000 M max	1001	5518	0.515	106 ± 3	103	3
5000 M max	1501	5492	0.892	129 ± 3	127	2
5000 M max	2001	5511	1.212	158 ± 2	147	7
5000 M max	2501	5465	1.634	189 ± 2	172	10

Table 4.2: Some SSS M-series mode-I SIF's; a comparison of DIC estimated- and theoretical calculated values.

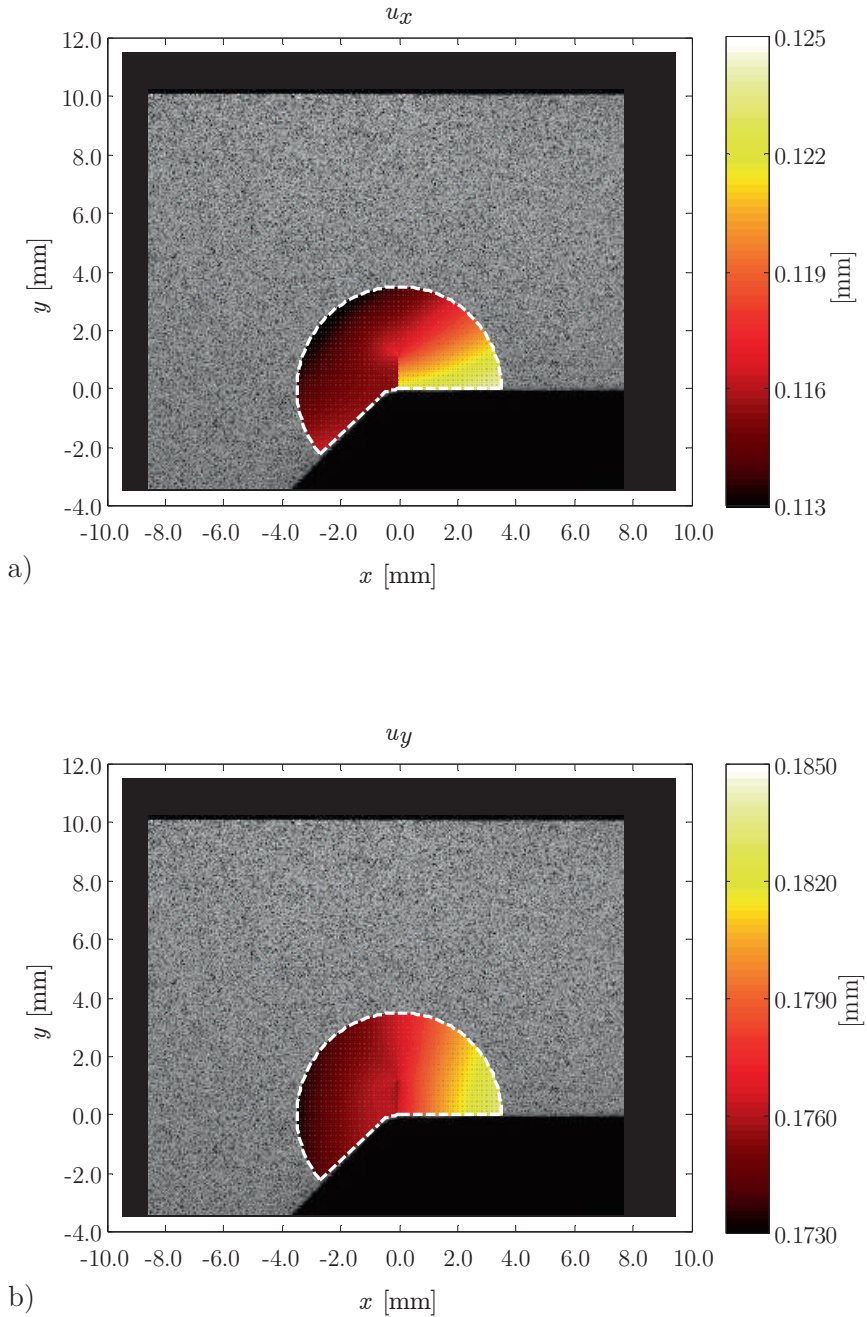


Figure 4.57: Typical subspace displacement fields $\{u_x, u_y\}$ including rigid body motions; M-series in max. load condition (notch Fig. 4.37; image 2001).

The crack tip (Fig. 4.56 and 4.57) is still located in the notch affected region; $\{a/t_b\} < 0.1\}$. The plastic zone may provide information concerning the type of crack growth behaviour (either monotonic or non-monotonic), i.e. may serve as elastoplasticity measure; indicate the coefficient n value. Rather than a 1st order crack tip plastic zone size estimate (Irwin, 1957), $r_p = (K_{I,max}/\sigma_y)^2/(2\pi)$ along the $(\theta = 0)$ -axis, size and shape can be obtained using the decomposed displacement field amplitudes and Von Mises' stress:

$$\sigma_{VM} = \sqrt{\sigma_{xx}^2 + \sigma_{yy}^2 - \sigma_{xx} \cdot \sigma_{yy} + 3\tau_{xy}^2} \quad (4.44)$$

with stress components (Malíková and Veselý, 2014)

$$\begin{aligned} \sigma_{xx} = \sum_n r^{\left(\frac{n}{2}-1\right)} & \left\{ \left(\frac{\omega_n}{\sqrt{2\pi}} \right) \left(\frac{n}{2} \right) \left[\left\{ 2 + \left(\frac{n}{2} \right) + (-1)^n \right\} \cos \left\{ \theta \left(\frac{n}{2} - 1 \right) \right\} - \right. \right. \\ & \left. \left(\frac{n}{2} - 1 \right) \cos \left\{ \theta \left(\frac{n}{2} - 3 \right) \right\} \right] - \\ & \left(\frac{v_n}{\sqrt{2\pi}} \right) \left(\frac{n}{2} \right) \left[\left\{ 2 + \left(\frac{n}{2} \right) - (-1)^n \right\} \sin \left\{ \theta \left(\frac{n}{2} - 1 \right) \right\} - \right. \\ & \left. \left(\frac{n}{2} - 1 \right) \sin \left\{ \theta \left(\frac{n}{2} - 3 \right) \right\} \right] \right\} \\ \sigma_{yy} = \sum_n r^{\left(\frac{n}{2}-1\right)} & \left\{ \left(\frac{\omega_n}{\sqrt{2\pi}} \right) \left(\frac{n}{2} \right) \left[\left\{ 2 - \left(\frac{n}{2} \right) - (-1)^n \right\} \cos \left\{ \theta \left(\frac{n}{2} - 1 \right) \right\} + \right. \right. \\ & \left. \left(\frac{n}{2} - 1 \right) \cos \left\{ \theta \left(\frac{n}{2} - 3 \right) \right\} \right] - \\ & \left(\frac{v_n}{\sqrt{2\pi}} \right) \left(\frac{n}{2} \right) \left[\left\{ 2 - \left(\frac{n}{2} \right) + (-1)^n \right\} \sin \left\{ \theta \left(\frac{n}{2} - 1 \right) \right\} + \right. \\ & \left. \left(\frac{n}{2} - 1 \right) \sin \left\{ \theta \left(\frac{n}{2} - 3 \right) \right\} \right] \right\} \\ \tau_{xy} = \sum_n r^{\left(\frac{n}{2}-1\right)} & \left\{ \left(\frac{\omega_n}{\sqrt{2\pi}} \right) \left(\frac{n}{2} \right) \left[- \left\{ \left(\frac{n}{2} \right) + (-1)^n \right\} \sin \left\{ \theta \left(\frac{n}{2} - 1 \right) \right\} + \right. \right. \\ & \left. \left(\frac{n}{2} - 1 \right) \sin \left\{ \theta \left(\frac{n}{2} - 3 \right) \right\} \right] + \\ & \left(\frac{v_n}{\sqrt{2\pi}} \right) \left(\frac{n}{2} \right) \left[- \left\{ \left(\frac{n}{2} \right) - (-1)^n \right\} \cos \left\{ \theta \left(\frac{n}{2} - 1 \right) \right\} + \right. \\ & \left. \left(\frac{n}{2} - 1 \right) \cos \left\{ \theta \left(\frac{n}{2} - 3 \right) \right\} \right] \right\} \end{aligned}$$

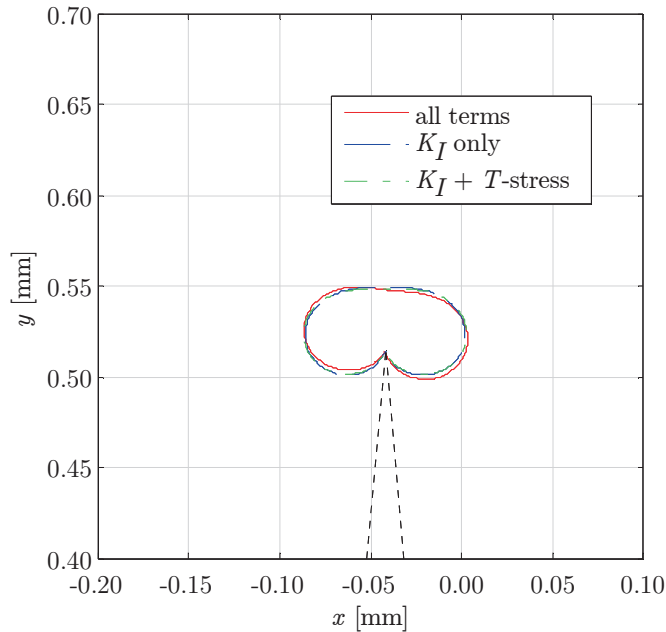


Figure 4.58: Typical plastic zone size and shape; M-series in maximum load condition (notch field Fig. 4.35; image 1001), $\Delta F_x = 5000$ [N].

For σ_{VM} exceeding the yield strength $\sigma_y = 228$ [MPa], the (plane stress) plastic zone size turns out to be one order of magnitude smaller compared to the crack length (Fig. 4.56). Assuming $\nu = 0.33$ [-], the plastic zone will be about 9 times smaller in case of plane strain (Janssen et al., 2002). Considering $\omega_1 = K_I$ only, the shape is obviously symmetric; adding ω_2 already includes more detail. Since the crack tip is still inside the notch affected region, the notch axis is still governing (Fig. 3.9); K_{II} is non-zero, introducing non-symmetry.

The T-stress (ω_2), a non-singular term acting parallel to the crack plane, affects the plastic zone size and shape (Fig. 4.58; Larsson and Carlsson, 1973) as well as crack path stability (Cottorell and Rice, 1980). If directionally stable, the T-stress is negative; positive if unstable. For image 1001, $\omega_2 = -26$ [MPa].

4.4.7 Time series analysis

The notch- and far field region for each individual image (Paragraph 4.4.5 and 4.4.6) contain spatial information only. The temporal solution correlates the crack tip location $a(n)$ at a particular number of cycles and the SIF $K_I(a)$, providing a crack growth relation ($da/dn = f(K_I(a))$). Both parameters (Fig. 4.57) however contain some noise, show some error. Suitable generic functions have been selected (because of derivative accuracy) and curve fitting is applied to obtain filtered $\{a(n), K_I(a)\}$ data.

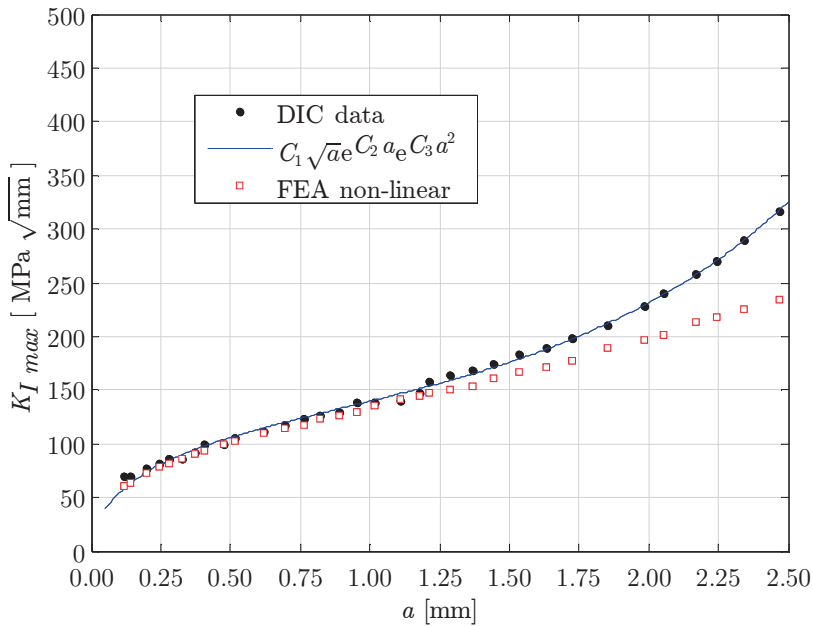
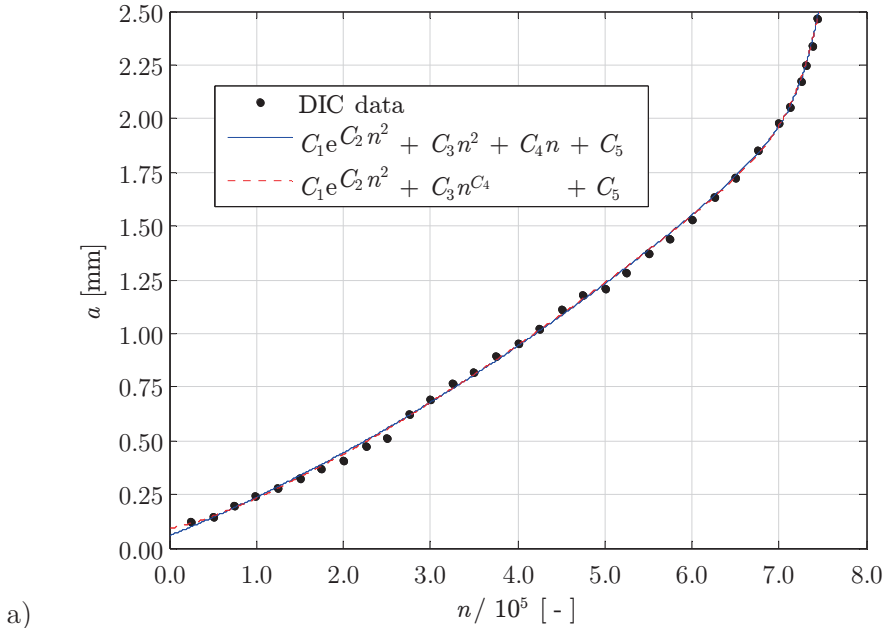


Figure 4.59: Typical a) crack length and b) SIF development in welded SSS; M-series in maximum load condition, $\Delta F_x = 5000$ [N].

Although the analysis did not involve any time constraints, the crack length data is monotonically increasing ($a_{i+1} > a_i$) as it should be (Fig. 4.59a) and is expected to return in the derivative; crack growth rate (da/dn) in the notch- and far field stable crack growth regions {I, II}. Different filter functions have been investigated, but results are similar. The SIF (Fig. 4.59b) shows principally monotonically increasing behaviour as well. Stress intensity errors become significant for ($a > 2$) and a new reference image taken halfway the test might solve this issue; an alternative solution could be a X-FEM based displacement field decomposition (Roux, Réthoré and Hild 2009).

For $\Delta\sigma_s = \sigma_{s,max} \cdot (1 - r_l)$, crack driving force estimates ΔK_I have been obtained. The crack growth characteristic shows obviously anomalous (notch affected) two-stage behaviour (Fig. 4.60). Raw data has been used rather than curve fitting based $\{a, K_{I,max}\}$ values, since the exponential functions dominate the solution introducing bi-linear crack growth on log-log scale. Applying the TS concept, slope $m \sim 3.7$ [-]; a realistic value in the customary range (3, 4). Coefficient $n_e \sim 10$ [-] suggests significant plasticity as reflected in the non-monotonic crack growth. Since the considered SSS is a welded one, the self-equilibrating residual stress is likely tensile in the notch affected region. The lasering process adopted to create an initial flaw may have contributed as well. The BSS concept elastoplasticity coefficient ($n = 2$) however seems insufficient.

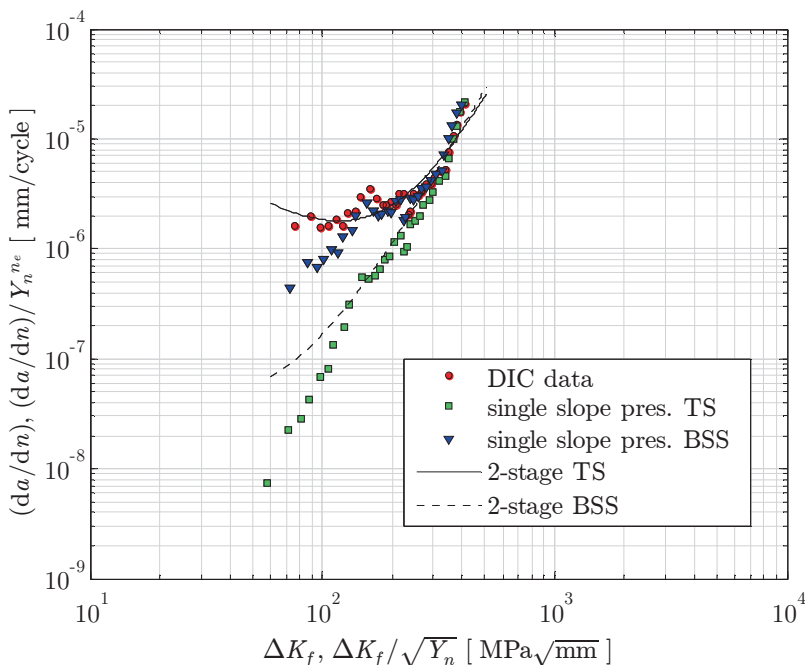


Figure 4.60: Typical welded SSS large/long crack growth- and two-stage single slope presentation; M-series, $\Delta F_x = 5000$ [N].

4.5 Conclusions

The crack growth rate of micro-cracks emanating at notches show elastoplastic wake field affected anomalies, i.e. monotonically increasing or non-monotonic behaviour beyond the material threshold. Modifying Paris' equation, a two-stage micro- and macro-crack growth law similarity is proposed to include both the weld notch- and far field characteristic contributions, elastoplasticity as well as remote mechanical- and thermal residual mean stress effects.

Investigated SSS experimental data sets suggest that non-monotonicity is predominantly related to a plane stress condition (i.e. thin specimen or DIC surface measurement obtained results). For {WM, HAZ} plane strain crack growth data showing monotonically increasing behaviour beyond the material threshold, the (self-equilibrating) residual stress might be compressive. Although the hull structure welded joint condition is typically plane strain, suggesting crack growth might be monotonically increasing, a significant (tensile) residual stress may keep the crack growth rate non-monotonic.

5

Welded Joint Fatigue Resistance

Only two things are infinite: the universe and human stupidity, and I am not sure about the former.
Albert Einstein (1879-1955, physicist)

5.1 Introduction

The (as) weld(ed) geometry in each cross-section along the (curved) weld seam is anything but simple. Joint parameters are principally random and affect the fatigue resistance, emphasising the importance of statistics in correlating the loading or structural response and life time of {SSS, LSS} fatigue resistance data; independent (deterministic)- and dependent (stochastic) variables.

Although a structural response parameter S does not include explicit fatigue damage process information, it is typically adopted as fatigue resistance criterion since S controls crack development related {micro, meso, macro}-plasticity. Using a global approach, principally the nominal stress range S_n and type of joint are explicitly taken into account, meaning model complexity is limited and required effort is low at the price of substantial inaccuracy; considerable life time uncertainty. Changing the approach to a local one, e.g. $S_n \rightarrow \{S_s, S_e\}$ meaning the nominal stress range turns into respectively the structural hot spot- or effective notch stress range, explicitly reflects local geometry and loading information and generally speaking accuracy increases. However, required effort and model complexity increase at the same time.

Response parameters $\{S_n, S_s, S_e\}$ are intact geometry, crack initiation, related. For a growth dominated process, a (local) crack damaged geometry parameter should be employed. Considering both initiation and growth, i.e. micro- and macro-crack growth in case of arc-welded joints in hull structures, the total stress concept (Chapter 2) has been introduced using the stress intensity (Chapter 3) as governing parameter to establish the weld notch governing and far field dominated crack growth contributions (Chapter 4).

Outline

The total stress range S_T will be defined first and its properties investigated (Paragraph 5.2). Single- and dual slope fatigue resistance formulations will be considered to be able to cover both medium- and high cycle fatigue (Paragraph 5.3). Regression analysis will be adopted to estimate model parameters, a likelihood approach in particular to deal with both complete- and right-censored data; failures and run-outs. Artificial fatigue test data of DS T-joints is investigated to determine the S_T parameter quality. As-welded SSS CA data has been used to establish a family of (damage tolerant engineering) joint S_T - N fatigue resistance design curves (Paragraph 5.4) to be able to estimate the fatigue life time N of welded joints (production quality is average) knowing the joint geometry and far field structural response. In order to demonstrate welded joint similarity, FSS representative CA LSS data has been examined to verify a SSS data scatter band fit (Paragraph 5.5). Since CA {SSS, LSS} fatigue resistance is principally used to estimate a VA FSS value adopting the Palmgren-Miner hypothesis, last but not least a scatter band fit is investigated for some VA SSS data (Paragraph 5.6) to obtain reliable fatigue damage estimates of some frame-stiffener connections in the slamming zone (Paragraph 5.7).

5.2 Total stress parameter

Straightforward integration of the Paris' equation based two-stage region {I, II} crack growth model (Eq. 4.7) yields a (Basquin type) single slope fatigue resistance relation; $\log(N) = C - m \cdot \log(S_T)$. The total stress range S_T , an equivalent structural response parameter, incorporates for weld toe notches the effective structural stress range $\Delta\sigma_s / (1 - r_l)^{1-\gamma}$ (Eq. 4.17 and 4.19) and a notch crack growth integral I_N including the size effects:

$$S_T = \frac{\Delta\sigma_s}{t_p^{(\prime) \frac{2-m}{2m}} \cdot I_N(r_s, n, m) \frac{1}{m} \cdot (1 - r_l)^{1-\gamma}} \quad (5.1)$$

with

$$I_N = \int_{\left(\frac{a_i}{t_p^{(\prime)}}\right)}^{\left(\frac{a_f}{t_p^{(\prime)}}\right)} \left[\frac{1}{\left\{ Y_n \left(\frac{a}{t_p^{(\prime)}} \right) \right\}^n \cdot \left\{ Y_f \left(\frac{a}{t_p^{(\prime)}} \right) \right\}^m \cdot \left(\frac{a}{t_p^{(\prime)}} \right)^{\frac{m}{2}}} \right] d \left(\frac{a}{t_p^{(\prime)}} \right)$$

To calculate I_N , boundary values are required: an initial- and final crack length $\{a_i, a_f\}$. The initial crack length is an important one because of LEFM assumptions, i.e. the integrand denominator contains the $(a/t_p^{(\prime)})^{m/2}$ factor thanks to the crack tip stress distribution square root asymptotic behaviour, meaning the introduction of a lower bound singularity. Adaptive Gauss-Kronrod quadrature for example is a suitable numerical integration scheme. The upper bound is typically

the plate thickness for a through-thickness crack, i.e. $\{a_f = t_p, a_f = t_p/2\}$ for $\{\text{SEN}, \text{DEN}\}$ HS type $\{A, C\}$ (non-) symmetry configurations; ($t_p^{(\prime)} = t_p$) and ($t_p^{(\prime)} = t_p/2$) respectively, and an artificial one for HS type B : $a_f = t_p'$; ($t_p^{(\prime)} = t_p'$). The integration variable a is turned into a dimensionless one ($a/t_p^{(\prime)}$), introducing $t_p^{(2-m)/2m}$ in the S_T dominator; basically a size or scale parameter (Paragraph 2.8.3), reduced to a thickness (i.e. crack path length) related one.

Similar to the effective notch stress concept intact geometry parameter ρ_e (Paragraph 2.11), its crack damaged equivalent can be defined as well (Sonsino et al., 1999): $a_e = a_i(\mu, \sigma) + a_f$. Defect size $a_i(\mu, \sigma)$ is principally expected to be independent of weld material volume; i.e. values are similar no matter t_p introducing a size effect. However, the relative effective defect size a_e turns out to be approximately constant (Sonsino et al., 1999) – although not mentioned; $(a_e/t_p) \approx 4.0 \cdot 10^{-2}$ [-] for aluminium welded joints. The relative defect size (a_i/t_p) , obtained using the characteristic fatigue strength of weld reinforcement removed aluminium butt joints (average $t_p = 10$), has a similar value (Atzori et al., 2008). The BSS concept on the other hand adopted a constant relative defect size $(a_i/t_p) = 1.0 \cdot 10^{-3}$ [-] as it corresponds to asymptotic $I_N^{1/m}$ behaviour (Dong and Hong, 2004); an engineering solution rather than physics based.

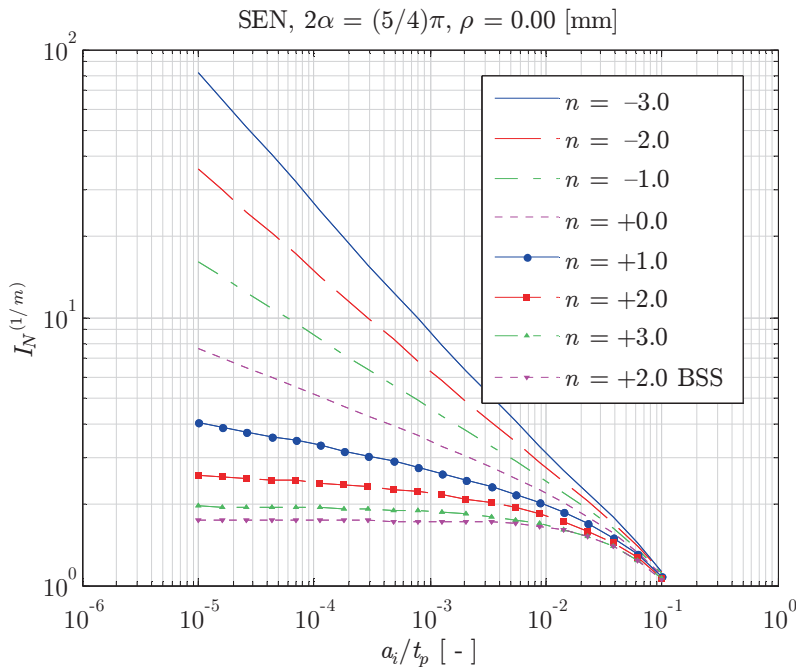


Figure 5.1: Typical defect size dependent notch crack growth integral behaviour (ideal fillet weld notch angle); $C_{bw} = 0$, $r_s = 0$, $m = 3.0$ [-].

The notch crack growth integral I_N is proportional to the fatigue life time N , meaning $I_N^{1/m}$ is inversely proportional to S_T (Eq. 5.1). For $(a_i/t_p) \rightarrow 0$, $I_N^{1/m}$ behaviour is typically divergent in case $n = \{-3.0, -2.0, -1.0\}$ and $m = 3.0$ (Figure 5.1); the crack growth rate (da/dn) is monotonically increasing, either structural threshold or notch compressive residual stress induced (elastic or even plastic). A special case: if no σ_n^r component is involved and $n = -2.0$, $(da/dn) \propto a$ according to the (generalised) F&D model (Paragraph 4.2). If $n = 0$, only region-II long crack growth is observed and $I_N^{1/m}$ is still sensitive to (a_i/t_p) , no matter its value. As soon as n increases, e.g. $n = 1.0$ if the total weld notch stress is elastic, (da/dn) starts to show non-monotonic behaviour. For $n > 1$ notch plasticity becomes involved and $I_N^{1/m}$ behaves asymptotically, converges, as noticed before (Maddox and Webber, 1978; Dong and Hong, 2004). The BSS concept assumes first order crack tip plasticity ($r_y \propto K_I^2$), i.e. $n = 2.0$ and shows in comparison to the TS concept a smaller asymptotic value because of the weld notch stress bi-linearisation and M_{kn} formulation. Values are different compared to the published ones (e.g. Dong and Hong, 2004) because of a different slope m and $(\pi^{m/2})$ is included in the fatigue strength constant $\log(C)$. In case $n = m = 3.0$ (involving the Paris equation), micro- and macro-crack growth behaviour is assumed to be similar and convergence is already obtained for $(a_i/t_p) \rightarrow 1.0 \cdot 10^{-3}$.

The elapsed part of fatigue life time N to obtain a typical crack size $a = 0.1$ [mm] at weld toe notches is estimated to be ~ 30 [%] (Lassen and Recho, 2009). Assuming σ_n^r is significant (e.g. $n = 2.0$), $(a_i/t_p) = O(10^{-4})$ and $t_p = 10$ [mm], the notch crack growth integral ratio $\{I_N^{1/m}(10^{-4}) - I_N^{1/m}(10^{-2})\}/I_N^{1/m}(10^{-4})$ can be used to obtain that information and is in the same range. Although LEFM is generally assumed to be not applicable for $a < 0.1$ [mm], micro-crack growth is even considered to be part of the initiation period, a reasonable estimate obtained using a crack damaged loading and geometry parameter (Fig. 5.1) is believed to be no coincidence for welded joints: (micro-)crack growth dominates N .

Convergence seems to be primarily a matter of the dominant singularity; the notch component Y_n^n or the (sharp) crack tip related one $(a/t_p)^{m/2}$. If Y_n^n is governing, asymptotic behaviour is observed. For $(\rho > 0)$, $(a/t_p)^{m/2}$ dominates by definition since the notch singularity has disappeared, meaning no convergence for $(a_i/t_p) \rightarrow 0$ at all (Fig. 5.2). However, ρ controls the $I_N^{1/m}$ slope. For $(a_i/t_p) \rightarrow 0$ it becomes equal no matter n . Increasing notch radius ρ , the difference in $I_N^{1/m}$ for varying n reduces. A similar effect is achieved using an intact geometry parameter, the effective notch radius, reducing the local fatigue strength scatter (Morgenstern et al., 2006a, 2006b). Although welded joints may have different elastoplasticity coefficients, the fatigue resistance scatter can still be limited if an appropriate (optimised) ρ value is adopted; a material related parameter. The BSS result hardly changes because of the σ_n bi-linearisation, i.e. the approximate zone 2 stress gradient effect is included at the price of losing zone 1 peak stress information. Keep in mind that $I_N^{1/m}$ is ρ sensitive (Fig. 5.3). If (da/dn) is monotonically increasing, S_T will increase for increasing ρ and seems paradoxical from fatigue resistance perspective; if non-monotonic, S_T decreases meaning an increased fatigue resistance as expected since for increasing ρ at constant n the zone 2 stress gradient decreases.

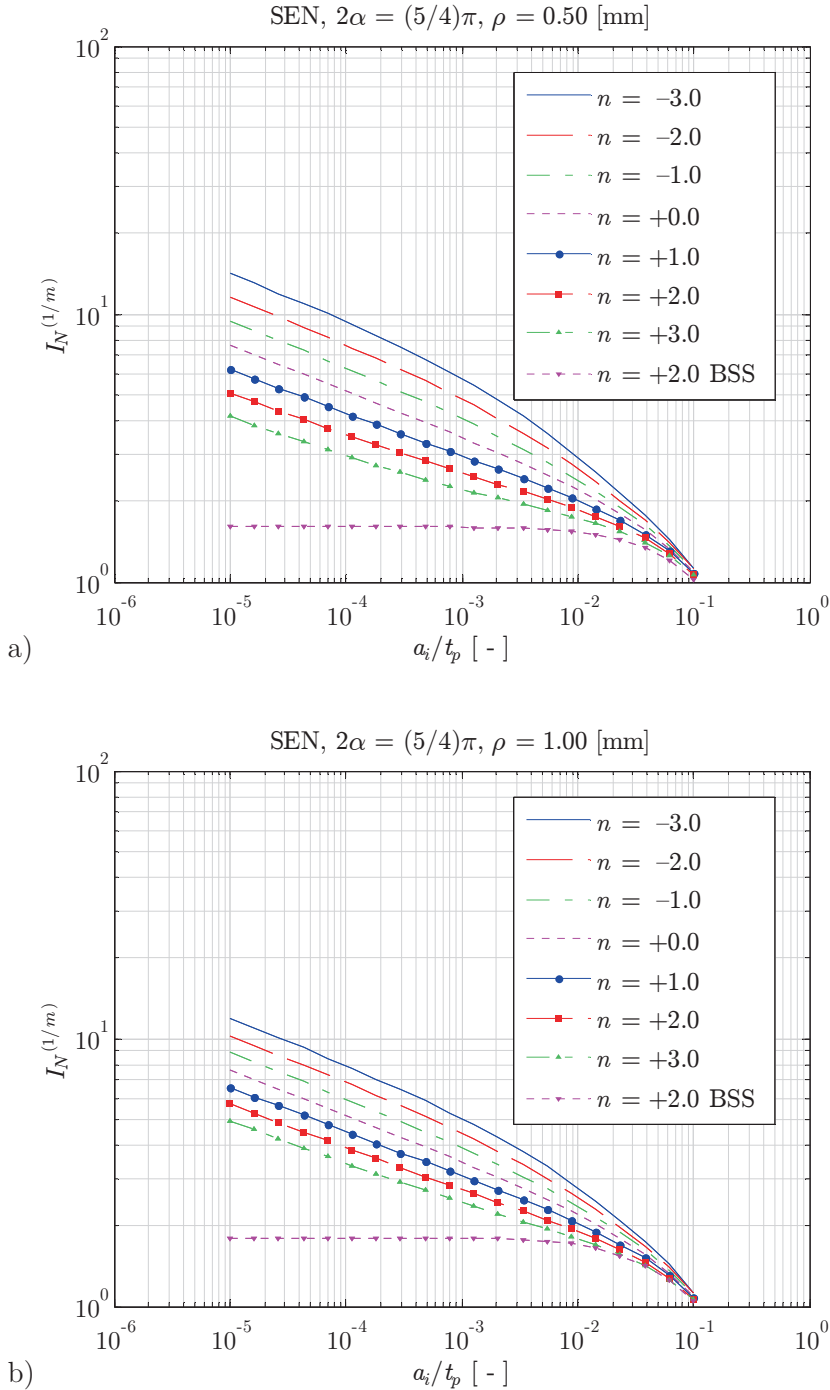


Figure 5.2: Typical defect size dependent notch crack growth integral behaviour (ideal fillet weld notch angle); $\rho = \{0.5, 1.0\}$, $r_s = 0$, $m = 3.0$ [-].

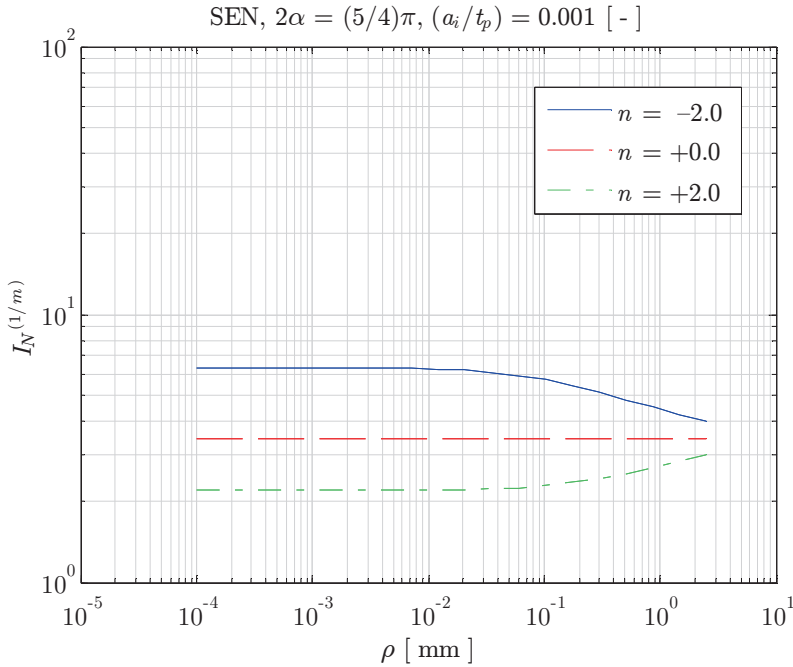


Figure 5.3: Typical notch radius dependent crack growth integral behaviour (ideal fillet weld notch angle); $C_{bw} = 0$, $r_s = 0$, slope $m = 3.0$ [-].

Weld load carrying coefficient C_{bw} controls the zone 2 (notch) stress gradient and may vary from $C_{bw} \rightarrow 0$ for NLC joints up to structural stress order of magnitude ($C_{bw} > 10^{-1}$) for heavy LC ones (Paragraph 2.6). Although no linear $C_{bw} - S_T$ relation exists, a significant C_{bw} value would significantly increase the fatigue strength in case ($n < 0$), but seems artificial (Fig. 5.4a). If notch/crack tip elastoplasticity is encountered ($n > 0$), e.g. ($r_y \propto K_I^2$), the fatigue strength may reduce up to 30 [%] for increasing C_{bw} ; the BSS concept NLC assumption ($r_t = 0.1t_p$, Paragraph 2.6.1) becomes non-conservative.

Comparing the fatigue strength for different far field stress distributions, differences will be at maximum for the extreme zone 3 gradient values $r_s = \{-\infty, 1\}$, as shown for load- and displacement controlled {LC, DC} conditions (Fig. 5.4b); i.e. respectively the remote mechanical- or (equilibrium equivalent) thermal residual stress is decisive. The proposed BSS polynomial $I_N^{1/m}(r_s)$ approximation for $m = 3.6$ (Dong et al., 2002; Dong, Hong and De Jesus, 2007) – 6th order seems exaggerated – is only valid for ($0 \leq r_s \leq 1$); a 1 DoF SEN based notch crack growth integral formulation for all weld (toe) notches. Obviously zone 3 far field stress gradient effects are negligible, for the same reason $I_N^{1/m}$ is hardly sensitive to any (a_f/t_p) outside the notch affected region. However, $C_{bw}(r_s)$ changes at the same time, meaning the fatigue strength is still affected because of a zone 2 stress gradient modification.

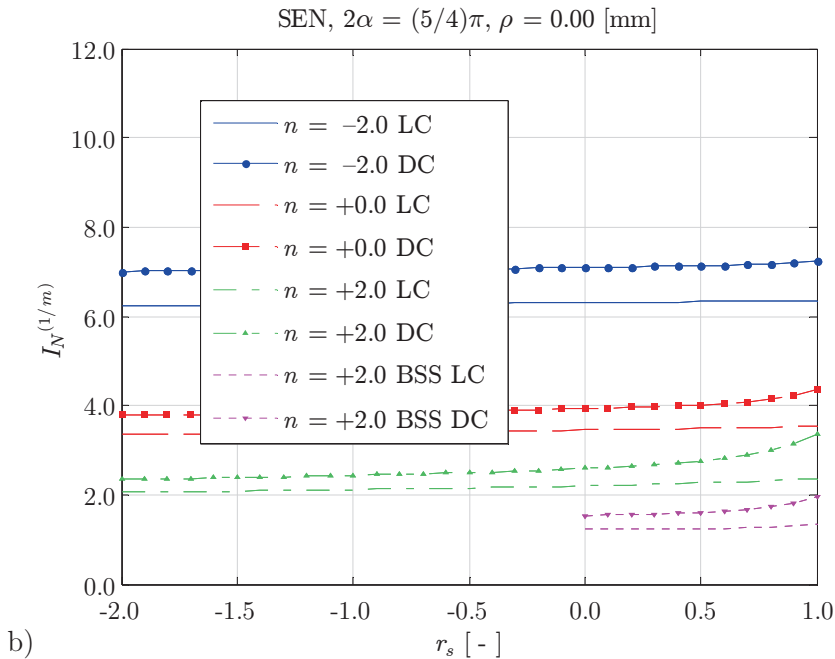
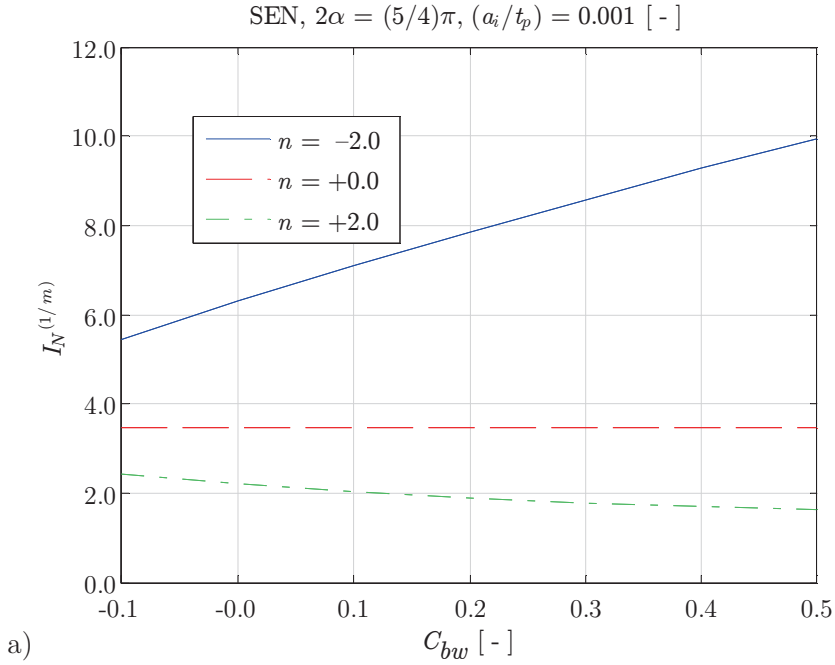


Figure 5.4: Typical a) C_{bw} ($r_s = 0$) dependent- and b) r_s ($C_{bw} = 0$) dependent crack growth integral behaviour (ideal fillet weld notch angle); $m = 3.0$ [-].

Principally S_T benefits from DC conditions in comparison to LC; ~ 15 [%], simply an offset. Approaching the DC pure bending load case, $I_N^{1/m}$ predominantly increases because of a domain singularity. The stress intensity becomes negative (Paragraph 3.8, Eq. 3.30) either for $\{r_s = 1, (a/t_p) = (\pi/4)\}$ or the other way around, meaning crack arrest. Because of low final crack length sensitivity, (a_f/t_p) has been reduced to plot the full $I_N^{1/m}(r_s)$ range (Fig. 5.4b).

Taking far field 3D effects ($a/c = 1/4$) into account (Fig. 5.5), i.e. comparing a single edge- and semi-elliptical formulation, S_T reduces (and N increases). Since C_{bw} remains unaffected (Paragraph 3.5.1); a notch affected zone contribution, $I_N^{1/m}(C_{bw})$ is shifting only. Depending on type of crack growth behaviour, {SEN, DEN} symmetry w.r.t. $(t_p/2)$ shows opposite effects. In case of an elastic structural notch response or (welding induced) compressive notch stress ($n < 0$), S_T reduces significantly for increasing C_{bw} . For tensile elastoplastic notch behaviour ($n > 0$), S_T increases and convergence is observed for ($C_{bw} \geq 0.1$); plasticity itself dominates.

A crack developing at one side only – a non-symmetry case w.r.t. $(t_p/2)$ – shows hardly any zone 3 far field stress gradient affects, no matter semi-elliptical 3D contributions (Fig. 5.6). Like for a DC structural response, the semi-elliptical crack requires the final crack length to be reduced because of crack arrest if bending becomes dominant. For symmetry on the other hand, r_s contributes significantly because of the symmetry condition affecting the zone 2 stress gradient at the same time.

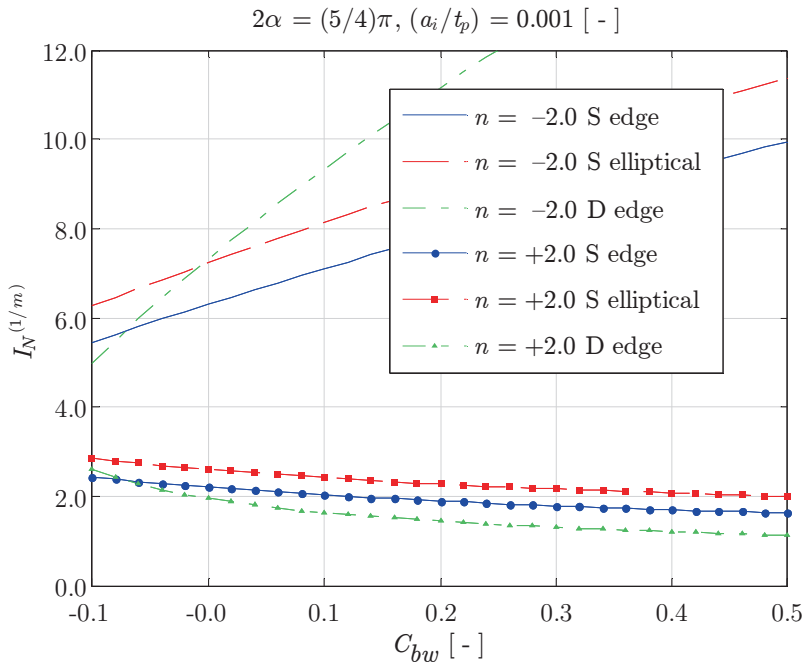


Figure 5.5: Typical (1st order) C_{bw} - and crack type dependent crack growth integral behaviour (ideal fillet weld notch angle); $r_s = 0$, $m = 3.0$ [-].

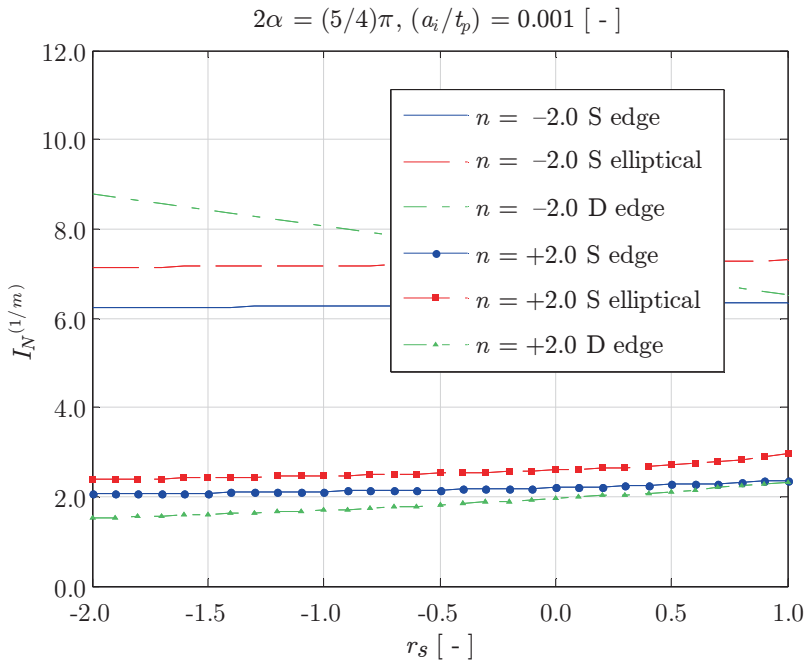


Figure 5.6: Typical r_s - and crack type dependent crack growth integral behaviour (ideal fillet weld notch angle); $C_{bw} = 0$, $m = 3.0 [-]$.

To be able to deal with weld root notches as well, the total stress formulation S_T (Eq. 5.1) needs to be generalised. The weld reinforcement explicitly contributes to the fatigue resistance $\{Y_n(Y_{nr}, Y_{nl}), Y_f(Y_{fw})\}$ and crack length a turns into a fictitious one; $(a_n + a)$. In case of symmetry (Fig. 2.35), $b_p = (b_p/2)$. For weld toe notches, $b_p \rightarrow t_p^{(\prime)}$.

$$S_T = \frac{\Delta\sigma_s}{\left(\frac{t_p^{(\prime)}}{b_p}\right)^{\frac{1}{m}} \cdot b_p^{\frac{2-m}{2m}} \cdot I_N(r_s, n, m)^{\frac{1}{m}} \cdot (1-r_l)^{1-\gamma}} \quad (5.2)$$

Although less dominant in comparison to the weld toe notch case (Fig. 5.1), the $I_N^{1/m}$ defect size dependency still holds (Fig. 5.7a). Both the notch- and crack tip induced singularity contribute for a weld toe; the notch component is in control for a weld root since the crack length has become fictitious $(a_n + a)$, i.e. no square root singular term. Note: the large scatter as quite often observed in weld root fatigue resistance data is predominantly because of the a_n distribution. Comparing $I_N^{1/m}$ for the {SEN, CN} geometry (Fig. 5.1 and 5.7a), the CN load-bearing cross-section is twice as large explaining why $I_N^{1/m}$ is twice as small. If $(\rho > 0)$, no singularity is involved at all and convergence is achieved no matter n (Fig. 5.7b).

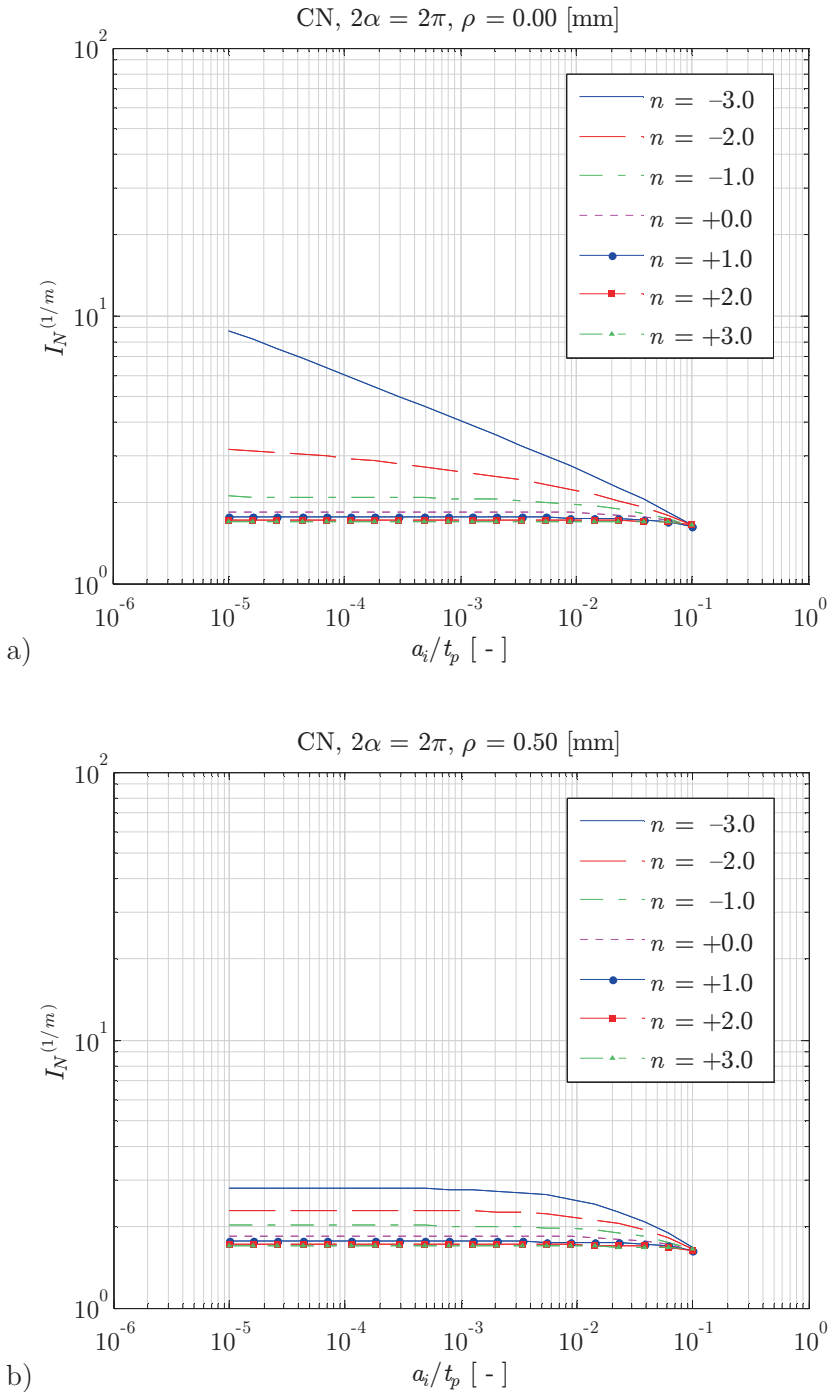


Figure 5.7: Typical defect size dependent notch crack growth integral behaviour (weld root notch in DS cruciform joint); $r_s = 0$, $m = 3.0$ [-].

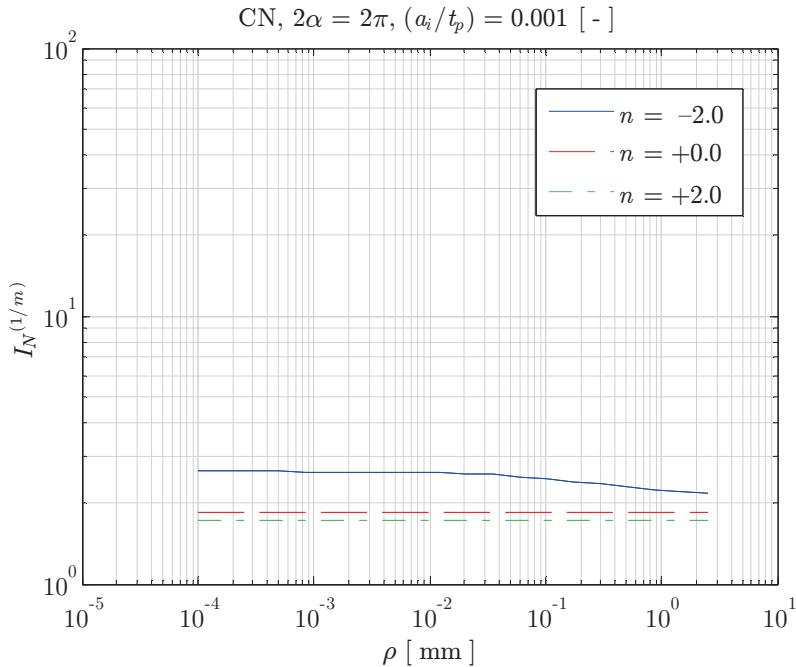


Figure 5.8: Typical ρ dependent notch crack growth integral behaviour (weld root notch in DS cruciform joint); $r_s = 0$, $m = 3.0$ [-].

Notch radius sensitivity is rather low (Fig. 5.8) in comparison to the weld toe notch case and limited to monotonically increasing crack growth behaviour. The fatigue resistance of weld root notches however shows a considerable degree of r_s dependency (Fig. 5.9), principally because of the far field membrane stress component σ_m . Far field bending remains bending in the weld root cross-section, i.e. $(\sigma_s = \sigma_b) \rightarrow \sigma_b^r$. In case of far field membrane loading, bending becomes involved as well; $(\sigma_s = \sigma_m) \rightarrow (\sigma_m^r, \sigma_b^r)$, meaning S_T significantly increases for constant σ_s and decreasing r_s .

Although the $\Delta\sigma_s$ and $I_N^{1/m}$ contributions to S_T are equally important, the range of {MCF, HCF} $\Delta\sigma_s$ values generally speaking exceeds the $I_N^{1/m}$ related one, meaning the (effective) structural stress range is still the governing fatigue resistance parameter like for the global and local concepts.

The total stress parameter S_T is in fact an equivalent one, i.e. its unit is not simply [MPa] or similar because of the involved Paris based crack growth law: the C dimension, $[\text{mm}/(\text{cycle} \cdot \text{MPa}\sqrt{\text{mm}})^m]$, ensures life time unit consistency in [cycles].

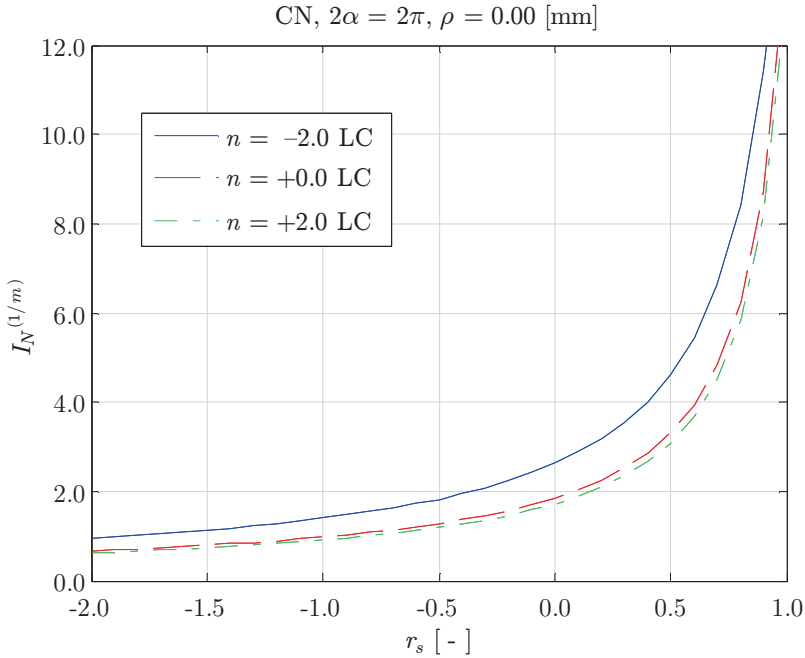


Figure 5.9: Typical zone 3 stress gradient dependent notch crack growth integral behaviour (weld root notch in DS cruciform joint); $m = 3.0$ [-].

5.3 Fatigue resistance statistics

Correlating a structural response parameter S and life time N in a particular {MCF, HCF} life time range, typically a(n approximately) log-log linear dependency is observed and a Basquin type of relation is naturally adopted:

$$\log(N) = C - m \cdot \log(S) \quad (5.3)$$

One way to estimate the single slope curve parameters $\{C, m\}$; scaling factor C and slope m (respectively the fatigue strength and damage mechanism parameter), is using (linear) regression:

$$\log(N) = C - m \cdot \log(S) + \sigma\varepsilon \quad (5.4)$$

An independent variable, predictor $\log(S)$, is related to the dependent one; response $\log(N)$. The Least Squares approach, minimising the sum of the square residuals $\varepsilon \sim N(0, 1)$, is a very popular concept to obtain the best parameter estimates. However, fatigue resistance data sets typically contain failures (complete data) as well as run-outs (right-censored data), that cannot be dealt with and a Likelihood approach (Dekking et al., 2005) will be employed.

A $\{S_j|N_j\}$ distribution assumption, i.e. probability density function (PDF) $f(\mu, \sigma)$ and corresponding cumulative distribution function (CDF) $F(\mu, \sigma)$, is required. Successful application of the basic life time distributions is based on probabilistic arguments and empirical success. The 2-parameter (mean μ and standard deviation σ , respectively location- and scale parameter) Lognormal distribution contains a lower bound $\log(N = 0) = 1$; a physical requirement and is flexible (explaining empirical success).

$$f = \frac{1}{\sigma\sqrt{2\pi}} \cdot \exp \left[-\frac{\{\log(N) - \mu\}^2}{2\sigma^2} \right] \quad (5.5)$$

$$F = \frac{1}{2} \left[1 + \operatorname{erf} \left\{ \frac{\log(N) - \mu}{\sqrt{2}\sigma} \right\} \right] \quad (5.6)$$

with

$$\mu = C - m \cdot \log(S)$$

The failure rate (f/F) however can be non-monotonic as it should be monotonically increasing, since early failures are excluded; probability of failure should increase over time considering $\{MCF, HCF\}$. The 2-parameter Weibull (extreme value) distribution, a $\{\text{location, scale}\}$ rather than $\{\text{shape, scale}\}$ formulation fits perfectly fatigue phenomena; after all, the weakest link in the structure defines life time N to failure. Its failure rate is monotonic by definition; the lower bound requirement and flexibility are maintained.

$$f = \frac{1}{\sigma} \cdot \exp \left[\frac{\{\log(N) - \mu\}}{\sigma} - \exp \left[\frac{\{\log(N) - \mu\}}{\sigma} \right] \right] \quad (5.7)$$

$$F = \exp \left[-\exp \left[\frac{\{\log(N) - \mu\}}{\sigma} \right] \right] \quad (5.8)$$

Considering a random sample $\{N_{j1}, N_{j2}, N_{j3}, \dots\}$ at $S = S_j$ statistically distributed according to $f(N|S_j; \theta)$ with $\theta = \{C, m, \sigma\}$, for single observation $\{N_{ji}|S_j\}$, a sample failure with probability density $f(N_{ji}|S_j; \theta)$, $\ell(\theta; N_{ji}|S_j)$ is a likelihood measure for θ corresponding to $\{N_{ji}|S_j\}$, i.e. $\ell(\theta; N_{ji}|S_j) = f(N_{ji}|S_j; \theta)$. Assuming all observations are independent, the sample likelihood L includes a joint probability density:

$$L(\theta; N_j|S_j) = \prod_{i=1}^n f(N_{ji}|S_j; \theta) \quad (5.9)$$

with

$$\theta = \{C, m, \sigma\}$$

From engineering perspective: regarding the likelihood, $\{N_j|S_j\}$ is fixed and θ variable; for the probability density the other way around. Provided an experimental data set including both failures and run-outs, the likelihood becomes:

$$L(\theta; N|S) = \prod_{j=1}^n \{f(N_j|S_j; \theta)\}^{\delta_j} \{1 - F(N_j|S_j; \theta)\}^{1-\delta_j} \quad (5.10)$$

with

$$\delta_j = 1$$

in case of failures; for run-outs

$$\delta_j = 0$$

The PDF interval of a failure is infinitesimally small at $N = N_j$. A run-out however contains only partial information. Some (unknown) part of the fatigue life time is dissipated and failure would appear at the interval $N = (N_j, \infty)$, the PDF right tail, i.e. (1-CDF). The likelihood will be turned into a log-likelihood formulation, valid since $\log(\cdot)$ is a monotonically increasing function, for convenience because of the $\{\text{PDF, CDF}\} \exp(\cdot)$ functions:

$$\begin{aligned} \mathcal{L}(\theta; N|S) &= \log\{L(\theta; N|S)\} \\ &= \sum_{j=1}^n \mathcal{L}_j(\theta; N_j|S_j) \end{aligned} \quad (5.11)$$

with

$$\mathcal{L}_j(\theta; N_j|S_j) = \delta_j \cdot \log\{f(N_j|S_j; \theta)\} + (1 - \delta_j) \cdot \log\{1 - F(N_j|S_j; \theta)\}$$

The maximum (log-)likelihood (maximum joint probability), an optimisation problem, needs to be solved for to obtain the most likely θ for the considered fatigue resistance data set, the parameter maximum likelihood estimates (MLE's) $\hat{\theta}$:

$$\max_{\theta} \{\mathcal{L}(\theta; N|S)\} \quad (5.12)$$

Using different $\{\text{PDF, CDF}\}$ assumptions, the best fit is obtained for the smallest $\max\{\mathcal{L}\}$, i.e. the smallest residual, provided the number of model parameters k is the same. However, if k differs from one distribution to another or S includes extra information – more parameters means generally speaking a better fit – Akaike's Information Criterion (AIC) should be adopted to take k into account (Pascual and Meeker, 1999). Increasing k principally increases AIC since $\max\{\mathcal{L}\}$ is negative.

$$\text{AIC} = -2[\max\{\mathcal{L}(\theta; N|S)\} - k] \quad (5.13)$$

One way to estimate MLE precision is using the (normalised) parameter profile likelihood (PL), obtained maximising $L(\theta_1, \boldsymbol{\theta}_2; N|S)$ relative to $L(\hat{\boldsymbol{\theta}})$:

$$L_r(\theta_1) = \max_{\boldsymbol{\theta}_2} \left\{ \frac{L(\theta_1, \boldsymbol{\theta}_2; N|S)}{L(\hat{\boldsymbol{\theta}}; N|S)} \right\} \quad (5.14)$$

A highly probable value is obtained for $L_r(\theta_1) \rightarrow 1$; a very unlikely one for $L_r(\theta_1) \rightarrow 0$. In between, a confidence interval (CI) can be defined. Since the central limit theorem holds, $\log\{L(\boldsymbol{\theta}; N|S)\} = \sum \log\{L_j(\boldsymbol{\theta}; N_j|S_j)\}$, the MLE's are asymptotically normal distributed. Normal approximate parameter confidence bounds (CB's) can be determined using the Fisher matrix, but accurate results require a relative large sample size. In general (i.e. no matter sample size) the likelihood ratio test can be adopted, since $\log\{L_r(\theta_1)^2\}$ is asymptotically chi-squared distributed. One parameter at the time is considered, meaning the number of degrees of freedom (nDoF) $k = 1$; required confidence level $c_l = 1 - \alpha$.

$$-2 \cdot \log\{L_r(\theta_1)\} \leq \chi^2_{k;1-\alpha} \quad (5.15)$$

The $R|p_s C|c_l$ fatigue resistance quantile/percentile corresponding to a required reliability or probability of survival- and confidence level, includes the mean $\hat{\mu}$ and a $\{p_s, c_l\}$ related correction term:

$$\log(N) = \hat{\mu} + \Phi(1 - p_s)\sigma \quad (5.16)$$

with

$$\hat{\mu} = \hat{C} - \hat{m} \cdot \log(S)$$

Standard(!) CDF $\Phi(1 - p_s)$ controls the reliability level. Standard deviation σ the confidence level. Parameter likelihood $L_r(\sigma)$ can be used to determine the (upper) CB at predefined c_l ; if not provided or unknown, MLE $\hat{\sigma}$ can be adopted. The confidence level is curve wise implemented, useful for design. Depending on the fatigue resistance data distribution, a point wise quantile/percentile may be preferred. However, to obtain a life time dependent parameter likelihood a reparameterisation is required. Using the fatigue strength parameter seems obvious; $C = \log(N_{ji}) + m \cdot \log(S_j) - \Phi(1 - p_s)\sigma$. At each stress level S_j the parameter likelihood is determined. Using the likelihood ratio test, the point wise quantile/percentile lower and upper CB's are obtained.

$$L_r(N_{ji}|S_j) = \max_{\boldsymbol{\theta}_2} \left\{ \frac{L(N_{ji}|S_j, \boldsymbol{\theta}_2; N|S)}{L(\hat{\boldsymbol{\theta}}; N|S)} \right\} \quad (5.17)$$

with

$$\boldsymbol{\theta}_2 = \{m, \sigma\}$$

The MLE $\hat{\sigma}$ is in fact a sample value and needs a correction to be valid for the population. In case the Lognormal distribution is adopted, $\varepsilon \sim \text{logN}(0, 1)$ and the bias corrected estimate simply becomes:

$$\sigma = \sqrt{\frac{n}{n-k}} \cdot \hat{\sigma} \quad (5.18)$$

Data vector length n is corrected for the common nDoF, i.e. $k = 2|\boldsymbol{\theta}| = \{C, m, \sigma\}$. Adopting a Weibull distribution, the residual $\varepsilon \sim \text{W}(0, 1)$ is the 63rd percentile with expected value $E(\varepsilon) = -\gamma$ (Euler constant) and standard deviation $sd(\varepsilon) = \pi/\sqrt{6}$. Unbiased parameter estimates require the regression model (and likelihood L) to be modified including a mean and standard deviation correction (Sarkani et al., 2007) to obtain a biased corrected residual $\varepsilon_c \sim \text{W}(\sqrt{6}/\pi \cdot \gamma, \sqrt{6}/\pi)$ with $E(\varepsilon_c) = 0$ and $sd(\varepsilon_c) = 1$:

$$\log(N) = C - m \cdot \log(S) + \frac{\sqrt{6}}{\pi} \cdot \gamma + \frac{\sqrt{6}}{\pi} \cdot \sigma \varepsilon_c \quad (5.19)$$

Specifying the structural response parameter S , e.g. $S = S_n$ in case the nominal stress range is adopted, $\boldsymbol{\theta} = \{C, m, \sigma\}$ remains unchanged. Using the effective structural stress $S = S_s/(1-r_l)^{1-\gamma}$, the load ratio coefficient is incorporated as well: $\boldsymbol{\theta} = \{C, m, \gamma, \sigma\}$. The total stress $S = S_T$ requires at least the elastoplasticity coefficient to be added; $\boldsymbol{\theta} = \{C, m, n, \gamma, \sigma\}$. Possible extensions include the effective defect size or -notch radius.

Correlating the {MCF, HCF} range at the same time, a transition in fatigue damage mechanism (i.e. growth dominant turns into initiation controlled), a slope change, has to be taken into account, introducing a dual slope formulation:

$$\log(N) = C - m_1 \cdot \log(S) - \left\{ \left(\frac{m_1}{m_2} \right) - 1 \right\} \cdot \log[1 + \exp\{\log(S) - \log(S_c)\}^{-m_2}] \quad (5.20)$$

If the HCF slope ($m_1 \rightarrow \infty$), the dual slope formulation (Eq. 5.20) will turn into a (random) fatigue limit model. From physical (i.e. material and loading) point of view the existence of a fatigue limit S_∞ , infinite life time, can be questioned (e.g. Bathias et al., 2001; Wang and Zheng, 2010; Pyttel et al., 2011; Cremer et al., 2013) as it is principally a right-censored data based hypothesis; insufficient HCF test data. Perfect or self-healing materials do not exist (yet), meaning the (micro-structural) weakest link will cause fatigue induced failure at last. The only criterion is sufficient testing time. If the loading is stochastic, somewhere in time a peak load will pass and breaks through S_∞ (or equivalent: stress intensity threshold ΔK_{th} , critical defect size a_0 ; Paragraph 4.2), starting a crack to initiate/grow.

From statistical point of view however a fatigue limit model can still be meaningful:

$$\log(N) = C - m \cdot \log(S - S_\infty(\mu, \sigma)) \quad (5.21)$$

The fatigue limit $S_\infty(\mu, \sigma)$ however is considered to be a stochastic variable (Pascual and Meeker, 1999) rather than a constant (Xiong and Shenoi, 2011) because of random micro-structural material parameters like grain-size and orientation, number of dislocations and inclusions.

The scatter range index (Radaaj, Sonsino and Fricke, 2006) related to $p_s = 0.10$ and $p_s = 0.90$ probability levels of survival will be adopted as data quality measure. In terms of the structural response parameter:

$$T_S = \frac{S_{R10}}{S_{R90}} \quad (5.22)$$

For welded joints, $T_S = 1:1.5$ is a characteristic value in case of good workmanship. A confidence level c_l is not explicitly considered, meaning the quantiles/percentiles should be formulated using the parameter MLE's. For a single slope fatigue resistance curve, the index becomes in terms of fatigue life time: $T_N = T_S^m$.

5.4 Small scale specimen CA fatigue resistance

Fatigue assessment concepts using an intact geometry parameter like the nominal-, structural hot spot- or effective notch stress $\{S_n, S_s, S_e\}$ typically introduce a number of FAT classes, reflecting the SSS fatigue strength at $N = 2 \cdot 10^6$ [cycles], to define the fatigue resistance curve(s). The slope, a fatigue damage mechanism measure, is the same for all. Adding (local) structural response information to a global geometry based parameter (i.e. the criterion application generalises at the same time), the number of FAT classes reduces ultimately up to one, like established for the effective notch (reference) stress concept. However, the curve parameters are data related estimates, meaning the variety in loading, geometry and quality defines the life time accuracy and limits the range of application, which – for the record – seems limited for the proposed S_e FAT class (Sonsino, 2009).

To reduce estimated life time uncertainty, a joint (family of) fatigue resistance curve(s) will be established using the total stress S_T , an equivalent structural response parameter like the BSS ΔS_s , using aluminium CA SSS artificial T-joint- and AW data series.

5.4.1 Artificial T-joint data

Crack growth behaviour at weld toe notches in aluminium arc-welded joint geometries is identified (Paragraph 4.4) up to $(a = t_p)$, meaning SSS fatigue resistance data is available at the same time and allows to verify (average) crack growth model parameter values.

The non-welded BM data is limited to the MCF range and a single slope formulation (Eq. 5.3) is adopted. Although the nominal stress concept, i.e. $S_n = (\Delta F/A)$, provides limited fatigue damage information – notch induced crack growth anomalies may affect scaling factor C and slope m – zone 3 far field stress gradient effects; in fact zone 2 contributions (Paragraph 5.2), can be observed (Fig. 5.10). At each stress level $S = S_j$, from the left to the right ($r_s = -0.6$) \rightarrow ($r_s = 0.0$) \rightarrow ($r_s = 0.4$), $\sigma_n(r/t_p)$ changes from monotonically increasing to non-monotonic, meaning the notch affected zone size decreases (Paragraph 2.6) and N increases.

The Normal $N(\mu, \sigma)$ - rather than Weibull distribution $W(\mu, \sigma)$ provides the best fit (Table 5.1). Eurocode 9 BM slope $m = 7$ is obviously crack initiation dominated and the data slope $m = 4.13$ turns out to be closer to the Eurocode 9 AW joint value $m = 3.4$, suggesting crack growth dominates the welded joint fatigue life time indeed. The (point wise R95C95 lower CB estimated, extrapolated) fatigue strength at $N = 2 \cdot 10^6$ is comparable to the Eurocode 9 welded joint value as well; FAT36.

distr.	C	m	σ	T_S	$\max\{\mathcal{L}\}$	AIC
$N(\mu, \sigma)$	13.27	4.13	0.23	1:1.40	-35.48	76.97
$W(\mu, \sigma)$	13.33	4.17	0.27	1:1.43	-37.83	81.66

Table 5.1: Parameter estimates DS T-joint crack growth specimen (non-welded, S_n).

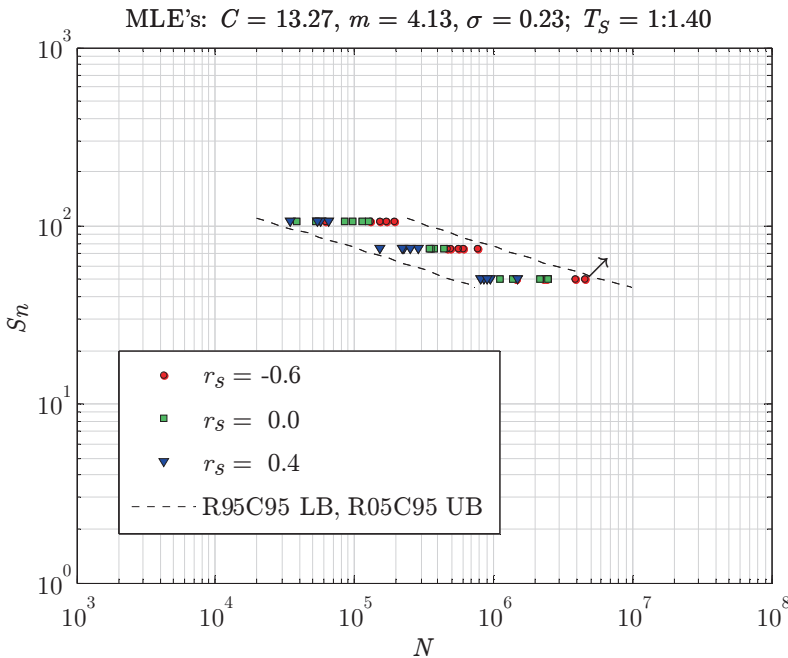


Figure 5.10: DS T-joint crack growth specimen nominal stress concept based fatigue resistance $\sim N(\mu, \sigma)$; non-welded data series $S_n = \{50, 75, 105\}$.

Material effects are limited as already confirmed for some crack growth data sets (e.g. Fig. 4.27), σ_n^r is of the self-equilibrium type and the scatter index is close to a typical as-welded joint data series value ($T_S \approx 1:1.5$), suggesting the initial crack size distribution $a_i \sim W(\mu, \sigma)$, including location- and scale parameter, is a realistic one.

However, the differences in life time N for the applied structural bending stress ratios r_s are not as large as expected. Since at 9 specimens (for each type of far field stress distribution 1 specimen at each load level) the actual far field strain distribution has been measured – using 1 strain gauge (SG) at the top and 1 at the bottom to capture both the membrane- and bending component (Fig. 5.11) – the obtained time series have been compared to the target values. Assuming $E = 70$ [GPa] and $\nu = 0.33$ [-], the SG M-series ($r_s = 0.0$) revealed that σ_{min} has never been reached, i.e. is approximately three times as high as the target value, meaning the effective stress range is smaller and load ratio r_l has increased (Table 5.2).

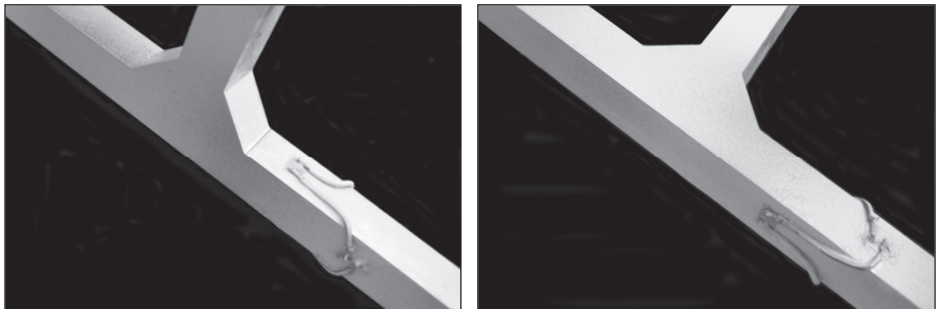


Figure 5.11: DS T-joint crack growth specimen SG's at top and bottom.

$S_n = 50$ M-series	σ_{max} top [MPa]	σ_{min} top [MPa]	$\Delta\sigma_m$ [MPa]	$\Delta\sigma_b$ [MPa]
target (non-lin.)	56 (57)	6 (6)	50	0 (1)
measured	53	15	37	1

$S_n = 75$ M-series	σ_{max} top [MPa]	σ_{min} top [MPa]	$\Delta\sigma_m$ [MPa]	$\Delta\sigma_b$ [MPa]
target (non-lin.)	83 (86)	8 (8)	75	0 (3)
measured	80	23	56	1

$S_n = 105$ M-series	σ_{max} top [MPa]	σ_{min} top [MPa]	$\Delta\sigma_m$ [MPa]	$\Delta\sigma_b$ [MPa]
target (non-lin.)	117 (122)	12 (12)	105	0 (5)
measured	114	32	76	7

Table 5.2: SG M-series characteristics, average load ratio at top: $r_l = 0.28$ [-]

Although the normal force measured- and target values are in agreement, accuracy issues may have been introduced because the operated MTS fatigue testing machine capacity is 100 [kN] and the minimum load condition is ≤ 1 [%] of the load cell range. Analysing (static) DIC displacement fields, i.e. photos at F_{min} condition, the (cyclic) SG results have been confirmed; $\sigma_s = \sigma_m |F_{min}$ shows a high level of scatter at the same time. Geometric non-linear behaviour introduced bending.

The {MBN, MBM} series r_s values are significantly smaller as supposed to be (Table 5.3 and 5.4), i.e. almost vanished: $r_s \sim \{-0.1, +0.1\}$. Specimen fixtures including sleeve bearings have been used aiming for frictionless hinges to ensure the required normal force and bending moment to operate in the weld toe cross-section no matter in-plane fixture misalignments. However, (Coulomb) friction induced counteracting bending still has been identified; the $\Delta\sigma_b$ measured- and target value ratio is about ~ 0.15 . The load ratios are different at top and bottom and the former value has been selected as governing one, assuming the major part of the fatigue life is spent in the notch affected micro-crack region.

To establish $\{r_s, r_l\}$ induced far field stress consequences, the effective structural stress $S_\gamma = S_s / (1 - r_l)^{1-\gamma}$ (Paragraph 4.2.4) will be adopted (Fig. 5.12). A considerable σ reduction has been observed. The maximum stress fatigue damage contribution turns out to be at least as much as the stress range; the load ratio coefficient γ MLE is slightly below the geometric mean. In comparison to the S_n based parameter MLE's, slope m remains principally unaffected as it should be, since the damage mechanism does not change. The Weibull distribution provides the better fit (Table 5.5), although the initial crack size is not explicitly considered yet.

$S_n = 50$ MBN-series	σ_{max} top [MPa]	σ_{min} top [MPa]	$\Delta\sigma_m$ [MPa]	$2\sigma_b$ [MPa]
target (non-lin.)	35 (40)	3 (4)	50	-19 (-14)
measured	44	10	36	-2

$S_n = 75$ MBN-series	σ_{max} top [MPa]	σ_{min} top [MPa]	$\Delta\sigma_m$ [MPa]	$2\sigma_b$ [MPa]
target (non-lin.)	52 (62)	5 (5)	75	-28 (-18)
measured	69	17	55	-3

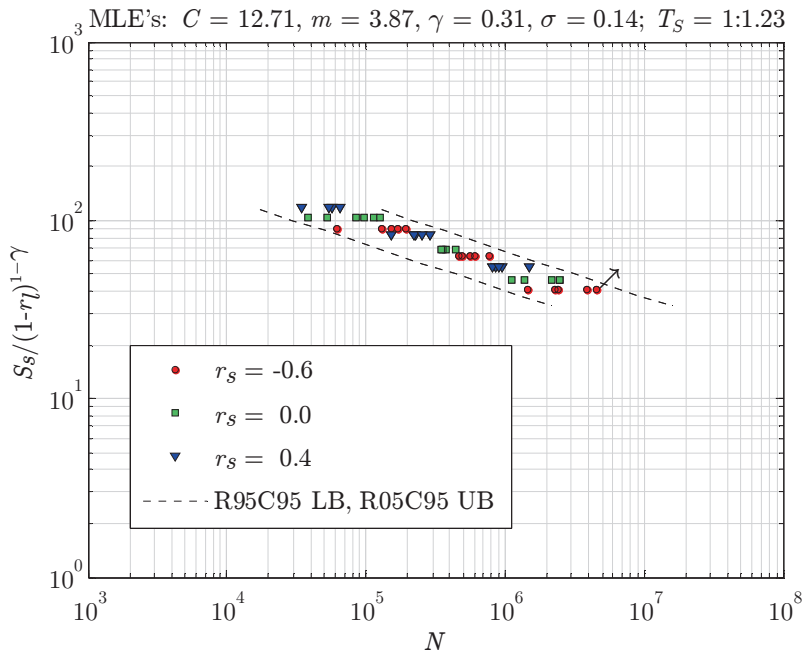
$S_n = 105$ MBN-series	σ_{max} top [MPa]	σ_{min} top [MPa]	$\Delta\sigma_m$ [MPa]	$2\sigma_b$ [MPa]
target (non-lin.)	73 (93)	7 (8)	105	-39 (-21)
measured	104	25	76	-3

Table 5.3: SG MBN-series characteristics, average load ratio at top: $r_l = 0.23$ [-]

$S_n = 50$ MBM-series	σ_{max} top [MPa]	σ_{min} top [MPa]	$\Delta\sigma_m$ [MPa]	$\Delta\sigma_b$ [MPa]
target (non-lin.)	93 (88)	8 (10)	50	33 (28)
measured	65	24	40	3

$S_n = 75$ MBM-series	σ_{max} top [MPa]	σ_{min} top [MPa]	$\Delta\sigma_m$ [MPa]	$\Delta\sigma_b$ [MPa]
target (non-lin.)	139 (127)	13 (13)	75	50 (39)
measured	93	33	54	6

$S_n = 105$ MBM-series	σ_{max} top [MPa]	σ_{min} top [MPa]	$\Delta\sigma_m$ [MPa]	$\Delta\sigma_b$ [MPa]
target (non-lin.)	194 (175)	18 (20)	105	70 (50)
measured	132	46	76	10

Table 5.4: SG MBM-series characteristics, average load ratio at top: $r_l = 0.36$ [-]Figure 5.12: DS T-joint crack growth specimen effective structural stress concept based fatigue resistance $\sim W(\mu, \sigma)$; non-welded data series.

distr.	C	m	γ	σ	T_S	$\max\{\mathcal{L}\}$	AIC
$N(\mu, \sigma)$	12.67	3.88	0.40	0.15	1:1.25	-14.04	36.08
$W(\mu, \sigma)$	12.71	3.87	0.31	0.14	1:1.23	-11.91	31.83

Table 5.5: Parameter estimates DS T-joint crack growth specimen (non-welded, S_γ).

Last but not least, the total stress parameter S_T is adopted; the initial crack size a_i is explicitly taken into account and the average notch/crack tip elastoplasticity coefficient n – principally a specimen loading and geometry specific parameter – is determined. Solving $\max\{\mathcal{L}\}$ does principally not involve constraint equations, but parameter constraints, e.g. $0 \leq \sigma \leq 1$, have been applied. The obtained scatter level is very small (Fig. 5.13) and T_S indicates the life time uncertainty has become below a factor 2; other structural response parameters are insufficient in this respect (i.e. local information is required). Crack growth behaviour is non-monotonic in average; $n_e = n + m/2 \sim 5$, likely a plane stress-, far field load level- and local laser heating induced contribution as already observed for a crack growth time series analysis (Paragraph 4.4.7). Because of $a_i \sim W(\mu, \sigma)$, $W(\theta; N|S_j)$ would make sense, but a slightly better fit is obtained using the Normal distribution (Table 5.6).

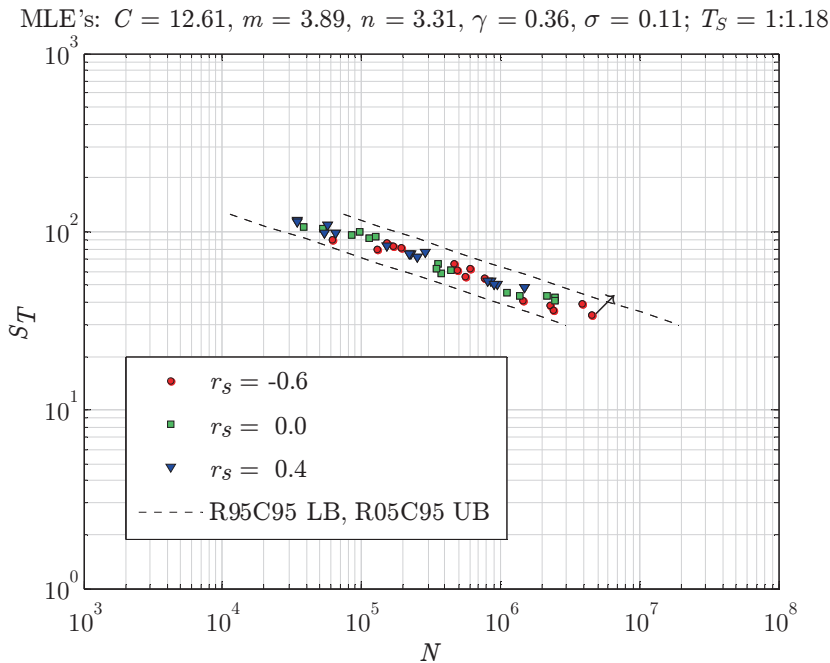


Figure 5.13: DS T-joint crack growth specimen total stress concept based fatigue resistance $\sim N(\mu, \sigma)$; non-welded data series.

distr.	C	m	n	γ	σ	T_S	$\max\{\mathcal{L}\}$	AIC
$N(\mu, \sigma)$	12.61	3.89	3.31	0.36	0.11	1:1.18	-0.47	10.93
$W(\mu, \sigma)$	12.70	3.88	3.59	0.26	0.12	1:1.18	-0.79	11.58

Table 5.6: Parameter estimates DS T-joint crack growth specimen (non-welded, S_T).

The identified peak stress importance ($\gamma < 0.5$) makes sense, in particular if the cyclic remote mechanical load component is governing (i.e. the quasi-constant residual stress contribution is negligible). After all, the peak stress (SCF) is responsible for the weld toe notch fatigue damage sensitivity.

Parameter profile likelihoods (Fig. 5.14 to 5.18) show a unique $\max\{\mathcal{L}\}$ solution; a global maximum is obtained. The resistance curve parameter $\{C, m, \sigma\}$ CB's indicate the confidence level is relatively high compared to the total stress parameter coefficient $\{n, \gamma\}$ values. Elastoplasticity coefficient n is loading and geometry dependent, specimen specific, meaning the MLE is an average one. Load ratio coefficient γ basically controls the scatter level, i.e. σ , as observed in the correlation matrix P (Table 5.7). Using the inverse of the (negative) Hessian $H(\boldsymbol{\theta}) = \partial^2 \mathcal{L}(\boldsymbol{\theta}) / (\partial \boldsymbol{\theta} \partial \boldsymbol{\theta}')$ as estimator of the asymptotic(ally Normal distributed) (co)variance matrix $V = (-H)^{-1}$, the scaled (co)variance- or correlation matrix P , $\rho_{ij} = V_{ij} / (\sqrt{V_{ii}} \sqrt{V_{jj}})$, is obtained. Parameters $\{C, m\}$ are highly correlated as it should be, since a changing slope affects the fatigue strength; n dependency is significant. The S_T parameter correlation $\rho_{n, \gamma}$ is limited. Elastoplasticity coefficient n hardly affects the standard deviation σ , suggesting it might be similar for all MCF data. The relatively large $\rho_{\gamma, \sigma}$ value shows that structural stress effectivity dominates the fatigue resistance scatter.

Initial crack size a_i is prescribed and n incorporates elastoplasticity, suggesting an average effective parameter estimate a_e is out of question. An average effective notch radius ρ_e – even though the stress gradient is taken into account and ρ_f (Paragraph 2.11) becomes obsolete – however is only useful if (at least) different (type of) welded joint geometries are involved. Solving $\max\{\mathcal{L}\}$ for a range of ρ_e values rather than ρ_e incorporated in parameter vector $\boldsymbol{\theta}$ because of the high $\{n, \rho_e\}$ correlation (both control notch elastoplasticity), for the non-welded crack growth specimen data a monotonically increasing function $AIC(\rho_e)$ is obtained (Fig. 5.19).

P	C	m	n	γ	σ
C	1.00	0.88	0.61	-0.05	-0.02
m		1.00	0.34	0.31	0.04
n			1.00	0.13	-0.01
γ				1.00	0.12
σ					1.00

Table 5.7: Correlation matrix DS T-joint crack growth specimen (non-welded, S_T).

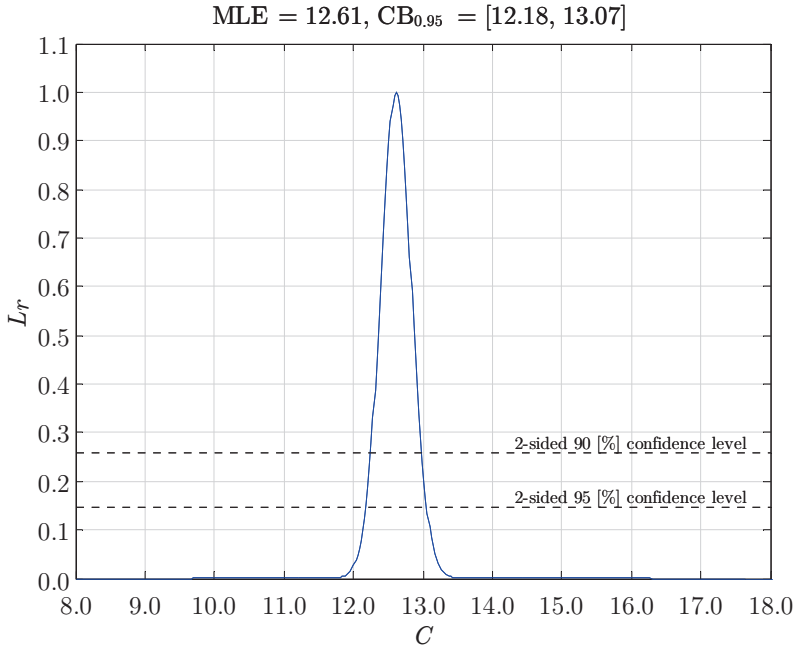


Figure 5.14: C relative parameter profile likelihood (non-welded specimen, S_T).

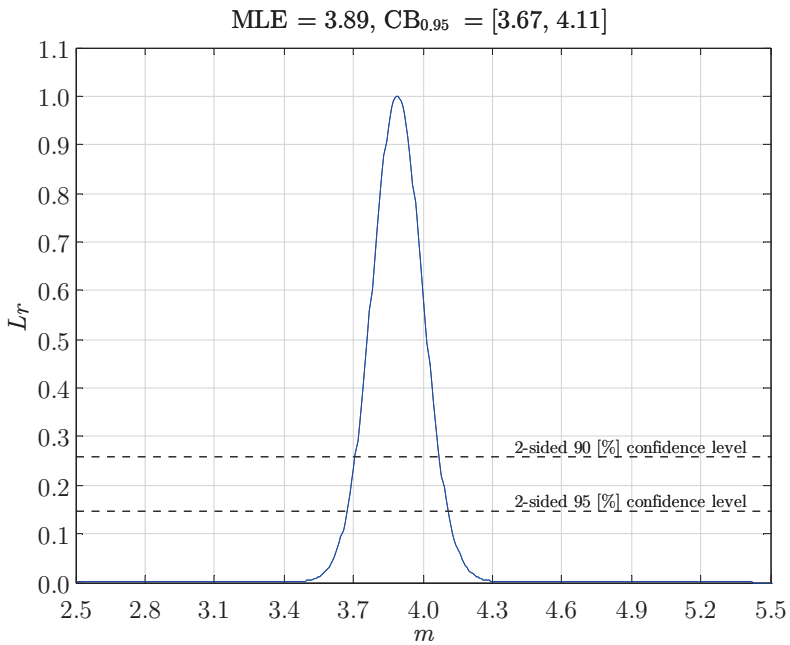


Figure 5.15: m relative parameter profile likelihood (non-welded specimen, S_T).

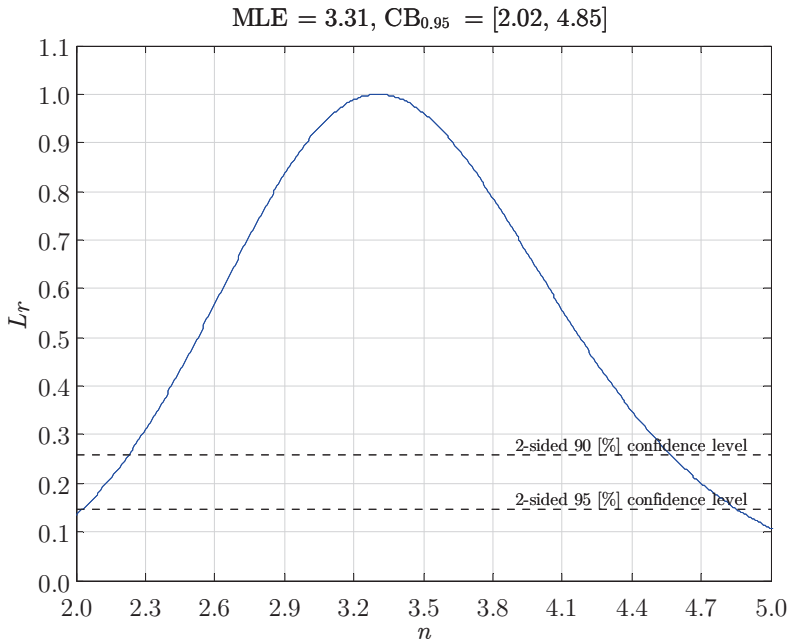


Figure 5.16: n relative parameter profile likelihood (non-welded specimen, S_T).

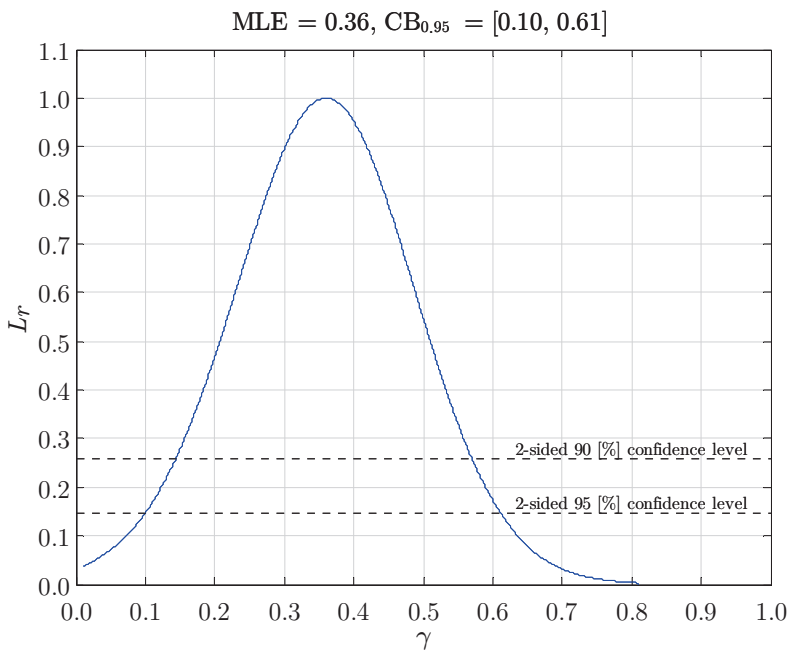


Figure 5.17: γ relative parameter profile likelihood (non-welded specimen, S_T).

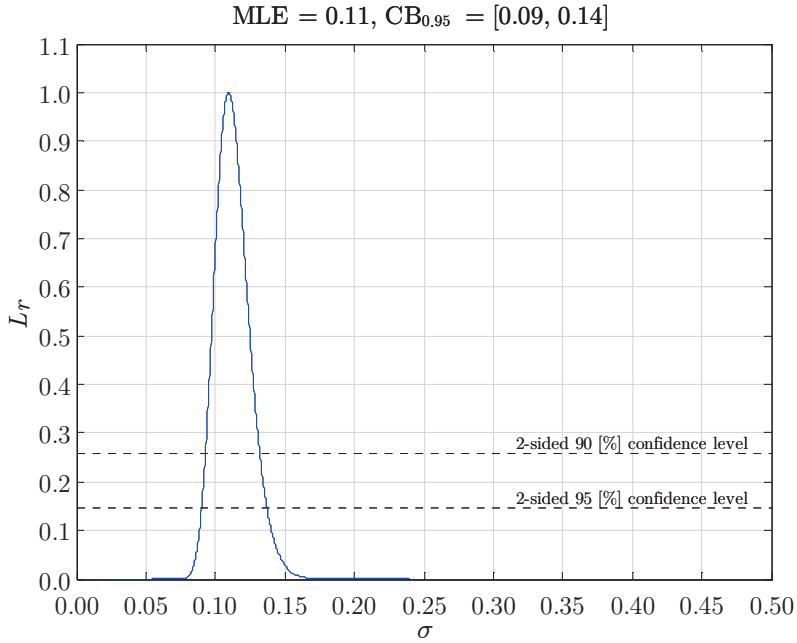


Figure 5.18: σ relative parameter profile likelihood (non-welded specimen, S_T).

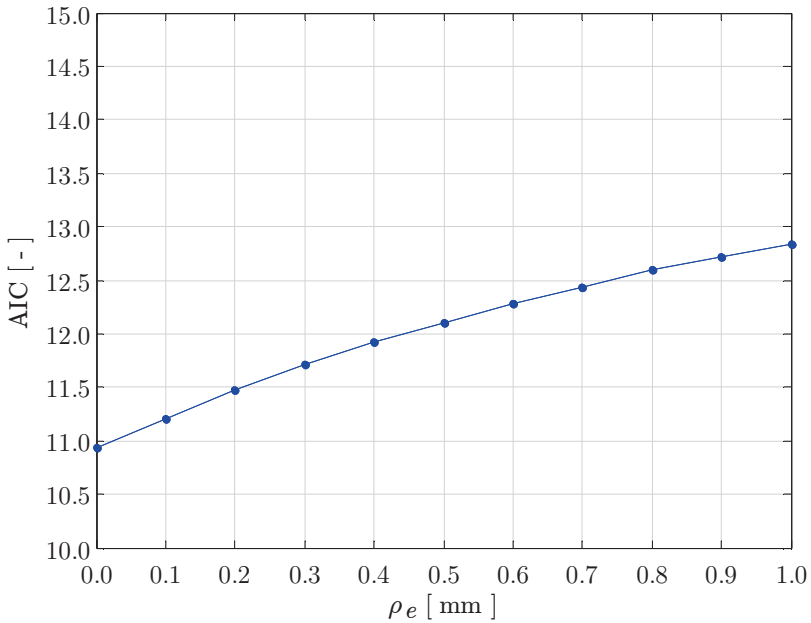


Figure 5.19: Akaike Information Criterion $AIC(\rho_e)$ for non-welded specimen; S_T .

Similarly, the welded DS T-joint crack growth specimen data series have been analysed. In comparison to the non-welded results (Fig. 5.10), the S_n data scatter (Fig. 5.20) has increased, likely a HAZ (micro-structure) material effect; defect size a_i is predefined. The Normal distribution still provides the better data fit (Table 5.8). The (estimated) FATigue class however has not changed as explained (Fig. 5.10 and 5.20); FAT36, although $\{C, m\}$ are different. Applied loading is slightly smaller and $\{S_{n,min}, N\}$ approaches the HCF range, i.e. the data scatter will typically increase and m starts to change.

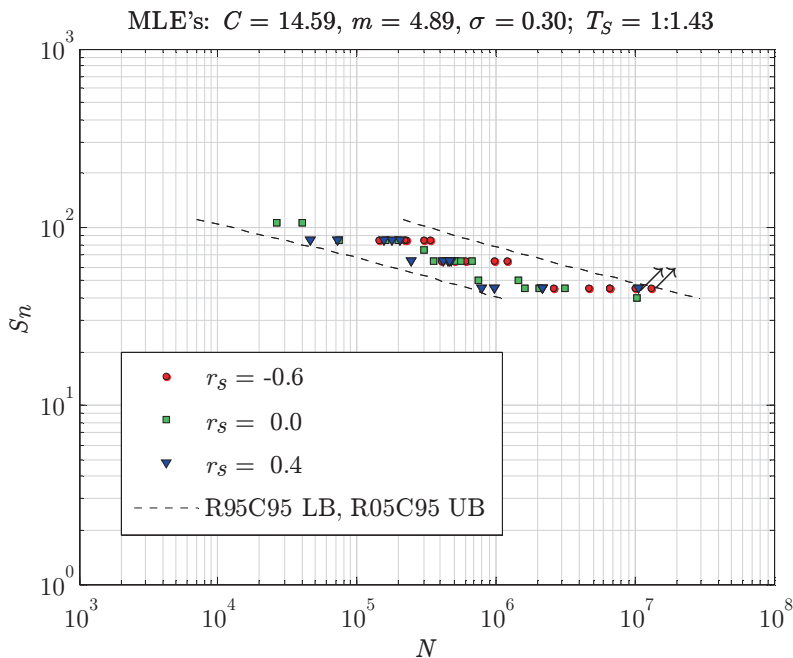


Figure 5.20: DS T-joint crack growth specimen nominal stress concept based fatigue resistance $\sim N(\mu, \sigma)$; welded data series $S_n = \{45, 65, 85\}$.

distr.	C	m	σ	T_S	$\max\{\mathcal{L}\}$	AIC
$N(\mu, \sigma)$	14.59	4.89	0.30	1:1.43	-47.52	101.0
$W(\mu, \sigma)$	15.69	5.51	0.34	1:1.41	-50.49	107.0

Table 5.8: Parameter estimates DS T-joint crack growth specimen (welded, S_n).

Assuming the far field stress distributions are similar to the non-welded series – no SG data is available and the test setup is the same – the membrane and bending amplitude have been scaled according to F_x and the single-slope S_T based fatigue resistance (Fig. 5.21, Table 5.9) has been obtained. The changing data slope for decreasing S_T has become visible. The load ratio coefficient ($\gamma = 0.85$) is in agreement with the common assumption that $\Delta\sigma$ dominates the welded joint fatigue damage process because of the high (quasi-static, self-equilibrating) tensile residual (notch) stress, meaning the remote mechanical loading induced σ_{max} is basically irrelevant.

Using a single slope formulation in case of {MCF, HCF} data provides average fatigue strength- and damage mechanism information only. For a dual slope model, the welded data m_1 value should become close to the non-welded data m like observed (Fig. 5.22, Table 5.10) since the fatigue damage mechanism should be the same: $m_1 \approx m \approx 4$. The AIC value has just slightly decreased (Table 5.9 and 5.10). Because of the limited HCF data, the m_2 slope uncertainty is large (Fig. 5.23). The transition location (Fig. 5.24), i.e. position of slope change; $S_c|N \sim 2 \cdot 10^6$ is a typically assumed one. For decreasing load ratio effects (Fig. 4.10) notch affected micro-crack growth becomes less pronounced (Fig. 4.8) – as the correlation coefficient $\rho_{n,\gamma}$ confirms (Table. 5.11) – and the elastoplasticity coefficient has reduced to ($n = 1.76$). Whether a coincidence or not, it is close to the crack growth test data based BSS value ($n = 2$). The transition- and structural stress effectivity parameters $\{m_2, S_c, \gamma\}$ define the fatigue resistance scatter.

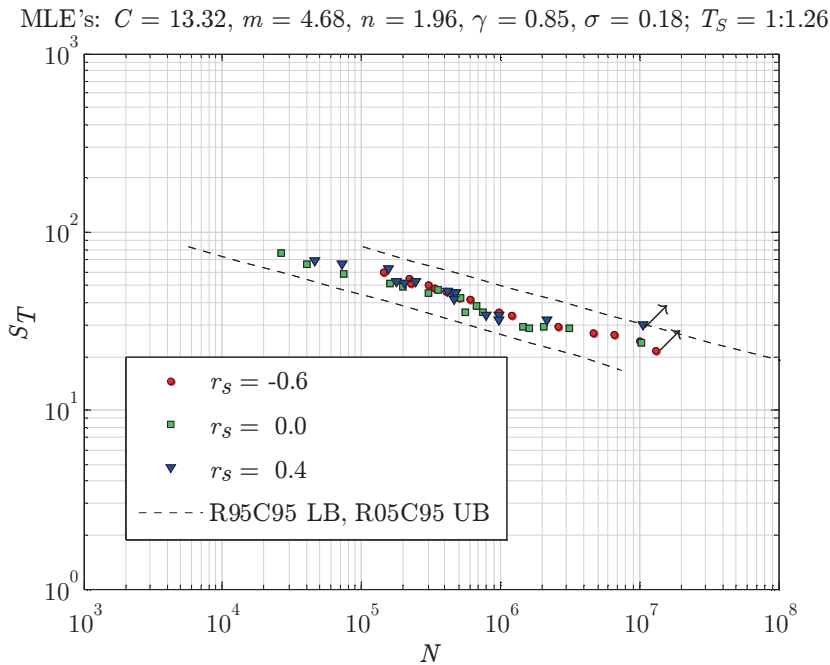


Figure 5.21: DS T-joint crack growth specimen total stress concept based fatigue resistance, 1-slope $\sim N(\mu, \sigma)$; welded data series.

distr.	C	m	n	γ	σ	T_S	$\max\{\mathcal{L}\}$	AIC
$N(\mu, \sigma)$	13.32	4.68	1.96	0.85	0.18	1:1.26	-24.66	59.31
$W(\mu, \sigma)$	13.81	5.07	1.98	0.95	0.26	1:1.32	-33.56	77.12

Table 5.9: Parameter MLE's DS T-joint crack growth specimen (welded, 1-slope S_T).

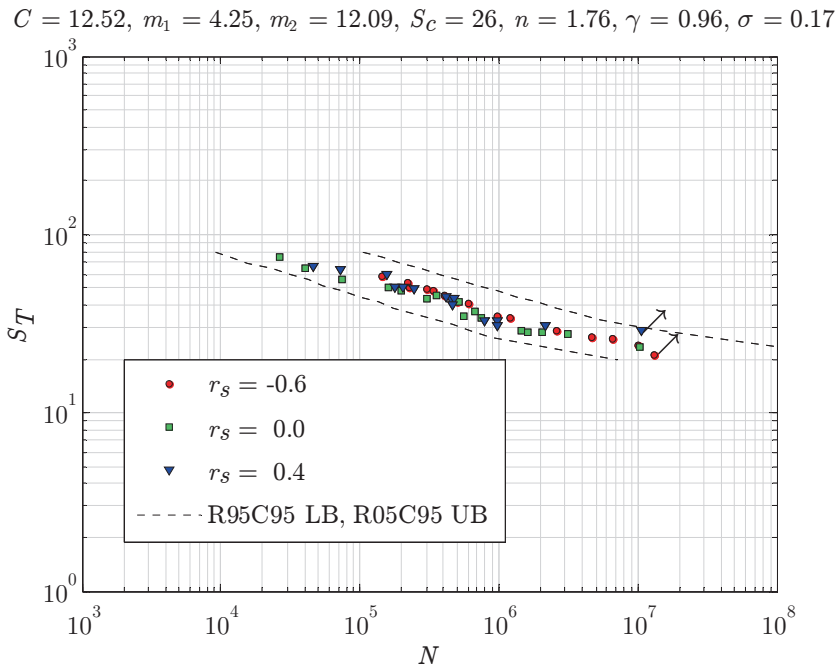


Figure 5.22: DS T-joint crack growth specimen total stress concept based fatigue resistance, 2-slope $\sim N(\mu, \sigma)$; welded data series.

distr.	C	m_1	m_2	S_c	n	γ	σ	T_S	AIC
$N(\mu, \sigma)$	12.52	4.25	12.1	26	1.76	0.96	0.17	1:1.27	56.33
$W(\mu, \sigma)$	11.89	4.02	7.81	29	0.55	1.00	0.25	1:1.41	77.25

Table 5.10: Parameter MLE's DS T-joint crack growth specimen (welded, 2-slope S_T).

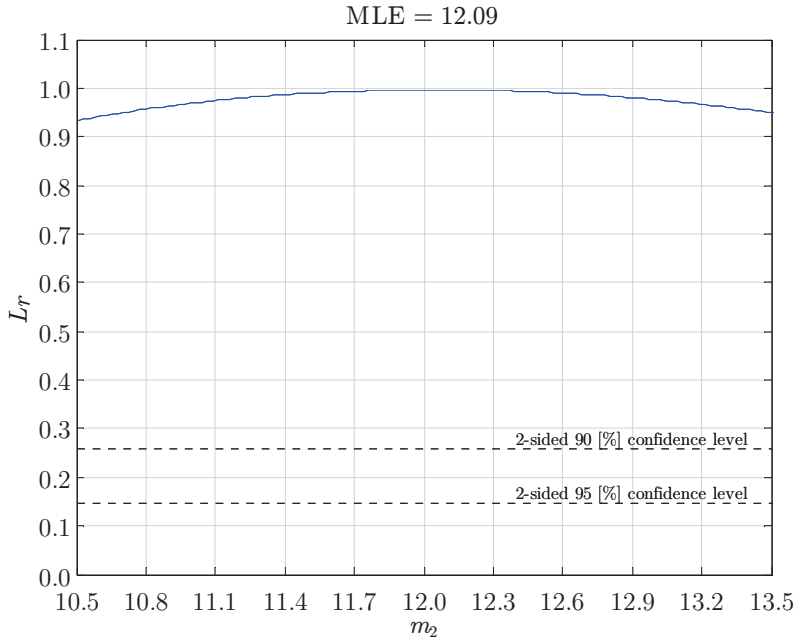


Figure 5.23: m_2 relative parameter profile likelihood (welded specimen, 2-slope S_T).

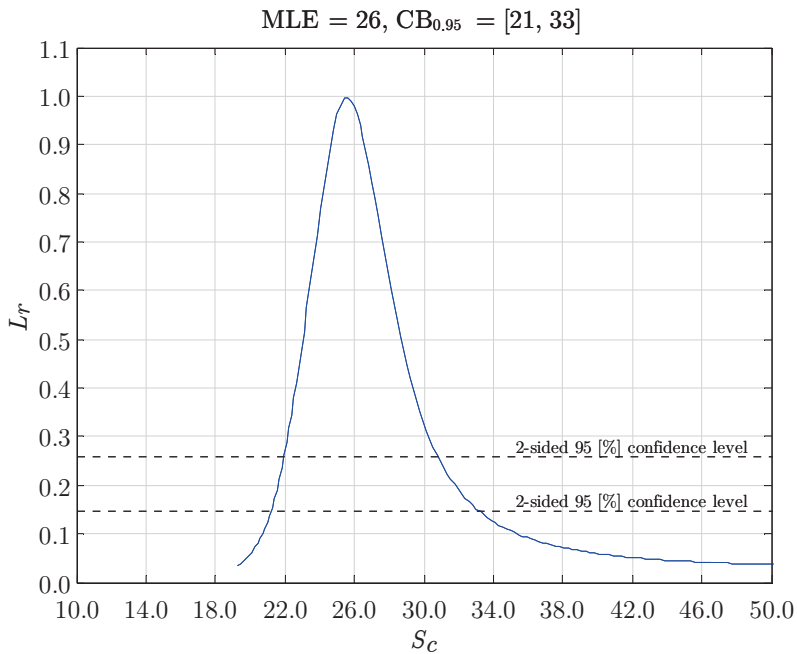


Figure 5.24: S_c relative parameter profile likelihood (welded specimen, 2-slope S_T).

P	C	m_1	m_2	S_c	n	γ	σ
C	1.00	0.99	-0.26	-0.14	-0.11	-0.21	-0.09
m_1		1.00	-0.37	-0.02	-0.20	-0.08	0.03
m_2			1.00	-0.68	0.35	-0.71	-0.75
S_c				1.00	-0.11	0.97	0.93
n					1.00	-0.19	-0.28
γ						1.00	0.93
σ							1.00

Table 5.11: Correlation matrix DS T-joint crack growth specimen (welded, 2-slope S_T).

Comparing the fatigue resistance curve parameter estimates (Table 5.6 and 5.10) for {non-welded, welded} geometry and loading controlled artificial T-joints, the fatigue strength C - and damage mechanism parameters $\{m, m_1\}$ are similar; only scatter parameter σ has increased for the welded series.

The slope $\{m, m_1\}$ for the considered crack damaged specimens has been observed way below the commonly adopted BM value ($m \sim 7$, Eurocode 9) and comparable to the (AW, HAZ) joint value ($m \sim 4$, Eurocode 9) suggesting crack growth is governing indeed. However, comparing the {BM, HAZ, WM} fatigue resistance of intact plane geometry ($K_t = 0$)- and notched ($K_t = 11.2$) specimens (Morgenstern, 2006b), a similar change in slope is observed. The fatigue (initiation and growth) damage mechanism seems predominantly be a matter of notch/crack tip elastoplasticity (for decreasing defect size the notch (singularity) becomes governing; Paragraph 5.2) rather than a material effect. After all, the BSS steel- and TS aluminium slope are comparable as well (Paragraph 5.4.2). The fatigue strength $\log(C)$ is much more material sensitive in that respect. The $\rho_{n,\sigma}$ correlation has increased since {MCF, HCF} is involved and notch/crack tip elastoplasticity changes for decreasing load level.

5.4.2 As-welded joint data

The relatively complicated AW joint geometry parameters like $\{l_w, h_w, \rho, a_i\}$ are principally random and production quality dependent at the same time, i.e. may vary from one fatigue resistance data set to another. Reinvestigating multiple CA Aluminium {5xxx, 6xxx} SSS series ($5 \leq t_p \leq 25$) available in literature, the average quality (mode-I) TS fatigue resistance statistics will be obtained in order to establish a design curve.

Both weld toe- and weld root induced failures (Ribeiro, 1993; Van Straalen et al., 1994a, 1994b, 1994c, 1994d; Hirt and Smith, 1995; Maddox, 1995; Matsuoka et al., 1995; Sharp, Nordmark and Menzemer, 1996; Haagenzen et al., 1998; Meneghetti, 1999; Brandt et al., 2000; Daniels, 2001; Aukes, 2004; Strik and Dijkstra, 2004; Mann, 2006; Morgenstern, 2006a, 2006b; Sidhom et al., 2007; Ye and Moan, 2007; Tveiten and Fjeldstad, 2009; Coughlin and Walbridge, 2012; Morinaga et al., 2014) are classified (Paragraph 2.2.) and processed. Obviously, fatigue is a matter of time in different ways.

Far field stress parameters $\{\sigma_s, r_s\}$ are calculated exploiting FEA, the idealised specimen geometry and applied nominal loading. The SSS structural response is defined as load controlled since no neighbour structural members are involved and the displacement controlled residual stress is assumed to be of the self-equilibrating type. Strain gauge based far field stress information has been incorporated if available, meaning any welding deformations induced secondary order bending is implicitly included up to some extent only.

Load ratio effects

The SSS data remote mechanical load ratio spectrum is relatively wide, i.e. in between ($-1.0 \leq r_l \leq 0.75$). For increasing r_l , increasing mean stress σ_r , the stress amplitude should decrease to avoid exceedance of the material ultimate strength ($\sigma < \sigma_{us}$), suggesting $C = f(\sigma_r/\sigma_{us})$; the yield strength σ_{ys} controls elastoplasticity. Welded joint fatigue test results typically suggest a non-linear mean stress dependency and an exponential relation has been proposed (Kwofie, 2001):

$$C = C_{r-1} \cdot \exp \left\{ -\alpha \left(\frac{\sigma_r}{\sigma_{us}} \right) \right\} \quad (5.23)$$

Fatigue strength coefficient C_{r-1} corresponds to the fully reversed load case ($r_l = -1.0$) and the (inverse) Basquin type of relation for any non-zero σ_r becomes:

$$\sigma = C_{r-1} \cdot \exp \left\{ -\alpha \left(\frac{\sigma_r}{\sigma_{us}} \right) \right\} \cdot N_{r-1}^{-\frac{1}{m}} \quad (5.24)$$

Assuming slope m is σ_r -invariant, σ (Eq. 5.24) at ($r_l = -1.0$) turns into:

$$\sigma_{r-1} = C_{r-1} \cdot N_{r-1}^{-\frac{1}{m}} \quad (5.25)$$

and quotient (σ/σ_{r-1}) denotes

$$\left(\frac{\sigma}{\sigma_{r-1}}\right) = \exp \left\{ -\alpha \left(\frac{\sigma_r}{\sigma_{us}}\right) \right\}. \quad (5.26)$$

Using a Maclaurin series expansion, a 1st order approximation is obtained:

$$\left(\frac{\sigma}{\sigma_{r-1}}\right) = \left\{ 1 - \alpha \left(\frac{\sigma_r}{\sigma_{us}}\right) \right\}, \quad (5.27)$$

basically a generalised formulation of several empirical mean stress models developed over time (Kwofie, 2001; Lobato da Silva et al., 2010).

1. For $(\alpha = 1)$, the Goodman relation (Dowling, 2007) is obtained:

$$\left(\frac{\sigma}{\sigma_{r-1}}\right) = \left\{ 1 - \left(\frac{\sigma_r}{\sigma_{us}}\right) \right\} \quad (5.28)$$

In case both mean stress and stress amplitude are relatively small; $(\sigma/\sigma_{r-1}) \rightarrow 1$ and $(\sigma_r/\sigma_{us}) \rightarrow 0$, the material behaviour is linear elastic.

2. For $(\alpha = \sigma_{us}/\sigma_{ys})$, using the yield stress rather than ultimate strength, the more conservative Soderberg relation (Herzberg, 1995) appears:

$$\left(\frac{\sigma}{\sigma_{r-1}}\right) = \left\{ 1 - \left(\frac{\sigma_r}{\sigma_{ys}}\right) \right\} \quad (5.29)$$

3. For $(\alpha = \sigma_r/\sigma_{us})$, the Gerber relation (Dowling, 2007) is acquired:

$$\left(\frac{\sigma}{\sigma_{r-1}}\right) = \left\{ 1 - \left(\frac{\sigma_r}{\sigma_{us}}\right)^2 \right\} \quad (5.30)$$

If plasticity cannot be neglected, i.e. (σ/σ_{r-1}) as well as (σ_r/σ_{us}) increase, mean stress effects become non-linear.

Exponential mean stress models have been developed in order to prevent for inaccurate fatigue lifetime estimates in case of relatively low σ and high σ_r , e.g. welded joints operating in the {MCF, HCF} region experiencing both a remote mechanical- and thermal residual mean stress contribution. The proposed formulation (Kwofie, 2001; Eq. 5.26) is a generalised one:

1. For $(\alpha = -\{\sigma_{us}/(2 \cdot \sigma_r)\} \cdot \ln\{(1 - r_l)/2\})$, a geometric mean of the stress cycle defining components $\{\Delta\sigma, \sigma_{max}\}$ is assumed (Smith, Watson and Topper, 1970; Paragraph 4.2.4):

$$\left(\frac{\sigma}{\sigma_{r-1}}\right) = \left(\frac{1 - r_l}{2}\right)^{\frac{1}{2}} \quad (5.31)$$

2. For $(\alpha = -\{\sigma_{us}/(\gamma \cdot \sigma_r)\} \cdot \ln\{(1 - r_l)/2\})$, fitting parameter γ substitutes the square root (Eq. 5.31); a load ratio coefficient (Walker, 1970; Paragraph 4.2.4):

$$\left(\frac{\sigma}{\sigma_{r-1}}\right) = \left(\frac{1 - r_l}{2}\right)^{\gamma} \quad (5.32)$$

In the notch affected region, elastoplasticity coefficient n' may take the total mean stress, i.e. remote mechanical and thermal residual contribution, into account (Eq. 4.19); the effective far field stress includes a remote mechanical component only, assuming either the residual stress is of the self-equilibrating type or any equilibrium equivalent part is incorporated in $\log(C')$. However, for varying remote mechanical load level, the relative residual stress contribution may be different and a smooth mean stress transition from the (displacement controlled) residual stress (at yield magnitude) governing in the notch affected region to (load controlled) remote mechanical dominated in the far field region can be achieved using a crack length dependent total load ratio, i.e. $r_l \rightarrow r_l^T$ (Eq. 4.19). For weld toe notches:

$$r_l^T = \frac{K_{I,min} + K_I^r}{K_{I,max} + K_I^r} \quad (5.33)$$

$$\begin{aligned} r_l^T &= \frac{\sigma_{s,min} Y_n Y_f + \left(\frac{\sigma_{ys}}{\sigma_{max}}\right) Y_n^r}{\sigma_{s,max} Y_n Y_f + \left(\frac{\sigma_{ys}}{\sigma_{max}}\right) Y_n^r} \\ &= \frac{Y_n \left\{ 2\sigma_s \left(\frac{r_l}{1 - r_l}\right) Y_f + \left(\frac{\sigma_{ys}}{\sigma_{max}}\right) \right\} - \left(\frac{\sigma_{ys}}{\sigma_{max}}\right)}{Y_n \left\{ 2\sigma_s \left(\frac{1}{1 - r_l}\right) Y_f + \left(\frac{\sigma_{ys}}{\sigma_{max}}\right) \right\} - \left(\frac{\sigma_{ys}}{\sigma_{max}}\right)} \end{aligned}$$

Both numerator and denominator have been divided by $\sqrt{\pi a}$. Remote mechanical and thermal residual stress distribution similarity (Paragraph 2.10 and 3.8) means $Y_n^r = (Y_n - 1)$; if any, the equilibrium equivalent residual stress part – incorporated in $\log(C')$ – is assumed to be similar for all AW joints.

Provided a far field stress at some level, the thermal residual contribution becomes increasingly important for decreasing r_l , as shown for an ideal fillet weld SEN geometry in a far field membrane loading condition (Fig. 5.25). Concerning high-speed craft, welded joints typically experience (repeated) impact loading,

meaning $r_l^T \rightarrow r_l$. Increasing σ_s at constant remote mechanical load ratio, $r_l^T \rightarrow r_l$ as well (Fig. 5.26). On the other hand, increases $(\sigma_{ys}/\sigma_{max})$ like for decreasing σ_s (MCF \rightarrow HCF), the more important r_l^T becomes. Yield stress sensitivity turns out to be relatively small and a typical value $\sigma_{ys} = 150$ [MPa] has been adopted; a monotonic value rather than a cyclic one since it reflects a quasi-constant mean stress.

Although the thermal residual stress contribution may seem small – realise the remote mechanical induced notch stress is already quite high – it is still very important since the major part of fatigue life time is spent in the notch affected region. If $\sigma_n^T(r/t_p \rightarrow 0) > 0$, load ratio coefficient ($\gamma = p$) anyway. For stress relieved SSS's; $(\sigma_{ys}/\sigma_{max}) = 0$ and $\{\gamma = p|r_l \geq 0, \gamma = 0|r_l < 0\}$. In case σ_n^r turns out to be compressive in the notch affected region (Paragraph 2.10), $(\sigma_{ys} = -\sigma_{ys})$ and $\{\gamma = p|r_l \geq 0, \gamma = 0|r_l < 0\}$.

Post-welding procedures like ultrasonic impact treatment (UIT) aim to improve the fatigue resistance, reducing the defect size and turning the highly tensile welding induced residual notch stress into a compressive one. A (technique dependent) improvement ratio r_i , governing in the notch affected micro-crack region, may be introduced to incorporate the fatigue strength consequences (den Besten and Huijsmans, 2011).

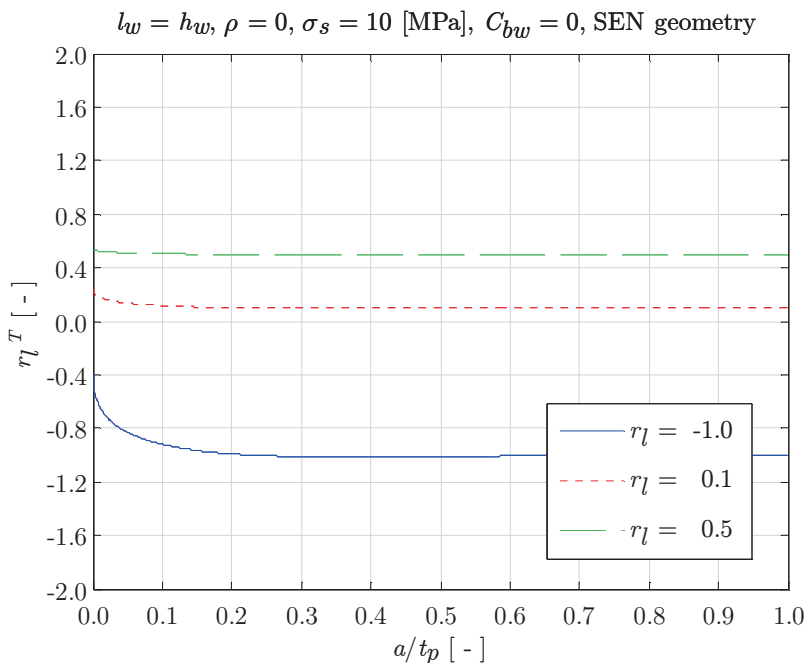


Figure 5.25: Total load ratio for different r_l , ($r_s = 0$).

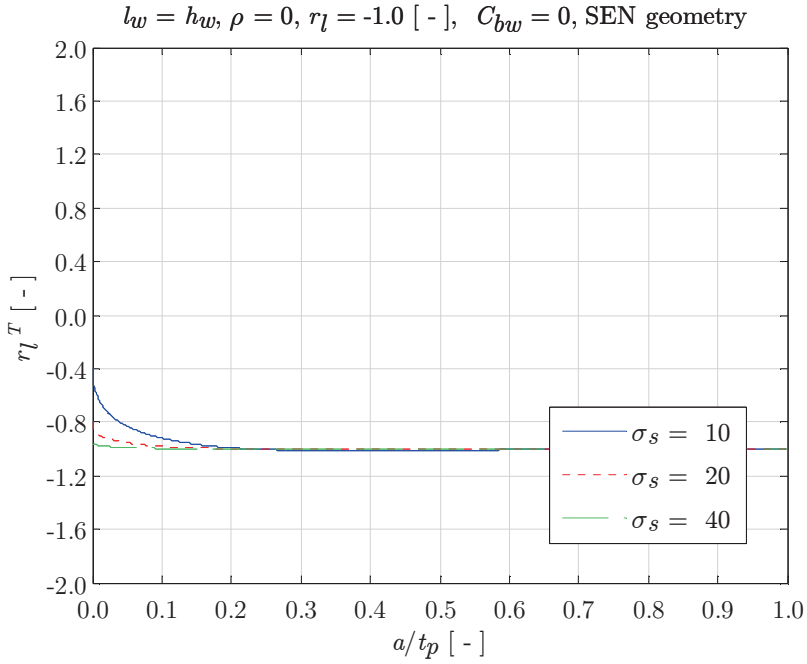


Figure 5.26: Total load ratio for different σ_s , ($r_s = 0$).

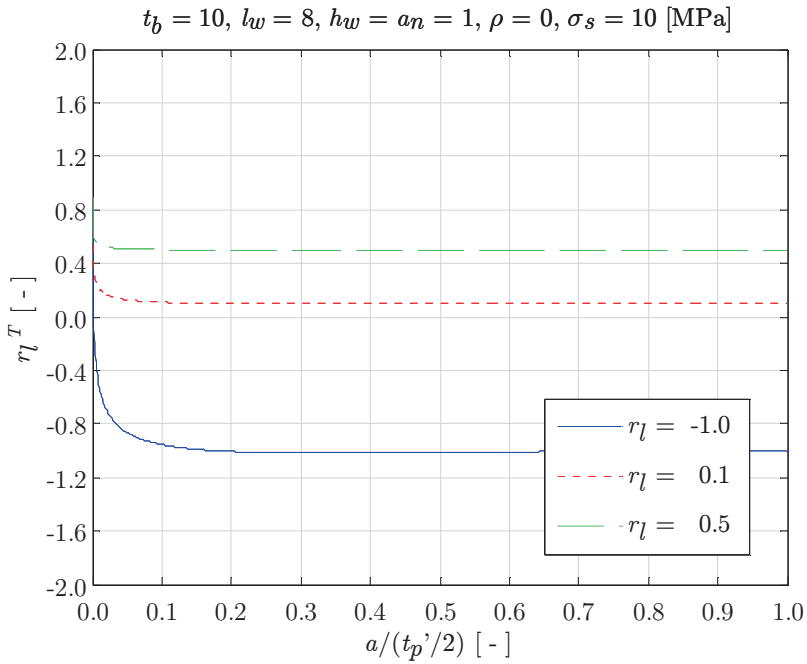


Figure 5.27: PP DS butt joint (loc. 5) total load ratio for different r_l , ($r_s = 0$).

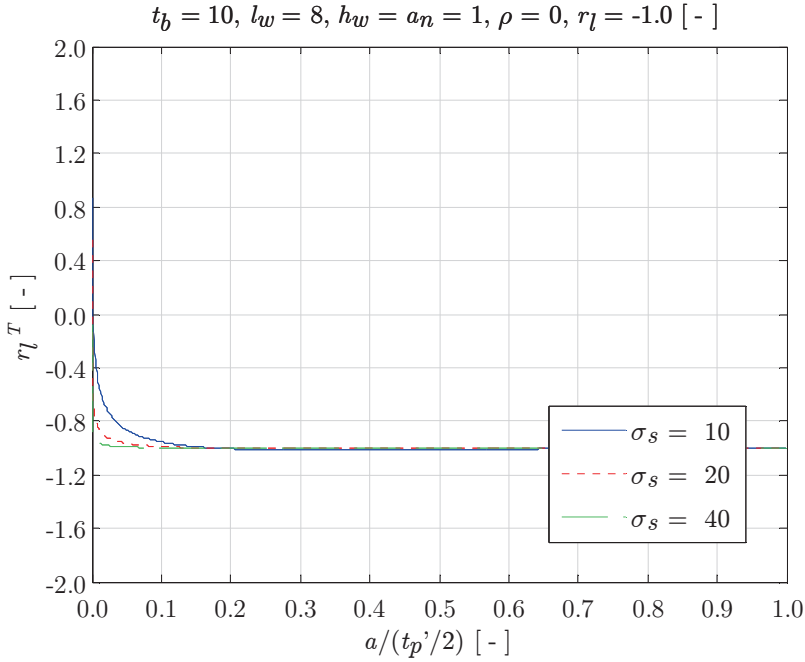


Figure 5.28: PP DS butt joint (loc. 5) total load ratio for different σ_s , ($r_s = 0$).

The total load ratio for weld root notches becomes:

$$r_l^T = \frac{2\sigma_s \left(\frac{r_l}{1-r_l} \right) Y_f + \left(\frac{\sigma_{ys}}{\sigma_{max}} \right) (Y_n - 1)}{2\sigma_s \left(\frac{1}{1-r_l} \right) Y_f + \left(\frac{\sigma_{ys}}{\sigma_{max}} \right) (Y_n - 1)} \quad (5.34)$$

As shown for a PP DS butt joint geometry (Fig. 5.27 and 5.28), r_l^T behaviour is similar to the weld toe notch case, although typically more pronounced. Since $r_l^T = f(a/t_p^{(\prime)})$, the total stress (Eq. 5.2) needs to be modified as well:

$$S_T = \frac{\Delta\sigma_s}{\left(\frac{t_p^{(\prime)}}{b_p} \right)^{\frac{1}{m}} \cdot b_p^{\frac{2-m}{2m}} \cdot I_N(r_s, r_l, n, m, \gamma)^{\frac{1}{m}}} \quad (5.35)$$

with

$$I_N = \int_{\left(\frac{a_i}{t_p^{(\prime)}} \right)}^{\left(\frac{a_f}{t_p^{(\prime)}} \right)} f_N d \left(\frac{a}{t_p^{(\prime)}} \right)$$

and

$$f_N = \frac{1}{\left\{ Y_n \left(\frac{a}{t_p^{(\rho)}} \right) \right\}^n \cdot \left\{ Y_f \left(\frac{a}{t_p^{(\rho)}} \right) \cdot (1 - r_l^T)^{1-\gamma} \right\}^m \cdot \left(\frac{a}{t_p^{(\rho)}} \right)^{\frac{m}{2}}}$$

Medium cycle fatigue resistance

Investigating MCF data first, a single slope S_T - N formulation (Eq. 5.3) will be adopted. The governing fatigue damage mechanism induced slope change, i.e. design curve based (MCF-HCF) transition, is assumed to be at $N \approx 5 \cdot 10^6$ (Eurocode 9, 2007); all failures $|N > 5 \cdot 10^6$ will be excluded for the moment as well as censored data (typically potential failures in the HCF region). Based on a preliminary analysis, 3 data points have been identified as outliers, have been excluded; 772 test results are taken into account.

Although welded joints (theoretically) may contain multiple geometrically similar weld toe notches because of symmetry; notch redundancy is implicitly included in the fatigue resistance data (scatter), typically 1 location is governing and from far field perspective a single edge type of crack – predominantly affecting Y_f – is assumed to develop anyway. A quasi-2D SEC formulation (Eq. 3.6 and 3.7) is considered for HS's type C along the weld seam; weld end type B develops a SEC by definition. However, because of 3D effects (e.g. Fig. 2.65) a semi-elliptical one (Eq. 3.10 and 3.11) is adopted for HS's type A . The type of crack developing at weld root notches (limited to HS type C) is assumed to be in agreement with the involved (non-) symmetry conditions. For a SEN geometry (e.g. PP SS butt joints) a slightly modified SEC formulation (Eq. 3.8) is required. In case of CC's developing at CN's, symmetry with respect to $(t_p/2)$ is maintained to prevent for far field stress definition issues (Paragraph 2.7). The Y_n formulation – quasi-2D for any hot spot – controls the notch affected zone size and includes (non-)symmetry as well.

Fillet- and groove weld geometries are assumed to be ideal, unambiguously defined using $\{l_w, h_w\}$. Since the (average) actual notch radius is typically not available, a worst case scenario value is adopted ($\rho = 0$); a conservative assumption.

Defect- or initial crack size a_i is typically unknown and includes a statistical component $a_i(\mu, \sigma)$. Since S_T explicitly includes an elastoplasticity coefficient n , the fictitious one a_f i.e. effective value a_e is irrelevant.

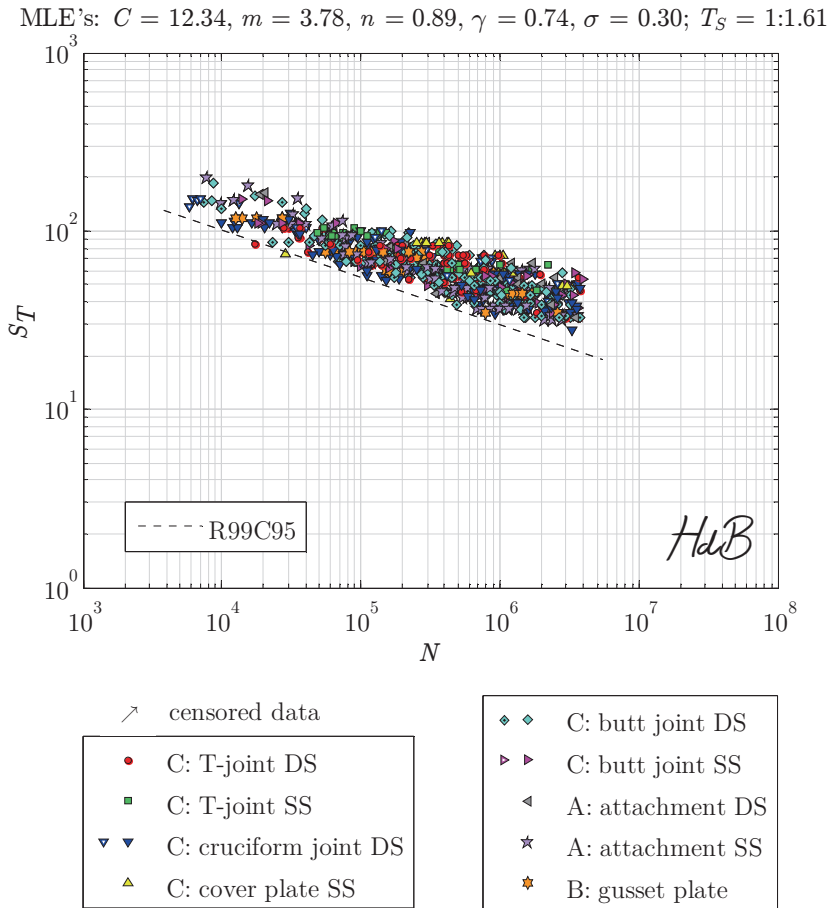


Figure 5.29: SSS total stress concept based MCF resistance data, 1-slope $\sim N(\mu, \sigma)$.

(a_i/t_p)	\mathcal{L}	T_S
$2 \cdot 10^{-3}$	-841.0	1:1.671
$4 \cdot 10^{-3}$	-822.1	1:1.622
$5 \cdot 10^{-3}$	-819.6	1:1.613
$6 \cdot 10^{-3}$	-819.6	1:1.608
$7 \cdot 10^{-3}$	-821.3	1:1.607
$8 \cdot 10^{-3}$	-824.3	1:1.608
$10 \cdot 10^{-3}$	-833.0	1:1.615

(a_i/t_p)	\mathcal{L}	T_S
$2 \cdot 10^{-3}$	-903.3	1:1.844
$4 \cdot 10^{-3}$	-889.0	1:1.783
$5 \cdot 10^{-3}$	-887.3	1:1.769
$6 \cdot 10^{-3}$	-887.8	1:1.762
$7 \cdot 10^{-3}$	-889.9	1:1.759
$8 \cdot 10^{-3}$	-893.1	1:1.761
$10 \cdot 10^{-3}$	-901.7	1:1.770

Table 5.12: Likelihood and scatter range index for varying (a_i/t_p) in case of a) $N(\mu, \sigma)$ and b) $W(\mu, \sigma)$.

Increasing (a_i/t_p) will shift S_T down. Its sensitivity for weld root notches is relatively small in comparison to weld toe notches (Fig. 5.1 and 5.7), meaning up to some extent the weld toe induced failures shift toward the weld root induced ones (centre marked symbols; Fig. 5.29). For a converged value, i.e. $(a_i/t_p \rightarrow 0)$, the notch induced (elastoplastic) response is in control and a crack initiation parameter could be a better choice. Adopting $(a_i/t_p) = C$, incorporating an average weld volume effect (Paragraph 2.8.3) only, the relative crack acuity is taken into account. Total stress S_T (Eq. 5.35) contains the absolute crack acuity $(a = a_i \rightarrow t_p)$, i.e. plate thickness scaling, as well. The single slope MCF resistance ‘Signac’¹ (Fig. 5.29) shows for both a Normal and Weibull distribution assumption a mean or most likely value, $(a_i/t_p) \approx 6 \cdot 10^{-3}$ (Table 5.12). The fatigue data life time scatter parameter σ includes the defect size scatter. Correlating defect size and weld seam length using an extreme value distribution $EV(a_r)$ would eliminate weld volume effects. The Normal distribution $N(\mu, \sigma)$ provides the better fit, i.e. maximum data joint probability density. In case $(t_p = 8)$; a common value in high-speed craft, $(a_i = 0.05 \sim 0.1)$ seems realistic (Paragraph 2.11, 4.4.1 and 5.4.1). The order of magnitude is similar to a scanning electron microscopy (SEM) measured most probable value $(a_i = a_r = 0.03)$ as well (Menzemer, 1992). For comparison: if the fatigue damage parameter would require a fictitious defect size, $(a_f/t_p) = C$ provides a most likely value as well (Sonsino et al., 1999): for $t_p = \{5, 25\}$, $a_f = \{0.20, 0.96\}$, although $(a_f/t_p) \approx 4 \cdot 10^{-2} \approx C$ seems not noticed. Note: $O(a_f/t_p) > O(a_r/t_p)$.

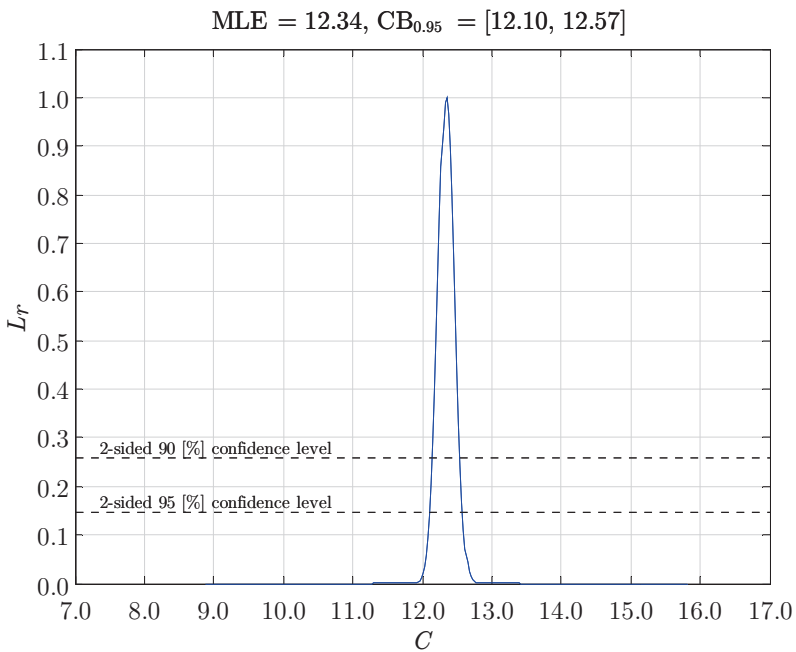
Using a most likely defect size, however, is in contrast to the BSS adopted converged value (Dong and Hong, 2004). Weld toe- and weld root induced failures are separately considered (Hong, 2010), even though the slopes m are similar (suggesting the damage mechanism is the same) and differences in {HAZ, WM} material behaviour are typically small (Paragraph 4.3). The weld root induced fatigue damage is simply considered to be smaller for similar $\sigma_{s(r)}$ in weld toe- and weld root cross-section; an observation rather than a physical explanation seems sufficient.

The parameter profile likelihoods (Fig. 5.30 to 5.34) and (two-sided) CB’s show the parameter confidence is quite high. Fatigue strength parameter C (Fig. 5.30), basically a quality indicator, seems to provide an excellent opportunity to compare its value to the ones obtained for other data sets. However, caution is required since C is highly correlated (Table 5.13) to the slope and elastoplasticity coefficient $\{m, n\}$. For example, C (as well as m) turns out to be surprisingly close to the artificial non-welded T-joint data series value (Table 5.6), though, n is different meaning any conclusion is incorrect in that respect.

¹ Pointillism artist, 1863-1935

P	C	m	n	γ	σ
C	1.00	0.98	0.59	-0.11	-0.04
m		1.00	0.42	-0.10	-0.06
n			1.00	0.07	0.03
γ				1.00	0.01
σ					1.00

Table 5.13: Correlation matrix MCF as-welded joint fatigue.

Figure 5.30: C relative parameter profile likelihood (AW MCF S_T resistance).

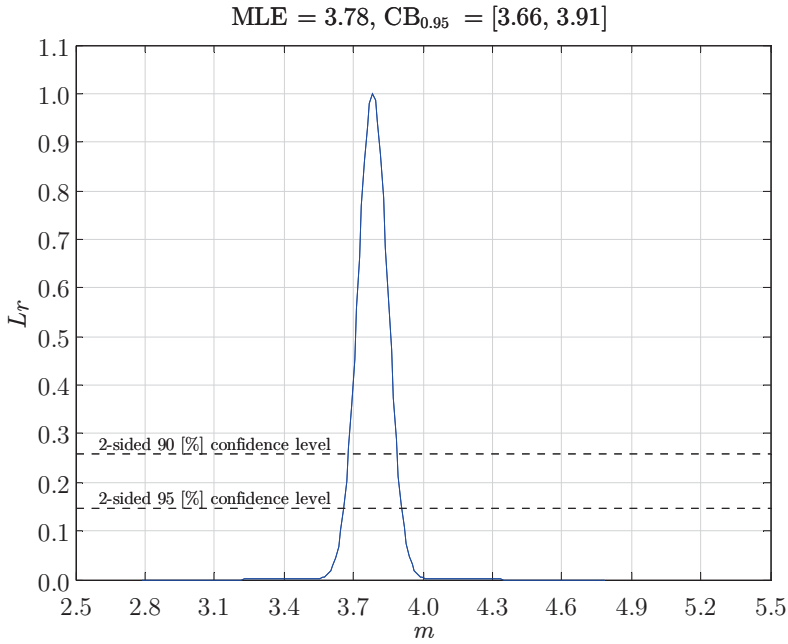


Figure 5.31: m relative parameter profile likelihood (AW MCF S_T resistance).

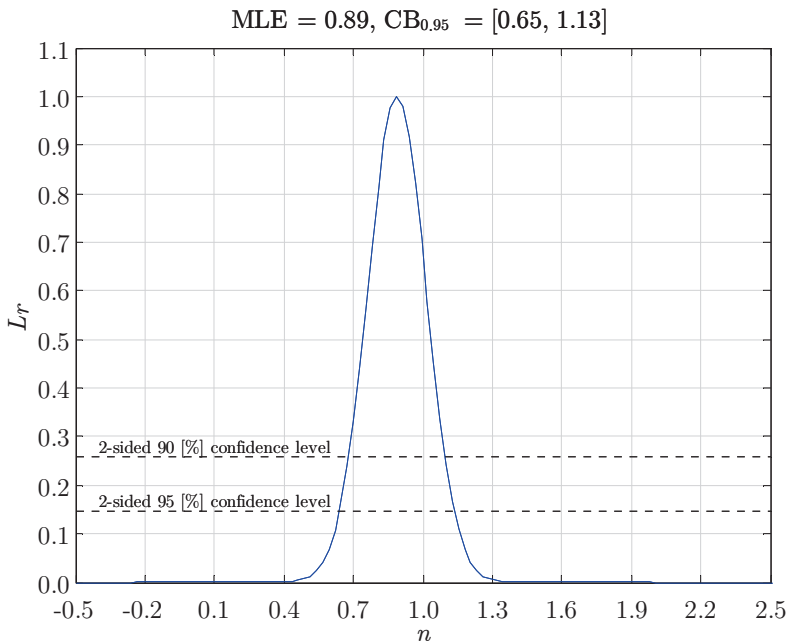
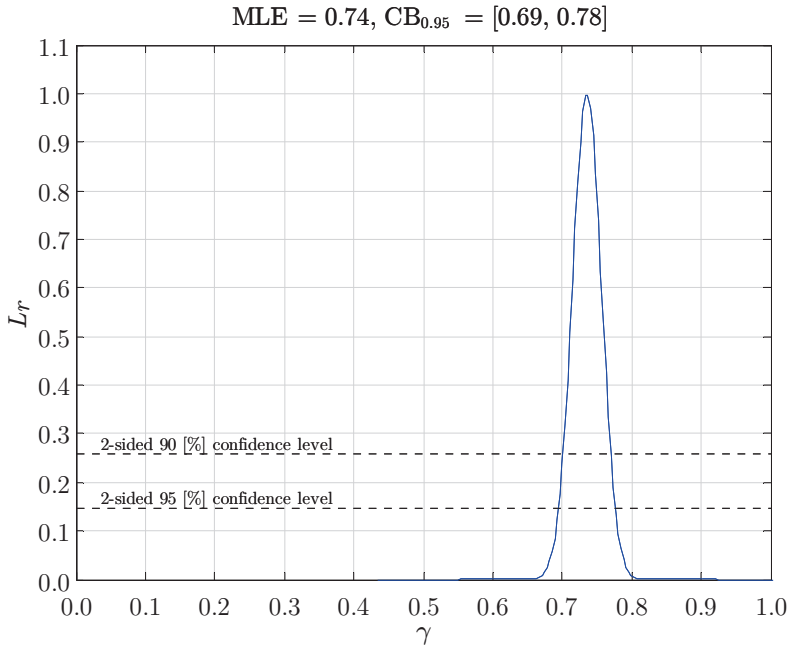
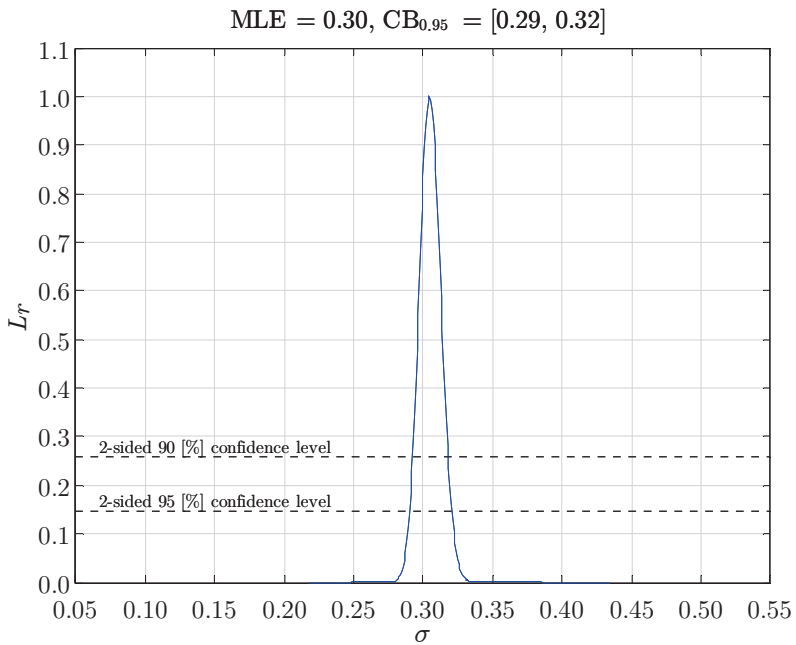


Figure 5.32: n relative parameter profile likelihood (AW MCF S_T resistance).

Figure 5.33: γ relative parameter profile likelihood (AW MCF S_T resistance).Figure 5.34: σ relative parameter profile likelihood (AW MCF S_T resistance).

The relevant nominal stress concept based Eurocode 9 (mode-I) slope is typically ($m = 3.4$); for FP butt joints however ($m = 4.3$) is adopted, suggesting the damage mechanism is different. Since the weld notch angle is principally a matter of fatigue strength, only a larger defect size – decreasing the (N_i/N_g) growth ratio – would be a reasonable (but unverified) explanation. The MCF AW data slope m (Fig. 5.31) turns out to be right in the middle and is comparable to the artificial T-joint data values ($m \sim 4$) as well (Paragraph 5.4.1). The $\rho_{m,n}$ correlation turns out to be significant (Table 5.13). Increasing the (cyclic) notch and/or crack tip plasticity increases n , increases the (N_i/N_g) ratio (because of decreasing N_g) and hence m at the same time (and vice versa).

Considering the (non-)welded artificial T-joint data and AW series, the average(!) elastoplasticity coefficient n (Fig. 5.32) seems to show some tendency. For increasing mean stress in the notch affected region, n reduces, suggesting the maximum stress dominates the stress range contribution (i.e. the quasi-static component – a residual stress contribution in particular – rather than the cyclic remote mechanical one is governing; Paragraph 4.2.4). Load ratio coefficient γ (Fig. 5.33) on the other hand shows the stress range is in charge in the far field dominated region; ($0.5 < \gamma \leq 1.0$). Since ($n \sim 1$), half the BSS value (Dong and Hong, 2004), $n_e = (n + m/2) > 1.0$ (Eq. 4.7) meaning plasticity is still involved and crack growth behaviour is non-monotonic. Even though the welded joint hot spot condition is typically plane strain (Paragraph 4.2.3), mean stress in the notch affected region is large in comparison to the far field component explaining why non-monotonicity is even pronounced (Fig. 4.10); $n_e \approx 2.7$.

At first glance, standard deviation MLE σ (Fig. 5.34), another quality indicator, may seem fairly high, although the average welded joint quality typically decreases (increasing σ) if an increased number of data sets is involved; an advantage from design perspective. At the same time, the fatigue resistance scatter band seems relatively constant in the MCF life time range (Fig. 5.29), suggesting convergence. Except the design curves, Eurocode 9 does not provide any data (scatter) information. Although not explicitly mentioned, likely the data investigated to establish the European Recommendations for Aluminium Alloy Structures (ERAAS) is involved, as well as some more recent test results (Jaccard, Kosteas and Ondra, 1995); both SSS and built-up beams (LSS), aiming for welded joint similarity (Paragraph 2.11 and 5.5).

The ERAAS (LSS) fatigue strength scatter parameter σ^s for different type of specimen is in the range $\sigma^s = (0.04, 0.10)$ based on a nominal stress concept (Kosteas and Ondra, 1995). Since $(S|N)$ - and $(N|S)$ regression is not the same, σ^s cannot be translated to a life time value. An average slope may be used to obtain an estimate only; ($m = 4$) has been proposed (Eurocode 9, 2007) meaning $\sigma = \sigma^n = (0.45, 0.56)$, a glaring contradiction in comparison to the only mentioned Eurocode 9 value ($\sigma = 0.18$). The mean standard deviation of the other test results (mode-I, ~ 1000 specimens; Jaccard, Kosteas and Ondra, 1995) turns out to be ($\sigma \approx 0.32$), knowing ($r_l \geq 0$). For the record: this data is partly included in the TS concept based analysis as well, e.g. (Hirt and Smith, 1995; Van Straalen et al, 1994). Keeping in mind an S_T - N quantile represents a family of mode-I governing welded joint

curves, i.e. FAT class uncertainties because a joint would not fit into the available prescribed ones do not exist, the TS σ MLE is considered to be a realistic one. In particular if compared to the S_n related data scatter (Fig. 5.35; legend Fig. 5.29). Scatter index $T_S = 1:1.6$ slightly exceeds the characteristic value $T_S = 1:1.5$ as obtained in case of good workmanship, limiting analysis results to ($r_l \geq 0$) data (Sonsino, 2007; Kranz and Sonsino, 2010); for decreasing remote mechanical load ratio, ($r_l < 0$) in particular, the scatter increases.

The family of S_T - N curves is typically a tension-tension (T-T) fatigue resistance relation, meaning that except the predominant tensile residual (notch) stress, the remote mechanical loading induced maximum stress is tensile as well: $\sigma_{max} = \Delta\sigma_s / (1 - r_l) > 0$ for $r_l = (-\infty, 1)$. The R99C95 quantile (Fig. 5.29) may serve as MCF design curve. Life time uncertainty is about a factor 6; ± 3 , explaining why N should be assessed in terms of order of magnitude rather than actual numbers.

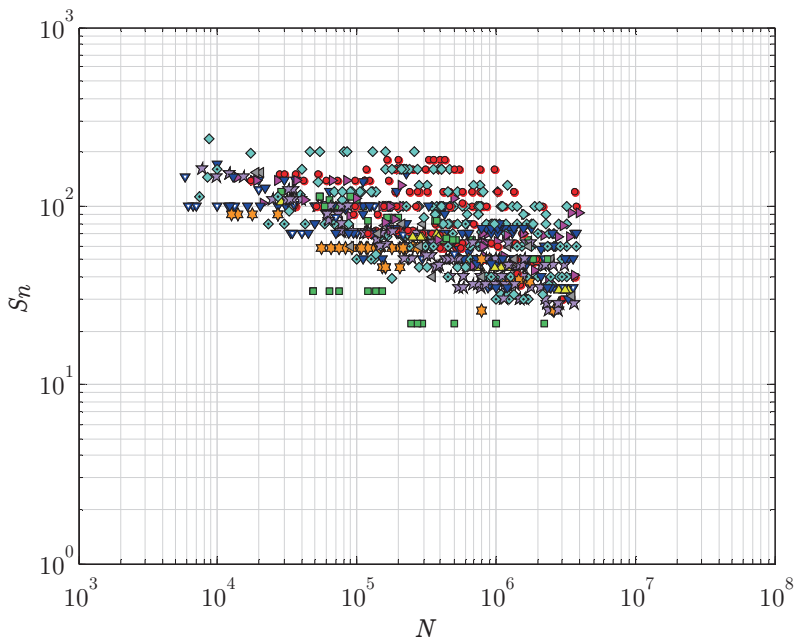


Figure 5.35: SSS S_n MCF resistance data.

The International Institute of Welding (IIW) defines the (MCF-HCF) transition at $N = 1 \cdot 10^7$ cycles (Hobbacher, 2009b), increasing the number of involved test results up to 805. In comparison to the Eurocode transition based results, m has slightly increased (Fig. 5.36, Table 5.14) – including censored data hardly affects the result – and turns out to be way beyond the IIW value ($m = 3$). Since the data slope tends to change for $N > 1 \cdot 10^6$, life time estimates close to the MCF upper bound will be (too) conservative. Although the residuals show no drift (Fig. 5.37), i.e. $\varepsilon(\mu) \approx 0$, some trend may be observed: approaching the {LCF, HCF} regions the error increases because of slope deviations. The residuals distribution (Fig. 5.38) is approximately symmetric and bell-shaped, suggesting the $\varepsilon \sim N(\mu, \sigma)$ assumption is valid.

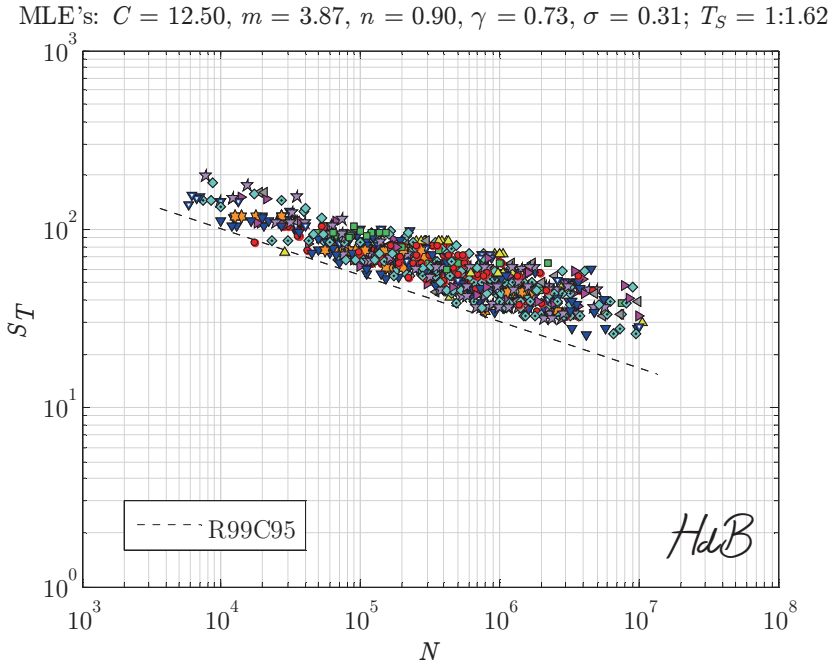


Figure 5.36: SSS S_T MCF resistance data (IIW definition), 1-slope $\sim N(\mu, \sigma)$.

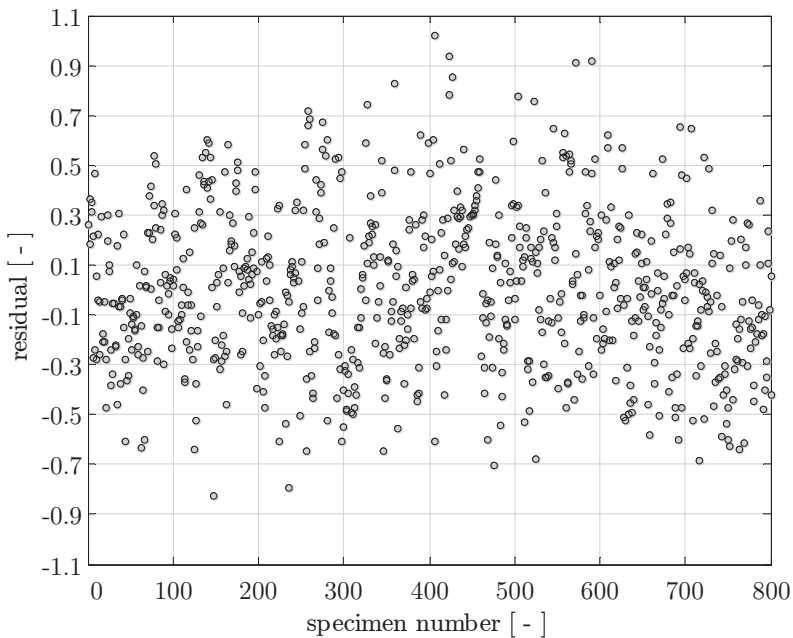


Figure 5.37: AW joints MCF life time residual plot.

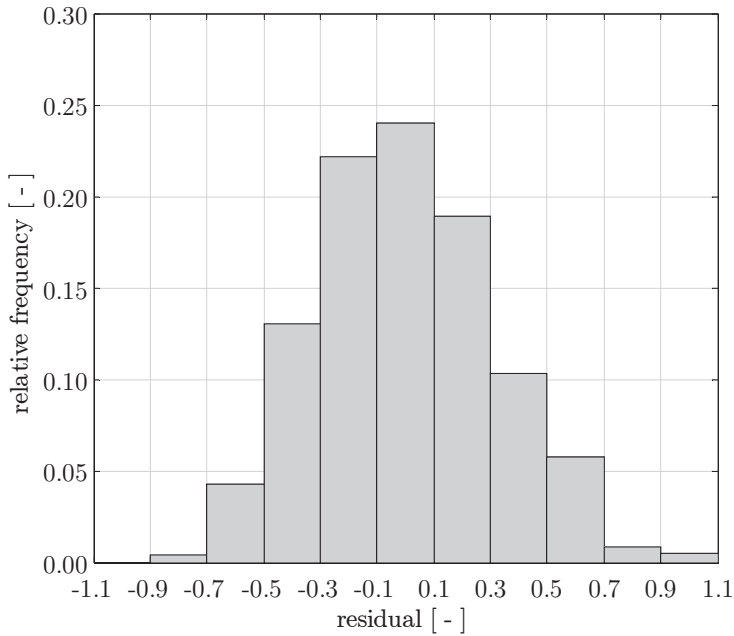


Figure 5.38: AW joints MCF (log) life time residual distribution.

parameter	MLE	0.95 LB	0.95 UB
C	12.50	12.25	12.73
m	3.87	3.73	3.99
n	0.90	0.66	1.14
γ	0.73	0.69	0.77
σ	0.31	0.30	0.33

Table 5.14: MCF resistance $\sim N(\mu, \sigma)$ parameter MLE's and 0.95 CB's.

The standard deviation and scatter index remain principally unaffected. However, $\sigma = 0.31$ seems in comparison to the IIW value (Hobbacher, 2009b; $\sigma = 0.25$) quite large. Even though the aluminium welded joint fatigue resistance scatter typically exceeds the steel one, IIW has adopted the same σ – and slope(!) – for both materials, considering material effects to be predominantly a matter of fatigue strength; the crack growth dominated damage mechanism is the same. The involved data sets are unknown. Fatigue resistance data scatter for steel welded joints according to {IIW, Battelle} – BSS weld toe induced failures only – share the same σ (Dong, Hong and De Jesus, 2007); root induced ones (Hong, 2010) typically show an increased scatter ($\sigma = 0.28$). A similar σ would be expected for the {IIW, TS} aluminium welded joint fatigue resistance as well, since the {BSS, TS} concepts are modelled along the same lines up to some extent.

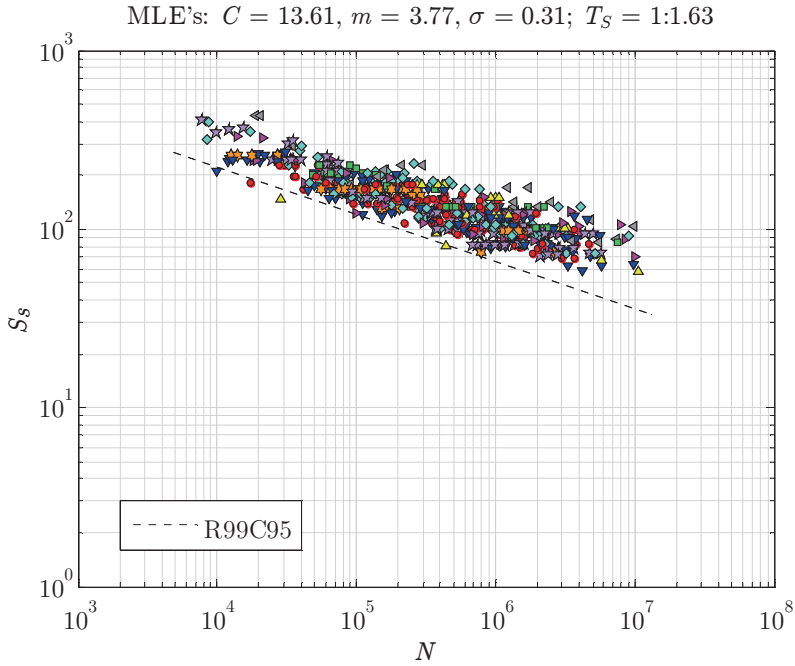


Figure 5.39: BSS S_g MCF resistance (load control); weld toe induced failures only.

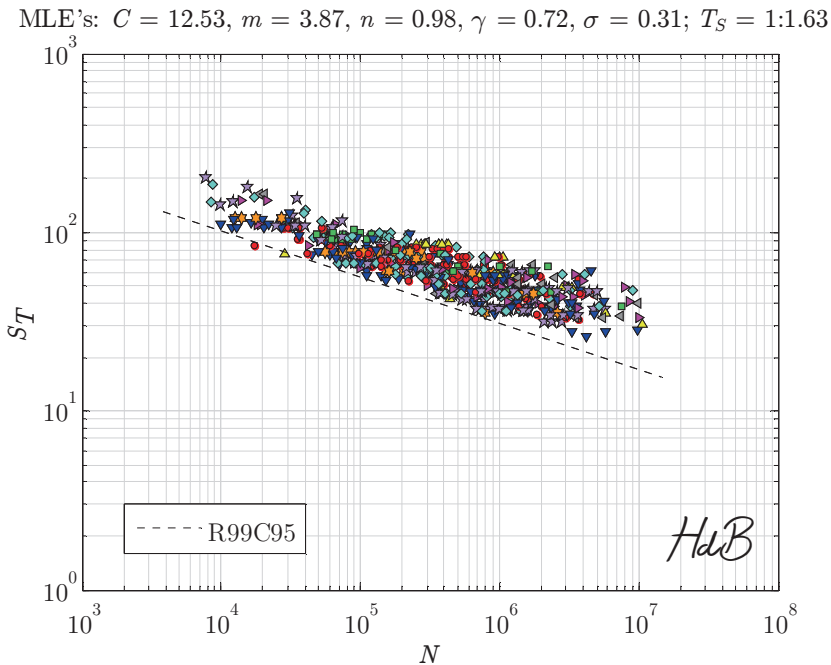


Figure 5.40: TS S_T MCF resistance; weld toe induced failures only.

An actual {BSS, TS} weld toe induced failure resistance comparison (Fig. 5.39 and 5.40) shows however the same scatter estimate; $\sigma = 0.31$, although the BSS fit shows some more outliers. The large number of data points in the scatter band core ensures σ is hardly affected. Comparing TS based (design) life time estimates N to the BSS obtained ones means that in some cases it will be better, in some others worse, but in average the same. The fatigue strength parameter C is quite different, predominantly because of different notch crack growth integral I_N formulation and elastoplasticity coefficient n . The BSS polynomial $(I_N)^{1/m}$ approximation (Dong, Hong and De Jesus, 2007) is based on $m = 3.6$; close to the MLE value. The effective BSS S_s (Dong and Hong et al., 2010) involves the geometric mean contribution of $\{\Delta\sigma_s^+, \sigma_{s,max}\}$.

Performing a quality check, a fair comparison of (some) joint specific {IIW, TS} FAT classes would require a nominal stress based re-analysis of the involved data. However, the IIW design values will be adopted to get a first estimate (Table 5.15). The TS FAT class is established at 25 [MPa] for $N = 2 \cdot 10^6$ cycles (Fig. 5.36). Using the S_T formulation (Eq. 5.35), the SSS joint specific FAT class can be calculated; $\Delta\sigma_s = \Delta\sigma_n$ if not specified and assumed to be a membrane component ($r_s = 0$). A worst case notch radius value has been selected ($\rho = 0$).

Generally speaking, the IIW FAT classes are slightly conservative in comparison to the TS ones as might be expected, although it seems in contradiction to the σ values. The involved r_l value might be a partial explanation, since IIW typically translates the design curves to an ($r_l = 0.5$) level; S_T includes an explicit contribution (Eq. 5.34). A $\{(1 - 0.5)/(1 - 0.1)\}^{1-\gamma}$ correction would increase the IIW FAT class ~ 15 [%] and the values approach the TS level, i.e. are in the same range as it should be, since the selected joint dimensions fit quite well the SSS dimensions as involved to establish the {IIW, TS} fatigue strength.

Weld reinforcement criteria and misalignment assumptions define the DS butt joint (weld toe induced failure) IIW FAT class at 32 [MPa]; slightly below the TS value. In case of weld root induced failure, the nominal stress is translated to the weld throat section value, ignoring any weld reinforcement contribution. The IIW does not define a notch length upper bound and an engineering value has been selected. The TS fatigue strength exceeds the IIW FAT class.

type	$t_b^{(\prime)}$	t_c	l_c	l_w	h_w	a_n	IIW	TS
butt joint DS (toe)	8.0	8.0	-	10.0	1.5	0.0	32	38
butt joint DS (root)	8.0	8.0	-	10.0	1.5	1.0	12	16
cruciform joint DS (toe)	8.0	8.0	-	8.0	8.0	0.0	28	37
cruciform joint DS (root)	8.0	8.0	-	8.0	8.0	2.0	12	18
cover plate SS (toe)	8.0	8.0	120.0	8.0	8.0	-	25	37
attachment SS (toe)	8.0	8.0	120.0	8.0	8.0	-	25	30
gusset plate (toe)	40.0	8.0	120.0	8.0	8.0	-	18	23

Table 5.15: Welded joint specific {TS, IIW} FAT class comparison; ($r_l = 0.1$).

According to IIW, a DS cruciform joint (weld toe induced failure) shows typically a lower FAT class in comparison to a DS butt joint – a matter of allowed misalignments; the TS fatigue strength has decreased just slightly. To compare the weld root FAT classes the TS based nominal stress is translated to the fillet weld throat value. IIW does not provide any a_n restrictions.

In comparison to the cruciform joint, the IIW SS cover plate fatigue strength has decreased. Although the cover plate length l_c typically exceeds the cruciform joint plate thickness t_c , C_{bw} effects are typically small (Fig. 5.4), explaining why the TS FAT class has hardly changed.

The SS attachment contains a weld end (HS type *A*), meaning a semi-elliptical crack type is involved because of 3D effects. Aspect ratio (a/c) is assumed to be similar to $t_b/(t_c/2 + l_w)$. Since $\Delta\sigma_s \neq \Delta\sigma_n$, a structural- to nominal stress conversion is involved. The IIW fatigue strength seems conservative, like for a gusset plate (HS type *B*).

Medium- and high cycle fatigue resistance

In order to correlate {MCF, HCF} data, a continuous dual slope formulation (Eq. 5.20) is adopted rather than a piecewise linear one to ensure a smooth transition. Analysis results (Fig. 5.41; legend Fig. 5.29, Table 5.16, 5.17 and 5.18) based on 911 complete and censored fatigue tests – after all, fatigue induced failure is an emergency – show the $N(\mu, \sigma)$ distribution overall still provides the better fit. The $\{C, m_1, m_2, S_c\}$ correlation is obvious.

The MCF slope has increased. Although the MCF data distribution is relatively constant and ($m_1 \sim 4$) still, at $N = 2 \cdot 10^6$; the characteristic fatigue strength related value, typically a data concentration is observed that may affect the overall MCF resistance fit. The HCF slope m_2 is in between the Eurocode 9 and IIW value, respectively ($m_2 = m_1 + 2$) and ($m_2 = 22$) based on 10 [%] fatigue resistance decrease per decade. However, its uncertainty is quite large (Fig. 5.42) since HCF data is limited and predominantly censored. The R99C95 quantile slope change in terms of life time is below any commonly defined {MCF, HCF} transition value, i.e. $N_c = 5 \cdot 10^6$ (Eurocode 9, 2007) or $N_c = 1 \cdot 10^7$ (IIW recommendations: Hobbacher, 2009b), but quite close to the characteristic fatigue strength related one, $N_c \approx 2 \cdot 10^6$ cycles.

$$C = 13.59, m_1 = 4.42, m_2 = 10.32, S_c = 29, n = 1.22, \gamma = 0.69, \sigma = 0.43$$

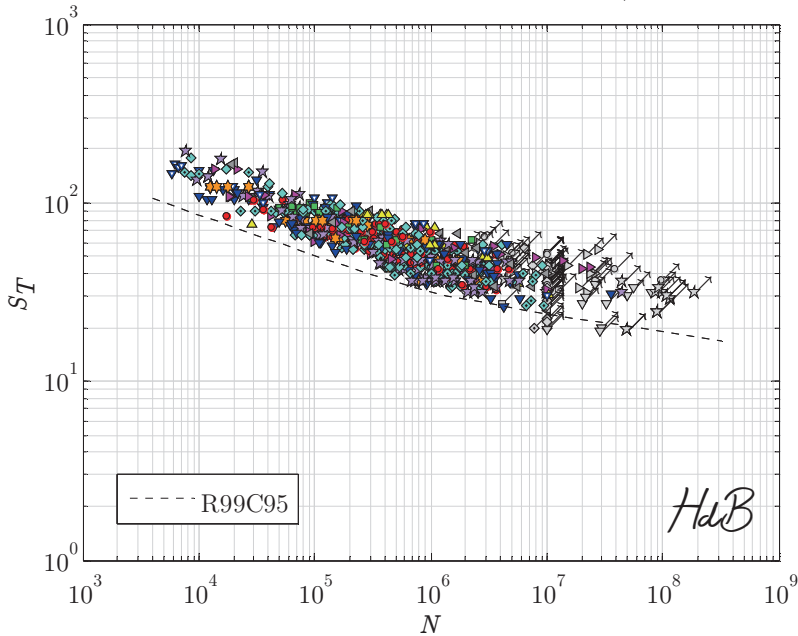


Figure 5.41: SSS S_T {MCF, HCF} resistance data; 2-slope $\sim N(\mu, \sigma)$.

distr.	C	m_1	m_2	S_c	n	γ	σ	T_S	$\max\{\mathcal{L}\}$
$N(\mu, \sigma)$	13.59	4.42	10.32	29	1.22	0.69	0.43	1:1.76	-1234
$W(\mu, \sigma)$	14.28	4.84	13.30	33	1.46	0.67	0.57	1:1.93	-1359

Table 5.16: Parameter MLE's {MCF, HCF} resistance data; 2-slope.

P	C	m_1	m_2	S_c	n	γ	σ
C	1.00	0.98	0.08	-0.31	0.63	-0.09	0.08
m_1		1.00	0.10	-0.31	0.50	-0.07	0.08
m_2			1.00	-0.37	-0.04	0.01	0.06
S_c				1.00	0.00	0.00	0.04
n					1.00	0.03	0.01
γ						1.00	-0.01
σ							1.00

Table 5.17: Correlation matrix {MCF, HCF} resistance; 2-slope $\sim N(\mu, \sigma)$.

parameter	MLE	0.95 LB	0.95 UB
C	13.59	13.27	13.92
m_1	4.42	4.25	4.59
m_2	10.32	-	-
S_c	29.00	25.00	35.00
n	1.22	0.91	1.53
γ	0.69	0.64	0.73
σ	0.43	0.41	0.45

Table 5.18: {MCF, HCF} resistance $\sim N(\mu, \sigma)$ parameter MLE's and 0.95 CB's.

For a decreasing remote mechanical load range, i.e. MCF \rightarrow HCF, the notch and/or crack tip elastoplasticity is hardly affected because of the highly tensile thermal residual stress; ($n \sim 1$) remains approximately unchanged. Only m_2 pretends to take care of the increasing (N_i/N_g) ratio, as a comparison of the $\rho_{m_1, n}$ and $\rho_{m_2, n}$ correlation coefficients confirms.

Load ratio coefficient γ has turned out to be an independent parameter (Table 5.17). The quasi-constant residual stress (in the notch affected region) is for all SSS approximately the same (at yield stress level) and the fatigue resistance mean stress effect as incorporated using Walker's model is approximately exponential indeed.

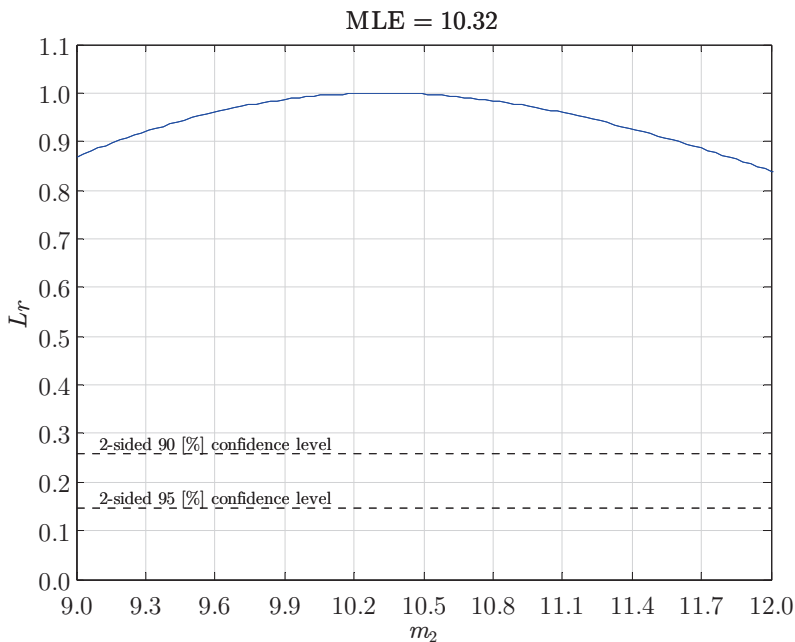


Figure 5.42: m_2 relative parameter profile likelihood ({MCF, HCF} data, 2-slope).

The data scatter parameter σ has significantly increased, predominantly because of the HCF censored data induced uncertainty. Note the HCF data life time scatter $O(10^2)$ as shown (Fig. 5.41) is fictitious in that respect, since the locations in N domain are based on the number of cycles up to the test stop rather than fatigue induced failure. A separate MCF- and HCF resistance analysis is considered to be no option. Even if a most likely transition location would be estimated using a connectivity constraint, the different σ 's introduce a quantile transition jump anyhow. Using a single level regression analysis, the MCF resistance uncertainty pays for an {MCF, HCF} formulation since only 1 residual term is involved. Though, if on the other hand application of the MCF σ in the HCF region (Morgenstern et al., 2006b; Sonsino, 2007) is supposed to be an alternative – meaning HCF life time estimates will be non-conservative – the {MCF, HCF} approach might be preferred, at least from high-speed craft design perspective.

The {MCF, HCF} slope change might be related to a S_T LB; a micro-structural barrier, a threshold, likely random because of the stochastic nature of grain size and orientation, number of dislocations and inclusions and welding induced defect size, introducing the random fatigue limit (RFL) model (Eq. 5.21). The (N_i/N_g) naturally increases up to $\lim_{S_T \rightarrow S_\infty} (N_i/N_g) \rightarrow \infty$. The {MCF, HCF} data scatter is naturally separated.

$$C = 12.17, m = 3.80, S_{\infty\mu} = 9.75, S_{\infty\sigma} = 2.77, n = 0.89, \gamma = 0.70, \sigma = 0.25$$

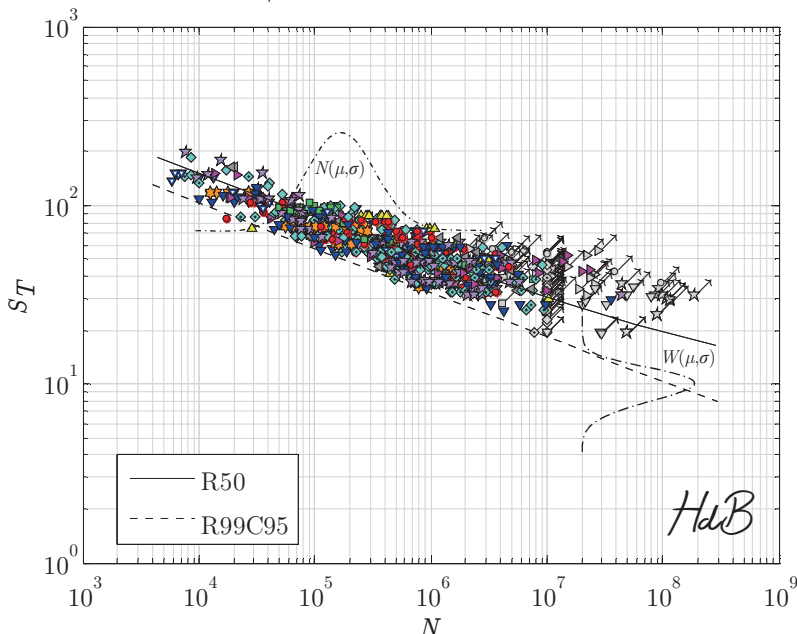


Figure 5.43: SSS S_T {MCF, HCF} resistance data (RFL $\sim \{N(\mu, \sigma), W(\mu, \sigma)\}$).

N distr.	S_∞ distr.	C	m_1	$S_{\infty,\mu}$	$S_{\infty,\sigma}$	n	γ	σ	$\max\{\mathcal{L}\}$
$N(\mu, \sigma)$	$N(\mu, \sigma)$	12.19	3.80	5.77	2.79	0.88	0.71	0.27	-1140
$N(\mu, \sigma)$	$W(\mu, \sigma)$	12.17	3.80	9.75	2.77	0.89	0.70	0.25	-667
$W(\mu, \sigma)$	$N(\mu, \sigma)$	11.90	3.65	8.20	2.37	0.47	0.70	0.61	-1165
$W(\mu, \sigma)$	$W(\mu, \sigma)$	11.89	3.67	12.07	2.37	0.43	0.69	0.61	-1151

Table 5.19: Parameter MLE's {MCF, HCF} resistance data; RFL model.

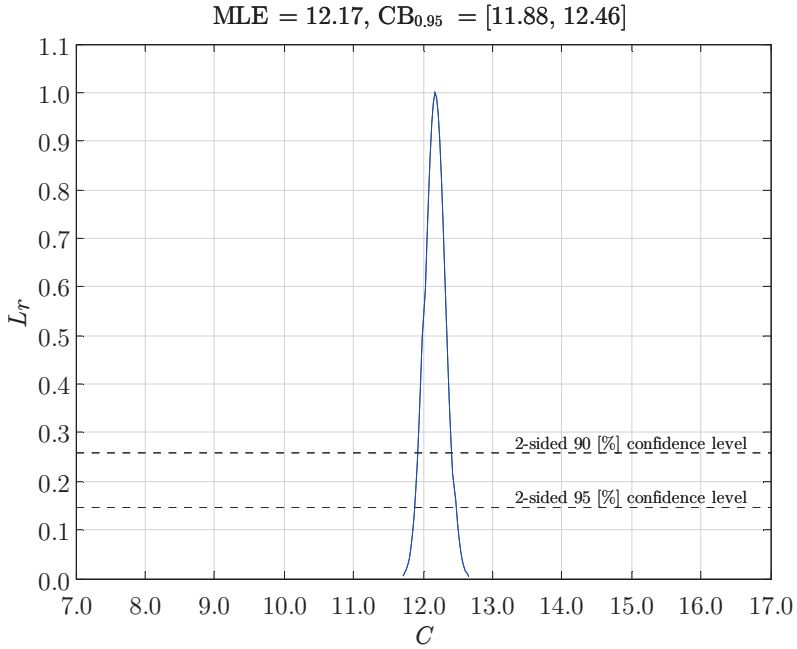
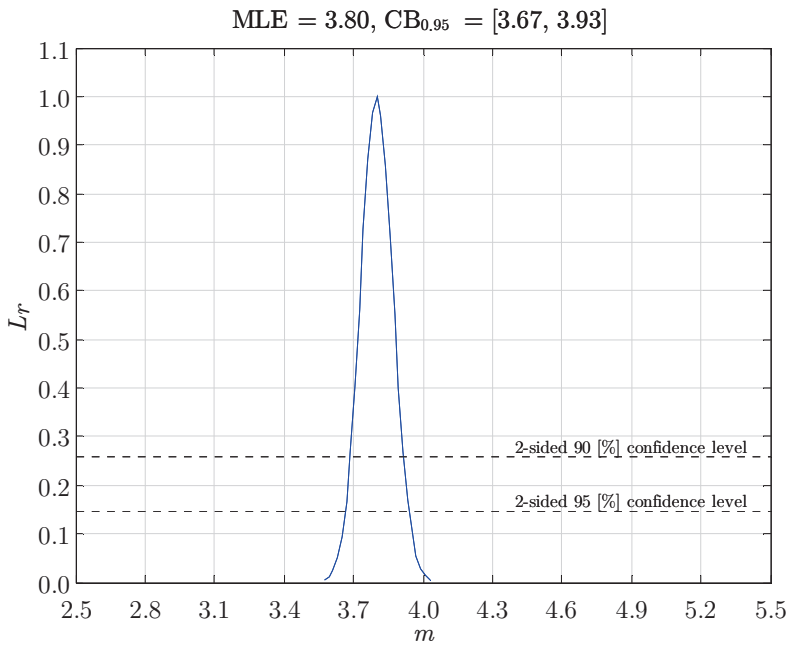
P	C	m	$S_{\infty,\mu}$	$S_{\infty,\sigma}$	n	γ	σ
C	1.00	0.97	-0.64	0.58	0.57	0.05	0.45
m		1.00	-0.52	0.45	0.47	0.05	0.37
$S_{\infty,\mu}$			1.00	-0.91	-0.15	-0.15	-0.60
$S_{\infty,\sigma}$				1.00	0.20	0.14	0.46
n					1.00	0.04	0.11
γ						1.00	0.04
σ							1.00

Table 5.20: Correlation matrix {MCF, HCF} resistance; RFL $\sim\{N(\mu, \sigma), W(\mu, \sigma)\}$.

A $N(\mu, \sigma)$ life time- and $W(\mu, \sigma)$ fatigue limit distribution assumption provides the best data fit (Fig. 5.43; legend Fig. 5.29, Table 5.19 and 5.20; Fig 5.44 to 5.50). Fatigue strength parameter C and slope m as well as the elastoplasticity- and load ratio coefficient $\{n, \gamma\}$ are close to the separate MCF resistance analysis results (Fig. 5.29). The life time data scatter parameter has reduced to $(\sigma = 0.25)$, suggesting the MCF UB is below $N_c = 5 \cdot 10^6$ (Fig. 5.29) or $N_c = 1 \cdot 10^7$ (Fig. 5.36) as already identified (Fig. 5.39). Scatter index T_S has become S_T dependent and cannot be unambiguously determined for comparison with other models; σ is considered to be sufficient in that respect.

The fatigue limit mean and standard deviation $\{S_{\infty,\mu} = 9.75, S_{\infty,\sigma} = 2.77\}$ in terms of shape and scale parameters $\{k = 3.98, \lambda = 10.20\}$ suggests a slightly skewed distribution (Fig. 5.43). The $(S_\infty - \sigma)$ sensitivity is quite high (Table 5.20). Note the R99C95 {MCF, HCF} RFL quantile is approximately a single slope curve up to $N = 1 \cdot 10^9$ cycles; a common assumption for fatigue resistance of aluminium alloys.

Comparing the dual slope- and RFL $\max(\mathcal{L})$; because of the same number of parameters Akaike's criterion does not provide additional information, the RFL model seems to be a better choice, predominantly because of the HCF slope m_2 uncertainty.

Figure 5.44: C relative parameter profile likelihood (AW RFL S_T resistance).Figure 5.45: m relative parameter profile likelihood (AW RFL S_T resistance).

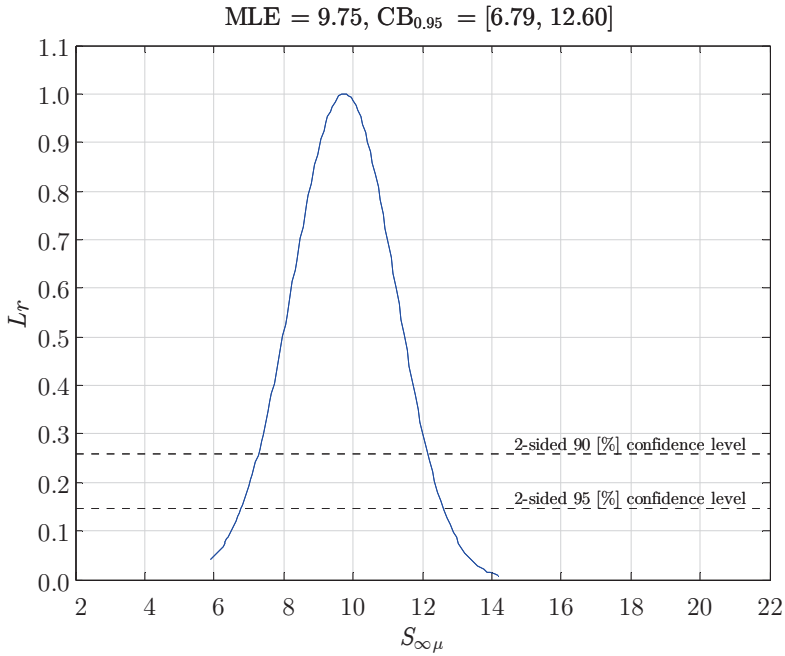


Figure 5.46: $S_{\infty\mu}$ relative parameter profile likelihood (AW RFL S_T resistance).

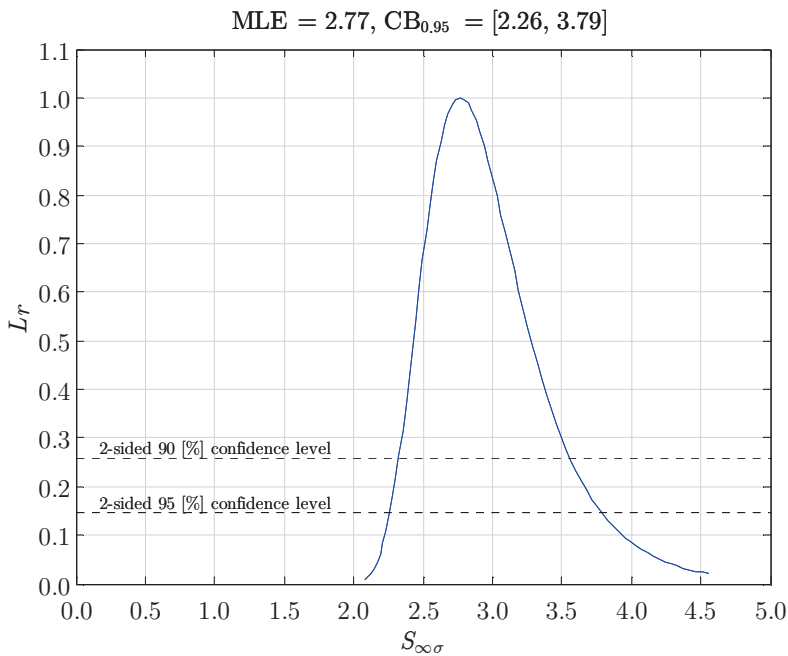
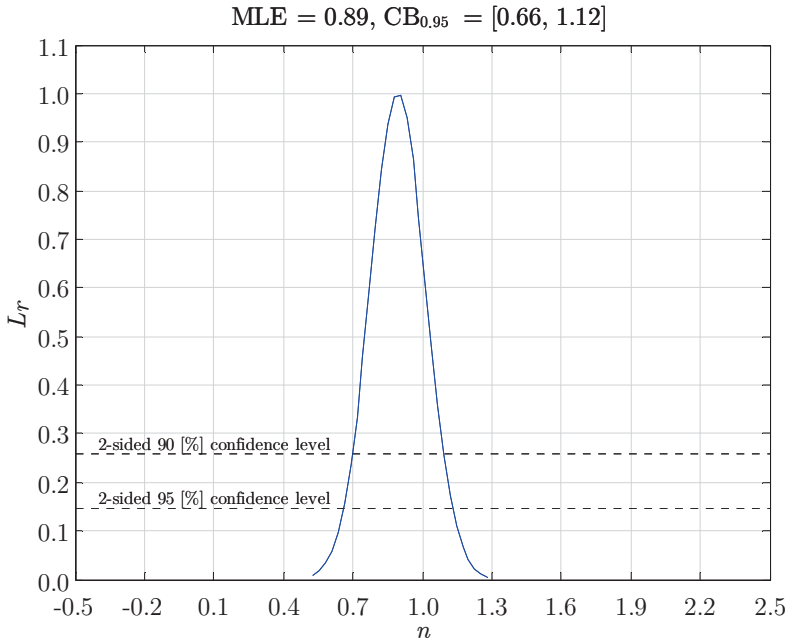
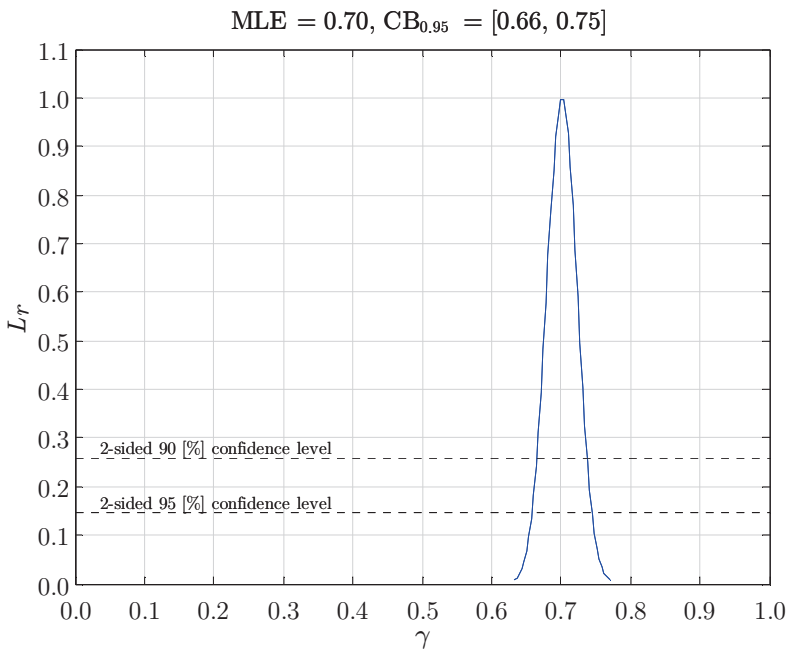


Figure 5.47: $S_{\infty\sigma}$ relative parameter profile likelihood (AW RFL S_T resistance).

Figure 5.48: n relative parameter profile likelihood (AW RFL S_T resistance).Figure 5.49: γ relative parameter profile likelihood (AW RFL S_T resistance).

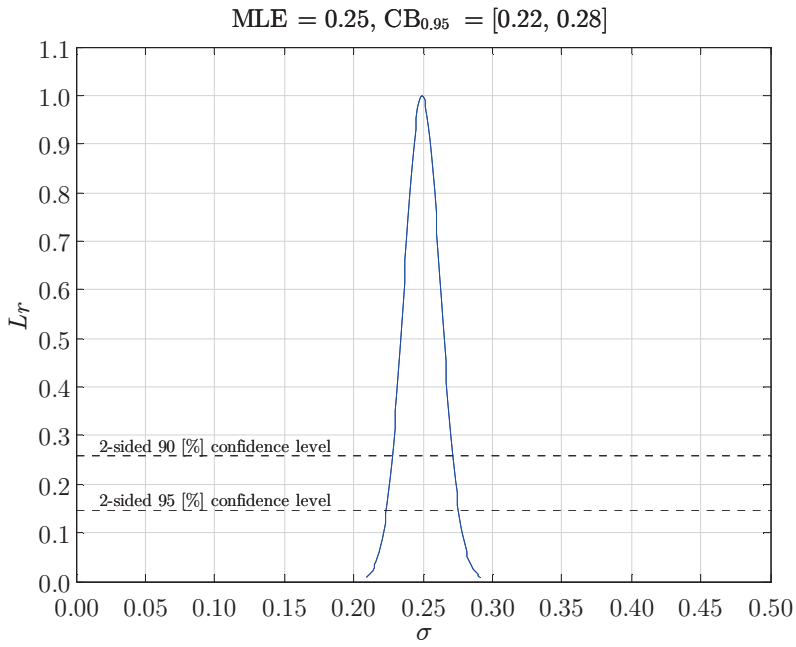


Figure 5.50: σ relative parameter profile likelihood (AW RFL S_T resistance).

5.5 Large scale specimen CA fatigue resistance

Since SSS test data is typically used to establish the fatigue resistance, FSS representative (one-bay) LSS data should fit the SSS data scatter band in order to demonstrate welded joint similarity (Paragraph 5.5.1), meaning the fatigue damage is the same (Paragraph 2.11). The classification {SSS, LSS, FSS} is not related to welded joint dimensions as well up to what extent neighbour structural members are involved (SSS include the welded joint only; LSS include some neighbour structural members as identified in stiffened panels, frames and trusses). The remote-mechanical stress is principally not affected, but the displacement controlled thermal residual stress in LSS however may introduce an equilibrium equivalent part, (slightly) affecting the total load ratio r_l^T . Special attention will be paid to fatigue data of three-bay stiffened panels exposed to repeated space-averaged pressure (den Besten and Kaminski, 2013; Paragraph 5.5.2). In contrast to a tensile remote far field stress, typical for {SSS, one-bay LSS} hot spots, a compressive one is introduced at fatigue sensitive locations like a frame-stiffener connection, affecting the fatigue resistance as already shown for a frame/truss structure related tubular welded joint (Mann, 2006).

5.5.1 One-bay {frame, plate-stiffener, stiffened panel} data

Fatigue sensitive locations in high-speed craft hull structures typically include frame corner- and frame-stiffener connections, with- or without bracket. Conducting LSS fatigue resistance experiments, typically a corner bending (Irving et al., 2005; Fig. 5.51) and three (Tveiten et al., 1999 and 2007; Sears et al., 2000; Polezhayeva et al., 2001; Fig. 5.52 and 5.53)- or four-point bending (De Vries et al., 2000; Ye et al., 2007; Fig. 5.54) setup is adopted using one-bay {frame, plate-stiffener, stiffened panel} structures.

The welded joint connecting the soft toe bracket to the frame corner (Fig. 5.51a) is classified as weld end (HS type *A*). To estimate the (non-symmetric) local weld geometry induced bending a SS cover plate geometry is involved. The cover plate height t_c equals the weld height h_w ; the bracket length is defined as cover plate length l_c . The FE model incorporates the (global) bracket induced load carrying effectiveness. Far field stress parameters $\{\sigma_s, r_s\}$ include the 3D effects (Paragraph 2.9); the semi-elliptical crack ratio $(a/c) = t_p/(t_c + 2l_w)$. In nested bracket configuration, the frame corner (Fig. 5.51b) contains a SS butt joint (HS type *C*).

Welding a frame/bulkhead stiffener to a (side) shell/deck stiffener flange introduces a governing HS type *B* (Fig. 5.52a); t_p' equals the stiffener web height. For a slightly different configuration (Fig. 5.52b); the brackets and frame/bulkhead stiffener (Fig. 5.52a) serve the same purpose here, the frame – T-stiffener connection, a DS T-joint, is dominant. In case of a continuous weld at mid-flange position a HS type *C* is governing; for a discontinuous one, i.e. welding the stiffener flange only partially, a HS type *B* is in charge again (t_p' equals half the flange width).

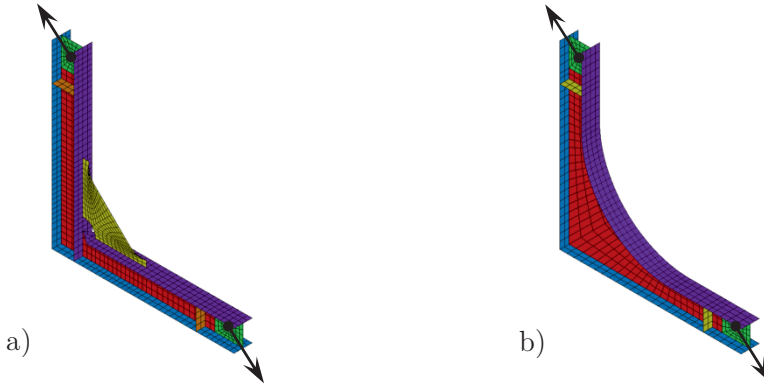


Figure 5.51: Corner bending setup (Irving et al., 2005) for a deck frame corner with soft toe- and nested bracket.

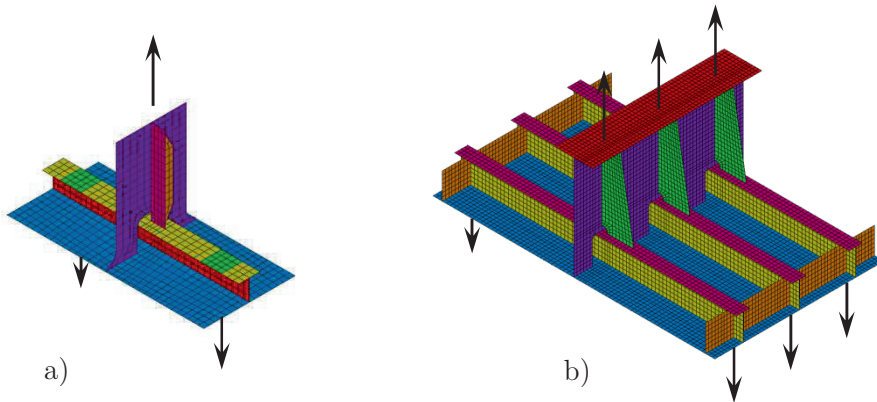


Figure 5.52: Three-point bending setup for frame – T-stiffener connections (Sears et al., 2000; Polezhayeva et al., 2001).

Frame – bulb stiffener connections are analysed as HS's type *C*, even if a bracket is involved (Fig. 5.53a) because of the small stiffener flange width; stresses are averaged along flange width direction. In case of a bracket, the SS cover plate is still used to estimate the weld geometry induced bending stress at the weld end (HS type *A*). If a plate-stiffener combination in between frames is subjected to (space-averaged) pressure loading, brackets typically reduce the effective span meaning the stress level decreases. Replacing a straight bracket by a curved one reduces the SCF at the weld toe; the governing hot spot (at the price of another BM hot spot in the curvature). However, for three-point bending the fatigue resistance for straight and curved brackets is similar. The frame – T-stiffener connection (Fig. 5.53b), a DS T-joint, contains a governing HS type *C* as well.

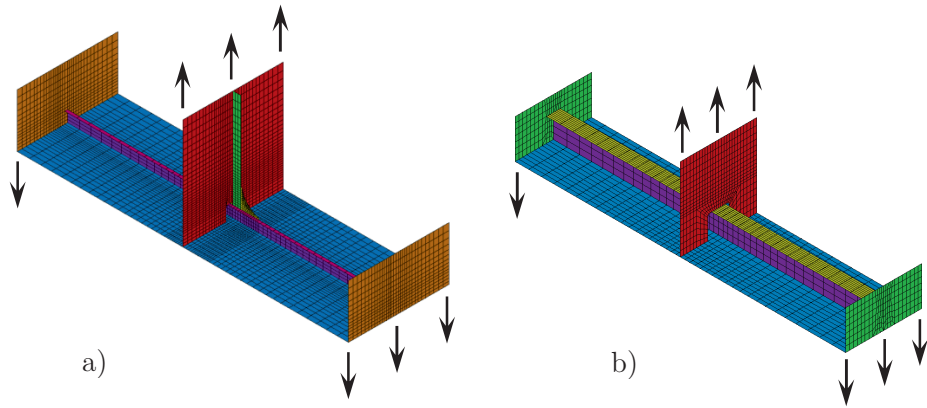


Figure 5.53: Three-point bending setup for frame – {bulb, T-} stiffener connections (Tveiten et al., 1999; 2007).

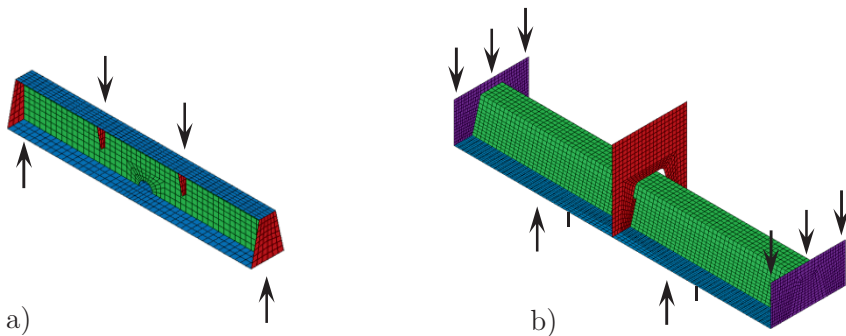


Figure 5.54: Four-point bending setup for a) stiffener scallop (De Vries et al., 2000) and b) frame – box stiffener connection (Ye et al., 2007).

Since a stiffener scallop weld end (Fig. 5.54a; HS type *A*) is typically a welding start/stop location (start over stop or stop over start, affecting the local geometry), its fatigue resistance has been investigated (De Vries et al., 2000). Nice feature: the through-thickness weld notch stress distribution is non-monotonic. Aiming for constant bending over some length along the plate-stiffener combination, a four-point bending setup has been adopted. A frame – box stiffener connection has been tested in 3 configurations (Ye et al., 2007): watertight (welding round about, HS type *C*), tight (welded along the inclined plates only, HS type *B*) and open (Fig. 5.54b, HS type *A*). The open configuration requires the 1st principal stress as mode-I component.

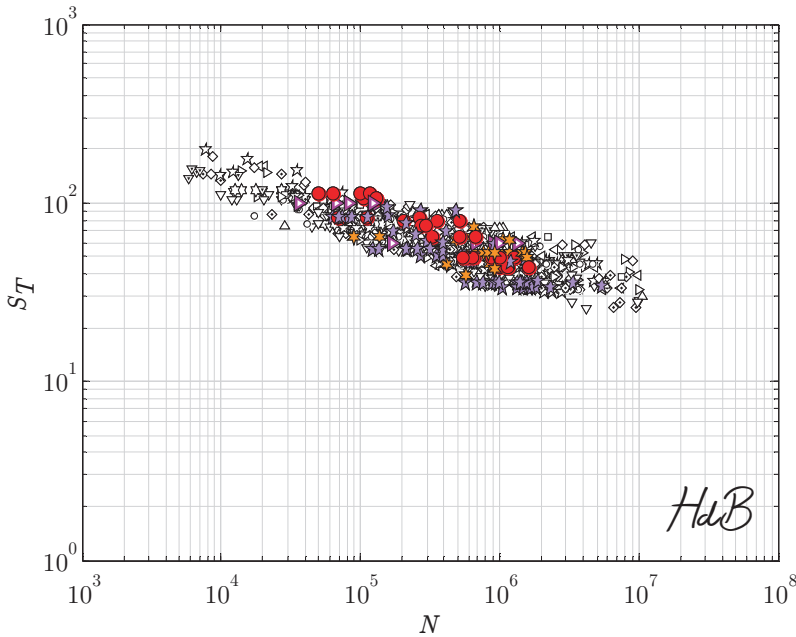


Figure 5.55: LSS data fitting the MCF SSS fatigue resistance scatterband.

The remote mechanical loading induced welded joint maximum far field stress $\sigma_{max} = \Delta\sigma_s / (1 - r_l)$ is tensile for all tests and seems at least to be a worst case scenario, e.g. space-averaged (water) pressure – a realistic type of hull bottom structure loading – introduces a compressive one. Principally, {SSS, LSS} data includes tensile remote mechanical- and tensile thermal residual stress, meaning the S_T - N fatigue resistance relation is a (T-T) curve. The LSS fatigue data perfectly fit the SSS (T-T) joint S_T - N curve data scatter band (Fig. 5.55; legend Fig. 5.29), i.e. the fatigue resistance is similar. Equilibrium equivalent residual stress contributions affecting r_l^T are limited.

5.5.2 Three-bay stiffened panel data

Applying a repeated (impact type of) space averaged pressure loading; $\Delta p \approx 1$ [bar] and $r_l \approx 0.1$ [-], to a three-bay stiffened panel (Fig. 5.56) to include realistic deformation restraints (i.e. residual stress distributions) as well as remote mechanical loading, a series of 3 LSS fatigue tests are conducted at the TNO Delft Structural Dynamics Laboratory (Drummen, Schiere and Tuitman, 2013). The two frames including web (200x6) and flange (50x6), the attachment (100x50x5) as well as the (stepped) base plate are produced using Al5083H321 material; all three HP80x3 stiffeners are Al6082 material extrusions.

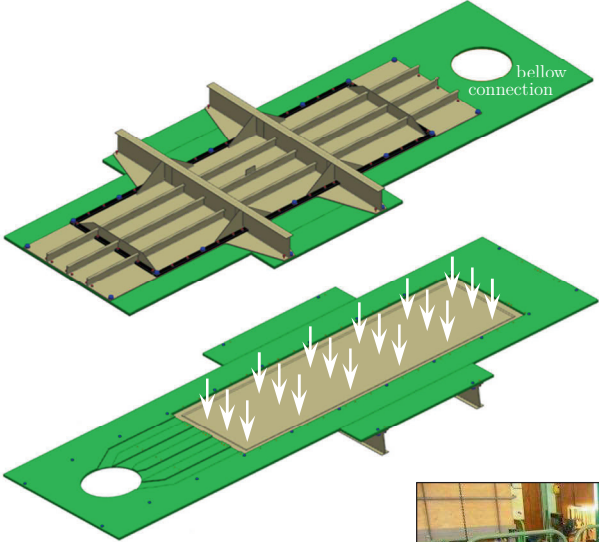
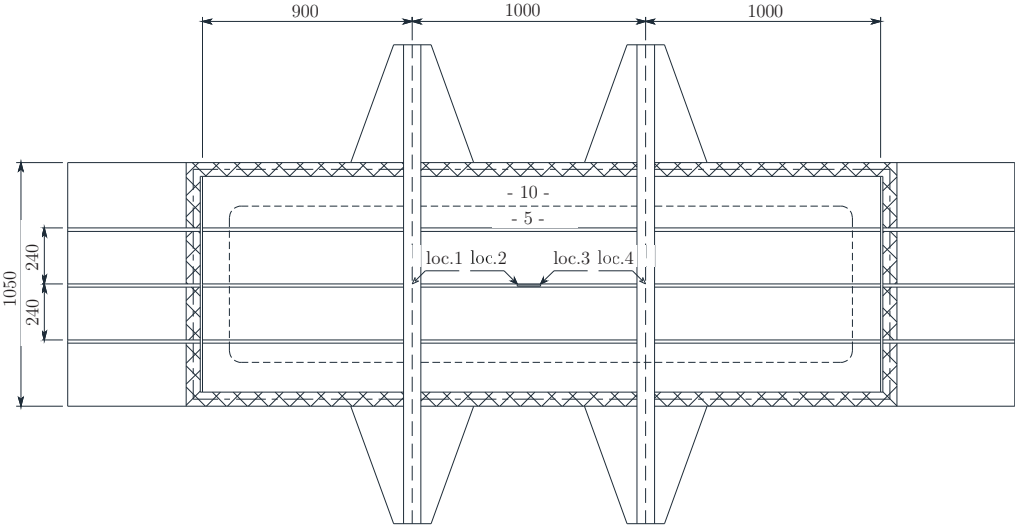


Figure 5.56: LSS layout and fatigue test setup

To control the number of fatigue sensitive locations, focus is on the middle stiffened panel bay; weld toes outside are grinded. The 2 frame-stiffener connections (1 redundant) at the middle-plate stiffener bay (loc. 1 \square and loc. 4 \triangleright) – the remote mechanical far field stress is compressive – include weld toe notches and will be governing. Halfway the span, an attachment has been welded on top of the stiffener to add 2 stiffener-attachment connections, weld toe notches (loc. 2 ∇ and loc. 3 \triangle) with a remote mechanical tensile far field stress for comparison.

Boundary conditions

For an accurate fatigue design life parameter estimate S_T of stiffened panel hot spots, the involved boundary conditions (BC's) are considered to be very important. The LSS's are mounted to the lab floor using bolts and strips (60x20); the strips are meant to distribute the bolt point loads along the panel boundaries (Fig. 5.56).

The observed panel deformations clearly showed some degree of BC rotational stiffness k_r , likely in between zero along the bolt row centre line and infinity over the strip, i.e. in between simply supported (SS) and clamped (CL) BC's. Although strain gauges (SG's) have been used to measure the structural response of the middle stiffened panel bay, to obtain BC estimates of the (overall) three-bay panel the SG signals are insufficient and the out-of-plane base plate displacement range Δd_z has been measured using lasers for LSS 3 (Fig. 5.57) only, assuming the BC's are similar for all 3 specimens.

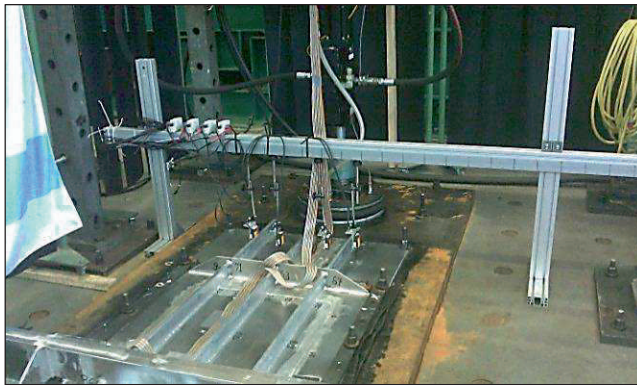


Figure 5.57: Laser displacement rang measurement setup.

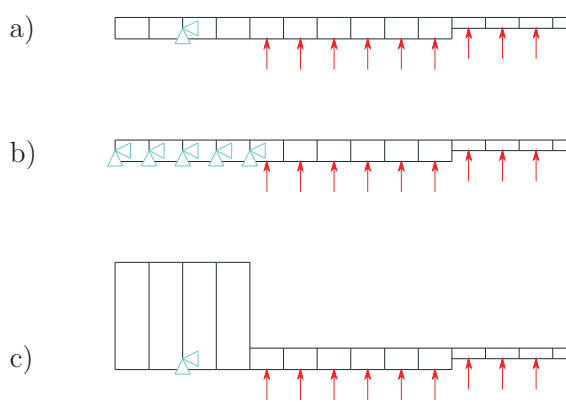


Figure 5.58: Model boundary conditions, a) SS along line, b) CL over strip, c) artificial increase of strip element thickness to simulate $k_r(0, \infty)$.

To include $k_r(0, \infty)$ in a shell/plate FE model, it seems straight forward to use torsional springs along the bolt row centre line. For $k_r \rightarrow \infty$ however, the stiffness matrix becomes ill-conditioned and the BC strips are still not fully constrained. Applying master-slave connections or linear springs over the strip width may solve this issue. Anyhow, spring elements predominantly include 2D behaviour and the solution adopted is to artificially increase the actual element thickness of the BC strip with SS BC's along the bolt row centre lines (Fig. 5.58); the k_r lower bound, if required up to approximately clamped BC's; the k_r upper bound, varying both bending and torsional stiffness to include 3D effects as well.

Using the out-of-plane base plate displacement range laser measurement grid table (9x4) and a relatively coarse meshed FE model, the total relative displacement error ε_d has been minimised employing 2 optimisation variables: the BC strip thickness at the long- and short sides $\{t_{BCl}, t_{BCs}\}$; a choice from design perspective. The obtained relative displacement range error (Fig. 5.59) for an applied pressure range $\Delta p = 0.88$ [bar] seems random; its mean is close to zero. The minimum objective $\varepsilon_d = 1.46$ [-], i.e. the average error at each grid point is less than 5 [%], reduces only if the number of t_{BCi} variables is increased. The optimum BC strip thicknesses $\{t_{BCl} \approx 50, t_{BCs} \approx 210\}$ intuitively make sense: the long side value is quite close to the sum of the actual base plate- and BC strip thickness; the short side value is significantly larger because of the involved (local) symmetry conditions and LSS panel aspect ratio.

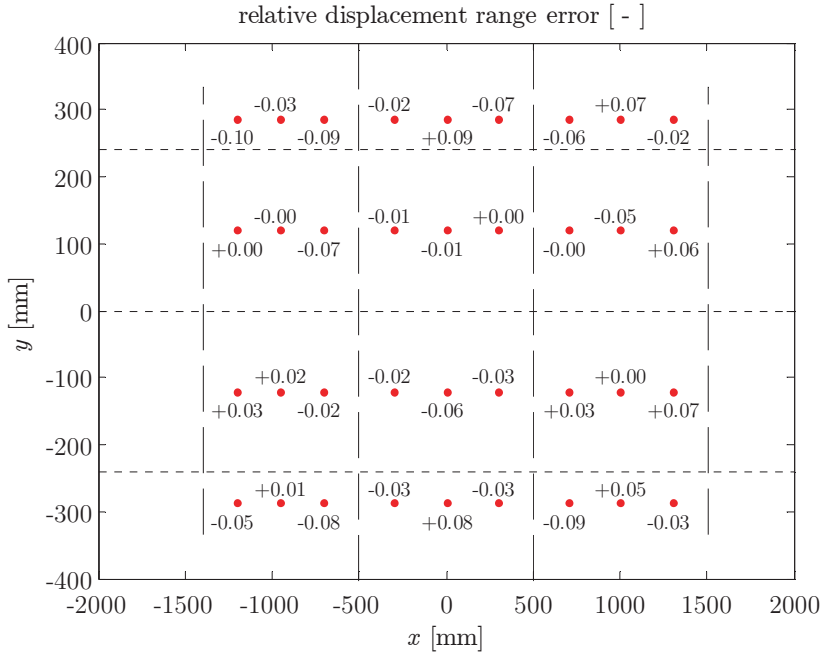


Figure 5.59: FE model out-of-plane displacements relative to laser measurements.

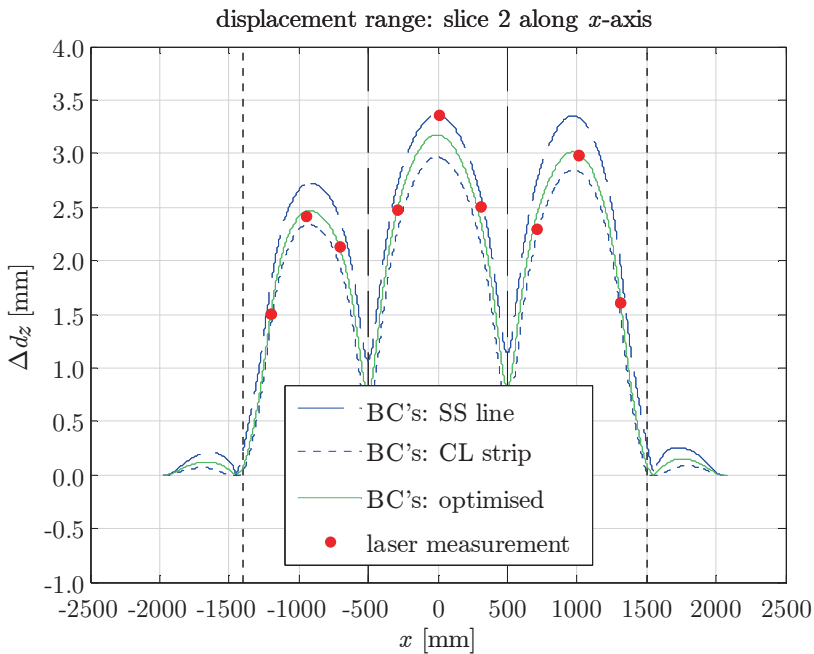
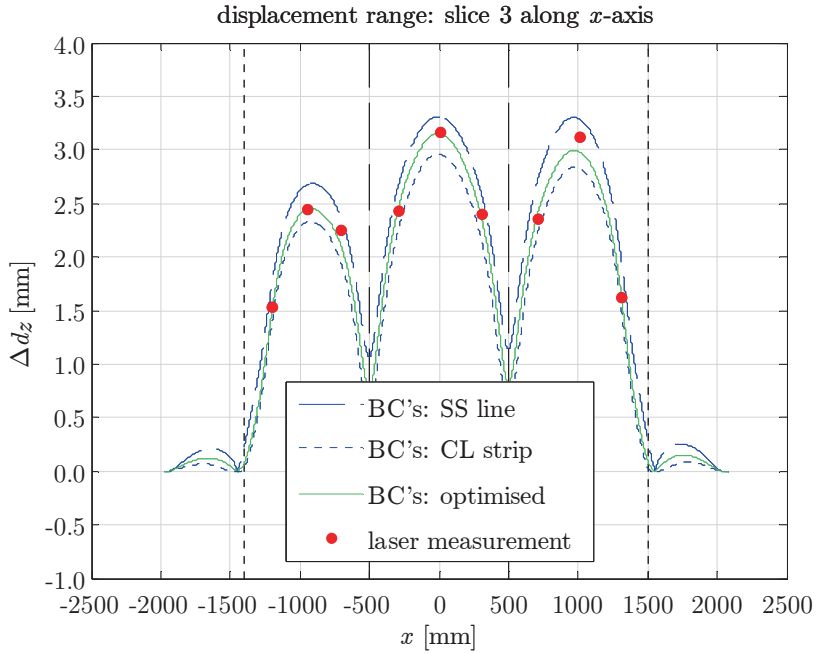
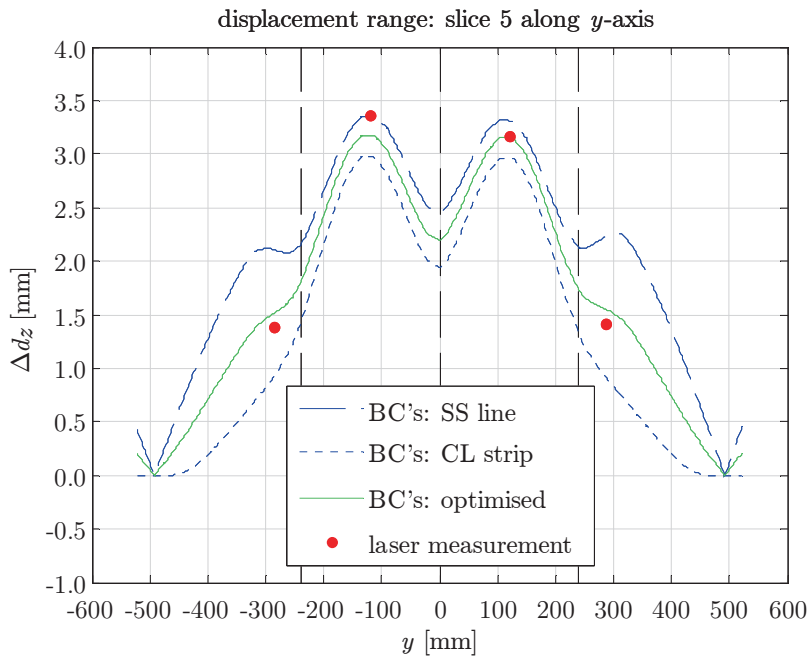


Figure 5.60: Displacement range along $y = -120$.

Figure 5.61: Displacement range along $y = 120$.Figure 5.62: Displacement range along $x = 0$.

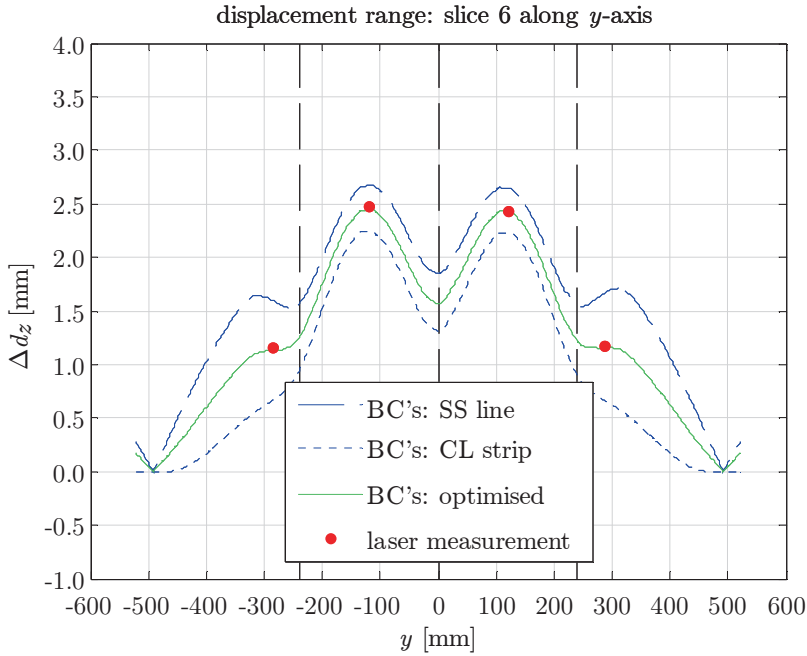


Figure 5.63: Displacement range along $x = -300$.

The out-of-plane base plate displacement range for both measurement- and model results, shown for 4 slices (Fig. 5.60, 5.61, 5.62 and 5.63), is in between the SS line and CL strip BC extremes indeed (except an individual outlier at the boundary).

Note that the $\{t_{BCl}, t_{BCs}\}$ values are related to the applied panel pressure range. Since Δp is measured at the bellow, it has been assumed that both values are equal. The SG measurement results may provide proof.

Strain response

Main purpose of the SG measurements is to obtain strain (drop and growth) information concerning the development of through thickness cracks at the hot spots and to measure the global structural response at some locations (Fig. 5.64).

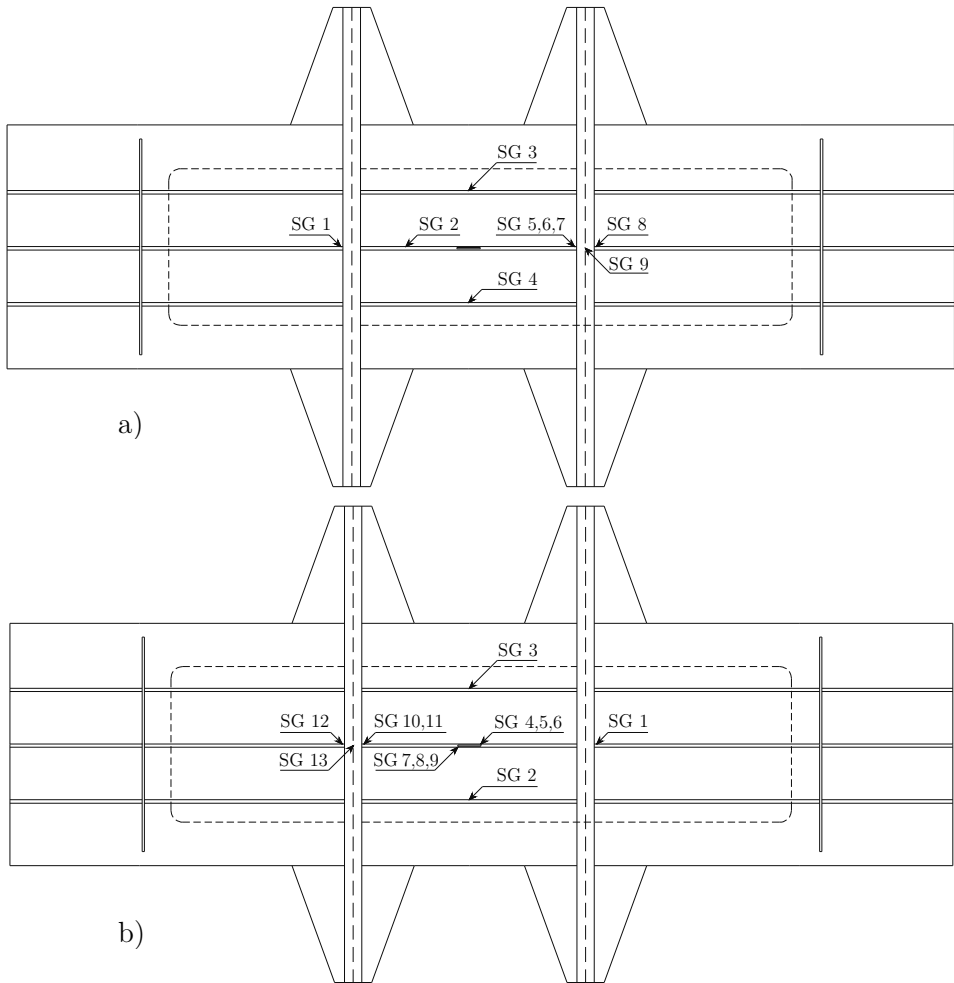


Figure 5.64: SG locations for a) LSS 1 and b) LSS {2, 3}.

The mean micro-strain range $\Delta\mu\epsilon$ value of the time series up to a number of cycles $n = 5 \cdot 10^4$, a MCF lifetime range value before significant through-thickness crack induced stiffness loss; engineering judgement, has been used to obtain intact geometry $\Delta\mu\epsilon$ values. Using the same FE model (Fig. 5.65) as involved for the displacement error optimisation, FE and SG global response data is compared for all LSS's (Table 5.21, 5.22 and 5.23).

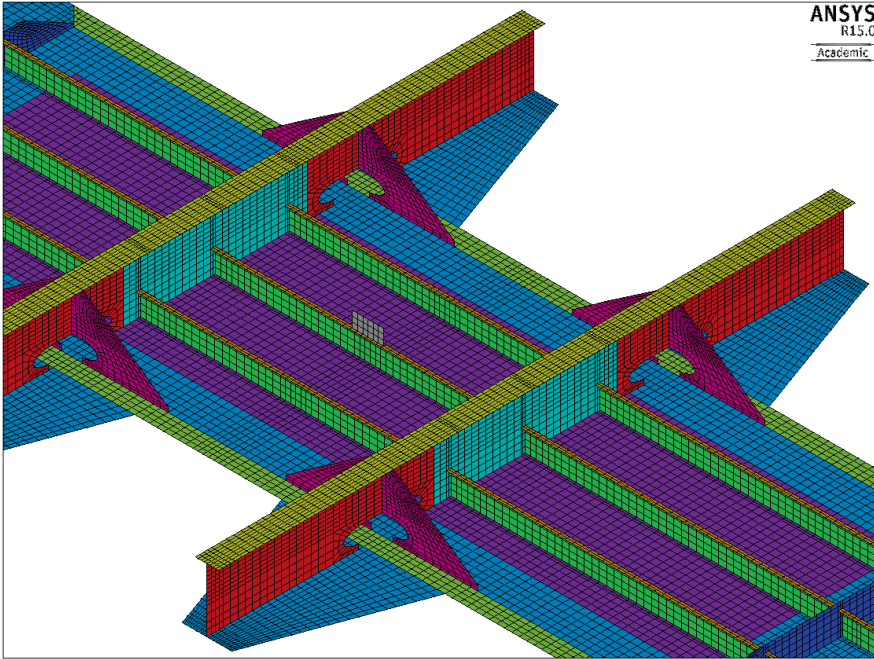


Figure 5.65: Relatively coarse meshed FE model, element size ~ 25 [mm].

Since the middle plate-stiffener combination in the frames behaves like a two-sided CL beam, SG's $\{1, 5, 6, 7, 8 | \text{LSS } 1\}$ and $\{1, 9, 11, 12 | \text{LSS } 2, \text{LSS } 3\}$ do not provide additional information in comparison to SG $\{2 | \text{LSS } 1\}$ and $\{6 | \text{LSS } 2, \text{LSS } 3\}$ or involves local information not included in the relatively coarse meshed FE model.

SG nr.	FE $\Delta\mu\varepsilon$	SG $\Delta\mu\varepsilon$	rel. error
2	296	317	- 0.071
3	806	769	+ 0.048
4	792	685	+ 0.156
9	705	833	- 0.154

Table 5.21: LSS 1 SG and FE strain, $\Delta p = 0.90$ [bar].

SG nr.	FE $\Delta\mu\varepsilon$	SG $\Delta\mu\varepsilon$	rel. error
2	740	762	- 0.029
3	752	836	- 0.100
6	995	1197	- 0.169
13	615	731	- 0.159

Table 5.22: LSS 2 SG and FE strain, $\Delta p = 0.84$ [bar].

SG nr.	FE $\Delta\mu\varepsilon$	SG $\Delta\mu\varepsilon$	rel. error
2	775	728	- 0.109
3	788	850	+ 0.065
4	1042	1170	- 0.073
9	644	704	- 0.085

Table 5.23: LSS 3 SG and FE strain, $\Delta p = 0.88$ [bar].

In general the strain is underestimated, meaning no or at most a very limited pressure loss in between bellow and panel. The influence of BC's to the FE $\Delta\mu\varepsilon$ values is limited as well because of the LSS panel stiffness hierarchy. The frame stiffness defines the plate-stiffener combination BC's, i.e. the strain on top of the stiffeners at SG {2, 3, 4; 2, 3, 6} for the different LSS's, and different $\{t_{BCl}, t_{BCs}\}$ values hardly affect the results. In fact, only the strain at the global response SG {9; 13} locations can be influenced within a few per cent. An optimisation using a weighted objective of the relative displacement- and strain error, e.g. $f_o = (4/40) \cdot \varepsilon_d + (36/40) \cdot \varepsilon_s$, even with increased or reduced panel pressure turns out not to improve the result, justifying the separate displacement based BC analysis. Since the FE model dimensions are according to drawing specifications; a design approach, the LSS strain error is accepted 'as built' representing a realistic hull bottom structure including production tolerances.

Fatigue life time parameter estimate

The SG time series for all LSS's have been investigated for the development of through-thickness cracks at the governing weld toe notches, HS locations {1, 2, 3, 4}, to identify the corresponding fatigue life time, i.e. number of cycles N until a through-thickness crack. Since the test (pressure) frequency is set to 0.5 [Hz], data is sampled at 10 [Hz] for LSS 1 and at 5 [Hz] for LSS {2, 3}, the strain time series $\varepsilon(t)$ are (FFT) low pass filtered first and translated to $\{\varepsilon_{min}, \varepsilon_{max}\}$ - and strain range $\Delta\mu\varepsilon$ data related to number of cycles n . Respectively a median and sophisticated moving average (mean) Savitzky-Golay filter have been applied to remove spikes and digital image correlation measurement (Drummen, Schiere and

Tuitman, 2013) induced interruptions to smoothen the data. Finally, piece-wise linear approximations are obtained in order to identify the through-thickness crack induced strain drops and -growths as show for LSS 2 (Fig. 5.66).

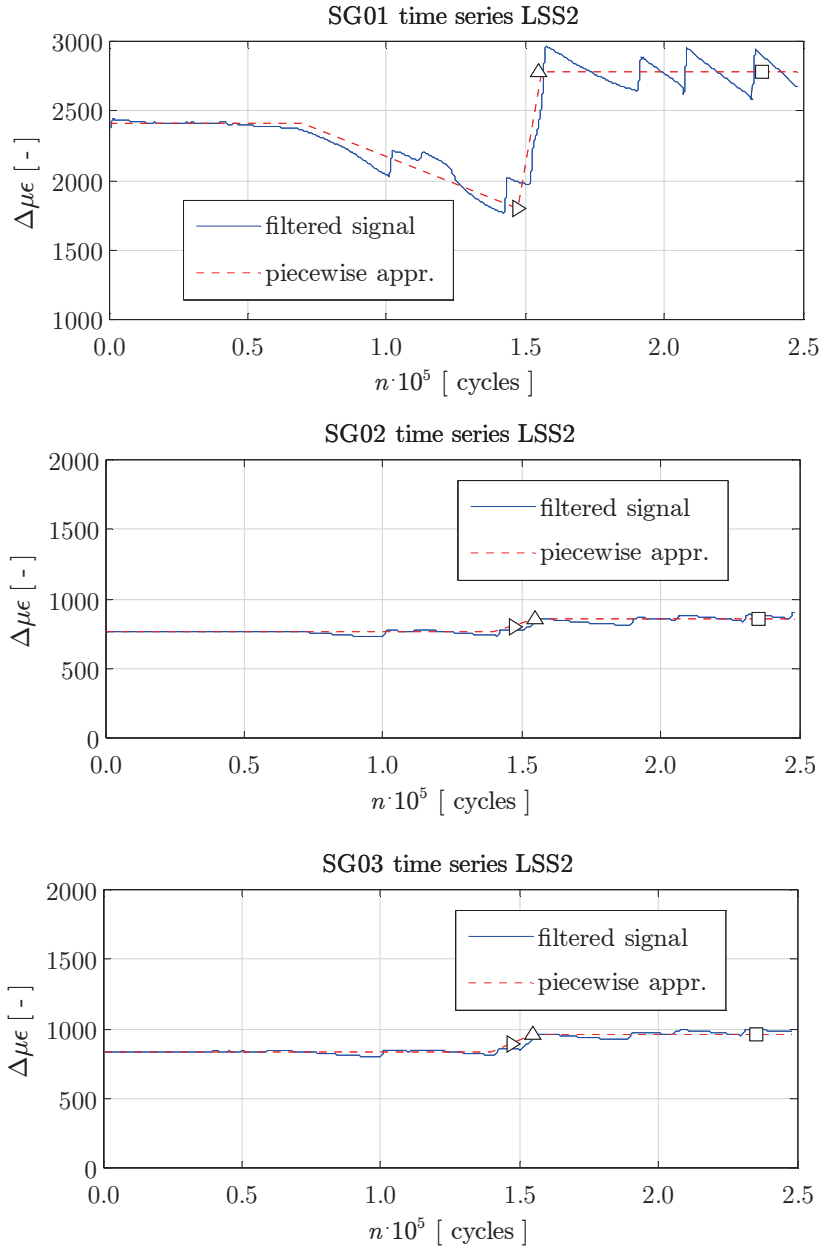


Figure 5.66a: Filtered SG data LSS 2.

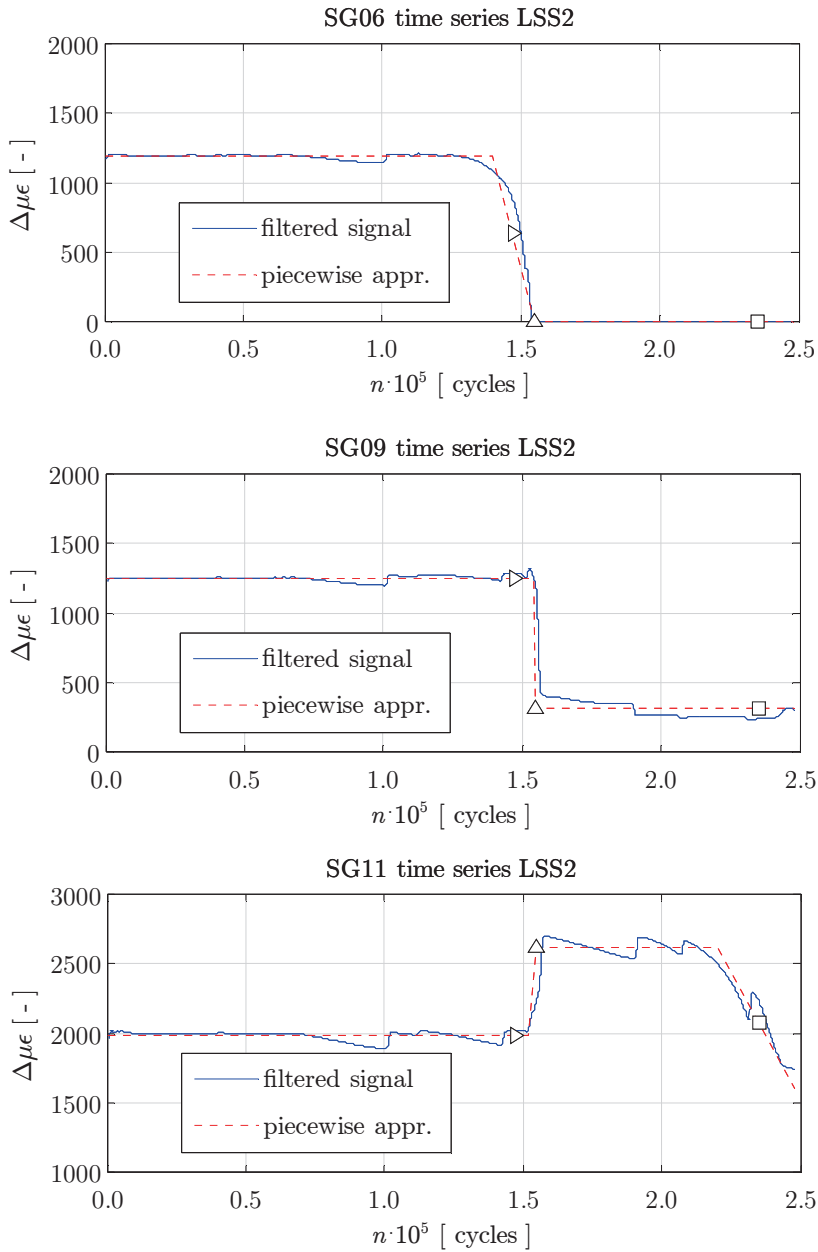


Figure 5.66b: Filtered SG data LSS 2.

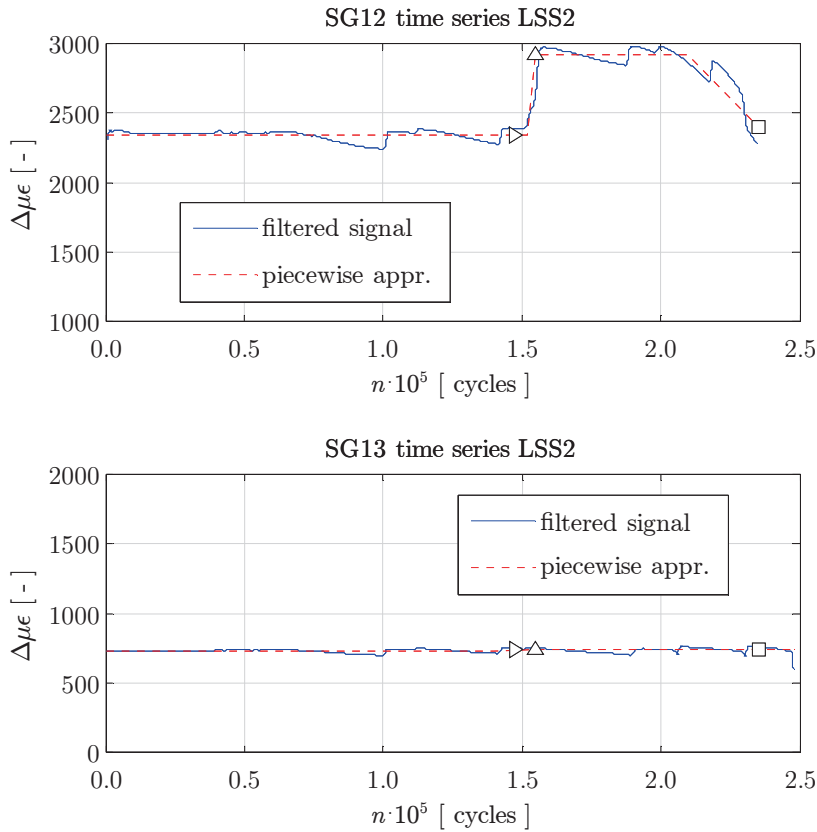


Figure 5.66c: Filtered SG data LSS 2.

At $n \sim 0.7 \cdot 10^5$ cycles a crack gradually starts to grow at loc. 4 \triangleright (SG 1), a frame-stiffener connection. Its size becomes through-(flange)thickness at $N \approx 1.47 \cdot 10^5$ cycles. The corresponding strain drop of about 30 [%] is in agreement with FE estimates. Crack growth appears to slow down, likely because the residual stress at that location becomes compressive as well. Other SG signals remain unaffected because the frame still imposes the displacement constraints, i.e. a compressive far field stress. Meanwhile, a rapid crack growth at loc. 2 ∇ (SG 6), a stiffener-attachment connection, can be identified and continues until the stiffener is completely cracked. Although a through-thickness crack corresponds approximately to a 75 [%] strain drop according to FE calculations, the through-thickness crack is set at $N \approx 1.55 \cdot 10^5$ cycles. At the same time, the strain significantly drops at loc. 3 (SG 9) as well. The middle plate-stiffener combination becomes unable to carry the pressure loading because of the stiffness loss and its neighbours take over since a stiffened panel is a parallel system: SG {1, 11, 12} values at the frame-stiffener connections increase to a greater extent in comparison to SG {2, 3} halfway the stiffener span. A third through-thickness crack has been identified at loc. 1 \square (SG

12) at $N \approx 2.35 \cdot 10^5$ cycles. The strain at SG 11 reduces as well, though unexpected based on the remote mechanical far field stress only. The frame structural response (SG 13) is insensitive to any crack induced stiffness loss. Note that some signals show saw-tooth shaped behaviour because of leakage and refilling issues; keeping the pressure level constant proved to be a challenge.

For LSS {1, 3} similar results have been obtained (Appendix B). The weld toe notch fatigue life time summary (Table 5.24) shows a reasonable level of scatter (factor 3).

loc.	LSS 1	LSS 2	LSS 3
1 \square	$1.10 \cdot 10^5$	$2.35 \cdot 10^5$	$0.50 \cdot 10^5$
2 ∇	$1.79 \cdot 10^5$	-	$2.36 \cdot 10^5$
3 \triangle	-	$1.55 \cdot 10^5$	-
4 \triangleright	$1.10 \cdot 10^5$	$1.47 \cdot 10^5$	$0.50 \cdot 10^5$

Table 5.24: Through-thickness cracks fatigue life time N .

Although the LSS's are overloaded in the first few cycles to simulate shake down, the residual stress is still tensile at the frame-stiffener connection since the crack is open in unloaded condition; a crack at the stiffener-attachment connection is open in loaded condition (Fig. 5.67).

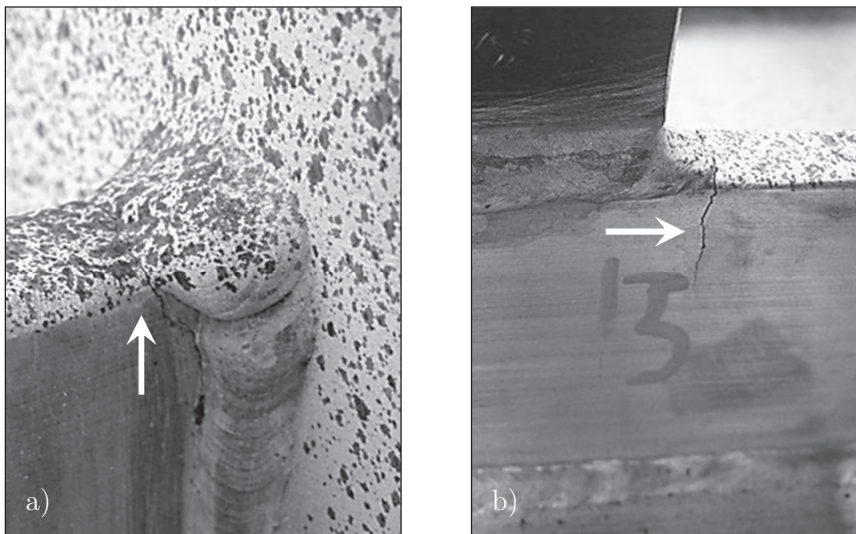


Figure 5.67: Cracks in LSS 1 at a) loc. 1 and b) loc. 2.

The total stress design parameter S_T requires a welded joint far field stress for all 4 notch locations and will be calculated using FE nodal forces (Fig. 5.68). The weld toe at the stiffener-attachment connections is identified as a hot spot type *A*. Since the weld end covers the total flange width (Fig. 5.67), average $\{\sigma_s, r_s\}$ values have been calculated like for the weld toe frame-stiffener connections; hot spots type *C*, rather than applying a virtual node method (Dong, 2005).

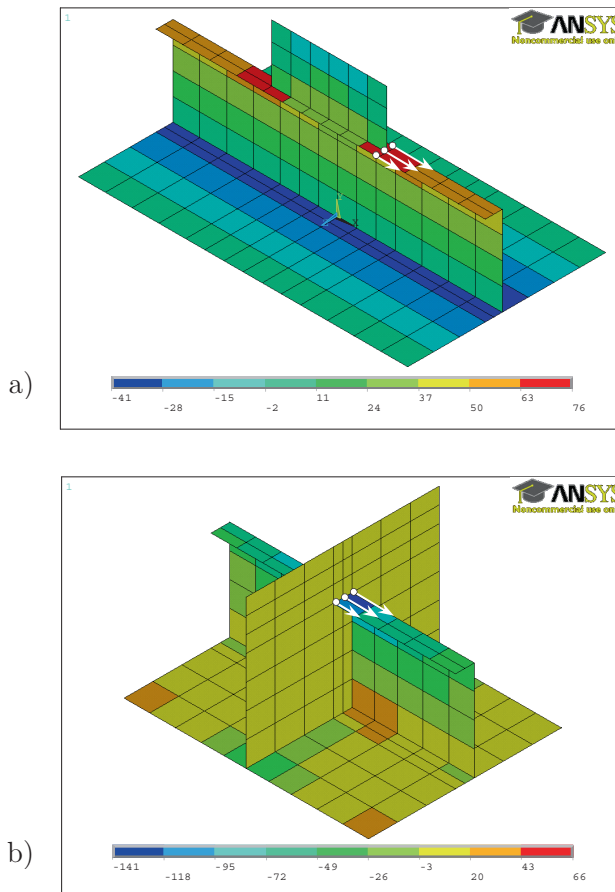


Figure 5.68: FE stress in x -direction and involved nodal forces to calculate $\{\sigma_s, r_s\}$ for a) stiffener-attachment and b) frame-stiffener connection.

All remote mechanical loading induced through-thickness weld toe notch stress distributions $\sigma_n(r/t_p)$ are monotonic and either fully compressive or fully tensile (Table 5.25).

$\Delta p = 0.90$ [bar]	LSS 1		
loc.	σ_s [MPa]	r_s [-]	$\Delta\sigma_s$ [MPa]
1 \square	-84	0.51	168
2 ∇	+44	0.31	88
3 \triangle	+43	0.31	86
4 \triangleright	-93	0.48	186

$\Delta p = 0.84$ [bar]	LSS 2		
loc.	σ_s [MPa]	r_s [-]	$\Delta\sigma_s$ [MPa]
1 \square	-78	0.51	156
2 ∇	+41	0.31	82
3 \triangle	+40	0.31	80
4 \triangleright	-87	0.48	174

$\Delta p = 0.88$ [bar]	LSS 3		
loc.	σ_s [MPa]	r_s [-]	$\Delta\sigma_s$ [MPa]
1 \square	-82	0.51	164
2 ∇	+43	0.31	86
3 \triangle	+42	0.31	84
4 \triangleright	-91	0.48	182

Table 5.25: Welded joint far field stress.

The obtained S_T - N curve is typically a SSS tension-tension (T-T) fatigue resistance relation, meaning that except the predominant tensile residual (notch) stress, the remote mechanical loading induced maximum stress is tensile as well: $\sigma_{max} = \Delta\sigma_s / (1 - r_l) > 0$ for $r_l \in (-\infty, 1)$. In case of full compression ($\sigma_{max} < 0$) however, $r_l \in (1, \infty)$ and a tension-compression (T-C) correction should be applied since the involved modified Walker model is based on the assumption that only the tensile part of the stress cycle contributes to fatigue damage meaning $r_l \in (-\infty, 1)$. Still using the (T-T) curve, it is proposed to define an equivalent remote mechanical load ratio $r_{l,eq}$ using the tensile case value ($r_l^t = 1/r_l$) of the fully compressive cycle ($r_l^t \geq 0$) and a relative one r_{lr} for translation to compression (Fig. 5.69):

$$r_{lr} = \frac{\sigma_{min,r}}{\sigma_{max,r}} \quad (5.36)$$

$$= - \left\{ 1 + \frac{1}{\frac{1}{2} + 2 \left(\frac{r_l^t}{1 - r_l^t} \right)} \right\}$$

Provided $\{r_l^t, r_{lr}\}$, the equivalent remote mechanical load ratio becomes:

$$r_{l,eq} = 1 - \frac{(1 - r_{lr})}{(1 - r_l^t)} \quad (5.37)$$

For ($r_l^t = 0$) corresponding to ($r_l = -\infty$): $r_{l,eq} = r_{lr} = -3$. In case ($r_l^t > 0$) \rightarrow ($r_{l,eq} < -3$). However, the equivalent load ratio to be used if $r_l \in (1, \infty)$ suggests its effect is similar to the tensile case $r_l = r_{l,eq} \in (-\infty, 1)$; a model peculiarity.

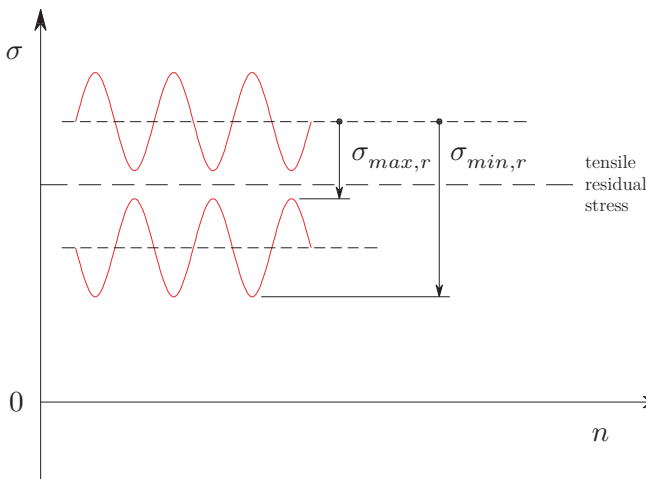


Figure 5.69: Relative load ratio effect for $r_l^t \geq 0$.

Since the γ MLE is relatively high, the effective stress will hardly change if ($r_{l,eq} = -3$) is adopted no matter $r_l \in (1, \infty)$; for consistency the same value is defined as lower bound if $r_l \in (-\infty, 1)$ as shown (Fig. 5.70). The total stress parameter (Eq. 5.35) turns into:

$$S_T = \frac{\Delta\sigma_s}{\left(\frac{t_p^{(\prime)}}{b_p}\right)^{\frac{1}{m}} \cdot b_p^{\frac{2-m}{2m}} \cdot I_N(r_s, r_{l,eq}, n, m, \gamma)^{\frac{1}{m}}} \quad (5.38)$$

The far field load reduction factor in case of (T-C) correction; $f_m = 1/(1 - r_{l,eq})^{1-\gamma} \approx 0.66$ [-], is close to $f_m = 0.6$ [-] as proposed in a classification note as lower bound (DNV, 2010); the only reference available in this respect, although related to steel base material rather than welded aluminium.

Adopting respectively a DS cruciform joint $\{t_b = 9.7, t_c = 6.0, l_w = h_w = 4.2, \rho = 0\}$ and SS attachment $\{t_b = 9.7, t_c = 6.0, l_c = 100, l_w = h_w = 4.2, \rho = 0\}$ geometry for the frame-stiffener and stiffener-attachment connections, finally the total stress design life parameters S_T can be obtained for the governing hot spots (Fig. 5.71).

The derived family of S_T - N welded joint fatigue resistance curves is damage tolerant, rather than fail safe philosophy based, since (micro-)cracks/defects are assumed to exist in an hull structure stiffened (curved) panel assembly; a parallel system.

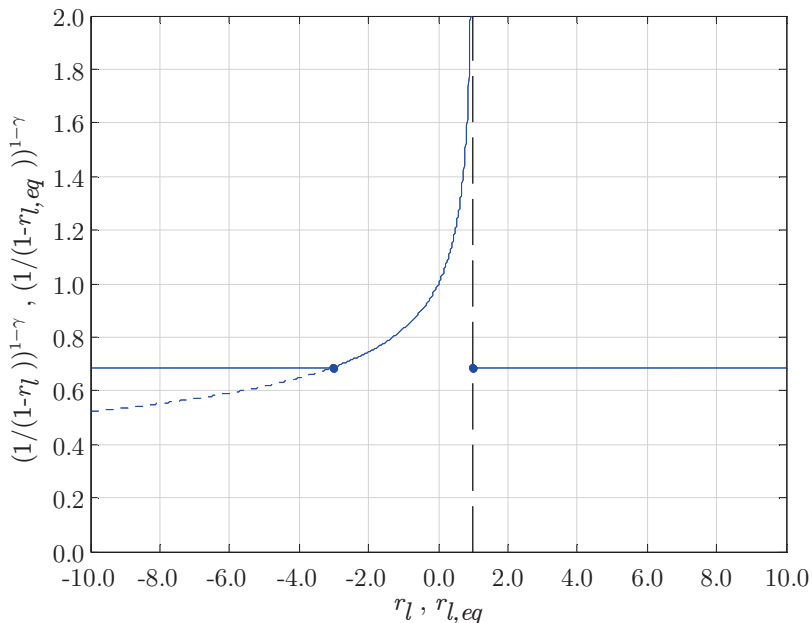


Figure 5.70: Far field reduction factor.

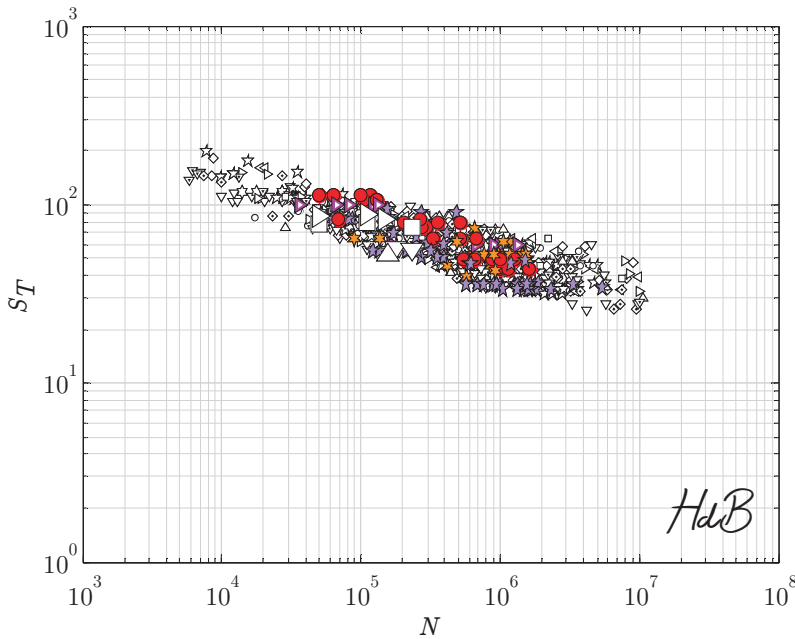


Figure 5.71: Stiffened panel data fitting the SSS fatigue resistance scatterband.

5.6 Small scale specimen VA fatigue resistance

Ocean/sea wave induced loading is highly stochastic; random, meaning the hull structural response shows VA- rather than CA behaviour. Assuming sequence effects are – on average – insignificant (i.e. crack growth {acceleration, deceleration} is balanced) and frequency related contributions are negligible, the Palmgren-Miner hypothesis is adopted to estimate (linearly) the fatigue damage: $\sum (n/N)_i \leq D$.

In general, D is considered to be load spectrum dependent (Fricke, 1997); a relatively large(r) contribution of small amplitude cycles increases fatigue life time N . A commonly recommended design value $D \leq 0.5$ (Kueppers and Sonsino, 2006) is typically based on a Gassner blocked program sequence with Gaussian-like loading distributions applied to SSS (Sonsino, 2004); $D \leq 1.0$ may provide non-conservative life time estimates. Applying WASH(W) wave load spectrum based time series to aluminium as-welded SSS, though, life times proved to be conservative for $D \leq 1.0$ using the corresponding CA fatigue resistance curve (Tveiten, 1999).

Variable amplitude data available in literature typically shows the spectrum only. However, the time series should be available to generate a rain flow matrix (or equivalent) providing the $n_i(\Delta\sigma_s | r_s, r_l)$ distribution; principally a rain flow cube $n_i(\Delta\sigma_s, r_s, r_l)$ if loading varies in both time and space like the FSS hull pressure distribution. Membrane and bending contributions are assumed to be proportional. Some DS cruciform joint data (Coughlin and Walbridge, 2012) for 2 different type of

characteristic VA time series (Fig. 5.72 and 5.73), yielding the corresponding rain flow matrices (Fig. 5.74 and 5.75) and spectra (Fig. 5.76 and 5.77), is investigated. Amplitudes have been scaled to obtain the fatigue resistance at a range of life times; r_s is constant since the spatial loading distribution does not change.

The RFL model (Eq. 5.21) will be adopted to address the VA fatigue resistance since the time series include {MCF, HCF} characteristic contributions, i.e. the large- as well as small amplitude contributions and corresponding resistance uncertainty needs to be taken into account. However, a possible design curve like the R99C95 quantile behaves approximately like a single slope formulation (Fig. 5.41) because of the HCF resistance uncertainty (meaning $m_1 \approx m_2$), i.e. natural filtering of (noise induced) small amplitude (high frequency) content is out of question and a significant fatigue damage contribution may be expected in that respect. Assuming a CA fatigue limit σ_∞ (threshold, micro-structural barrier) – if it exists – should be neglected (extrapolating the curve) in VA loading conditions since σ_∞ will be violated at some point in time, may seem to provide effectively the same result. A sequence effect based argument like this, though, is invalid if the Palmgren-Miner hypothesis is adopted. A single slope formulation sec, either based on MCF- or {MCF, HCF} data, is assumed to be too conservative anyway. To judge RFL model performance, let time be the interpreter...

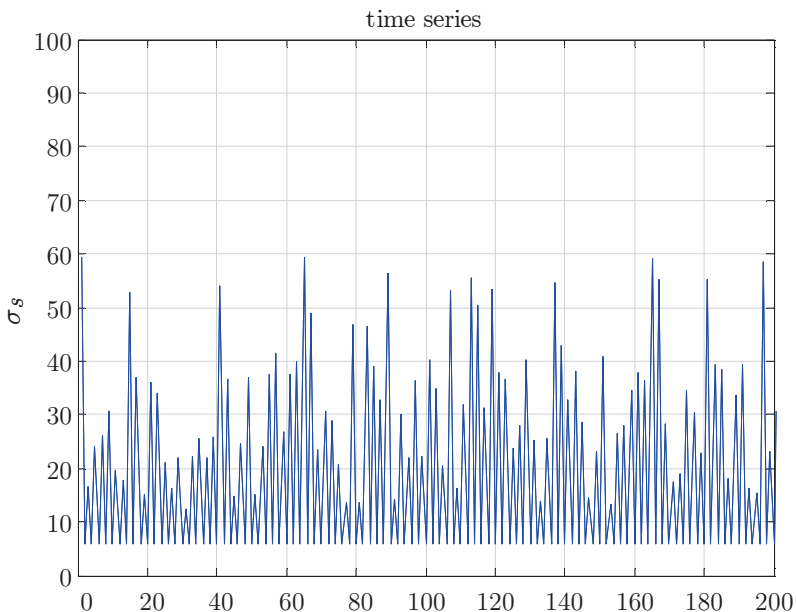


Figure 5.72: Characteristic time series 1 (Coughlin et al., 2012); $f = \{8, 28\}$ [Hz].

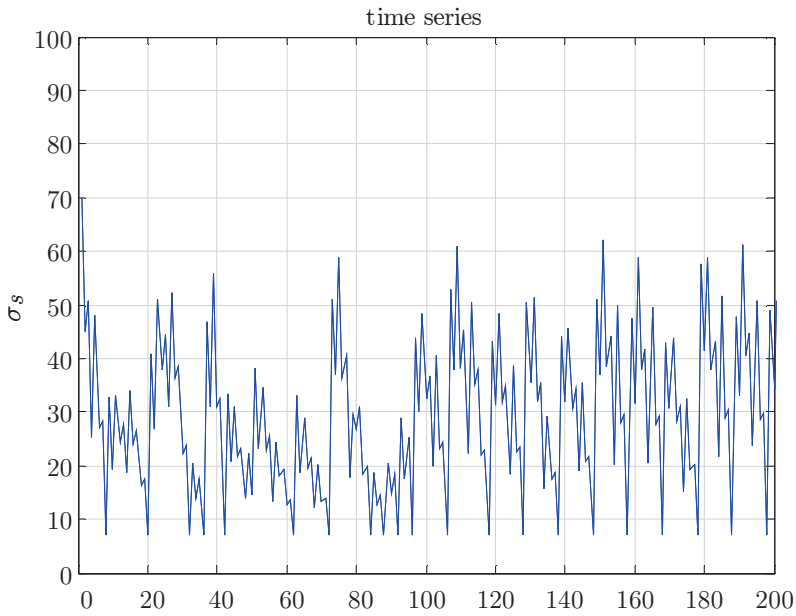


Figure 5.73: Characteristic time series 2 (Coughlin et al., 2012); $f = \{8, 28\}$ [Hz].

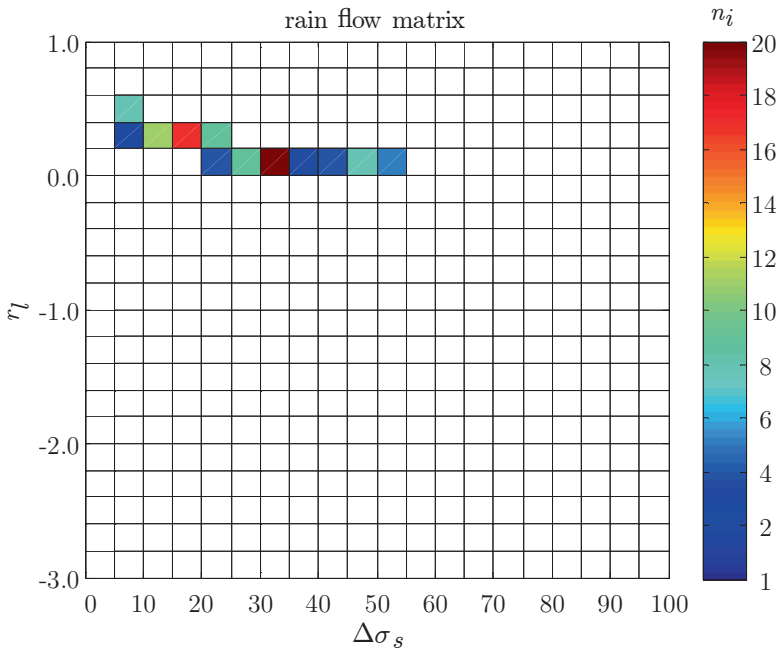


Figure 5.74: Rain flow matrix characteristic time series 1 (100 cycles).

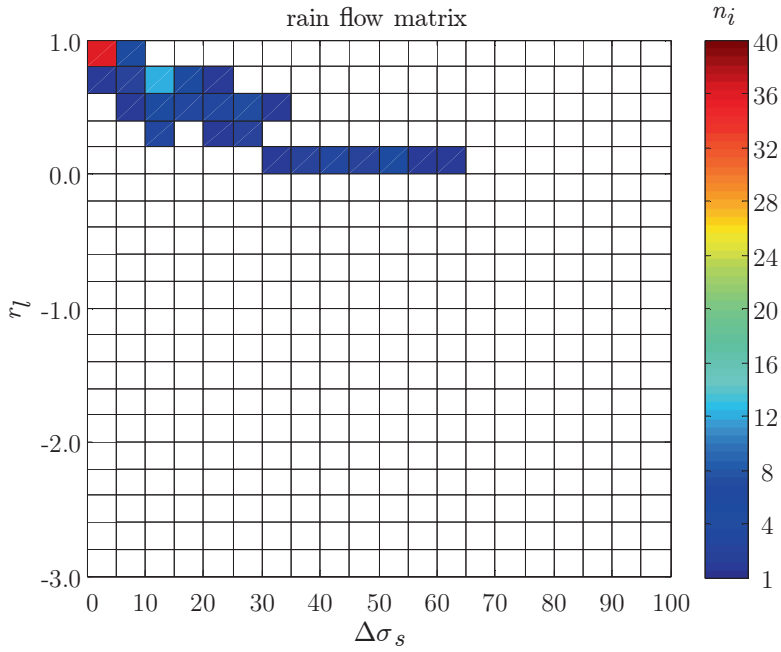


Figure 5.75: Rain flow matrix characteristic time series 2 (100 cycles).

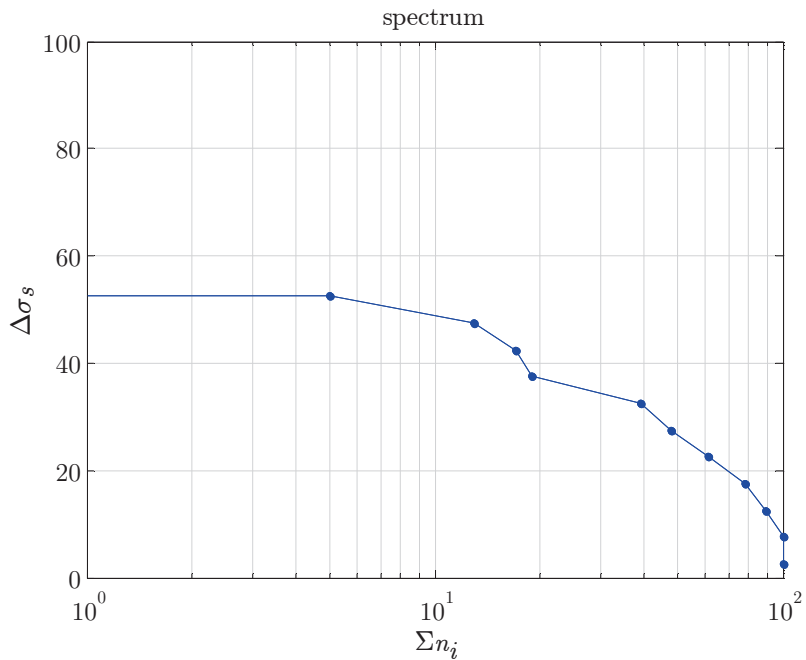


Figure 5.76: Structural stress spectrum characteristic time series 1.

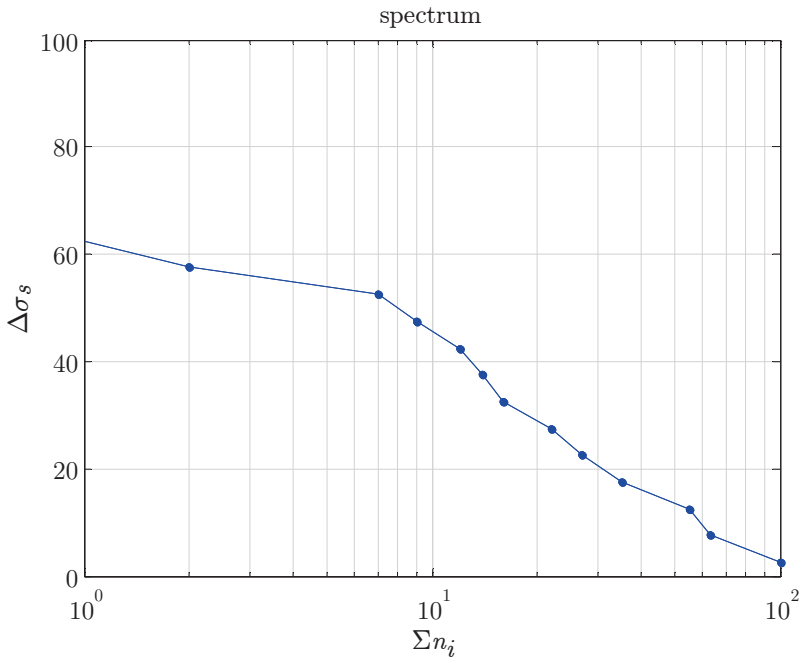


Figure 5.77: Structural stress spectrum characteristic time series 2.

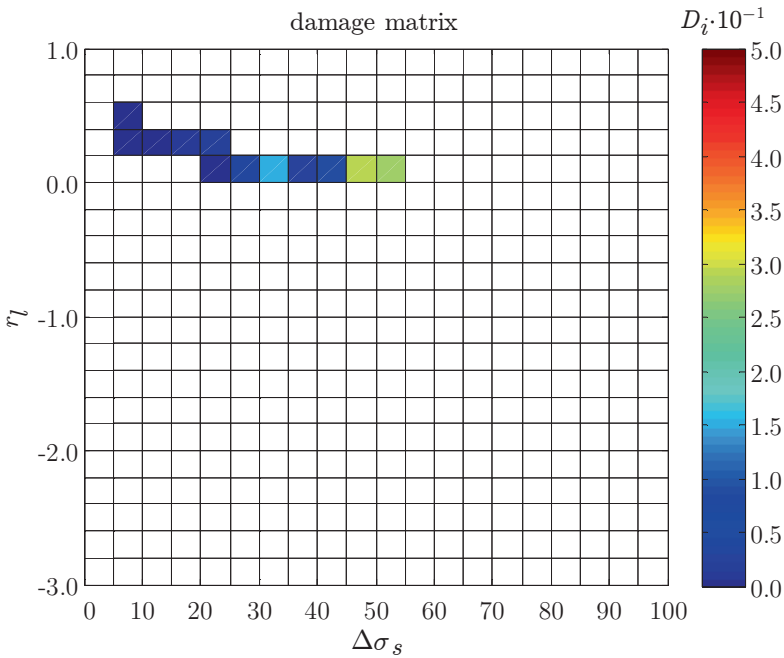


Figure 5.78: Damage matrix SSS 01 (characteristic time series 1; median curve).

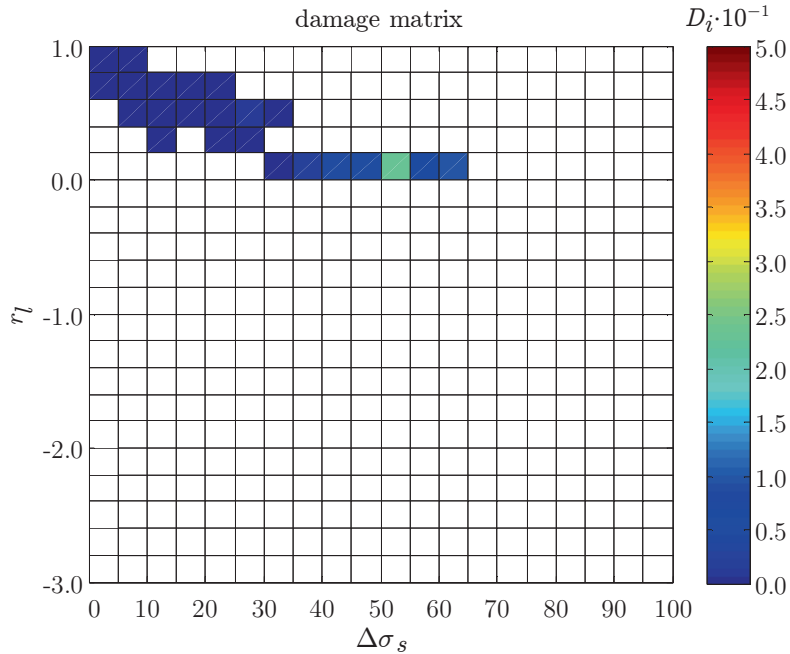


Figure 5.79: Damage matrix SSS 15 (characteristic time series 2; median curve).

Test data requires the definition of an equivalent total stress parameter:

$$S_{T,eq} = \left\{ \frac{\sum [n_i \cdot \{S_{T,i} - S_\infty(\mu, \sigma)\}^m]}{N} \right\}^{\frac{1}{m}} + S_\infty(\mu, \sigma) \quad (5.39)$$

with

$$S_{T,i} = \frac{\Delta\sigma_{s,i}}{\left(\frac{t_p^{(r)}}{b_p}\right)^{\frac{1}{m}} \cdot b_p^{\frac{2-m}{2m}} \cdot I_N(r_{s,i}, r_{l,eq,i}, n, m, \gamma)^{\frac{1}{m}}}$$

Comparing the rain flow- and damage matrix (Fig. {5.74, 5.75} and {5.78, 5.79}) for a particular SSS in characteristic time series {1, 2} loading condition, the large(r) stress range cycles typically dominate the total fatigue damage – no matter r_l – since differences between number of cycles for all bins is just 1 order of magnitude $O(10^1)$. Generally speaking, $D_i(\Delta\sigma_{si}, r_{li}) > D_j(\Delta\sigma_{sj}, r_{lj})$ for $(\Delta\sigma_{sj} > \Delta\sigma_{si})$ only if $O(n_i/n_j) \geq O(\{[\Delta\sigma_{sj}/(1-r_{lj})^{1-\gamma}] - [\Delta\sigma_{si}/(1-r_{li})^{1-\gamma}]\}^m)$.

Although the involved VA SSS fatigue resistance data is limited, a CA SSS scatter band fit is obtained (Fig. 5.80; legend Fig. 5.29) and the average VA damage with respect to the CA median ($D \approx 1.0$) suggests a design(!) criterion $D \leq 1.0$ is sufficient for the proposed R99C95 quantile.

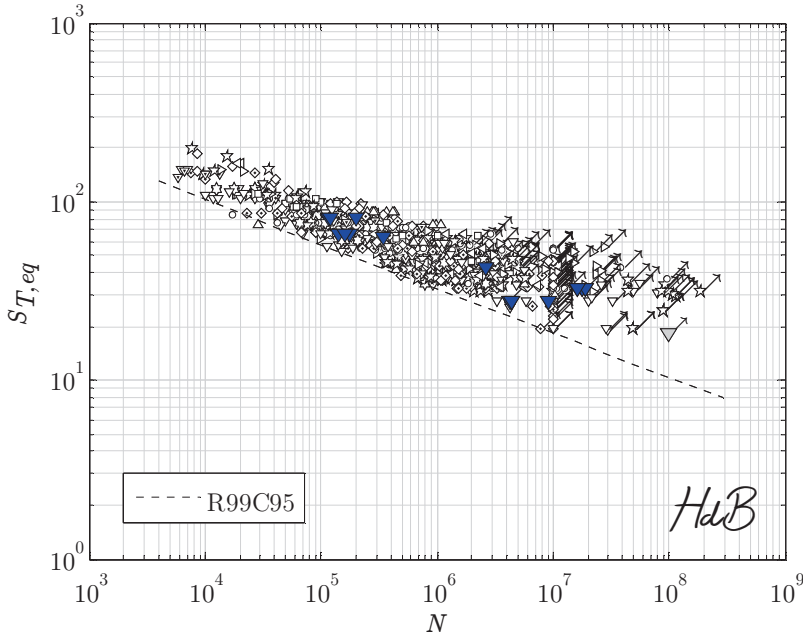


Figure 5.80: VA SSS data fitting the CA SSS fatigue resistance scatterband.

5.7 Full scale structure VA fatigue damage estimate

The FSS response of a Damen Stan Patrol 1204 (Fig. 1.1) has been measured in several trials at the North Sea (Drummen, Schiere and Tuitman, 2013; Schiere and Drummen, 2014). Some SG's on top of the stiffener flange halfway the span in the bottom slamming zone (Fig. 5.81) in between frame 7 and 9 (access issues prevented for instrumentation up to frame 10) have been used to get an idea of the (governing) local plate-stiffener bending response; any global longitudinal hull girder contribution is assumed to be negligible because of the relatively small hull girder length. For a (20 minutes) run at constant speed in head waves of the 2nd trial; $V_s \sim 15$ [knots] and wave height $H_s \sim 1$ [m], the far field structural response and (hourly) fatigue damage estimate of a frame-stiffener connection; a hot spot location (Paragraph 5.5), will be investigated.

To correlate the structural response at the stiffener flange halfway the span σ_{sh} to the frame-stiffener connection far field- or structural stress σ_s and establish the transfer function, the required spatial and temporal hull pressure distribution may be estimated using the measured undisturbed incoming wave and simulation software like FASTship (Delft University of Technology) and applied to a 3D FE model. The still water pressure distribution is an engineering alternative. As a first step, however, the plate-stiffener combinations will be assumed to be in fully space-averaged pressure loading condition and fully clamped in between the frames because of symmetry and structural hierarchy, meaning $\sigma_s = -2\sigma_{sh}$; a conservative assumption. Measured

r_s information is not available, but the stiffener flange thickness is relatively small in comparison to the stiffener height, suggesting $\sigma_s \approx \sigma_m$.

Data has been sampled at $f_s = 1000$ [Hz] to ensure that bottom slamming events are fully captured. Discrete Fourier transformation (DFT) provides amplitude spectra and revealed that signal power is typically in the 0 – 20 [Hz] frequency band (even though an impact- or impulse excitation contains all frequencies), as shown for SG 11 (Fig. 5.82). Because of limited natural damage filtering of noise induced small amplitude high frequency content, filter parameters should be carefully defined.

The 1st dry natural frequency is identified at $f_{d1} \sim 180$ [Hz]; a stiffener tripping mode. The relevant plate-stiffener bending mode is established at $f_{d2} \sim 480$ [Hz], close to the Nyquist-frequency ($f_s/2$). Including a simplified added mass contribution; $m_a = (\pi/2)\rho_w s_s^2 \sim 15$ [kg/m] versus the structural mass $m_s = \sim 5$ [kg/m], reduces the natural frequency to $f_{w2} \sim 240$ [Hz] but is still way beyond 20 [Hz]. Natural mode excitation is not observed in the amplitude spectrum.

The cut-off frequency is set at $f_c = 20$ [Hz]. Still > 98 [%] signal power is maintained and impact induced response amplitudes – period is ~ 0.2 [s] – are hardly affected as shown for a time series interval of SG 11 (Fig. 5.83). Besides, the involved frequencies are well within the considered fatigue testing frequency range; local heating or strain rate contributions as can be expected in resonance tests, $f \sim O(\text{kHz})$, may affect the fatigue damage process and should be taken into account.

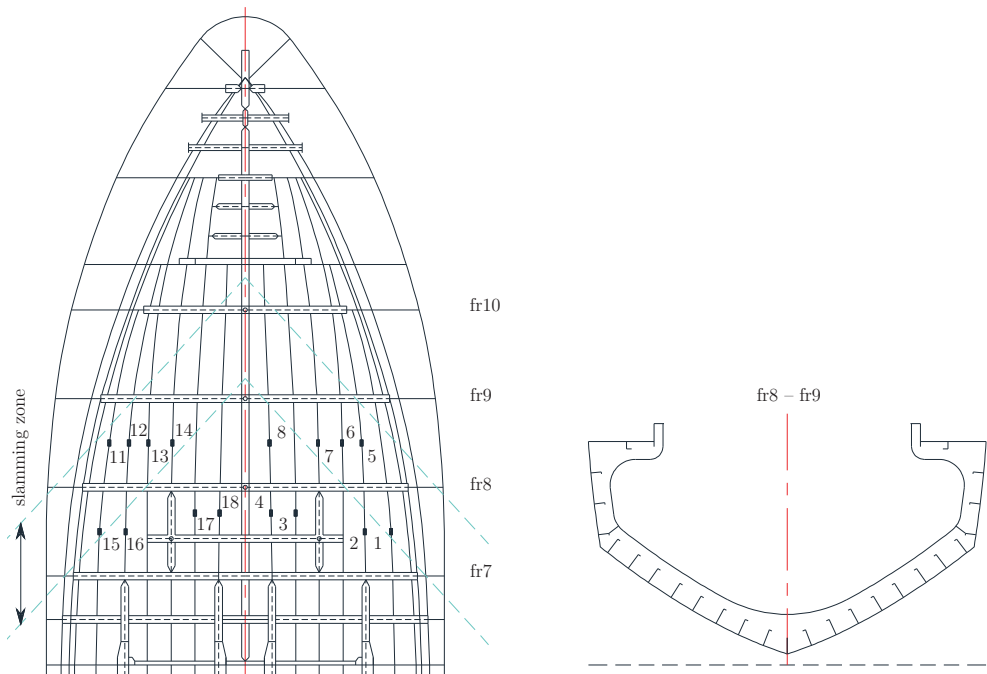
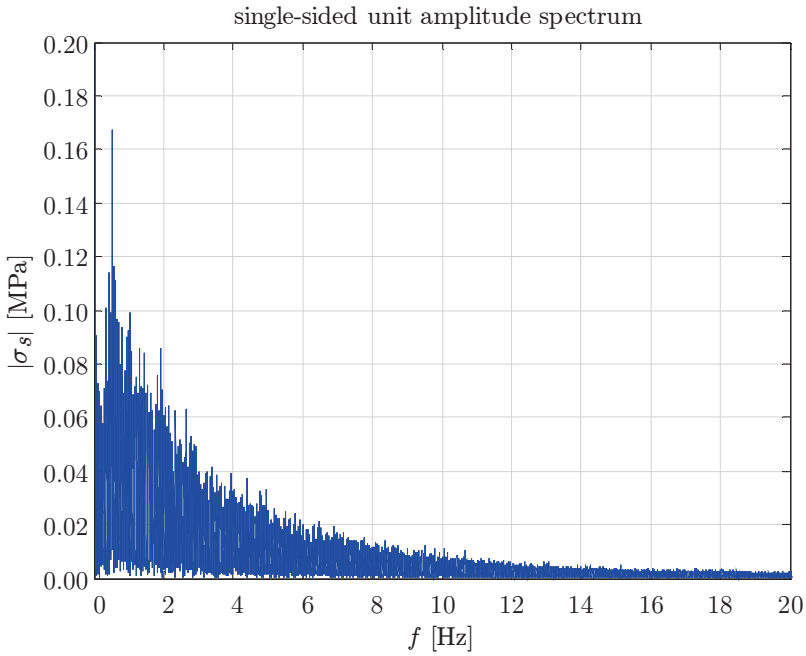
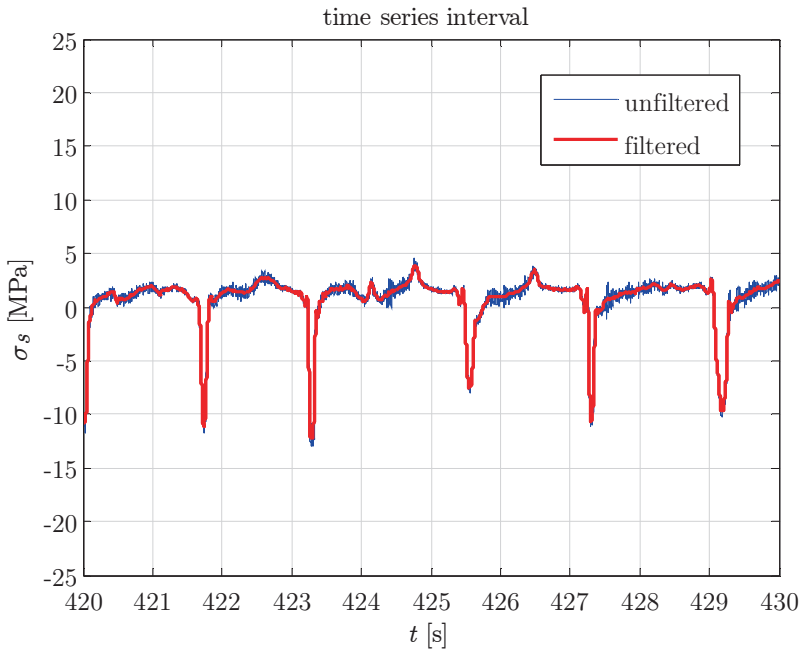
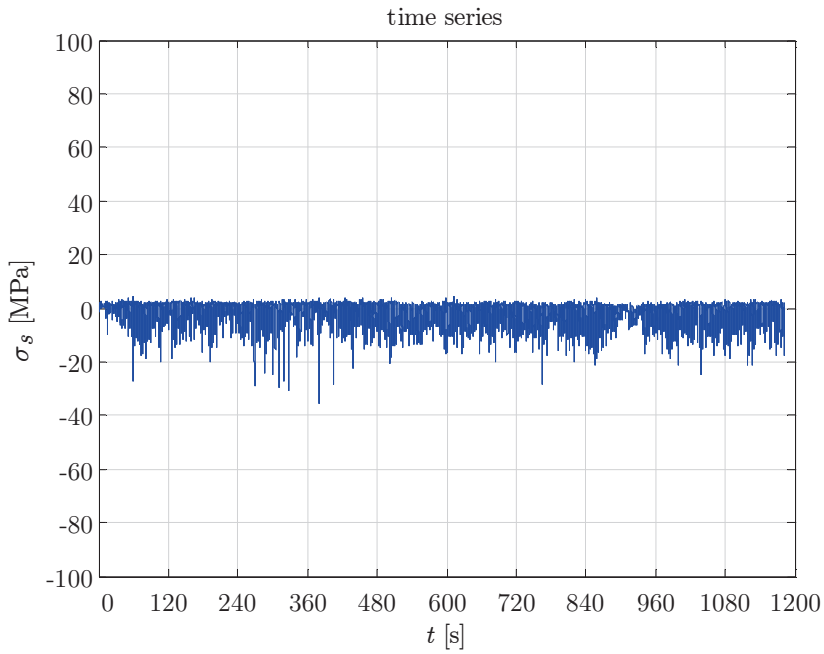
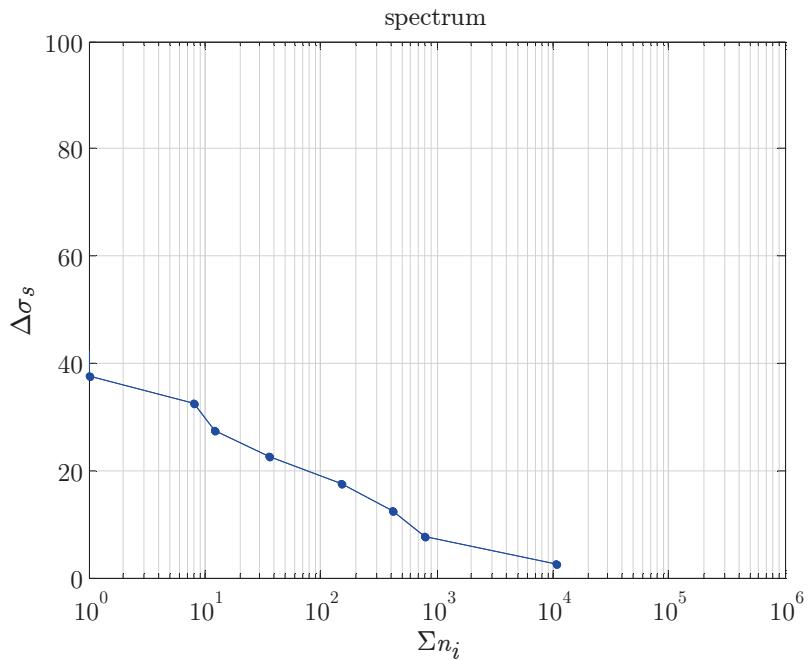


Figure 5.81: Strain gauge locations and numbers.

Figure 5.82: SG 11 unfiltered σ_s DFT amplitude spectrum.Figure 5.83: SG 11 σ_s time series interval.

Figure 5.84: SG 11 filtered σ_s time series.Figure 5.85: SG 11 filtered σ_s spectrum.

Time series observations confirmed impact induced repeated loading ($r_l \sim 0.0$) introducing a (remote mechanical) compressive far field stress $\sigma_s(t)$ at the frame-stiffener connections. Because of the relatively large structural stiffness and high speed, the overall response contains predominantly low amplitude high frequency content as shown for SG 11 (Fig. 5.84 and 5.85). Mean encounter period $T_e \sim 4$ [s]. Note that filtering reduced the number of cycles up to ~ 10 [%] of the measured signal; 1 order of magnitude, practically 0-5 $\Delta\sigma_s$ bin content only.

Rain flow counting typically shows that the vast majority of n is stored in the bin extremes, i.e. the smallest $\Delta\sigma_s$ either fully compressive or highly tensile like shown for SG 11 (Fig. 5.86). Basically, the ($\Delta\sigma_s|r_l = -2.9$) cycles are related to the impact event itself; ($\Delta\sigma_s|r_l = 0.9$) cycles are observed in between impact events. The frame-stiffener rain flow matrix composition is different from the SSS ones (Fig. 5.74 and 5.75), i.e. is quite pronounced and L-shaped.

However, the direct impact induced fatigue damage still dominates as shown for SG 11 (Fig. 5.87) since $O(n_i|\{\Delta\sigma_{s,i}, r_{l,i}\}/n_j|\{\Delta\sigma_{s,j}, r_{l,j}\})$ does not compensate a smaller total stress S_T with a (significantly) larger number of cycles. The structural response $\sigma_s(t)$ at frame 7-8 is smaller – in extremis for SG {3, 4, 17, 18} because of the reduced plate-stiffener span – if compared to $\sigma_s(t)$ in the actual bottom slamming zone at frame 8-9 and pays off in relatively low hourly fatigue damage estimates D_h (Fig. 5.88 and 5.89). Since the considered run is conducted in (near) head waves, (weak) port side – starboard symmetry is identified, although in terms of damage frame 7-8 shows the opposite of frame 8-9: respectively star board and port side is governing.

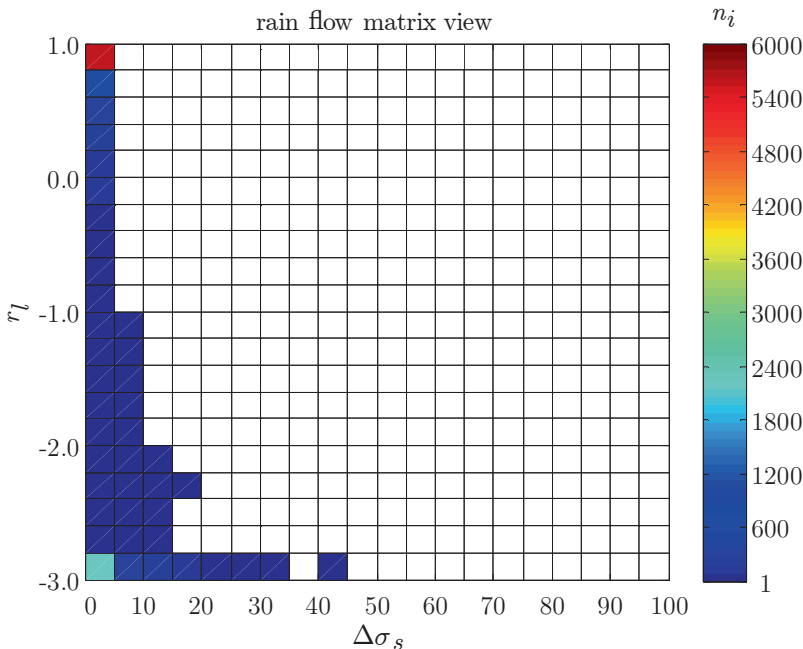


Figure 5.86: Rain flow matrix SG 11, ($\Delta\sigma_s, r_l$) view.

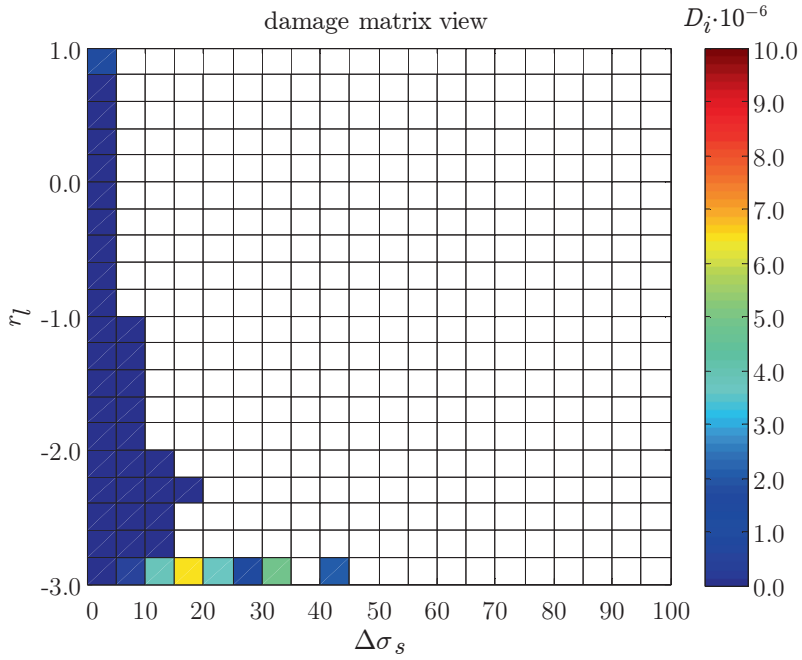


Figure 5.87: Damage matrix SG 11, $(\Delta\sigma_s, r_L)$ view.

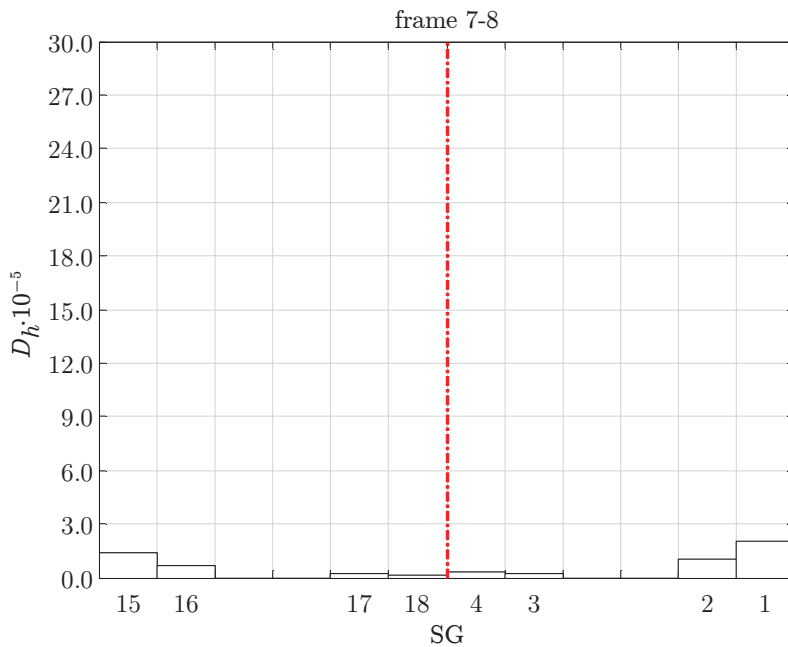


Figure 5.88: Hourly fatigue damage estimate frame-stiffener connections fr. 7-8.

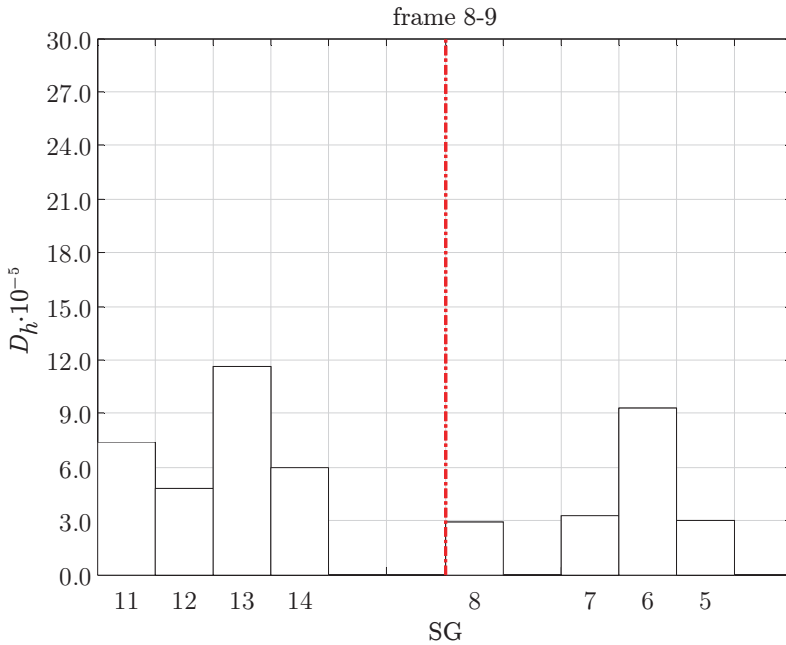


Figure 5.89: Hourly fatigue damage estimate frame-stiffener connections fr. 8-9.

The hourly damage estimate D_h reduced up to 30 [%] relative to the unfiltered signal because of filtered low amplitude high frequency content. Governing damage at frame 7-8 is observed at frame-stiffener connections nearest the slamming zone; SG {15, 1}. Frame 8-9 damage estimates D_h based on SG {6, 13} as well as SG 11 up to some extent are relatively large in comparison to the values obtained for the neighbour plate-stiffener combinations; eventually up to a factor ~ 2 . Looking at the rain flow- and damage matrices, basically 2 compositions have been identified. For SG {6, 11, 13} the actual impact related cycles ($\Delta\sigma_s | r_l = -2.9$) dominate D_h ; the damage related to cycles in between the wave slamming events – typically small(er) amplitude high frequency content – dominate for SG {5, 7, 12, 14}. The SG 12 rain flow- and damage matrix are shown for convenience (Fig. 5.90 and 5.91). The L-shape shows some relaxation, i.e. more amplitude variations are identified. Important observation in that respect: the signal mean stress for SG {6, 11, 13} is slightly smaller if compared to the SG {5, 7, 12, 14} values, respectively close to zero and slightly tensile, meaning larger D_h contributions from a few bins only ($r_l \rightarrow -3$) in contrast to smaller contributions from multiple bins in the $(-3 \leq r_l \leq -1)$ range. Whether a matter of sensor zeroing or physics does not need to be decided yet; simulation results may help in that respect. Average signal sensitivity for $(\Delta\sigma_s, r_l) \rightarrow 0$ is quite obvious anyway.

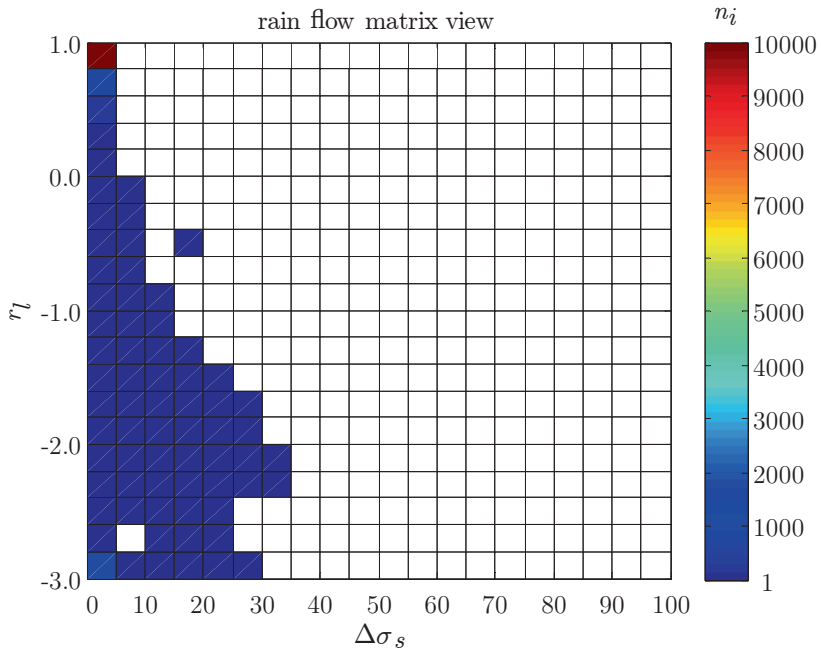


Figure 5.90: Rain flow matrix SG 12, $(\Delta\sigma_s, r_l)$ view.

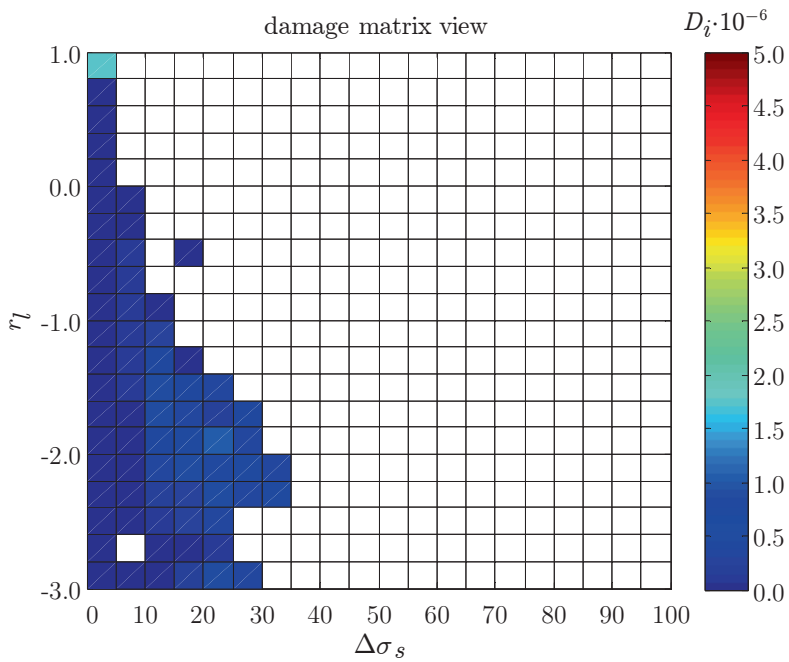


Figure 5.91: Damage matrix SG 12, $(\Delta\sigma_s, r_l)$ view.

To be able to compare measurement and simulation D_h estimates, wave spectral JONSWAP parameters have been established first using the undisturbed incoming wave. Adopting FASTship, a 2.5D strip theory based high speed craft seakeeping code, ~ 200 minutes simulation time (10 times trial run time) is generated in 15 realisations; wave component phase angles are random. The wave relative impact velocity $V_i(t)$, body submergence $z(t)$ as well as wedge dead rise angle β_w are input for the strip wise applied modified Logvinovich impact model (MLM; Korobkin and Malenica, 2005). The strip wise obtained MLM impact force $F_i(t)$ is converted into space averaged pressure distributions, rather than the water entry characteristic one, using the wetted area $A_w(\beta_w, z, t)$ and applied to a 3D FE model to calculate the quasi-static structural response (Bosman, 2008; Drummen, Schiere and Tuitman, 2013). Note the FASTship- and MLM impact force can be different, just like the water pile up affected A_w .

A fair comparison requires the structural stress at the frame-stiffener connection to be estimated using $\sigma_s = -2\sigma_{sh}$. The SG11 simulation time series $\sigma_s(t)$ and $\Delta\sigma_s$ spectrum (Fig. 5.92 and 5.93) show in comparison to the measurement results (Fig. 5.84 and 5.85) typically larger (impact induced) values – the total number of cycles $\sum n_i$ is similar – as confirmed in the rain flow matrix (Fig. 5.94), meaning the damage estimates are larger as well (Fig. 5.95). The L-shaped damage profile is even more pronounced if compared to the measured equivalent (Fig. 5.87). Hardly any ($\Delta\sigma_s/r_l \rightarrow 1$) content is identified and the direct impact induced contributions dominate. Note that quite a substantial part is in the (CA) HCF range; resistance uncertainty is very high.

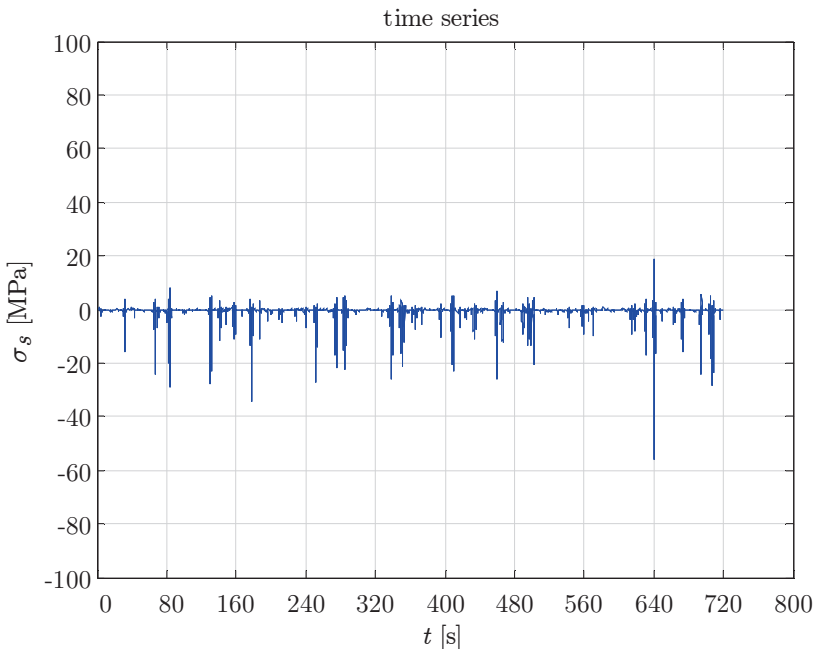


Figure 5.92: σ_s simulation time series based on SG 11 position (realisation 1).

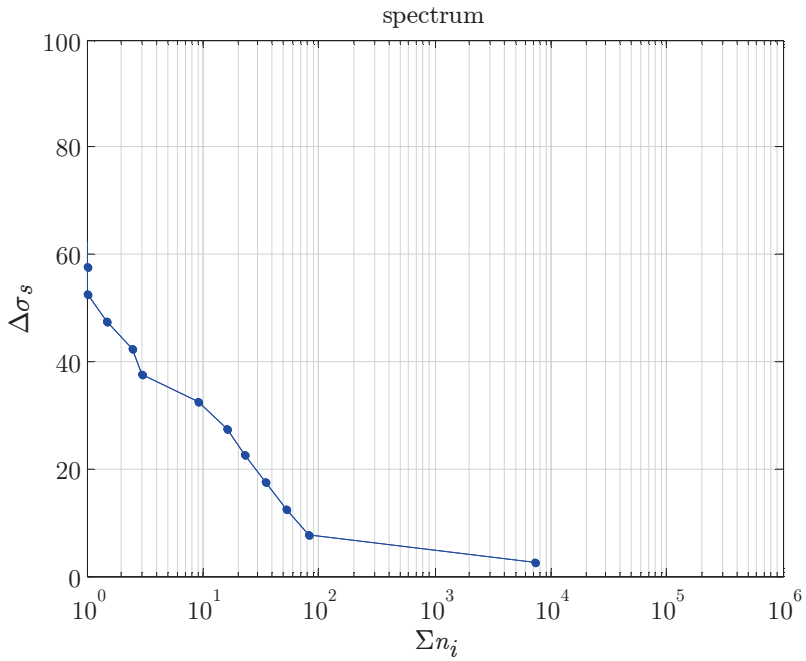


Figure 5.93: σ_s simulation spectrum based on SG 11 position (realisation 1).

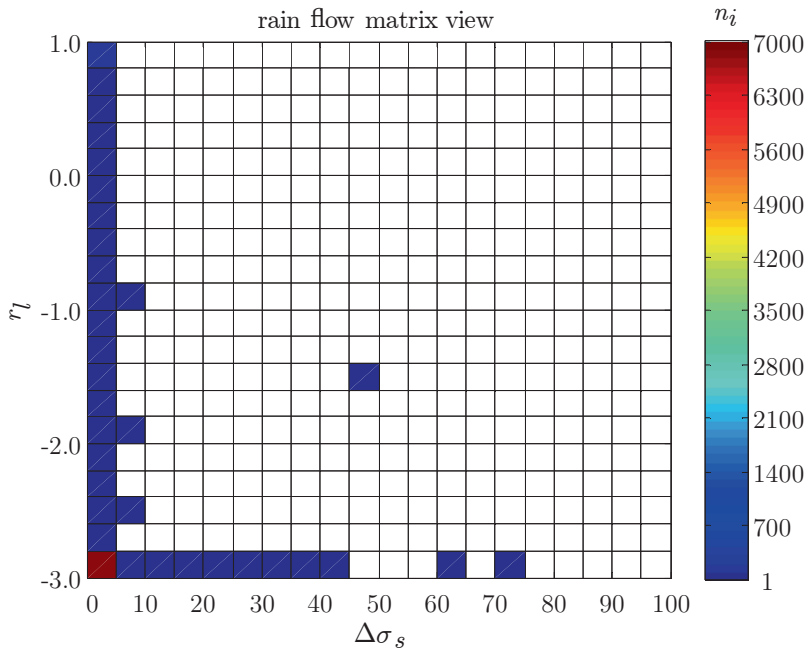


Figure 5.94: Rain flow matrix SG 11 position, $(\Delta\sigma_s, r_l)$ view (sim. realisation 1).

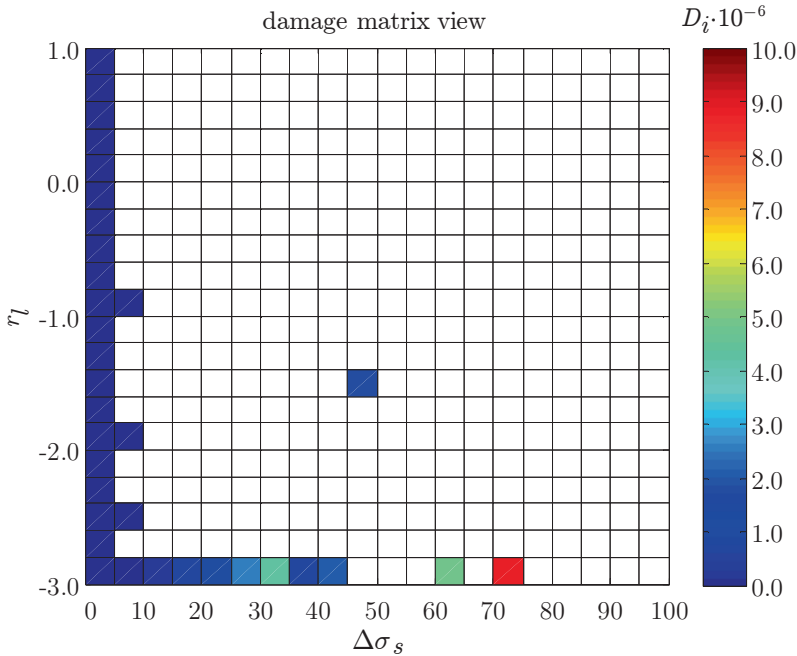


Figure 5.95: Damage matrix SG 11 position, $(\Delta\sigma_s, r_l)$ view (sim. realisation 1).

Looking at the frame 8-9 mean hourly fatigue damage simulation estimates (Fig. 5.96), from the centre line up to SG {12, 5} the (mean) slamming zone explains the observed D_h values. Frame-stiffener connections related to SG {13, 6} in the centre of the slamming zone are confirmed to be fatigue damage governing. Beyond, however, SG 11 throws a spanner in the works. The occasional/extreme impact events introduce a few large amplitude cycles in between a relatively low amplitude high frequency content contributing significantly to D_h , in contrast to continuous wave dominated fatigue damage as typically observed for displacement ships. Simulation typically overestimates D_h about a factor 2, except close to the slamming zone boundaries (regions of relatively low response levels); D_h is comparable to $\sigma_s(t)$ measurement based estimates. The small level of non-symmetry observed in simulation results, e.g. SG {13, 6} is a consequence of mesh irregularities. Since bottom slamming is a non-linear phenomenon, simulation uncertainties are significant.

Differences in damage matrix composition, like observed for measurement based D_h , do not appear in simulations. Still pronounced L-shapes are obtained as shown for SG 12 (Fig. 5.97) although the amplitude level is relatively small. Direct impact induced contributions are still governing like for all other locations. Apparently the time series mean value is important indeed and affects the composition. Because of the small tensile mean, the measured $\sigma_s(t)$ based damage is overestimated.

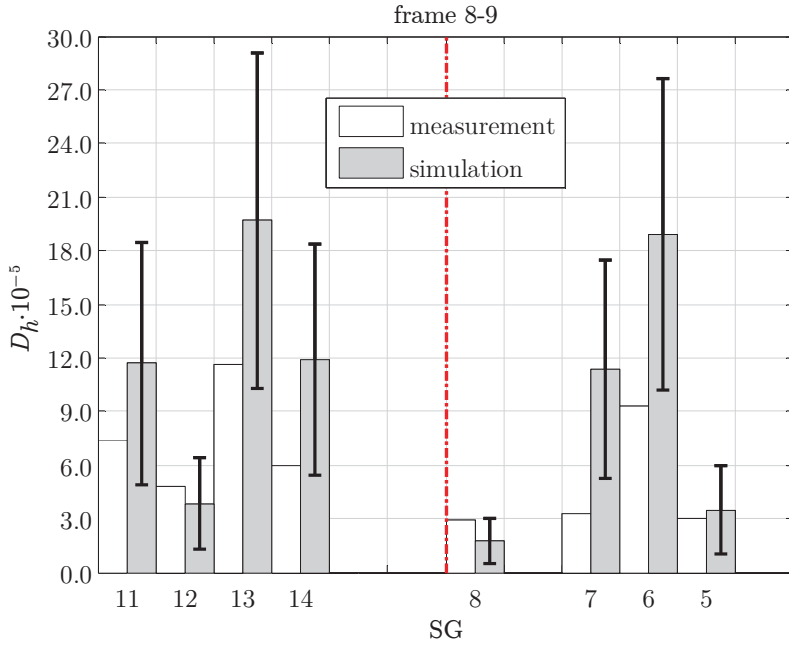


Figure 5.96: Hourly fatigue damage estimates frame-stiffener connections fr. 8-9.

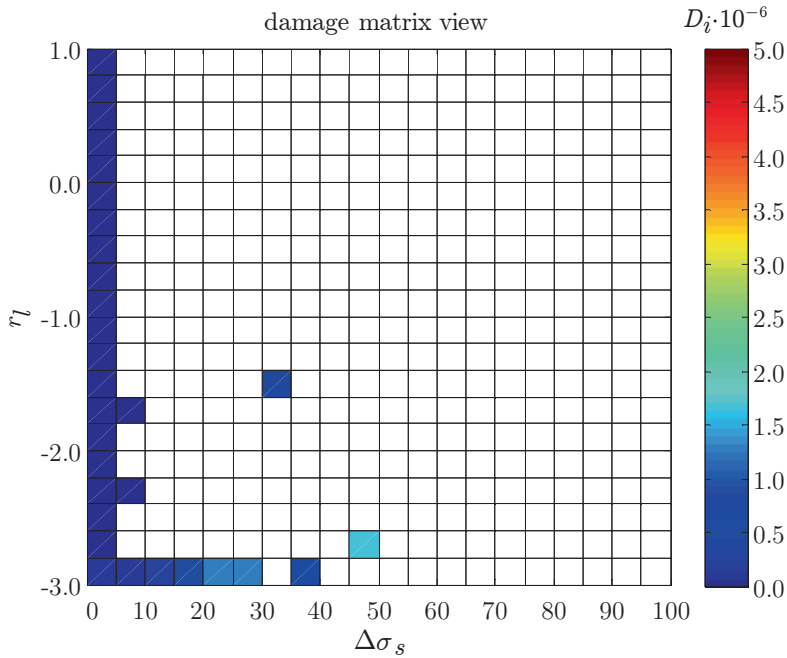


Figure 5.97: Damage matrix SG 12 position, $(\Delta\sigma_s, r_l)$ view (sim. realisation 1).

The wave simulation induced D_h uncertainty is about a factor 2.5 (using $\mu + 3\sigma$), quite close to the MCF fatigue resistance value of 3 (R99Cxx – R50Cxx $\approx 3\sigma$).

Note the same level of hourly fatigue damage estimates is obtained for structural details in deck structures of large steel container ships (hull girder length of a completely different order of magnitude in comparison to high speed craft and the hull shape is a displacement- rather than planing one) including both the continuous wave induced (high amplitude) low frequency- and whipping/springing induced (low amplitude) high frequency content (e.g. Drummen et al., 2008; Tuitman, 2010; Li and Ringsberg, 2011). The rain flow matrix composition, by the way, is comparable to the VA SSS test characteristic time series 2.

5.8 Conclusions

To estimate hull structure longevity, arc-welded joint fatigue life times, in an early design stage, the total stress concept has been developed using the equivalent stress parameter S_T to balance accuracy, effort and model complexity. Including local geometry- and far field stress information a welded joint (family of) S_T - N curve formulation(s) has been established.

Investigating artificial T-joint MCF resistance data, S_T shows the fatigue life time uncertainty can be reduced up to a factor 2; ($T_S \approx 1:1.2$). For a combined a number of series AW joint test results available in literature, reducing the (production) quality level to an average one, the MCF life time uncertainty bandwidth increases up to a factor 6, i.e. ($T_S \approx 1:1.6$). In the hull structure (HCF) design region uncertainty is significant, predominantly because of lacking complete data. SSS (T-T) CA fatigue resistance relation parameters have been established.

Aiming for weld notch stress distribution-, weld notch stress intensity-, weld {notch affected micro, far field dominated macro} crack growth- as well as crack path similarities, the total stress concept proved {SSS, LSS, FSS} welded joint fatigue resistance similarity as well. Full scale structure representative large scale specimen CA- as well as SSS VA data fit the CA small scale data scatter band. In case of (fully) compressive far field stress, a proposed (T-C) correction using a relative load ratio should be adopted.

Hourly fatigue damage estimates D_h , as obtained for some frame-stiffener connections in the slamming zone of an aluminium high-speed craft using the FSS response as measured for several trials at the North Sea, show the wave (loading) statistics induced D_h uncertainty is about a factor 2.5 comparing the measured- and simulation structural response based values; quite close to the MCF fatigue design resistance value of 3 (R99Cxx – R50Cxx).



Weld Notch Stress Equations

V-shaped notch stress components including notch radius

Weld toe formulation:

$$\begin{aligned}
 \sigma_{rr} \left(\frac{r''}{t_p} \right) = & -\sigma_s \left[\mu_s \left\{ \left(\frac{r''}{t_p} \right)^{\lambda_s-1} \lambda_s [(\lambda_s + 1) \cos\{(\lambda_s + 1)\beta\} - \right. \right. & (A.1) \\
 & \chi_s(\lambda_s - 3) \cos\{(\lambda_s - 1)\beta\}] + \\
 & \left. \left(\frac{r''}{t_p} \right)^{\zeta_s-1} \left(\frac{r_0}{t_p} \right)^{\lambda_s-\zeta_s} \lambda_s \frac{\left(\frac{2\alpha}{\pi} \right)}{4 \left\{ \left(\frac{2\alpha}{\pi} \right) - 1 \right\}} \cdot \right. \\
 & \left. [\omega_{s1} \cos\{(\zeta_s + 1)\beta\} + \right. \\
 & \left. \omega_{s2}(\zeta_s - 3) \cos\{(\zeta_s - 1)\beta\}] \right\} + \\
 \mu_a \left\{ \left(\frac{r''}{t_p} \right)^{\lambda_a-1} \lambda_a [(\lambda_a + 1) \sin\{(\lambda_a + 1)\beta\} - \right. & \\
 & \chi_a(\lambda_a - 3) \sin\{(\lambda_a - 1)\beta\}] + \\
 & \left. \left(\frac{r''}{t_p} \right)^{\zeta_a-1} \left(\frac{r_0}{t_p} \right)^{\lambda_a-\zeta_a} \lambda_a \frac{1}{4(\zeta_a - 1)} \cdot \right. \\
 & \left. [\omega_{a1} \sin\{(\zeta_a + 1)\beta\} + \right. \\
 & \left. \omega_{a2}(\zeta_a - 3) \sin\{(\zeta_a - 1)\beta\}] \right\} \left. \right]
 \end{aligned}$$

$$\begin{aligned}
\sigma_{\theta\theta} \left(\frac{r''}{t_p} \right) = \sigma_s \left[\mu_s \left\{ \left(\frac{r''}{t_p} \right)^{\lambda_s - 1} \lambda_s (\lambda_s + 1) [\cos\{(\lambda_s + 1)\beta\} - \right. \right. & \quad (A.2) \\
& \quad \left. \left. \chi_s \cos\{(\lambda_s - 1)\beta\} \right] + \right. \\
& \quad \left. \left(\frac{r''}{t_p} \right)^{\zeta_s - 1} \left(\frac{r_0}{t_p} \right)^{\lambda_s - \zeta_s} \lambda_s \frac{\left(\frac{2\alpha}{\pi} \right)}{4 \left\{ \left(\frac{2\alpha}{\pi} \right) - 1 \right\}} \cdot \right. \\
& \quad \left. [\omega_{s1} \cos\{(\zeta_s + 1)\beta\} + \right. \\
& \quad \left. \omega_{s2} (\zeta_s + 1) \cos\{(\zeta_s - 1)\beta\} \right] \left. \right\} + \\
\mu_a \left\{ \left(\frac{r''}{t_p} \right)^{\lambda_a - 1} \lambda_a (\lambda_a + 1) [\sin\{(\lambda_a + 1)\beta\} - \right. & \\
& \quad \left. \chi_a \sin\{(\lambda_a - 1)\beta\} \right] + \\
& \quad \left(\frac{r''}{t_p} \right)^{\zeta_a - 1} \left(\frac{r_0}{t_p} \right)^{\lambda_a - \zeta_a} \lambda_a \frac{1}{4(\zeta_a - 1)} \cdot \\
& \quad [\omega_{a1} \sin\{(\zeta_a + 1)\beta\} + \\
& \quad \left. \omega_{a2} (\zeta_a + 1) \sin\{(\zeta_a - 1)\beta\} \right] \left. \right\} \left. \right]
\end{aligned}$$

$$\begin{aligned}
 \sigma_{r\theta} \left(\frac{r''}{t_p} \right) = \sigma_s \left[\mu_s \left\{ \left(\frac{r''}{t_p} \right)^{\lambda_s-1} \lambda_s [(\lambda_s + 1)\sin\{(\lambda_s + 1)\beta\} - \right. \right. & \quad (A.3) \\
 \chi_s (\lambda_s - 1)\sin\{(\lambda_s - 1)\beta\}] + & \\
 \left. \left(\frac{r''}{t_p} \right)^{\zeta_s-1} \left(\frac{r_0}{t_p} \right)^{\lambda_s-\zeta_s} \lambda_s \frac{\left(\frac{2\alpha}{\pi} \right)}{4 \left\{ \left(\frac{2\alpha}{\pi} \right) - 1 \right\}} \cdot \right. & \\
 \left. [\omega_{s1} \sin\{(\zeta_s + 1)\beta\} + \right. & \\
 \left. \omega_{s2}(\zeta_s - 1) \sin\{(\zeta_s - 1)\beta\}] \right\} - & \\
 \mu_a \left\{ \left(\frac{r''}{t_p} \right)^{\lambda_a-1} \lambda_a [(\lambda_a + 1)\cos\{(\lambda_a + 1)\beta\} - \right. & \\
 \chi_a (\lambda_a - 1)\cos\{(\lambda_a - 1)\beta\}] + & \\
 \left. \left(\frac{r''}{t_p} \right)^{\zeta_a-1} \left(\frac{r_0}{t_p} \right)^{\lambda_a-\zeta_a} \lambda_a \frac{1}{4(\zeta_a - 1)} \cdot \right. & \\
 \left. [\omega_{a1} \cos\{(\zeta_a + 1)\beta\} + \right. & \\
 \left. \omega_{a2}(\zeta_a - 1) \cos\{(\zeta_a - 1)\beta\}] \right\} &
 \end{aligned}$$

The (first) eigenvalues $\{\zeta_s, \zeta_a\}$ can be implicitly solved for using:

$$\begin{aligned}
 \omega_{s1} \cos\{(\zeta_s + 1)\alpha\} + \omega_{s2} (\zeta_s + 1)\cos\{(\zeta_s - 1)\alpha\} = 0 & \\
 \omega_{a1} \cos\{(\zeta_a + 1)\alpha\} + \omega_{a2} (\zeta_a - 1)\cos\{(\zeta_a - 1)\alpha\} = 0 & \quad (A.4)
 \end{aligned}$$

with

$$\begin{aligned}
 \omega_{s1} = & \quad \{\chi_s(\lambda_s - 3) - (\lambda_s + 1)\} \left\{ (\zeta_s - 1)^2 - \frac{(\zeta_s + 1)}{\left(\frac{2\alpha}{\pi} \right)} \right\} + (\zeta_s - 3)\varepsilon_s \\
 \omega_{s2} = & \quad \{\chi_s(\lambda_s - 3) - (\lambda_s + 1)\} \left\{ \frac{1 - \left(\frac{2\alpha}{\pi} \right) (\zeta_s + 1)}{\left(\frac{2\alpha}{\pi} \right)} \right\} - \varepsilon_s \\
 \omega_{a1} = & \quad \{\chi_a(\lambda_a - 1) - (\lambda_a + 1)\}(\zeta_a - 1) \left\{ 2 - \frac{\left(\frac{2\alpha}{\pi} \right) (\zeta_a - 3)}{\left(\frac{2\alpha}{\pi} \right)} \right\} - (\zeta_a - 1)\varepsilon_a \\
 \omega_{a2} = & \quad \{\chi_a(\lambda_a - 1) - (\lambda_a + 1)\} \left\{ \frac{\left(\frac{2\alpha}{\pi} \right) (\zeta_a + 1) - 2}{\left(\frac{2\alpha}{\pi} \right)} \right\} + \varepsilon_a
 \end{aligned}$$

and

$$\begin{aligned}\varepsilon_s &= (\lambda_s + 1)^2 - \chi_s(\lambda_s - 1)^2 + \frac{1}{\left(\frac{2\alpha}{\pi}\right)}(\chi_s - 1)(\lambda_s + 1) \\ \varepsilon_a &= (\lambda_a + 1)^2 - \chi_a(\lambda_a - 3)(\lambda_a - 1) + \frac{2}{\left(\frac{2\alpha}{\pi}\right)}\{\chi_a(\lambda_a - 1) - (\lambda_a + 1)\}\end{aligned}$$

The system of equations to be solved for a non-symmetry case:

$$\begin{bmatrix} C_{11} & C_{12} \\ C_{21} & C_{22} \end{bmatrix} \begin{Bmatrix} \mu_s \\ \mu_a \end{Bmatrix} = \begin{Bmatrix} F_1 \\ F_2 \end{Bmatrix} \quad (\text{A.5})$$

with

$$\begin{aligned}C_{11} &= \lambda_s(\lambda_s + 1)[\cos\{(\lambda_s + 1)\beta\} - \chi_s \cos\{(\lambda_s - 1)\beta\}]F_{\lambda_s}^f + \\ &\quad \left(\frac{r_0}{t_p}\right)^{\lambda_s - \zeta_s} \lambda_s \frac{\left(\frac{2\alpha}{\pi}\right)}{4\left\{\left(\frac{2\alpha}{\pi}\right) - 1\right\}} \cdot \\ &\quad [\omega_{s1} \cos\{(\zeta_s + 1)\beta\} + \omega_{s2}(\zeta_s + 1) \cos\{(\zeta_s - 1)\beta\}]F_{\zeta_s}^f\end{aligned}$$

$$\begin{aligned}C_{12} &= \lambda_a(\lambda_a + 1)[\sin\{(\lambda_a + 1)\beta\} - \chi_a \sin\{(\lambda_a - 1)\beta\}]F_{\lambda_a}^f + \\ &\quad \left(\frac{r_0}{t_p}\right)^{\lambda_a - \zeta_a} \lambda_a \frac{1}{4(\zeta_a - 1)} \cdot \\ &\quad [\omega_{a1} \sin\{(\zeta_a + 1)\beta\} + \omega_{a2}(\zeta_a + 1) \sin\{(\zeta_a - 1)\beta\}]F_{\zeta_a}^f\end{aligned}$$

$$\begin{aligned}C_{21} &= \lambda_s(\lambda_s + 1)[\cos\{(\lambda_s + 1)\beta\} - \chi_s \cos\{(\lambda_s - 1)\beta\}]M_{\lambda_s}^f + \\ &\quad \left(\frac{r_0}{t_p}\right)^{\lambda_s - \zeta_s} \lambda_s \frac{\left(\frac{2\alpha}{\pi}\right)}{4\left\{\left(\frac{2\alpha}{\pi}\right) - 1\right\}} \cdot \\ &\quad [\omega_{s1} \cos\{(\zeta_s + 1)\beta\} + \omega_{s2}(\zeta_s + 1) \cos\{(\zeta_s - 1)\beta\}]M_{\zeta_s}^f\end{aligned}$$

$$\begin{aligned}C_{22} &= \lambda_a(\lambda_a + 1)[\sin\{(\lambda_a + 1)\beta\} - \chi_a \sin\{(\lambda_a - 1)\beta\}]M_{\lambda_a}^f + \\ &\quad \left(\frac{r_0}{t_p}\right)^{\lambda_a - \zeta_a} \lambda_a \frac{1}{4(\zeta_a - 1)} \cdot \\ &\quad [\omega_{a1} \sin\{(\zeta_a + 1)\beta\} + \omega_{a2}(\zeta_a + 1) \sin\{(\zeta_a - 1)\beta\}]M_{\zeta_a}^f\end{aligned}$$

$$F_1 = 1$$

$$F_2 = \frac{1}{2} - \frac{C_{bw}}{6}$$

and

$$F_x^f = \int_0^1 \left\{ \left(\frac{r}{t_p} \right)^2 + 2\cos(\beta) \left(\frac{r_0}{t_p} \right) \left(\frac{r}{t_p} \right) + \left(\frac{r_0}{t_p} \right)^2 \right\}^{\frac{x-1}{2}} d \left(\frac{r}{t_p} \right)$$

$$M_x^f = \int_0^1 \left(\frac{r}{t_p} \right) \left\{ \left(\frac{r}{t_p} \right)^2 + 2\cos(\beta) \left(\frac{r_0}{t_p} \right) \left(\frac{r}{t_p} \right) + \left(\frac{r_0}{t_p} \right)^2 \right\}^{\frac{x-1}{2}} d \left(\frac{r}{t_p} \right)$$

The system of equations to be solved for a symmetry case:

$$\begin{bmatrix} C_{11} & C_{12} \\ C_{21} & C_{22} \\ C_{31} & C_{32} \end{bmatrix} \begin{Bmatrix} \mu_s \\ \mu_a \end{Bmatrix} = \begin{Bmatrix} F_1 \\ F_2 \\ F_3 \end{Bmatrix} \tag{A.6}$$

with

$$C_{11} = \lambda_s(\lambda_s + 1)[\cos\{(\lambda_s + 1)\beta\} - \chi_s \cos\{(\lambda_s - 1)\beta\}]F_{\lambda_s}^f +$$

$$\left(\frac{r_0}{t_p} \right)^{\lambda_s - \zeta_s} \lambda_s \frac{\left(\frac{2\alpha}{\pi} \right)}{4 \left\{ \left(\frac{2\alpha}{\pi} \right) - 1 \right\}}$$

$$[\omega_{s1} \cos\{(\zeta_s + 1)\beta\} + \omega_{s2}(\zeta_s + 1) \cos\{(\zeta_s - 1)\beta\}]F_{\zeta_s}^f$$

$$C_{12} = \lambda_a(\lambda_a + 1)[\sin\{(\lambda_a + 1)\beta\} - \chi_a \sin\{(\lambda_a - 1)\beta\}]F_{\lambda_a}^f +$$

$$\left(\frac{r_0}{t_p} \right)^{\lambda_a - \zeta_a} \lambda_a \frac{1}{4(\zeta_a - 1)}$$

$$[\omega_{a1} \sin\{(\zeta_a + 1)\beta\} + \omega_{a2}(\zeta_a + 1) \sin\{(\zeta_a - 1)\beta\}]F_{\zeta_a}^f$$

$$C_{21} = \lambda_s(\lambda_s + 1)[\cos\{(\lambda_s + 1)\beta\} - \chi_s \cos\{(\lambda_s - 1)\beta\}]M_{\lambda_s}^f +$$

$$\left(\frac{r_0}{t_p} \right)^{\lambda_s - \zeta_s} \lambda_s \frac{\left(\frac{2\alpha}{\pi} \right)}{4 \left\{ \left(\frac{2\alpha}{\pi} \right) - 1 \right\}}$$

$$[\omega_{s1} \cos\{(\zeta_s + 1)\beta\} + \omega_{s2}(\zeta_s + 1) \cos\{(\zeta_s - 1)\beta\}]M_{\zeta_s}^f$$

$$C_{22} = \lambda_a(\lambda_a + 1)[\sin\{(\lambda_a + 1)\beta\} - \chi_a \sin\{(\lambda_a - 1)\beta\}]M_{\lambda_a}^f + \left(\frac{r_0}{t_p}\right)^{\lambda_a - \zeta_a} \lambda_a \frac{1}{4(\zeta_a - 1)} \cdot [\omega_{a1} \sin\{(\zeta_a + 1)\beta\} + \omega_{a2}(\zeta_a + 1) \sin\{(\zeta_a - 1)\beta\}]M_{\zeta_a}^f$$

$$C_{31} = \lambda_s(\lambda_s + 1)[\cos\{(\lambda_s + 1)\beta\} - \chi_s \cos\{(\lambda_s - 1)\beta\}]D_{\lambda_s} + \left(\frac{r_0}{t_p}\right)^{\lambda_s - \zeta_s} \lambda_s \frac{\left(\frac{2\alpha}{\pi}\right)}{4\left\{\left(\frac{2\alpha}{\pi}\right) - 1\right\}} \cdot [\omega_{s1} \cos\{(\zeta_s + 1)\beta\} + \omega_{s2}(\zeta_s + 1) \cos\{(\zeta_s - 1)\beta\}]D_{\zeta_s}$$

$$C_{32} = \lambda_a(\lambda_a + 1)[\sin\{(\lambda_a + 1)\beta\} - \chi_a \sin\{(\lambda_a - 1)\beta\}]D_{\lambda_a} + \left(\frac{r_0}{t_p}\right)^{\lambda_a - \zeta_a} \lambda_a \frac{1}{4(\zeta_a - 1)} \cdot [\omega_{a1} \sin\{(\zeta_a + 1)\beta\} + \omega_{a2}(\zeta_a + 1) \sin\{(\zeta_a - 1)\beta\}]D_{\zeta_a}$$

$$F_1 = \frac{1}{2}$$

$$F_2 = \frac{1}{8} - \frac{C_{bw}}{24}$$

$$F_3 = -4C_{bw}$$

and

$$F_x^f = \int_0^{\frac{1}{2}} \left\{ \left(\frac{r}{t_p}\right)^2 + 2\cos(\beta) \left(\frac{r_0}{t_p}\right) \left(\frac{r}{t_p}\right) + \left(\frac{r_0}{t_p}\right)^2 \right\}^{\frac{x-1}{2}} d\left(\frac{r}{t_p}\right)$$

$$M_x^f = \int_0^{\frac{1}{2}} \left(\frac{r}{t_p}\right) \left\{ \left(\frac{r}{t_p}\right)^2 + 2\cos(\beta) \left(\frac{r_0}{t_p}\right) \left(\frac{r}{t_p}\right) + \left(\frac{r_0}{t_p}\right)^2 \right\}^{\frac{x-1}{2}} d\left(\frac{r}{t_p}\right)$$

$$D_x = \left(\frac{x-1}{2}\right) \left\{ \left(\frac{1}{2}\right)^2 + 2\cos(\beta) \left(\frac{r_0}{t_p}\right) \left(\frac{1}{2}\right) + \left(\frac{r_0}{t_p}\right)^2 \right\}^{\frac{x-3}{2}} \cdot \left\{ 1 + 2\cos(\beta) \left(\frac{r_0}{t_b}\right) \right\}$$

Note that a least squares solution is obtained.

Weld root formulation:

$$\begin{aligned}
 \sigma_{rr} \left(\frac{r''}{t_p'} \right) = -\sigma_{sr} \left[\sum_{i=1}^n \mu_{1i} \left\{ \left(\frac{r''}{t_p'} \right)^{\lambda_i-1} \lambda_i [(\lambda_i + 1) \cos\{(\lambda_i + 1)\beta\} - \right. \right. & \quad (A.7) \\
 \chi_i(\lambda_i - 3) \cos\{(\lambda_i - 1)\beta\}] + & \\
 \left. \left(\frac{r''}{t_p'} \right)^{\zeta_i-1} \left(\frac{r_0}{t_p'} \right)^{\lambda_i-\zeta_i} \frac{\lambda_i}{2} \cdot \right. & \\
 \left. [\omega_{1i} \cos\{(\zeta_i + 1)\beta\} + \right. & \\
 \left. \omega_{2i}(\zeta_i - 3) \cos\{(\zeta_i - 1)\beta\}] \right\} + & \\
 \mu_{3i} \left\{ \left(\frac{r''}{t_p'} \right)^{\lambda_i-1} \lambda_i [(\lambda_i + 1) \sin\{(\lambda_i + 1)\beta\} - \right. & \\
 \chi_i(\lambda_i - 3) \sin\{(\lambda_i - 1)\beta\}] + & \\
 \left. \left(\frac{r''}{t_p'} \right)^{\zeta_i-1} \left(\frac{r_0}{t_p'} \right)^{\lambda_i-\zeta_i} \lambda_i \frac{1}{4(\zeta_i - 1)} \cdot \right. & \\
 \left. [\omega_{1i} \sin\{(\zeta_i + 1)\beta\} + \right. & \\
 \left. \omega_{2i}(\zeta_i - 3) \sin\{(\zeta_i - 1)\beta\}] \right\} \Big] &
 \end{aligned}$$

$$\begin{aligned}
\sigma_{\theta\theta} \left(\frac{r''}{t_p'} \right) = \sigma_{sr} \sum_{i=1}^n \left[\mu_{1i} \left\{ \left(\frac{r''}{t_p'} \right)^{\lambda_i-1} \lambda_i (\lambda_i + 1) [\cos\{(\lambda_i + 1)\beta\} - \right. \right. & \quad (A.8) \\
& \chi_i \cos\{(\lambda_i - 1)\beta\}] + \\
& \left. \left(\frac{r''}{t_p'} \right)^{\zeta_i-1} \left(\frac{r_0}{t_p'} \right)^{\lambda_i-\zeta_i} \frac{\lambda_i}{2} \cdot \right. \\
& \left. [\omega_{1i} \cos\{(\zeta_i + 1)\beta\} + \right. \\
& \left. \omega_{2i}(\zeta_i + 1) \cos\{(\zeta_i - 1)\beta\}] \right\} + \\
\mu_{3i} \left\{ \left(\frac{r''}{t_p'} \right)^{\lambda_i-1} \lambda_i (\lambda_i + 1) [\sin\{(\lambda_i + 1)\beta\} - \right. & \\
& \chi_i \sin\{(\lambda_i - 1)\beta\}] + \\
& \left. \left(\frac{r''}{t_p'} \right)^{\zeta_i-1} \left(\frac{r_0}{t_p'} \right)^{\lambda_i-\zeta_i} \lambda_i \frac{1}{4(\zeta_i - 1)} \cdot \right. \\
& \left. [\omega_{1i} \sin\{(\zeta_i + 1)\beta\} + \right. \\
& \left. \omega_{2i}(\zeta_i + 1) \sin\{(\zeta_i - 1)\beta\}] \right\} \left. \right]
\end{aligned}$$

$$\begin{aligned}
 \sigma_{r\theta} \left(\frac{r''}{t_p} \right) = \sigma_{sr} \sum_{i=1}^n \left[\mu_{1i} \left\{ \left(\frac{r''}{t_p} \right)^{\lambda_i-1} \lambda_i [(\lambda_i + 1) \sin\{(\lambda_i + 1)\beta\} - \right. \right. & \quad (A.9) \\
 \chi_i (\lambda_i - 1) \sin\{(\lambda_i - 1)\beta\}] + & \\
 \left(\frac{r''}{t_p} \right)^{\zeta_i-1} \left(\frac{r_0}{t_p} \right)^{\lambda_i-\zeta_i} \frac{\lambda_i}{2} \cdot & \\
 [\omega_{1i} \sin\{(\zeta_i + 1)\beta\} + & \\
 \omega_{2i} (\zeta_i - 1) \sin\{(\zeta_i - 1)\beta\}] \left. \right\} - & \\
 \mu_{3i} \left\{ \left(\frac{r''}{t_p} \right)^{\lambda_i-1} \lambda_i [(\lambda_i + 1) \cos\{(\lambda_i + 1)\beta\} - \right. & \\
 \chi_i (\lambda_i - 1) \cos\{(\lambda_i - 1)\beta\}] + & \\
 \left(\frac{r''}{t_p} \right)^{\zeta_i-1} \left(\frac{r_0}{t_p} \right)^{\lambda_i-\zeta_i} \lambda_i \frac{1}{4(\zeta_i - 1)} \cdot & \\
 [\omega_{1i} \cos\{(\zeta_i + 1)\beta\} + & \\
 \omega_{2i} (\zeta_i - 1) \cos\{(\zeta_i - 1)\beta\}] \left. \right\} &
 \end{aligned}$$

Along the bisector, $\beta = 0$ meaning $\sigma_{r\theta} = 0$. Eigenvalues ζ_i and corresponding coefficients $\{\omega_{1i}, \omega_{2i}, \varepsilon_1\}$ can be obtained using:

$$\zeta_i = \frac{\chi_i \{(\lambda_i - 1)^2 - 2\} - (\lambda_i + 1)^2}{\chi_i (\lambda_i - 3) - (\lambda_i + 1)} - 1 \quad (A.10)$$

with

$$\begin{aligned}
 \omega_{1i} &= \{\chi_i (\lambda_i - 3) - (\lambda_i + 1)\} \left\{ (\zeta_i - 1)^2 - \frac{(\zeta_i + 1)}{2} \right\} + (\zeta_i - 3) \varepsilon_i \\
 \omega_{2i} &= \{\chi_i (\lambda_i - 3) - (\lambda_i + 1)\} \left\{ \frac{1 - 2(\zeta_i + 1)}{2} \right\} - \varepsilon_i
 \end{aligned}$$

and

$$\varepsilon_i = (\lambda_i + 1)^2 - \chi_i (\lambda_i - 1)^2 + \frac{(\chi_i - 1)(\lambda_i + 1)}{2}$$

The system of equations to be solved for ($\beta = 0$):

$$\begin{bmatrix} C_{11} & \cdots & C_{15} \\ \vdots & \ddots & \vdots \\ C_{51} & \cdots & C_{55} \end{bmatrix} \begin{Bmatrix} \mu_1 \\ \vdots \\ \mu_5 \end{Bmatrix} = \begin{Bmatrix} F_1 \\ \vdots \\ F_5 \end{Bmatrix} \quad (\text{A.11})$$

with:

$$C_{1i} = \lambda_i(\lambda_i + 1)(1 - \chi_i)F_{\lambda_i}^f + \left(\frac{r_0}{t_p'}\right)^{\lambda_i - \zeta_i} (\lambda_i/2)\{\omega_{1i} + \omega_{2i}(\zeta_i + 1)\}F_{\zeta_i}^f$$

$$C_{2i} = \lambda_i(\lambda_i + 1)(1 - \chi_i)M_{\lambda_i}^f + \left(\frac{r_0}{t_p'}\right)^{\lambda_i - \zeta_i} (\lambda_i/2)\{\omega_{1i} + \omega_{2i}(\zeta_i + 1)\}M_{\zeta_i}^f$$

$$C_{3i} = \lambda_i(\lambda_i + 1)(1 - \chi_i)R_{\lambda_i}^1 + \left(\frac{r_0}{t_p'}\right)^{\lambda_i - \zeta_i} (\lambda_i/2)\{\omega_{1i} + \omega_{2i}(\zeta_i + 1)\}R_{\zeta_i}^1$$

$$C_{4i} = \lambda_i(\lambda_i + 1)(1 - \chi_i)R_{\lambda_i}^2 + \left(\frac{r_0}{t_p'}\right)^{\lambda_i - \zeta_i} (\lambda_i/2)\{\omega_{1i} + \omega_{2i}(\zeta_i + 1)\}R_{\zeta_i}^2$$

$$C_{5i} = \lambda_i(\lambda_i + 1)(1 - \chi_i)R_{\lambda_i}^3 + \left(\frac{r_0}{t_p'}\right)^{\lambda_i - \zeta_i} (\lambda_i/2)\{\omega_{1i} + \omega_{2i}(\zeta_i + 1)\}R_{\zeta_i}^3$$

$$F_1 = 1 - r_{sr}$$

$$F_2 = \frac{1 - r_{sr}}{2} - \frac{r_{sr}}{6}$$

$$F_3 = \frac{\sigma_{nr1}}{\sigma_{sr}}$$

$$F_4 = \frac{\sigma_{nr2}}{\sigma_{sr}}$$

$$F_5 = \frac{\sigma_{nr3}}{\sigma_{sr}}$$

and

$$F_x^f = \int_0^1 \left\{ \left(\frac{r''}{t_p'}\right)^2 + 2\left(\frac{r_0}{t_p'}\right)\left(\frac{r''}{t_p'}\right) + \left(\frac{r_0}{t_p'}\right)^2 \right\}^{\frac{x-1}{2}} d\left(\frac{r''}{t_p'}\right)$$

$$M_x^f = \int_0^1 \left(\frac{r}{t_p'}\right) \left\{ \left(\frac{r''}{t_p'}\right)^2 + 2\left(\frac{r_0}{t_p'}\right)\left(\frac{r''}{t_p'}\right) + \left(\frac{r_0}{t_p'}\right)^2 \right\}^{\frac{x-1}{2}} d\left(\frac{r''}{t_p'}\right)$$

$$R_x^n = \left\{ \left(\frac{r_n}{t_p'}\right)^2 + 2\left(\frac{r_0}{t_p'}\right)\left(\frac{r_n}{t_p'}\right) + \left(\frac{r_0}{t_p'}\right)^2 \right\}^{\frac{x-1}{2}}$$

B

Large Scale Specimen Data

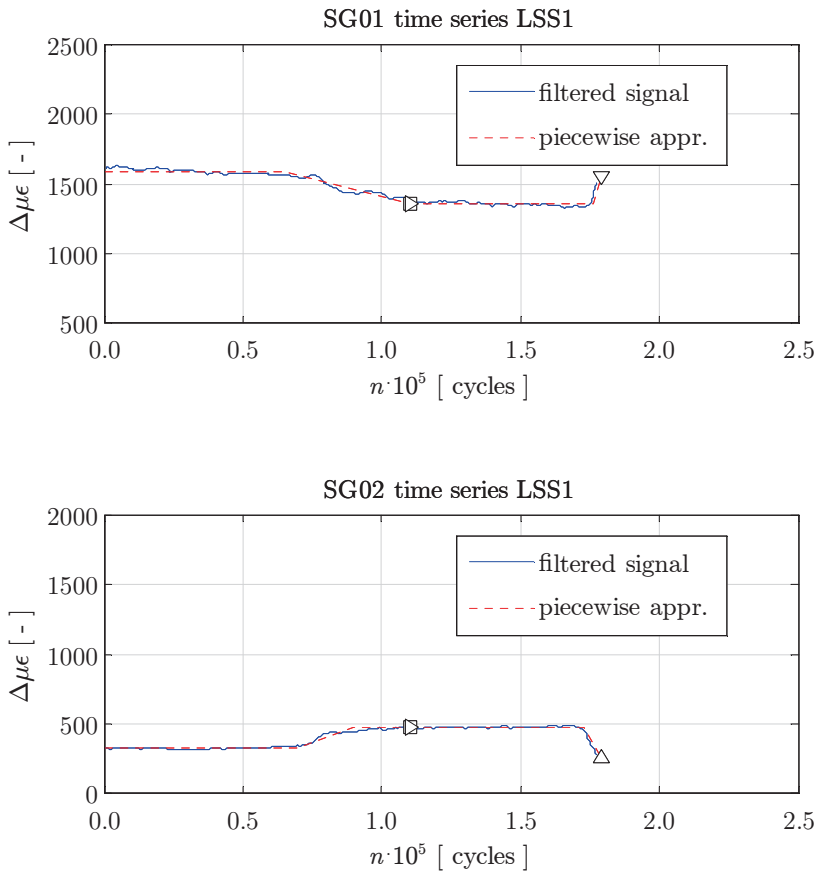


Figure B.1a: Filtered SG data three-bay LSS 1.

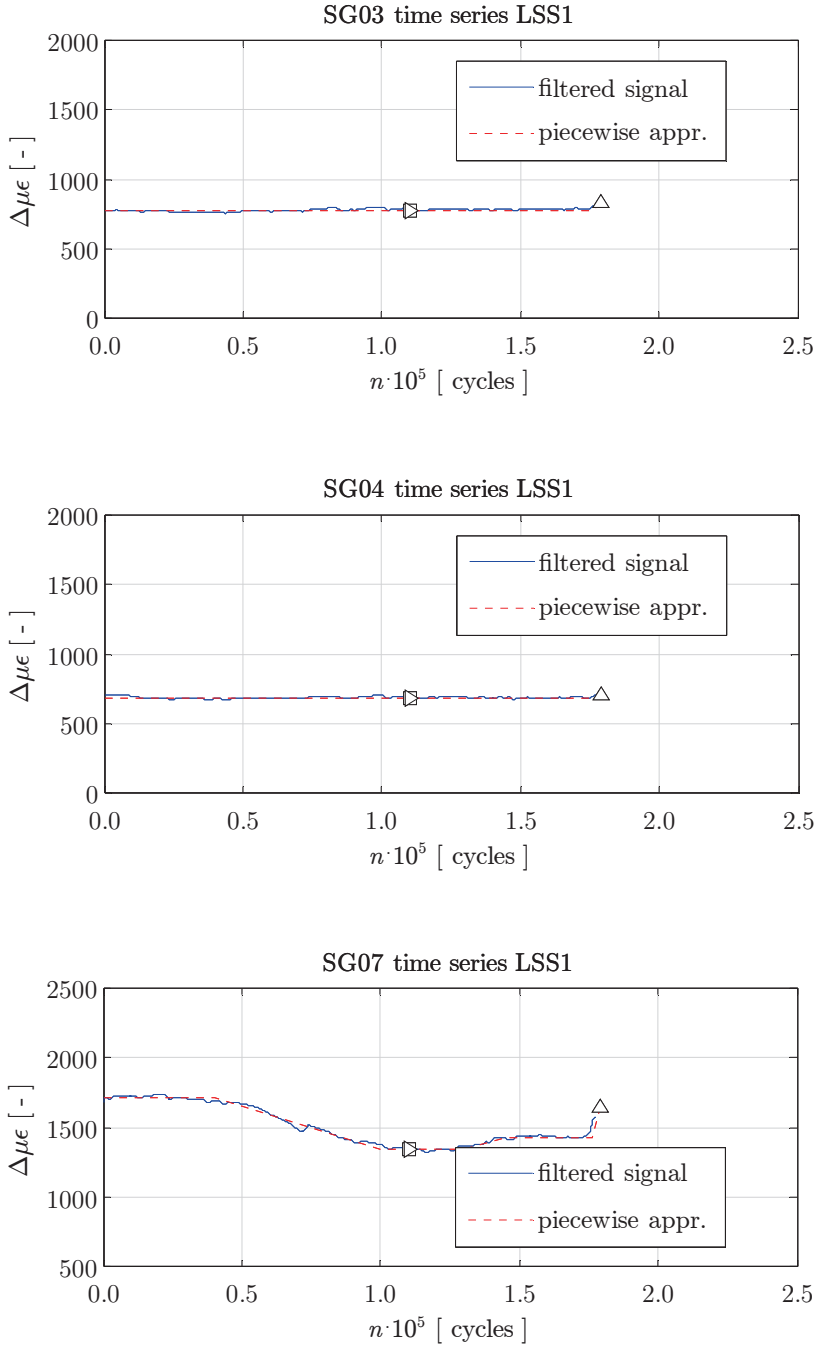


Figure B.1b: Filtered SG data three-bay LSS 1.

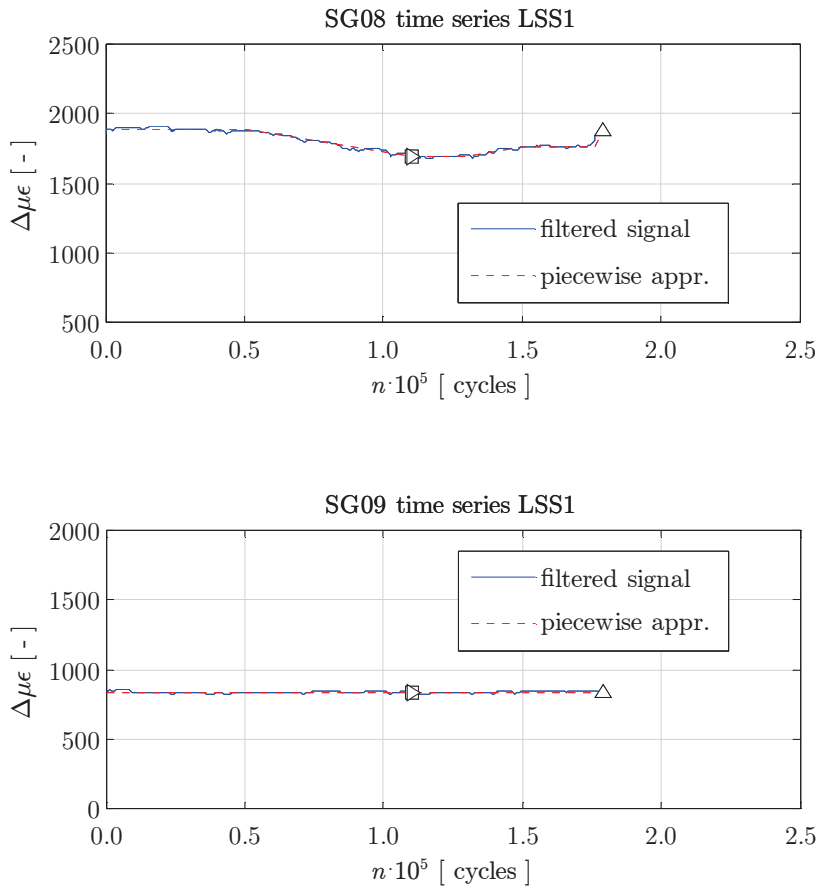


Figure B.1c: Filtered SG data three-bay LSS 1.

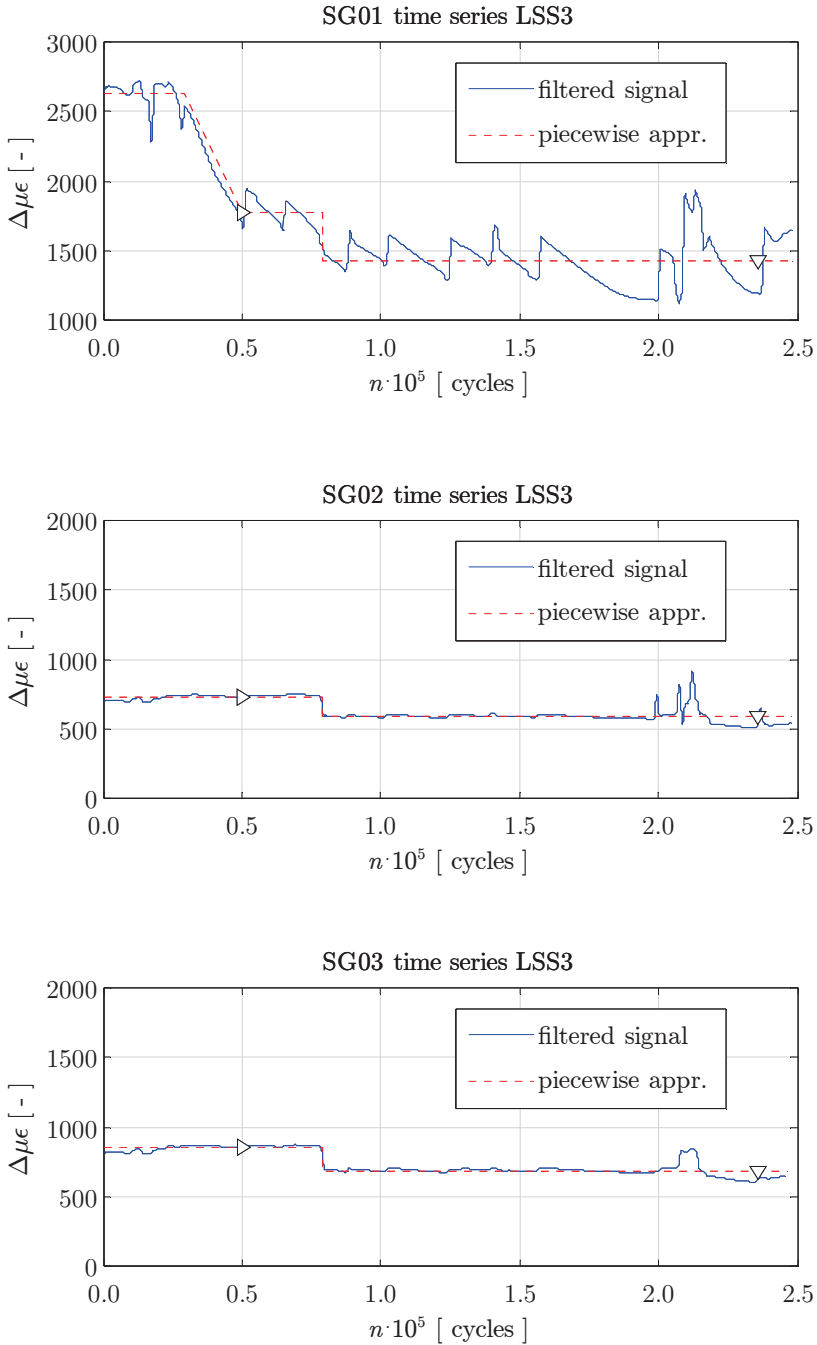


Figure B.2a: Filtered SG data three-bay LSS 3.

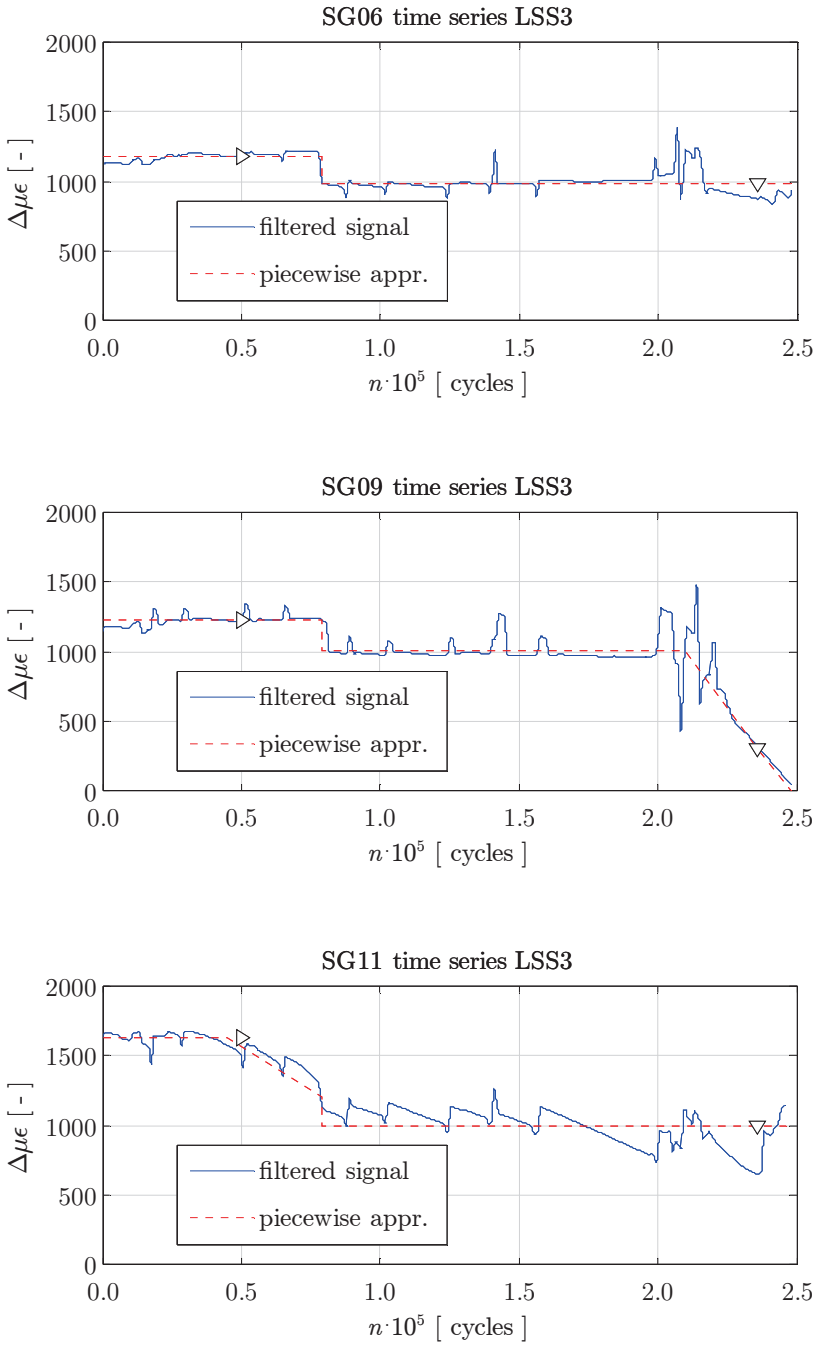


Figure B.2b: Filtered SG data three-bay LSS 3.

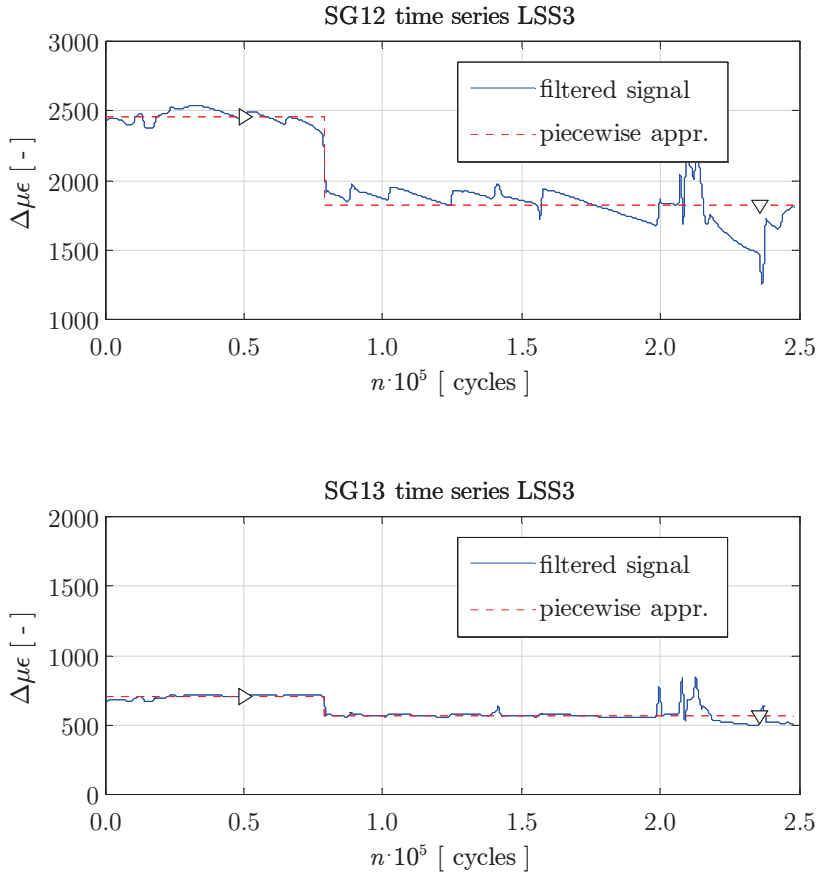


Figure B.2c: Filtered SG data three-bay LSS 3.

Review

The total stress concept welded joint fatigue design parameter S_T is a line (i.e. {plate, shell} thickness t_p related) equivalent point criterion. Correlation to life time N provides a joint S_T - N curve to estimate (hull) structure longevity. The weld notch stress distribution-, weld notch stress intensity- and even weld notch affected crack growth as well as crack path similarities may be qualified as modelling assumptions, but the TS concept proves at least {SSS, LSS, FSS} welded joint fatigue resistance similarity. Translating the total stress FAT class to dedicated SSS nominal stress based ones, a comparison to IIW shows values in the same range in favour of TS.

The Battelle structural stress concept involves a line equivalent point criterion as well; S_s . The MCF {TS, BSS} fatigue resistance data scatter turns out to be the same, showing that different parameters defined at the same scale (although S_T includes more detail) provide similar accuracy levels. However, in terms of modelling S_T may solve some S_s issues. Because of the developed semi-analytical remote mechanical loading induced weld notch stress formulations, bi-linear approximations are not required meaning the actual rather than compromised zone 1 peak stress and zone {2, 3} stress gradients are included. A weld load carrying stress related transition point assumption is prevented for as well, although a FE beam model based C_{bw} value may be considered as a disadvantage too. In case of symmetry with respect to ($t_p/2$) the welded joint far field stress definition can be maintained preventing for a double standard in scaling parameter assumption and no solid FE modelling is needed to capture the structural field stress distribution. For the same reason the BSS concept based weld {toe, root} induced failures have to be dealt with separately, i.e. involve different fatigue resistance curves. Translating the intact geometry related notch stress distribution to a crack damaged equivalent, the SIF K is finite for ($a \rightarrow 0$) by definition; the BSS singularity seems artificial since higher order terms of Williams' asymptotic solution do not contain singularities. The TS two-stage crack growth model allows for elastoplasticity induced monotonically increasing- as well as non-monotonic behaviour rather than non-monotonic only including a fixed elastoplasticity coefficient ($n = 2$) based on crack growth data series rather than as-welded joint fatigue resistance data. Crack growth model integration provides for the {TS, BSS} concepts a single slope fatigue resistance relation. The majority of the available data is MCF related; for the BSS concept only (SEC) failures seem to be considered and run-outs are ignored. In the actual (hull) structure (HCF) design region data is limited and typically censored, meaning uncertainty is significant and at least complete data is required to improve life time estimates. At the same time crack initiation may become dominant because of decreasing load level, meaning the resistance curve should include a slope change like the RFL model as adopted for the TS concept. All TS model parameter estimates are obtained using regression

analysis of as-welded joint fatigue resistance data to ensure {SSS, LSS, FSS} similarity in that respect. Statistics itself have no physical meaning, but the model parameters do. The MCF {TS aluminium, BSS steel} slopes $m \sim \{3.8, 3.6\}$ are comparable; rather governing damage mechanism (crack growth) than material dependent. The TS elastoplasticity coefficient estimate ($n \sim 1$) is half the BSS value (claimed to be the same value for different materials). Although S_s includes the geometric mean contribution of $\{\Delta\sigma_s, \sigma_{s,max}\}$, i.e. $\gamma = 0.5$, the range slightly dominates ($\gamma \sim 0.7$); at least for aluminium.

The parameter S_T involves the {intact, crack damaged} geometry fatigue sensitivity parameters $\{\rho, a\}$ and the corresponding effective values may include a real-, fictitious- and statistical part. Since the stress gradient as well as (average) notch and/or crack tip elastoplasticity is explicitly taken into account, the fictitious parts have become obsolete. The (average) real defect size (a_i/t_p) is estimated optimising the fatigue resistance residual. The real notch radius involves a worst case assumption ($\rho = 0$). The statistical components (distribution) – not incorporated yet – should be determined using direct measurements and can be used to include weld volume effects and to deal with different weld qualities.

The total stress concept may be extended to a total life concept, including both crack initiation and growth. To correlate an intact- and crack damaged geometry parameter in a two-stage two-parameter concept, the {micro-structural support, micro-crack} length should be involved since the fatigue sensitivity parameters $\{\rho^*, a_0\}$ share the same purpose; are similar. Another option might be to adopt a two-stage one-parameter concept and develop a load level dependent elastoplasticity coefficient $n(S)$; for decreasing S , n should decrease turning crack growth behaviour from non-monotonic into monotonically increasing.

Bibliography

Abildgaard P.M., Larsen M.J., Jensen J.J. (2000). Udmattelsesforsøg med små aluminiums-modeller – forstudie. SASAK-RAP-LE-AKS-DTU-0004-01, Danmark Tekniske Universitet.

Albrecht P., Yamada K. (1977). Rapid calculation of stress intensity factors. *Journal of the Structural Division of American Society of Civil Engineers (ASCE)*, vol. 103, pp. 377-389.

Al-Mukhtar A., Biermann H., Henkel S., Hübner S. (2009). Comparison of the stress intensity factor of load-carrying cruciform welded joints with different geometries. *J. of Materials Engineering and Performance*, vol. 19, pp. 802-809.

Anthes R.J., Köttger V.B., Seeger T. (1990). Kerbformzahlen von Stumpfstößen und Doppel-T-Stößen. *Schweißen und Schneiden*, vol. 45, pp. 685-688.

Atzori B., Lazzarin P., Tovo R. (1997). Stress distributions for V-shaped notches under tensile and bending loads. *Fatigue & Fracture of Engineering Materials*, vol. 20, pp. 1083-1092.

Atzori B., Meneghetti G. (1998). A physical interpretation of the scale effect in fatigue of fillet welded aluminium alloys. *Proc. of the 7th Int. Conf. on Joints in Aluminium, INALCO 1998, Cambridge, UK*.

Atzori B., Lazzarin P., Tovo R. (1999). From a local stress approach to fracture mechanics: a comprehensive evaluation of the fatigue strength of welded joints. *Fatigue & Fracture of Engineering Materials & Structures*, vol. 22, pp. 369-381.

Atzori B., Lazzarin P. (2000). Notch sensitivity and defect sensitivity under fatigue loading: two sides of the same medal. *Int. J. of Fracture*, vol. 107, L3-L8.

Atzori B., Meneghetti G., Susmel L. (2002). Estimation of the fatigue strength of light alloy welds by an equivalent notch stress analysis. *Int. J. of Fatigue*, vol. 24, pp. 591-599.

Atzori B., Lazzarin P., Meneghetti G. (2008). Fatigue strength assessment of welded joints: from the integration of Paris' law to a synthesis based on the notch stress intensity factors of the uncracked geometries. *Engineering Fracture Mechanics*, vol. 75, pp. 364-378.

Aukes M. (2004). A design method for hot spot stress fatigue assessment of welded aluminium ship details. MSc thesis, Delft University of Technology, The Netherlands.

- Banks-Sills L. (1991). Application of the finite element method to linear elastic fracture mechanics. *Applied Mechanics Reviews (ASME)*, vol. 44, pp. 447-461.
- Barber J.R. (2002). *Solid mechanics and its applications*. ISBN 1-4020-0966-6, Kluwer Academic Publishers.
- Barsoum Z., Lundbäck A. (2009). Simplified FE welding simulation of fillet welds – 3D effects on the formation of residual stresses. *Engineering Failure Analysis*, vol. 16, pp. 2281-2289.
- Bathias C., Drouillac L., Le François P. (2001). How and why the fatigue S-N curve does not approach a horizontal asymptote. *Int. J. of Fatigue*, vol. 23, pp. S143-S151.
- Bell R. (1987). Stress intensity factors for weld toe cracks in welded “T” plate joints. DSS Contract Report 22ST.23440-2-9083/1, Faculty of Engineering, Carleton University, Ottawa, Canada.
- Bertini L., Fontanari V., Straffellini G. (1998). Influence of post weld treatments on fatigue behaviour of Al-alloy welded joints. *Int. J. of Fatigue*, vol. 20, pp. 749-755.
- Besten J.H. den, Huijsmans R.H.M. (2010). Fatigue in high-speed ships: crack propagation in aluminum. *Proc. of the 11th Int. Symposium on Practical Design of Ships and other Floating Structures, PRADS 2010, Rio de Janeiro, Brazil*.
- Besten J.H. den, Huijsmans R.H.M. (2011). Fatigue of high-speed aluminium ships: a master curve formulation. *Proc. of the 3rd Int. Conf. on Marine Structures, MARSTRUCT 2011, Hamburg, Germany*.
- Besten J.H. den, Huijsmans R.H.M. (2011). Fatigue master curve approach for arc-welded aluminium joints ~ mean stress effects. *Proc. of the 30th Int. Conf. on Ocean, Offshore and Arctic Engineering, OMAE 2011, Rotterdam, The Netherlands*.
- Besten J.H. den, Kaminski M.L. (2013). Fatigue in aluminium high-speed craft: a large scale specimen design life parameter estimate. *Proc. of the 12th Int. Conf. on Fast Sea Transportation, FAST 2013, Amsterdam, The Netherlands*.
- Besten J.H. den, Kaminski M.L., Huijsmans R.H.M. (2013). Stress intensity factor analysis using digital image correlation: a post-processing approach. *Proc. of the 4th Int. Conf. on Marine Structures, MARSTRUCT 2013, Espoo, Finland*.
- Brandt U., Lawrence F.V., Sonsino C.M. (2001). Fatigue crack initiation and growth in AlMg4.5Mn butt weldments. *Fatigue & Fracture of Engineering Materials & Structures*, vol. 24, pp. 117-126.
- Bosman T. (2008). Dynamic response analysis of a D1204. VOMAS MIIP report.

- BS7910 (2005). Guidance on methods for assessing the acceptability of flaws in fusion welded structures. British Standard Institution (BSI), London, UK.
- Bueckner H.F. (1987). Weight functions and fundamental fields for the penny-shaped and half-plane crack in three-space. *Int. J. of Solids and Structures*, vol. 23, pp. 57-93.
- Collette M. (2005). Strength and reliability of aluminium stiffened panels. PhD thesis, University of Newcastle upon Tyne, UK.
- Cornell Fracture Group, <http://www.cfg.cornell.edu> (2010).
- Cottorell B., Rice J.R. (1980). Slightly curved or kinked cracks. *Int. J. of Fracture*, vol. 16, pp. 155-169.
- Coughlin R., Walbridge S. Fatigue testing and analysis of aluminum welds under in-service highway bridge loading conditions. *J. of Bridge Engineering*, vol. 17, pp. 409-419.
- Cremer M., Zimmermann M., Christ H.J. (2013). High-frequency cyclic testing of welded aluminium alloy joints in the region of very high cycle fatigue (VHCF). *Int. J. of Fatigue*, vol. 57, pp. 120-130.
- Cui W. (2002). A state-of-the-art review on fatigue life prediction methods for metal structures. *Journal of Marine Science and Technology*, vol. 7, pp. 43-56.
- Dang Van K. (1993). Macro-micro approach in high-cycle multiaxial fatigue. *Advances in multiaxial fatigue*, ASTM STP 1191, pp. 120-130.
- Dang Van K., Bignonnet A., Fayard J.L., Janosch J.J. (2001). Assessment of welded structures by a local multiaxial fatigue approach. *Fatigue & Fracture of Engineering Materials & Structures*, vol. 24, pp. 369-376.
- Daniels N. (2001). Fatigue of Al5083 based on the hot spot stress. MSc. Thesis, Delft University of Technology, The Netherlands.
- Dekking F.M., Kraaikamp C., Lopuhaä, Meester L.E. (2005). A modern introduction to probability and statistics – understanding why and how (1st ed.). ISBN: 978-1-85233-896-1. Springer-Verlag, London, UK.
- Det Norske Veritas (2010). Fatigue assessment of ship structures. DNV classification notes No. 30.7.
- Ding F., Feng M., Jiang Y. (2007). Modeling of fatigue crack growth from a notch. *Int. J. of Plasticity*, vol., 23, pp. 1167-1188.

Donald K.J., Paris P.C. (1999). An evaluation of ΔK_{eff} estimation procedures on 6061-T6 and 2024-T3 aluminium alloys. *Int. J. of Fatigue*, vol. 21, pp. S47-S57.

Dong P. (2001). A structural stress definition and numerical implementation for fatigue analysis of welded joints. *Int. J. of Fatigue*, vol. 23, pp. 865-876.

Dong P., Hong J.K. (2001). Residual stresses, notch stresses and stress intensities at welds: an unified assessment procedure with self-consistency. *Proc. of the 16th Int. Conference on Structural Mechanics in Reactor Technology, SMiRT 16*, Washington DC, USA.

Dong P., Hong J.K., Osage D.A., Prager M. (2002). Master S-N curve method for fatigue evaluation of welded components. WRC bulletin 474. Welding Research Council, New York, USA.

Dong P., Hong J.K., Cao Z. (2003). Stresses and stress intensities at notches: 'anomalous crack growth' revisited. *Int. J. of Fatigue*, vol. 25, pp. 811-825.

Dong P. (2004). The mesh-insensitive structural stress and master S-N curve method for ship structures. *Proc. specialty conference on integrity of FPSO systems (OMAE 2004)*, Houston, Texas.

Dong P., Hong J.K. (2004). The master S-N curve approach to fatigue evaluation of offshore and marine structures. *Proc. of the 23rd Int. Conf. on Offshore Mechanics and Arctic Engineering, OMAE 2004*, Vancouver, British Columbia, Canada.

Dong P., Hong J.K. (2004). A two-stage crack growth model incorporating environmental effects. *Proc. of the ASME Pressure Vessels and Piping Conf., PVP vol. 482: Computer Technology and Applications*, pp 105-113, San Diego, California USA.

Dong P., Hong J.K., Cao Z. (2004). A robust K estimation scheme using mesh-insensitive structural stresses. *Welding in the World*, vol. 48, pp. 28-39.

Dong P. (2005). A robust structural stress method for fatigue analysis of offshore/marine structures. *J. of Offshore Mechanics and Arctic Engineering*, vol. 127, pp. 68-74.

Dong P., Hong J.K., De Jesus A.M.P. (2007). Analysis of recent fatigue data using the structural stress procedure in ASME Div. 2 Rewrite. *J. of Pressure Vessel Technology*, vol. 129, pp. 355-362.

Dong, P. (2008). Length scale of secondary stresses in fracture and fatigue. *Int. J. of Pressure Vessels and Piping*, vol. 85, pp. 128-143.

- Dong P., Hong J.K., Osage D.A., Dewees D.J., Prager M. (2010). The master S-N curve method: an implementation for fatigue evaluation of welded components in the ASME B&PV code, section VIII, Division 2 and API 579-1/ASME FSS-1. WRC bulletin 523. Welding Research Council, New York, USA.
- Dowling N.E. (2007). Mechanical behaviour of materials (3rd ed.). ISBN: 978-0-13186-312-5. Prentice Hall, Englewood Cliffs, UK.
- Dowling N.E., Calhoun C.A., Arcari A. (2009). Mean stress effects in stress-life fatigue and the Walker equation. *Fatigue & Fracture of Engineering Materials & Structures*, vol. 32, pp. 163-179.
- Drummen I., Storhaug G., Moan T. (2008). Experimental and numerical investigation of fatigue damage due to wave-induced vibrations in a containership in head seas. *J. of Marine Science and Technology*, vol. 13, pp. 428-445.
- Drummen I., Schiere M., Tuitman J. (2013). Fatigue in high-speed aluminium craft: evaluating a design methodology for predicting the fatigue life using large scale tests and full scale trials. Proc. of the 12th Int. Conf. on Fast Sea Transportation, FAST 2013, Amsterdam, The Netherlands.
- Elber W. (1971). The significance of fatigue crack closure. *Damage Tolerance in Aircraft Structures*, ASTM STP 486, American Society for Testing and Materials, pp. 230-242.
- El Haddad M.H., Smith K.N., Topper T.H. (1979). Fatigue crack propagation at short cracks. *J. of Engineering Materials and Technology*, vol. 101, pp. 42-46.
- El Haddad M.H., Topper T.H., Smith K.N. (1979). Prediction of non-propagating cracks. *Engineering Fracture Mechanics*, vol. 11, pp. 573-584.
- El Haddad M.H., Dowling N.E., Topper T.H., Smith K.N. (1980). J-integral applications for short fatigue cracks at notches. *Int. J. of Fracture*, vol. 16, pp. 15-30.
- El Haddad M.H., Topper T.H., Topper T.N. (1981). Fatigue life predictions of smooth and notched specimens based on fracture mechanics. *J. of Engineering Materials and Technology*, vol. 103, pp. 91-96.
- Eurocode 9, Design of aluminium structures – part 1-3: structures susceptible to fatigue (2007). EN-1999-1-3, Brussels, CEN.
- Ferro P., Berto F., Lazzarin P. (2005). Generalised stress intensity factors due to steady and transient thermal loads with applications to welded joints. *Fatigue & Fracture of Engineering Materials & Structures*, vol. 29, pp. 440-453.

Filippi S., Lazzarin P., Tovo R. (2002). Developments of some explicit formulas useful to describe elastic stress fields ahead of notches in plates. *Int. J. of Solids and Structures*, vol. 39, pp. 4543-4565.

Filippi S., Ciavarella M., Lazzarin P. (2002). An approximate, analytical approach to the 'HRR'-solution for sharp V-notches. *Int. J. of Fracture*, vol. 117, pp. 269-286.

Fischer C., Fricke W. (2013). Realistic fatigue life prediction of weld toe and weld root failure in load-carrying cruciform joints by crack propagation analysis. *Analysis and Design of Marine Structures, Proc. of the 4th Int. Conf. on Marine Structures, MARSTRUCT 2013, Espoo, Finland.*

Frank K.H., Fisher J.W. (1979). Fatigue strength of fillet welded cruciform joints. *J. of the Structural Division*, vol. 105, pp. 1727-1741.

Fricke W., Petershagen H., Paetzold H. (1997). Fatigue strength of ship structures, part I: basic principles. GL-Technology, Germanischer Lloyd, Hamburg.

Fricke W. (2002). Recommended hot-spot analysis procedure for structural details of ships and FPSO's based on Round-Robin FE analyses. *Int. J. of Offshore and Polar Engineering*, vol. 12, pp. 40-47.

Fricke W. (2003). Fatigue analysis of welded joints: state of development. *Marine Structures*, vol. 16, pp. 185-200.

Fricke W., Kahl A., Paetzold H. (2005). Fatigue strength of fillet welds predominantly subjected to throat bending. *Proc. of the 11th Int. Congress of the Int. Maritime Association of the Mediterranean, IMAM 2005, Lisbon, Portugal.*

Fricke W. (2012). IIW recommendations for the fatigue assessment of welded structures by notch stress analysis. ISBN: 978-0-85709-855-9, Woodhead Publishing Limited, Abington, Cambridge, UK.

Fricke W. (2013). IIW guideline for the assessment of weld root fatigue. *Welding in the World*, vol. 57, pp 753-791.

Fricke W., Kahl A. (2008). Numerical and experimental investigation of weld root fatigue in fillet-welded structures. *Int. Shipbuilding Progress*, vol. 55, pp. 29-45.

Frost N.E., Dugdale D.S. (1958). The propagation of fatigue cracks in sheet specimens. *J. of the Mechanics and Physics in Solids*, vol. 6, pp. 92-110.

Gavras A.G., Lados D.A., Donald J.K. (2013). A unified method of design for fatigue crack growth resistance in structural materials. *Int. J. of Fatigue*, vol. 47, pp. 58-70.

- Gross B., Mendelson A. (1972). Plane elastostatic analysis of V-notched plates. *Int. J. of Fracture Mechanics*, vol. 8, pp. 267-276.
- Gurney T.R. (1991). *The fatigue strength of transverse fillet welded joints – a study of the influence of joint geometry*. Abington Publishing, Cambridge, UK.
- Haagensen P.J., Statnikov E.S., Lopez-Martinez L. (1998). Introductory fatigue tests on welded joints in high strength steel and aluminium improved by various methods including ultrasonic impact treatment. IIW document XIII-1748-98. International Institute of Welding.
- Herzberg R.W. (1995). *Deformation and fracture mechanics of engineering materials* (4th ed.). ISBN: 978-0-47101-214-6. John Wiley & Sons, New York, US.
- Hild F., Roux S. (2006). Digital image correlation: from displacement measurement to identification of elastic properties – a review. *Strain*, vol. 42, pp. 69-80.
- Hild F., Roux S. (2008). CorreliQ4: a software for “finite element” displacement field measurements by digital image correlation. LMT-Cachan, internal report 269.
- Hirt M.A., Smith I.F.C. (1995). Fatigue behaviour of aluminium beams with welded attachments. *Proc. of the 3rd Int. Conf. on Steel and Aluminium Structures, ICSAS'95, Istanbul, Turkey*.
- Hobbacher A. (1993). Stress intensity factors of welded joints. *Engineering Fracture Mechanics*, vol. 46, pp. 173-182.
- Hobbacher A.F. (2009a). The new IIW recommendations for fatigue assessment of welded joints and components – a comprehensive code recently updated. *Int. J. of Fatigue*, vol. 31, pp. 50-58.
- Hobbacher A. (2009b). Recommendations for fatigue design of welded joints and components. WRC bulletin 520. Welding Research Council, New York, USA.
- Hong J.K. (2010). Evaluation of weld root failure using Battelle structural stress method. *Proc. of the 29th Int. Conf. on Offshore Mechanics and Arctic Engineering, OMAE 2010, Shanghai, China*.
- Huang J. et al. (2013). Digital image correlation with self-adaptive Gaussian windows. *Experimental Mechanics*, vol. 52, brief technical note.
- Iida K., Uemura T. (1996). Stress concentration factor formulae widely used in Japan. *Fatigue & Fracture of Engineering Materials & Structures*, vol. 19, pp. 779-786.

International Ship and Offshore Structures Congress Proceedings (2012). Editors: Fricke W. and Bronsart R. ISBN: 978-3-87700-131-5,8. CRC press (Taylor & Francis Group), London, UK.

Irwin G.R. (1957). Analysis of stresses and strains near the end of a crack traversing a plate. *Journal of Applied Mechanics*, vol. 24, pp. 361-364.

Jaccard R., Kosteas D., Ondra R. (1995). Background document to fatigue design curves for welded aluminium components. IIW document XIII-1588-95. International Institute of Welding.

Janssen M., Zuidema J., Wanhill R.J.H. (2002). *Fracture mechanics* (2nd ed.). ISBN: 90-407-2221-8. Delft University Press, Delft, The Netherlands.

Jones R., Molent L., Pitt S. (2007a). Crack growth of physically small cracks. *Int. J. of Fatigue*, vol. 29, pp. 1658-1667.

Jones R., Chen B., Pitt S. (2007b). Similitude: fatigue cracking in steels. *Theoretical and Applied Fracture Mechanics*, vol. 48, pp. 161-168.

Jones R., Molent L. (2010). Critical review of the generalised Frost-Dugdale approach to crack growth in F/A18 Hornet Structural materials. Australian Defence Science and Technology Organisation, Centre of Expertise in Structural Mechanics, report DSTO-RR-0350.

Kim J.S., Kim C., Jin T.E., Dong P. (2006). Mean load effect on fatigue of welded joints using structural stress and fracture mechanics approach. *Nuclear Engineering and Technology*, vol. 38, pp. 277-284.

Kitagawa H., Takahashi S. (1976). Application of fracture mechanics to very small cracks. *Proc. of the 2nd Int. Conf. on Mechanical Behaviour of Materials, ICM2*, ASM Metal Park, Ohio.

Korobkin A., Malenica Š. (2005). Modified Logvinovich model for hydrodynamic loads on asymmetric contours entering water. *International Workshop on Water Waves and Floating Bodies, IWWF 2005*, Oslo, Norway.

Kosteas D., Ondra R. (1995). Safety and reliability in aluminium design. *Proc. of the 6th Int. Conf. on Aluminium Weldments*, Cleveland, Ohio, USA.

Kranenburg K. van, Riemsag T., Zuidema J., Benedictus-de Vries S., Veer F. (2001). Crack closure and fatigue threshold of AA5083 alloy in air and seawater by two determination methods. *Materials Science*, vol. 37, pp. 970-974.

- Kranenburg C. van (2010). Fatigue crack growth in aluminium alloys. PhD thesis, Delft University of Technology, The Netherlands.
- Kranz B., Sonsino C.M. (2010). Verification of FAT values for the application of the notch stress concept with the reference radii $r_{ref} = 1.00$ and 0.05 mm. *Welding in the World*, vol. 54, pp. r218-r224.
- Krupp U. (2007). Fatigue crack propagation in metals and alloys. ISBN: 978-3-527-31537-6. WILEY-VCH Verlag GmbH & Co. KGaA, Osnabrück, Germany.
- Kueppers M., Sonsino C.M. (2006). Assessment of the fatigue behaviour of welded aluminium joints under multiaxial spectrum loading by a critical plane approach. *Int. J. of Fatigue*, vol. 28, pp. 540-546.
- Kujawski D. (2001). A fatigue crack driving force parameter with load ratio effects. *Int. J. of Fatigue*, vol. 23, pp. S239-S246.
- Kwofie S. (2001). An exponential stress function for predicting fatigue strength and life due to mean stresses. *Int. J. of Fatigue*, vol. 23, pp. 829-836.
- Lados D.A., Apelian D., Donald J.K. (2007). Fracture mechanics analysis for residual stress and crack closure corrections. *Int. J. of Fatigue*, vol. 29, pp. 687-694.
- Larsson S.G., Carlsson A.J. (1973). Influence of non-singular stress terms and specimen geometry on small-scale yielding at crack tips in elastic-plastic materials. *J. Mech. Phys. Solids*, vol. 21, pp. 263-277.
- Lassen T., Darcis Ph., Recho N. (2005). Fatigue behaviour of welded joints part 1 – statistical methods for fatigue life prediction. *Welding Journal*, vol. 84, pp. 183s-187s.
- Lassen T., Darcis Ph., Recho N. (2006). Fatigue behaviour of welded joints part 2 – physical modelling of the fatigue process. *Welding Journal*, vol. 85, pp. 19s-26s.
- Lassen T., Recho N. (2009). Proposal for a more accurate physically based S-N curve for welded steel joints. *Int. J. of Fatigue*, vol. 31, pp. 70-78.
- Lazzarin P., Tovo R. (1996). A unified approach to the evaluation of linear elastic stress fields in the neighbourhood of cracks and notches. *Int. J. of Fracture*, vol. 78, pp. 3-19.
- Lazzarin P., Tovo R. (1998). A notch intensity factor approach to the stress analysis of welds. *Fatigue & Fracture of Engineering Materials & Structures*, vol. 21, pp. 1089-1103.

Lazzarin P., Livieri P. (2001). Notch stress intensity factors and fatigue strength of aluminium and steel welded joints. *Int. J. of Fatigue*, vol. 23, pp. 225-232.

Lazzarin P., Zambardi R., Livieri P. (2001). Plastic notch stress intensity factors for large V-shaped notches under mixed loading conditions. *Int. J. of Fracture*, vol. 107, pp. 361-377.

Lazzarin P., Filippi S. (2006). A generalized stress intensity factor to be applied to rounded V-shaped notches. *Int. J. of Solids and Structures*, vol. 43, pp. 2461-2478.

Li W.F., Zhang X.P. (2001). Study on the effects of notch tip and crack tip plasticity on small fatigue crack growth. *Proc. of the 10th Int. Conf. on Fracture, ICF10, Honolulu (Hawaii), USA.*

Li Z., Ringsberg J.W. (2011). Fatigue routing of container ships – assessment of contributions to fatigue damage from wave induced torsion and horizontal and vertical bending. *Ships and Offshore Structures*, vol. 7, pp. 119-131.

Liljedahl C.D.M. et al. (2009). Weld residual stress effects on fatigue crack growth behaviour of aluminium alloy 2024-T351. *Int. J. of Fatigue*, vol. 31, pp. 1081-1088.

Liu Y., Mahadevan S. (2009). Fatigue limit prediction of notched components using short crack growth theory and an asymptotic interpolation method. *Eng. Fract. Mech.*, vol. 76, pp. 2317-2331.

Livieri P., Lazzarin P. (2005). Fatigue strength of steel and aluminium welded joints based on generalised stress intensity factors and local strain energy values. *Int. J. of Fracture*, vol. 133, pp. 247-276.

Lobato da Silva B. et al. (2010). Influence of mean stress on the fatigue strength of ASTM A743 CA6NM alloy steel. *Frattura ed Integrità Strutturale*, vol. 14, pp. 17-26.

Maddox S.J. (1975). The effect of mean stress on fatigue crack propagation; a literature review. *Int. J. of Fracture*, vol. 11, pp. 389-408.

Maddox S.J., Webber D. (1978). Fatigue crack propagation in Aluminium-Zinc-Magnesium alloy fillet-welded joints. *Fatigue Testing of Weldments*, American Society for Testing and Materials (ASTM) Special Technical Publication (STP) 648, Hoepfner D.W. (editor), pp. 159-184.

Maddox S.J., Lechocki J.P., Andrews R.M. (1986). Fatigue analysis for the revision of PD6493: 1980. The Welding Institute, report 3873/1/86, Cambridge, UK.

Maddox S.J. (1987). The effect of plate thickness on the fatigue strength of fillet welded joints. ISBN: 0-853-00208-8. The Welding Institute, Abington, Cambridge, UK.

Maddox S.J. (1995). Scale effect in fatigue of fillet welded aluminium alloys. Proc. of the 6th Int. Conf. on Aluminium Weldments, INALCO 1995, Cleveland, Ohio, USA.

Maddox S.J. (2003). Review of fatigue assessment procedures for welded aluminium structures. *Int. J. of Fatigue*, vol. 25, pp. 1359-1378.

Malíková L., Veselý V. (2014). The influence of higher order terms of Williams series on a more accurate description of stress fields around the crack tip. *Fatigue & Fracture of Engineering Materials & Structures*, vol. 38, pp 91-103.

Mann T. (2006). Fatigue assessment methods for welded structures and their application to an aluminium T-joint. PhD thesis, Norwegian University of Science and Technology.

Mann T. (2007). The influence of mean stress on fatigue crack propagation in aluminium alloys. *Int. J. of Fatigue*, vol. 29, pp. 1393-1401.

Mathieu F., Hild F., Roux S. (2012). Identification of a crack propagation law by digital image correlation. *Int. J. of Fatigue*, vol. 36, pp. 146-154.

Matic T., Domazet Z. (2005). Determination of structural stress for fatigue analysis of welded aluminium components subjected to bending. *Fatigue & Fracture of Engineering Materials & Structures*, vol. 28, pp. 835-844.

Matsuoka K., Uemura T., Fujita Y. (1995). Fatigue strength of welded joints of Al-Mg-Si alloy (6N01) extrusions. Proc. of the 6th Int. Conf. on Aluminium Weldments, Cleveland, Ohio, USA.

McEvily A.J. (1983). On the quantitative analysis of fatigue crack propagation. *Fatigue Mechanisms: Advances in Quantative Measurements of Physical Damage*, ASTM STP811, American Society for Testing and Materials, pp. 283-312.

McEvily A.J., Minakawa K. (1984). Crack closure and the growth of short and long fatigue cracks. *Scripta Metallurgica*, vol. 18, pp. 71-76.

Meneghetti G., Tovo R., Patricolo M., Volpone M. (1999). Experimental determination of fatigue strength of structural details in welded light alloys. *Welding International*, vol. 13, pp. 461-464.

- Menzemer C. C. (1992). Fatigue behaviour of welded aluminium structures. PhD thesis, Lehigh University, Bethlehem, Pennsylvania, USA.
- Molent L., Jones R., Barter S., Pitt S. (2006). Recent developments in fatigue crack growth assessment. *Int. J. of Fatigue*, vol. 28, pp. 1759-1768.
- Morgenstern C. (2006a). Kerbgrundkonzepte für die schwingfeste Auslegung von Aluminiumschweißverbindungen am Beispiel der naturharten Legierung AlMg4,5Mn (AW-5083) und der warmausgehärteten Legierung AlMgSi1T6 (AW-6082 T6). PhD thesis, Technische Universität Darmstadt, Germany.
- Morgenstern C., Sonsino C.M., Hobbacher A., Sorbo F. (2006b). Fatigue design of aluminium welded joints by the local stress concept with the fictitious notch radius of $r_f = 1$ mm. *Int. J. of Fatigue*, vol. 28, pp. 881-890.
- Morinaga K. et al. (2014). Fatigue strength assessment by hot spot stress approach for welded aluminium structures: 1st report. Proc. of the 24th Int. Ocean and Polar Eng. Conf., ISOPE 2014, Busan, Korea.
- Murakami Y. (1987). Stress intensity factors handbook (1st ed.) p. 59 (vol. 1), pp. 698-699 (vol. 2). ISBN: 0-08-034809-2, Pergamon Press, Oxford, UK.
- Neuber H. (1937, 1958, 1985, 2001). Kerbspannungslehre (4. Aufl.). ISBN: 3-540-67657-0. Springer-Verlag, Berlin, Germany.
- Newman J.C., Raju I.S. (1981). An empirical stress intensity factor equation for the surface crack. *Engineering Fracture Mechanics*, vol. 15, pp. 185-192.
- Newman J.C. et al. (2000). Small-crack growth and fatigue life predictions for high-strength aluminium alloys. Part II: crack closure and fatigue analyses. *Fatigue & Fracture of Engineering Materials & Structures*, vol. 23, pp. 59-72.
- Niemi E. (1995). Stress determination for fatigue analysis of welded components. ISBN: 1-85573-213-0, Abington Publishing, Abington, Cambridge, UK.
- Niemi E., Fricke W., S.J. Maddox (2006). Fatigue analysis of welded components – designer's guide to the structural hot spot stress approach. ISBN: 978-1-84569-124-0, Woodhead Publishing Limited, Abington, Cambridge, UK.
- Nieslony A., El Dsoki C., Kaufmann, H., Krug P. (2008). New method for evaluation of the Manson-Coffin-Basquin and Ramberg-Osgood equations with respect to compatibility. *Int. J. of Fatigue*, vol. 30, pp. 1967-1977.

- Nitschke-Pagel T., Dilger K. (2011). Residual stresses in welded steels with longitudinal stiffeners. Proc. of the 21st Int. Offshore and Polar Engineering Conf., ISOPE 2011, Maui, Hawaii, USA.
- Noblett J.E., Andrews R.M. (2000). A stress intensity factor solution for root defects in fillet and partial penetration welds. Fatigue core research from TWI, pp. 120-144. ISBN: 1-85573-520-2, Woodhead Publishing Ltd, Abington, Cambridge, UK.
- Noroozi A.H., Glinka G., Lambert S. (2005). A two parameter driving force for fatigue crack growth analysis. Int. J. of Fatigue, vol. 27, pp. 1277-1296.
- Obrtlík K., Man J., Polák J. (2004). Effect of mean stress on short crack growth in fatigued 316L stainless steel. Proc. of the 15th European Conference on Fracture, ECF15, Stockholm, Sweden.
- Paris P.C., Erdogan F. (1963). Critical analysis of crack growth propagation laws. ASME Transactions, J. of Basic Engineering, vol. 85, pp. 528-534.
- Pascual, F.G., Meeker W.Q. (1999). Estimating fatigue curves with the random fatigue limit model. Technometrics, vol. 41, pp. 277-302.
- Polezhayeva H., Malinowski W. (2001). Fatigue strength of aluminium structural details of special service craft. Proc. of the 6th Int. Conf. on Fast Sea Transportation, FAST 2001, Southampton, UK.
- Poutiainen I., Tanskanen P., Marquis G. (2004a). Finite element methods for structural hot spot stress determination – a comparison of procedures. Int. J. of Fatigue, vol. 26, pp. 1147-1157.
- Poutiainen I., Marquis G. (2004b). A single-point structural stress assessment procedure for load-carrying fillet welds. IIW document XIII-2013-04, International Institute of Welding.
- Poutiainen I., Marquis G. (2006). A fatigue assessment method based on weld stress. Int. J. of Fatigue, vol. 28, pp. 1037-1046.
- Pyttel B., Schwerdt D., Berger C. (2011). Very high cycle fatigue – is there a fatigue limit? Int. J. of Fatigue, vol. 33, pp. 49-58.
- Radaj D., Zhang S. (1990). Multiparameter design optimisation in respect of stress concentrations. Proc. of the Int. Conf. on Engineering Optimization in Design Processes, Karlsruhe Nuclear Research Center, Germany.

Radaj D., Sonsino C.M., Fricke W. (2006). Fatigue assessment of welded joints by local approaches (2nd ed.). ISBN: 978-1-85573-948-2. Woodhead Publishing Limited, Cambridge, UK.

Radaj D., Lazzarin P., Berto F. (2013). Generalised Neuber concept of fictitious notch rounding. *Int. J. of Fatigue*, Vol. 51, pp. 105-115.

Radaj D., Vormwald M. (2013). Advanced methods of fatigue assessment (1st ed.). ISBN: 978-3-642-30739-3. Springer-Verlag, Berlin, Germany.

Ribeiro A. (1993). Efeito da fase de iniciação na previsão do compartimento à fadiga de estruturas soldadas. PhD. Thesis, Universidade de Trás-os-montes e Alto Douro (UTAD), Portugal.

Ribeiro A.S., de Jesus A.M.P. (2011). Fatigue behaviour of welded joints made of 6061-T651 Aluminium alloy. Aluminium alloys, theory and applications. ISBN: 978-953-307-244-9. Intech, Kvacakaj T. (editor), pp. 135-156.

Ritchie R.O., Yu W., Holm D.K., Blom A.F. (1988). Development of fatigue crack closure with the extension of long and short cracks in aluminium alloy 2124: a comparison of experimental and numerical results. *Mechanics of Fatigue Crack Closure*, ASTM STP 982, American Society for Testing and Materials, pp. 300-316.

Rizzo C.M. (2011). Application of advanced notch stress approaches to assess fatigue strength of ship structural details: literature review. ISBN:978-3-89220-655-2. Technische Universität Hamburg-Harburg.

Roux S., Hild F. (2006). Stress intensity factor measurements from digital image correlation: post-processing and integrated approaches. *Int. J. of Fracture*, vol. 140, pp. 141-157.

Roux S., Réthoré J., Hild F. (2009). Digital image correlation and fracture: an advanced technique for estimating stress intensity factors of 2D and 3D cracks. *J. of Physics D: Applied Physics*, vol. 42, No. 21.

Sadananda K., Vasudevan A.K. (1998). Short crack growth and internal stresses. *Int. J. of Fatigue*, vol. 19, supp. 1, pp. s99-s108.

Sadananda K., Vasudevan A.K. (2004). Crack tip driving forces and crack growth representation under fatigue. *Int. J. of Fatigue*, vol. 26, pp. 39-47.

Sarkani S., Mazzuchi T.A., Lewandowski D., Kihl D.P. (2007). Runout analysis in fatigue investigation. *Engineering Fracture Mechanics*, vol. 74, pp. 2971-2980.

- Savitzky A., Golay M.J.E. (1964). Smoothing and differentiation of data by simplified least square procedures. *Analytical Chemistry*, vol. 36, pp. 1627-1639.
- Schiere M., Drummen I. (2014). MARIN VOMAS JIP data analysis report no. 22690-1-HSS.
- Schijve J. (1988). Fatigue crack closure: observations and technical significance. *Mechanics of Fatigue Crack Closure*, ASTM STP 982, American Society for Testing and Materials, pp. 5-34.
- Schijve J. (2009). *Fatigue of structures and materials* (2nd ed.). ISBN: 978-1-4020-6808-9. Springer, Berlin, Germany.
- Schijve J. (2012). Fatigue predictions of welded joints and the effective notch stress concept. *Int. J. of Fatigue*, vol. 45, pp 31-38.
- Sehitoglu H., Gall K., García A.M. (1996). Recent advances in fatigue crack growth modelling. *Int. J. of Fracture*, vol. 80, pp. 165-192.
- Shankar K., Wu W. (2002). Effect of welding and weld repair on crack propagation behaviour in aluminium alloy 5083 plates. *Materials and Design*, vol. 23, pp. 201-208.
- Sharp M.L., Nordmark G.E., Menzemer C.C. (1996). *Fatigue design of aluminum components & structures*. ISBN: 0-07-056970-3. McGraw-Hill, New York, USA.
- Shin C.S., Smith R.A. (1988). Fatigue crack growth at stress concentrations – the role of notch plasticity and crack closure. *Engineering Fracture Mechanics*, vol. 29, pp. 301-315.
- Sidhom N., Laamouri A., Fathallah R., Braham C., Lieurade H.P. (2005). Fatigue strength improvement of 5083-H11 Al-alloy T-welded joints by shot peening: experimental characterization and predictive approach. *Int. J. of Fatigue*, vol. 27, pp. 729-745.
- Sidhom N., Braham C., Lieurade H.P. (2007). Fatigue life evaluation of shot peened Al-alloys 5083H11 T-welded joints by experimental and numerical approaches. *Welding in the World*, vol. 51, pp. 50-57.
- Smith R.N., Watson P., Tupper T.H. (1970). A stress-strain parameter for the fatigue of metals. *J. of Materials*, vol. 5, pp. 767-778.
- Smith R.A., Miller K.J. (1979). Prediction of fatigue regimes in notched components. *Int. J. of Mechanical Science*, vol. 20, pp. 201-206.

Sonsino C.M., Radaj D., Brandt U., Lehrke H.P. (1999). Fatigue assessment of welded joints in AlMg 4.5Mn aluminium alloy (AA 5083) by local approaches. *Int. J. of Fatigue*, vol. 21, pp. 985-999.

Sonsino C.M., Radaj D., Brandt U., Lehrke H.P. (1999). Fatigue assessment of welded joints in AlMg 4.5Mn aluminium alloy (AA 5083) by local approaches. *Int. J. of Fatigue*, vol. 21, pp. 985-999.

Sonsino C.M. (2004). Principles of variable amplitude fatigue design and testing. *J. of ASTM International*, vol. 1.

Sonsino C.M. (2007). Course of SN-curves especially in the high-cycle fatigue regime with regard to component design and safety. *Int. J. of Fatigue*, vol. 29, pp. 2246-2258.

Sonsino, C.M. (2009). A consideration of allowable equivalent stresses for fatigue design of welded joints according to the notch stress concept with the reference radii $r_{ref} = 1.00$ and 0.05 mm. *Welding in the World*, vol. 53, No. 3/4, pp. 64-75.

Sonsino C.M., Fricke W., de Bruyne F., Hoppe A., Ahmadi A., Zhang G. (2012). Notch stress concepts for the fatigue assessment of welded joints – background and applications. *Int. J. of Fatigue*, vol. 34, pp. 2-16.

Sørensen J.D., Tychsen J., Andersen J.U., Brandstrup R.D. (2006). Fatigue analysis of load-carrying fillet welds. *ASME Transactions, Journal of Offshore Mechanics and Arctic Engineering*, vol. 128, pp. 65-74.

Spagnoli A. (2005). Self-similarity and fractals in the Paris range of fatigue crack growth. *Mechanics of Materials*, vol. 37, pp. 519-529.

Straalen van IJ.J., Soetens F., Dijkstra O.D. (1994a). Eureka 269 – fatigue tests on transverse butt welds. TNO-report 94-CON-R1563, TNO, Delft, The Netherlands.

Straalen van IJ.J., Soetens F., Dijkstra O.D. (1994b). Eureka 269 – fatigue tests on transverse non-load carrying fillet welds. TNO-report 94-CON-R1564, TNO, Delft, The Netherlands.

Straalen van IJ.J., Soetens F., Dijkstra O.D. (1994c). Eureka 269 – fatigue tests on transverse load carrying fillet welds. TNO-report 94-CON-R1565, TNO, Delft, The Netherlands.

Straalen van IJ.J., Soetens F., Dijkstra O.D. (1994d). Eureka 269 – fatigue tests on longitudinal non-load carrying fillet welds. TNO-report 94-CON-R1566, TNO, Delft, The Netherlands.

- Straalen van I.J.J., Soetens F. (1995). Thickness effect in fatigue of welded aluminium structures – evaluation of EUREKA 269 result. TNO report, 95-CON-R0451, TNO Building and Construction Research, The Netherlands.
- Strik J.H.A., Dijkstra O.D. (2004). Ontwerpmethodiek voor aluminium hogesnelheidsschepen met lange vermoeiingslevensduur. TNO-report, TNO, Delft, The Netherlands.
- Suresh S., Ritchie R.O. (1984). Propagation of short fatigue cracks. *Int. Metals Reviews*, vol. 29, pp. 445-475.
- Tada H., Paris P.C. (1981). The stress intensity factor for a crack perpendicular to the welding bead. *Int. J. of Fracture*, vol. 21, pp. 279-284.
- Tada H., Paris P.C., Irwin G.R. (2000). *The stress analysis of cracks handbook* (3rd ed.). ISBN: 1-86058-304-0. ASME press, New York, USA.
- Tuitman J.T. (2010). Hydro-elastic response of ship structures to slamming induced whipping. PhD thesis, Delft University of Technology, Delft, The Netherlands.
- Tveiten B.W. (1999). Fatigue assessment of welded aluminium ship details. PhD thesis, Norwegian University of Science and Technology, Trondheim, Norway.
- Tveiten B.W., Fjeldstad A. (2009). Fatigue assessment of aluminium rectangular hollow section T-joints by hot-spot stress approach. *Proc. of the 19th Int. Offshore and Polar Eng. Conf., ISOPE 2009*, Osaka, Japan.
- Verreman Y., Nie B. (1996). Early development of fatigue cracking at manual fillet welds. *Fatigue & Fracture of Engineering Materials & Structures*, vol. 19, pp. 669-681.
- Vries de B.A., Vink J.H., Boon B. (2000). Fatigue life of a typical construction detail for aluminium high-speed ships. *Proc. of the 4th Int. Forum on Aluminium in Ships*, New Orleans, USA.
- Walker, K. (1970). The effects of stress ratio during crack propagation and fatigue for 2024-T3 and 7075-T6 Aluminium. *Effects of Environment and Complex Load History on Fatigue Life*, ASTM STP 462, American Society for Testing and Materials, pp. 1-14.
- Wang Y., Cui W., Wu X., Wang F., Huang X. (2008). The extended McEvily model for fatigue crack growth analysis of metal structures. *Int. J. of Fatigue*, vol. 30, pp. 1851-1860.

Williams M.L. (1952). Stress singularities resulting from various boundary conditions in angular corners of plates in extension. *ASME Journal of Applied Mechanics*, vol. 19, pp. 526-528.

Wormsen A., Fjeldstad A., Härkegård G. (2006). The application of asymptotic solutions to a semi-elliptical crack at the root of a notch. *Eng. Fract. Mech.*, vol. 73, pp. 1899-1912.

Xiao Z.G., Yamada K. (2004). A method of determining geometric stress for fatigue strength evaluation of steel welded joints. *Int. J. of Fatigue*, vol. 26, pp. 1277-1293.

Xiong J.J., Shenoi R.A. (2011). *Fatigue and fracture reliability engineering*. ISBN: 978-0-85729-217-9. Springer-Verlag, London, UK.

Xu T., Bea R. (1997). Load shedding of fatigue fracture in ship structures. *Marine Structures*, vol. 10, pp. 49-80.

Ye N., Moan T. (2007). Improving fatigue life for aluminum cruciform joints by weld toe grinding. *Proc. of the 10th Int. Symposium on Practical Ship Design and Other Floating Structures, PRADS 2007, Houston, Texas, USA.*

Zhang G. (2012). Method of effective stress for fatigue: part I – a general theory. *Int. J. of Fatigue*, vol. 37, pp. 17-23.

Zhang G., Sonsino C.M., Sundermeier R. (2012). Method of effective stress for fatigue: part II: applications to V-notches and seam welds. *Int. J. of Fatigue*, vol. 37, pp. 24-40.

Zhao T., Zhang J., Jiang Y. (2008). A study of fatigue crack growth of 7075-T651 aluminium alloy. *Int. J. of Fatigue*, vol. 30, pp. 1169-1180.

Curriculum Vitae

Johannes Hendrik (Henk) den Besten

Education

- 2001 – 2005: B.Eng. degree in Mechanical Engineering (cum laude)
The Hague University of Applied Sciences;
Technische Hogeschool Rijswijk
- 2005 – 2008: M.Sc. degree in Marine Technology (cum laude)
Delft University of Technology

Employment Record

- 2008 – 2015: Ph.D. candidate
Delft University of Technology;
Maritime and Transport Technology Department
- 2015 – present: Assistant Professor
Delft University of Technology;
Maritime and Transport Technology Department

Professional Memberships

- 2013 – present: International Ship and Offshore Structures Congress (ISSC)
III.2 Fatigue and Fracture committee member

Research Focus

Fatigue and fracture in {common, advanced} materials, hydroelasticity

Teaching

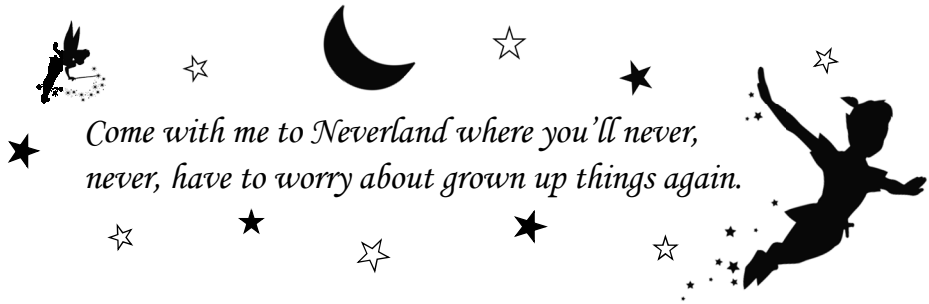
Fatigue and fracture in marine structures

Awards and Honours

- B.Eng. award: Best graduate student 2005
M.Sc. thesis award: Unilever Research Prize 2008

Publications

- 2009: Besten J.H. den, Huijsmans R.H.M., Hydrodynamic impact of sandwich structures with flexible core and structural damping properties. Proc. of the 5th Int. Conf. on Hydroelasticity in Marine Technology, HYEL 2009, Southampton, UK.
- Besten J.H. den, Huijsmans R.H.M., Hydrodynamic impact of sandwich structures with vibration isolation and structural damping properties. Int. Shipbuilding Progress, vol. 58, pp 1-57.
- 2010: Besten J.H. den, Huijsmans R.H.M., Fatigue in high-speed ships: crack propagation in aluminium. Proc. of the 11th Int. Symposium on Practical Design of Ships and other Floating Structures, PRADS 2010, Rio de Janeiro, Brazil.
- 2011: Besten J.H. den, Huijsmans R.H.M., Fatigue of high-speed aluminium ships: a master curve formulation. Proc. of the 3rd Int. Conf. on Marine Structures, MARSTRUCT 2011, Hamburg, Germany.
- Besten J.H. den, Huijsmans R.H.M., Fatigue master curve approach for arc-welded aluminium joints ~ mean stress effects. Proc. of the 30th Int. Conf. on Ocean, Offshore and Arctic Engineering, OMAE 2011, Rotterdam, The Netherlands.
- 2013: Besten J.H. den, Kaminski M.L., Fatigue in aluminium high-speed craft: a large scale specimen design life parameter estimate. Proc. of the 12th Int. Conf. on Fast Sea Transportation, FAST 2013, Amsterdam, The Netherlands.
- Besten J.H. den, Kaminski M.L., Huijsmans R.H.M., Stress intensity factor analysis using digital image correlation: a post-processing approach. Proc. of the 4th Int. Conf. on Marine Structures, MARSTRUCT, 2013, Espoo, Finland.



Theatre play "Peter Pan" (J.M. Barrie, 1904).

